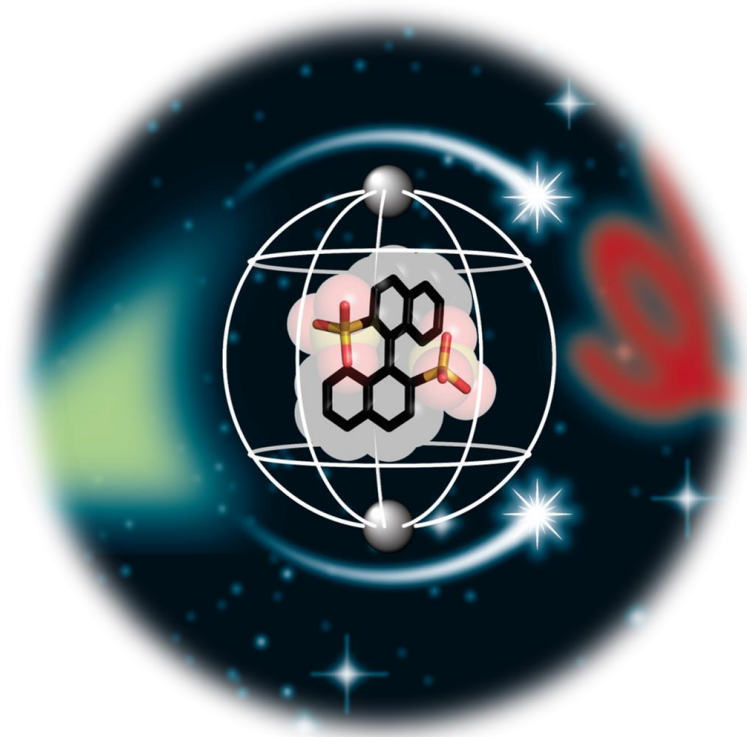# Systematic Studies on Heteroleptic Coordination Cages

Thesis for the degree of Doctor rerum naturalium

(Dr. rer. nat.)

TU Dortmund University

Department for Chemistry and Chemical Biology

Kristina E. Ebbert

from Schermbeck

DOB: September 2nd 1988

The beginning of wisdom is the statement 'I do not know'.
The person who cannot make that statement is one who will
never learn anything. And I have prided myself on my ability
to learn.

Thrall, The Earth-Warder, Cycle of Hatred by Keith R.A. DeCandido

Principal advisor: Prof. Dr. Guido H. Clever

Secondary surveyor: Prof. Dr. Christian Merten

Filed on: 26.02.2024

Eidesstattliche Versicherung (Affidavit)

_____   _____
Name, Vorname   Matrikel-Nr.
(Surname, first name)   (Enrolment number)

<table>
<tr>
<td>

Belehrung:

Wer vorsätzlich gegen eine die Täuschung über Prüfungsleistungen betreffende Regelung einer Hochschulprüfungsordnung verstößt, handelt ordnungswidrig. Die Ordnungswidrigkeit kann mit einer Geldbuße von bis zu 50.000,00 € geahndet werden. Zuständige Verwaltungsbehörde für die Verfolgung und Ahndung von Ordnungswidrigkeiten ist der Kanzler/die Kanzlerin der Technischen Universität Dortmund. Im Falle eines mehrfachen oder sonstigen schwerwiegenden Täuschungsversuches kann der Prüfling zudem exmatrikuliert werden, § 63 Abs. 5 Hochschulgesetz NRW.

Die Abgabe einer falschen Versicherung an Eides statt ist strafbar.

Wer vorsätzlich eine falsche Versicherung an Eides statt abgibt, kann mit einer Freiheitsstrafe bis zu drei Jahren oder mit Geldstrafe bestraft werden, § 156 StGB. Die fahrlässige Abgabe einer falschen Versicherung an Eides statt kann mit einer Freiheitsstrafe bis zu einem Jahr oder Geldstrafe bestraft werden, § 161 StGB.

Die oben stehende Belehrung habe ich zur Kenntnis genommen:

</td>
<td>

Official notification:

Any person who intentionally breaches any regulation of university examination regulations relating to deception in examination performance is acting improperly. This offence can be punished with a fine of up to EUR 50,000.00. The competent administrative authority for the pursuit and prosecution of offences of this type is the chancellor of the TU Dortmund University. In the case of multiple or other serious attempts at deception, the candidate can also be unenrolled, Section 63, paragraph 5 of the Universities Act of North Rhine-Westphalia.

The submission of a false affidavit is punishable.

Any person who intentionally submits a false affidavit can be punished with a prison sentence of up to three years or a fine, Section 156 of the Criminal Code. The negligent submission of a false affidavit can be punished with a prison sentence of up to one year or a fine, Section 161 of the Criminal Code.

I have taken note of the above official notification.

</td>
</tr>
</table>

_____   _____
Ort, Datum   Unterschrift
(Place, date)   (Signature)

Titel der Dissertation:
(Title of the thesis):

_____

_____

_____

<table>
<tr>
<td>

Ich versichere hiermit an Eides statt, dass ich die vorliegende Dissertation mit dem Titel selbstständig und ohne unzulässige fremde Hilfe angefertigt habe. Ich habe keine anderen als die angegebenen Quellen und Hilfs- mittel benutzt sowie wörtliche und sinngemäße Zitate kenntlich gemacht.
Die Arbeit hat in gegenwärtiger oder in einer anderen Fassung weder der TU Dortmund noch einer anderen Hochschule im Zusammenhang mit einer staatlichen oder akademischen Prüfung vorgelegen.

</td>
<td>

I hereby swear that I have completed the present dissertation independently and without inadmissible external support. I have not used any sources or tools other than those indicated and have identified literal and analogous quotations.

The thesis in its current version or another version has not been presented to the TU Dortmund University or another university in connection with a state or academic examination.*

</td>
</tr>
</table>

*Please be aware that solely the German version of the affidavit ("Eidesstattliche Versicherung") for the PhD thesis is the official and legally binding version.

_____   _____
Ort, Datum   Unterschrift
(Place, date)   (Signature)

Table of Contents

VI

Abstract

Metal-mediated self-assembly is one of the most prominent approaches to form supramolecules, here defined as dynamic self-assemblies, from smaller building blocks in a facile and controlled manner. Depending on the metal of choice and the corresponding ligand(s), chemists gained access to a plethora of two- and three-dimensional assemblies, of which coordination cages with a defined cavity emerged as promising structures for further application in catalysis, molecular recognition and separation. Supramolecular coordination cages based on square-planar Pd(II) cations in combination with bis-monodentate ligands equipped with pyridine, respectively isoquinoline donor groups, form a subclass of lantern-shaped coordination cages and assemblies that has been extensively studied. In recent years, efforts towards the development of functional coordination cages have been made, with the usual approach to achieve this goal being the incorporation of a functional backbone followed by careful choice of linker and donor-groups. Tuning the donor-groups and linkers allowed the synthesis of heteroleptic coordination cages by designing shape-complementary ligands (SCA). This approach has been utilized to form a wide array of heteroleptic coordination assemblies.
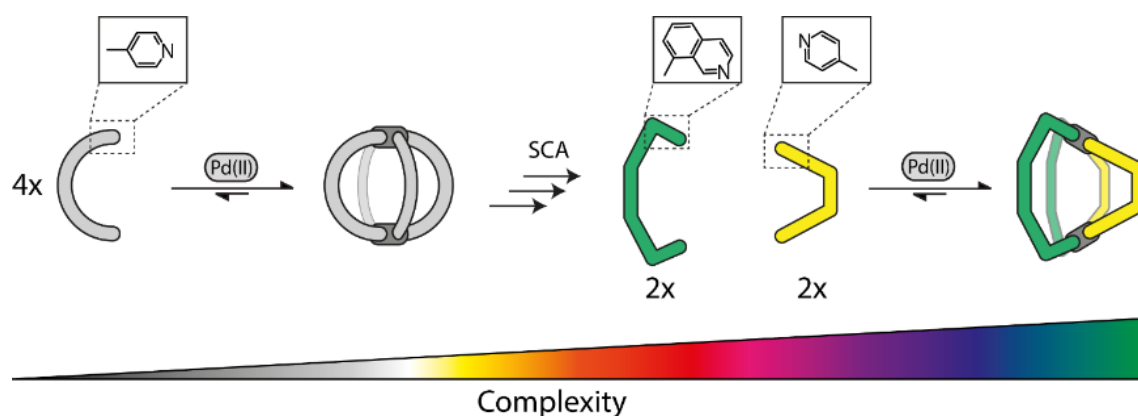
Figure 1: Schematic representation of the increase in structural diversity going from homoleptic coordination cages to heteroleptic ones using the shape-complementarity approach.

This thesis examines a diverse array of heteroleptic Pd(II)-based coordination cages in regard to four major subtopics. Firstly, the heteroleptic approach has been used to limit the number of cages formed from a 1:1:1:1 mixture of four different ligands, of which two each are shape complementary, forming a total of ten different coordination cages including two isomers. The mixture was analyzed via ion-mobility mass spectrometry and successful discrimination of all ten species including the isomers has been achieved. This setup proved valuable in the evaluation of ion-mobility as a method to discriminate

minor differences in closely related structures, thus adding to the wide array of analytical methods used in the field.

The second part describes a solvent switching system, that has been established within the scope of a previous master thesis. A strained heteroleptic coordination cage formed in DMSO has been shown to undergo strain release in CD_3CN. This inherent property of the system has been used to achieve guest-induced post-assembly separation leaving only one homoleptic species in solution with the other precipitating alongside the employed chemical trigger. Furthermore, the strong association of this guest molecule to one of the homoleptic components of the system has been exploited in competition experiments resulting in host-guest self-sorting with a selectivity of up to 90%.

In the third chapter, the utilization of SCA to establish a heteroleptic coordination cage with two complementary chromophores, effectively bringing them in close proximity to achieve energy-transfer in form of FRET and a complementary control system, replacing the donor chromophore with an inactive backbone was achieved. The cavity of the formed cages has then been used to incorporate a chiral guest molecule, yielding CD and CPL responses by chirality transfer from guest to host, thus forming an interacting three-component system from ligand L^A, ligand L^B and the chiral guest.

Lastly in the fourth part, rigid ligands were designed and found to form heteroleptic structures with a novel, unprecedented $Pd_3L^A_3L^B_3$ topology. A total of five new structures, based on an emissive ligand L^A and a small ligand L^B, based upon an aromatic six-membered ring system, have been described with a high tolerance for functional groups and promising photophysical properties. L^A maintained its emissive properties upon Pd(II) coordination in all structures and host-guest experiments with a chiral guest yielded respectable g_{lum} values. The behavior of the system in response to structural changes in the small ligand L^B has been thoroughly studied in regard to bulk, electrochemical repulsion and angle increase. All aforementioned approaches led to a nuclearity increase and the formation of four unprecedented $Pd_4L^A_4L^B_4$ assemblies. Furthermore, studies with common bis-sulfonate dyes of varying structure proved three different binding motifs of the respective dye to the bowl-shaped host molecules depending on the orientation of the anionic sulfonate group. Observed were 2:3, 2:1 and 1:1 host-guest complexes, with the different binding motifs having been shown to be translated into distinct changes in regard to the optic properties of the dye.

All systems have been extensively studied using 1D- and 2D NMR techniques, as well as ESI mass spectrometry, extended by ion-mobility mass spectrometry, X-ray analysis, *in silico* calculations and photophysical methods, if the systems required so.

Zusammenfassung

Metall-vermittelte Selbst-Assemblierung ist eine der am weitesten verbreiteten Strategien um mittels einfacher und kontrollierter Techniken Supramoleküle, hier definiert als dynamische, selbstassemblierte Moleküle, aus kleineren Bausteinen zu formen. Forschende konnten durch gezielte Wahl von Metallzentrum und komplementärer Ligandengeometrie eine Vielzahl zwei- und dreidimensionaler Strukturen erhalten, aus welcher Koordinationskäfige mit definierter Kavität besonders bemerkenswert waren, speziell in Bezug auf zukünftige Anwendungen in Bereichen wie Katalyse, sowie in molekularen Erkennungs- und Trennverfahren. Darunter bilden supramolekulare Käfige basierend auf quadratisch-planaren Pd(II) Kationen in Verbindung mit bis-monodentaten Liganden, welche Pyridin oder Isoquinolin Donor-Gruppen aufweisen, eine Untergruppe laternenförmiger Käfige und verwandter Strukturen, deren Bildung und Eigenschaften ausgiebig erforscht wurden. Zuletzt wurden immer mehr funktionelle Käfigstrukturen beschrieben, welche häufig mittels Einbaus eines funktionellen Rückgrads in Verbindung mit passenden Linker- und Donor-Gruppen realisiert wurden. Sorgfältige Einstellung der Donor-Gruppen und der Linkerart eröffnete ferner die Möglichkeit, zwei formkomplementäre Liganden in einem Käfig zu kombinieren und so heteroleptische Koordinationskäfige zu synthetisieren (Formkomplementärer Ansatz; FKA).
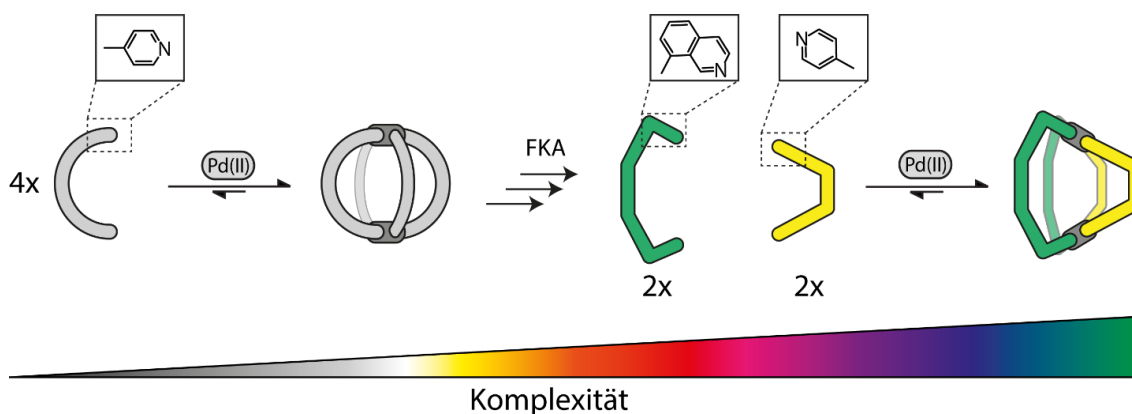
Figure 2: Schematische Darstellung der Steigerung struktureller Komplexität, welche durch den Übergang von rein homoleptischen Architekturen zu heteroleptischen Käfigen unter Verwendung des Form-Komplementären Ansatzes (FKA) initiiert wird.

Diese Arbeit untersucht eine diverse Reihe heteroleptischer Pd(II)-basierter Koordindationskäfige in vier Unterkapiteln, welche einzelne Aspekte dieser Strukturen genauer beleuchten. Zuerst wurde der heteroleptische Ansatz verwendet, um die Anzahl möglicher Strukturen zu limitieren, welche aus einer Mischung von vier Liganden, von welchen jeweils zwei formkomplementär sind, mit Pd(II) hervorgehen. Die entstandene Mischung von 10 heteroleptischen Koordinationskäfigen, von welchen zwei

X

Regioisomere sind, konnte erfolgreich mittels Ionenmobilitätsmessungen analysiert werden, was speziell in Bezug auf die Unterscheidung der Isomere beindruckend war. Dieser Ansatz konnte zeigen, dass Ionenmobilität als Methode zur Unterscheidung minimaler Größenunterschiede eng verwandter Strukturen eine wertvolle Ergänzung des analytischen Methodenschatzes in der supramolekularen Chemie darstellt.

Das zweite Kapitel befasst sich mit einem System, welches ein lösungsmittelabhängiges Schaltverhalten zwischen heteroleptischem Käfig und Mischung aus homoleptischen und heteroleptischen Strukturen aufweist und in der vorangegangenen Masterarbeit etabliert wurde. Ein heteroleptischer Koordinationskäfig, welcher einer gewissen Spannung der implementierten Alkin-Linker unterliegt, toleriert diese Spannung in DMSO, aber nicht in CD_3CN. Diese Eigenschaft des Systems wurde verwendet, um nach Bildung des heteroleptischen Käfigs durch Wechsel des Lösungsmittels gefolgt von Gast-induzierter Fällung einer der homoleptischen Spezies, die andere homoleptische Spezies in ihrer Reinform zu erhalten. Weiterhin wurde die starke Assoziation des Gastmoleküls zu einer der homoleptischen Komponenten genutzt, um in einem 4-Komponenten System mit je zwei supramolekularen Strukturen und zwei Gästen eine Selektivität von bis zu 90% in Bezug auf die Wirt-Gast Selbstsortierung zu erreichen.

Das dritte Kapitel behandelt die Anwendung des FKA zur Synthese eines heteroleptischen Koordinationskäfigs bestehend aus zwei komplementären Chromophoren, welche bedingt durch ihre räumliche Nähe in der Lage waren Energietransfer in Form von FRET zu zeigen. Ferner wurde ein Kontrollsystem etabliert, in welchem das Donor-Rückgrat durch ein inaktives, aber weiterhin formkomplementäres Molekül ersetzt wurde. Die gebildete Kavität des Käfigs wurde genutzt, um ein chirales Gastmolekül zu binden und der Wirt-Gast Komplex wurde mittels CD und CPL untersucht. Sowohl FRET, als auch Chiralitätstransfer von Gast zu Wirt konnte auf diese Weise nachgewiesen werden.

Im vierten und letzten Kapitel wurden starre Liganden designt, welche heteroleptische Strukturen mit einer neuartigen Topologie, $Pd_3L^A_3L^B_3$, bildeten. Insgesamt wurden fünf neue Strukturen, basierend auf einerseits einem Fluorenon-basierten Liganden L^A und andererseits einem kleinen Liganden L^B, basierend auf einem aromatischen Sechsring, mit hoher Toleranz in Bezug auf funktionelle Gruppen und interessanten optischen Eigenschaften beschrieben. Die Lumineszenz von L^A blieb auch nach Pd(II) Koordination erhalten und Wirt-Gast Experimente mit einem chiralen Gast resultierten in exzellenten g_{lum} Werten. Strukturelle Analysen zeigten, dass Modifikation von L^B im Bezug auf die Einführung von sterisch anspruchsvollen oder elektrochemisch repulsiven Gruppen, sowie durch Änderung des Donorwinkels zu einem Anstieg der Nuklearität führte, was zur Bildung von vier neuartigen $Pd_4L^A_4L^B_4$ Strukturen führte. Weiterhin

zeigten Studien mit Bissulfonat-basierten Farbstoffen drei verschiedene Bindungsmotive, je nach Orientierung der Bissulfonatgruppen. Beobachtet wurden 2:3, 2:1 und 1:1 Stöchiometrie, wobei jedes Bindungsmotiv einem spezifischen optischen Verhalten zugeordnet werden konnte.

Alle Systeme wurden mittels 1D- und 2D NMR, ESI-MS, erweitert durch IMS, Einkristallröntgen-strukturanalyse, *in silico* Methoden und fotophysikalische Messungen, so denn sinnvoll, untersucht.

1   Introduction

Cavities and confined spaces are a common occurrence in natural chemical environments like e.g. proteins, especially enzymes, and are of essential need for these structures to function the way they do. Oftentimes, an incredible amount of preorganization of substrates and a strong structure-activity relationship at the active site of the respective biomolecule is given, with functional groups orientated in a well-defined manner and substrate binding pockets forming to accommodate very specific molecules. Enzymes and other biomolecules allow catalysis, enable electron transfer processes, transport and stabilization of volatile molecules (e.g. gases like O_2) and many more chemical processes that would not readily proceed without the defined chemical environment. A few examples of the aforementioned proteins involved in such processes are given in Figure 3 below.
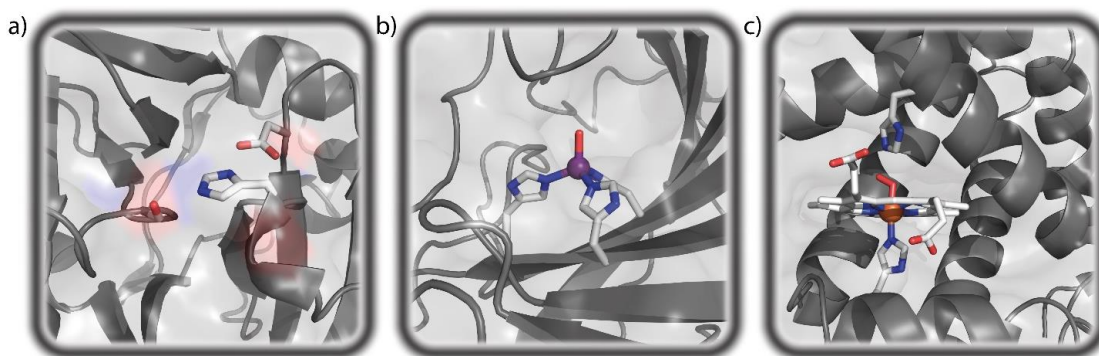

Figure 3: Representation of the active sites of a) serine protease I (PDB: 1arb)[1], b) human carbonic anhydrase II (PDB: 1ca2)[2] and c) myoglobin (PDB: 1mbo)[3].

Figure 3 a) shows the catalytic triad of the lysine-specific serine protease I found in ACHROMOBACTER LYTICUS (PDB: 1arb).[1] This triad consists of the amino acids histidine, aspartic acid and serine (here: H-57, D-113, S-194). Proteases catalyze the N-C bond cleavage of amides by a series of proton transfer processes under consumption of one molecule of H_2O to form a free primary amine and a carboxylic acid. The enzyme's active site is recovered after the reaction. Figure 3 b) depicts the active site of human carbonic anhydrase II (PDB: 1ca2).[2] The active site consists of a Zn(II) co-factor held in place by three structural histidines (H-94, H-96, H-119) with a water molecule coordinated to its vacant coordination site. The enzyme catalyzes the reversible reaction from CO_2 and H_2O to HCO_3^- and H^+ which facilitates e.g. the transport of CO_2 from the cells to the lungs. Figure 3 c) does not depict an enzyme but the transport protein myoglobin with one molecule O_2 reversibly bound to its active site (oxymyoglobin; PDB: 1mbo).[3] Predominant structural features are an Fe(II) center coordinated inside a porphyrin ring

system, forming a so called Heme-center, which is held in place by a proximal histidine ligand (H-93) coordinating the iron center from below and a distal histidine (H-64) above the porphyrin system. While the distal histidine does not seem to be involved in the coordination of the iron, it serves a very distinct purpose, namely altering the affinity of CO to the iron center. CO is normally a much stronger ligand for Fe(II), derived from its π-backbonding. However, it is a linear molecule, thus the steric demand in the distal area is increased as compared to O_2 which is sterically blocked by the histidine in this case, changing the affinity in favor of O_2. However, studies showed, that hydrogen-bonding from the distal histidine to O_2 might also play a vital role in controlling O_2 and CO affinity to Mb.[4] All three processes require a strict preorganization of the functional groups inside the cavity with enough flexibility for transformation processes and substrate binding, yet structural closeness of the involved functional groups to interact with one another. Furthermore, Figure 3 b) and c) depict functional biomolecules incorporating transition metals, which is not a rare occurrence but it is estimated that 50% of all proteins could very well be metalloproteins.[5]

In nature, these nanomolecular host molecules and enzymes have been developed through evolutionary processes over the course of billions of years. The desire to understand the processes, the importance of each individual component and the exact mechanisms has been driving researchers ever since with two main approaches being prevalent.

While the top-down approach, which would include e.g. enzyme modification by site-directed mutagenesis[6] to evaluate the effect of changes in amino acid sequence among other things has to be mentioned herein for the sake of completeness, it is a highly complex procedure and taxing in terms of financial and human resources. The bottom-up approach whereas starts from the most basic structures to first understand these and then complexity is generated expanding from there.

For a better understanding of recognition processes observed in natural occurring systems, like e.g. the lock-and-key model proposed in 1894 by EMIL FISCHER[7], chemists started researching the intermolecular bond.[8] Thus, the field of supramolecular chemistry was established, which has been defined by one of its pioneers, JEAN-MARIE LEHN, as "the chemistry of the intermolecular bond". Since then, a plethora of synthetic host molecules has been established, which can be divided into two subcategories, namely fully organic host systems and metal-based coordination assemblies. Structural diversity in fully organic host systems ranges from nanomolecular cation binders[9–15] and macrocyclic compounds[16–19] to fully three-dimensional cage architectures,[20] whose

synthesis is based upon the dynamic covalent chemistry (DCC) approach. The premise of the aforementioned is the generation of larger structures like macrocycles and 3D molecular cages using reversible covalent bond formation reactions like e.g. imine or boronic ester formations.[21] A summary of fully organic host molecules is given below in Figure 4:.
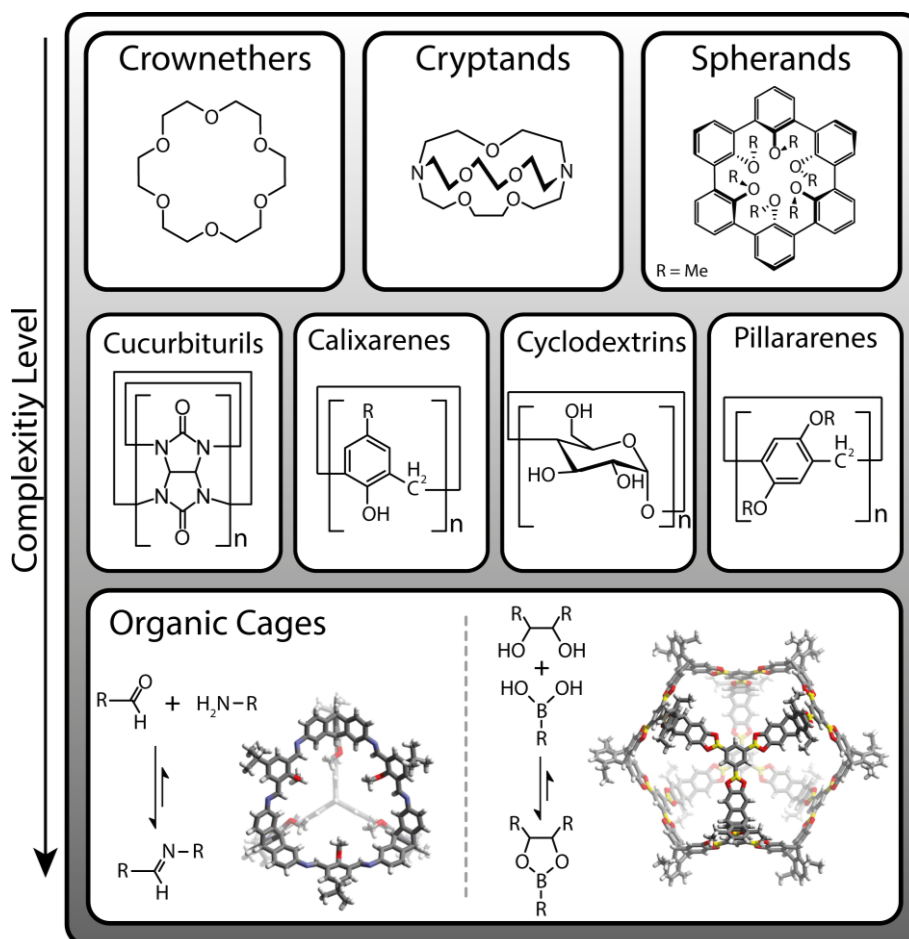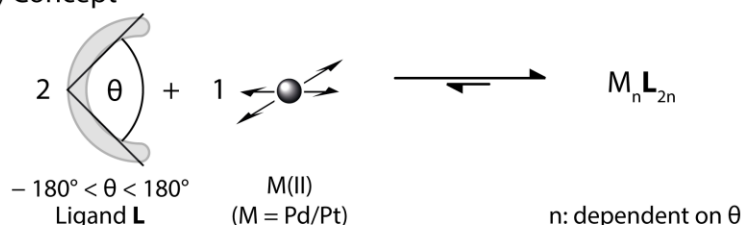

Figure 4: Common fully organic receptor molecules. Pictures for organic cages taken from[20]

The first row of Figure 4 shows the cation receptor molecules LEHN[11–14], PEDERSEN[10] and CRAM[9,15] published, which lead to the award of the Nobel prize in 1987 for "development and use of molecules with structure-specific interactions of high selectivity".[22] Depending on the size of the ring and thus the distance of the oxygen atoms, different cations like e.g. Na^+ or K^+ are bound selectively,[23] making these macrocycles selective hosts for small cationic guests. The second row of Figure 4, depicts cucurbiturils[18,24], calixarenes[19], cyclodextrins[16,25] and pillararenes[17], all of which are macrocyclic molecules formed from a repetitive subunit like e.g. glycoluril (cucurbiturils) or phenol (calixarenes). It is noted, that cyclodextrins are occurring naturally and have first been described by VILLIERS in 1891.[25] Another example for a macrocyclic structure like the aforementioned ones that is not depicted in Figure 4 are
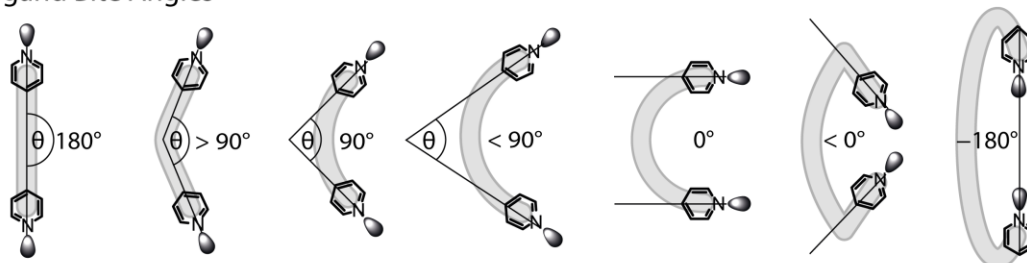
dyn[n]arenes, macrocycles based on 1,4-bisthiophenols.[26] All of these form macrocyclic containers with a defined wall and an aperture on each, top and bottom of the structure, as well as rich host-guest chemistry.[27] Finally, the last row of Figure 4 shows two examples of porous organic cages (POCs) formed via dynamic covalent chemistry, one using imine condensation reactions[28] and the other relying on boronic ester condensation.[29] The formed cages are fully organic, three-dimensional structures with a defined cavity.[20] Recent advances show the potential of these molecules in sensing and catalysis, among other applications.[30,31] However, a common drawback of these structures is the yield of the respective formation reaction oftentimes not being quantitative[28] and the nature of the systems themselves demanding the presence of certain functional groups in a repetitive manner, limiting structural diversity. As mentioned before, a second strategy can be used to design nanomolecular assemblies in a facile and directed manner, namely metal-mediated self-assembly. The overall structure is hereby defined by two factors, the metal coordination geometry and the ligand design. Transition metals especially have very diverse coordination geometries based on their d-electron configuration, ranging from linear coordinated Ag(I) or Au(I),[32] an octahedral geometry in e.g. Co(II) or Fe(II),[33,34] square planar coordination in Pd(II) and Pt(II)[33–35] to more exotic coordination environments like hexagonal bipyramidal coordination in e.g. uranyl-carboxylate complexes.[36] Since this thesis focusses on coordination assemblies based on square-planar coordinated Pd(II), other metals will not be discussed unless needed for comparison.

Choosing Pd(II) as the structure-determining metal has several advantages. The square planar coordination environment of Pd(II) makes the outcome of coordination events more predictable and the self-healing ability of the complexes mediated by on-off coordination of the ligands allows defect correction,[37,38] which is not as readily happening in e.g. Pt(II) coordination assemblies, which exhibit a stronger coordination of nitrogen atom to the central Pt(II) cation. Combined with bis-monodentate ligands, ligands with two isolated coordination donor sites, well defined $Pd_n\mathbf{L}_{2n}$ structures can be accessed, whose nuclearity n depends on the donor- or bite-angle of the complementary ligand.[39] A summary of the assembly principle of coordination cages based on square-planar coordinated M(II) cations and the corresponding bite-angle to nuclearity relationship is given below in Figure 5.

a) Concept

b) Ligand Bite Angles

c) Assemblies

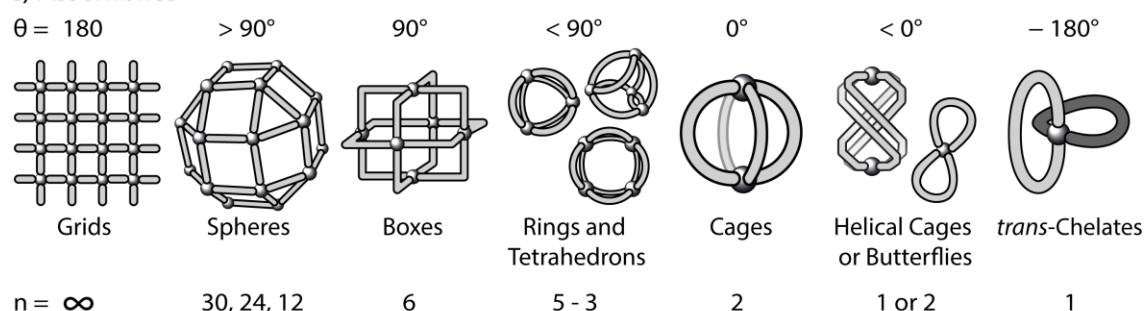| $\theta =$ 180	> 90°	90°	< 90°	0°	< 0°	− 180°
Grids	Spheres	Boxes	Rings and Tetrahedrons	Cages	Helical Cages or Butterflies	*trans*-Chelates
n = ∞	30, 24, 12	6	5 - 3	2	1 or 2	1

Figure 5: Graphic representation of a) the concept of coordination assembly formation using square planar Pd(II) cations and bis-dentate ligands; b) representation of the bite angles predetermined by a certain N-donor orientation in rigid ligands and c) corresponding assemblies formed by combining the above mentioned ligands and Pd(II) cations in a 2:1 manner. Figure recreated from[39].

As Figure 5 a) shows, the basic principle is the 2:1 combination of a ligand with bite-angle θ and a square-planar coordinated metal(II) cation M(II). Figure 5 b) depicts possible bite-angles and Figure 5 c) gives the respective assemblies and associated nuclearity n. While ligands with a bite-angle of 180° would form grids and thus 2D coordination polymers, smaller bite angles lead to a decrease in nuclearity and thus assembly size. Bite-angles of $\theta > 90°$ lead to the formation of spheres of varying sizes, as shown by FUJITA and co-workers in multiple examples.[40–43] Donor-angles of exactly 90° result in the formation of Pd_6L_{12} boxes,[44–46] while those with $\theta < 90°$ form 3-[47–51] or 4-rings[47,49,52] and/or tetrahedrons.[51,53] Lantern-shaped Pd_2L_4 coordination cages formed from banana-shaped bis-monodentate ligands with a bite angle of $\theta = 0°$, with parallel oriented donor-groups, are of special interest due to their well defined cavity and straight forward assembly.[54,55]. If $\theta < 0°$, helical M_2L_4 cages[56–58] or ML_2 butterfly assemblies[59] are formed depending on the closeness of the respective donor groups. The last

structure, that can be formed with the aforementioned bis-monodentate ligands is similar to the butterfly motif, however the ligands do not coordinate to the central metal cation in a *cis*-, but in a *trans*-conformation forming ML_2 *trans*-chelates.[59] Understanding the basic relation of ligand bite-angle, predetermined coordination geometry and outcome of the assembly formation as shown in Figure 5, allows the educated design of ligands to target a certain assembly formation. As this thesis focusses on palladium(II)-based coordination cages, the underlying design principle of ligands used in this work is given in Figure 6.

Balancing Structure and Function - A Modular Approach
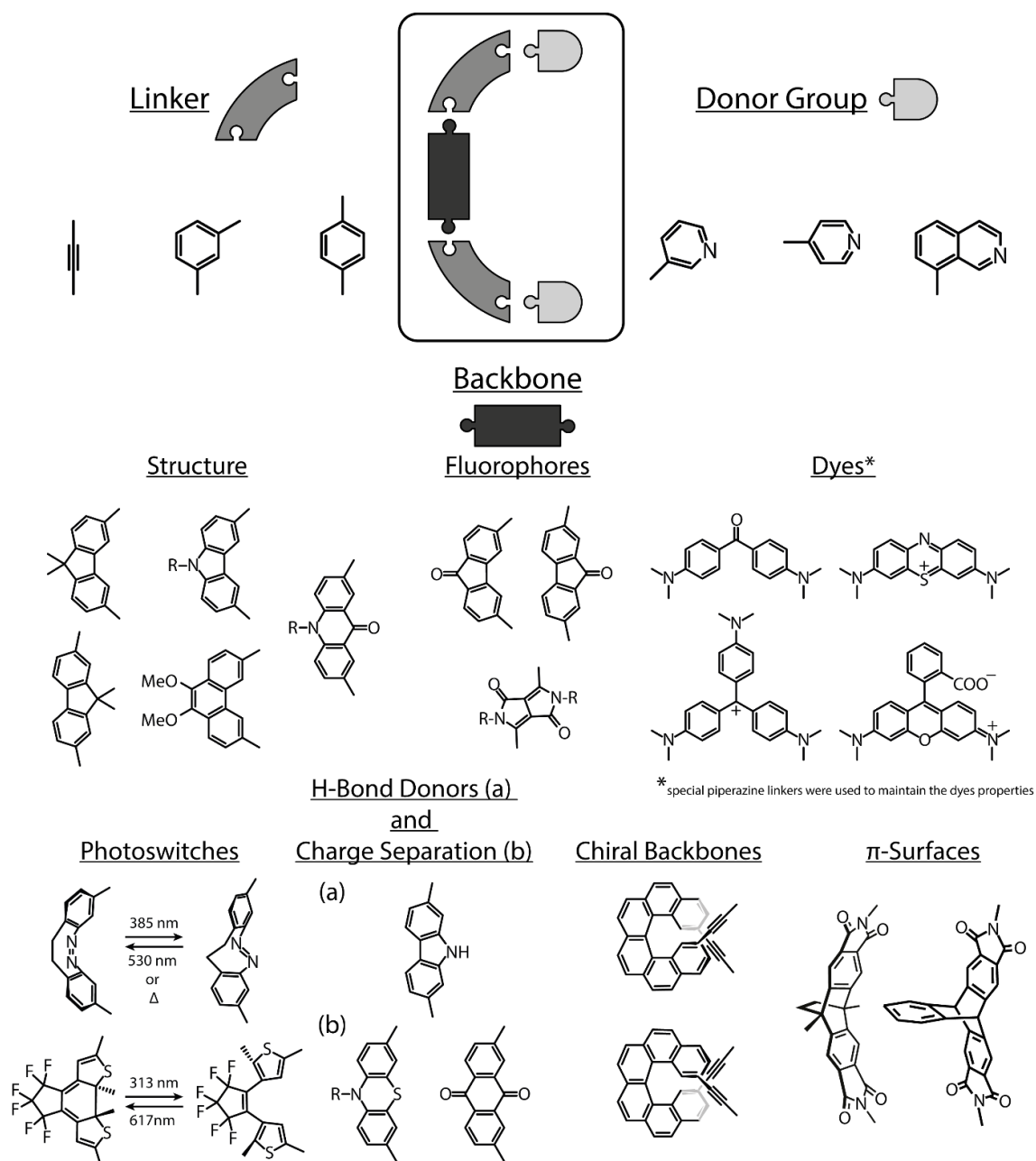
Figure 6: Graphic representation of the basic ligand design principle including exemplary backbones, linkers and donor-groups used in the CLEVER group.

As shown in Figure 6, the structure of bis-monodentate ligands can be categorized into three subunits, namely the backbone, the linker and the donor-group. While there are examples for ligands with reduced symmetry found in literature,[60–62] this thesis focusses on a fully symmetric ligand design. Each individual element of the ligand can be utilized to achieve a) the desired donor-angle, which is often controlled via linker and donor-group and b) a certain function, which is mostly derived from the backbone. Figure 6 gives examples of different functional backbones, that have been utilized by our group in recent years. The classification is to be understood as broadly formulated, since functional backbones with e.g. H-bond acceptor functionality like acridone can also be used for purely structural purposes.[57] The array of backbones ranges from ones used purely for their geometry, like 3,6- or 2,7-fluorene derivatives[63] or 3,6-phenanthrene[57,64–66], to fluorophores like fluorenone[51,67,68] or diketopyrrolopyrrole (DPP)[69], photoswitches,[50,70–72] H-bond donors,[65] phenothiazine in combination with anthracene-9,10-dione for charge separation,[73] chiral molecules like helicene[67,74] to π-surfaces.[75–79] An additional function, that has been implemented into coordination cages and helices in this group, are coal-tar dyes, though a special piperazine linker had to be introduced to maintain the electronic structure and properties of the parental dye.[58,69]

To access further and more complex systems, the targeted combination of two different ligands within one heteroleptic coordination cage has emerged as a promising field in recent years.[80,81] However, the combination of two different ligands can lead to three different outcomes of the self-assembly process as depicted in Figure 7.
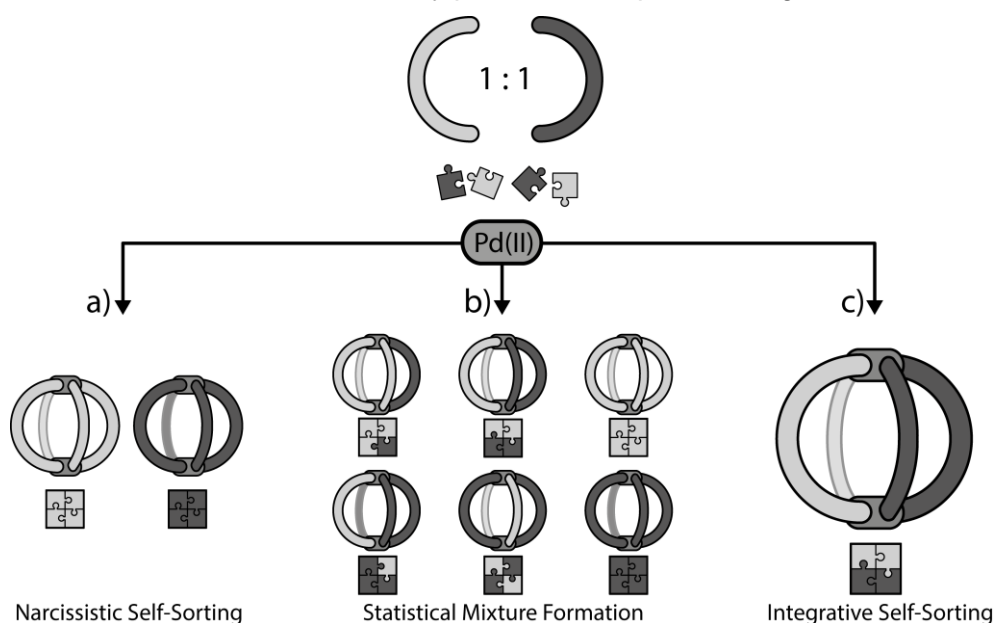

Figure 7: Three different outcomes of the coordination driven self-assembly process of a 1:1:1 combination of two different ligands L^A and L^B with Pd(II) cations; a) narcissistic self-sorting, b) statistical assembly yielding a mixture according to a BOLTZMANN distribution, c) integrative self-sorting yielding a clean heteroleptic structure (here cis-$Pd_2L^A_2L^B_2$).

The first possible outcome is the sorting of the involved ligands in a narcissistic fashion, meaning the individual ligands form homoleptic assemblies with no regard for the other ligand (Figure 7 a)). The second option is purely statistical assembly formation of the ligands according to a BOLTZMANN distribution. This usually is given if the structure of both ligands is very similar, thus no discrimination within the self-assembly process is given. While it is inherently possible to analyze statistic mixtures in regard to a certain property, like e.g. shown by FRANK et al. for light-induced charge separation,[73] it is usually difficult to gain insight into the structure-activity relationship if there is no single structure to track the observed property back to. Thus, the desired option for the coordination driven self-assembly process of a 1:1:1 combination of two different ligands L^A and L^B with Pd(II) cations is integrative self-sorting. For dinuclear Pd_2L_4 assemblies this leads to the formation of one distinct structure, in which the ligands can be organized in *cis*- or *trans* conformation.[81] As integrative self-sorting has to work against entropic factors of the system, the enthalpic gain has to be controlled. Possible strategies to access clean heteroleptic cage formation are depicted below in Figure 8.
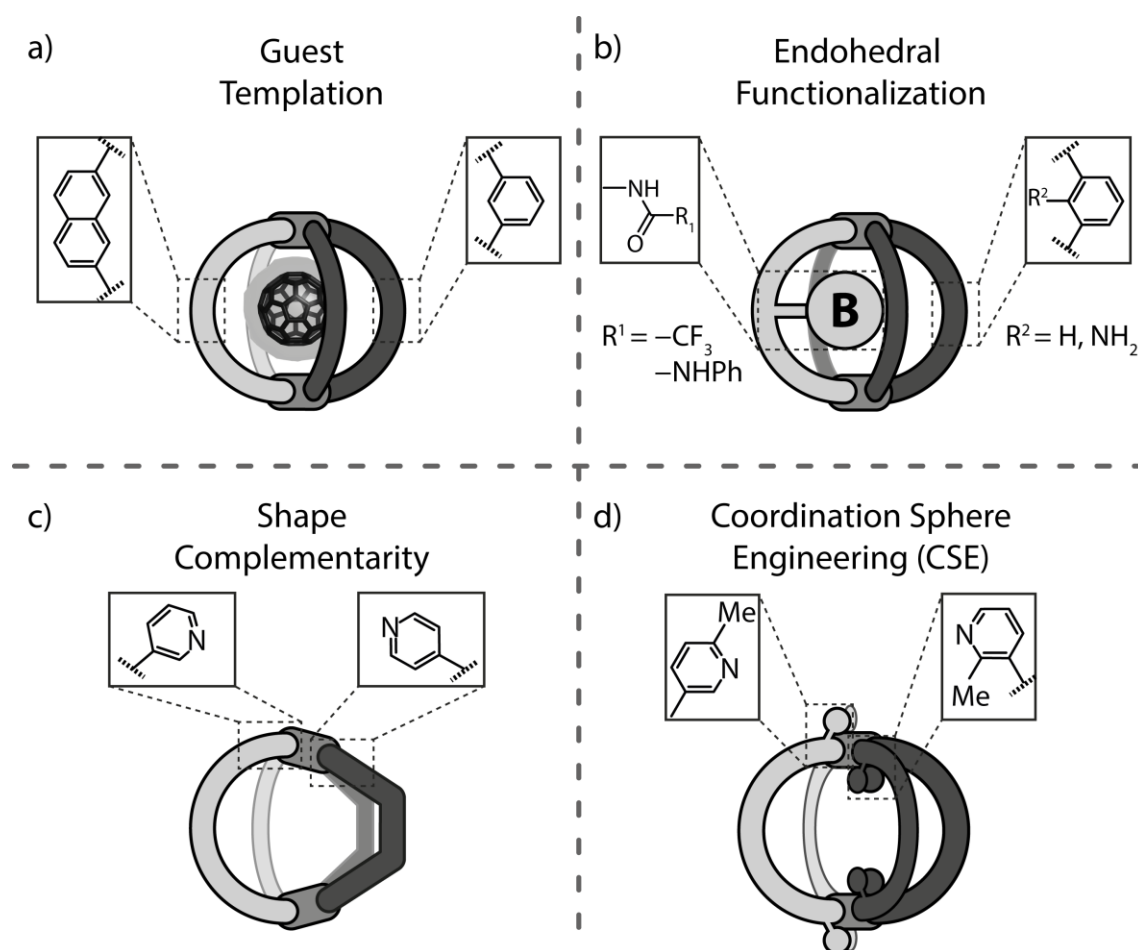
Figure 8: Different strategies to access the clean formation of heteroleptic coordination cages; a) via guest templation; b) using endohedral functionalization and thus bulk; c) the incorporation of shape-complementary ligands and d) coordination sphere engineering (CSE).

Figure 8 a) shows the guest templation approach that has been reported by YAMASHINA et al. in 2015 using two different backbones, benzene and naphthalene, in ligands functionalized with anthracene linkers equipped with pyridine-donor groups. The individual ligands form homoleptic $Pd_2L^{A/B}_4$ cages, however upon introduction of C_{60} into the system, frame rearrangement takes place and the heteroleptic cage $[C_{60}@Pd_2L^A_2L^B_2]$ emerges in a clean fashion.[82] A second approach has been proposed by JOHNSON et al. in 2011 (Figure 8 b)), who added an endohedral functionalized ligand L^A, carrying a bulky substituent, to three other ligands L^B, successfully forming a heteroleptic $Pd_2L^A_1L^B_3$ cage.[83] Both approaches, however, have the significant disadvantage of losing the cavity to form the heteroleptic assembly. Two strategies for heteroleptic cage synthesis maintain the cavity and thus preserve the possibility for further functional increase by means of host-guest chemistry are depicted in Figure 8 c) and d). Figure 8 d) shows a coordination dependent approach[84] for the generation of heteroleptic coordination cages via coordination sphere engineering. Prominent examples for $Pd_2L^A_2L^B_2$ cages synthesized using this method are PRESTON et al. in 2016 using amino-groups directly next to the coordinating pyridines[85] and ZHU et al. in 2018 exploiting methyl-groups in a similar way.[86] This strategy can also be applied to generate ligand deficient systems and Pd_2L_2 rings in which the vacant positions are occupied by coordinating solvent molecules.[75–77] The most commonly used strategy to access heteroleptic coordination cages popularized in our group is the shape-complementarity approach (SCA).[57,64,81,87–89] This strategy applies a careful balance of enthalpic and/or entropic penalties for the homoleptic assemblies by either constructing the ligands bite-angles in a way, that the homoleptic assemblies have higher nuclearity than the assumed heteroleptic ones or have to adapt non-optimal coordination environments, like e.g. in helically twisted Pd_2L_4 cages.[57] A well-functioning approach for the synthesis of $Pd_2L^A_2L^B_2$ coordination cages has been proposed by BLOCH et al. in 2016.[57,64] This approach focusses on the design of ligand pairs with complementary length and donor-group orientation effectively creating coordination cages in which the two palladium centers are no longer parallel to one another, but tipped out of plane. The SCA in combination with the modular ligand approach shown in Figure 6 not only allows a wide array of functional groups to be incorporated into heteroleptic coordination cages, but furthermore maintains the cavity generated in these lantern-shaped coordination cages. For the sake of completeness, a fifth recently proposed strategy by TESSAROLO et al. in 2021 is outside steric hinderance to form heteroleptic tetrahedral assemblies,[51] however this is a relative special case and the approach not widely applicable.

This thesis will fully focus on the shape-complementarity approach, possible applications and uses in method evaluation and systems chemistry, the combination of complementary functions and the boundaries of the approach.

2 Motivation

The creation of metal-based coordination cages is a facile method to establish complex, three-dimensional host molecules equipped with a cavity to enable guest binding. The successful introduction of the shape-complementarity approach (SCA) to access heteroleptic coordination cages, structures with two or more different ligands, opened up a multitude of possible applications, however, opportunities rarely come without challenges.

This thesis is partitioned into four sub-chapters, each addressing a particular aspect of heteroleptic coordination cage formation by using the shape-complementarity approach. These partitions can be summarized as:

1. Ion-Mobility Mass Spectrometry: A novel method enabling gas-phase dimensional analysis of coordination cages will be challenged using the shape-complementarity approach to establish a system of ten heteroleptic coordination cages, which are structurally extremely close related.

2. Systems transformations – a previous master thesis could show a solvent switching behavior of a strained heteroleptic coordination cage. Further analysis of the system in regard to its solvent susceptibility will be performed and the scope of further transformations in special regard to systems chemistry is explored.

3. Functional Heteroleptic coordination cages – The shape-complementarity approach is used to purposefully combine complementary chromophores, a fluorenone-based ligand L^A as a donor and diketopyrrolopyrrole-based ligand L^B as an acceptor, to form one lantern-shaped coordination cage and analyze it in regard to its photophysical and guest-binding properties. The aim is thereby the synthesis of a multi-functional system in which each element has a specific purpose and then analyze their interaction with one another.

4. Limits of the shape-complementarity approach – While alkyne-linkers allow a certain mismatch of ligand donor-angle and Pd(II) coordination geometry by bending the aforementioned alkyne-bonds, rigid ligands with slightly mismatched and thus no longer complementary donor angles will be combined with Pd(II) cations to examine the outcome of the coordination event. With purposeful ligand choice, having the homoleptic species experience either enthalpic or entropic penalty, the outcome of this "restrained" shape-complementarity approach will be thoroughly examined.

All Systems are to be analyzed using NMR and ESI-MS methods, complemented by X-ray diffraction and *in silico* methods. Furthermore, systems containing the fluorenone-

based ligand, thus possessing interesting photophysical properties, will be examined using further methods including UV-Vis absorption-, fluorescence-, CD and CPL spectroscopy.

3   Results

3.1   Ion-Mobility Mass Spectrometry (IMS) – A Valuable Tool for Supramolecular Chemists

3.1.1 Introduction: Methods in Supramolecular Chemistry

The analysis of supramolecular systems relies heavily on the availability of potent analytic techniques to help understanding the formed structures and processes taking place on the nanoscale level. The "big three" analytic methods in supramolecular chemistry are nuclear magnetic resonance (NMR) spectroscopy, mass spectrometry (MS) and single crystal X-ray analysis.[90]

While the latter is an extremely potent method to obtain structural information of a system, as it yields direct and undeniable information on the absolute configuration of molecules, including anions and potential guest molecules, within a solid-state crystalline matter, there are certainly some drawbacks to consider. First, one of the strengths of X-ray analysis can be its weakness depending on what information one wants to obtain. Accurate structural information due to rather static atom orientation in a crystalline state means, that little to no information regarding dynamic processes can be obtained. As the crystallization process often requires another solvent to diffuse into the stock solution of the assembly, the environment is subjected to invasive changes in polarity which might alter the thermodynamic equilibrium. Additionally, the crystallization of coordination cages is not straight forward and the right conditions concerning counter solvent and potential anions can be hard to determine. Furthermore, the formed crystals might not even be comprised of the mayor product in solution, but a smaller subspecies that readily crystallizes instead. If the desired species does crystallize, the crystals are often too small for regular diffractometers and require synchrotron radiation, making single crystal X-ray analysis a cumbersome method that requires external expertise to measure.

Another method that is commonly used in supramolecular chemistry is NMR spectroscopy, which is a method that is mostly used for liquid sample analysis. While there are solid state NMR techniques,[91] these are by far not the most commonly used ones in this field. NMR analysis is extremely potent for the investigation of supramolecular systems,[92] as they are mostly synthesized in solution, thus this physical state being their "native" one. Structural analysis is enabled by 2D NMR techniques like ^1H-^1H COSY and ^1H-^1H NOESY, as well as 1D and 2D heteroatom studies, as long as

the corresponding heteroatom is an NMR active nucleus. The most commonly analyzed nuclei in supramolecular chemistry are ^{1}H, ^{13}C, ^{19}F and sometimes ^{31}P. Furthermore, NMR spectroscopy allows binding-, as well as kinetic studies, and, with additional experiments like ^{1}H DOSY NMR,[90] it is possible to access information regarding the diffusion coefficient which can be readily translated to the hydrodynamic radius of the species and thus its size. Where there is strength, there is also weakness, so while NMR spectroscopy is extremely diverse in its applications and investigative prowess, there are limits to its applicability. As mentioned before, the nucleus to be analyzed needs to be an NMR-active nucleus and the natural abundance needs to be in a reasonable range to achieve sufficient signal-to-noise ratio and thus usable results. Nuclearity assignment in metallo-supramolecular coordination cages via NMR analysis is only feasible by educated guess based on the hydrodynamic radius in combination with *in silico* studies or by using an internal standard with known signal count, as the signal intensity is relative and the information obtained is only the number of protons in different chemical environments relative to one another. Furthermore, samples containing paramagnetic nuclei like Co^{2+} or Cu^{2+} often complicate even simple ^{1}H experiments. While measuring samples containing paramagnetic nuclei is possible,[93,94] most supramolecular chemists actively avoid them due to the aforementioned reason. Another point to consider is the NMR timescale, as it is in the range of seconds to milliseconds depending on what exactly one is looking at,[95] thus not allowing to follow extremely fast processes in solution.

The last one out of the "big three" methods is MS analysis, which allows the analysis of charged species and yields information on the composition of the species and their nuclearity. The sample amount in MS experiments can be extremely low, making it a very resourceful method, in which small sample sizes suffice. Furthermore, in redox-active systems, it gives information on the charge state of e.g. $Fe^{2+/3+}$ species.[96] Mass spectrometry can also yield information on atom connectivity by means of collision-induced fragmentation experiments[97,98] and thus yield valuable data on the structure of e.g. natural products.[99] Guest association studies can be performed,[74,100,101] yielding a valuable addition or even alternative to NMR experiments, where guest addition might lead to broadening of signals and thus leading to non-conclusive results. Additionally, further tandem experiments help analyzing highly complex mixtures or molecules.[102] MS is inherently an invasive method, thus results have to be analyzed with utmost care and consideration, e.g. dilution of the sample with a solvent of different polarity might lead to a change in the system or precipitation of the analyte or higher ordered structures are

not observed due to fragmentation or disassembly caused by elevated ionization energy and dilution.

While the results in mass spectrometry are usually filtered by one parameter, the m/z value, ion mobility spectrometry adds a second sorting parameter, namely the ion mobility K of the ion,[103] which can be translated using equations 2, 3 and 4 (see experimental part) to the experimental collisional cross section (eCCS). This second sorting parameter allows the discrimination of e.g. isomers since while they do have inherently the exact same m/z value, their spatial extent is different due to different atom orientation. There are five different methods for measuring ion-mobility at the moment, namely drift tube ion mobility mass spectrometry (DTIMS), travelling wave ion mobility mass spectrometry (TWIMS), trapped ion mobility mass spectrometry (TIMS), field asymmetric ion mobility mass spectrometry (FAIMS) and differential mobility mass spectrometry (DMS).[104] The method applied in this chapter is TIMS, which is relatively new method for measuring ion mobility with a high resolving power. The basic principle of the utilized TIMS cell is depicted in Figure 9.
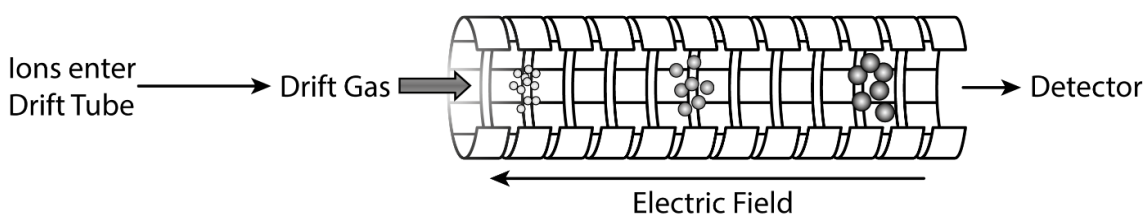
Figure 9: Schematic representation of the function of the TIMS cell used for the herein reported experiments.

As shown in Figure 9, the charged molecules, that were previously ionized using an ESI source, travel through the drift tube in the direction of the drift gas flow and are accumulated and trapped inside by means of the counteracting electric field.[105,106] While other methods allow the observation of all ions in a parallel fashion without changing the experimental parameters, TIMS analyzes the species once eluted from the drift tube by means of changes in the electric field after previously capturing the ion.[104] This accumulation allows a very high resolving power (that increases, the longer the ions are trapped) as opposed to other ion-mobility methods, that can range between up to 200-400 $K/\Delta K$.[107,108] The tunable selectivity makes it highly valuable for the analysis of complex mixtures containing structures that pose extremely close spatial extent and the resolving power enables the resolution of very minor size differences, which would not be possible to analyze with e.g. ^{1}H DOSY NMR.

In this chapter, an ion-mobility setup with a trapped ion mobility (TIMS) cell and a time-of-flight (TOF) m/z analyzer will be challenged with the separation and identification of

different coordination cages, testing its viability as an analytic method in supramolecular chemistry with special emphasis on later applications in systems chemistry.

3.1.2 Abstract

The herein reported system consists of four different bis-monodentate ligands (Scheme 1, experimental part) of which two each (L^{C1}/L^{F1}, respectively L^{P1}/L^{P2}) are shape complementary to the other set.

L^{C1} and L^{F1} carry a very similar backbone structure, L^{C1} being based on carbazole, while L^{F1} is based on fluorenone, and are both equipped with alkyne linkers and meta-pyridine coordination donor groups. This leads to two congruent ligands, only differing slightly in donor angle due to the heteroatom implemented in L^{C1}. Additionally, L^{C1} carries a hexyl-chain, increasing its size as compared to L^{F1}, which only sports a carbonyl group.

The chosen counter ligands L^{P1} and L^{P2} are both based on a phenanthrene backbone and para pyridine donor groups with the only difference being an alkyne group introduced in between backbone and donor group for L^{P2}. While the inherent bite angle remains unaltered, the distance of the two donor-groups thus increases. This leads to an increased size of L^{P2} as compared to L^{P1}.

Each ligand forms clean homoleptic assemblies when combined with Pd(II) cations, while a 1:1 combination of two individual shape-complementary ligands leads to the formation of a clean, heteroleptic coordination cage in either DMSO or CD_3CN (see Figure 10).

The results reported in this chapter have been published in: *Resolution of minor size differences in a family of heteroleptic coordination cages by trapped ion mobility ESI-MS* (K. E. Ebbert, L. Schneider, A. Platzek, C. Drechsler, B. Chen, R. Rudolf and G. H. Clever, *Dalton Trans.*, **2019**, *48*, 11070-11075).[66]
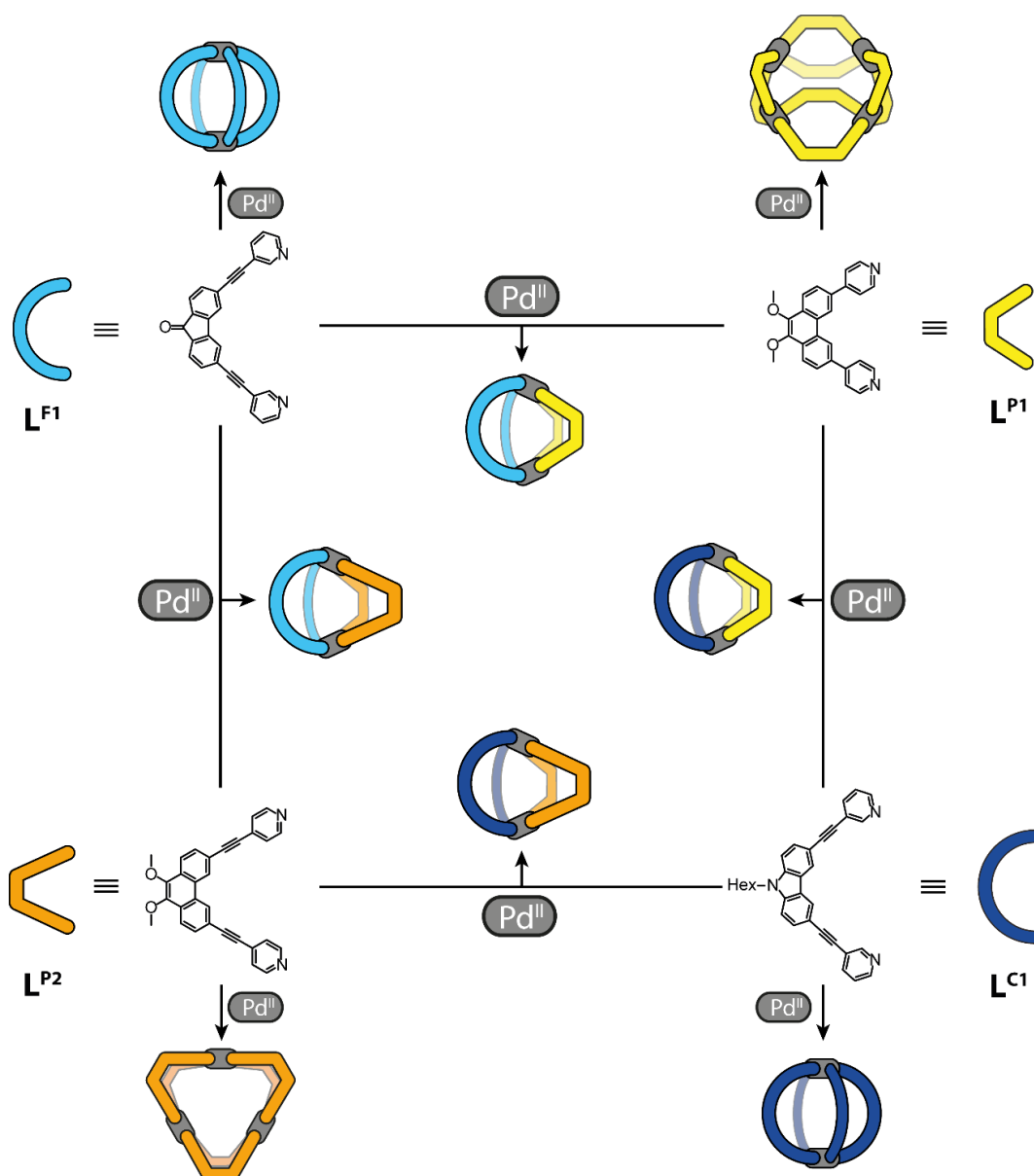
Figure 10: Overview of utilized ligands, corresponding homoleptic assemblies and heterolpetic assemblies formed upon 1:1 combination of shape-complementary ligands (blue/teal + yellow/orange) with Pd(II) cations.

L^{C1} and L^{F1} individually form Pd_2L_4 coordination cages upon treatment with Pd(II) cations, while L^{P1} and L^{P2} form species of higher nuclearity $n \in \{3,4\}$. L^{P1} forms a clean Pd_4L_8 assembly in DMSO but a mixture of homoleptic Pd_3L_6 and Pd_4L_8 assemblies in CD_3CN. This behavior is not reflected in related L^{P2}, which forms Pd_3L_6 assemblies in both solvents, likely due to the introduction of more flexibility by means of alkyne bridges. While heteroleptic cage formation from L^{C1} and L^{P1} with Pd(II) cations has been shown previously,[64] the other three heteroleptic assemblies $Pd_2L^{F1}_2L^{P1}_2$, $Pd_2L^{F1}_2L^{P2}_2$ and $Pd_2L^{C1}_2L^{P2}_2$ were unprecedented and have first been shown in the associated publication, respectively the preceding master thesis.[66,109]

The ^1H NMR spectra of ligand L^{P1} and L^{P2}, their homoleptic assemblies, the homoleptic $Pd_2L^{F1}_4$ cage and the related heteroleptic assemblies $Pd_2L^{F1}_2L^{P1}_2$ and $Pd_2L^{F1}_2L^{P2}_2$ are depicted in Figure 11.
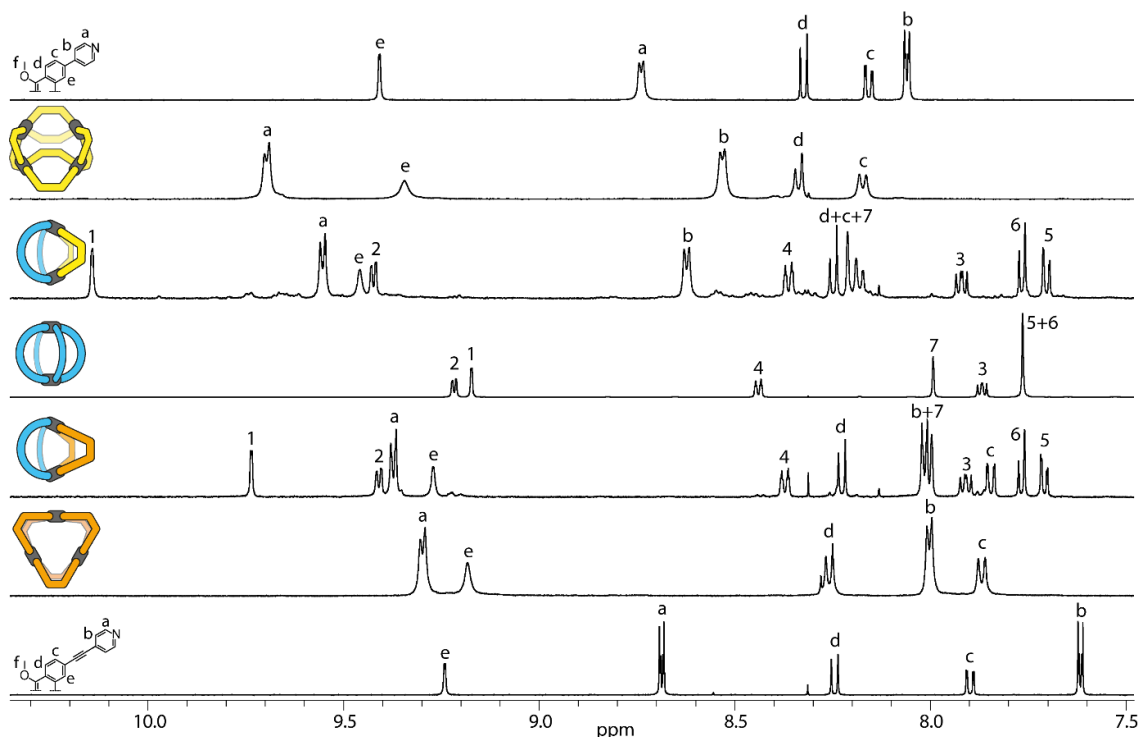
Figure 11: Partial ^1H NMR spectra of L^{P2}, $Pd_3L^{P2}_6$, $Pd_2L^{F1}_2L^{P2}_2$, $Pd_2L^{F1}_4$ (600 MHz), $Pd_2L^{F1}_2L^{P1}_2$, $Pd_4L^{P1}_8$ and L^{P1} in DMSO-d_6 at 298 K. Spectra were measured at 500 MHz if not stated otherwise.

As evident from Figure 11, all assigned species form with no free ligand present in the spectra of the homoleptic, nor the heteroleptic assemblies, and no homoleptic species being detected in the spectra of heteroleptic $Pd_2L^{F1}_2L^{P1}_2$ or $Pd_2L^{F1}_2L^{P3}_2$. All signals of protons around the coordination sphere, like H^a and H^b, of L^{P1} and L^{P2} experience a mayor downfield shift upon coordination to Pd(II) and formation of the homoleptic assemblies, while the signal of proton H^e, located inside formed the assembly, shifts upfield. While the signals of H^b and H^e shift even further downfield in the heteroleptic assemblies, the signal of H^a shows further downfield shifting only for $Pd_2L^{F1}_2L^{P2}_2$, but not for $Pd_2L^{F1}_2L^{P1}_2$, where a less pronounced downfield shift as compared to the homolpetic assembly is observed. Most notably however, is the shift of proton H^1, located inside the formed coordination cages directly next to the donor-nitrogen. While its shift is $\delta = 9.17$ ppm in homolpetic $Pd_2L^{F1}_4$, it is $\delta = 9.74$ ppm in case of $Pd_2L^{F1}_2L^{P2}_2$ and $\delta = 10.15$ ppm for $Pd_2L^{F1}_2L^{P1}_2$, indicating deshielding of this specific proton in a heteroleptic environment, which is even more pronounced for the combination of L^{F1} and L^{P1}.

The other system including the heteroleptic coordination cages $Pd_2L^{C1}_2L^{P1}_2$ and $Pd_2L^{C1}_2L^{P2}_2$ was characterized likewise with the same behavior of proton H^1 being observable,[66,109] thus it can be attributed directly to the coordination environment and not the solvent.

As evident from Figure 11 and Figure 26 (see experimental part), ligand L^{P2} does form heteroleptic cages just as well as its shorter analogue L^{P1} despite its donor atoms being further apart. Single crystals suitable for X-ray diffraction could be obtained for both, homoleptic $Pd_3L^{P2}_6$ and heteroleptic $Pd_2L^{C1}_2L^{P2}_2$ and were derived from slow vapor diffusion of benzene into DMSO, respectively CD_3CN. This helped to provide further structural insight (Figure 12).
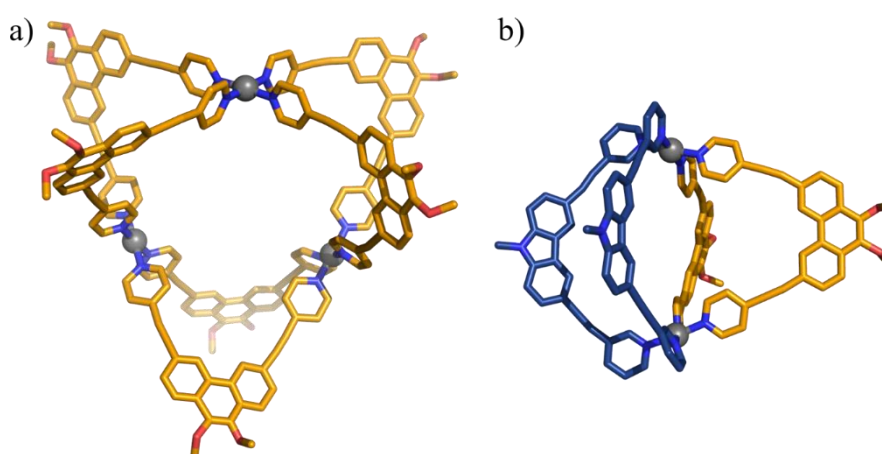
Figure 12: X-ray structures of a) homoleptic $Pd_3L^{P2}_6$ and b) heteroleptic $Pd_2L^{C1}_2L^{P2}_2$.

As proposed previously already, the introduction of alkyne-linkers adds more flexibility to ligand L^{P2}, which allows the formation of smaller, entropically more favored, homoleptic assemblies $Pd_3L^{P2}_6$ independent of the solvent. The observed alkyne angles in the solid-state structure of $Pd_3L^{P2}_6$ range from approximately $\alpha \approx 168\text{-}176°$ with the bending obvious from the depicted structure (Figure 12, a)). The same effect could be observed for the heteroleptic $Pd_2L^{C1}_2L^{P2}_2$ assembly, where the alkyne angle in incorporated L^{P2} ranges from approximately $\alpha \approx 165\text{-}171°$, while it is $\beta \approx 171\text{-}178°$ in L^{C1} (Figure 12, b). While bending of the alkyne-linkers will yield a positive enthalpic contribution to the system, a heteroleptic $Pd_2L^A_2L^B_2$ cage is overall the thermodynamic product in all four 1:1:1 (L^A:L^B:Pd(II)) combinations.

All herein mentioned heteroleptic cages were also analyzed regarding their spatial extent with the most commonly used technique being ^1H DOSY NMR analysis, as single X-ray diffraction is a powerful tool for structure elucidation, yet obtaining single crystals suitable for diffraction is not always trivial.

Trapped Ion Mobility Mass Spectrometry (TIMS) is valuable tool for the analysis of complex mixtures, especially regarding size elucidation in the gas phase, as opposed to ^{1}H DOSY NMR in solution. Both methods will be challenged with the previously described system regarding their ability to still differentiate minimal structural changes with the complexity of the mixtures being increased iteratively.

3.1.3 The System – A Complex, yet Defined Mixture

While 1:1 combinations of two shape-complementary ligands each (**L^{C1}**/**L^{F1}** and **L^{P1}**/**L^{P2}**) yield clean and readily analyzable spectra in 1D and 2D NMR studies, as well as standard MS techniques, analyzing mixtures containing three different ligands pose ascending difficulty levels and demand for more sophisticated, diverse methods. To directly compare the standard ^{1}H DOSY NMR technique and ion mobility in regard to their effectiveness to discriminate three-component mixtures formed by **L^{C1}**, respectively **L^{F1}** with both **L^{P1}** and **L^{P2}**, the corresponding solutions were set up and subjected to both analytic methods.
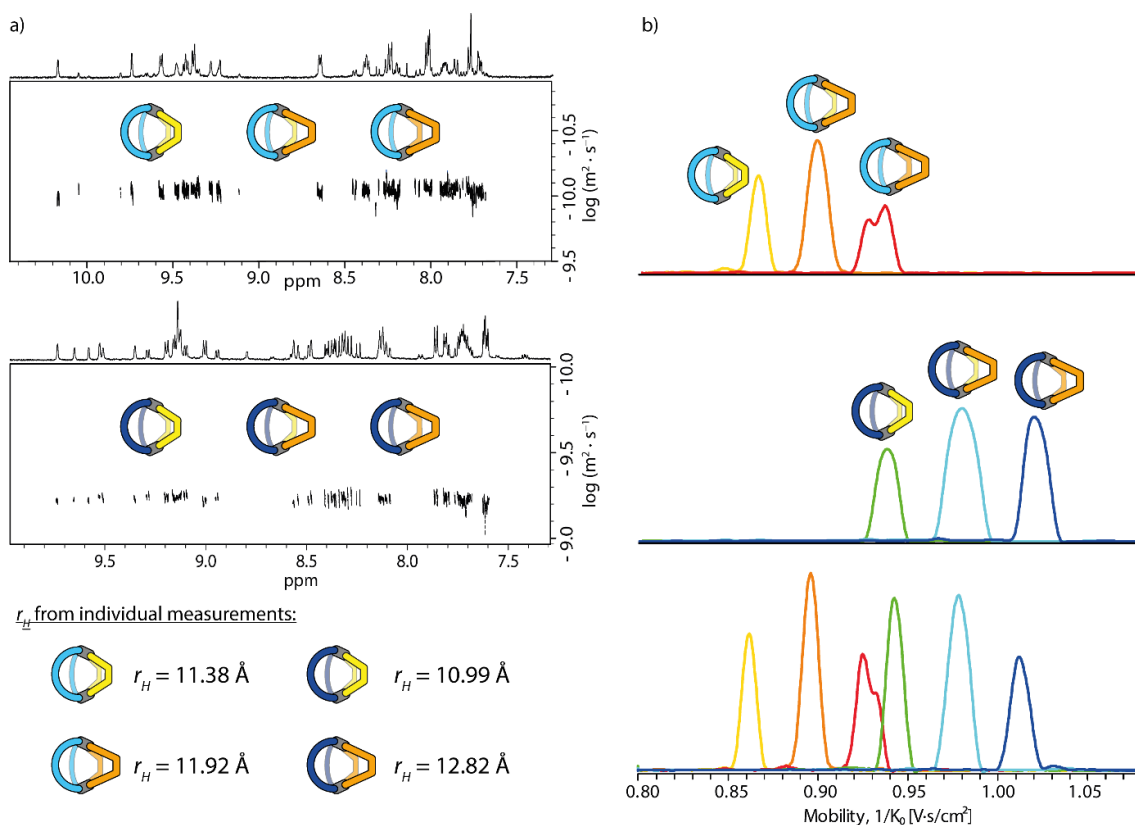
Figure 13: Comparision of the resolution of (a) ^{1}H DOSY NMR of mixed spectra obtained from **L^{F1}** + **L^{P1}** + **L^{P2}** after the addition of Pd(II) cations in DMSO-d_6 (top), **L^{C1}** + **L^{P1}** + **L^{P2}** after the addition of Pd(II) cations in CD$_3$CN (middle) and the hydrodynamic radii of the clean species (bottom) with IMS analysis of same mixtures (b, top and middle) and a six-component mixture (b, bottom).

As evident from the ^{1}H NMR spectra (Figure 13, a)), both combinations led to the formation of a mixture of heteroleptic coordination cages, without the presence of homoleptic species. While ^{1}H DOSY NMR allowed size discrimination in single species without any problems, as the given values for all clean systems show, analysis of a three-component mixture poses more of a challenge. The mixed spectra obtained from three-ligand mixtures in either DMSO ($L^{F1} + L^{P1} + L^{P2}$) or CD_3CN ($L^{C1} + L^{P1} + L^{P2}$) can be analyzed via ^{1}H DOSY NMR, however broadening and overlap of the corresponding signals complicates the assignment of a clear hydrodynamic radius r_H to the individual species (Figure 13, a)). On the other hand, the very same mixture subjected to IMS measurement shows clearly distinguishable mobility traces that were each measured choosing the $[Cage + BF_4]^{3+}$ species peak, yielding collisional cross-section (CCS) values that can be directly translated to the gas phase radius of the assembly (Figure 13, b)).

The given formula relates the radius of the analyzed molecule, the kinetic radius[110] of the collision gas and the measured CCS value is given by equation 1:[111]

$$CCS = \pi(r_1 + r_2)^2 \qquad (1)$$

In case of nitrogen, the kinetic radius (based on its kinetic diameter) is given as $r(N_2) = 1.82$ Å.[112] Summarized data is given in Table 1.

Table 1: Summary of formed coordination Cages with assigned CCS values and therefore derived kinetic radii r_K in the gas phase determined from the individual three-component mixtures (TCM) shown in Figure 13.

Species	CCS (Å^2)	Radius r_K (Å)
$Pd_2L^{F1}{}_2L^{P1}{}_2$	527.6	11.14
$Pd_2L^{F1}{}_2L^{P1}L^{P2}$	547.3	11.38
$Pd_2L^{F1}{}_2L^{P2}{}_2$	569.1	11.64
$Pd_2L^{C1}{}_2L^{P1}{}_2$	574.8	11.71
$Pd_2L^{C1}{}_2L^{P1}L^{P2}$	599.2	11.99
$Pd_2L^{C1}{}_2L^{P2}{}_2$	619.2	12.22

The measured kinetic radii obtained from the IMS measurement are generally smaller than the ones obtained for the hydrodynamic radius by 2.11-2.35% and in case of $Pd_2L^{C1}{}_2L^{P2}{}_2$ by 4.69%, with the exception of the values for $Pd_2L^{C1}{}_2L^{P1}{}_2$. This discrepancy can potentially be explained by increased folding of the attached chains into the cage's vicinity, though further studies to explain this behavior would be required, since the same effect could not be observed for $Pd_2L^{C1}{}_2L^{P2}{}_2$.

While the size-discrimination of coordination cages in three-, and even six-component mixtures has been proven to be very feasible using IMS studies, the provided system

has the potential to challenge the method even further. Combining equimolar amounts of all four ligands, L^{C1}, L^{F1}, L^{P1} and L^{P2}, with Pd(II) led to the formation of a highly complex, yet defined mixture. The outcome of the coordination event is limited by the SCA and thus, only 10 different species of varying composition can form, while a total of 55 would be possible without that restriction. While one could argue, that the three-component mixtures discussed before are still eligible to be differentiated by ^{1}H DOSY NMR, this becomes definitely unmanageable in a ten-component mixture, thus NMR studies are not suitable from this point on. The partial ESI-MS spectrum showing the $[BF_4@Cage]^{3+}$ species of this mixture is given below.
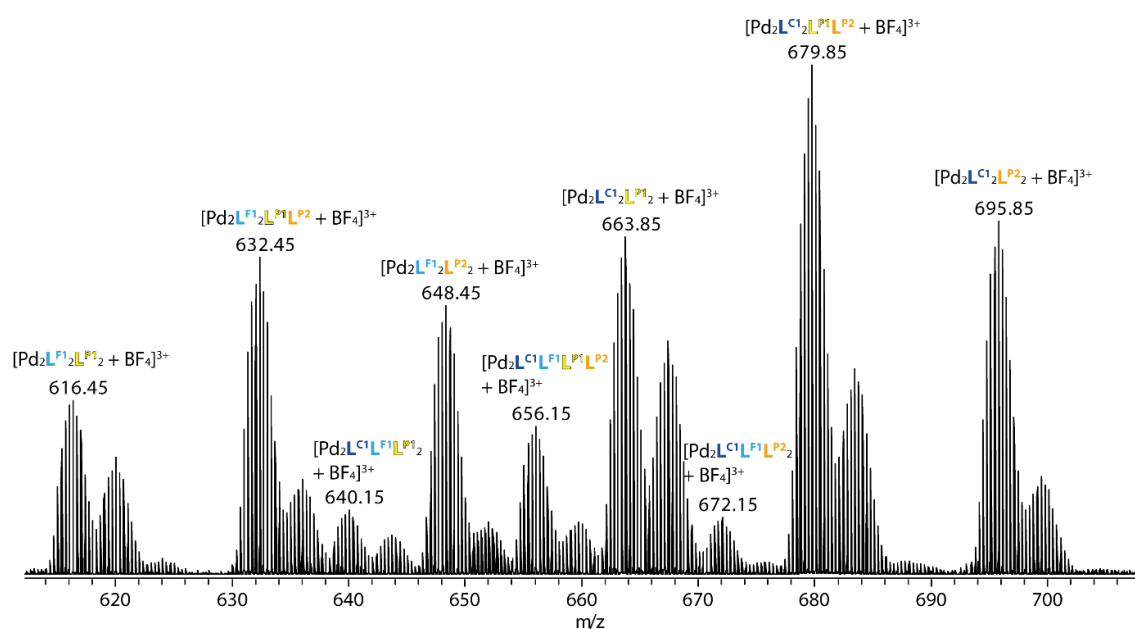
Figure 14: Partial ESI-MS spectrum of the *m/z* =3+ species of all 10 possible Pd_2L_4 coordination cages formed by a 1:1:1:1 combination of ligands L^{C1}, L^{F1}, L^{P1} and L^{P2} with Pd(II).

As evident from Figure 14, all expected Pd_2L_4 combinations formed and can be detected according to their m/z value. Additional adducts with varying anions lead a more intricate spectrum, yet assignment of all 9 m/z values to the according species was performed without any complications. The isomeric nature of $Pd_2L^{C1}L^{F1}L^{P1}L^{P2}$, the assembly containing all four different ligands, yields to the peak at m/z = 656.15 featuring in fact two species with identical mass. A depiction of the 10 formed structures is given in Figure 15.
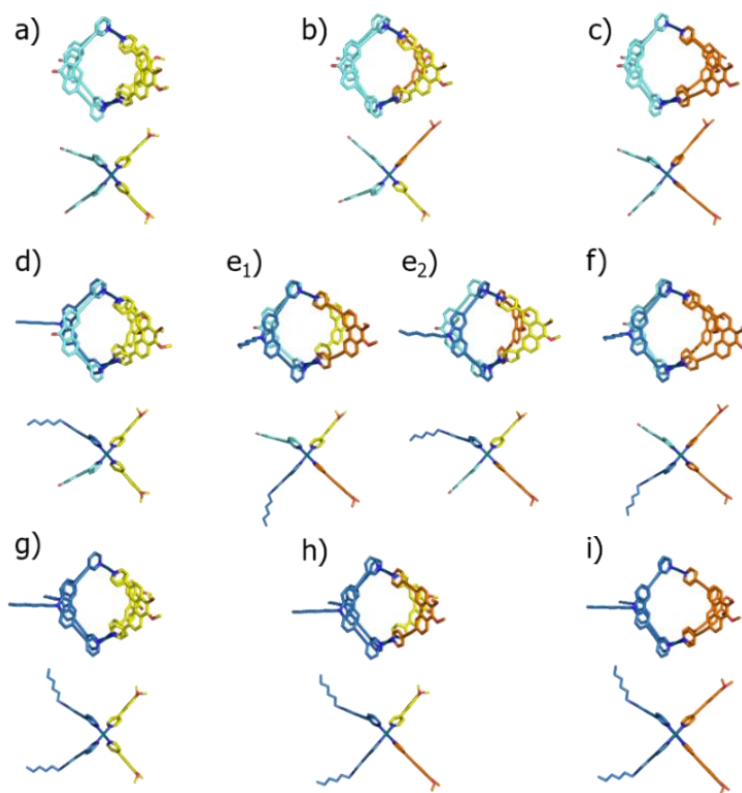
Figure 15: Geometry optimized structures (PM6) of (a) $[Pd_2L^{F1}_2L^{P1}_2]^{4+}$; (b) $[Pd_2L^{F1}_2L^{P1}L^{P2}]^{4+}$; (c) $[Pd_2L^{F1}_2L^{P2}_2]^{4+}$; (d) $[Pd_2L^{C1}L^{F1}L^{P1}_2]^{4+}$; (e_1) *cis*-$[Pd_2L^{C1}L^{F1}L^{P1}L^{P2}]^{4+}$; (e_2) *trans*-$[Pd_2L^{C1}L^{F1}L^{P1}L^{P2}]^{4+}$; (f) $[Pd_2L^{C1}L^{F1}L^{P2}_2]^{4+}$; (g) $[Pd_2L^{C1}_2L^{P1}_2]^{4+}$; (h) $[Pd_2L^{C1}_2L^{P1}L^{P2}]^{4+}$ and (i) $[Pd_2L^{C1}L^{F1}L^{P2}_2]^{4+}$ (each in top and side view).

Most notable for the evaluation of the potential of IMS in the analysis of complex mixtures of supramolecular assemblies are the isomeric structures with the composition $Pd_2L^{C1}L^{F1}L^{P1}L^{P2}$. The nature of these two coordination assemblies is not purely random due to the restriction applied using the SCA. A detailed analysis can be performed using Figure 16.
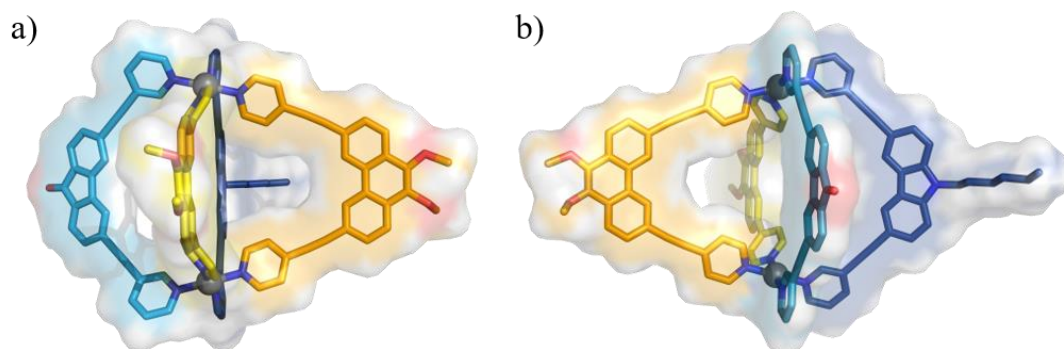
Figure 16: *In silico* models (PM6) of the two isomeres (a) *cis*-$[Pd_2L^{C1}L^{F1}L^{P1}L^{P2}]^{4+}$ with the two ligands of smaller extend, L^{P1} and L^{F1}, neighboring each other and (b) *trans*-$[Pd_2L^{C1}L^{F1}L^{P1}L^{P2}]^{4+}$, where L^{P1} and L^{F1} stand *trans* to oneanother, formed from the 1:1:1:1 combination of ligands L^{C1}, L^{F1}, L^{P1} and L^{P2} with Pd(II) cations (hydrogens omnitted for clarity). To emphasize on the spatial extent of the molecules, the surface representation is given.

The SCA limited L^{C1} and L^{F1} (blue and teal) as well as L^{P1} and L^{P2} (yellow and orange) to always coordinate in a *cis*-conformation to one another (Figure 16). Thus, the more sterically demanding ligand L^{C1}, with its hexyl-chain can only be located next to (Figure 16 a)) or opposite (Figure 16 b)) from the other sterically demanding L^{P2} with its increased linker-backbone distance introduced by alkyne spacers. The size difference between these two structures is incredibly small, especially considering the potential of the hexyl-chain to fold itself to the cage structure due to dispersive forces. This led to the system posing a challenge to the newly applied method not only in regard to the sheer number of species but also in regard to these two, structurally very closely related structures. However, the resolution of an IMS measurement can be increased by sacrificing spectral width.[104] Figure 17 shows the IMS measurement of the 10-component mixture with all species assigned according to nomenclature given in Figure 15.
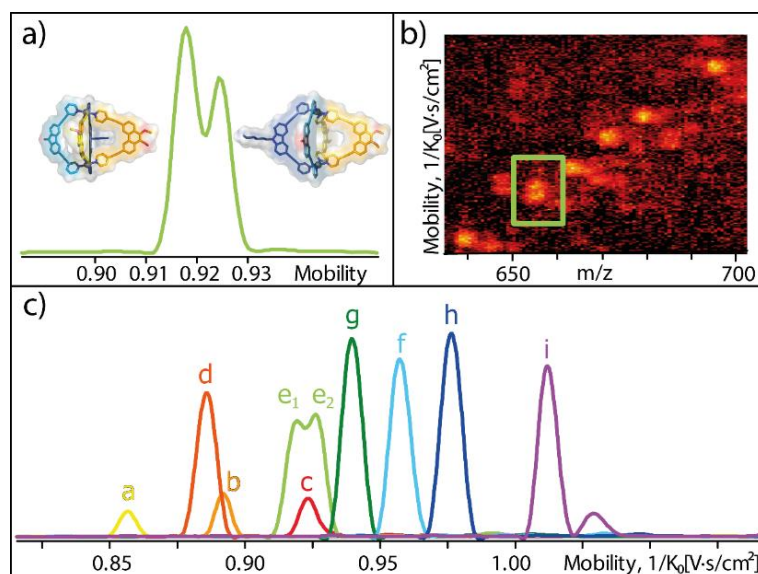
Figure 17: a) High-resolution ion mobility measurement (160 $1/K_0$) of the the peak representing the two isomeric $Pd_2L^{C1}L^{F1}L^{P1}L^{P2}$ structures b) heatmap showing the mobility related to the m/z value with special emphasis on the double spot at $m/z = 656.15$ c) Mobilogram of all detected species depicted in Figure 16.

The full spectrum of all 10 mobilities measured is clear and it is straightforward to assign a mobility to the given MS peak obtained from the same measurement (Figure 17) for all non-isomeric species. The isomers could be distinguished in not only the high-resolution measurement (160 $1/K_0$, Figure 17, a)), but already under standard measurement conditions (Figure 17, c)). This is remarkable considering the difference in CCS attributes to only 4.3 $Å^2$. This difference is also visible in the heatmap depicted in Figure 17, b), where a prominent double spot can be observed at $m/z = 656.15$, while only a single mobility is obtained for the other m/z values.

With the CCS measurement inherently being subject to a certain error, the 10-component mixture was measured five times on different days with freshly prepared mixtures to

validate the results. The obtained mean values (values for single and three-cage systems have been included if applicable), respective errors and derived kinetic radii r_K are given in Table 2.

Table 2: Measurement data obtained and averaged from all collective measurements of the experimental CCS value (eCCS) of the m/z = 3+ peak of all ten analyzed coordination cages $[Cage + BF_4]^{3+}$. Mean value and standard deviation (SD) are given.

Species	eCCS (Å^2)	SD eCCS (Å^2)	Radius r_K (Å)
$Pd_2L^{F1}_2L^{P1}_2$	526.3	0.7	$11.12 \pm 8.6 \cdot 10^{-3}$
$Pd_2L^{F1}_2L^{P1}L^{P2}$	547.9	0.5	$11.39 \pm 6.0 \cdot 10^{-3}$
$Pd_2L^{F1}_2L^{P2}_2$	566.1	1.3	$11.60 \pm 1.5 \cdot 10^{-2}$
$Pd_2L^{C1}L^{F1}L^{P1}_2$	543.8	0.4	$11.34 \pm 4.8 \cdot 10^{-3}$
$Pd_2L^{C1}L^{F1}L^{P1}L^{P2}$	562.9	1.0	$11.57 \pm 1.2 \cdot 10^{-2}$
$Pd_2L^{C1}L^{F1}L^{P1}L^{P2}$	567.2	0.8	$11.62 \pm 9.5 \cdot 10^{-3}$
$Pd_2L^{C1}L^{F1}L^{P2}_2$	587.2	0.7	$11.85 \pm 8.1 \cdot 10^{-3}$
$Pd_2L^{C1}_2L^{P1}_2$	575.2	1.1	$11.71 \pm 1.3 \cdot 10^{-2}$
$Pd_2L^{C1}_2L^{P1}L^{P2}$	598.2	1.0	$11.98 \pm 1.2 \cdot 10^{-2}$
$Pd_2L^{C1}_2L^{P2}_2$	619.1	1.2	$12.22 \pm 1.2 \cdot 10^{-2}$

While the differentiation of the two isomers has been proven to be possible by means of the herein presented data, the assignment of the two structures to the corresponding mobility is not straightforward. An educated guess would be, that both sterically demanding ligands L^{C1} and L^{P2} standing *trans* to each other would lead to a species with the higher kinetic radius due to fast rotational motion in the gas phase averaging the longest inter-cage distance to a conclusively higher CCS value as opposed to L^{C1} and L^{P2} standing *cis* to one another leading to a lower averaged kinetic radius and thus CCS value.

To prove this point and to further validate the obtained results, theoretical CCS calculations have been performed using three different *in silico* methods to determine theoretical CCS values (tCCS). These calculations were performed as a collaboration within the research group by fellow PhD student, Christoph Drechsler. The methods for tCCS determination included IMoS,[113,114] using the 'projected area method', in which hard spheres based on Van der Waals radii are assigned to the atoms and the projected 2D area is averaged over 500 orientations. (a factor ξ = 1.2 for compensating the neglect of momentum transfer and long-range interactions is applied) and a method based on the 'trajectory method' (MOBCAL[115,116]) in which a simulation of the interaction of analyte and collision gas is performed. The tCCS calculations were performed on the PM6 optimized structures shown in Figure 7. A summary of tCCS values as compared to eCCS values obtained from the measurements is given in Figure 18.
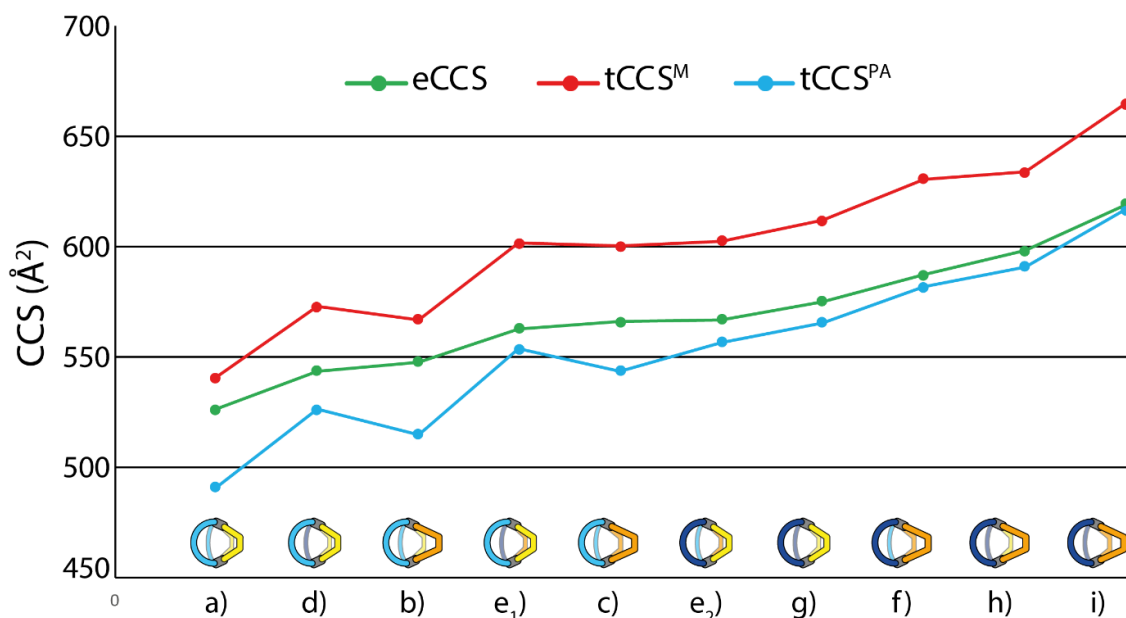
Figure 18: Comparison of experimental (eCCS; green) values of the $[Cage + BF_4]^{3+}$ species and calculated values (tCCS) either using the trajectory method ($tCCS^M$) or the projected area method ($tCCS^{PA}$).

Both methods are able to reproduce the trend of the eCCS values nicely with minor deviation, though the trajectory method generally overestimated the tCCS values, while the projected area method results in tCCS values lower than the actual experimental results. Aside from this, all methods yielded the same trend for the isomeric structures, with *cis*-$Pd_2L^{C1}L^{F1}L^{P1}L^{P2}$ being slightly smaller than *trans*-$Pd_2L^{C1}L^{F1}L^{P1}L^{P2}$. Since all computational methods support the previously stated educated guess, assigning the structure to the measured mobility as depicted in Figure 17 a) is reasonable.

Further details regarding the *in silico* methods including the exact calculated values can be obtained from the published literature[66] and the experimental part.

3.1.4 Conclusion and Outlook

In summary, we were able to design a system of heteroleptic cages formed from four different ligands of which two ligands each were shape-complementary to the other set. This restriction limited the degree of statistical self-sorting to the formation of only 10 heteroleptic coordination cages of the Pd_2L_4 type, instead of 55 assemblies, that would form without restrictions by means of the SCA. Two of the 10 formed assemblies were isomeric, thus having the exact same *m/z* value. The complex mixture was subjected to ion-mobility mass spectrometry and the method was tested in regard to its potential in the analysis of complex mixtures. A chapter summary is depicted in Figure 19.
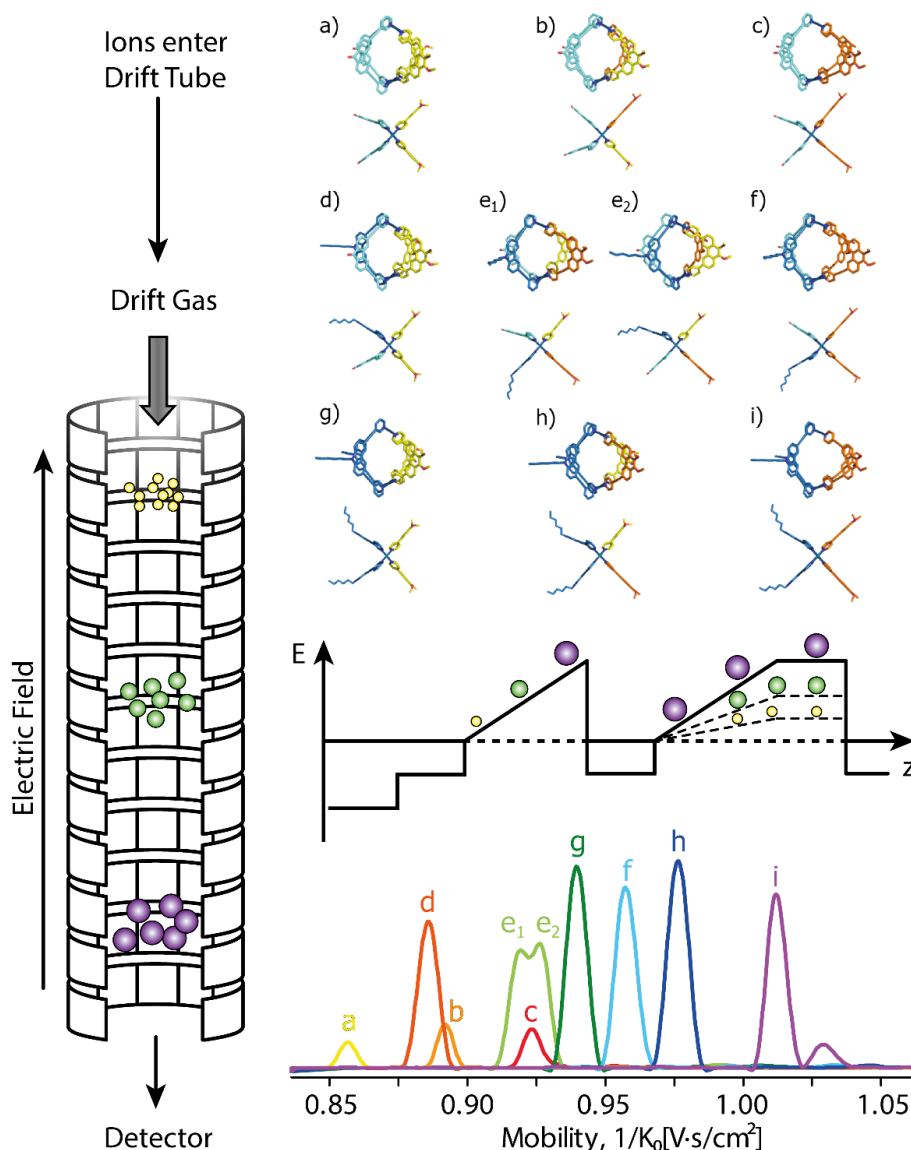
Figure 19: Summary of the method used in this chapter and the corresponding results.

Not only was IMS indeed able to differentiate the assemblies, which one could argue, would be possible by mass alone since cages of different composition do possess different *m/z* values, but the method proved to yield accurate values regarding the spatial extent of the corresponding molecules. Furthermore, the two isomeric assemblies could be differentiated using this method, while they possess a difference in eCCS value as low as 4.3 Å^2. The herein reported system proved to be a valuable evaluation tool for the potential IMS as a method has for the analysis of supramolecular coordination assemblies in regard to minimal changes in their spatial extent. These changes can be induced by structural differences, as described in this chapter with isomeric structures to be differentiated, or by guest-binding and conformational changes due to external triggers.

3.1.5 Experimental Part

3.1.5.1 Ligand Synthesis

All Ligands (Scheme 1) were prepared according to literature procedures.[57,66,117]
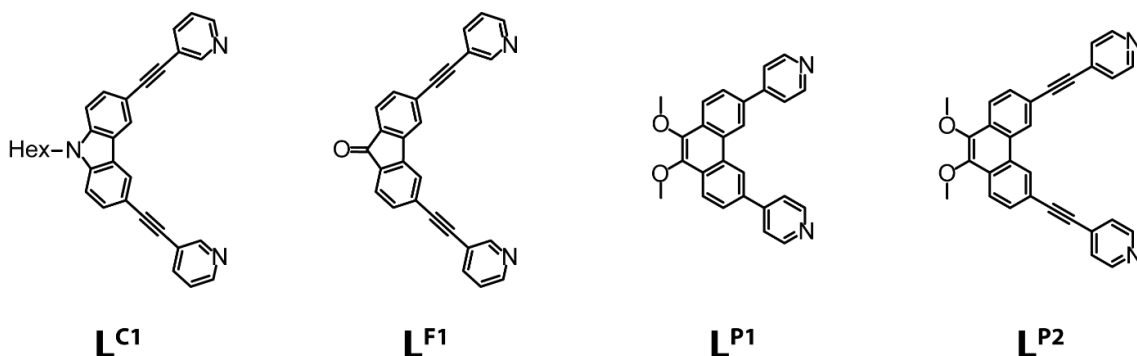
Scheme 1: Structure of the utilized ligands **L**^{C1}, **L**^{F1}, **L**^{P1} and **L**^{P2}.

3.1.5.2 Coordination Cage Synthesis

Formation of homoleptic cages Pd$_2$**L**$^{C1}_4$ and Pd$_4$**L**$^{P1}_8$

Formation of homoleptic cages [Pd$_2$**L**$^{C1}_4$] and [Pd$_4$**L**$^{P1}_8$] have been previously reported in CD$_3$CN, respectively DMSO-d_6.[57,64,117]

Formation of homoleptic Pd$_2$**L**$^{F1}_4$

A solution of [Pd(CH$_3$CN)$_4$](BF$_4$)$_2$ (60 µL, 15 mM in DMSO-d_6) was combined with a suspension of **L**^{F1} (540 µL, 3.11 mM in DMSO-d_6) at room temperature to afford [Pd$_2$**L**$^{F1}_4$] in quantitative yield.
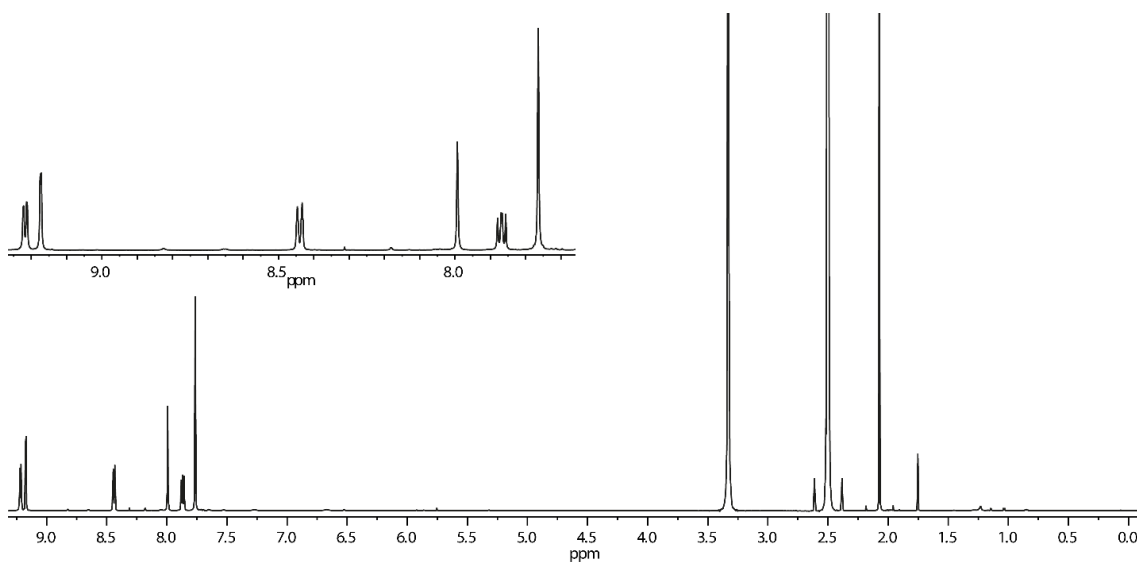
Figure 20: ^{1}H NMR spectrum (600 MHz, DMSO-d_6, 298 K) of [Pd$_2$**L**$^{F1}_4$] including a zoom in the aromatic region.

^{1}H NMR (600 MHz, DMSO-d_6, 298 K): δ = 9.22 (dd, ^3J = 6.0, ^4J = 1.1, 8H, H^f), 9.17 (d, ^4J = 1.7, 8H, H^g), 8.43 (dt, ^3J = 8.0, ^5J = 1.6, 8H, H^e), 7.99 (s (br), 8H, H^c), 7.86 (dd, ^3J = 6.1, ^4J = 1.7, 8H, H^d), 7.76 (s (br), 16H, H^a, H^b).
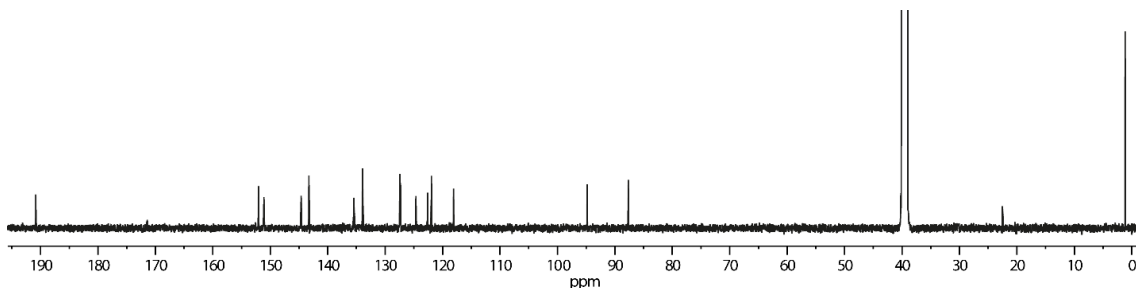
Figure 21: ^{13}C NMR spectrum (151 MHz, DMSO-d_6, 298 K) of [Pd$_2$**L**$^{F1}_4$].

^{13}C{^{1}H} NMR (150 MHz, DMSO-d_6, 298 K): δ = 190.8, 152.0, 151.1, 144.6, 143.3, 135.4, 133.9, 127.4, 127.3, 124.6, 122.6, 122.0, 118.1, 94.8, 87.7.
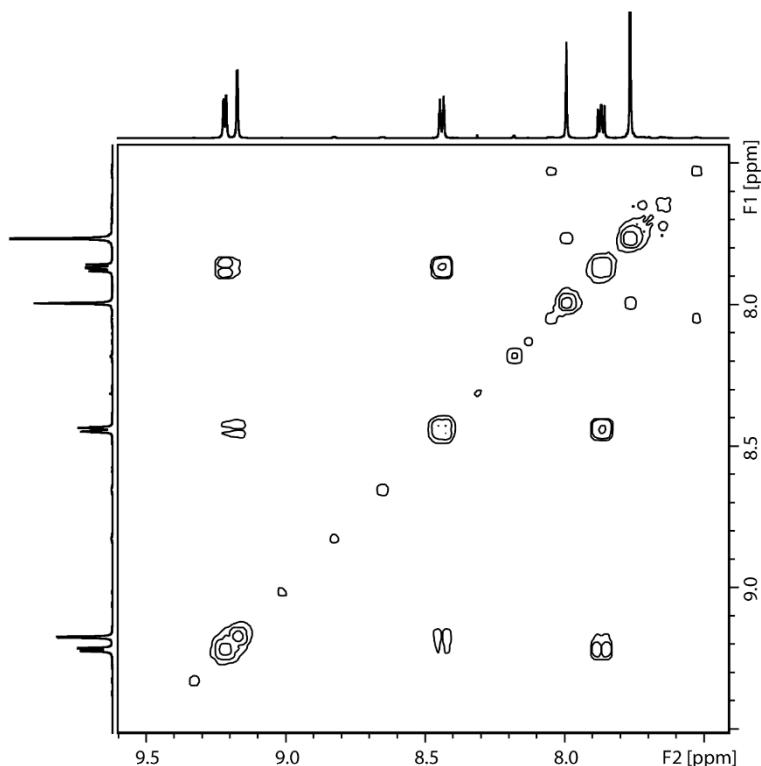
Figure 22: Partial ^{1}H−^{1}H COSY spectrum (600 MHz, DMSO-d_6, 298 K) of [Pd$_2$**L**$^{F1}_4$].

Synthesis of Pd$_2$**L**$^{F1}_2$**L**$^{P1}_2$

A solution of [Pd(CH$_3$CN)$_4$](BF$_4$)$_2$ (60 µL, 15 mM in DMSO-d_6) was combined with a solution of **L**^{P1} (270 µL, 3.11 mM in DMSO-d_6) and a suspension of **L**^{F1} (270 µL, 3.11 mM in DMSO-d_6) and left to sit at room temperature for 2 h to afford [Pd$_2$**L**$^{F1}_2$**L**$^{P1}_2$] in quantitative yield.
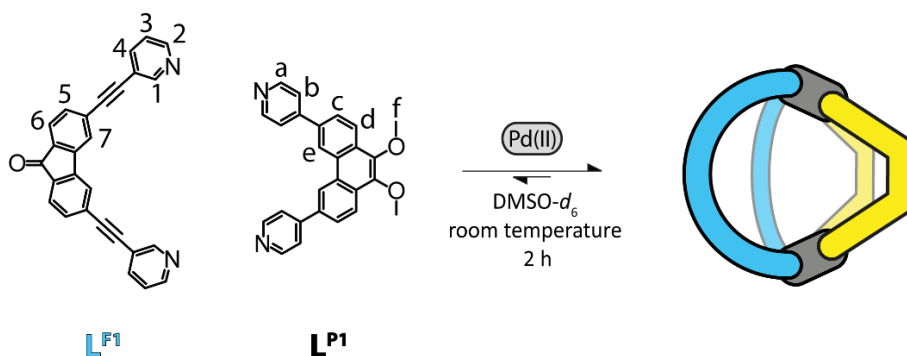
Scheme 2: Formation of Pd$_2$L$^{F1}_2$L$^{P1}_2$ with consecutive proton labels.
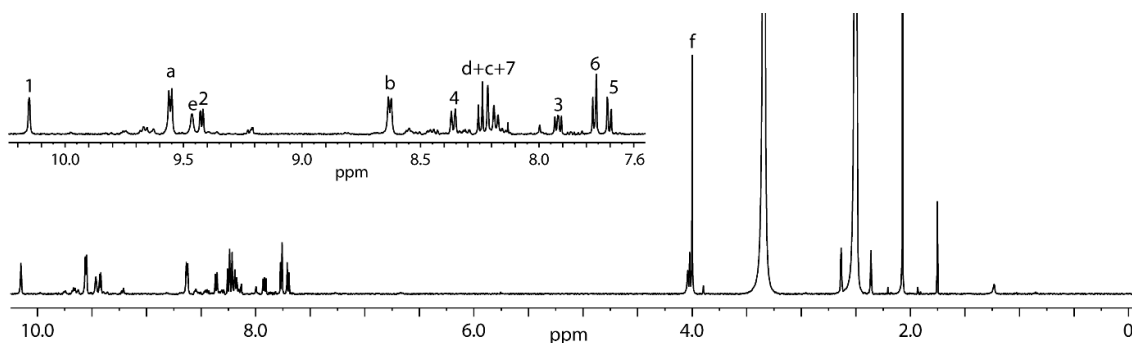
Figure 23: ^{1}H NMR spectrum (600 MHz, DMSO-d_6, 298 K) of [Pd$_2$L$^{F1}_2$L$^{P1}_2$] including a zoom in the aromatic region.

^{1}H NMR (600 MHz, DMSO-d_6, 298 K): δ = 10.15 (s, 4H, H^1), 9.55 (d, ^3J = 7.7, 4H, H^a), 9.46 (s, 4H, H^e), 9.41 (d, ^3J = 5.8, 4H, H^2), 8.63 (d, ^3J = 7.8, 4H, H^b), 8.36 (d, ^3J = 9.8, 4H, H^4), 8.21 (m, 16H, H^d, H^c, H$_7$), 7.92 (dd, ^3J = 7.1, ^4J = 2.5, 4H, H^3), 7.76 (d, ^3J = 9.1, 4H, H^6), 7.70 (dd, ^3J = 9.1, ^4J = 1.2, 4H, H^5), 4.00 (s, 12H, H^f).
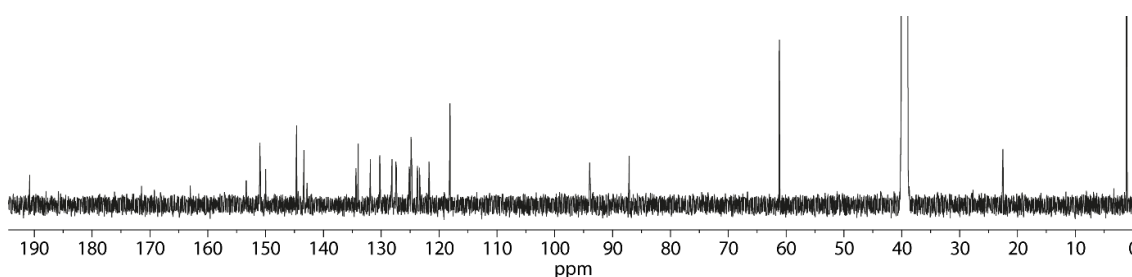
Figure 24: ^{13}C NMR spectrum (151 MHz, DMSO-d_6, 298 K) of [Pd$_2$L$^{F1}_2$L$^{P1}_2$].

^{13}C {^{1}H} NMR (150 MHz, DMSO-d_6, 298 K): δ = 190.8, 171.4, 163.1, 153.3, 151.0, 150.0, 144.7, 143.4, 142.8, 134.4, 134.0, 131.9, 130.3, 128.1, 127.5, 127.4, 125.2, 124.9, 124.7, 123.7, 123.4, 121.7, 118.1, 94.0, 87.1, 61.2.
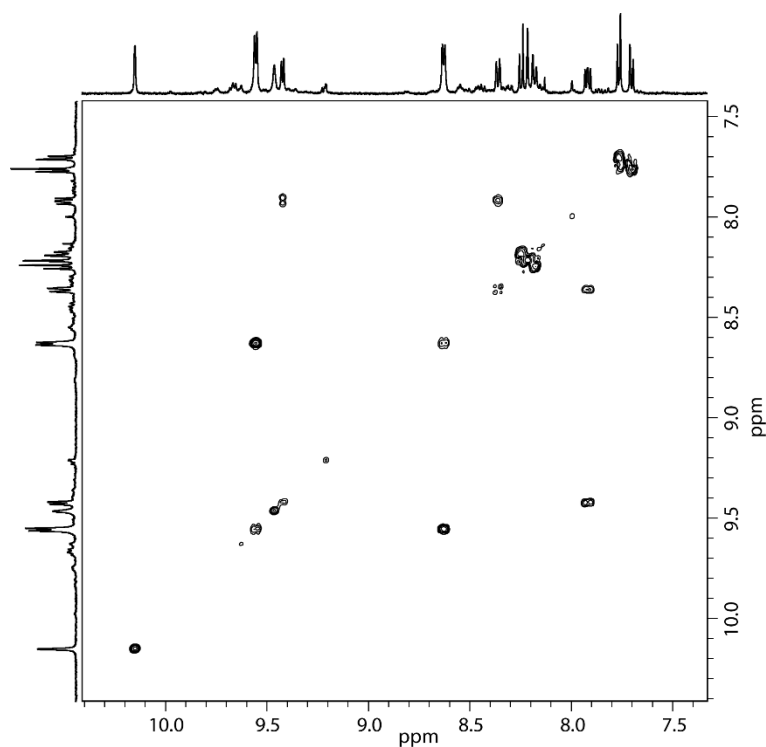
Figure 25: Partial ^{1}H−^{1}H COSY spectrum (600 MHz, DMSO-d_6, 298 K) of [Pd$_2$**L$^{F1}_2$L$^{P1}_2$**].

Synthesis of Pd$_2$**L$^{F1}_2$L$^{P2}_2$**

A solution of [Pd(CH$_3$CN)$_4$](BF$_4$)$_2$ (60 µL, 15 mM in DMSO-d_6) was combined with a suspension of **L^{P2}** (270 µL, 3.11 mM in DMSO-d_6) and a suspension of **L^{F1}** (270 µL, 3.11 mM in DMSO-d_6) and left to sit at room temperature for 2 h to afford [Pd$_2$**L$^{F1}_2$L$^{P2}_2$**] in quantitative yield.
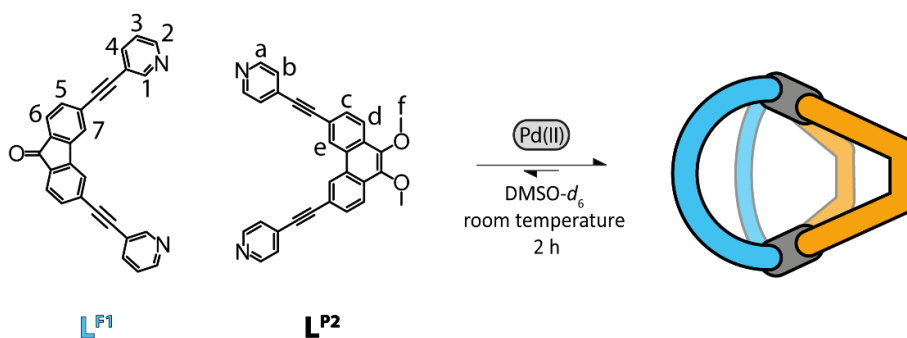
Scheme 3: Formation of Pd$_2$**L$^{F1}_2$L$^{P2}_2$** with consecutive proton labels.
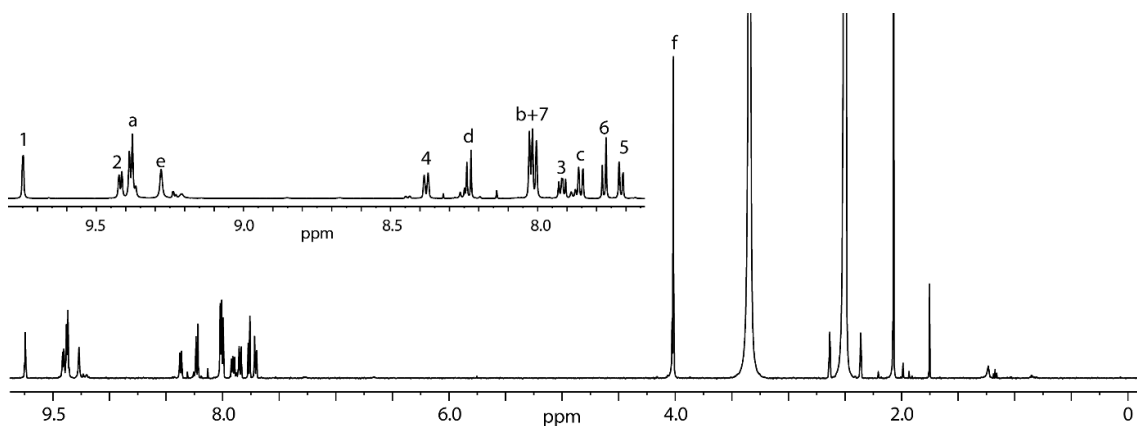
Figure 26: ^{1}H NMR spectrum (600 MHz, DMSO-d_6, 298 K) of [Pd$_2$**L**$^{F1}_2$**L**$^{P2}_2$] including a zoom in the aromatic region.

^{1}H NMR (600 MHz, DMSO-d_6, 298 K): δ = 9.74 (d, ^4J = 1.3, 4H, H^1), 9.41 (d, ^3J = 5.3, 4H, H^2), 9.37 (d, ^3J = 6.7, 4H, H^a), 9.27 (s, 4H, H^e), 8.37 (d, ^3J = 9.7, 4H, H^4), 8.22 (d, ^3J = 10.2, 4H, H^d), 8.00 (m, 12H, H^b, H^7), 7.90 (dd, ^3J = 6.9, ^4J = 2.4, 4H, H^3), 7.84 (dd, ^3J = 10.4, ^4J = 1.3, 4H, H^c), 7.76 (d, ^3J = 9.3, 4H, H^6), 7.70 (dd, ^3J = 9.1, ^4J = 1.3, 4H, H^5), 4.02 (s, 12H, H^f).
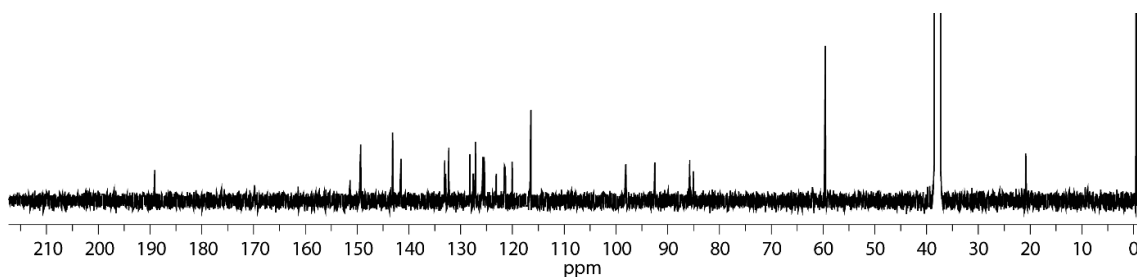
Figure 27: ^{13}C NMR spectrum (151 MHz, DMSO-d_6, 298 K) of [Pd$_2$**L**$^{F1}_2$**L**$^{P2}_2$].

^{13}C{^{1}H} NMR (150 MHz, DMSO-d_6, 298 K): δ = 189.1, 151.4, 149.3, 143.2, 141.7, 141.5, 133.1, 132.9, 132.3, 128.2, 128.1, 127.6, 127.2, 125.8, 125.7, 125.6, 123.1, 121.5, 121.3, 120.1, 116.6, 116.4, 98.1, 92.5, 85.8, 85.1, 59.6.
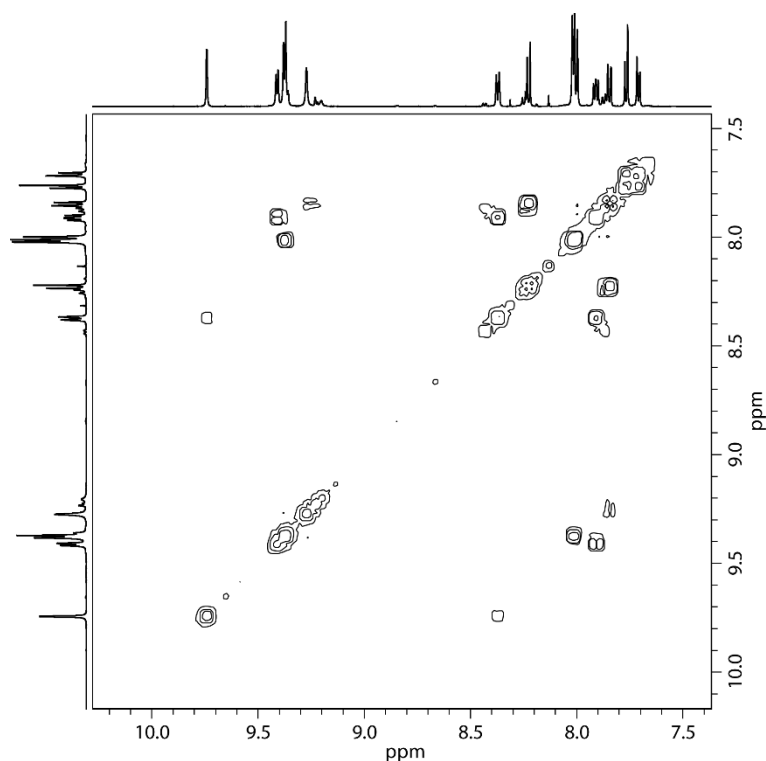
Figure 28: Partial ^{1}H−^{1}H COSY spectrum (600 MHz, DMSO-d_6, 298 K) of [Pd$_2$L$^{F1}_2$L$^{P2}_2$].

Synthesis of Pd$_2$L$^{C1}_2$L$^{P1}_2$

Synthesis and characterization of [Pd$_2$L$^{C1}_2$L$^{P1}_2$] has been previously described in CD$_3$CN.[64]

Synthesis of Pd$_2$L$^{C1}_2$L$^{P2}_2$

Synthesis and characterization of [Pd$_2$L$^{C1}_2$L$^{P2}_2$] has been previously described in CD$_3$CN.[109]

Setup of three-component Mixtures

A solution of [Pd(CH$_3$CN)$_4$](BF$_4$)$_2$ (60 µL, 15 mM in DMSO-d_6) was combined with L^{P1} (135 µL, 2.8 mM in DMSO-d_6) L^{P2} (135 µL, 2.8 mM in DMSO-d_6) and L^{F1} (270 µL, 2.8 mM in DMSO-d_6) at room temperature for 2 h to afford a mixture of [Pd$_2$L$^{F1}_2$L$^{P1}_2$], [Pd$_2$L$^{F1}_2$L^{P1}L^{P2}] and [Pd$_2$L$^{F1}_2$L$^{P2}_2$].

A solution of [Pd(CH$_3$CN)$_4$](BF$_4$)$_2$ (60 µL, 15 mM in CD$_3$CN) was combined with L^{P1} (135 µL, 2.8 mM in CD$_3$CN) L^{P2} (135 µL, 2.8 mM in CD$_3$CN) and L^{C1} (270 µL, 2.8 mM in CD$_3$CN) and heated at 70°C for 5 h to afford a mixture of [Pd$_2$L$^{C1}_2$L$^{P1}_2$], [Pd$_2$L$^{C1}_2$L^{P1}L^{P2}] and [Pd$_2$L$^{C1}_2$L$^{P2}_2$].

3.1.5.3 Special NMR Measurements
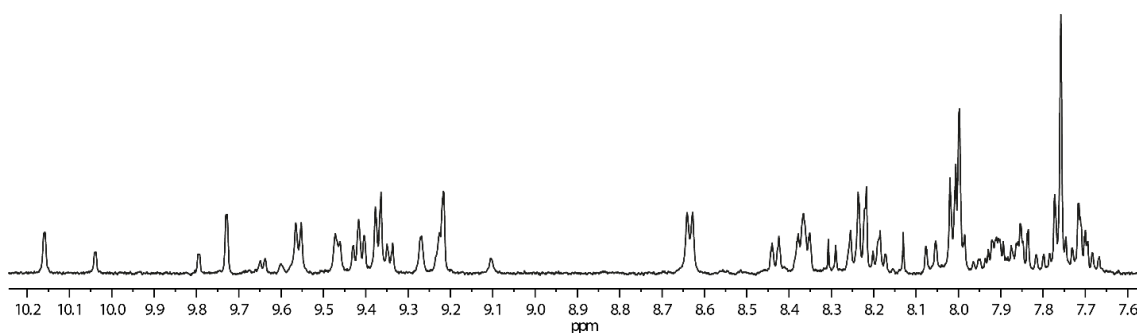
Figure 29: Partial ^{1}H NMR spectrum (500 MHz, DMSO-d_6, 298 K) of a mixture of [Pd$_2$L$^{F1}_2$L$^{P1}_2$], [Pd$_2$L$^{F1}_2$L^{P1}L^{P2}] and [Pd$_2$L$^{F1}_2$L$^{P2}_2$]. The ratio of the three species (calculated from the relative ^{1}H signals corresponding to each structure) equals approximately 1:1:1.
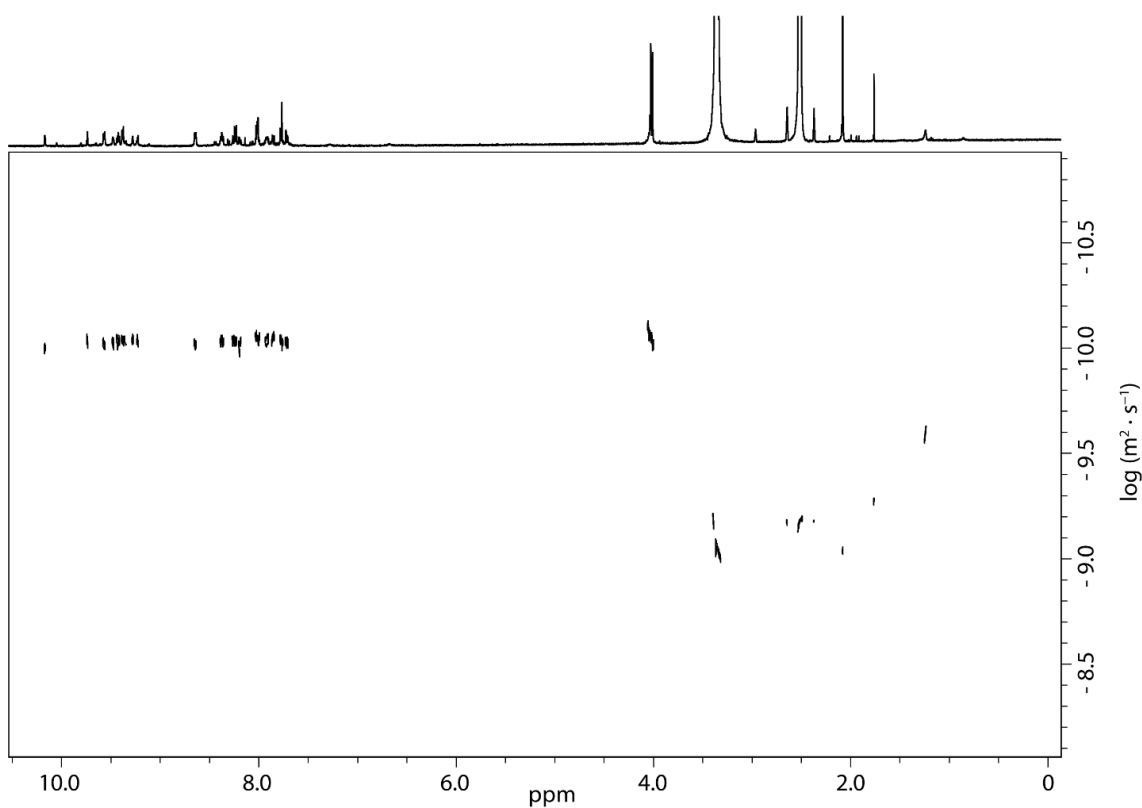
Figure 30: ^{1}H DOSY NMR spectrum (500 MHz, DMSO-d_6, 298 K) of a mixture of [Pd$_2$L$^{F1}_2$L$^{P1}_2$], [Pd$_2$L$^{F1}_2$L^{P1}L^{P2}] and [Pd$_2$L$^{F1}_2$L$^{P2}_2$].
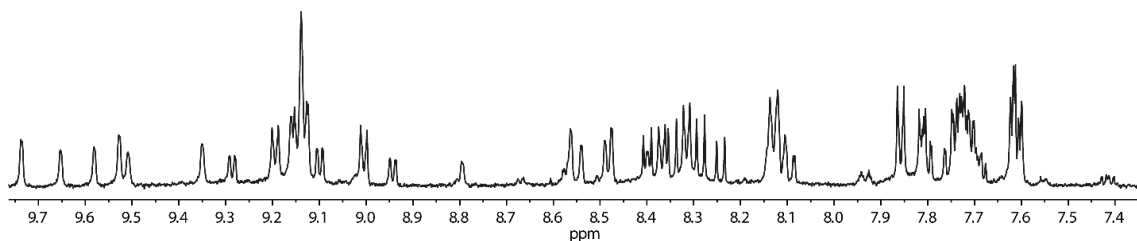
Figure 31: Partial ^{1}H NMR spectrum (500 MHz, CD$_3$CN, 298 K) of a mixture of [Pd$_2$L$^{C1}_2$L$^{P1}_2$], [Pd$_2$L$^{C1}_2$L^{P1}L^{P2}] and [Pd$_2$L$^{C1}_2$L$^{P2}_2$]. The ratio of the three species (calculated from the relative ^{1}H signals corresponding to each structure) equals approximately 1:2:1.
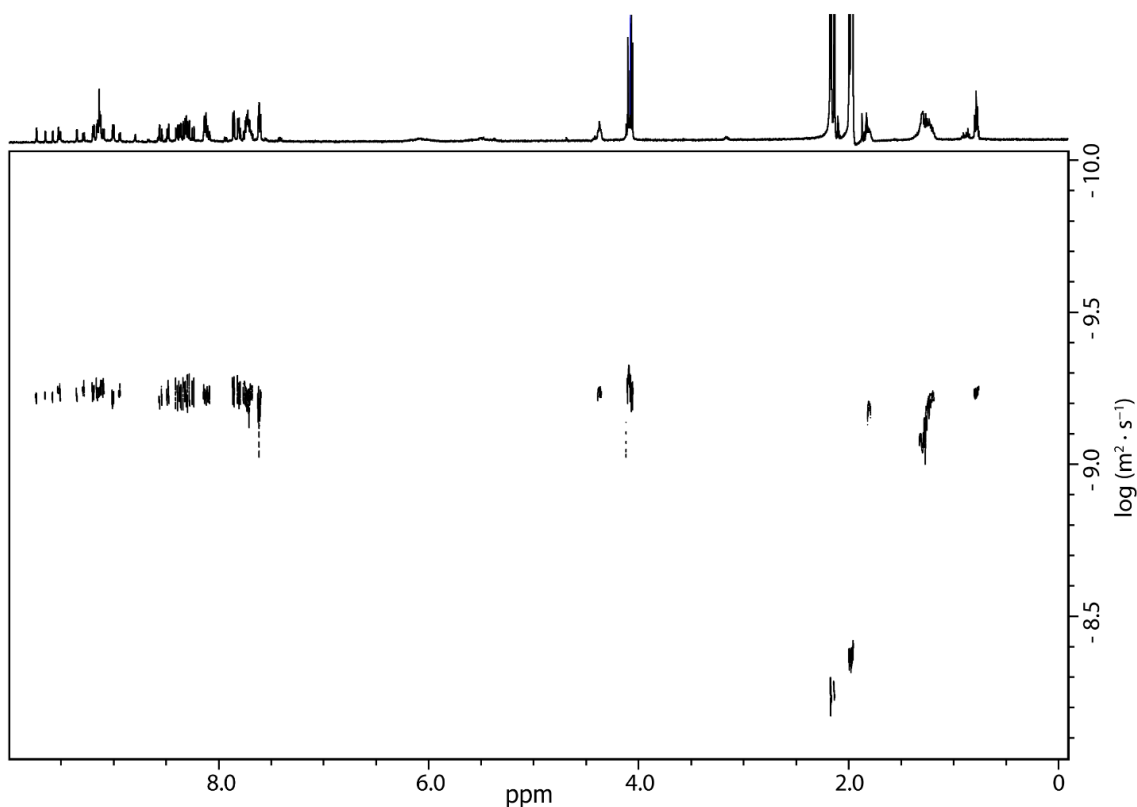
Figure 32: ^{1}H DOSY NMR spectrum (500 MHz, CD$_3$CN, 298 K) of a mixture of [Pd$_2$L^{C1}$_2$L^{P1}$_2$], [Pd$_2$L^{C1}$_2$L^{P1}L^{P2}] and [Pd$_2$L^{C1}$_2$L^{P2}$_2$].

3.1.5.4 ESI-MS

Pd$_2$L^{F1}$_2$L^{P1}$_2$
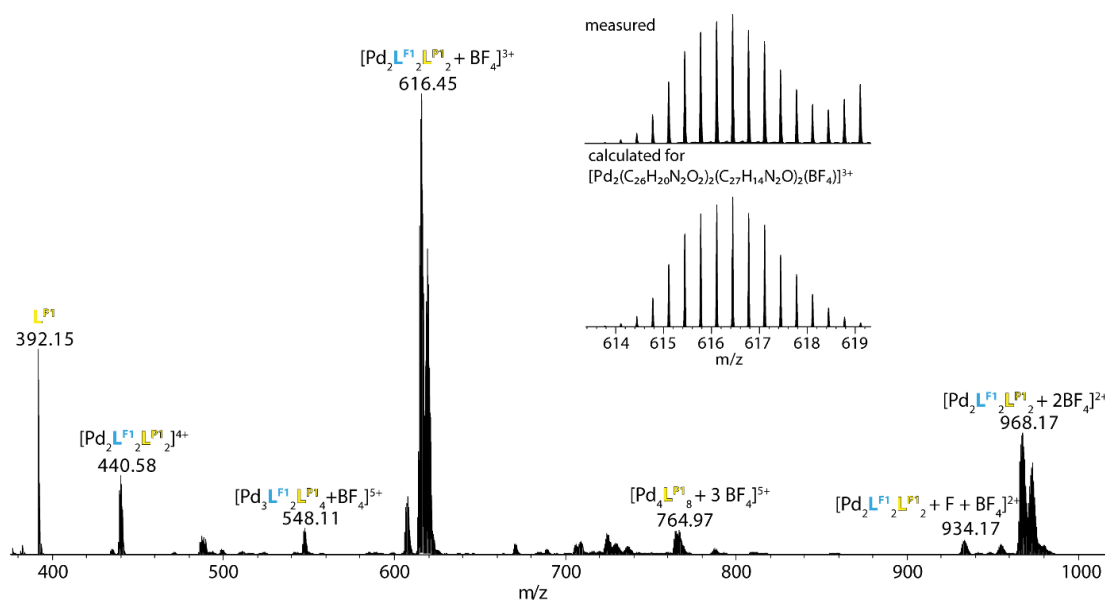
Figure 33: ESI-MS spectrum of [Pd$_2$L^{F1}$_2$L^{P1}$_2$]. The calculated patterns for [Pd$_2$L^{F1}$_2$L^{P1}$_2$ + BF$_4$]$^{3+}$ is shown in the inset.
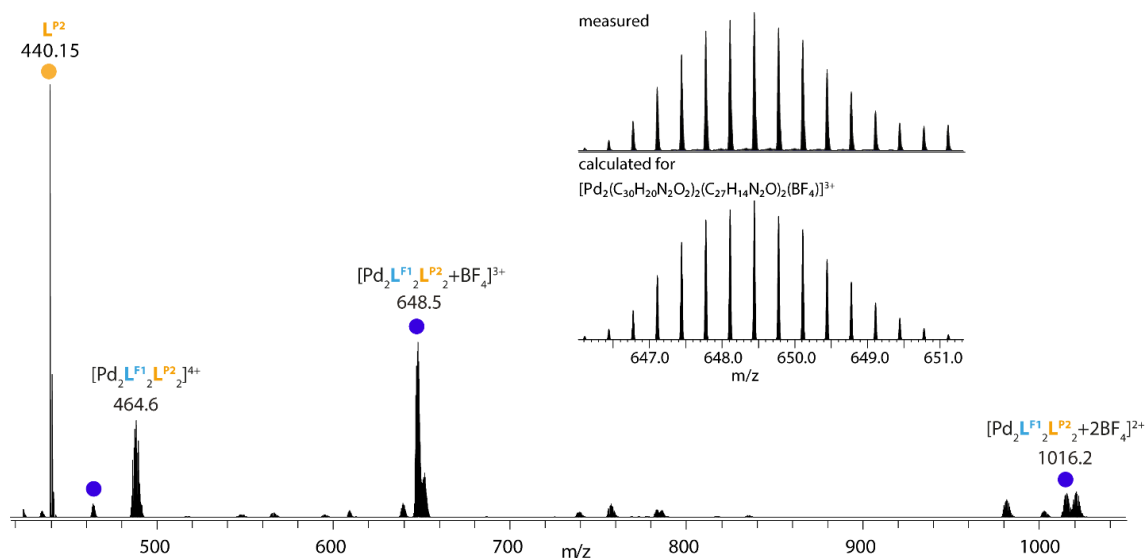
Pd$_2$**L$^{F1}_2$L$^{P2}_2$**

Figure 34: ESI-MS spectrum of [Pd$_2$**L$^{F1}_2$L$^{P2}_2$**]. The calculated patterns for [Pd$_2$**L$^{F1}_2$L$^{P2}_2$** + BF$_4$]$^{3+}$ is shown in the inset.

Mixture of [Pd$_2$**L$^{F1}_2$L$^{P1}_2$**] [Pd$_2$**L$^{F1}_2$L^{P1}L^{P2}**] and [Pd$_2$**L$^{F1}_2$L$^{P2}_2$**]
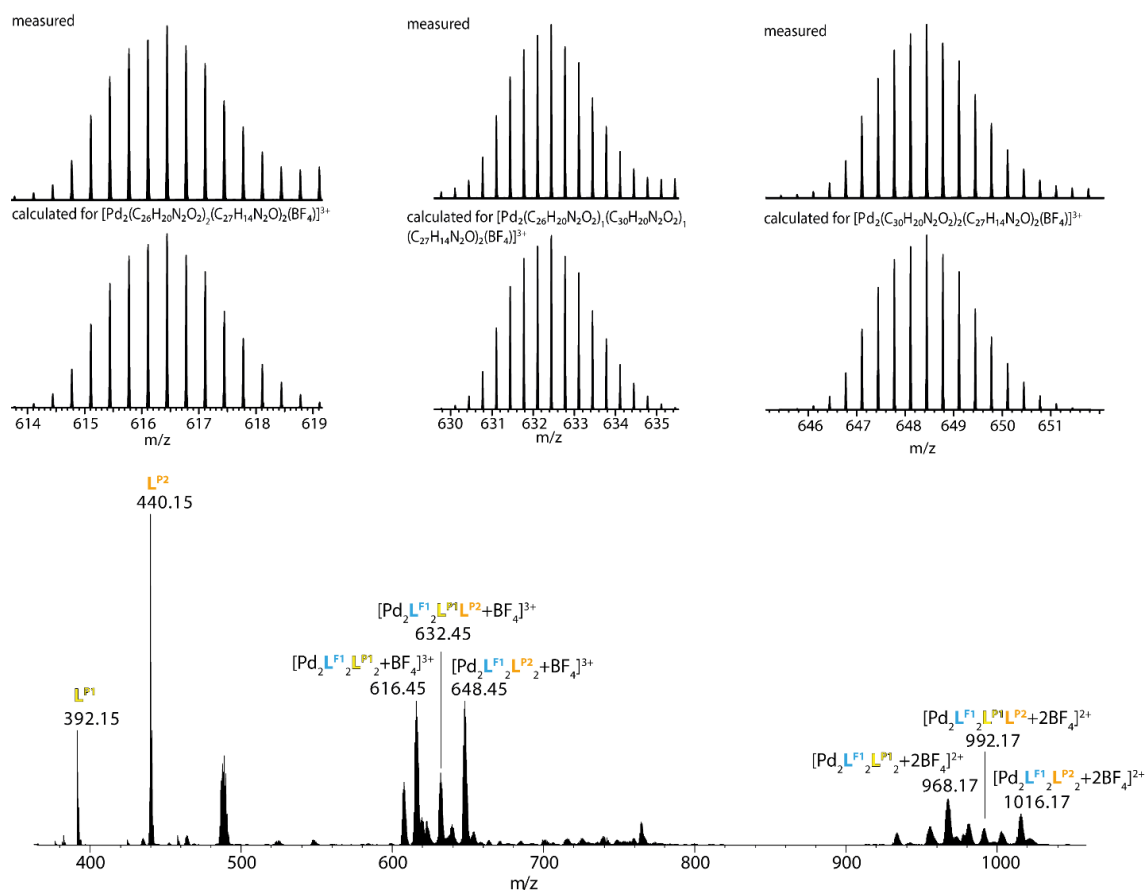
Figure 35: ESI-MS spectrum of a mixture of [Pd$_2$**L$^{F1}_2$L$^{P1}_2$**], [Pd$_2$**L$^{F1}_2$L^{P1}L^{P2}**] and [Pd$_2$**L$^{F1}_2$L$^{P2}_2$**]. The calculated patterns for [Pd$_2$**L$^{F1}_2$L$^{P1}_2$** + BF$_4$]$^{3+}$, [Pd$_2$**L$^{F1}_2$L^{P1}L^{P2}** + BF$_4$]$^{3+}$ and [Pd$_2$**L$^{F1}_2$L$^{P2}_2$** + BF$_4$]$^{3+}$ are shown in the insets.

Mixture [Pd$_2$**L$^{C1}_2$L$^{P1}_2$**] [Pd$_2$**L$^{C1}_2$L^{P1}L^{P2}**] and [Pd$_2$**L$^{C1}_2$L$^{P2}_2$**]
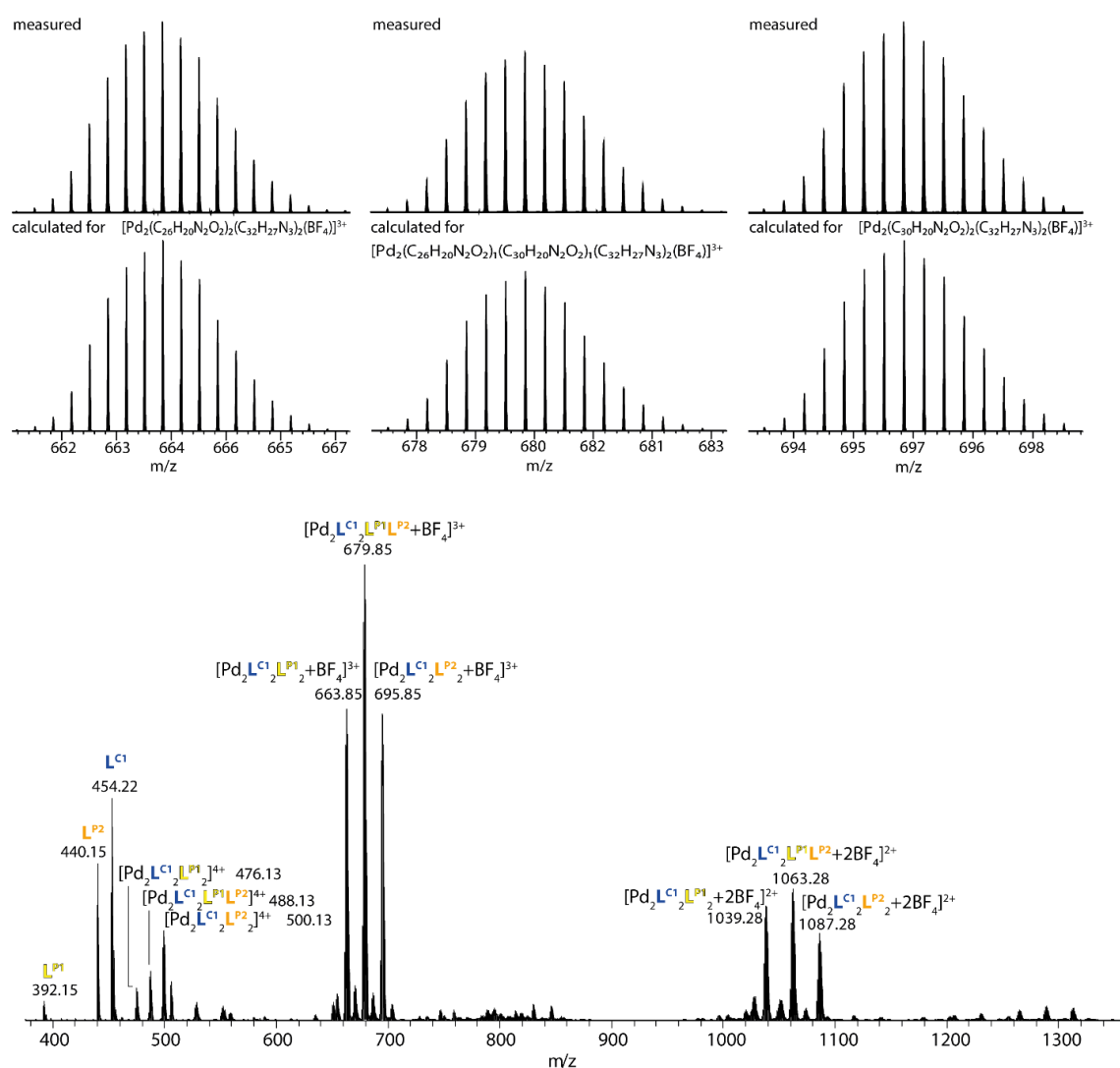
Figure 36: ESI-MS spectrum of mixture of [Pd$_2$**L$^{C1}_2$L$^{P1}_2$**], [Pd$_2$**L$^{C1}_2$L^{P1}L^{P2}**] and [Pd$_2$**L$^{C1}_2$L$^{P2}_2$**]. The calculated patterns for [Pd$_2$**L$^{C1}_2$L$^{P1}_2$** + BF$_4$]$^{3+}$, [Pd$_2$**L$^{C1}_2$L^{P1}L^{P2}** + BF$_4$]$^{3+}$ and [Pd$_2$**L$^{C1}_2$L$^{P2}_2$** + BF$_4$]$^{3+}$ are shown in the insets.

Mixture of all six heteroleptic cages
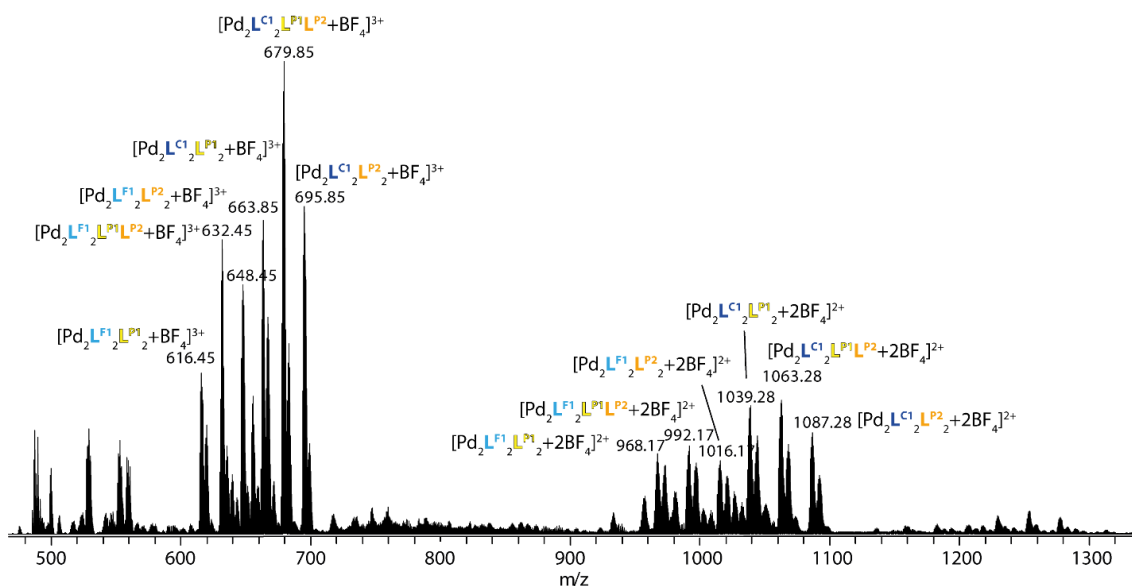
Figure 37: Total ESI-MS spectrum of mixture of [$Pd_2L^{F1}_2L^{P1}_2$], [$Pd_2L^{F1}_2L^{P1}L^{P2}$], [$Pd_2L^{F1}_2L^{P2}_2$] and [$Pd_2L^{C1}_2L^{P1}_2$], [$Pd_2L^{C1}_2L^{P1}L^{P2}$], [$Pd_2L^{C1}_2L^{P2}_2$]. The multitude of peaks arises due to the respective cage species with a combination of different counter anions (F^-, NO_3^-, BF_4^-). A zoom into the region from m/z = 610-705 can be found in the main text (Figure 14).

3.1.5.5 Ion Mobility Measurements

Ion mobility measurements were performed on a Bruker timsTOF instrument combining a trapped ion mobility (TIMS) with a time-of-flight (TOF) mass spectrometer in one instrument. In contrast to the conventional drift tube method to determine mobility data, where ions are carried by an electric field through a stationary drift gas, the TIMS method is based on an electric field ramp to hold ions in place against a carrier gas pushing them in the direction of the analyzer. Consequently, larger sized ions that experience more carrier gas impacts leave the TIMS units first and smaller ions elute later. This method offers a much higher mobility resolution despite a smaller device size.

Measurement: After the ion generation by electrospray ionization (ESI, conditions see Table 3) the desired ions were orthogonally deflected into the TIMS cell consisting of an entrance funnel, the TIMS analyzer (carrier gas: N_2, conditions see Table 3). As a result, the ions are stationary trapped. After accumulation (accumulation time see below), a stepwise reduction of the electric field strength leads to a release of ion packages separated by their mobility. After a subsequent focusing, the separated ions are transferred to the TOF-analyzer.[106,118,119]

The ion mobility K was directly calculated from the trapping electric field strength E and the velocity of the carrier gas stream v_g via

$$K = \frac{v_g}{E} = \frac{A}{U_{release} - U_{out}} \tag{2}$$

where A is a calibration constant (based on calibration standards), $U_{release}$ is the voltage at which the ions are released from the analyzer and U_{out} is the voltage applied to the exit of the tube. The ion mobility is corrected to standard gas density *via*

$$K_0 = K \frac{P}{1013 \text{ hPa}} \frac{273 \text{ K}}{T} \tag{3}$$

to obtain the reduced mobility K_0, where P is the pressure and T is the temperature. By using the Mason-Schamp equation, the collisional cross-section Ω (eCCS) can be calculated:

$$\Omega = \frac{(18\pi)^{\frac{1}{2}}}{16} \frac{ze}{(k_B T)^{\frac{1}{2}}} \left[\frac{1}{\mu}\right]^{\frac{1}{2}} \frac{1}{K_0} \frac{1}{N_0} \tag{4}$$

where ze is the ion charge, k_B is the Boltzmann constant, μ is the reduced mass of analyte and carrier gas and N_0 is the number density of the neutral gas.[106,118,119]

For calibration of both the TIMS and TOF analyzers, commercially available Agilent ESI tune mix was used (https://www.agilent.com/cs/library/certificateofanalysis/G1969-85000cofa872022-U-LB86189.pdf). The instrument was calibrated before each measurement, including each change in the ion mobility resolution mode ("imeX" settings: survey, detect or ultra).

M/z peaks of species that can be compared (3+ peaks of cages containing one BF_4^- counter anion) were picked in the mass traces and the respective ion mobility was isolated and is shown in the mobilograms depicted in this paper. All mobilograms were smoothened using the Savitzky-Golay method with a factor of 0.005 with exception of the high-resolution measurement of the isomeric cage (smoothened by factor 0.003).

Table 3: Ion Mobility measurement conditions for each experiment.

Measurement	Solvent	capillary voltage	end plate offset voltage	nebulizer gas pressure	dry gas flow rate	dry temperature	carrier gas
Standard	DMSO/MeCN (1:20)	3600 V	500 V	0.3 bar	3.0 L/min	200 °C	N_2
High Res. Isomer	DMSO/MeCN (1:20)	3500 V	500 V	0.3 bar	3.5 L/min	200 °C	N_2
	temperature TIMS	entrance pressure	exit pressure	IMS imeX ramp end	IMS imeX ramp start	accumulation time	IMS imeX mode
Standard	305 K	2.59 mbar	0.89 mbar	1.90 $1/K_0$	0.5 $1/K_0$	5.0 ms	Detect
High Res. Isomer	305 K	2.61 mbar	0.91 mbar	1.03 $1/K_0$	0.87 $1/K_0$	5.0 ms	Ultra

Entrance pressure in standard measurements raged from 2.57 – 2.61 mbar while exit pressure ranged from 0.89 – 0.91 mbar.

All samples were prepared and subsequently diluted 1:20 in a mixture of DMSO/MeCN and measured with the same IMS conditions to keep the results comparable. The measurements for the calculation of the error have been executed on different days with freshly diluted samples and injection of calibrant before or after the measurement.

Ion Mobility of $[Pd_2L^{F1}_2L^{P1}_2 + BF_4]^{3+}$

CCS: 539.0 Å^2
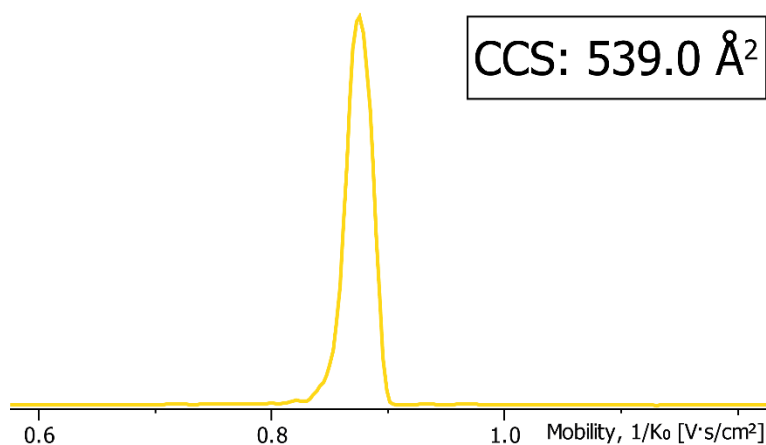
Figure 38: Ion Mobility spectrum of $[Pd_2L^{F1}_2L^{P1}_2 + BF_4]^{3+}$, from a clean solution of $Pd_2L^{F1}_2L^{P1}_2$ in DMSO-d_6.

Ion Mobility of $[Pd_2L^{F1}_2L^{P2}_2 + BF_4]^{3+}$

CCS: 570.6 Å^2
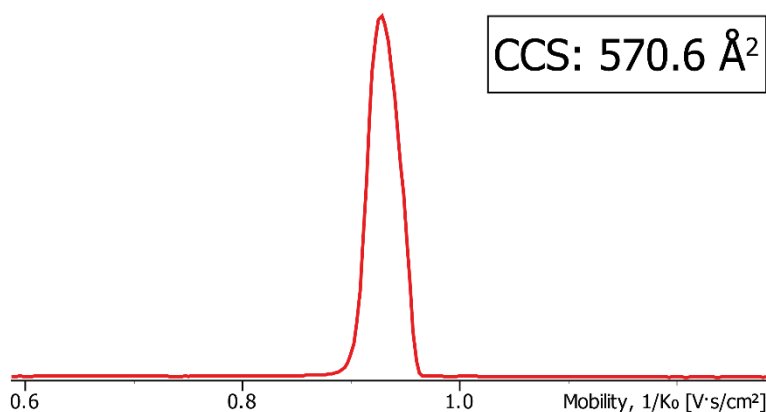
Figure 39: Ion Mobility spectrum of $[Pd_2L^{F1}_2L^{P2}_2 + BF_4]^{3+}$, from a clean solution of $Pd_2L^{F1}_2L^{P2}_2$ in DMSO-d_6.

Ion Mobility of $[Pd_2L^{C1}{}_2L^{P1}{}_2 + BF_4]^{3+}$
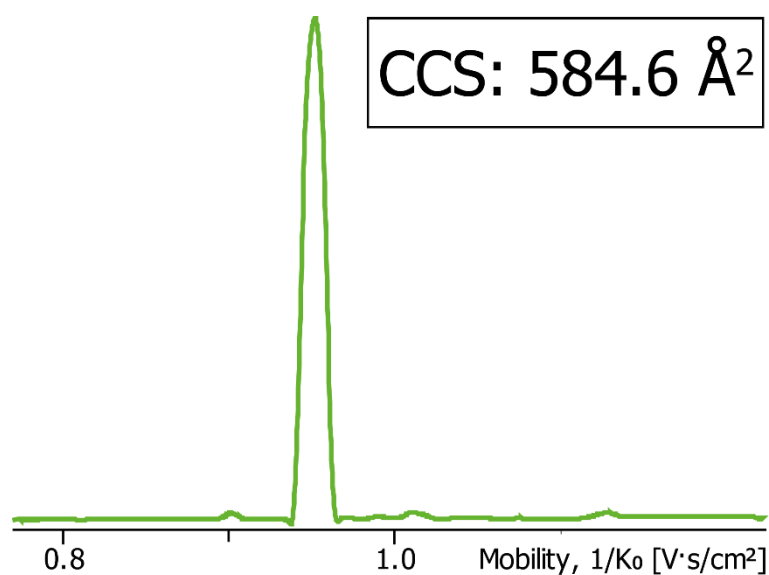
Figure 40: Ion Mobility spectrum of $[Pd_2L^{C1}{}_2L^{P1}{}_2 + BF_4]^{3+}$, from a clean solution of $Pd_2L^{C1}{}_2L^{P1}{}_2$ in CD_3CN.

Ion Mobility of $[Pd_2L^{C1}{}_2L^{P2}{}_2 + BF_4]^{3+}$
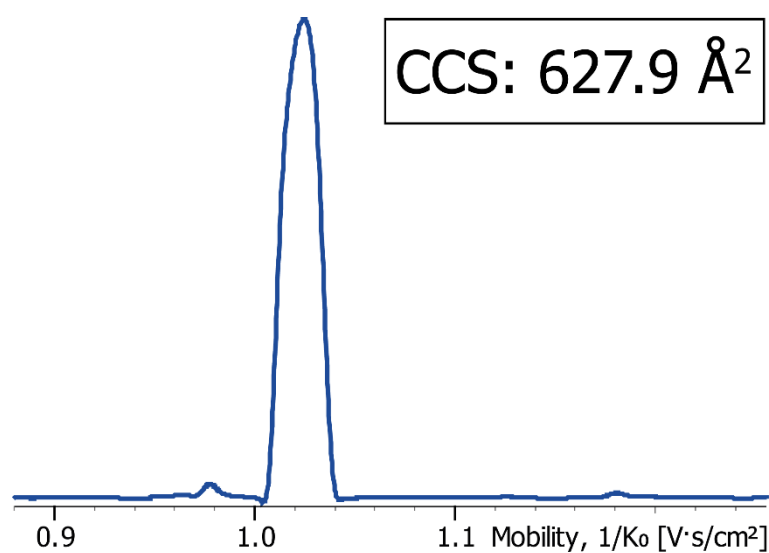
Figure 41: Ion Mobility spectrum of $[Pd_2L^{C1}{}_2L^{P2}{}_2 + BF_4]^{3+}$, from a clean solution of $Pd_2L^{C1}{}_2L^{P2}{}_2$ in CD_3CN.

<u>Ion Mobility of [Pd$_2$**L$^{F1}_2$L$^{P1}_2$** + BF$_4$]$^{3+}$, [Pd$_2$**L$^{F1}_2$L^{P1}L^{P2}** + BF$_4$]$^{3+}$and [Pd$_2$**L$^{F1}_2$L$^{P2}_2$** + BF$_4$]$^{3+}$ in a Mixture</u>
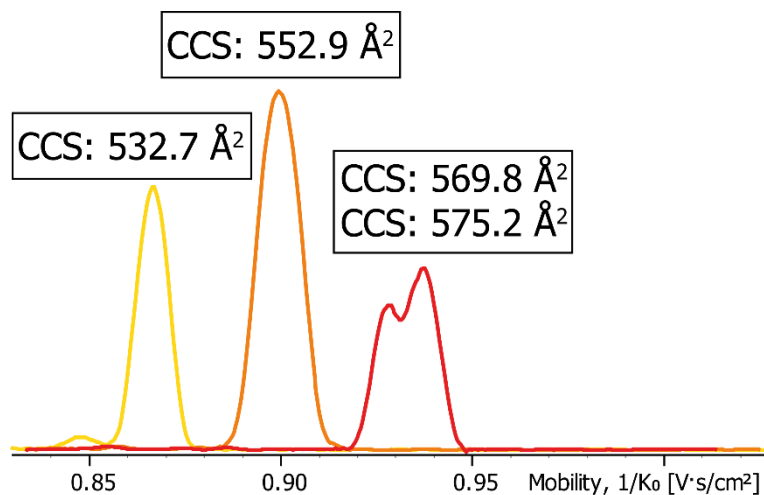
Figure 42: Ion Mobility spectrum of [Pd$_2$**L$^{F1}_2$L$^{P1}_2$** + BF$_4$]$^{3+}$, [Pd$_2$**L$^{F1}_2$L^{P1}L^{P2}** + BF$_4$]$^{3+}$ and [Pd$_2$**L$^{F1}_2$L$^{P2}_2$** + BF$_4$]$^{3+}$ measured from one sample.

<u>Ion Mobility of [Pd$_2$**L$^{C1}_2$L$^{P1}_2$** + BF$_4$]$^{3+}$, [Pd$_2$**L$^{C1}_2$L^{P1}L^{P2}** + BF$_4$]$^{3+}$and [Pd$_2$**L$^{C1}_2$L$^{P2}_2$** + BF$_4$]$^{3+}$ in a Mixture</u>
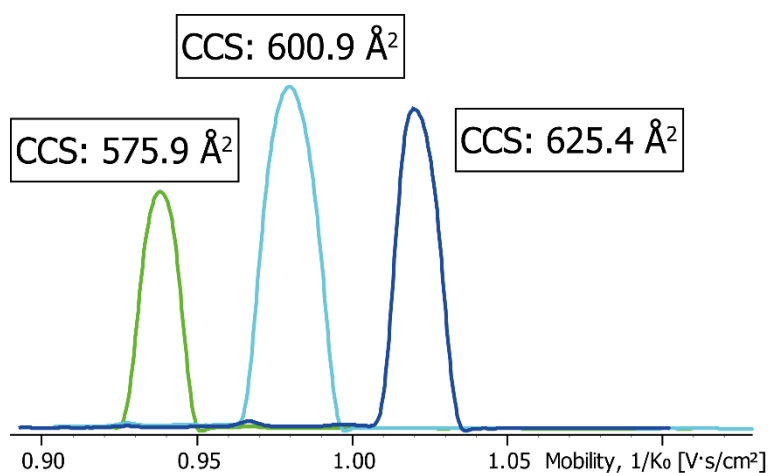
Figure 43: Ion Mobility spectrum of [Pd$_2$**L$^{C1}_2$L$^{P1}_2$** + BF$_4$]$^{3+}$, [Pd$_2$**L$^{C1}_2$L^{P1}L^{P2}** + BF$_4$]$^{3+}$ and [Pd$_2$**L$^{C1}_2$L$^{P2}_2$** + BF$_4$]$^{3+}$ measured from one sample.

Ion Mobility of a mixture containing all six cages

CCS: 529.4 Å²   CCS: 550.2 Å²   CCS: 567.9 Å²   CCS: 578.2 Å²   CCS: 599.9 Å²   CCS: 619.9 Å²
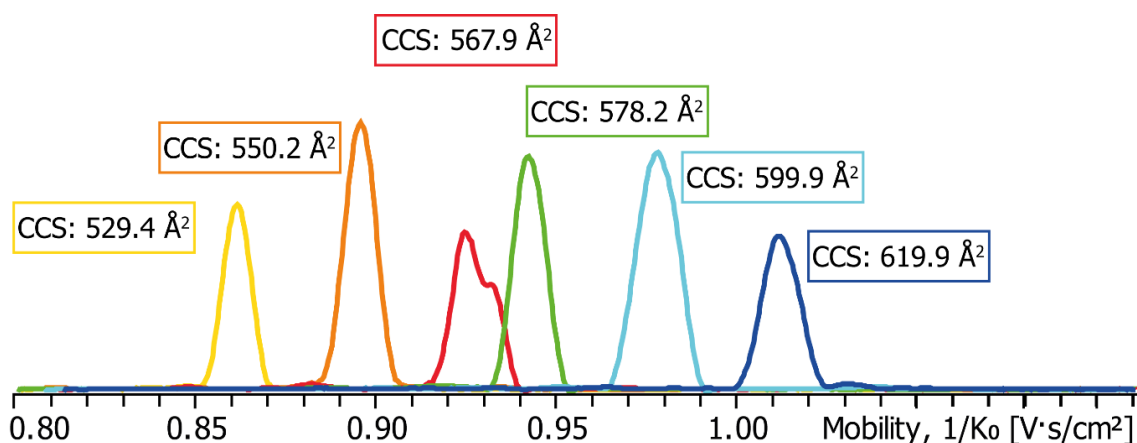
Figure 44: Ion Mobility spectrum of $[Pd_2L^{F1}_2L^{P1}_2 + BF_4]^{3+}$, $[Pd_2L^{F1}_2L^{P1}L^{P2} + BF_4]^{3+}$, $[Pd_2L^{F1}_2L^{P2}_2 + BF_4]^{3+}$ and $[Pd_2L^{C1}_2L^{P1}_2 + BF_4]^{3+}$, $[Pd_2L^{C1}_2L^{P1}L^{P2} + BF_4]^{3+}$, $[Pd_2L^{C1}_2L^{P2}_2 + BF_4]^{3+}$ from one single mixture.

CCS Determination – Error and molecular radius from eCCS values

The error for the experimental CCS values has been calculated from all measurements for each species as it is given in **Table 4**. To validate the values, the ten-cage system has been measured five times on different days with a freshly prepared dilution of the sample. Measurements for the single cage systems and three cage systems have been included into the error calculation.

Table 4: Data achieved from measuring the collisional cross section (CCS) of the different systems. Measurement 1-5 ($M1_{10}$-$M5_{10}$) includes all ten cages, the system containing three cages (TCM) and the single cage measurements (SCM). Mean value and standard deviation (SD) are given.

Species	$M1_{10}$ CCS [Å²]	$M2_{10}$ CCS [Å²]	$M3_{10}$ CCS [Å²]	$M4_{10}$ CCS [Å²]	$M5_{10}$ CCS [Å²]	TCM CCS [Å²]	SCM CCS [Å²]	Mean CCS [Å²]	SD CCS [Å²]
$[Pd_2L^{F1}_2L^{P1}_2]$	526.5	525.5	526.9	526.3	525.9	527.6	526.0	526.3	0.7
$[Pd_2L^{F1}_2L^{P1}L^{P2}]$	547.9	548.4	548.7	547.8	547.4	547.3		547.9	0.5
$[Pd_2L^{F1}_2L^{P2}_2]$	566.8	565.4	567.0	565.9	565.7	569.1	566.1	566.1	1.3
$[Pd_2L^{C1}L^{F1}L^{P1}_2 + BF_4]^{3+}$	544.1	543.8	544.5	543.7	543.5			543.8	0.4
a) $[Pd_2L^{C1}L^{F1}L^{P1}L^{P2} + BF_4]^{3+}$	564.1	561.6	564.0	562.9	562.7			562.9	1.0
b) $[Pd_2L^{C1}L^{F1}L^{P1}L^{P2} + BF_4]^{3+}$	568.6	567.2	568.6	567.2	566.9			567.2	0.8
$[Pd_2L^{C1}L^{F1}L^{P2}_2 + BF_4]^{3+}$	587.2	585.9	587.8	587.2	586.9			587.2	0.7
$[Pd_2L^{C1}_2L^{P1}_2]$	576.3	574.7	576.5	575.6	575.2	574.8	573.4	575.2	1.1
$[Pd_2L^{C1}_2L^{P1}L^{P2}]$	598.6	596.7	598.8	597.7	597.2	599.2		598.2	1.0
$[Pd_2L^{C1}_2L^{P2}_2]$	620.2	616.8	619.9	619.1	618.9	619.2	617.9	619.1	1.2

The formula for a system containing two colliding molecules with different radii (here: cage and collision gas N_2) is given in equation 1 (see main text):[111]

For scattering events in the gas phase, the radius taken into consideration is the kinetic radius determining the size of the sphere of influence of the molecule in question.[110] For the diatomic nitrogen molecule, this radius is given as $r(N_2) = 1.82$ Å[112] derived from its kinetic diameter. The averaged radii of all species calculated based on equation 1 can be found in Table 4.

3.1.5.6 Calculation of theoretical CCS values (tCCS)

In order to obtain refined theoretically determined collisional cross sections three different programs, MOBCAL,[115,116] and IMoS[113,114] were used. With MOBCAL the trajectory method, which consists of a simulation of the interaction of the analyte with the collision gas, was chosen. With IMoS a different method, the projected area method averaging the projected 2D area according to Van der Waals radii (using the correction factor $\xi = 1.2$), was used. In preparation for the CCS calculations, we used PM6 as a method for geometry optimization. This way, for each cage, two values (tCCS^{PA} and tCCS^{M}) were obtained. Interestingly, MOBCAL and IMoS are able to reproduce the experimentally observed, gradual CCS increase from $[Pd_2L^{F1}_2L^{P1}_2 + BF_4]^{3+}$ to $[Pd_2L^{C1}_2L^{P2}_2 + BF_4]^{3+}$ quite well (with MOBCAL values in average about 6% overestimated, IMoS values about 2% underestimated) (see Figure 18, main text).

Table 5: Comparison of experimental (eCCS) values with results derived from softwares MOBCAL (tCCS^{M}) and IMoS (tCCS^{PA}) based on the GFN-xTB optimized models with one encapsulated BF_4^- counter anion.

Species	eCCS [Å^2]	tCCS^{PA} [Å^2]	tCCS^{M} [Å^2]
$[Pd_2L^{F1}_2L^{P1}_2 + BF_4]^{3+}$	526.3 ± 0.7	491.0	540.8
$[Pd_2L^{F1}_2L^{P1}L^{P2} + BF_4]^{3+}$	547.9 ± 0.5	515.1	566.9
$[Pd_2L^{F1}_2L^{P2}_2 + BF_4]^{3+}$	566.1 ± 1.3	543.7	600.4
$[Pd_2L^{C1}L^{F1}L^{P1}_2 + BF_4]^{3+}$	543.8 ± 0.4	526.1	572.9
a) $[Pd_2L^{C1}L^{F1}L^{P1}L^{P2} + BF_4]^{3+}$	562.9 ± 1.0	553.7	601.8
b) $[Pd_2L^{C1}L^{F1}L^{P1}L^{P2} + BF_4]^{3+}$	567.2 ± 0.8	556.6	602.6
$[Pd_2L^{C1}L^{F1}L^{P2}_2 + BF_4]^{3+}$	587.2 ± 0.7	581.7	630.6
$[Pd_2L^{C1}_2L^{P1}_2 + BF_4]^{3+}$	575.2 ± 1.1	565.7	611.9
$[Pd_2L^{C1}_2L^{P1}L^{P2} + BF_4]^{3+}$	598.2 ± 1.0	591.1	633.8
$[Pd_2L^{C1}_2L^{P2}_2 + BF_4]^{3+}$	619.1 ± 1.2	616.7	664.8

3.2 Bent Cages – An introduction to systems chemistry and stimuli-controlled cage transformations

3.2.1 Introduction

The previous chapter 3.1 explored a valuable method to analyze complex, yet semi-statistical mixtures using ion-mobility mass spectrometry. However, to evaluate the properties of a system and gain insight into its structure-activity relationship, it is often crucial to achieve controlled formation of a defined structure. Over the course of recent years, a plethora of coordination assemblies have been published yielding a wide scope of structural and functional diversity. The formation of these assemblies often relies on a dynamic metal-ligand bond which provides the system with the ability of self-correction and further enables the prospect of systems chemistry. One aspect of the aforementioned is the ability of a certain system to change upon applying a certain stimulus. The supramolecular system can hereby be subjected to a multitude of possible triggers and undergoes one or more transformations. A summary of possible system transformations is given below in Figure 45.
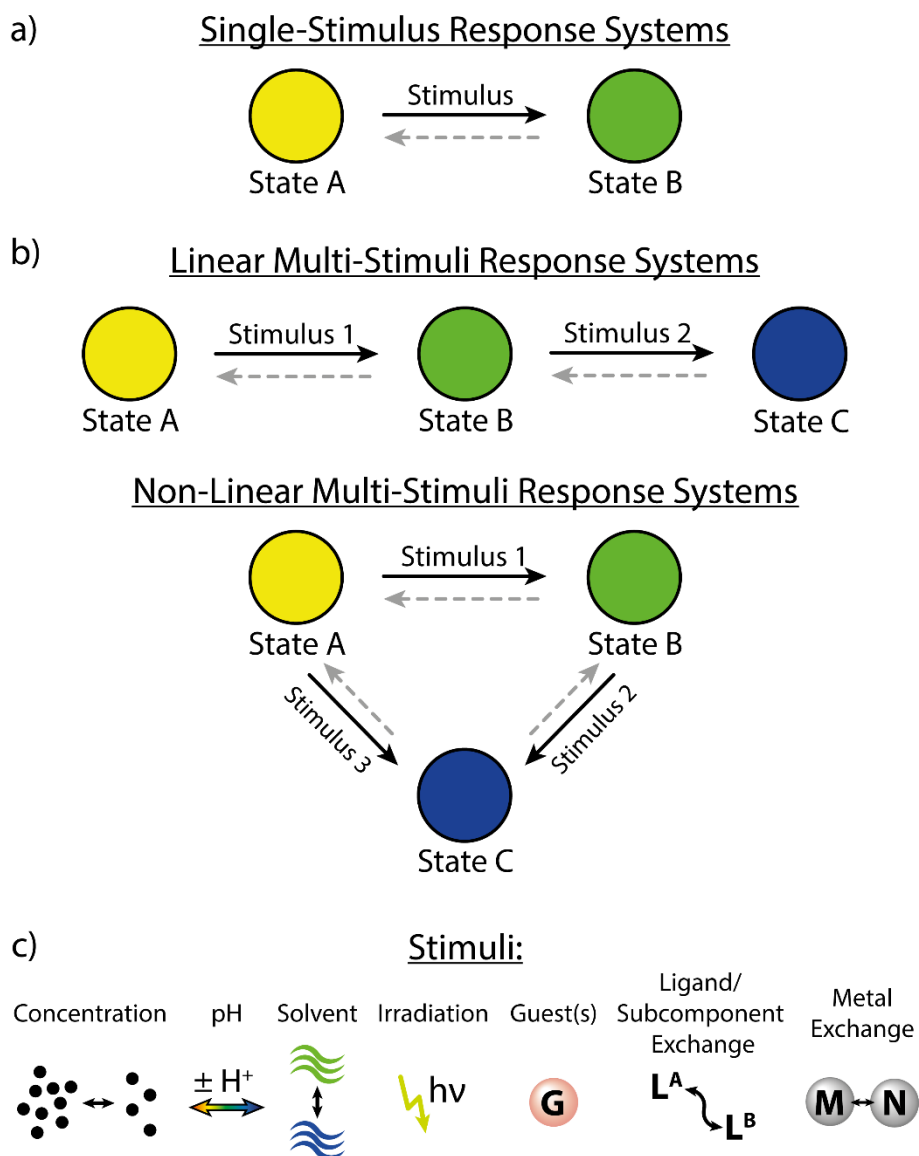
Figure 45: Schematic representation of stimuli responsiveness in systems chemistry with a) a single stimulus being applied and b) a representation of either linear or non-linear multi-stimuli systems; c) shows the most commonly used stimuli applied in systems chemistry on coordination assemblies.

The simplest transformation is given in Figure 45 a) being the change of a system in state **A** upon introduction of a certain stimulus to state **B**. This transformation can be reversible, as it is often the case for e.g. systems incorporating photo switches[50,70–72], or irreversible and end in a thermodynamic minimum or kinetic trap of the system. An extension of the simple systems chemistry approach from Figure 45 a) using only one stimulus is the further transformation of the system using a second, or even more stimuli accessing diverse structural outcomes thereby. Multi-stimuli responsive systems like these can be divided into two sub-classes, namely linear stimuli response systems, in which one transformation follows the other and the final outcome cannot be reached using other routes or shortcuts and non-linear stimuli response systems, in which the final structure can be reached using multiple routes or even allowing a wider array of

outcomes to be accessed (Figure 45 b). Researchers have published a wide variety of works utilizing certain stimuli to induce these transformations including changes in concentration[120–122], pH[123,124], solvent[63,121,125,126], irradiation[50,70–72], introduction of guest molecules[82,127–131] or templating anions[117,132–138], ligand[76,85,139,140] or subcomponent exchange[51,64,86] and metal exchange[141,142] (Figure 45 c).

The stimuli in these multi-stimuli system transformations can either be from the same family, as e.g. iterative ligand exchange as shown by BANDI et al. in 2016[143] as well as SAMANTA et al. in 2014[144], that lead to the formation of different Pd(II)-based architectures as well as another example provided by ZHANG et al. in 2017[49], in which different anions templated the size of the host-assembly via anion metathesis forming Pd(II) complexes with nuclearity ranging from n = 3-7. The other option is the utilization of stimuli, that differ in their nature as e.g. RIDDELL et al. in 2014[145] showed structural rearrangement of a ligand initially forming a Cd_2L_3-complex which is first subjected to structural rearrangement by means of anion templation, forming a Cd_8L_{12}-complex with ClO_4^- and a $Cd_{12}L_{18}$-complex in presence of AsF_6^-, followed by secondary transformations replacing Cd(II) with Fe(II). Further examples of system chemistry applications applying different stimuli are e.g. the group of NITSCHKE using concertation and bulky guest molecules (2022)[146], different subcomponents, metal equivalents and solvents (2019)[147] and post-assembly modification, subcomponent exchange and a templating anion (2018)[148].

As mentioned previously, most of these transformations lead to the formation of a final structure or host guest complex that is the thermodynamic minimum of the system, making further transformations hard to achieve. The exception here being photo-switchable systems and concentration-dependent ones, as well as some rarer examples of reversible transformations upon guest extraction[128,131]. The following chapter will explore a multi-stimuli responsive system using the solvent switching behavior of a heteroleptic coordination cage followed by guest induced post-assembly separation, extracting one ligand and the introduced guest in a clean, controlled fashion. This can perspectively be followed up by the re-formation of the heteroleptic cage by means of a cage-to-cage transformation in the original solvent system.

3.2.2 The system – A recap

Previous research[109] (and Chapter 3.1) showed, that the introduction of an alkyne linker into L^{P1} to form L^{P2} did not affect its feasibility in heteroleptic coordination cage formation with the exact same counter ligands as previously described for L^{P1}. Another known counter ligand for L^{P1}, that forms Pd(II) complexes is L^{A1}, based on an acridone backbone and equipped with isoquinoline donor-groups (see Scheme 4). Previous work[109] showed the successful formation of $Pd_2L^{A1}_2L^{P2}_2$ in DMSO-d_6. The reaction was set up mixing 270 µl of a 3.11 mM solution of L^{A1} in DMSO-d_6 and 270 µl of a 3.11 mM solution of L^{P2} in DMSO-d_6 with 60 µl of a 15 mM solution of $[Pd(CH_3CN)_4](BF_4)_2$ in a 5 mm standard NMR tube and either heated to 70°C for 10 minutes or let to rest at room temperature for 2h to afford $Pd_2L^{A1}_2L^{P2}_2$ (Scheme 4).
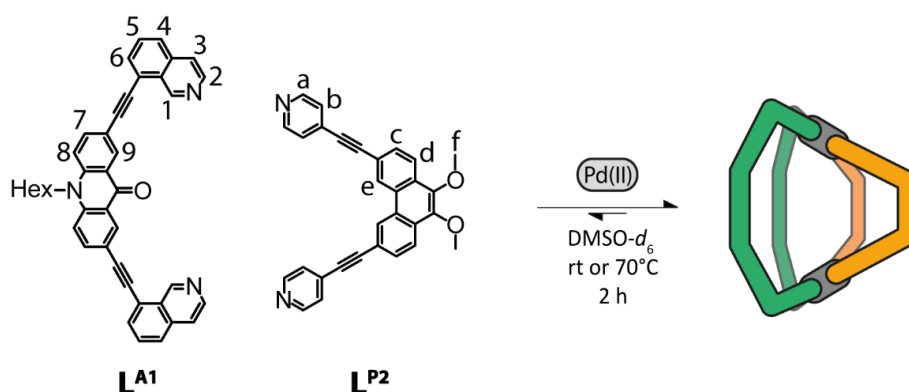
Scheme 4: Formation of $Pd_2L^{A1}_2L^{P2}_2$ with consecutive proton labels.

Figure 46 depicts the successful formation of a single species compared to the spectra of the free ligands L^{A1} and L^{P2} and the homoleptic species $Pd_2L^{A1}_4$ and $Pd_3L^{P2}_6$ in DMSO-d_6.
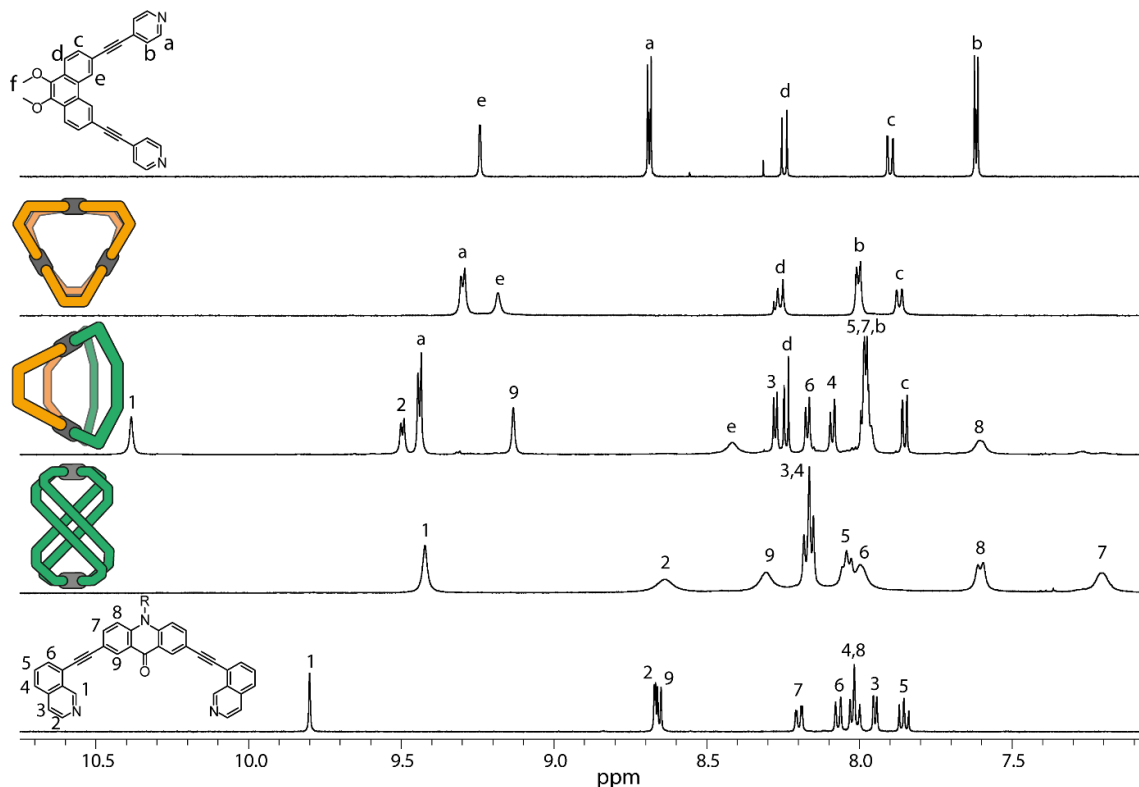
Figure 46: Partial stacked ^{1}H NMR spectra of (bottom to top) ligand $\mathbf{L^{A1}}$ (500 MHz, 298 K, DMSO-d_6), the corresponding homoleptic cage Pd$_2\mathbf{L^{A1}}_4$ (500 MHz, 298 K, DMSO-d_6) formed upon addition of 0.55 equiv. Pd(II) to ligand $\mathbf{L^{A1}}$, the heteroleptic assembly Pd$_2\mathbf{L^{A1}}_2\mathbf{L^{P2}}_2$ (600 MHz, 298 K, DMSO-d_6), the Pd$_3\mathbf{L^{P2}}_6$ ring ligand $\mathbf{L^{P2}}$ forms upon addition of 0.55 equiv. Pd(II) (600 MHz, 298 K, DMSO-d_6) and ligand $\mathbf{L^{P2}}$ (500 MHz, 298 K, DMSO-d_6).

As Figure 46 shows, the heteroleptic Pd$_2\mathbf{L^{A1}}_2\mathbf{L^{P2}}_2$ coordination cage forms in a clean fashion without homoleptic assemblies being present in solution. 2D NMR techniques allowed the assignment of all proton signals (data see master thesis).[109] Especially the proton signals close to the coordination sphere, like H^1 and H^2 or H^a and H^b experience a mayor downfield shift as compared to the signals in the free ligands due to deshielding caused by the formation of the coordinative bond. Furthermore, the signal assigned to proton H^9, pointing to the inside cavity of the formed coordination cage, also experiences downfield shifting, whereas proton H^e shifts upfield indicating increased shielding in the assembly as compared to the free ligand. The hydrodynamic radius of the species in DMSO-d_6 amounted to $r_H = 13.02 \pm 0.005$ Å derived from a diffusion coefficient of $D = 8.4225 \pm 0.03 \cdot 10^{-11}$ m$^2\cdot$s^{-1} and ESI-MS analysis showed detected peaks at $m/z = 564.15$ ([Pd$_2\mathbf{L^{A1}}_2\mathbf{L^{P2}}_2$]$^{4+}$), 781.20 ([Pd$_2\mathbf{L^{A1}}_2\mathbf{L^{P2}}_2$+BF$_4$]$^{3+}$) and 1215.31 ([Pd$_2\mathbf{L^{A1}}_2\mathbf{L^{P2}}_2$+2BF$_4$]$^{2+}$).

Obtaining an MS spectrum of the herein described structure however proved to be difficult, as an equilibrium shift from the purely heteroleptic species in DMSO to a mixture of homoleptic and heteroleptic species in CH$_3$CN, that was used to dilute the MS sample,

was observed, thus requiring the sample to be measured immediately after dilution via direct-injection to prevent ligand rearrangement.

To analyze the situation in CD$_3$CN, a clean sample of Pd$_2$**L**$^{A1}_2$**L**$^{P2}_2$ in DMSO-d_6 was subjected to lyophilization and the residual yellow power was redissolved in CD$_3$CN. The mixture was heated until the solid had dissolved and ^{1}H NMR spectra were measured until the spectrum did not show changes anymore. It was then compared to the homoleptic Pd$_2$**L**$^{A1}_4$ and Pd$_3$**L**$^{P2}_6$ species the individual ligands form in CD$_3$CN (Figure 47).
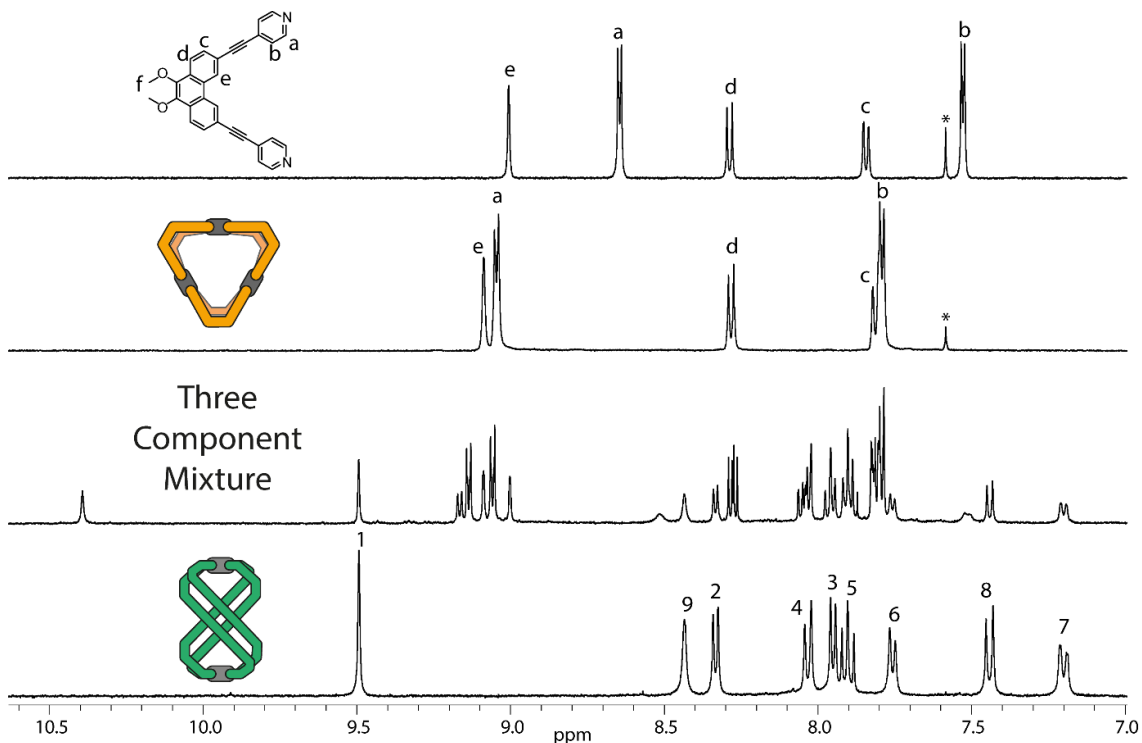
Figure 47: Partial stacked ^{1}H NMR spectra of (bottom to top) homoleptic cage Pd$_2$**L**$^{A1}_4$ (600 MHz, 298 K, CD$_3$CN) formed upon addition of 0.55 equiv. Pd(II) to ligand **L**^{A1}, the mixture of heteroleptic assembly Pd$_2$**L**$^{A1}_2$**L**$^{P2}_2$, homoleptic Pd$_2$**L**$^{A1}_4$ cage and homoleptic Pd$_3$**L**$^{P2}_6$ ring (600 MHz, 298 K, CD$_3$CN), the Pd$_3$**L**$^{P2}_6$ ring ligand **L**^{P2} forms upon addition of 0.55 equiv. Pd(II) (600 MHz, 298 K, CD$_3$CN) and ligand **L**^{P2} (500 MHz, 298 K, CD$_3$CN).

As evident from Figure 47, the heteroleptic Pd$_2$**L**$^{A1}_2$**L**$^{P2}_2$ still forms alongside with the homoleptic binuclear helical Pd$_2$**L**$^{A1}_4$ assembly and the trinuclear Pd$_3$**L**$^{P2}_6$ ring, which has been described before in the previous chapter. The calculated ratio of these three assemblies based on integration of proton signals H^1 (heteroleptic Pd$_2$**L**$^{A1}_2$**L**$^{P2}_2$ and homolpetic Pd$_2$**L**$^{A1}_4$ cage) and H^e (Pd$_3$**L**$^{P2}_6$ ring) amounts to $1:2:\frac{4}{3}$.

The existence of all three species could be confirmed by ESI-MS studies and ^{1}H DOSY NMR measurement with elevated acquisition time as depicted below (Figure 48).
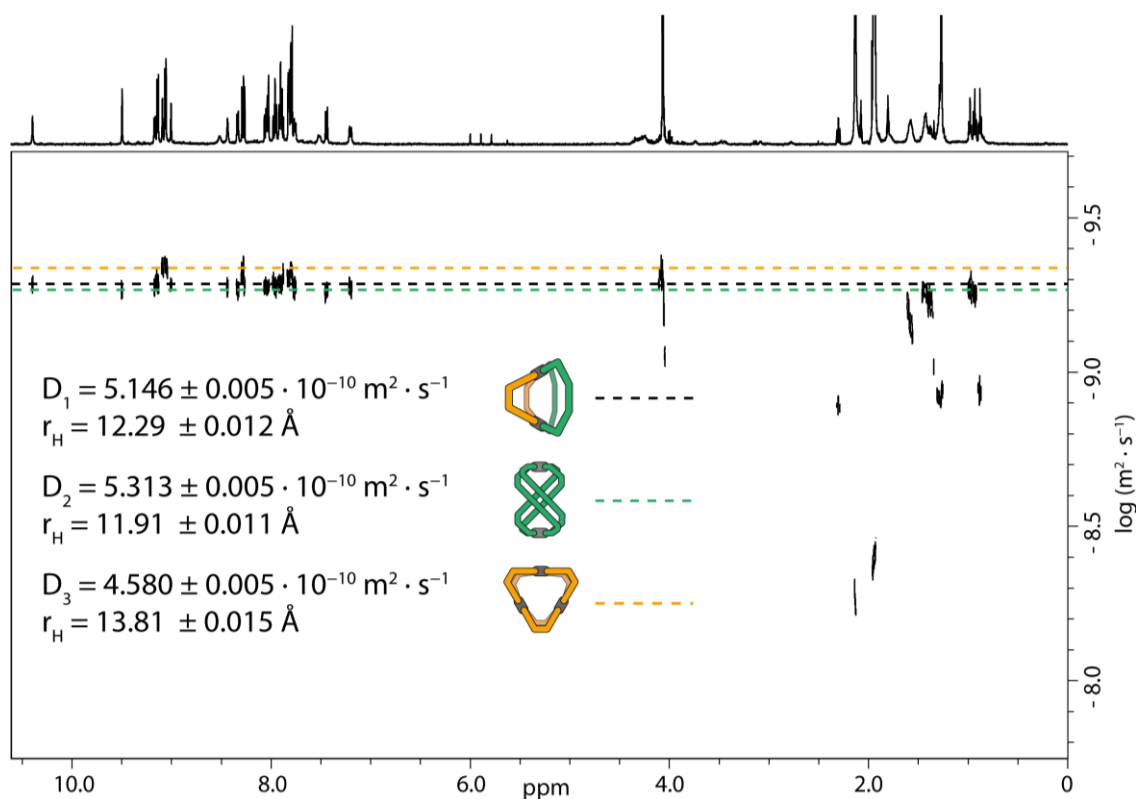
Figure 48: ^{1}H DOSY NMR spectrum (500 MHz, 298 K, CD$_3$CN) of the mixture of heteroleptic Pd$_2$L$^{A1}_2$L$^{P2}_2$, homoleptic Pd$_2$L$^{A1}_4$ cage and homoleptic Pd$_3$L$^{P2}_6$ ring.

The spectrum shows the mixture after re-equilibration in CD$_3$CN. The signal-overlap of the three species is, by a lucky coincidence, very minimal which enabled the differentiation of the three species by extended ^{1}H DOSY NMR measurement. The species showed hydrodynamic radii of r_H = 12.29 Å (Pd$_2$L$^{A1}_2$L$^{P2}_2$), r_H = 11.91 Å (Pd$_2$L$^{A1}_4$) and r_H = 13.81 Å (Pd$_3$L$^{P2}_6$) matching well with the values obtained from DMSO-d_6 (Figure 76; experimental part).

This change in the thermodynamic equilibrium cannot be readily explained by entropy changes based on the assemblies alone, since the homoleptic species, Pd$_2$L$^{A1}_4$ and Pd$_3$L$^{P2}_6$, form in either CD$_3$CN or DMSO. A nuclearity change as for example for the homoleptic species L^{P1} forms (Pd$_4$L$^{P1}_8$ ring in DMSO-d_6; Pd$_3$L$^{P1}_6$- and Pd$_4$L$^{P1}_8$ ring and Pd$_4$L$^{P1}_8$ tetrahedron in CD$_3$CN[135]) is not given. An analysis of previously described Pd$_2$L$^{C1}_2$L$^{P1}_2$ and Pd$_2$L$^{C1}_2$L$^{P2}_2$, that have been described previously in CD$_3$CN[64,66,109], regarding their behavior when exchanging CD$_3$CN for DMSO led to no evident change in regard to the outcome of the coordination cage formation (see experimental part). Thus, the coordination assemblies formed by L^{C1} and L^{P1}, respectively L^{P2}, do not seem to be affected whether CD$_3$CN or DMSO is used. Neither does Pd$_2$L$^{A1}_2$L$^{P1}_2$, which has been shown to form in DMSO and CD$_3$CN[57], leaving Pd$_2$L$^{A1}_2$L$^{P2}_2$ to be the sole system

that forms in one of the two solvents but experiences an equilibrium shift once subjected to the other.

A summary of the complete system is shown in Figure 49.
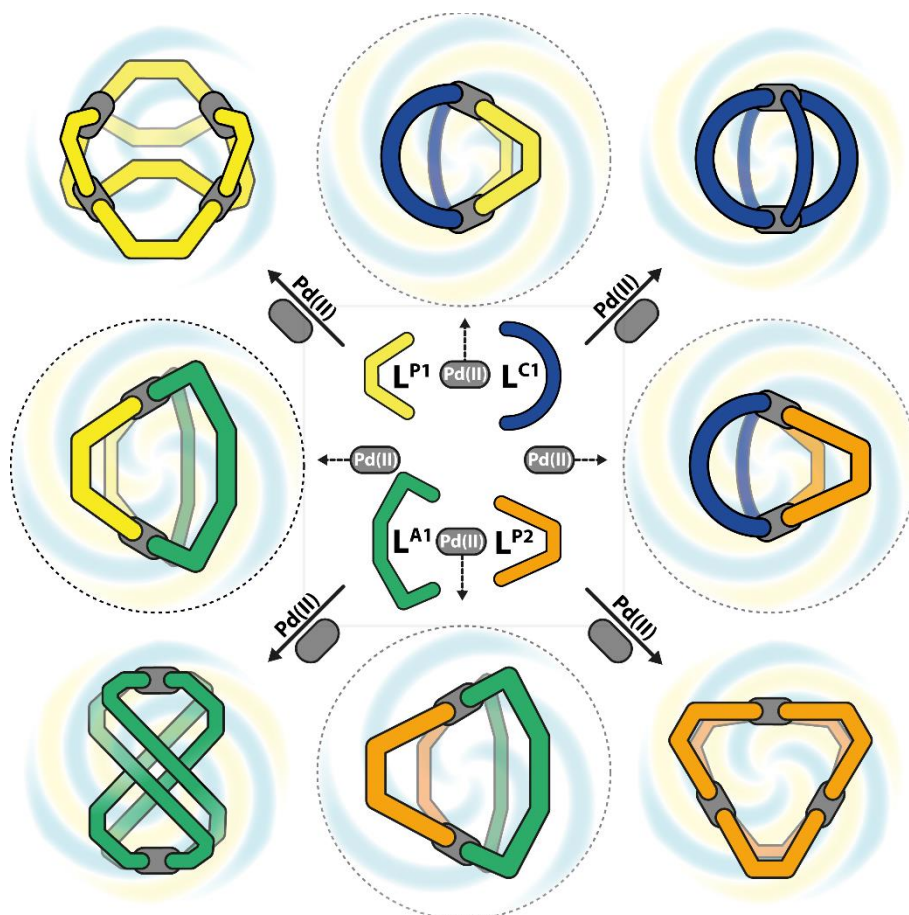
Figure 49: Schematic representation of all Pd(II)-based coordination cages formed from the two ligands L^{C1}, respectively L^{A1}, with their shape complementary counterparts L^{P1}, respectively L^{P2}. In addition, all homoleptic assemblies are given with the respective solvent system indicated by color (DMSO-d_6: blue; CD$_3$CN: yellow).

All herein described systems, heteroleptic or homoleptic, form in both, CD$_3$CN (yellow) or DMSO (blue) with the sole exceptions being the homoleptic assembly of L^{P1} and the heteroleptic assembly formed by L^{A1} and L^{P2}.

In science, the logical conclusion after an observation is either of theoretical nature, posing the question "Can I explain it?", or of practical nature asking "Can I use it?".

Since this behavior does not seem to be based on entropic factors, at least when only regarding the stoichiometry of the homoleptic assemblies, extensive *in silico* studies have been performed to explain, why the system undergoes this solvent-dependent equilibrium change. Preliminary results from these calculations by FABIAN SENDZIK and PROF. DR. S. KAST are able to reproduce the observed effect and support the experimental results (manuscript in preparation).

While these studies will help to obtain a deeper understanding of the thermodynamic contributions in complex coordination cage systems especially regarding the solvent environment, the observed effect can potentially be used in systems chemistry transformations.

3.2.3 Host-Guest Chemistry or "Multi-Trigger post assembly separation"

Host-guest experiments conducted with $Pd_3L^{P2}_6$ showed, that the addition of a linear bis-sulfonate guest, 1,3-propanedisulfonate (G^1), leads to precipitation of the host-guest complex and thus successive removal of both, guest and host from the mother liquor. The aromatic region of the ^1H titration experiment is shown in Figure 50 below.
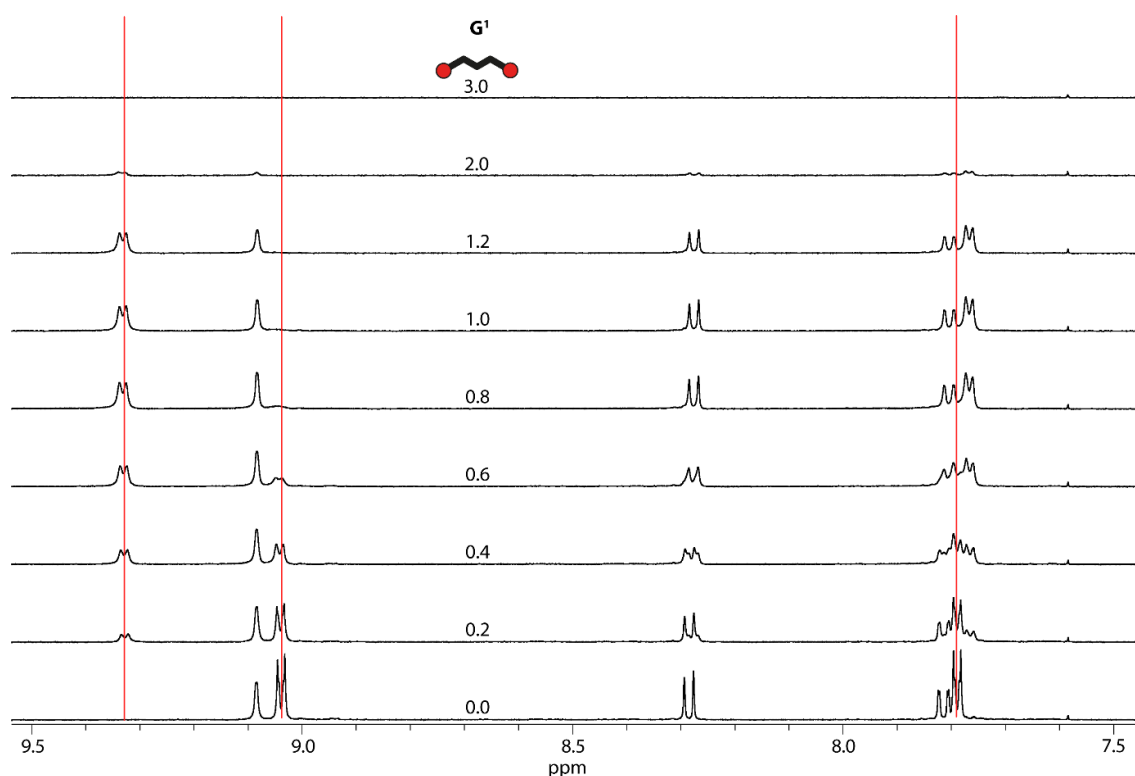
Figure 50: Aromatic region of the ^1H NMR titration (500 MHz, 298K, CD_3CN) of $Pd_3L^{P2}_6$ (0.233 mM in CD_3CN) with G^1 (17.5 mM solution in CD_3CN).

Upon addition of G^1, the proton signals of the $Pd_3L^{P2}_6$ ring show splitting. While the signal of H^a splits from $\delta = 9.04$ ppm to 9.33 ppm, signals further away from the coordination sphere show less pronounced splitting, like e.g. H^b only splitting from $\delta = 7.79$ ppm to 7.765 ppm. While this behavior does indicate slow exchange kinetics of G^1 to the $Pd_3L^{P2}_6$ ring, the determination of a binding constant is not possible due to the lack of free host or guest signals, signal overlap and the observed precipitation of the host-guest complex starting from 1 equiv. G^1 total. This precipitation can be easily followed by ^1H NMR and

after the addition of 3 equiv. total G^1, the host-guest complex is completely removed from the CD$_3$CN solution.

As much as a conclusive statement regarding the binding motif of [G^1@Pd$_3$L$^{P2}_6$] cannot be made, the clean removal of a host-guest complex from solution by simple means of precipitation and successive filtration could provide to be a second stage trigger in the heteroleptic system, after the first stage trigger being the solvent control.

To confirm this, the heteroleptic cage was setup in DMSO-d_6. After clean formation had been confirmed, the solvent was removed via lyophilization and the remaining solid was redissolved in 600 µl CD$_3$CN. After equilibration, the three-component mixture consisting of Pd$_2$L$^{A1}_4$, Pd$_2$L$^{A1}_2$L$^{P2}_2$ and Pd$_3$L$^{P2}_6$ was subjected to successive addition of G^1. The process was followed by ^{1}H NMR measurement (Figure 51).
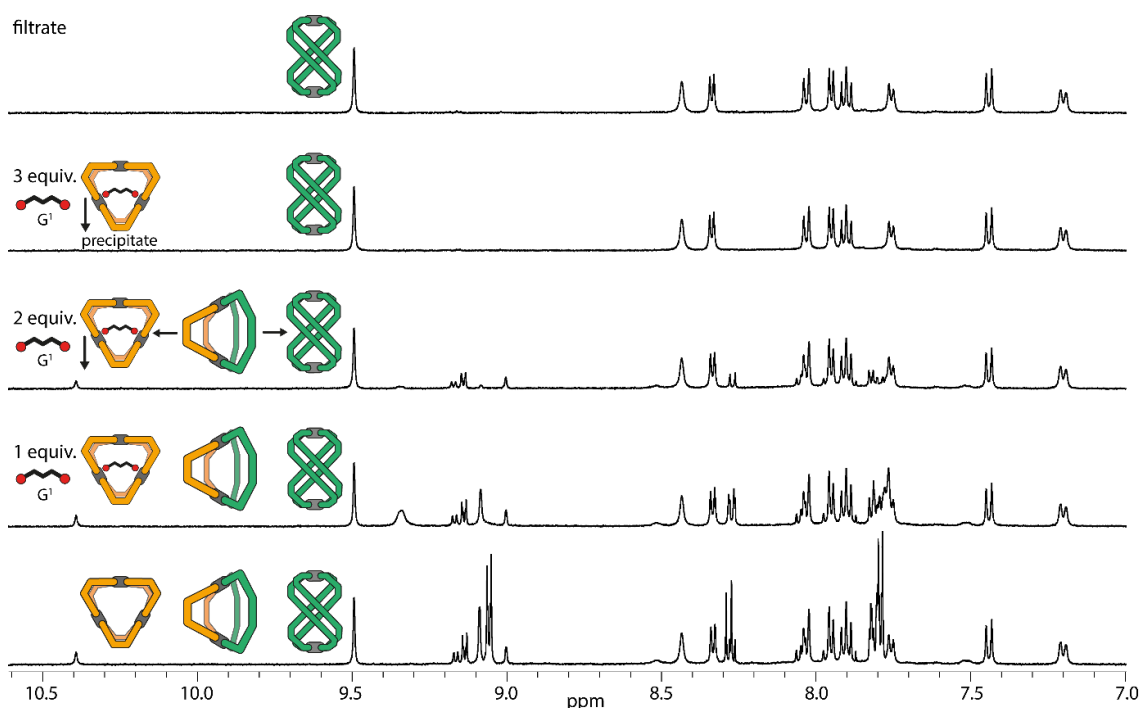
Figure 51: Partial ^{1}H NMR spectra (500 MHz, 298 K, CD$_3$CN) of the mixture of heteroleptic assembly Pd$_2$L$^{A1}_2$L$^{P2}_2$, homoleptic Pd$_2$L$^{A1}_4$ cage and homoleptic Pd$_3$L$^{P2}_6$ ring with consecutive addition of G^1 and finally of the filtrate being purely homoleptic Pd$_2$L$^{A1}_4$ cage (bottom to top).

The addition of 1 equiv. G^1 (in respect to the total amount of Pd$_3$L$^{P2}_6$ ring) led to a new signal appearing at $\delta = 9.34$ ppm. The arising signal is corresponding to proton H^a and its shift is consistent with the one observed in the single component titration (Figure 50). Further changes can be observed for H^b, though signal overlap makes this observation less reliable. It is notable, that the addition of G^1, a bis-sulfonate guest, which are known to bind into Pd$_2$L$_4$ coordination cages quite well, does affect neither the signals of the heteroleptic Pd$_2$L$^{A1}_2$L$^{P2}_2$ cage nor the ones of the helical Pd$_2$L$^{A1}_4$ assembly. Further addition of G^1 led to an equilibrium change due to the commencing precipitation of

[3G^1@Pd$_3$L$^{P2}_6$] with the final result after the addition of 3 equiv. G^1 being all of Pd$_3$L$^{P2}_6$ having precipitated alongside G^1 with L^{A1} remaining in solution as a helically twisted, homoleptic assembly alongside tetrabutylammonium, the former counter cation of G^1.

There are two interesting observations to be taken from this experiment, 1st being that the heteroleptic cage is completely unaffected by the guest and 2nd how clean the removal of [3G^1@Pd$_3$L$^{P2}_6$] proceeds. While an interaction with helical Pd$_2$L$^{A1}_4$ was not expected due to a lack of an adequate cavity, the strong affinity of G^1 to Pd$_3$L$^{P2}_6$ causing it to interact solely with the ring while not affecting the Pd$_2$L$^{A1}_2$L$^{P2}_2$ cage at all is surely surprising.

While the determination of a binding constant of G^1 to Pd$_2$L$^{A1}_2$L$^{P2}_2$ could only be carried out in DMSO (see experimental part), it amounted to K = 7995 ± 652 M^{-1} by using the software Bindfit[49], thus being significantly higher than the binding constants for naphthyl-based bis-sulfonates that were analyzed for the smaller Pd$_2$L$^{A1}_2$L$^{P1}_2$ cage previously[57]. As previously discussed, a binding constant for [G^1@Pd$_3$L$^{P2}_6$] could not be determined, since even dilution of the sample led to no free host complex being observable in presence of G^1. This shows how strong the association of G^1@Pd$_3$L$^{P2}_6$ is, even if no numbers can be determined.

After the cage-to-cage transformation had been progressed, the solution was filtered and the precipitate was redissolved in DMSO-d_6. The resulting spectra and reference spectra of the same species directly formed in the respective solvent, are compared in Figure 52.
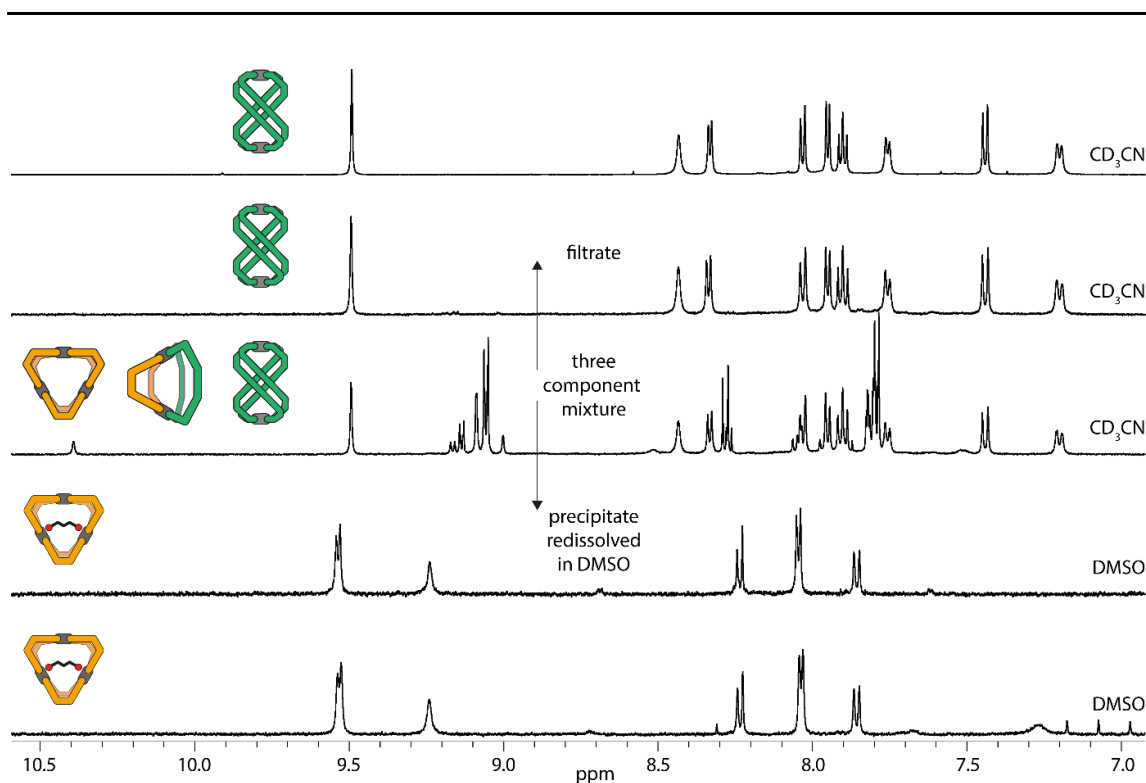
Figure 52: Partial ^{1}H NMR spectra (bottom to top) of homoleptic Pd$_3$L$^{P2}_6$ ring after addition of 2 equiv. **G^1** (500 MHz, DMSO-d_6), the precipitate of [x**G^1**@Pd$_3$L$^{P2}_6$] ring redissolved in DMSO-d_6 (500 MHz, DMSO-d_6); the mixture of heteroleptic assembly Pd$_2$L$^{A1}_2$L$^{P2}_2$, homoleptic Pd$_2$L$^{A1}_4$ cage and homoleptic Pd$_3$L$^{P2}_6$ ring (600 MHz, CD$_3$CN); the filtrate recovered from the mixture after treatment with 3 equiv. **G^1** (500 MHz, CD$_3$CN); the helical homoleptic Pd$_2$L$^{A1}_4$ cage (600 MHz, CD$_3$CN). All spectra were measured at 298 K.

As evident from Figure 52, the filtrate of the post-assembly cage separation is congruent with the one of the helical Pd$_2$L$^{A1}_4$ cage directly formed in CD$_3$CN. The same can be observed for the [**G^1**@Pd$_3$L$^{P2}_6$] complex though it is noted, that the complex [3**G^1**@Pd$_3$L$^{P2}_6$] precipitates also in DMSO at an initial Pd$_3$L$^{P2}_6$ ring concentration of 0.233 mM (see experimental part, Figure 81 and Figure 82), thus the spectrum used for comparison is [2**G^1**@Pd$_3$L$^{P2}_6$]. There are two possibilities as to why the spectra of redissolved [3**G^1**@Pd$_3$L$^{P2}_6$] precipitate and [2**G^1**@Pd$_3$L$^{P2}_6$] match nevertheless, one would be that the dilution factor of redissolved [3**G^1**@Pd$_3$L$^{P2}_6$] in DMSO is higher in the depicted case, and the complex is in fact soluble at that concentration, and the other that the complex ends up losing 1 equiv. **G^1** in the filtration process. The solubility of [**G^1**@Pd$_3$L$^{P2}_6$] differs depending on the solvent, as precipitation starts from 1 equiv. in CD$_3$CN, while it takes 2 equiv. in DMSO-d_6 before precipitation can be observed (see Figure 80 to Figure 82, experimental part).

Figure 53 summarized the herein presented post-assembly cage separation.
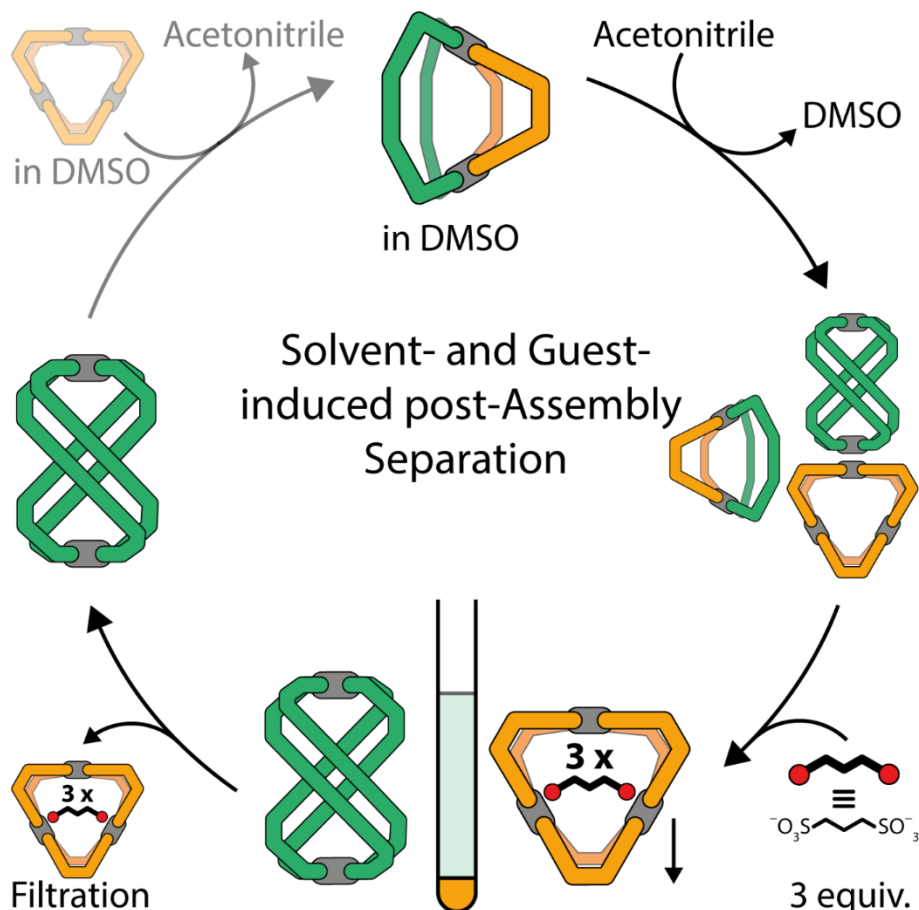
Figure 53: Schematic representation of a solvent- and guest-induced post assembly separation.

A clean Pd$_2$L$^{A1}_2$L$^{P2}_2$ cage solution in DMSO-d_6 undergoes an equilibrium change upon replacement of DMSO-d_6 with CD$_3$CN. A mixture of heteroleptic Pd$_2$L$^{A1}_2$L$^{P2}_2$ cage and homoleptic Pd$_2$L$^{A1}_4$ helix, respectively Pd$_3$L$^{P2}_6$ ring emerges. Upon treatment of this mixture with a linear bis-sulfonate guest **G^1**, the ring is precipitated in the form of [3**G^1**@Pd$_3$L$^{P2}_6$], while the helical Pd$_2$L$^{A1}_4$ assembly remains in solution unaltered. The precipitation induced the second equilibrium change by removing **L^{P2}** and thus inducing the cage-to-cage transformation of residual heteroleptic Pd$_2$L$^{A1}_2$L$^{P2}_2$ cage to the homoleptic assemblies with successive precipitation of Pd$_3$L$^{P2}_6$ ring. Filtering the solid of the solution leaves only helical Pd$_2$L$^{A1}_4$ assembly and the former counter cation of **G^1**, tetra-*n*-butylammonium, in CD$_3$CN.

As evident from the last step being grayed-out, the cage-to-cage transformation from Pd$_3$L$^{P2}_6$ ring with helical Pd$_2$L$^{A1}_4$ cage has yet to be performed to finalize the cycle. While it should be feasible to recover ligand **L^{P2}** from the filtrate by simple organic workup procedures, **G^1** and Pd(II) would end up being simultaneously fuel and waste in the proposed cycle. A waste-free switch, solely fueled by the solvent change, could be achieved if the [3**G^1**@Pd$_3$L$^{P2}_6$] precipitate is directly combined with helical Pd$_2$L$^{A1}_4$ assembly in DMSO-d_6 after evaporation of CD$_3$CN. This transformation could yield the

host-guest complex [G^1@$Pd_2L^{A1}_2L^{P2}_2$], since it has been found to tolerate up to 2 equiv. G^1 in the clean system host-guest titration experiment (Figure 89/Figure 90, experimental part). The resulting system however would no longer be a cycle but a back and forth switch going directly from [G^1@$Pd_2L^{A1}_2L^{P2}_2$] in DMSO-d_6 to the helical $Pd_2L^{A1}_4$ cage and [$3G^1$@$Pd_3L^{P2}_6$] precipitate in CD_3CN.

Aside from the proposed cyclic process, the strong binding of G^1 to the ring with total disregard of the present heteroleptic $Pd_2L^{A1}_2L^{P2}_2$ cage poses the question of selectivity. Thus, a second guest molecule G^2 is introduced in the following part.

3.2.4 Host-Guest self-sorting

While the binding of G^1 to $Pd_3L^{P2}_6$ ring is a slow exchange process with strong binding in CD_3CN, the binding kinetics change in DMSO-d_6, where fast exchange kinetics are observed. The system will be challenged by means of the introduction of a second guest G^2, that is known to bind preferably to bent heteroleptic cages[57]. While G^2 has been shown to have a binding constant of K ≈ 5200 M^{-1} to $Pd_2L^{A1}_2L^{P1}_2$ in DMSO-d_6, the change from L^{P1} to L^{P2} and thus size increase of the cage cavity (Pd−Pd distance increase from 12.6 Å to 14.0 Å, measurements taken from DFT models) leads to an even higher binding constant for [G^2@$Pd_2L^{A1}_2L^{P2}_2$] amounting to K ≈ 10750 ± 535 M^{-1}. A control experiment found the binding constant for [G^1@$Pd_2L^{A1}_2L^{P2}_2$] amounting to K ≈ 7995 ± 652 M^{-1}, thus being slightly lower emphasizing not only stronger binding of the guests to the new $Pd_2L^{A1}_2L^{P2}_2$ cage as opposed to its smaller $Pd_2L^{A1}_2L^{P1}_2$ analogue, but also an increase in attractive forces for the naphthyl-based G^2 as opposed to the alkane-based G^1 likely due to attractive π-π interactions in the former case.

The following competition experiments have all been conducted in DMSO-d_6, to prevent precipitation tipping the equilibrium by removing components from solution. A strict 1:1:1:1 (Cage:Ring:G^1:G^2) ratio has been kept, since control experiments (Figure 89-Figure 94; experimental part) showed precipitation only from 2 equiv. G^1, respectively G^2 in DMSO-d_6. Mixtures of heteroleptic $Pd_2L^{A1}_2L^{P2}_2$ cage and homoleptic $Pd_3L^{P2}_6$ ring have been prepared setting up a ligand stock solution with a ratio of 1 equiv. L^{A1} and 4 equiv. L^{P2}. The solvent was removed by lyophilization and [$Pd(CH_3CN)_4$](BF_4)$_2$ has been added to form a mixture of 0.7 mM heteroleptic $Pd_2L^{A1}_2L^{P2}_2$ cage and equimolar amounts of homoleptic $Pd_3L^{P2}_6$ ring. G^1 and G^2 have been setup in 17.5 mM solutions and were added simultaneously in all competition experiments.

A comparison of the single titration experiments of $[G^1@Pd_2L^{A1}_2L^{P2}_2]$ and $[G^2@Pd_2L^{A1}_2L^{P2}_2]$ and the three-component titration of simultaneously G^1 and G^2 to the heteroleptic $Pd_2L^{A1}_2L^{P2}_2$ cage is shown in Figure 54.
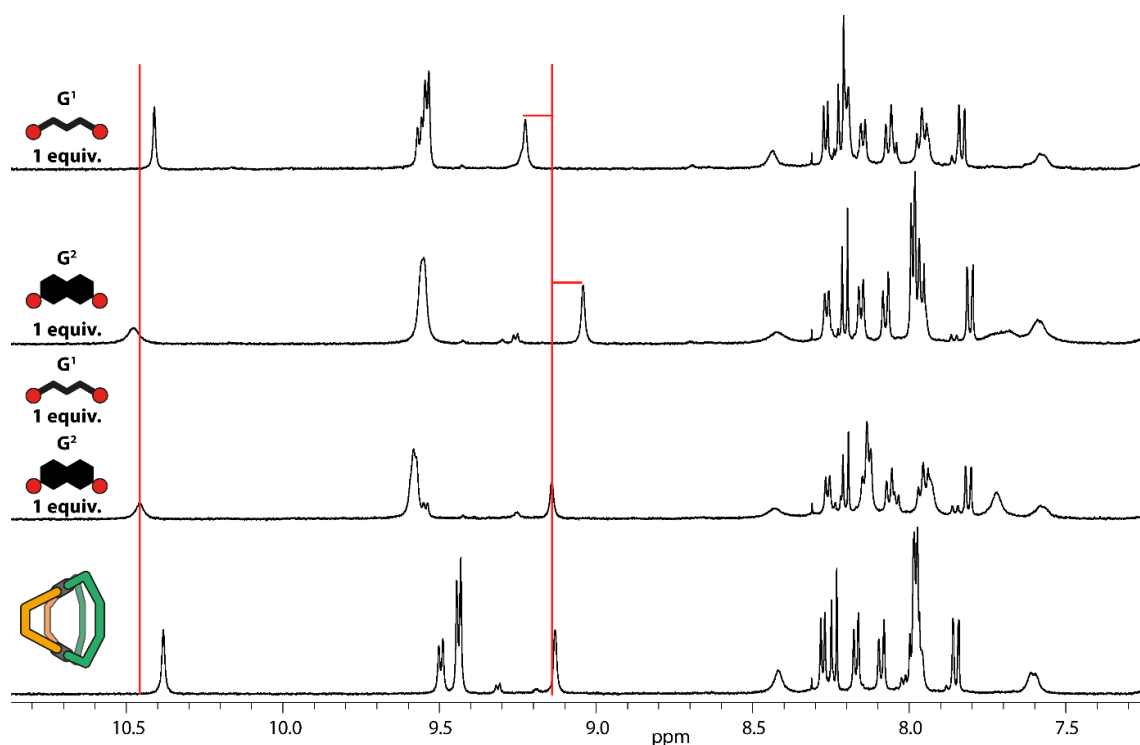
Figure 54: Partial ^{1}H NMR spectra (bottom to top) of heteroleptic $Pd_2L^{A1}_2L^{P2}_2$; after treatment with 1 equiv. G^1 and G^2; after treatment with 1 equiv. G^2; after treatment with 1 equiv. G^1 (500 MHz, 298 K, DMSO-d_6). The red bars indicate the inner protons H^1 and H^9 and their behavior upon guest addition.

Figure 54 shows the heteroleptic $Pd_2L^{A1}_2L^{P2}_2$ cage (bottom spectrum) compared to the spectra of the latter mentioned after the addition of both guests, G^1 and G^2, and after addition of just 1 equiv. of each guest individually. While H^1 remains sharp and H^9 shifts downfield after addition of G^1, the addition of G^2 leads to broadening of H^1 and an upfield shift of H^9. Furthermore, the downfield shift of H^1 is more pronounced upon addition of G^2, shifting from $\delta = 10.38$ ppm to $\delta = 10.48$ ppm, while it only shifts to $\delta = 10.41$ ppm upon addition of 1 equiv. G^1. The proton shift of H^1 in the mixed guest titration experiment amounts to $\delta = 10.45$ ppm, though it has to be considered, that at this point two equivalents of bis-sulfonate guest are present around the cage thus the overall ion concentration in solution differs slightly for the compared cases. While H^1 is close to the coordination sphere and could thus also be influenced by outside binding of anions on a cationic cage, H^9 is pointing to the inside of the assembly, thus its shift should be affected mostly by guest association inside the cavity. Interestingly, the signal of this specific proton upon addition of 1 equiv. G^1 shifts downfield from $\delta = 9.14$ ppm to $\delta = 9.23$ ppm but upfield to $\delta = 9.04$ ppm upon addition of 1 equiv. G^2. However, this specific signal shows close to no shift in the mixed guest titration, being always around $\delta = 9.14$ ppm.

While the single guest experiments clearly showed, that both guests bind inside the cavity of $Pd_2L^{A1}_2L^{P2}_2$, thus the possibility of the cage not interacting with the guest can be ruled out, the signal's shift of protons H^1 and H^9 averages almost perfectly on the mean of the shifts in both single guest titrations. Furthermore, there is no significant change from 0.5 equiv. of each G^1 and G^2 added to 1.0 equiv. of both guest molecules. This proves both guests being in fast exchange and the cage showing no selectivity regarding one or the other guest molecule. This is overall not surprising, since the determined binding constants for G^1 or G^2 in $Pd_2L^{A1}_2L^{P2}_2$ are in a similar range. However, this also shows that the signal of proton H^9 is a very good indicator for the binding of the individual guest molecules, which will be of use in the following four-component experiment.

A system containing equimolar amounts of $Pd_2L^{A1}_2L^{P2}_2$ cage and $Pd_3L^{P2}_6$ ring with a ligand ratio of 1:4 (L^{A1}:L^{P2}) has been setup to contain a total concentration of 0.7 mM of both assemblies in DMSO-d_6. The two-component mixture was then successively treated with first, 1 equiv. G^1 followed by 1 equiv. G^2 to analyze competitive guest binding in a four-component system. The resulting spectra and a comparison with $[G^2@Pd_2L^{A1}_2L^{P2}_2]$ are shown in Figure 55.
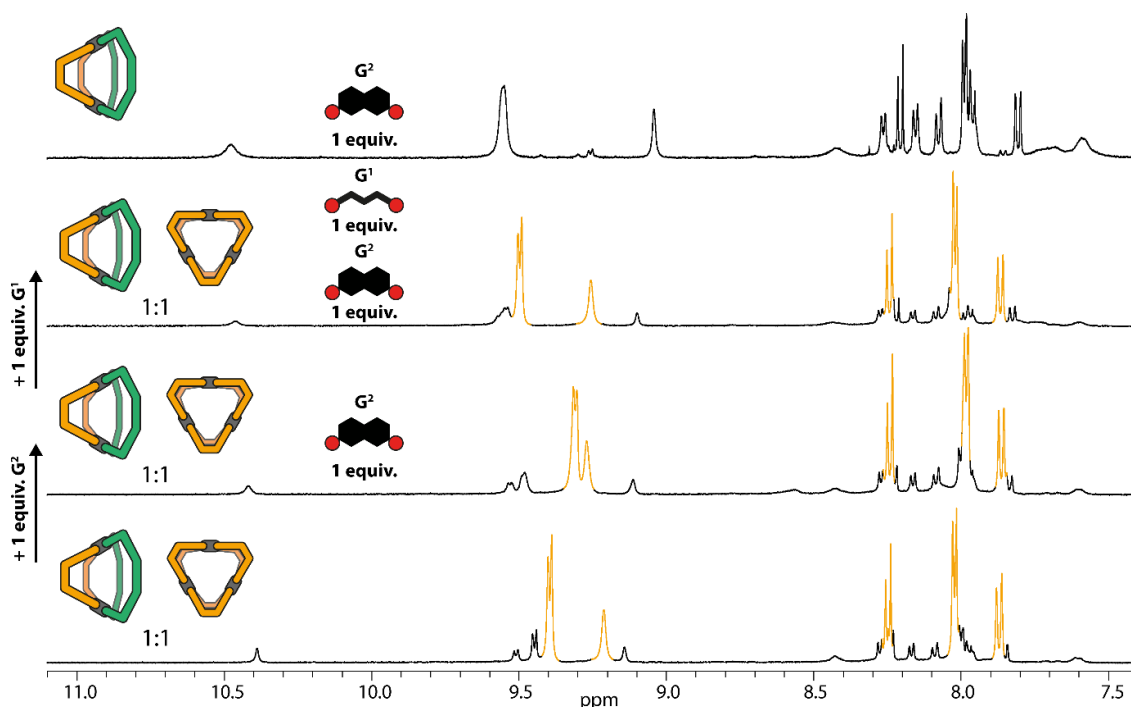
Figure 55: Partial ^1H NMR spectra (bottom to top) of an equimolar mixture of heteroleptic $Pd_2L^{A1}_2L^{P2}_2$ and homoleptic $Pd_3L^{P2}_6$ ring (both 0.7 mM); the same mixture after addition of 1 equiv. G^2; after addition of 1 equiv. G^2 and G^1 and the clean heteroleptic $Pd_2L^{A1}_2L^{P2}_2$ after addition of 1 equiv. G^2 for reference (500 MHz, 298 K, DMSO-d_6). The signals of homoleptic $Pd_3L^{P2}_6$ are highlighted in yellow.

As evident from Figure 55, the signals of the $Pd_2L^{A1}{}_2L^{P2}{}_2$ cage show broadening upon addition of G^2 to the two-component mixture with H^1 shifting slightly downfield and H^9 shows a slight upfield shift indicating partly inside binding of $[G^2@Pd_2L^{A1}{}_2L^{P2}{}_2]$. However, an apparent change can be detected in the shifts of H^a and H^e of $Pd_3L^{P2}{}_6$ with H^a shifting upfield and H^e downfield, indicating binding of G^2 to both assemblies. Upon addition of G^1, the shift of proton H^a changes quite drastically as it sports a downfield shift from previously $\delta = 9.30$ ppm to $\delta = 9.49$ ppm indicating guest exchange from $[G^2@Pd_3L^{P2}{}_6]$ to $[G^1@Pd_3L^{P2}{}_6]$. The inner protons of the heteroleptic $Pd_2L^{A1}{}_2L^{P2}{}_2$ cage are also affected by the addition of G^1 as H^1 shifts further downfield to $\delta = 10.42$ ppm and shows increased broadening and H^9 shifting even further upfield from $\delta = 9.12$ ppm to $\delta = 9.09$ ppm. The behavior of both signals upon addition of the second guest indicates the increase in binding of $[G^2@Pd_2L^{A1}{}_2L^{P2}{}_2]$ which is in good accordance to G^1 preferably binding to the trinuclear $Pd_3L^{P2}{}_6$ ring.

To further verify the claim, that G^1 associates to the $Pd_3L^{P2}{}_6$ ring even with G^2 being available, thus the ring selectively "choosing" one bis-sulfonate guest over the other in presence of the cage, a comparison of the 1:1:1:1 four-component mixture and the spectra of the two component titration experiments of $[G^1@Pd_3L^{P2}{}_6]$ and $[G^2@Pd_3L^{P2}{}_6]$, each after the addition of 1, respectively 2 equiv. guest, is shown below in Figure 56.
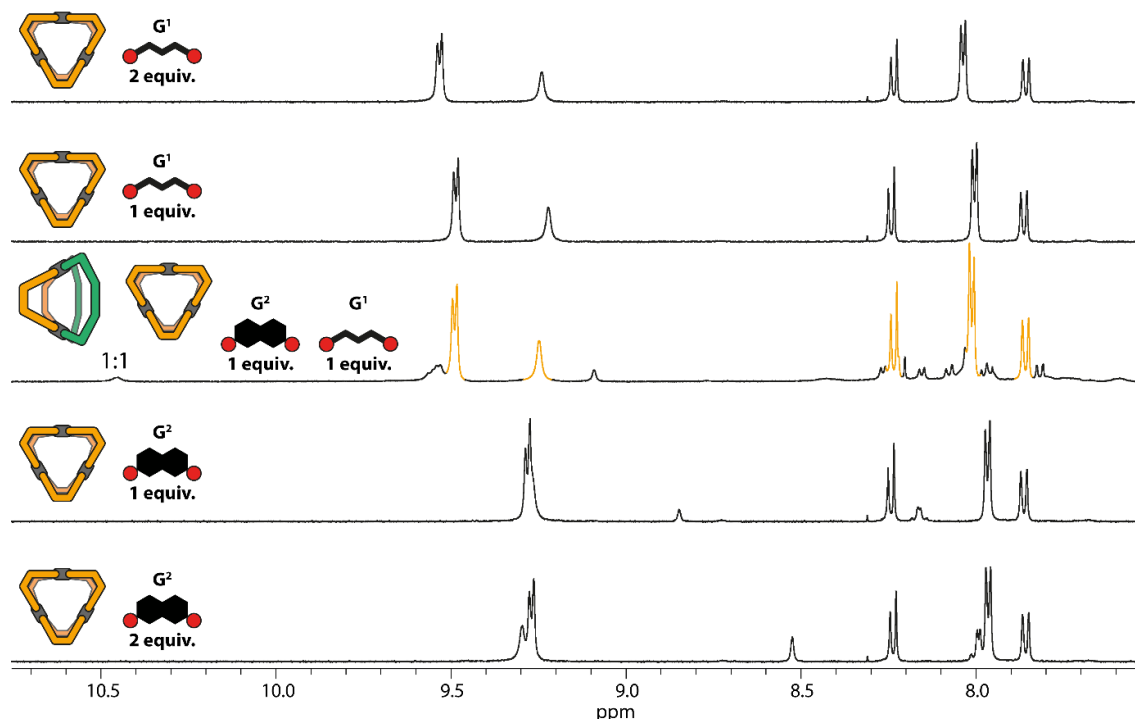
Figure 56: Partial ^{1}H NMR spectra (bottom to top) of homoleptic $Pd_3L^{P2}{}_6$ ring after addition of 2 equiv. G^2; homoleptic $Pd_3L^{P2}{}_6$ ring after addition of 1 equiv. G^2; an equimolar mixture of heteroleptic $Pd_2L^{A1}{}_2L^{P2}{}_2$ and homoleptic $Pd_3L^{P2}{}_6$ ring (both 0.7 mM) after addition of 1 equiv. G^1 and 1 equiv. G^2; homoleptic $Pd_3L^{P2}{}_6$ ring after addition of 1 equiv. G^1; homoleptic $Pd_3L^{P2}{}_6$ ring after addition of 2 equiv. G^1 (500 MHz, 298 K, DMSO-d_6). The signals of homoleptic $Pd_3L^{P2}{}_6$ are highlighted in yellow in the spectrum of the four-component mixture.

Figure 56 shows the spectra of the $Pd_3L^{P2}{}_6$ upon addition of 1, respectively 2 equiv. $\mathbf{G^1}$ (top spectra) and the ones after addition of 1, respectively 2 equiv. $\mathbf{G^2}$ (bottom spectra) compared to the equimolar mixture of $Pd_3L^{P2}{}_6$ ring and $Pd_2L^{A1}{}_2L^{P2}{}_2$ cage (middle) treated with 1 equiv. of both guests. The direct comparison of the spectra via ¹H NMR stack provides very good insight as to which guest is associated to the ring in the four-component mixture as the central spectrum closely resembles the upper two ([$\mathbf{G^1}$@$Pd_3L^{P2}{}_6$]), while being quite different from the bottom two ([$\mathbf{G^2}$@$Pd_3L^{P2}{}_6$]). While the signal H^a of the $Pd_3L^{P2}{}_6$ ring is almost congruent in the spectra of the $\mathbf{G^1}$@$Pd_3L^{P2}{}_6$ two-component mixture and the four-component mixture, the shift of H^e differs slightly being a tad bit more downfield shifted in the four-component mixture. This could be attributed to a small amount of $\mathbf{G^2}$ being associated to the $Pd_3L^{P2}{}_6$ ring or the overall ion concentration that causes the signals to shift. Taking the comparison with $\mathbf{G^2}$@$Pd_3L^{P2}{}_6$ into consideration, the former possibility is likely since the signal of H^e is further downfield shifted, though the effect seems to be minimal. As for the conclusion of the comparison, the shift of both protons can definitely be correlated with the one of $\mathbf{G^1}$ associating to the ring and not $\mathbf{G^2}$, thus showing the system demonstrating the self-sorting behavior of two bis-sulfonate guest molecules having the same charge and differing only in one containing an aromatic system, yielding a rigid structure, and one being aliphatic with a way more flexible core.

While it has already been stated, that the analysis of selective binding in this multi-component system is challenging by ¹H NMR analysis with the overall ion concentration leading to slight proton shifting and signal overlap making especially quantitative analysis impossible, ESI-MS analysis provides extremely detailed information especially in regard of quantification.

While ESI-MS spectrometry is usually not applicable in guest selectivity studies due to its invasive nature and the guests associating differently to a hexa-cationic species ($Pd_3L^{P2}{}_6$) as opposed to a tetra-cationic one ($Pd_2L^{A1}{}_2L^{P2}{}_2$), a quantitative comparative analysis of the individual peaks of [$\mathbf{G^1}$@$Pd_2L^{A1}{}_2L^{P2}{}_2$]²⁺ with [$\mathbf{G^2}$@$Pd_2L^{A1}{}_2L^{P2}{}_2$]²⁺, respectively [$\mathbf{G^1}$@$Pd_3L^{P2}{}_6$]⁴⁺ with [$\mathbf{G^2}$@$Pd_3L^{P2}{}_6$]⁴⁺, is possible due to the only difference being the structure of the guest while the species binding it, the overall charge of the peak and the charge of the guest are constant. The ESI-MS spectrum of the 1:1:1:1 four-component mixture of $Pd_2L^{A1}{}_2L^{P2}{}_2$ cage, $Pd_3L^{P2}{}_6$ ring, $\mathbf{G^1}$ and $\mathbf{G^2}$ is shown in Figure 57.
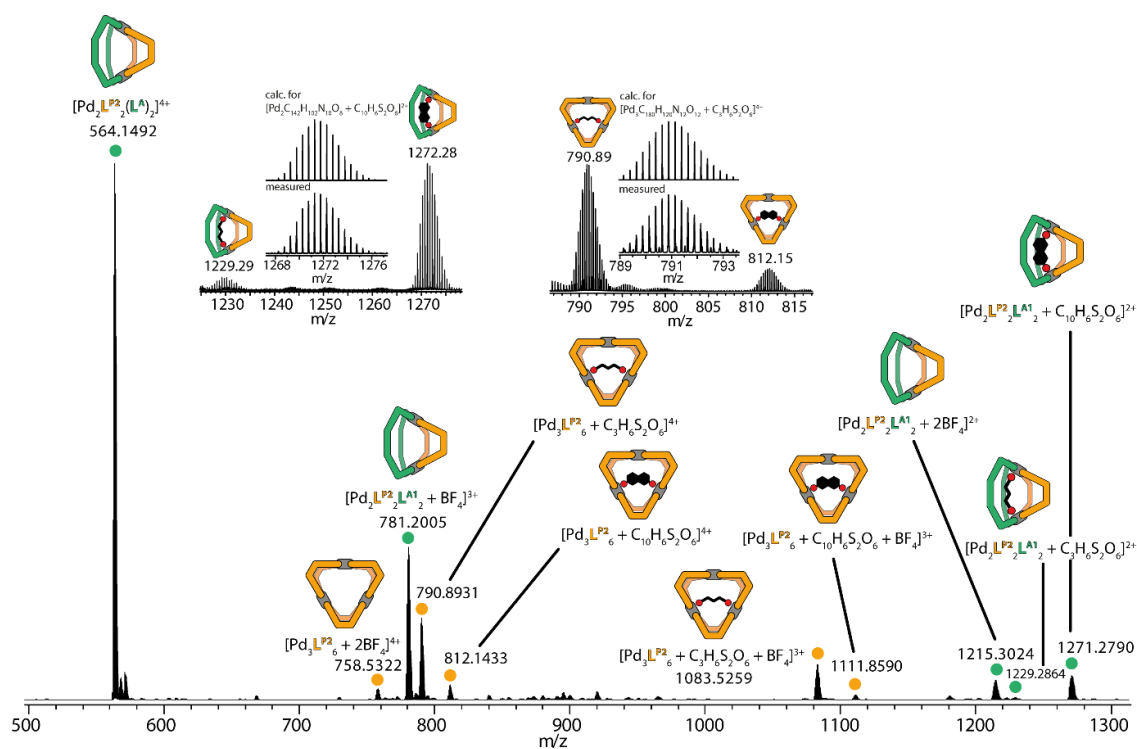
Figure 57: ESI-MS spectrum of a mixture of $[Pd_2L^{P2}_2L^{A1}_2 + xBF_4]^{(4-x)+}$ and $[Pd_3L^{P2}_6 + xBF_4]^{(6-x)+}+$ 1 equiv. of $\mathbf{G^1}$ and 1 equiv. $\mathbf{G^2}$. The observed and calculated isotopic patterns of $[\mathbf{G^2}@Pd_2L^{A1}_2L^{P2}_2]^{2+}$ and $[\mathbf{G^1}@Pd_3L^{P2}_6]^{4+}$ are shown in the inset, as well as the ratio of $[\mathbf{G^1}@Pd_2L^{A1}_2L^{P2}_2]^{2+}$ to $[\mathbf{G^2}@Pd_2L^{A1}_2L^{P2}_2]^{2+}$ and $[\mathbf{G^1}@Pd_3L^{P2}_6]^{4+}$ to $[\mathbf{G^2}@Pd_3L^{P2}_6]^{4+}$.

Figure 57 shows the full ESI-MS spectrum of the 1:1:1:1 four-component mixture with all species assigned and indicated by color (green: $Pd_2L^{A1}_2L^{P2}_2$ cage species; orange: $Pd_3L^{P2}_6$ ring species). The insets show the direct comparison of the peaks assigned to $\mathbf{G^1}$, respectively $\mathbf{G^2}$ associated to heteroleptic $Pd_2L^{A1}_2L^{P2}_2$ cage, respectively $Pd_3L^{P2}_6$ ring with a comparison of the isotopic pattern of simulated and measured peak of the most prominent species. Since the compared species carry the same charge, 2+ for $[\mathbf{G}@Pd_2L^{A1}_2L^{P2}_2]$ and 4+ $[\mathbf{G}@Pd_3L^{P2}_6]$, and only the same species with different guests $\mathbf{G^1}$ and $\mathbf{G^2}$, both being di-anionic bis-sulfonates, are compared, the intensity difference of the detected peaks can be directly attributed to the abundance in solution. As evident from the insets shown in Figure 57, ESI-MS supports the claims previously made based on ^{1}H NMR experiments. In case of the $Pd_3L^{P2}_6$ ring, the intensity of the peak assigned to the ring associating to the linear bis-sulfonate, $[\mathbf{G^1}@Pd_3L^{P2}_6]^{4+}$, is significantly higher than the one of $[\mathbf{G^2}@Pd_3L^{P2}_6]^{4+}$ (Figure 57, right inset). The exact opposite trend can be observed for the peak assigned to $[\mathbf{G^1}@Pd_2L^{A1}_2L^{P2}_2]^{2+}$, which is substantially lower in intensity as compared to $[\mathbf{G^2}@Pd_2L^{A1}_2L^{P2}_2]^{2+}$ (Figure 57, left inset).

If the total intensity of both peaks, $\mathbf{G^1}@Pd_3L^{P2}_6$ and $\mathbf{G^2}@Pd_3L^{P2}_6$ is summed up and set to 100%, $[\mathbf{G^1}@Pd_3L^{P2}_6]^{4+}$ amounts to 84%, while $[\mathbf{G^2}@Pd_3L^{P2}_6]^{4+}$ amounts to only 16%. The same procedure yields 10% $[\mathbf{G^1}@Pd_2L^{A1}_2L^{P2}_2]^{2+}$, as opposed to 90%

$[\mathbf{G^2}@Pd_2\mathbf{L^{A1}}_2\mathbf{L^{P2}}_2]^{2+}$. While an objection regarding the analytic procedure could be, that the species are still showing different ionization behavior despite only the structural backbone of the guest being changed, it would a) not justify the extent of the observed differences and b) be highly unlikely to favor a species with $\mathbf{G^1}$ in one case and one with $\mathbf{G^2}$ in the other. The experiment could be repeated multiple more times to validate the results and determine error values. Within this, the experimental setup could further be screened in regard to ionization energies and other measurements conditions, to rule out any effect of the experimental setup on the result.

Figure 58 summarizes the full scope of the host-guest self-sorting experiment and its most important results.
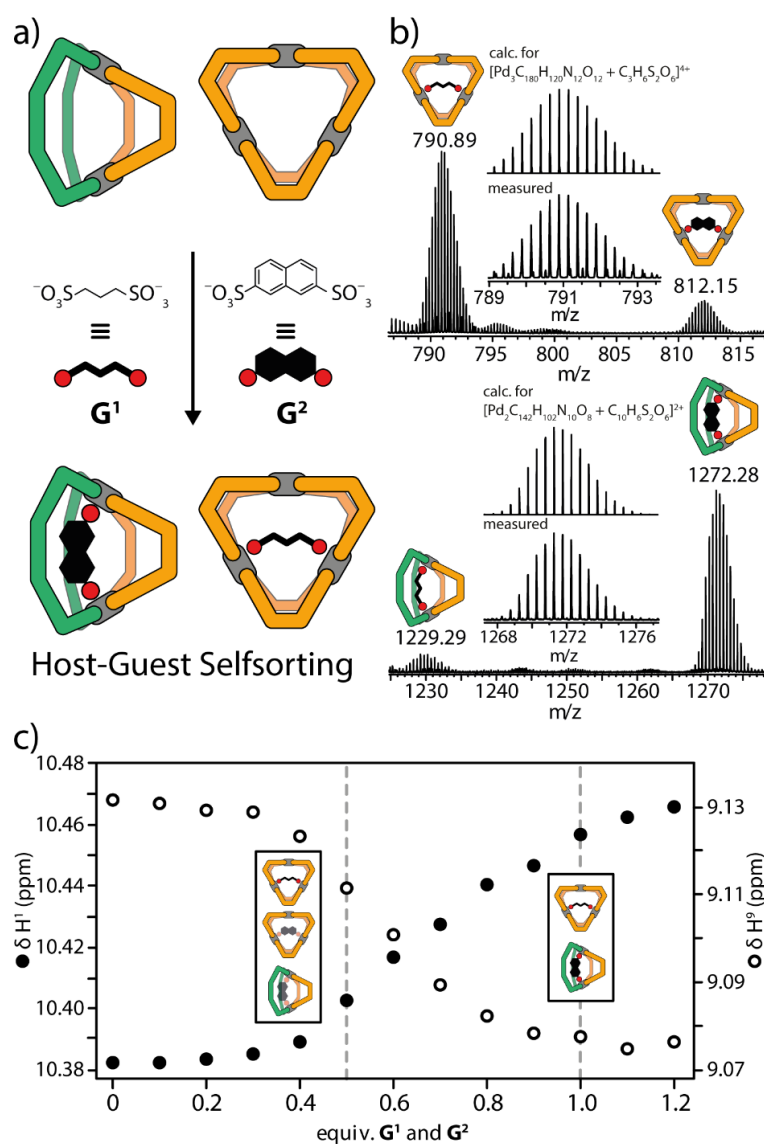
Figure 58: a) Schematic representation of the observed host-guest self-sorting of $\mathbf{G^1}$ and $\mathbf{G^2}$ to heteroleptic $Pd_2\mathbf{L^{A1}}_2\mathbf{L^{P2}}_2$ and homoleptic $Pd_3\mathbf{L^{P2}}_6$; b) partial ESI-MS spectra of the host-guest complexes $[\mathbf{G^1}@Pd_3\mathbf{L^{P2}}_6]$ and $[\mathbf{G^1}@Pd_3\mathbf{L^{P2}}_6]$, respectively $[\mathbf{G^1}@Pd_2\mathbf{L^{A1}}_2\mathbf{L^{P2}}_2]$ and $[\mathbf{G^2}@Pd_2\mathbf{L^{A1}}_2\mathbf{L^{P2}}_2]$, the observed and calculated isotopic pattern of the highest peak each are shown in the inset; c) observed shift of the inner protons H^1 and H^9 of $Pd_2\mathbf{L^{A1}}_2\mathbf{L^{P2}}_2$ with increasing concentration of $\mathbf{G^1}$ and $\mathbf{G^2}$.

A complex system consisting of two Pd(II)-based coordination assemblies, one heteroleptic $Pd_2L^{A1}{}_2L^{P2}{}_2$ cage species and an homoleptic $Pd_3L^{P2}{}_6$ ring, was treated with two dianionic bis-sulfonate guest molecules G^1 and G^2. Both assemblies have been shown to bind both guests individually in two-component titrations in DMSO-d_6 showing fast exchange kinetics in all four cases. If an equimolar amount of both assemblies is treated with 1 equiv. of each guest G^1 and G^2 simultaneously, the four-component system shows remarkable sorting behavior, whereby G^1 associates preferably to the homoleptic $Pd_3L^{P2}{}_6$ ring and G^2 to the heteroleptic $Pd_2L^{A1}{}_2L^{P2}{}_2$ cage (Figure 58, a)). This behavior could be followed by an ESI-MS experiment in which the four-component mixture was analyzed regarding to the intensity of the individual species relative to one another (Figure 58, b)). Due to the nature of the experiment and the close structural relation of the two guests to each other, quantification of the aforementioned self-sorting behavior was possible resulting in a 90% selectivity for $[G^2@Pd_2L^{A1}{}_2L^{P2}{}_2]$ and 84% selectivity for $[G^1@Pd_3L^{P2}{}_6]$. Statistically more relevant results could be obtained by acquisition of more measurements while furthermore altering the measurement parameters. Iterative addition of both guest molecules to an equimolar solution of both assemblies has also been analyzed via ^{1}H NMR titration experiments. While the ring has a higher affinity to bind both guests initially, likely due to its higher charge (6+ as compared to 4+ for the cage), self-sorting behavior of both guests can be observed once a certain threshold of total guest concentration is reached (≥0.4 equiv. of both guests). The process could be followed by analyzing the shifts of the inner protons H^1 and H^9 of the heteroleptic $Pd_2L^{A1}{}_2L^{P2}{}_2$ cage. The shift of H^9 could even be used as an indicator to differentiate both guests, as it was shifting upfield for G^2 but downfield for G^1. Thus, the continuous upfield shifting of H^9 as shown in Figure 58c) indicates the presence of more and more $[G^2@Pd_2L^{A1}{}_2L^{P2}{}_2]$, whereas the curve saturates after the addition of 1.1 equiv. of both guests. This slightly late saturation could occur due to small concentration inaccuracies. The observed shifts in the four-component system did not quite reach the values observed for the two-component titration experiments, which was to be expected since the ESI-MS experiment showed only 90% selectivity and the overall increase in ion-concentration will also affect the chemical shifts of the two species.

3.2.5 Experimental Part

3.2.5.1 Synthesis of the Heteroleptic Assemblies

Synthesis of Pd$_2$L$^{C1}_2$L$^{P1}_2$
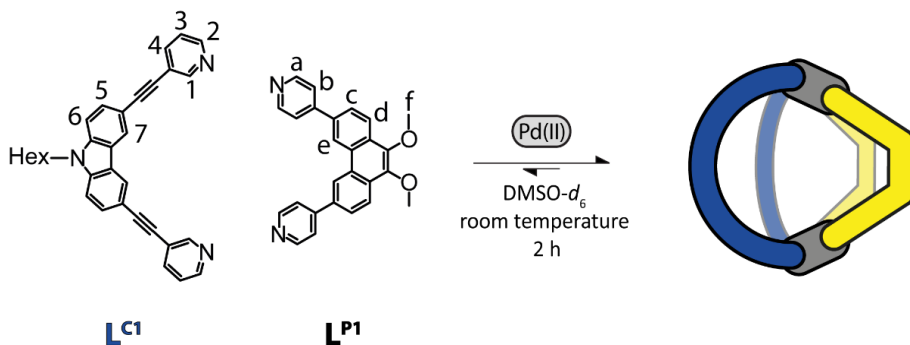
Scheme 5: Formation of Pd$_2$L$^{C1}_2$L$^{P1}_2$ with consecutive proton labels.

A mixture of ligand L^{P1} (270 µL of a 3.11 mM solution in DMSO-d_6), ligand L^{C1} (270 µL of a 3.11 mM solution in DMSO-d_6) and [Pd(CH$_3$CN)$_4$](BF$_4$)$_2$ (60 µL of a 15 mM solution in DMSO-d_6) was left to rest at room temperature for 2h to afford the heteroleptic coordination cage Pd$_2$L$^{P1}_2$L$^{C1}_2$.
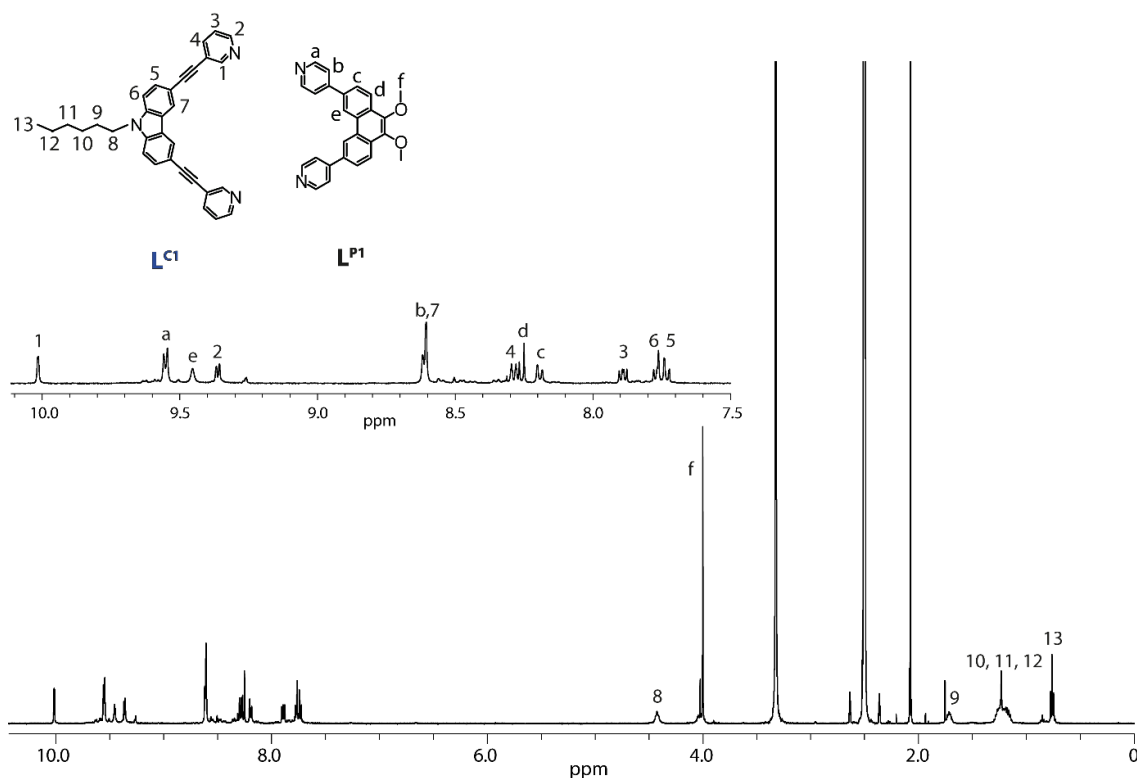
Figure 59: Full ^{1}H NMR spectrum (600 MHz, 298 K, DMSO-d_6) of Pd$_2$L$^{C1}_2$L$^{P1}_2$. The inset shows a zoom of the aromatic region.

^{1}H NMR (600 MHz, 298 K, DMSO-d_6) δ 10.02 (d, ^4J = 1.1 Hz, 4H, H^1), 9.55 (d, ^3J = 6.4 Hz, 8H, H^a), 9.45 (s, 4H, H^e), 9.36 (dd, ^3J = 5.8 Hz, ^4J = 0.95 Hz, 4H, H^2), 8.59 – 8.64 (m, 12H, H^b+H^7), 8.29 (dt, ^3J = 8.05 Hz, ^4J = 1.3 Hz, 4H, H^4), 8.26 (d, ^3J = 8.6 Hz, 4H, H^d), 8.19 (d, ^3J = 8.6 Hz, 4H, H^c), 7.89 (dd, ^3J = 8.4, 5.8 Hz, 4H, H^3), 7.75 – 7.79 (m, 4H, H^6), 7.73 (dd, ^3J = 8.5 Hz, ^4J = 1.3 Hz, 4H, H^5), 4.42 (t, ^3J = 6.2 Hz, 4H, H^8), 4.00 (s, 12H, H^f), 1.71 (quint, ^3J = 6.75 Hz, 4H, H^9), 1.11 – 1.32 (m, 12H, H$^{10\text{-}12}$), 0.76 (t, ^3J = 7.1 Hz, 6H, H^{13}) ppm.
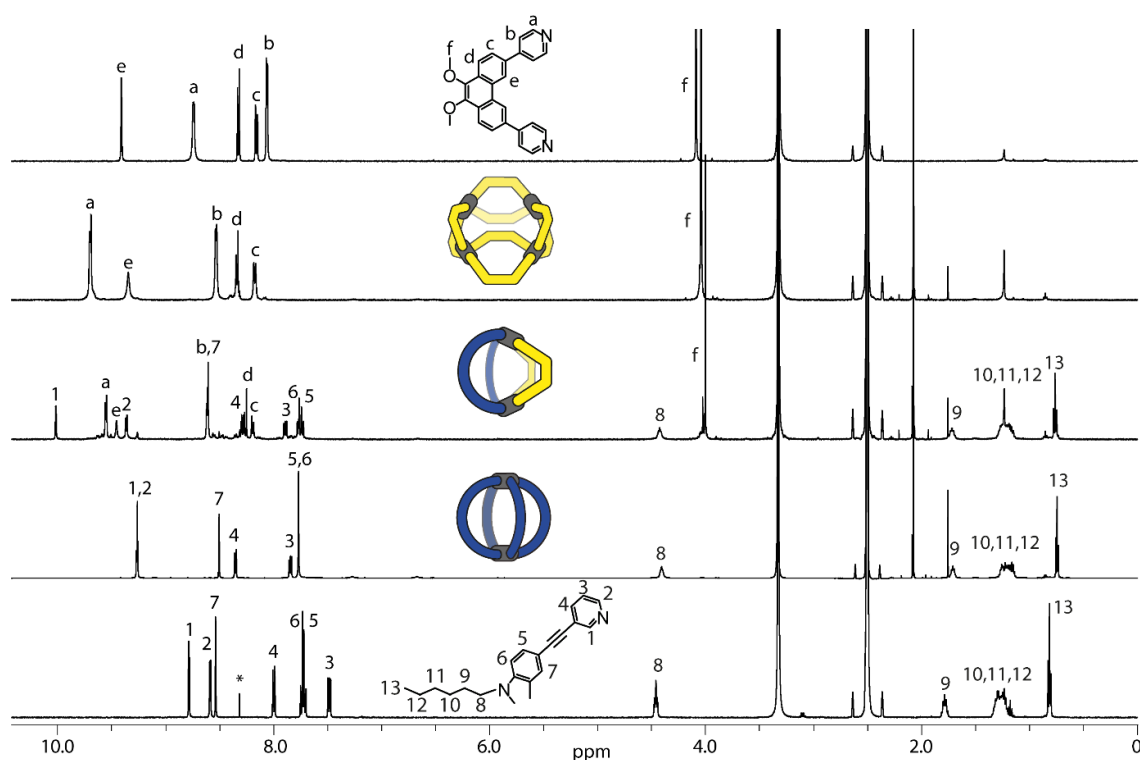
Figure 60: Full stacked ^{1}H NMR spectra of (bottom to top) ligand **L^{C1}** (500 MHz, 298 K, DMSO-d_6), the corresponding homoleptic cage Pd$_2$**L^{C1}**$_4$ (600 MHz, 298 K, DMSO-d_6) formed upon addition of 0.55 equiv. Pd(II) to ligand **L^{C1}**, the heteroleptic assembly Pd$_2$**L^{C1}**$_2$**L^{P2}**$_2$ (600 MHz, 298 K, DMSO-d_6), the Pd$_4$**L^{P1}**$_8$ ring ligand **L^{P1}** forms upon addition of 0.55 equiv. Pd(II) (500 MHz, 298 K, DMSO-d_6) and ligand **L^{P1}** (500 MHz, 298 K, DMSO-d_6).
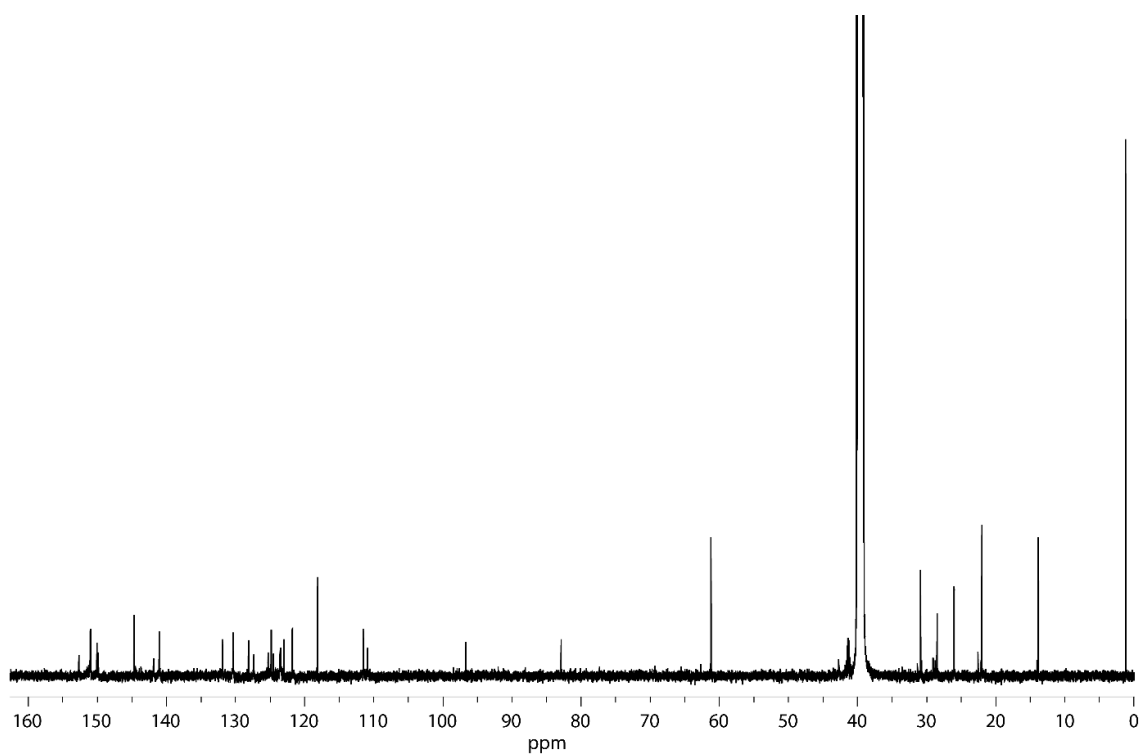
Figure 61: ^{13}C NMR spectrum (151 MHz, 298 K, DMSO-d_6) of Pd$_2$**L**^{C1}$_2$**L**^{P1}$_2$.

^{13}C{^{1}H} (151 MHz, 298 K, DMSO-d_6) δ 152.60, 150.95, 150.00, 149.82, 144.64, 141.77, 140.99, 131.84, 130.32, 130.28, 128.07, 127.33, 125.24, 124.79, 124.48, 123.51, 123.42, 122.95, 121.73, 111.46, 110.87, 96.64, 82.84, 61.15, 42.68, 30.83, 29.03, 25.97, 21.96, 13.78 ppm.
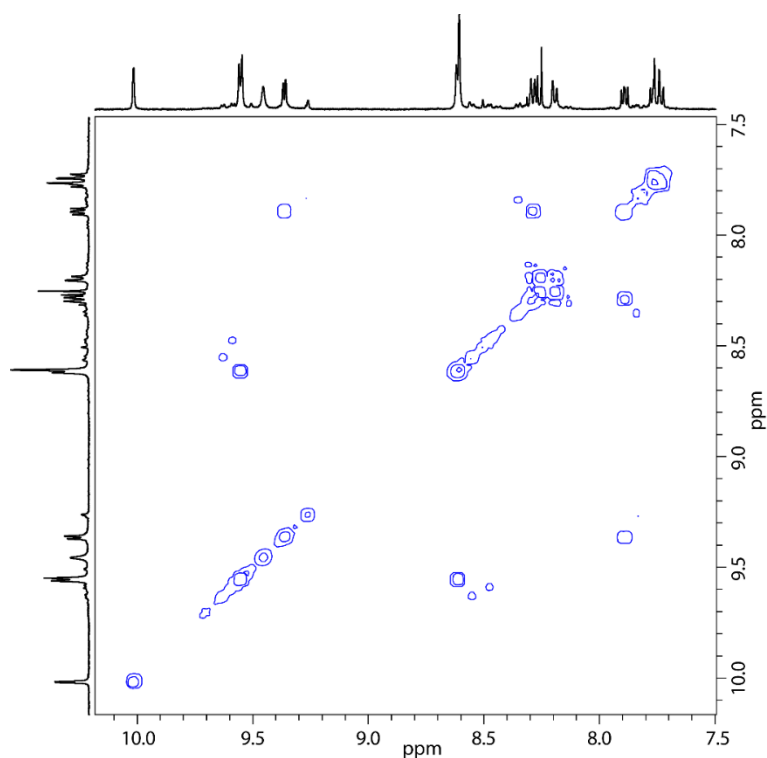
Figure 62: Partial ^{1}H-^{1}H COSY NMR spectrum (600 MHz, 298 K, DMSO-d_6) of Pd$_2$**L**^{C1}$_2$**L**^{P1}$_2$.
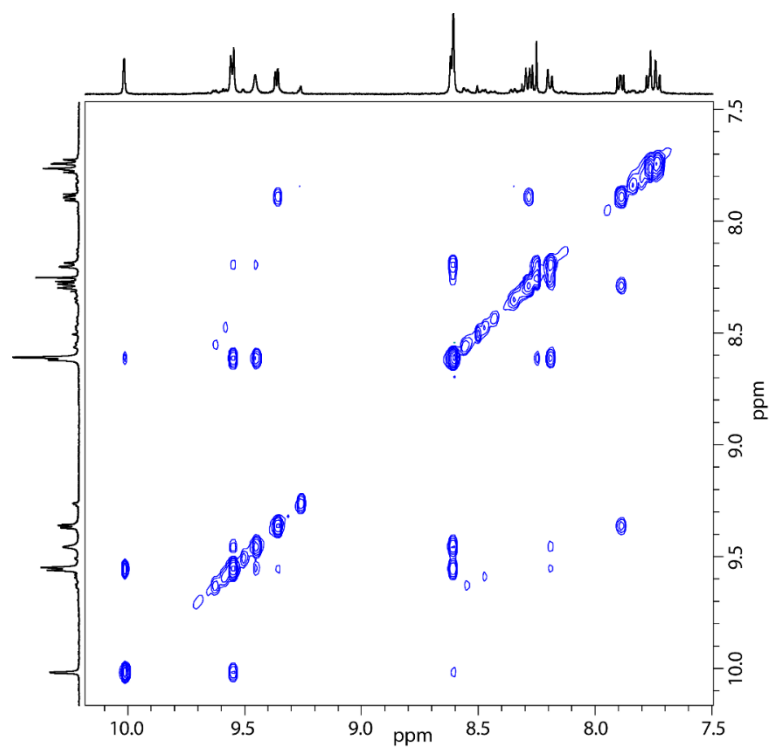
Figure 63: Partial ^{1}H-^{1}H NOESY NMR spectrum (600 MHz, 298 K, DMSO-d_6) of Pd$_2$**L^{C1}**$_2$**L^{P1}**$_2$.

$D_1 = 9.056 \pm 0.003 \cdot 10^{-11}\ m^2 \cdot s^{-1}$
$r_H = 12.11 \pm 0.001$ Å
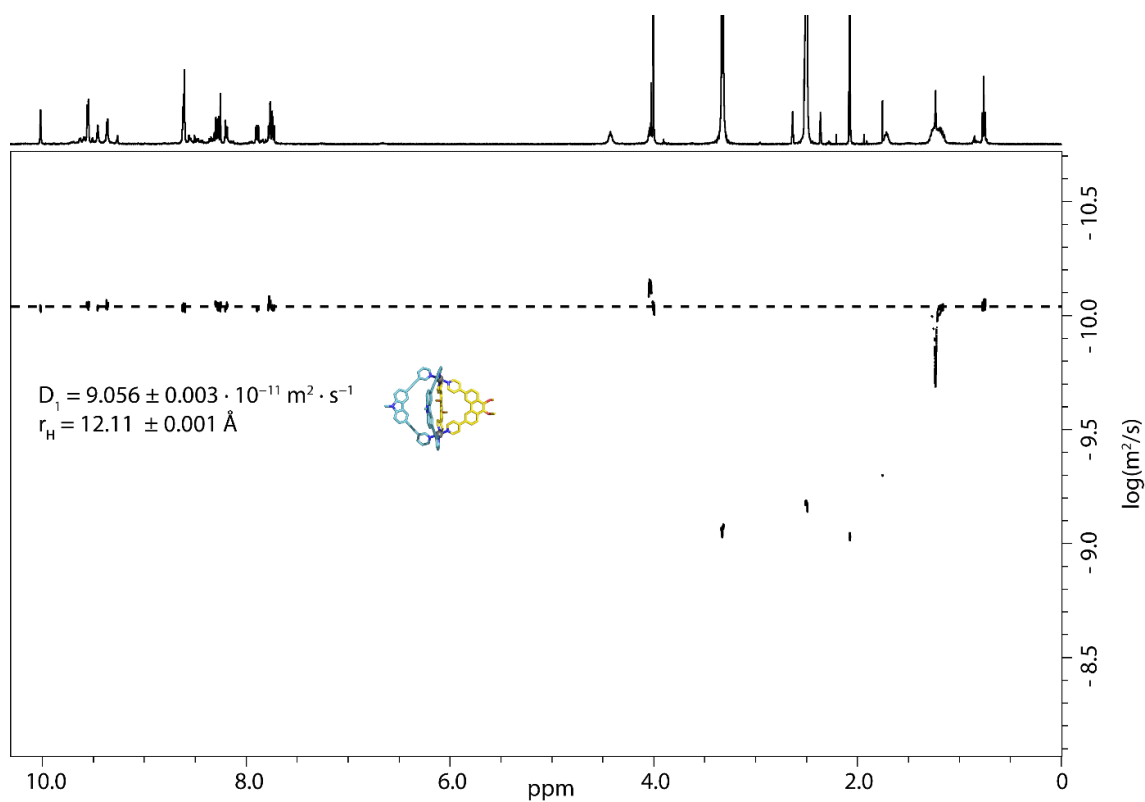
Figure 64: ^{1}H DOSY NMR spectrum (500 MHz, 298 K, DMSO-d_6) of Pd$_2$**L^{C1}**$_2$**L^{P1}**$_2$.

Synthesis of Pd$_2$L$^{C1}_2$L$^{P2}_2$
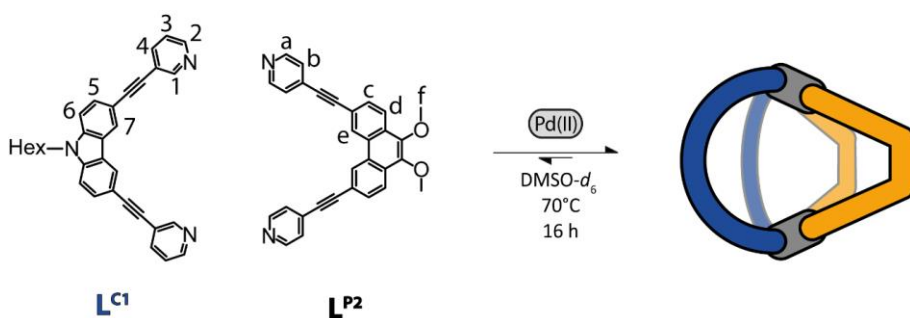
Scheme 6: Formation of Pd$_2$L$^{C1}_2$L$^{P2}_2$ with consecutive proton labels.

A mixture of ligand **L**^{C1} (270 µL of a 3.11 mM solution in DMSO-d_6), ligand **L**^{P2} (270 µL of a 3.11 mM solution in DMSO-d_6) and [Pd(CH$_3$CN)$_4$](BF$_4$)$_2$ (60 µL of a 15 mM solution in DMSO-d_6) was heated to 70°C overnight to afford the heteroleptic coordination cage Pd$_2$L$^{C1}_2$L$^{P2}_2$.
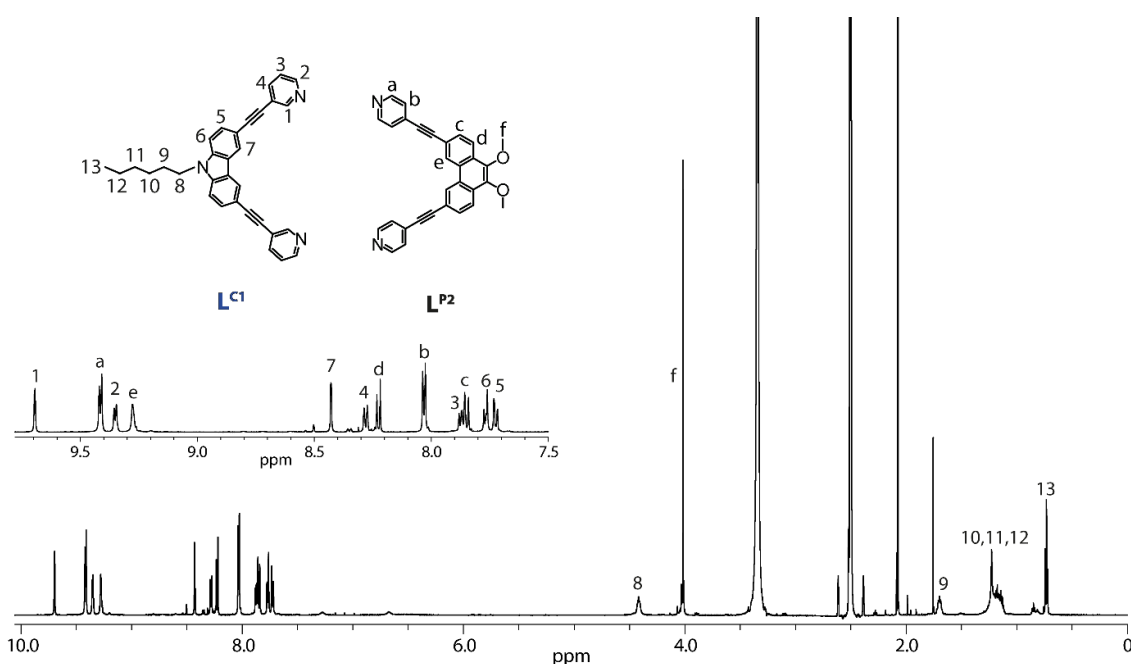
Figure 65: Full ^{1}H NMR spectrum (600 MHz, 298 K, DMSO-d_6) of Pd$_2$L$^{C1}_2$L$^{P2}_2$. The inset shows a zoom of the aromatic region.

^{1}H NMR (600 MHz, 298 K, DMSO-d_6) δ 9.70 (d, ^4J = 1.6 Hz, 4H, H^1), 9.41 (d, ^3J = 6.6 Hz, 8H, H^a), 9.35 (d, ^3J = 5.6 Hz, 4H, H^2), 9.28 (s, 4H, H^e), 8.43 (d, ^4J = 0.95 Hz, 4H, H^7), 8.28 (d, ^3J = 7.95 Hz, ^4J = 1.55 Hz, 4H, H^4), 8.23 (d, ^3J = 8.5 Hz, 4H, H^d), 8.03 (d, ^3J = 6.85 Hz, 8H, H^b), 7.83 – 7.89 (m, 8H, H^3+H^c), 7.75 – 7.79 (m, 4H, H^6), 7.72 (dd, ^3J = 8.5 Hz, ^4J = 1.4 Hz, 4H, H^5), 4.42 (t, ^3J = 6.3 Hz, 4H, H^8), 4.01 (s, 12H, H^f), 1.70 (quint, ^3J = 6.9 Hz, 4H, H^9), 1.10 – 1.32 (m, 12H, H$^{10\text{-}12}$), 0.73 (t, ^3J = 7.1 Hz, 6H, H^{13}) ppm.
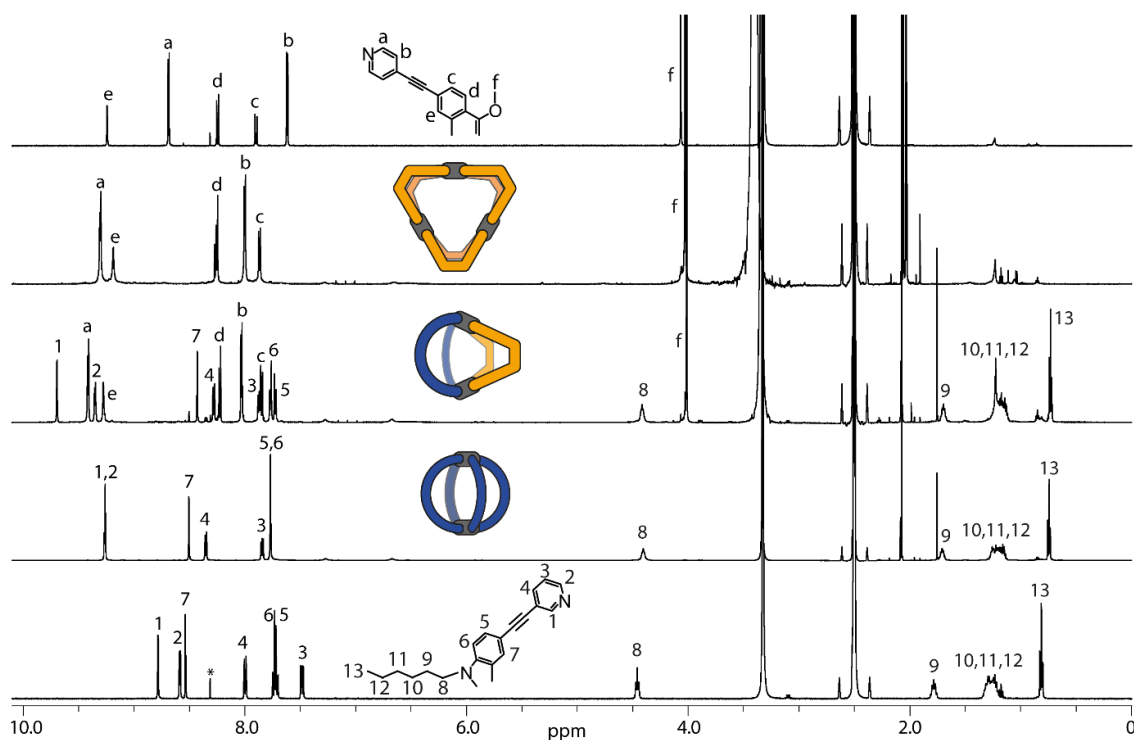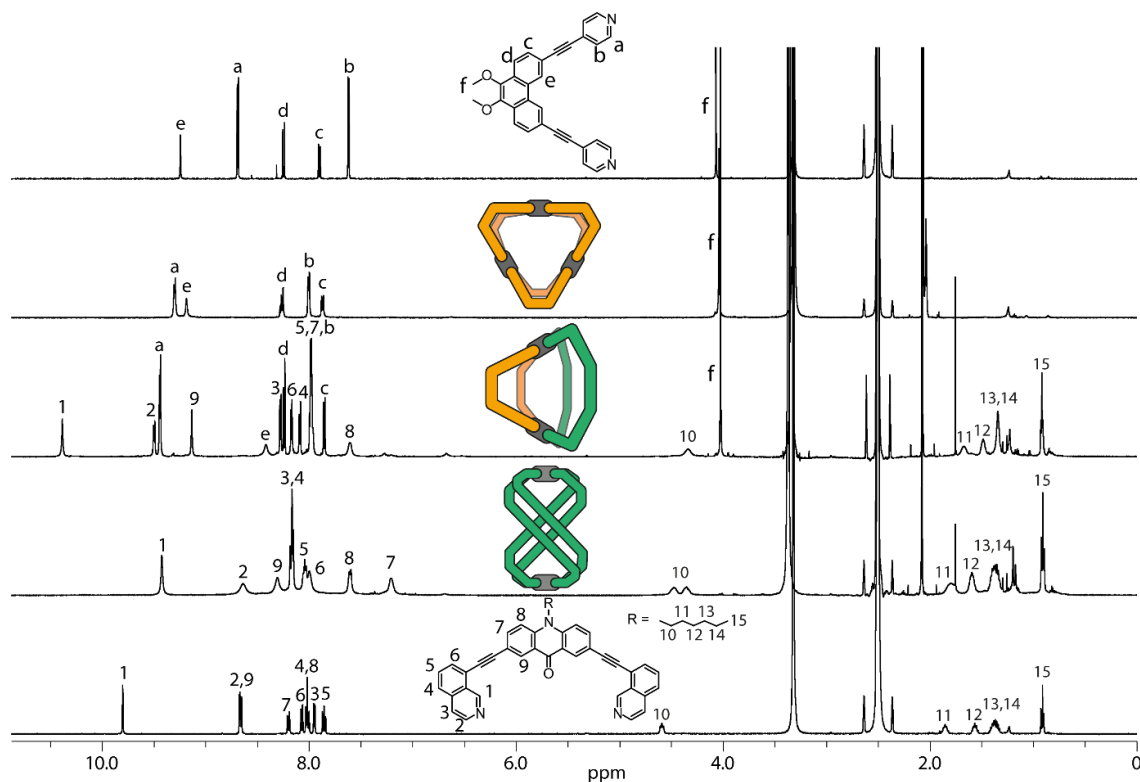
Figure 66: Full stacked ^{1}H NMR spectra of (bottom to top) ligand $\mathbf{L^{C1}}$ (500 MHz, 298 K, DMSO-d_6), the corresponding homoleptic cage Pd$_2$$\mathbf{L^{C1}}_4$ (600 MHz, 298 K, DMSO-d_6) formed upon addition of 0.55 equiv. Pd(II) to ligand $\mathbf{L^{C1}}$, the heteroleptic assembly Pd$_2$$\mathbf{L^{C1}}_2$$\mathbf{L^{P2}}_2$ (600 MHz, 298 K, DMSO-d_6), the Pd$_3$$\mathbf{L^{P2}}_6$ ring ligand $\mathbf{L^{P2}}$ forms upon addition of 0.55 equiv. Pd(II) (600 MHz, 298 K, DMSO-d_6) and ligand $\mathbf{L^{P2}}$ (500 MHz, 298 K, DMSO-d_6).

Figure 67: ^{13}C NMR spectrum (151 MHz, 298 K, DMSO-d_6) of Pd$_2$$\mathbf{L^{C1}}_2$$\mathbf{L^{P2}}_2$.

^{13}C{^{1}H} (151 MHz, 298 K, DMSO-d_6) δ 152.34, 151.02, 149.68, 144.81, 142.27, 140.96, 134.71, 130.55, 129.89, 129.70, 128.81, 127.42, 127.12, 123.82, 123.38, 123.02, 122.89, 121.59, 118.24, 111.44, 110.96, 99.71, 96.77, 86.67, 83.04, 61.21, 30.80, 29.03, 28.39, 21.93, 13.74 ppm.

The NCH$_2$ carbon signal could not be resolved.
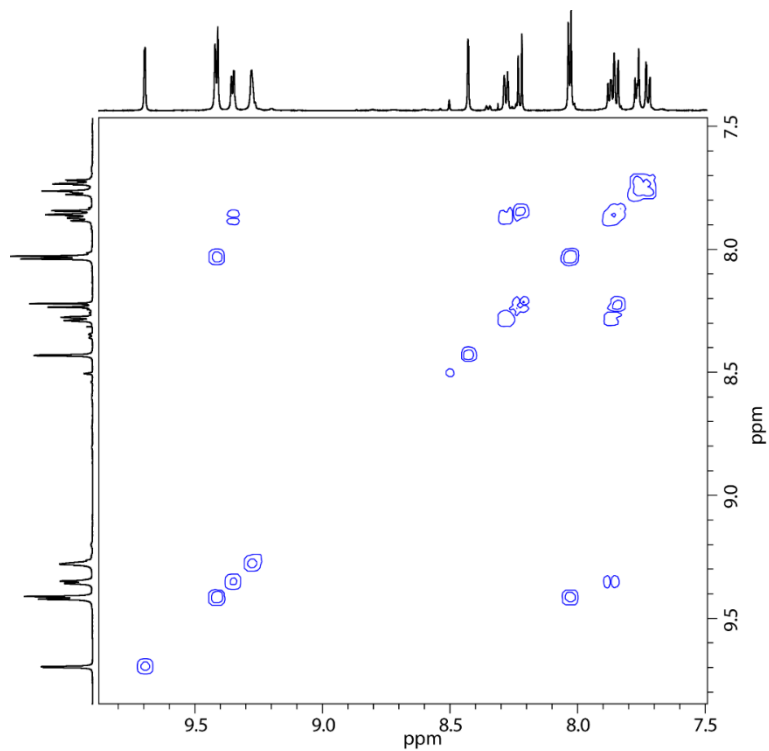
Figure 68: Partial ^{1}H-^{1}H COSY NMR spectrum (600 MHz, 298 K, DMSO-d_6) of Pd$_2$**L^{C1}**$_2$**L^{P2}**$_2$.
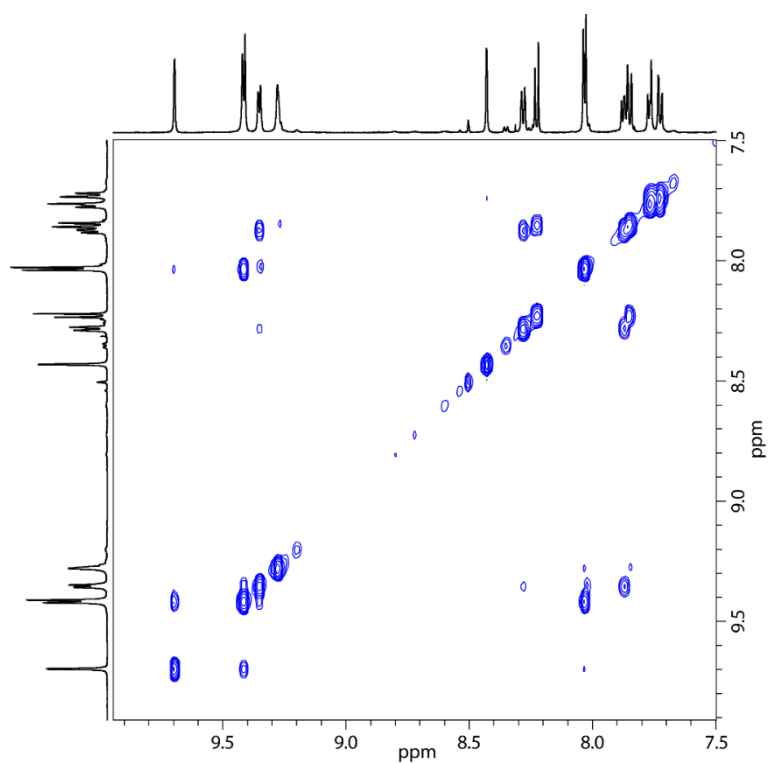
Figure 69: Partial ^{1}H-^{1}H NOESY NMR spectrum (600 MHz, 298 K, DMSO-d_6) of Pd$_2$**L^{C1}**$_2$**L^{P2}**$_2$.
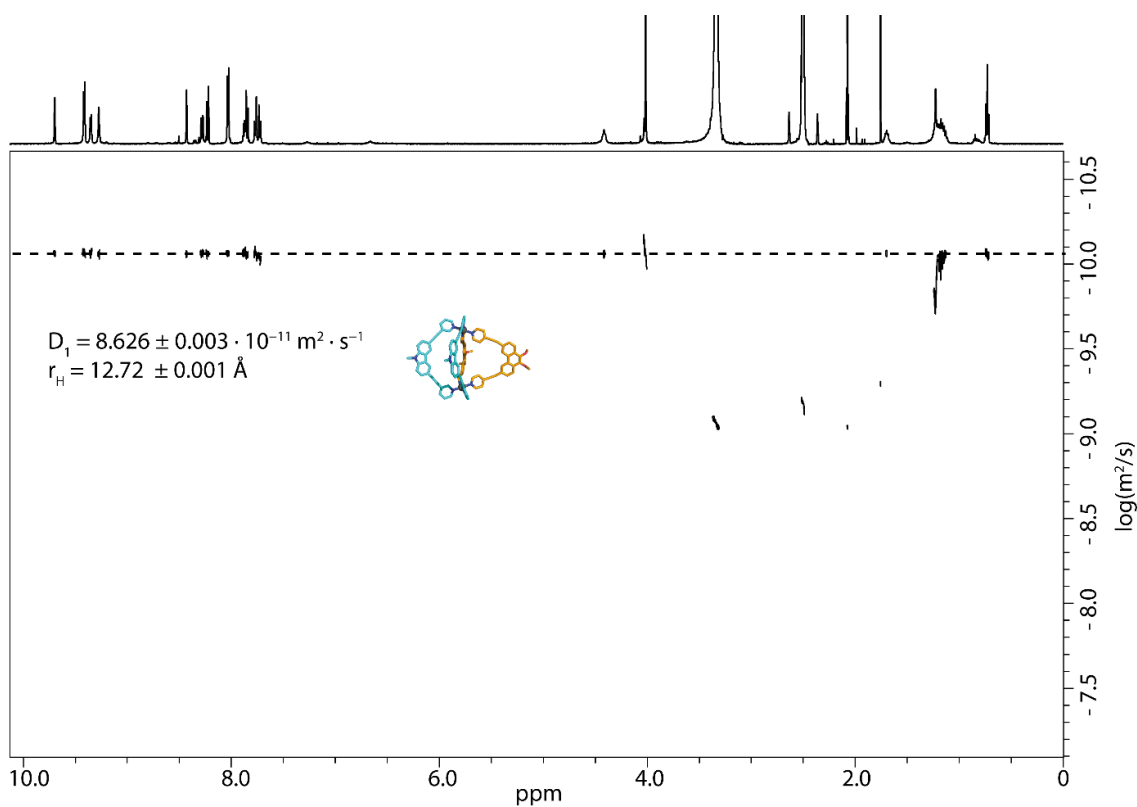
Figure 70: ^{1}H DOSY NMR spectrum (500 MHz, 298 K, DMSO-d_6) of Pd$_2$L$^{C1}_2$L$^{P2}_2$.

Synthesis of Pd$_2$L$^{A1}_2$L$^{P2}_2$

A mixture of ligand **L^{P2}** (270 µL of a 3.11 mM solution in DMSO-d_6), ligand **L^{A1}** (270 µL of a 3.11 mM solution in DMSO-d_6) and [Pd(CH$_3$CN)$_4$](BF$_4$)$_2$ (60 µL of a 15 mM solution in DMSO-d_6) was left to rest at room temperature for 2h to afford the heteroleptic coordination cage Pd$_2$L$^{P2}_2$L$^{A1}_2$.
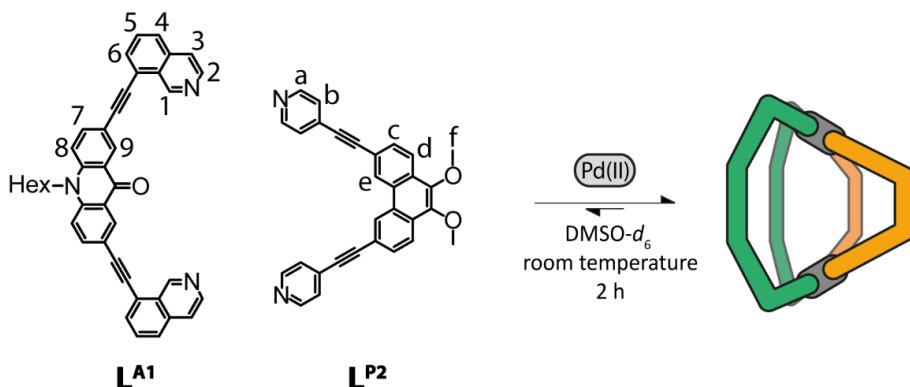
Scheme 7: Formation of Pd$_2$L$^{A1}_2$L$^{P2}_2$ with consecutive proton labels.
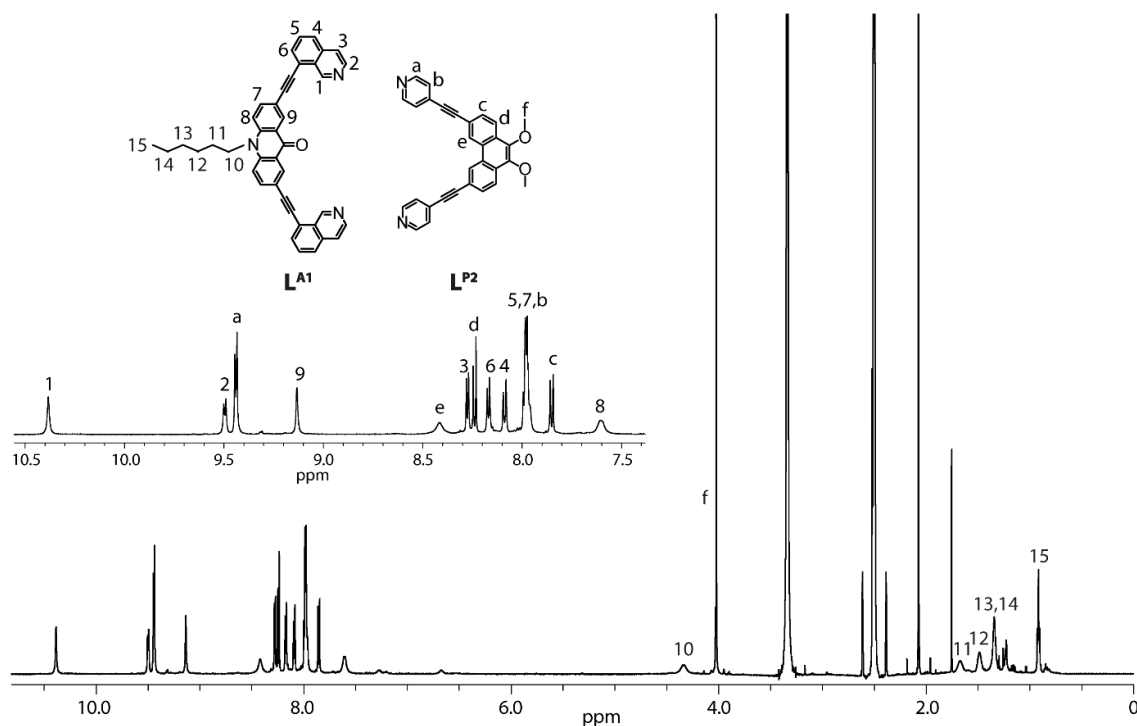
Figure 71: Full ^{1}H NMR spectrum (600 MHz, 298 K, DMSO-d_6) of Pd$_2$**L**$^{A1}_2$**L**$^{P2}_2$. The inset shows an enlargement of the aromatic region.

^{1}H NMR (600 MHz, 298 K, DMSO-d_6) δ 10.39 (s, 4H, H^1), 9.49 (d, ^3J = 6.4 Hz, 4H, H^2), 9.44 (d, ^3J = 6.7 Hz, 8H, H^a), 9.13 (s, 4H, H9), 8.42 (s (br), 4H, H^e), 8.28 (d, ^3J = 6.5 Hz, 4H, H^3), 8.24 (d, ^3J = 8.6 Hz, 4H, H^d), 8.17 (d, ^3J = 7.2 Hz, 4H, H^6), 8.09 (d, ^3J = 8.4 Hz, 4H, H^4), 7.94 – 8.00 (m, 16H, H^{5+7+b}), 7.85 (d, ^3J = 8.6 Hz, 4H, H^c), 7.60 (s (br), 4H, H^8), 4.34 (s (br), 4H, H^{10}), 4.02 (s, 12H, H^f), 1.67 (s (br), 4H, H^{11}), 1.48 (s (br), 4H, H^{12}), 1.3 – 1.4 (m, 8H, H^{13+14}), 0.92 (t, ^3J = 6.95 Hz, 6H, H^{15}) ppm.

Figure 72: Full stacked ^{1}H NMR spectra of (bottom to top) ligand $\mathbf{L^{A1}}$ (500 MHz, 298 K, DMSO-d_6), the corresponding homoleptic cage Pd$_2\mathbf{L^{A1}}_4$ (500 MHz, 298 K, DMSO-d_6) formed upon addition of 0.55 equiv. Pd(II) to ligand $\mathbf{L^{A1}}$, the heteroleptic assembly Pd$_2\mathbf{L^{A1}}_2\mathbf{L^{P2}}_2$ (600 MHz, 298 K, DMSO-d_6), the Pd$_3\mathbf{L^{P2}}_6$ ring ligand $\mathbf{L^{P2}}$ forms upon addition of 0.55 equiv. Pd(II) (600 MHz, 298 K, DMSO-d_6) and ligand $\mathbf{L^{P2}}$ (500 MHz, 298 K, DMSO-d_6).

Figure 73: ^{13}C NMR spectrum (151 MHz, 298 K, DMSO-d_6) of Pd$_2\mathbf{L^{A1}}_2\mathbf{L^{P2}}_2$.

$^{13}C\{^1H\}$ (151 MHz, 298 K, DMSO-d_6) δ 175.17, 152.89, 151.48, 144.65, 142.85, 140.79, 137.24, 136.07, 136.05, 135.95, 134.55, 133.76, 129.78, 129.67, 128.53, 128.33, 127.73, 127.38, 127.13, 125.00, 122.99, 121.33, 121.12, 118.26, 116.64, 114.56, 98.76, 96.59, 86.09, 85.55, 61.20, 31.05, 29.03, 25.57, 22.15, 13.95 ppm.

NCH_2 carbon signal cannot be found due to overlap with DMSO solvent signal.
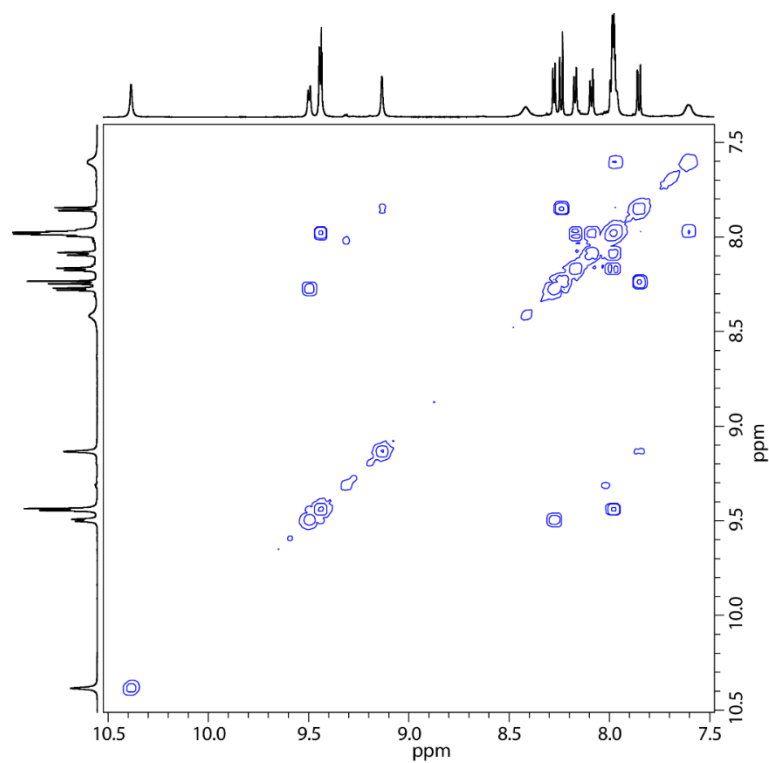
Figure 74: Partial ^1H-^1H COSY NMR spectrum (600 MHz, 298 K, DMSO-d_6) of Pd$_2$**L**^{A1}$_2$**L**^{P2}$_2$.
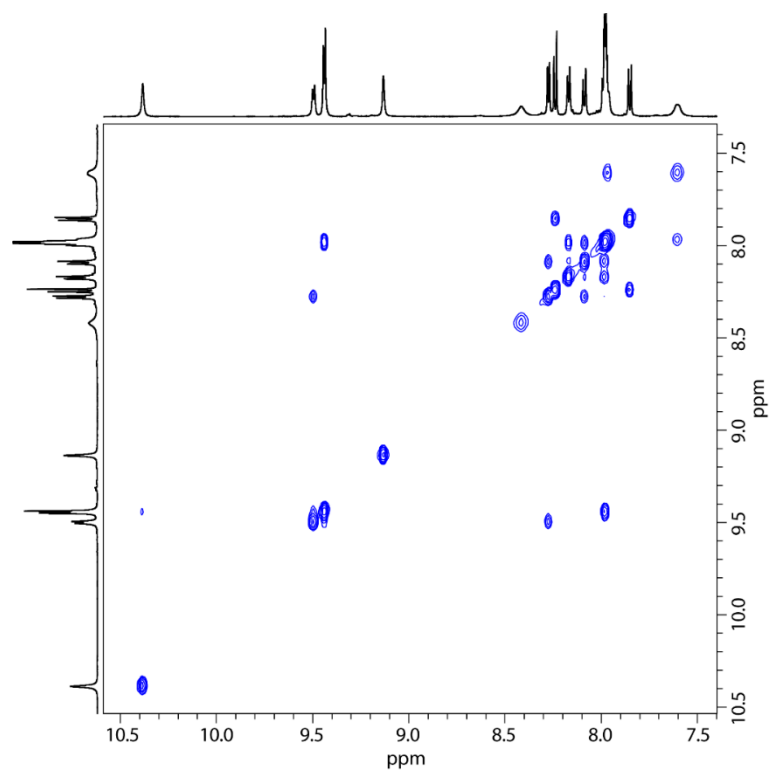
Figure 75: Partial ^{1}H-^{1}H NOESY NMR spectrum (600 MHz, 298 K, DMSO-d_6) of Pd$_2$**L**$^{A1}_2$**L**$^{P2}_2$.

$D_1 = 8.4225 \pm 0.003 \cdot 10^{-11}$ m$^2 \cdot$ s^{-1}
$r_H = 13.02 \pm 0.005$ Å
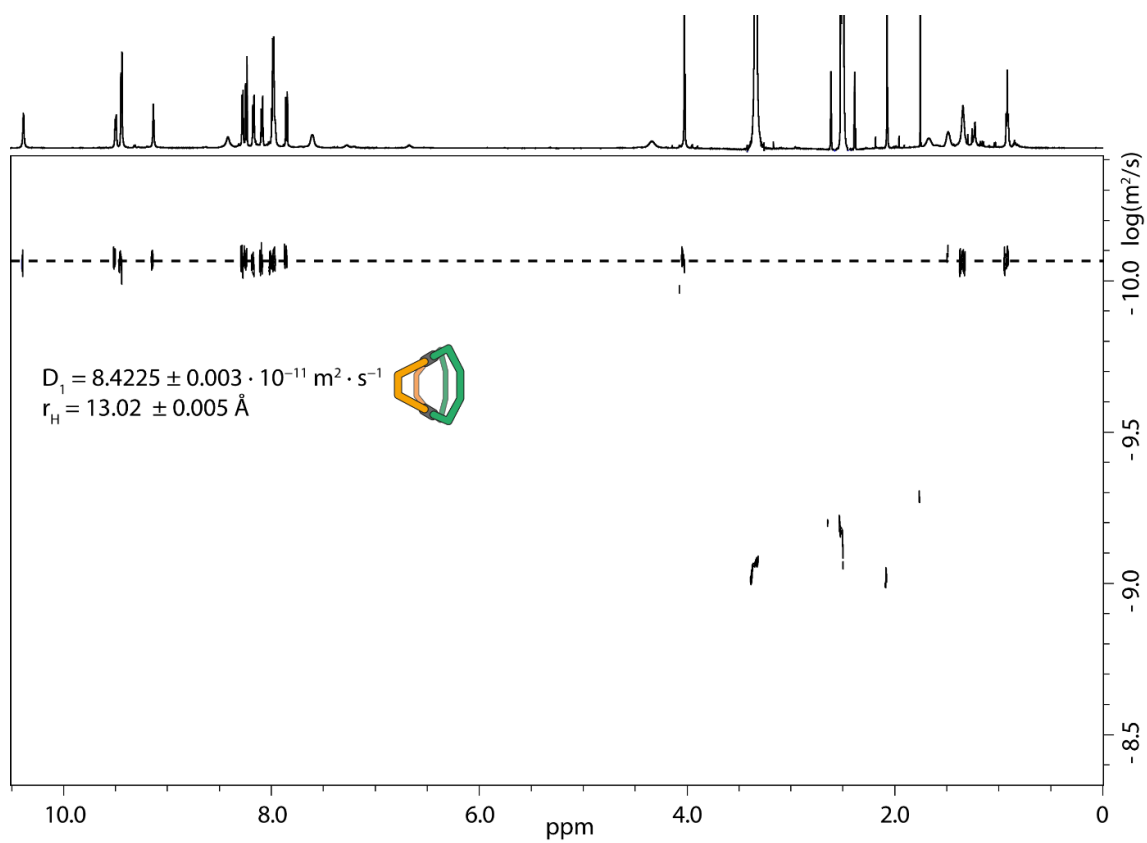
Figure 76: ^{1}H DOSY NMR spectrum (500 MHz, 298 K, DMSO-d_6) of Pd$_2$**L**$^{A1}_2$**L**$^{P2}_2$.

Synthesis of the three-component mixture in CD$_3$CN

Pd$_2$**L$^{P2}_2$L$^{A1}_2$** was formed in DMSO-d_6 according to previously described procedure. The solvent was removed via lyophilization and the yellow powder was redissolved in 600 µl CD$_3$CN. The solution was heated to equilibrate until no changes could be observed anymore.
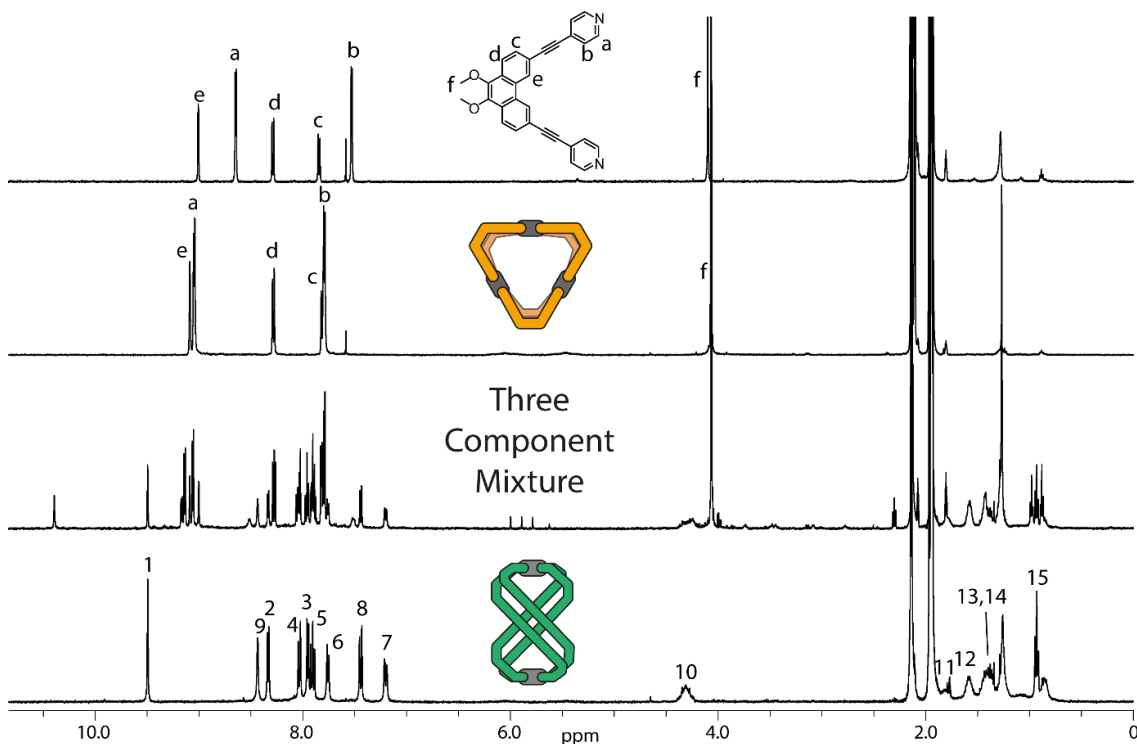
Figure 77: Full stacked ^{1}H NMR spectra of (bottom to top) homoleptic cage Pd$_2$**L$^{A1}_4$** (600 MHz, 298 K, CD$_3$CN) formed upon addition of 0.55 equiv. Pd(II) to ligand **L^{A1}**, the mixture of heteroleptic assembly Pd$_2$**L$^{A1}_2$L$^{P2}_2$**, homoleptic Pd$_2$**L$^{A1}_4$** cage and homoleptic Pd$_3$**L$^{P2}_6$** ring (600 MHz, 298 K, CD$_3$CN), the Pd$_3$**L$^{P2}_6$** ring ligand **L^{P2}** forms upon addition of 0.55 equiv. Pd(II) (600 MHz, 298 K, CD$_3$CN) and ligand **L^{P2}** (500 MHz, 298 K, CD$_3$CN).

3.2.5.2 Multi-Trigger Post-Assembly Cage-Separation

Pd$_2$**L$^{P2}_2$L$^{A1}_2$** was formed in DMSO-d$_6$ according to previously described procedure. The solvent was removed via lyophilization and the yellow powder was redissolved in 600 µl CD$_3$CN. 3 equiv. (24 µl) propane-1,3-bissulfonate (equivalents given in respect to maximal Pd$_3$**L$^{P2}_6$** ring concentration of 0.2$\overline{3}$ mM, **G^1**) were added stepwise. The solution was heated to 70 °C for 5 minutes in-between measurements to assure equilibrium adaptation.
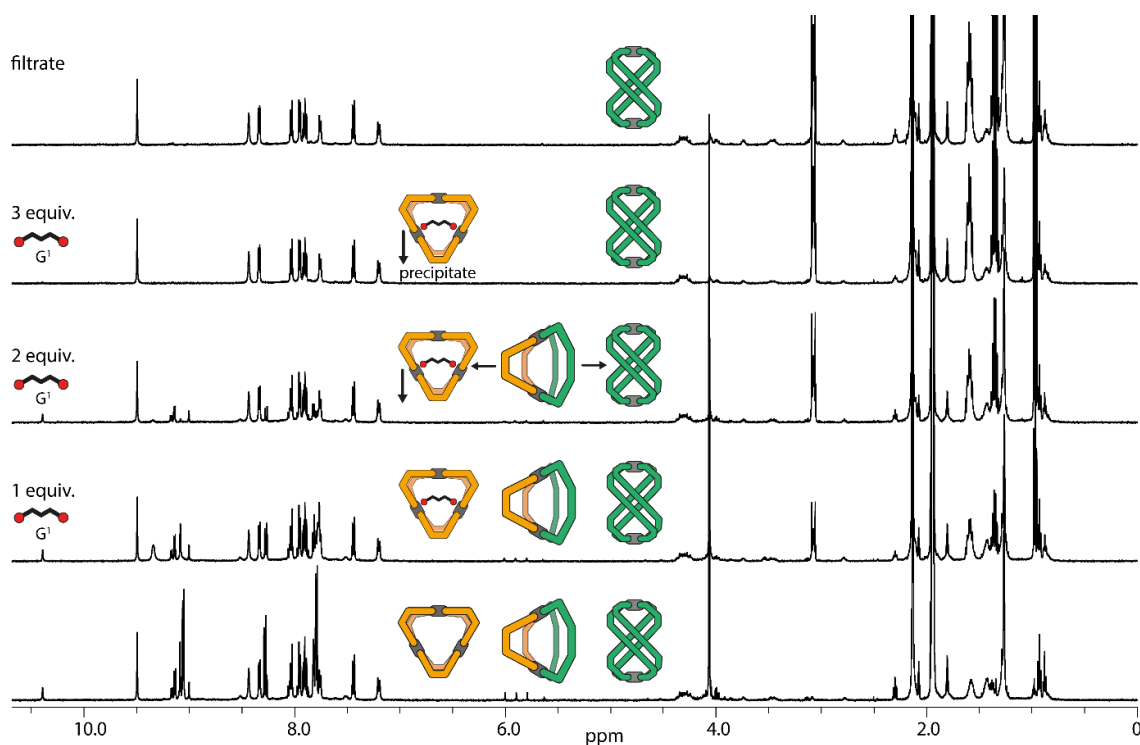
Figure 78: Full ^{1}H NMR spectra (500 MHz, 298 K, CD$_3$CN) of the mixture of heteroleptic assembly Pd$_2$L$^{A1}_2$L$^{P2}_2$, homoleptic Pd$_2$L$^{A1}_4$ cage and homoleptic Pd$_3$L$^{P2}_6$ ring with consecutive addition of **G^1** and finally of the filtrate being purely homoleptic Pd$_2$L$^{A1}_4$ cage (bottom to top).
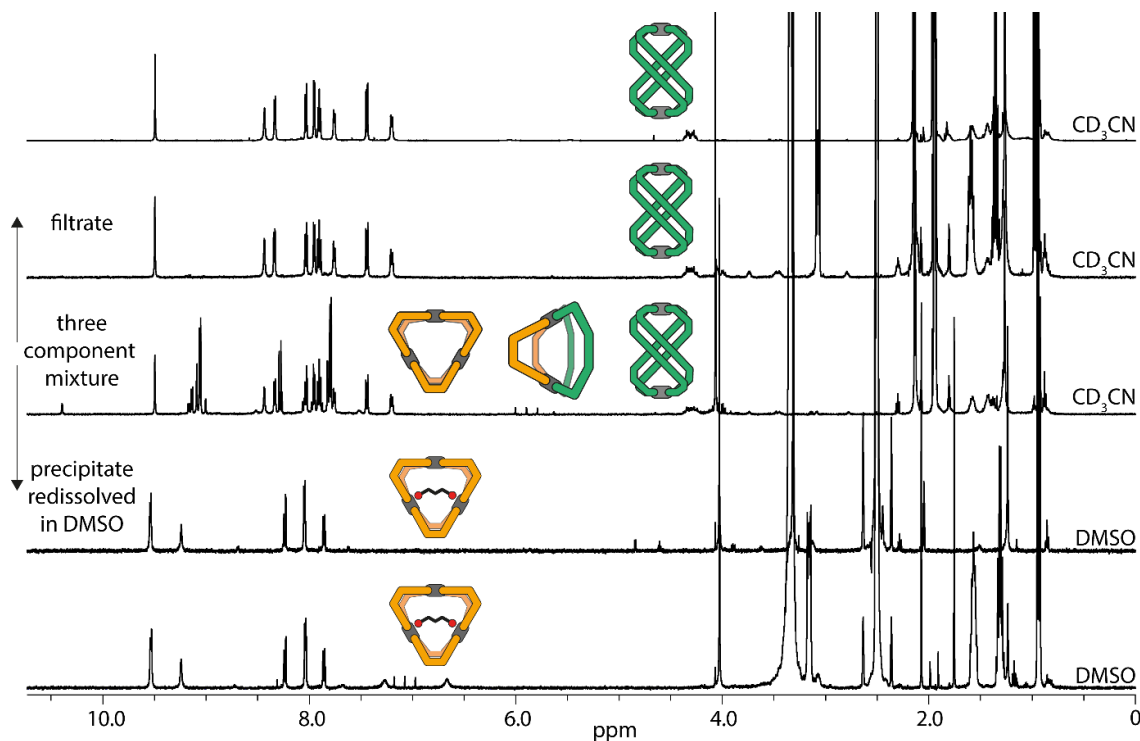
Figure 79: Full ^{1}H NMR spectra (bottom to top) of homoleptic Pd$_3$L$^{P2}_6$ ring after addition of 2 equiv. **G^1** (500 MHz, DMSO-d_6), the precipitate of [x**G^1**@Pd$_3$L$^{P2}_6$] ring redissolved in DMSO-d_6 (500 MHz, DMSO-d_6); the mixture of heteroleptic assembly Pd$_2$L$^{A1}_2$L$^{P2}_2$, homoleptic Pd$_2$L$^{A1}_4$ cage and homoleptic Pd$_3$L$^{P2}_6$ ring (600 MHz, CD$_3$CN); the filtrate recovered from the mixture after treatment with 3 equiv. **G^1** (500 MHz, CD$_3$CN); the helical homoleptic Pd$_2$L$^{A1}_4$ cage (600 MHz, CD$_3$CN). All spectra were measured at 298 K.

3.2.5.3 Host-Guest Chemistry

Titration of Pd$_3$L$^{P2}_6$ with G^1
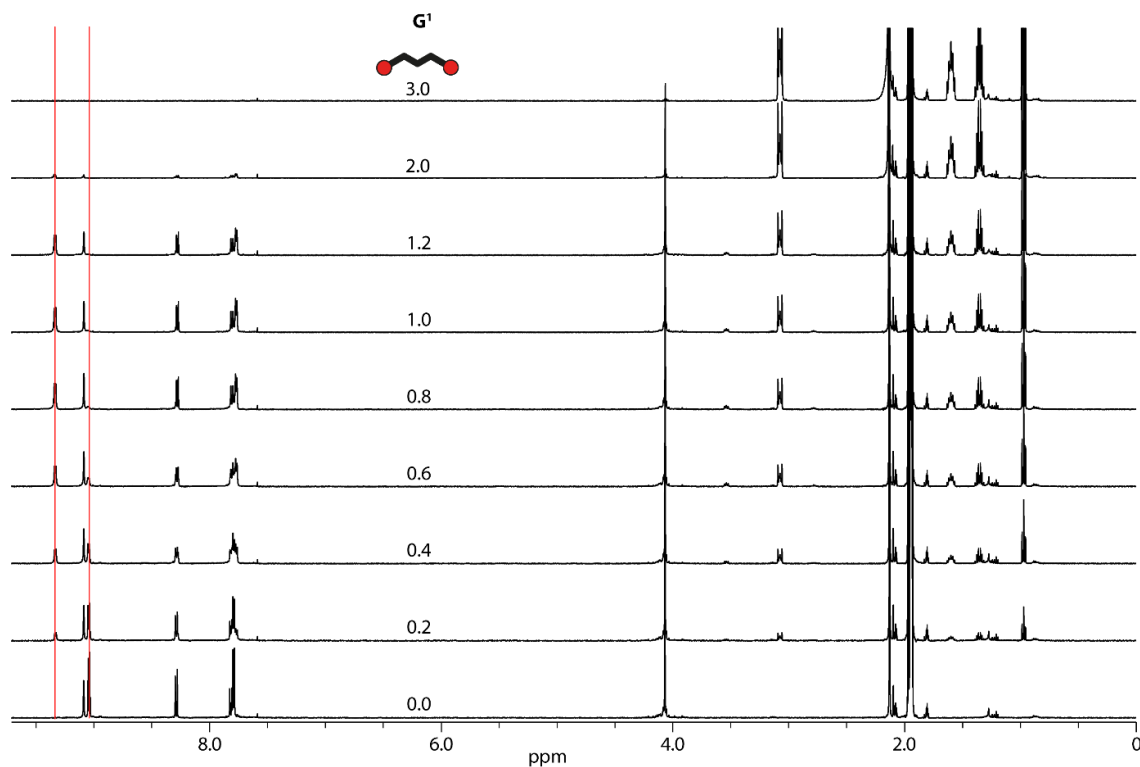
Figure 80: ^{1}H NMR titration (500 MHz, 298K, CD$_3$CN) of Pd$_3$L$^{P2}_6$ (0.233 mM in CD$_3$CN) with G^1 (17.5 mM solution in CD$_3$CN).
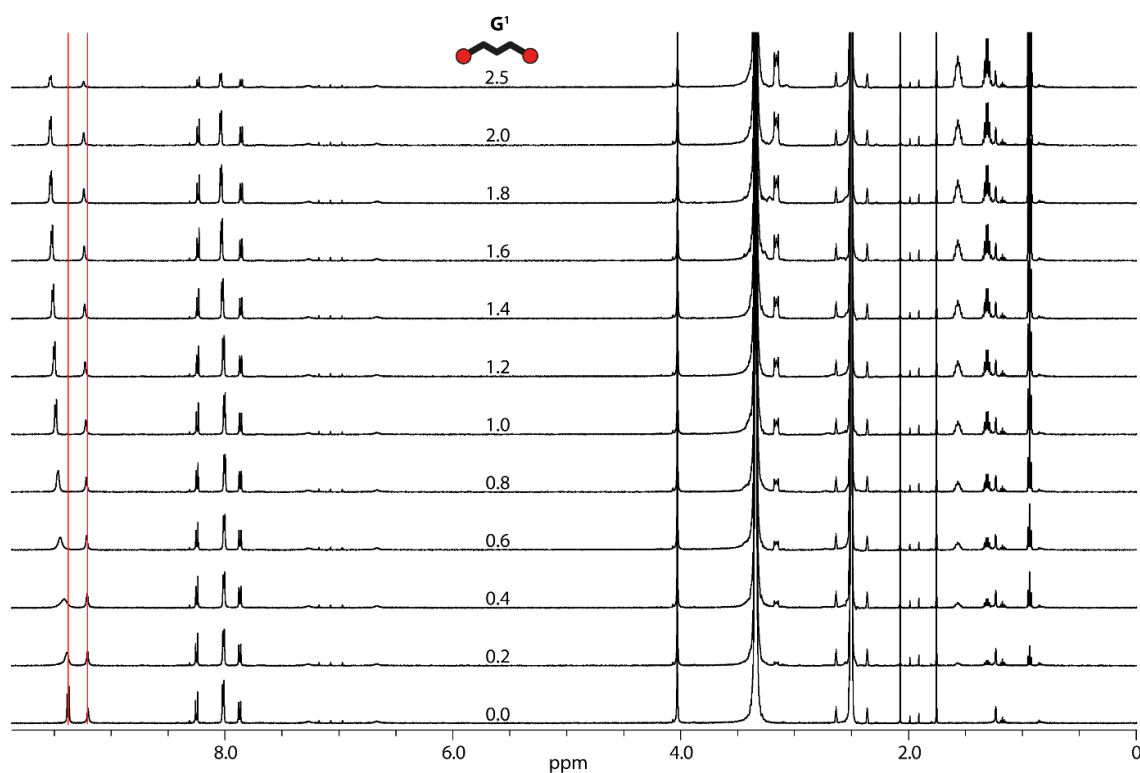
Figure 81: ^{1}H NMR titration (500 MHz, 298K, DMSO-d_6) of Pd$_3$L$^{P2}_6$ (0.233 mM in DMSO-d_6) with G^1 (17.5 mM solution in DMSO-d_6).
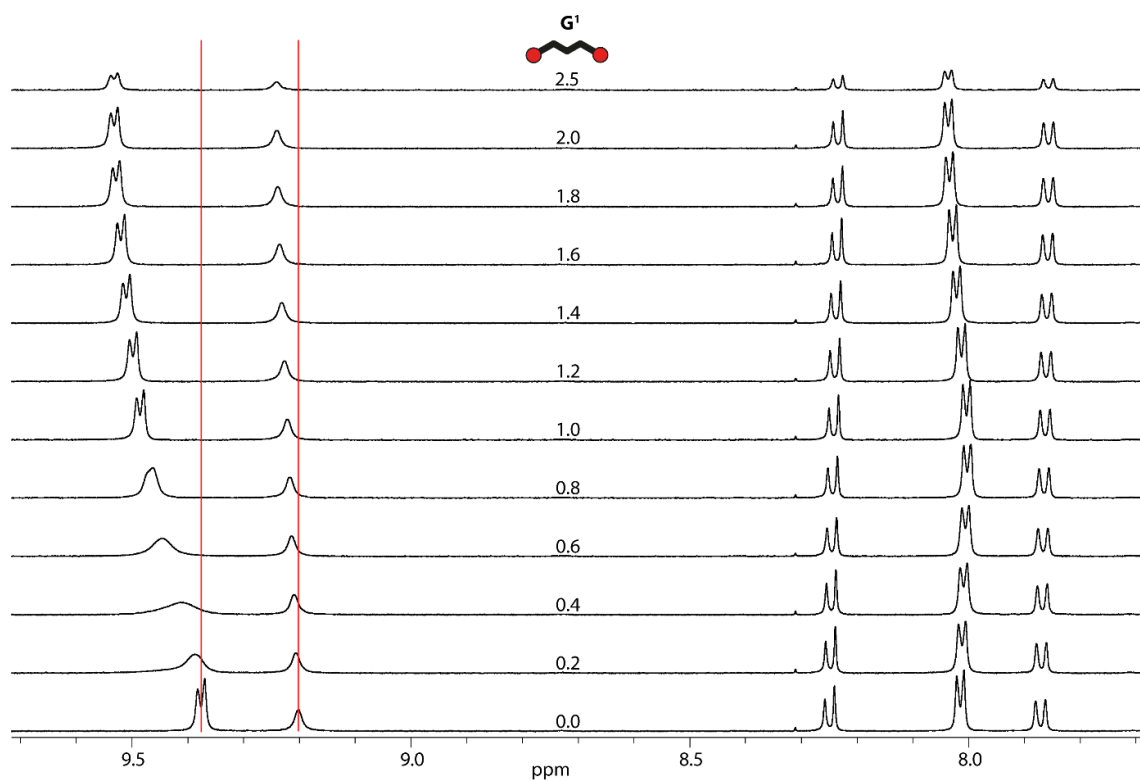
Figure 82: Aromatic region of the ^{1}H NMR titration (500 MHz, 298K, DMSO-d_6) of Pd$_3$**L^{P2}**$_6$ (0.233 mM in DMSO-d_6) with **G^1** (17.5 mM solution in DMSO-d_6).
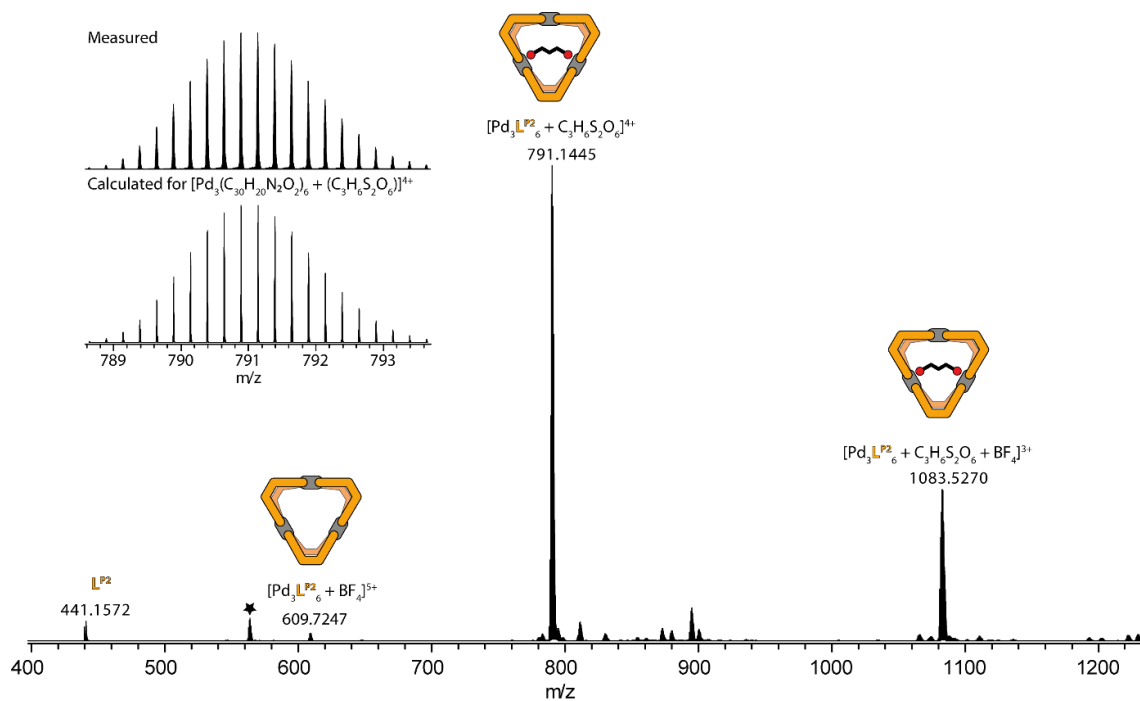
Figure 83: ESI-MS spectrum of [Pd$_3$**L^{P2}**$_6$ + xBF$_4$]$^{(6−x)+}$ + 1 equiv. of **G^1**. The observed and calculated isotopic pattern of [**G^1**@ Pd$_3$**L^{P2}**$_6$]$^{2+}$ are shown in the inset.

Titration of Pd₃L^{P2}₆ with **G²**
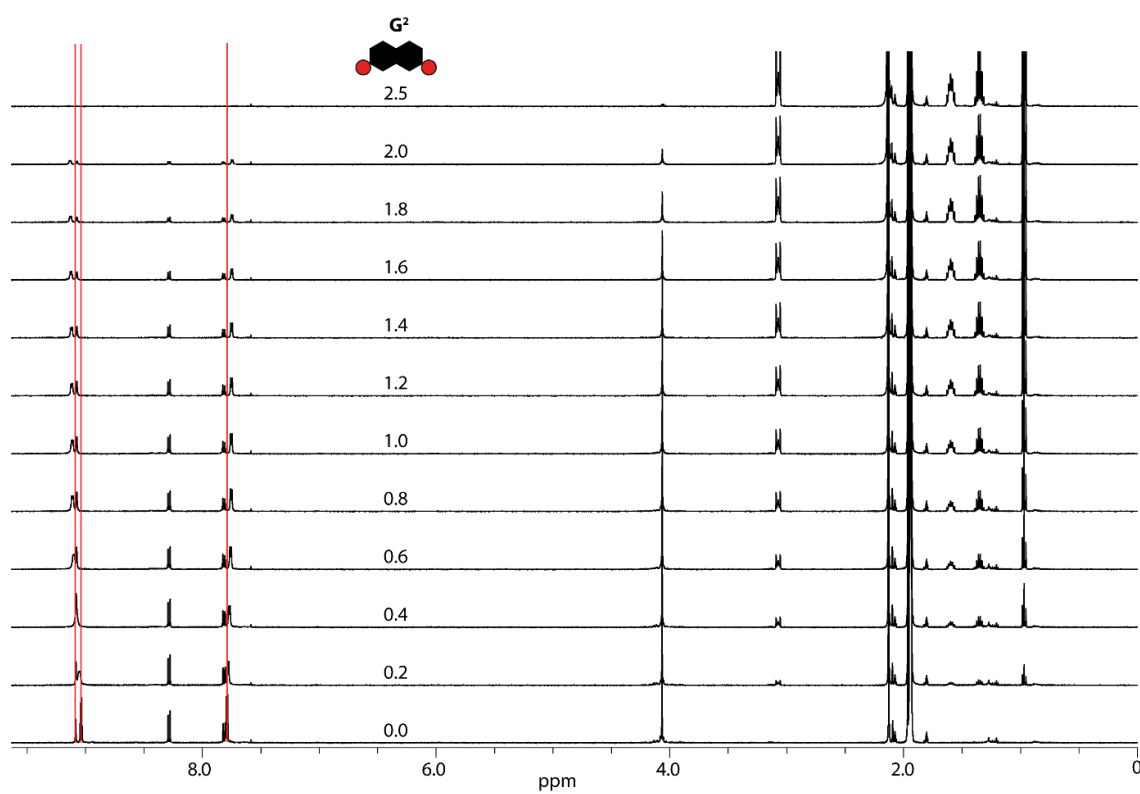
Figure 84: ^{1}H NMR titration (500 MHz, 298K, CD$_3$CN) of Pd$_3$L^{P2}$_6$ (0.233 mM in CD$_3$CN) with **G²** (17.5 mM solution in CD$_3$CN).
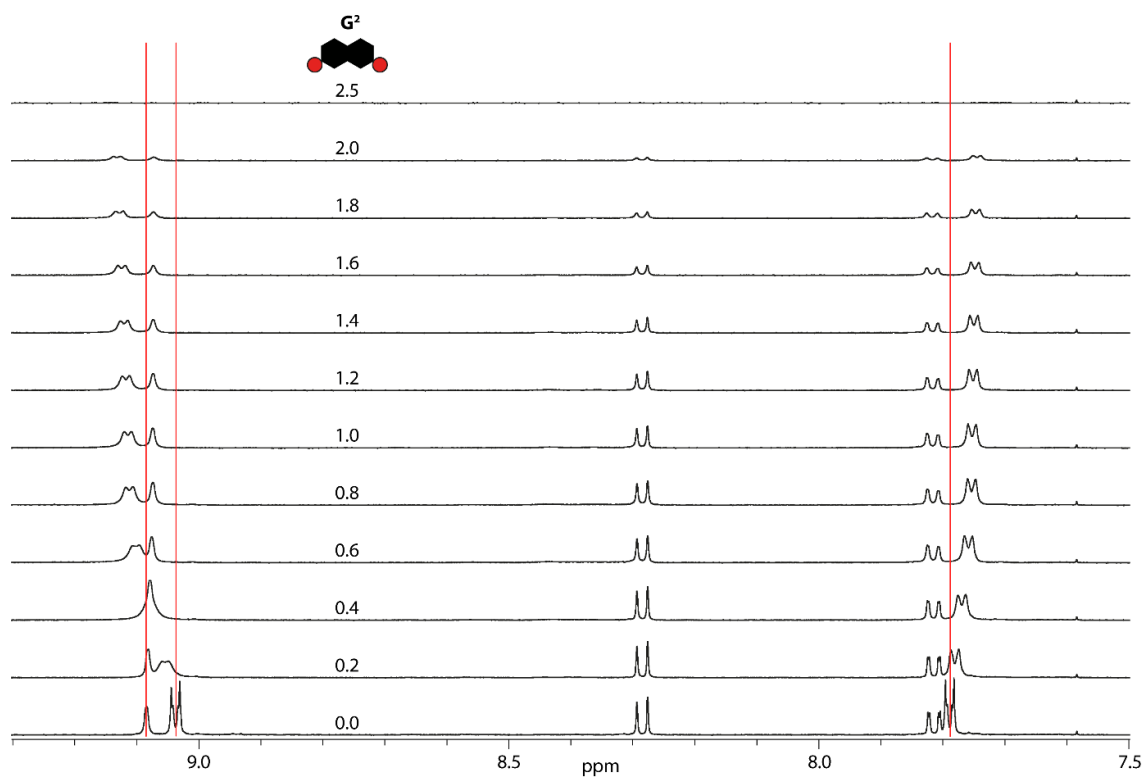
Figure 85: Aromatic region of the ^{1}H NMR titration (500 MHz, 298K, CD$_3$CN) of Pd$_3$L^{P2}$_6$ (0.233 mM in CD$_3$CN) with **G²** (17.5 mM solution in CD$_3$CN).
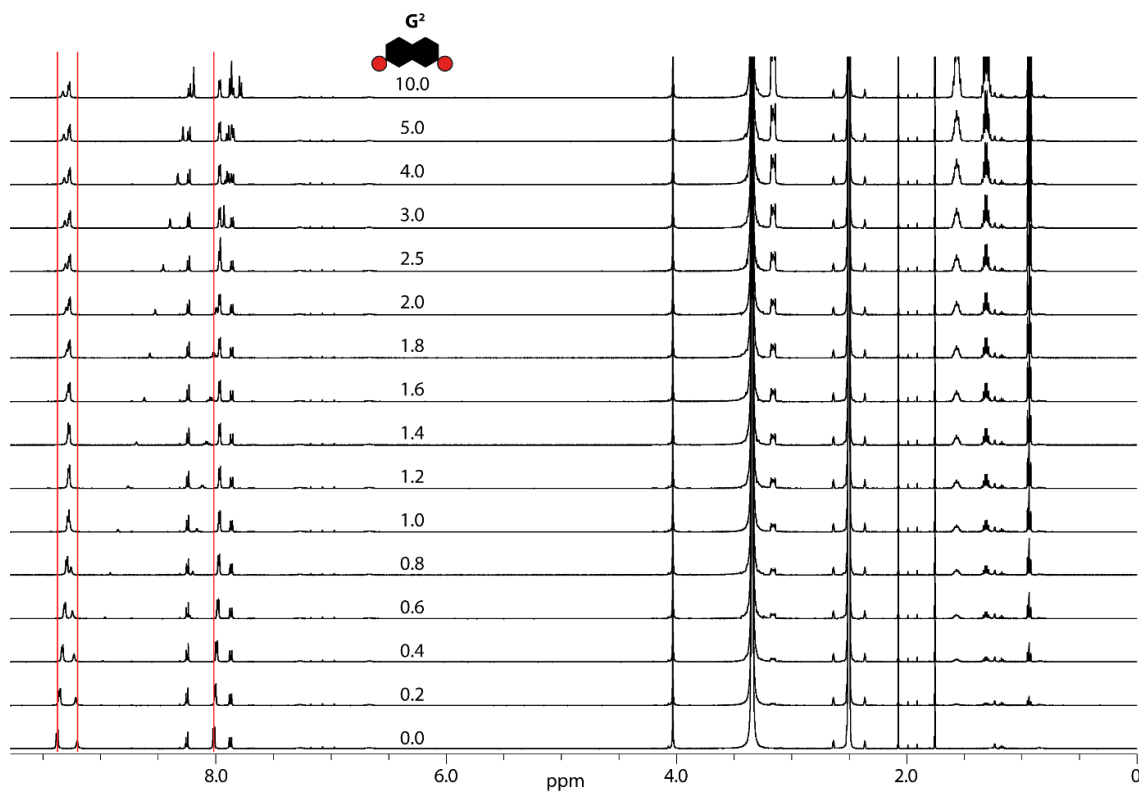
Figure 86: ^{1}H NMR titration (500 MHz, 298K, DMSO-d_6) of Pd$_3$**L**$^{P2}_6$ (0.233 mM in DMSO-d_6) with **G^2** (17.5 mM solution in DMSO-d_6).
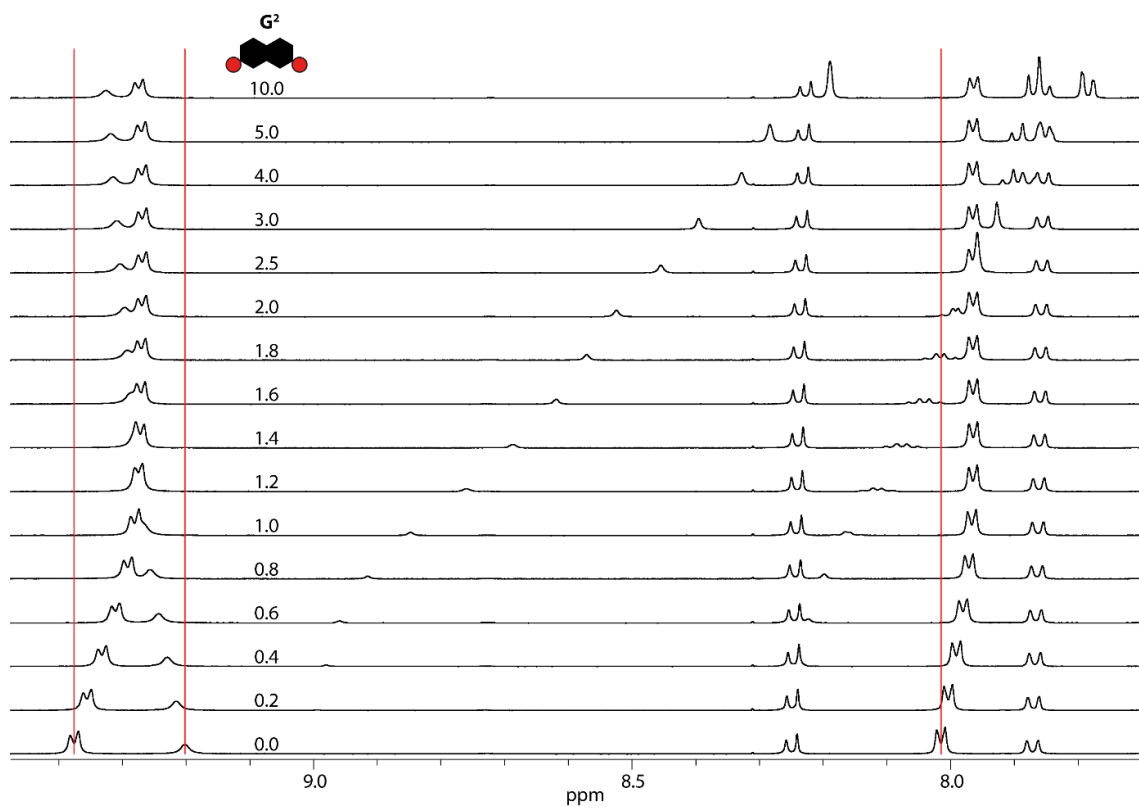
Figure 87: Aromatic region of the ^{1}H NMR titration (500 MHz, 298K, DMSO-d_6) of Pd$_3$**L**$^{P2}_6$ (0.233 mM in DMSO-d_6) with **G^2** (17.5 mM solution in DMSO-d_6).
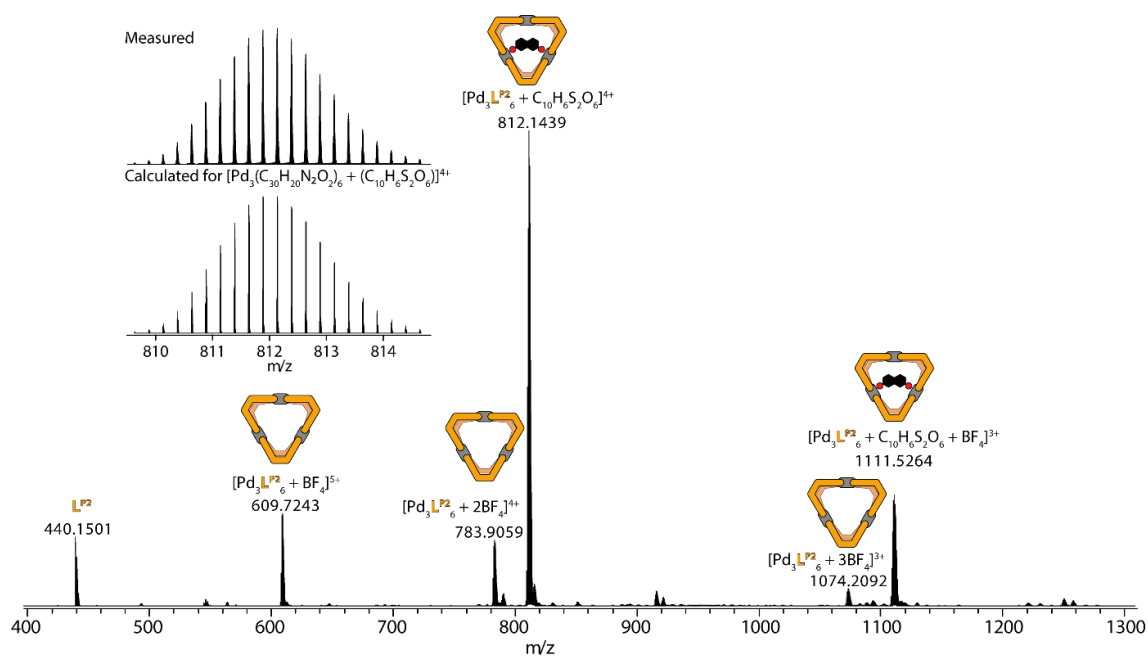
Figure 88: ESI-MS spectrum of $[Pd_3L^{P2}_6 + xBF_4]^{(6-x)+}$ + 1 equiv. of **G²**. The observed and calculated isotopic pattern of $[G^2@ Pd_3L^{P2}_6]^{2+}$ are shown in the inset.

Titration of $Pd_2L^{A1}_2L^{P2}_2$ with **G¹**
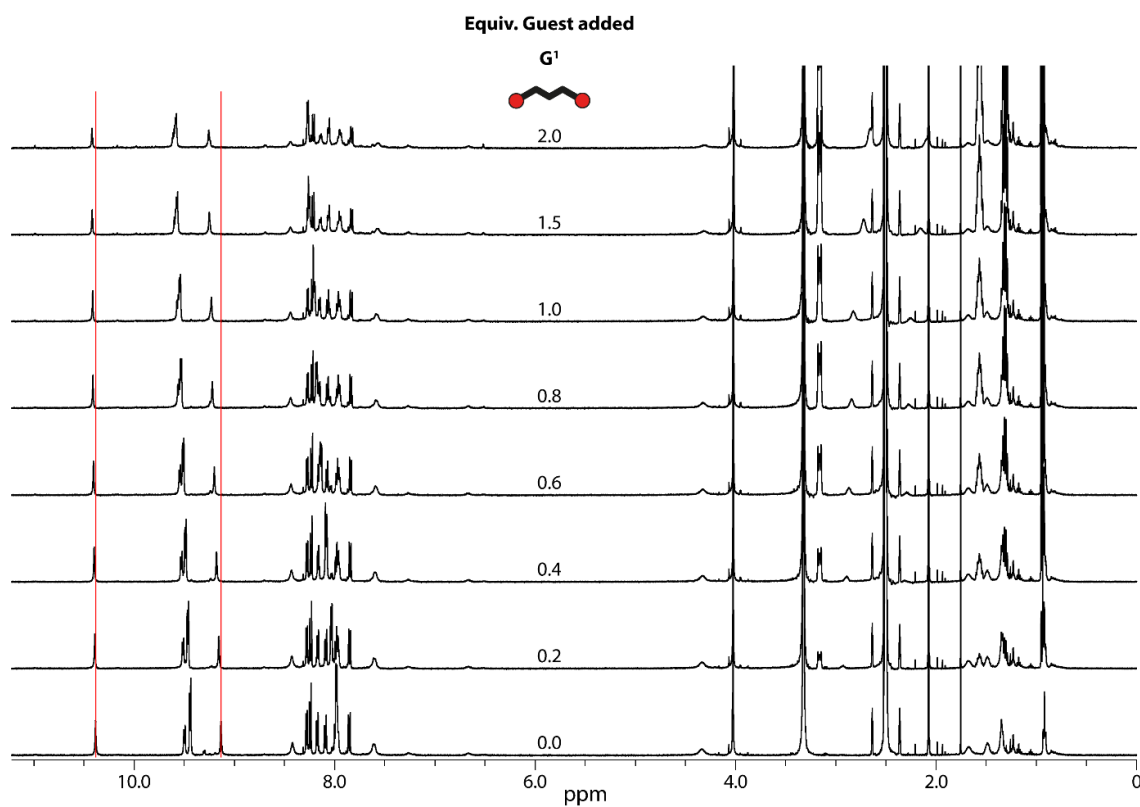
Figure 89: ¹H NMR titration (500 MHz, 298K, DMSO-d_6) of $Pd_2L^{A1}_2L^{P2}_2$ (0.7 mM in DMSO-d_6) with **G¹** (17.5 mM solution in DMSO-d_6).
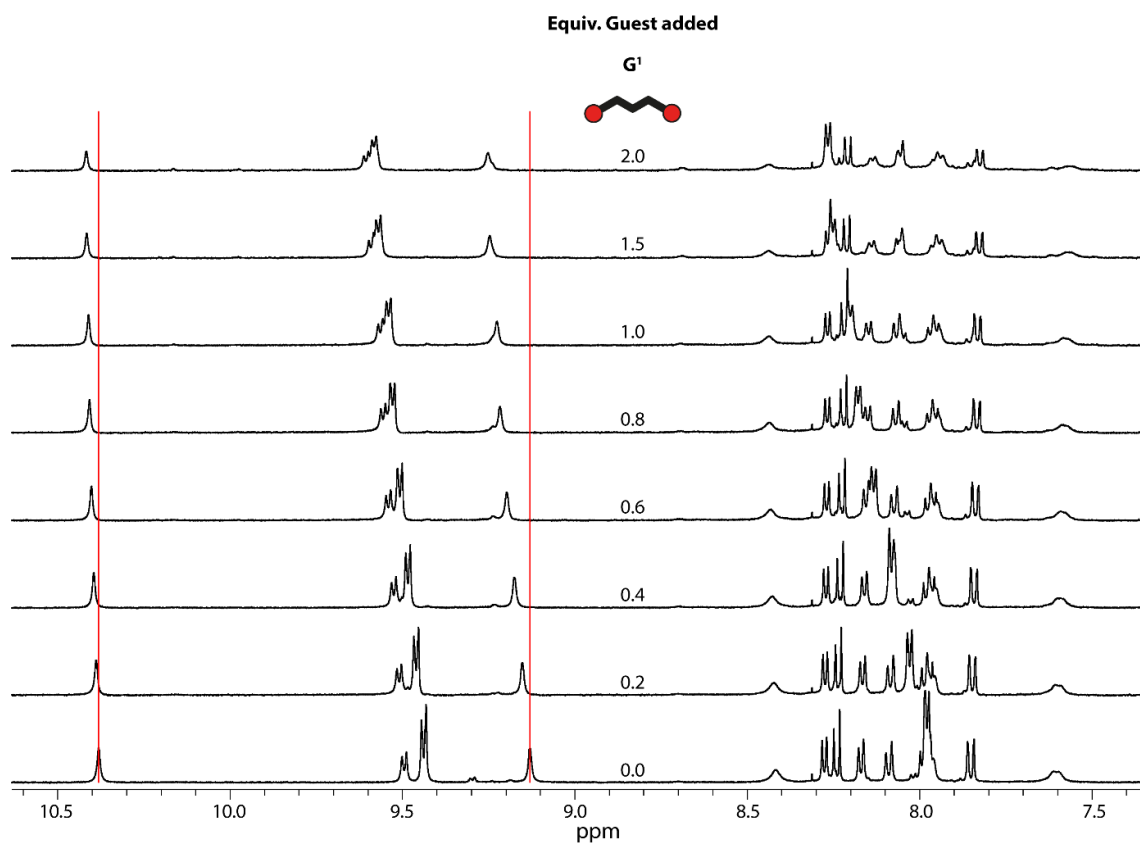
Figure 90: Aromatic region of the ^{1}H NMR titration (500 MHz, 298K, DMSO-d_6) of Pd$_2$**L**$^{A1}_2$**L**$^{P2}_2$ (0.7 mM in DMSO-d_6) with **G^1** (17.5 mM solution in DMSO-d_6).
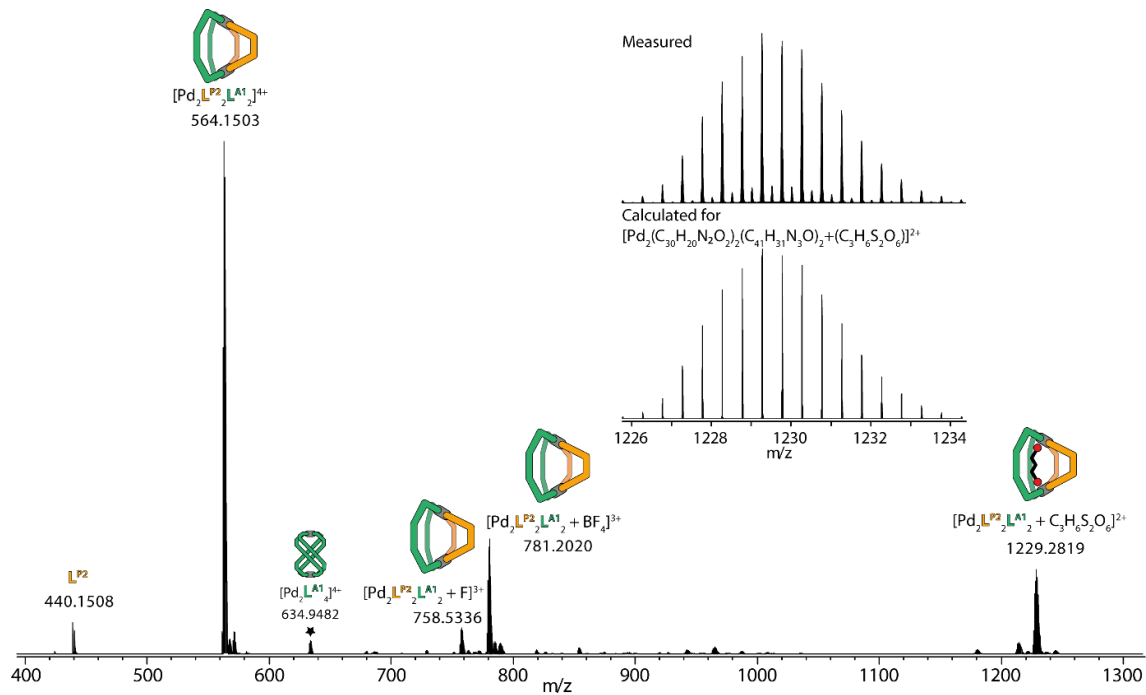
Figure 91: ESI-MS spectrum of [Pd$_2$**L**$^{A1}_2$**L**$^{P2}_2$ + xBF$_4$]$^{(4-x)+}$ + 1 equiv. of **G^1**. The observed and calculated isotopic pattern of [**G^1**@Pd$_2$**L**$^{A1}_2$**L**$^{P2}_2$]$^{2+}$ are shown in the inset.

Titration of Pd$_2$L$^{A1}_2$L$^{P2}_2$ with **G^2**
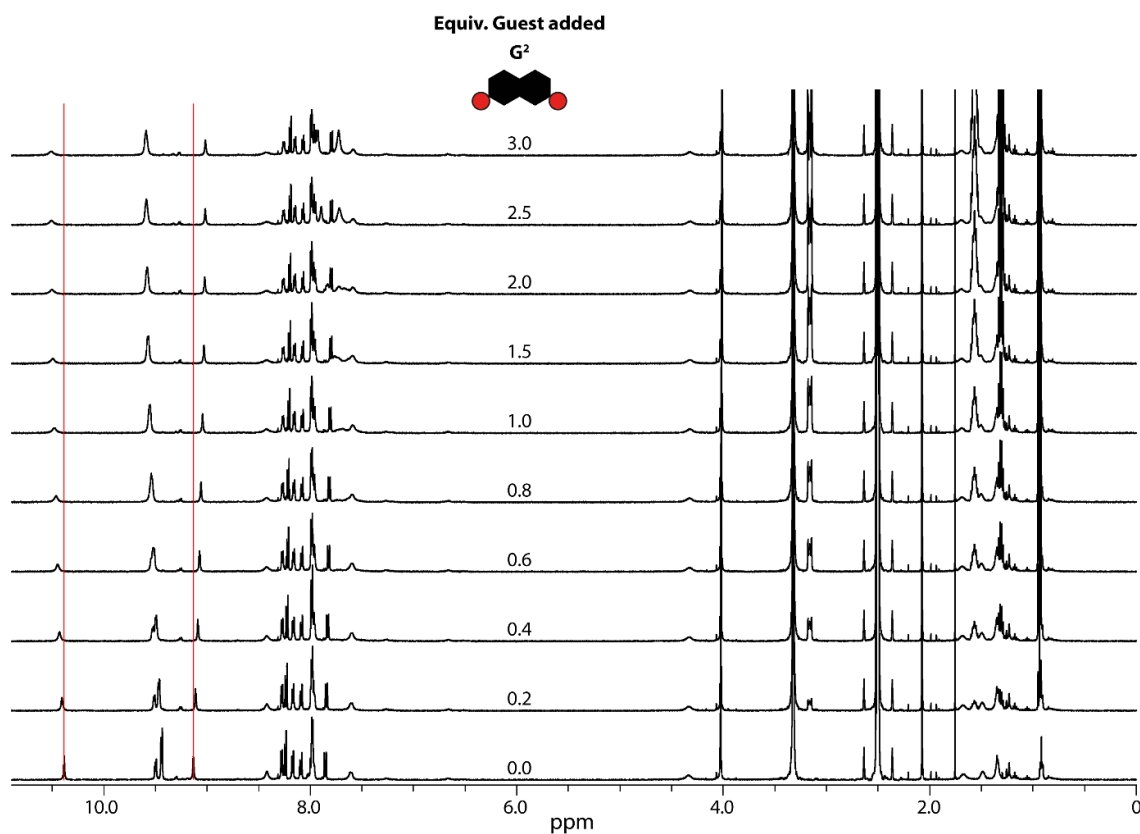
Figure 92: ^{1}H NMR titration (500 MHz, 298K, DMSO-d_6) of Pd$_2$L$^{A1}_2$L$^{P2}_2$ (0.7 mM in DMSO-d_6) with **G^2** (17.5 mM solution in DMSO-d_6).
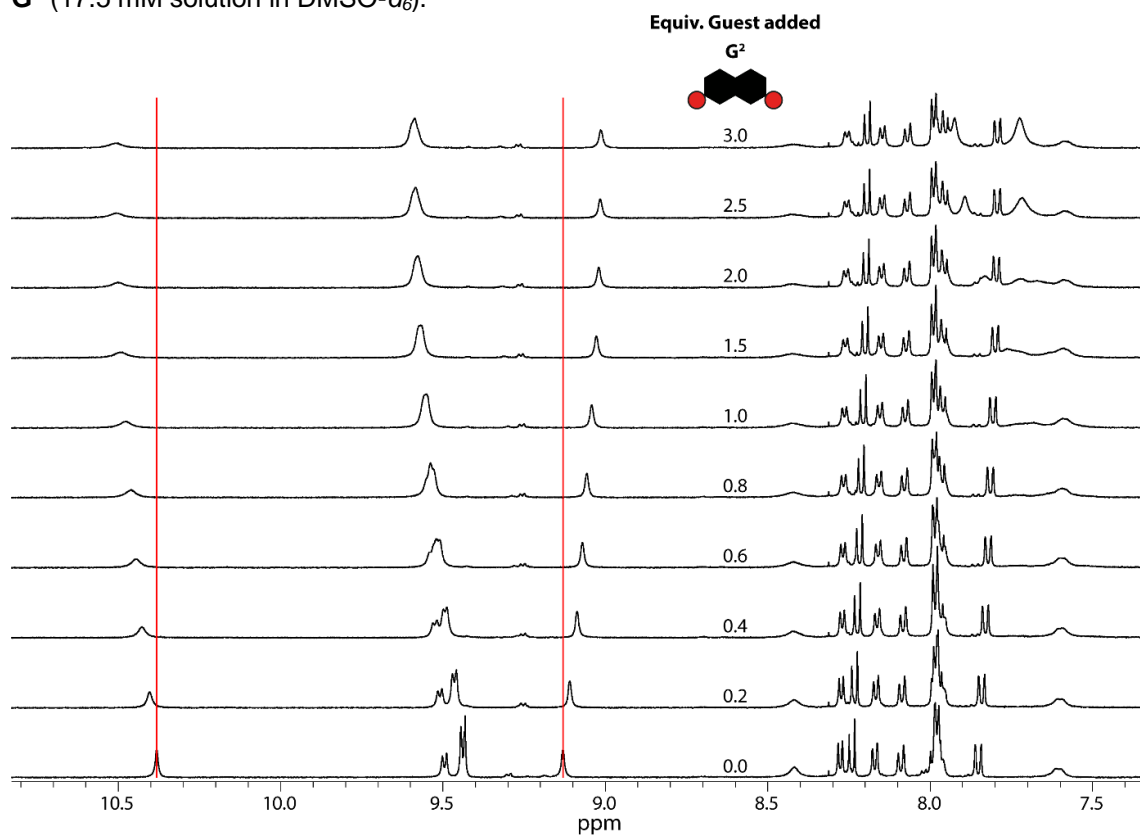
Figure 93: Aromatic region of the ^{1}H NMR titration (500 MHz, 298K, DMSO-d_6) of Pd$_2$L$^{A1}_2$L$^{P2}_2$ (0.7 mM in DMSO-d_6) with **G^2** (17.5 mM solution in DMSO-d_6).
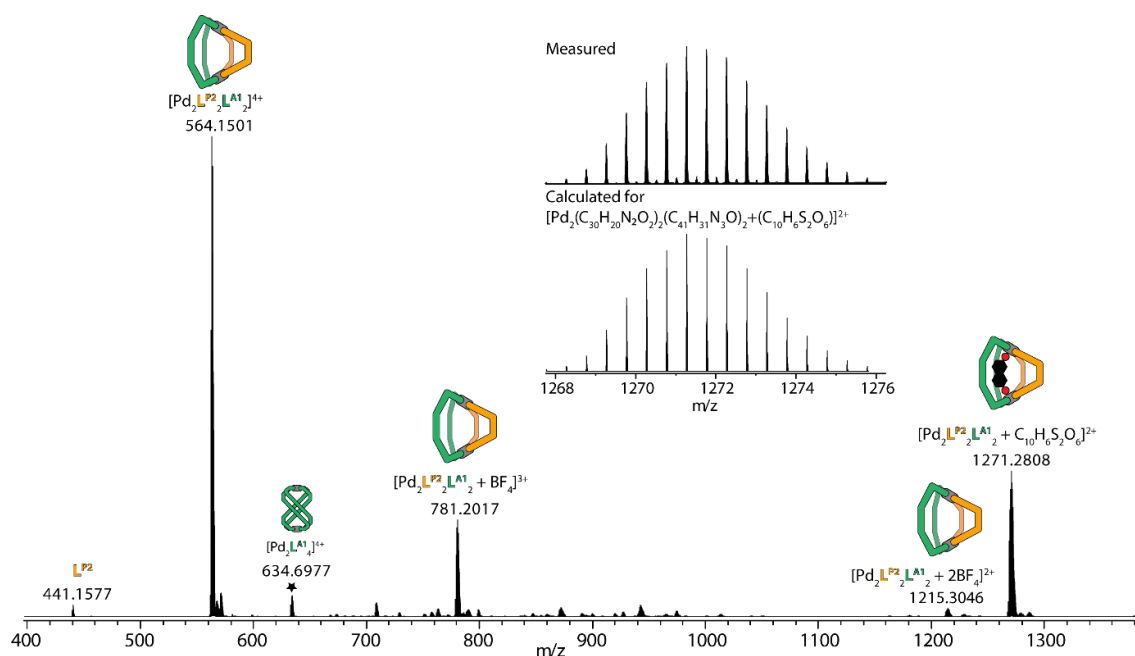
Figure 94: ESI-MS spectrum of $[Pd_2L^{A1}{}_2L^{P2}{}_2 + xBF_4]^{(4-x)+}$ + 1 equiv. of **G²**. The observed and calculated isotopic pattern of $[G^2@Pd_2L^{A1}{}_2L^{P2}{}_2]^{2+}$ are shown in the inset.

Multi-Component Titration of Pd₃L^{P2}₆ and Pd₂L^{A1}₂L^{P2}₂ with **G¹** and **G²**
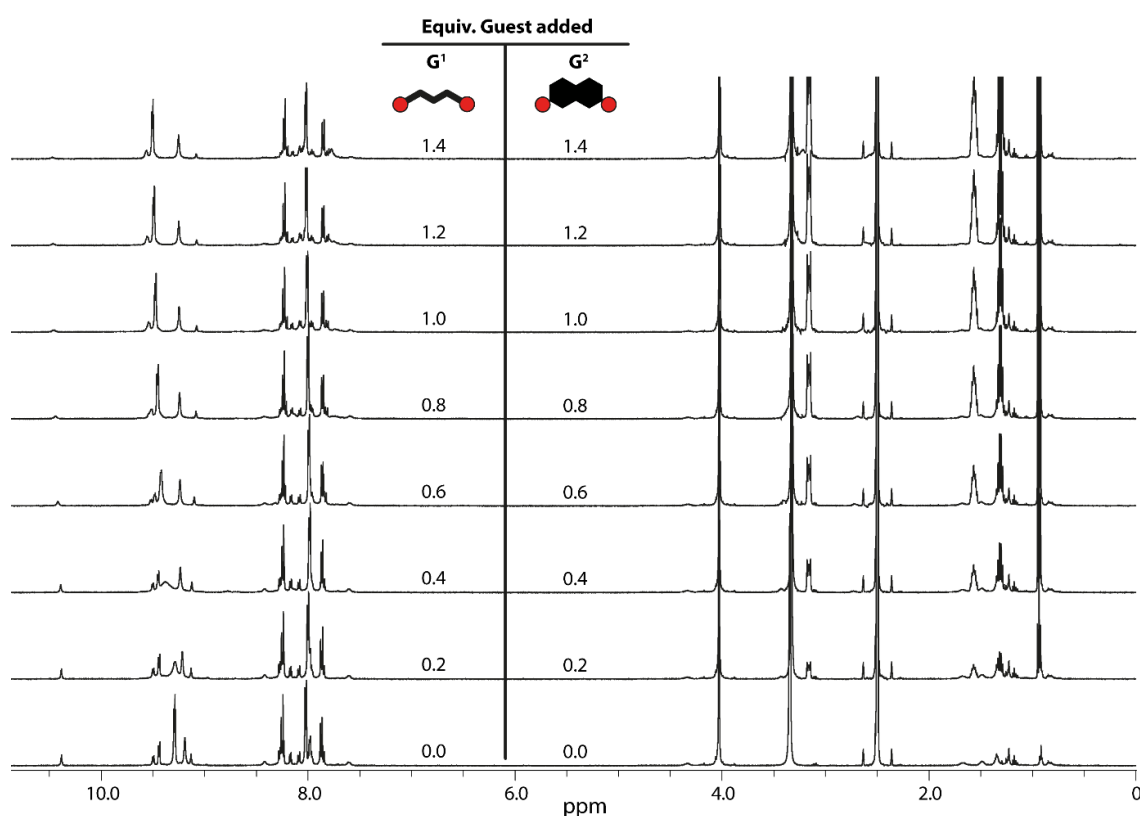
Figure 95: Simultaneous ¹H NMR titration (500 MHz, 298K, DMSO-d_6) of **G¹** and **G²** (each 17.5 mM in DMSO-d_6) to a mixture of Pd₂L^{A1}₂L^{P2}₂ and Pd₃L^{P2}₆ (each 0.7 mM in DMSO-d_6). The samples were heated to 70°C for 5 minutes each after guest addition.
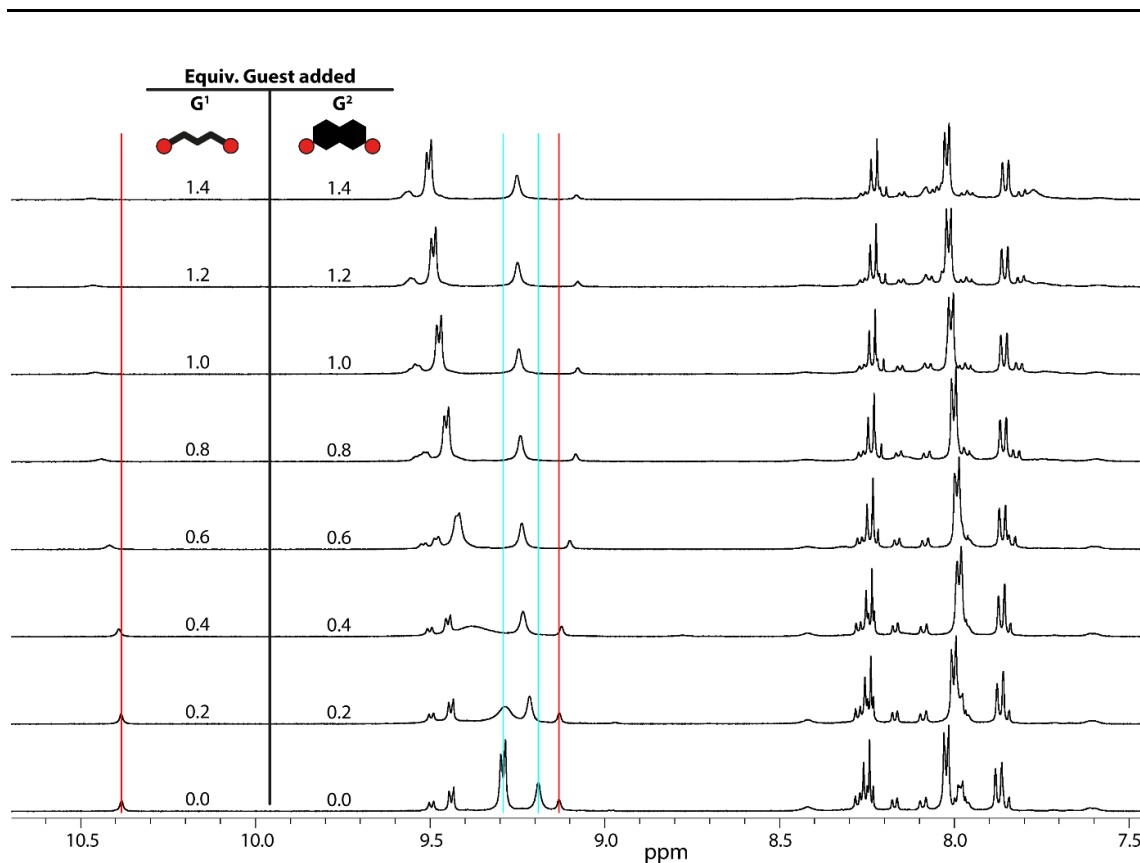
Figure 96: Aromatic region of the simultaneous ^{1}H NMR titration (500 MHz, 298K, DMSO-d_6) of **G^1** and **G^2** (each 17.5 mM in DMSO-d_6) to a mixture of Pd$_2$**L^{A1}**$_2$**L^{P2}**$_2$ and Pd$_3$**L^{P2}**$_6$ (each 0.7 mM in DMSO-d_6).
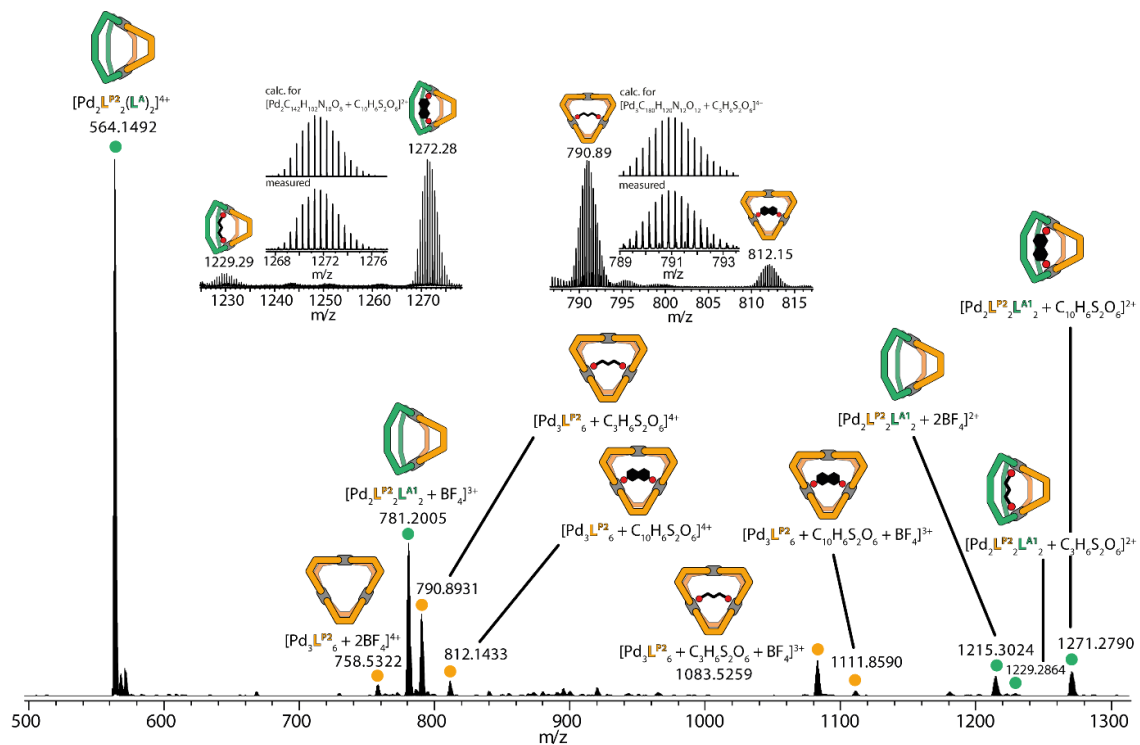
Figure 97: ESI-MS spectrum of a mixture of [Pd$_2$**L^{P2}**$_2$**L^{A1}**$_2$ + xBF$_4$]$^{(4-x)+}$ and [Pd$_3$**L^{P2}**$_6$ + xBF$_4$]$^{(6-x)+}$+ 1 equiv. of **G^1** and 1 equiv. **G^2**. The observed and calculated isotopic patterns of [**G^2**@Pd$_2$**L^{A1}**$_2$**L^{P2}**$_2$]$^{2+}$ and [**G^1**@Pd$_3$**L^{P2}**$_6$]$^{4+}$ are shown in the inset, as well as the ratio of [**G^1**@Pd$_2$**L^{A1}**$_2$**L^{P2}**$_2$]$^{2+}$ to [**G^2**@Pd$_2$**L^{A1}**$_2$**L^{P2}**$_2$]$^{2+}$ and [**G^1**@Pd$_3$**L^{P2}**$_6$]$^{4+}$ to [**G^2**@Pd$_3$**L^{P2}**$_6$]$^{4+}$.

3.3 Combining complementary Functions: A FRET Pair forming a heteroleptic Coordination Cage

3.3.1 Introduction

As shown previously, coordination cages provide a facile method to generate hollow molecular hosts combining the advantages of molecular confinement with chemical functions by means of different implemented backbones. Over the course of recent years, a multitude of functional coordination cages has been described and their application scope is gradually increasing, ranging from switchable systems, as for example described in the previous chapter, host-guest interactions as e.g described for C_{60},[46,76–78,82] and catalysis up to using coordination cages to generate amphiphilic structures, like membranes and vesicles.[149] Assorted functional backbones used in our group include chromophores[69,150], photo-switches[50,71,72], hydrogen-bond donors and/or -acceptors[65] and chiral molecules such as e.g. helicene.[67,74] While the combination of these aforementioned functions with the confinement effects provided by the coordination cage approach in and of itself led to fascinating results, the heteroleptic SCA allows the combination of multiple functional backbones in one structure, still providing a distinct cavity for guest binding.

An example given for the purposeful combination of two ligands with different functionality forming a heteroleptic coordination cage in which the functional groups directly communicate with one another has been published by our group in 2022 (see Figure 98).[67]
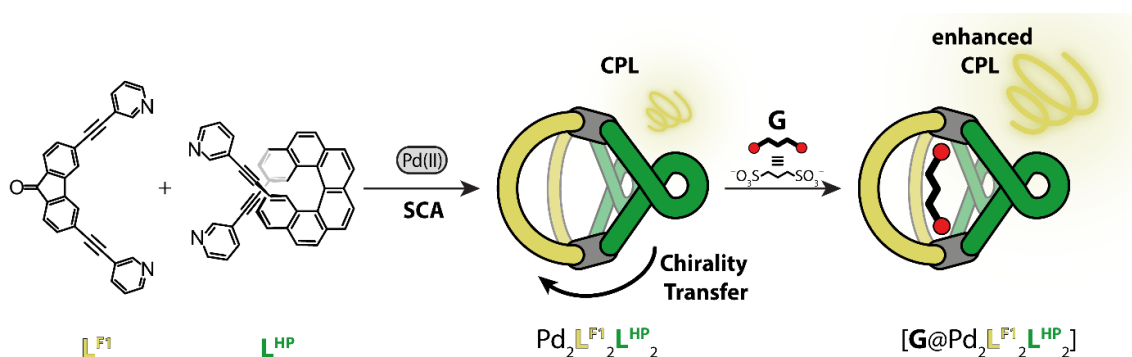

Figure 98: Schematic depiction of guest-induced CPL enhancement in a heteroleptic coordination cage consisting of a chiral ligand L^{HP}, based on helicene, and an emitting ligand L^{F1}. Reproduced from [67].[67]

The authors combined luminescent ligands L^{F1}, respectively L^{F2}, with an enantiopure chiral ligand based upon a helicene-backbone in either its M or P conformation using the SCA and forming heteroleptic assemblies in a non-statistical manner. CD and CPL

measurements proved transfer of chirality from the helicene-based ligand to the non-chiral emissive ligands and the binding of a bis-sulfonate guest inside the cage cavity led to an overall 4-fold increase of the CPL intensity.[67] This example nicely shows the utilization of the SCA to bring two functional groups in close structural proximity to have them interact with one another, additionally utilizing the formed cavity to further modify and enhance the properties of the system. Results from a follow-up work using the same fluorophore **L^F1** but a different chiral ligand, based on a cyclohexane-backbone, provided the perspective of tuning the CPL output of a system by means of altering the properties of the counter ligand.[68]

The luminescent fluorenone backbone used in the previous examples is one of the rarer examples of backbones, that maintain their luminescence upon Pd(II) coordination. While there are a few other examples to be found in the literature, the chromophore is either attached outside of the central ligand system,[151,152] or the coordination to Pd(II) leads to quenching of fluorescence due to different relaxation pathways involving the metal center.[73] While the seemingly obvious solution to Pd(II)-coordination quenching fluorophores would be to use Pt(II) as the metal center instead, heteroleptic platinum coordination cages without the use of *cis*-protected Pt(II) have, to the best of my knowledge, not yet been described. Thus, the choice of chromophore is rather important if one wants to analyze such optical properties in heteroleptic Pd(II) coordination cages, as the emission has to prevail upon coordination.

While the interaction of a chromophore with a chiral molecule has been shown in the previous example, the combination of two complementary chromophores can lead to another fascinating phenomenon, namely Förster-resonance energy transfer (FRET). The general process of how FRET works is depicted below in Figure 99.
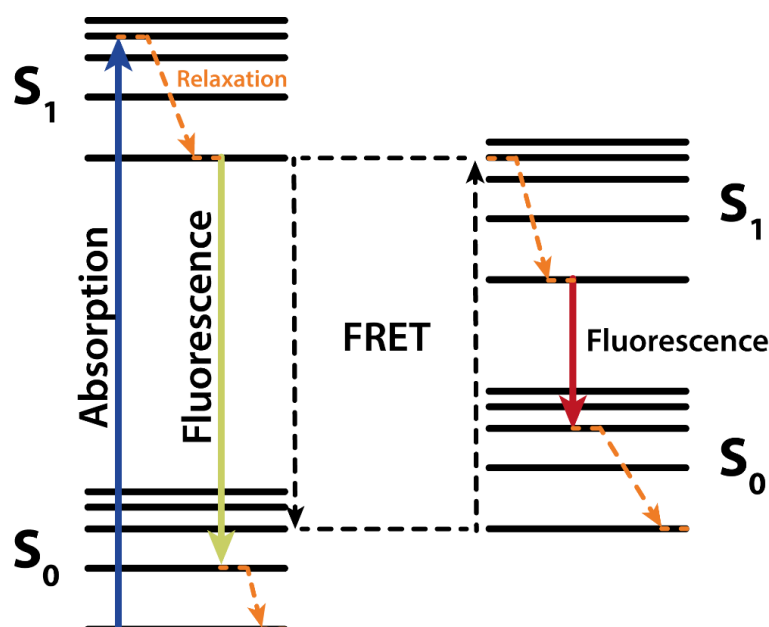
Figure 99: Schematic representation of the Jablonski diagram showing the FRET process.[153]

Figure 99 shows the ground state and excited state levels of chromophore A on the left side and the ones of a complementary chromophore B on the right. Upon absorption of light, an electron traverses from the ground state into the excited state. From there, multiple relaxation modes are available with one being fluorescence, which is the process of the electron falling back into the ground state while emitting light of lower energy than previously used to excite it. Another occurring process can be the previously mentioned interaction with a metal center leading to quenching of fluorescence due to the electron relaxing via non-radiative pathways. FRET, on the other hand, occurs, when the energy, which the electron of chromophore A would give of in the form of emission matches the energy needed to excite another electron in a complementary chromophore B in direct proximity to the first one. The proximity of both chromophores, donor and acceptor, is rather important, as the efficiency E of FRET decreases with an inverse 6th power law as given by equation 5,

$$E = \frac{1}{1 + \left(\frac{r}{R_0}\right)^6}$$

(5)

with R_0 being the Förster radius, the radius at which FRET efficiency is 50% and r is the distance separating both chromophores. [153]

As coordination chemistry can be used to a) form host molecules that have the potential to encapsulate guests, which in succession interact with their hosts and b) provide a facile method to bring two molecules in close structural proximity, various researchers have exploited this approach to look into FRET processes in coordination assemblies.

The groups of MINGMING ZHANG and HAI-BO YANG could show FRET within coordination boxes formed by using *cis*-protected Pt(II) and linear ligands either based on boron-dipyrromethene (BODIPY)[154] or equipped with side chains attached to rhodamine B in combination with tetradentate tetraphenylethylene (TPE) based counter ligands.[155] A different approach to FRET in coordination assemblies has been shown by the group of CHENG HE, who could show FRET from a TPE-based ligand organized in a Zn(II) coordination box to an encapsulated sulforhodamine guest, effectively showing host-guest FRET.[156]

The aforementioned approaches either relied on *cis*-protected Pt(II)[154,155] to prevent non-radiative quenching caused by transition to Pd(II) or showed FRET from a coordination host to an encapsulated acceptor guest molecule.[156]

We herein report an emissive, heteroleptic Pd(II)-based coordination cage using two complementary chromophores based on fluorenone, respectively diketopyrrolopyrrole (DPP), in which FRET from chromophore A (fluorenone) to chromophore B (DPP) could be realized. Furthermore, the formed cavity has been used to bind a chiral guest molecule G, effectively inducing chirality into the system, which has consequently been analyzed using CD and CPL (I. Regeni, K. E. Ebbert et al. Manuscript in preparation).

3.3.2 System and Characterization

Herein reported is a system consisting of two fluorene-derivative-based ligands L^{F2} and L^{C2} (Scheme 9 and Scheme 10) equipped with 3-pyridine donor groups and 1,4-phenyl-linkers that each form a heteroleptic coordination cage with the shape-complementary ligand L^{IR}, a ligand based on diketopyrrolopyrrole (DPP) equipped with 4-pyridine donor-groups and 1,3 phenyl-linkers (Scheme 8). A special feature of the system is the capacity of ligands L^{F2} and L^{IR} to maintain their emissive properties even upon Pd(II) coordination. A combination of both ligands in a heteroleptic environment was used to analyze ligand interaction, when in close proximity to one another in special regard to the systems photophysical and host-guest binding properties. Ligand L^{C2}, which loses its emissive properties upon Pd(II) coordination has been chosen for control purposes.

Ligands L^{F2} and L^{C2}, as well as their homoleptic assemblies, were synthesized and characterized in DMSO-d_6 according to procedures reported in the experimental part of this chapter. While the fluorenone-based ligand L^{F2} forms a complex mixture of $Pd_nL^{F2}{}_{2n}$ (n = 2-5) assemblies upon Pd(II) addition, the carbazole-based ligand L^{C2} forms a mixture of $Pd_2L^{F2}{}_4$ cages and $Pd_3L^{F2}{}_6$ rings in an approximate ratio of 2:1 (based on ^{1}H proton signal integration of the signal assigned to H^1). As both ligands pose a relatively inflexible phenyl-linker group, an adaptivity to the smaller assembly is hindered and the system can no longer fully yield to entropic pressure like their analogues with alkyne-based linkers L^{F1} and L^{C1}, which both form clean Pd_2L_4 assemblies (see chapter 3.1). Ligand L^{IR} forms a mixture of $Pd_3L^{IR}{}_6$ and $Pd_4L^{IR}{}_8$ rings that has been described in the thesis of Dr. Irene Regeni, alongside the synthesis and characterization of the ligand.[69]

Heteroleptic coordination cages were synthesized using 270 µl of a 3.11 mM solution of L^{F2}, respectively L^{C2}, in DMSO-d_6 combined with equimolar amounts of L^{IR} (270 µl, 3.11 mM in DMSO-d_6) and 60 µl of a 15 mM solution of $[Pd(CH_3CN)_4](BF_4)_2$ in a 5 mm standard NMR tube and heating the mixture to 70°C for 2h.

The synthesis of the fluorenone-based heteroleptic coordination cage $Pd_2L^{F2}{}_2L^{IR}{}_2$ is shown in Scheme 8 alongside the proton nomenclature of the ligands. The synthesis of its carbazole-based analogue $Pd_2L^{C2}{}_2L^{IR}{}_2$ follows the same procedure and is shown in the experimental part (Scheme 14). The proton designation for L^{C2} (Scheme 10 and Scheme 14) follows the same pattern as given for L^{F2} (Scheme 8 and Scheme 9).
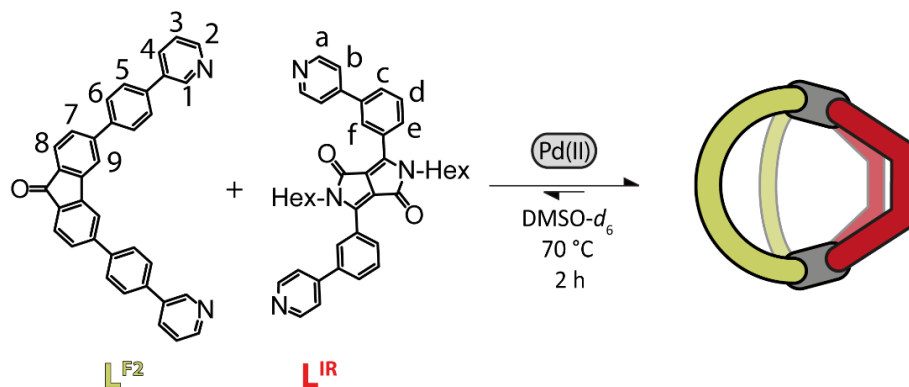
Scheme 8: Formation of Pd$_2$L$^{F2}_2$L$^{IR}_2$ with consecutive proton labels.

The systems were meticulously described using analytic procedures such as 1D/2D NMR spectroscopy and ESI-MS. Figure 100 shows the aromatic region of the ^{1}H NMR spectra of all ligands L^{F2} (Figure 100, a)), L^{C2} (Figure 100, g))and L^{IR} (Figure 100, d)), the homoleptic mixtures L^{F2} and L^{C2} form upon Pd(II) addition (Figure 100, b) and f)) and of the heteroleptic assemblies Pd$_2$L$^{F2}_2$L$^{IR}_2$ (Figure 100, c)) and Pd$_2$L$^{C2}_2$L$^{IR}_2$ (Figure 100, e)). The individual ^{1}H NMR stacks, including the homoleptic mixture of Pd$_3$L$^{IR}_6$ and Pd$_4$L$^{IR}_8$, rings can be found in the experimental part (Figure 131 and Figure 140).
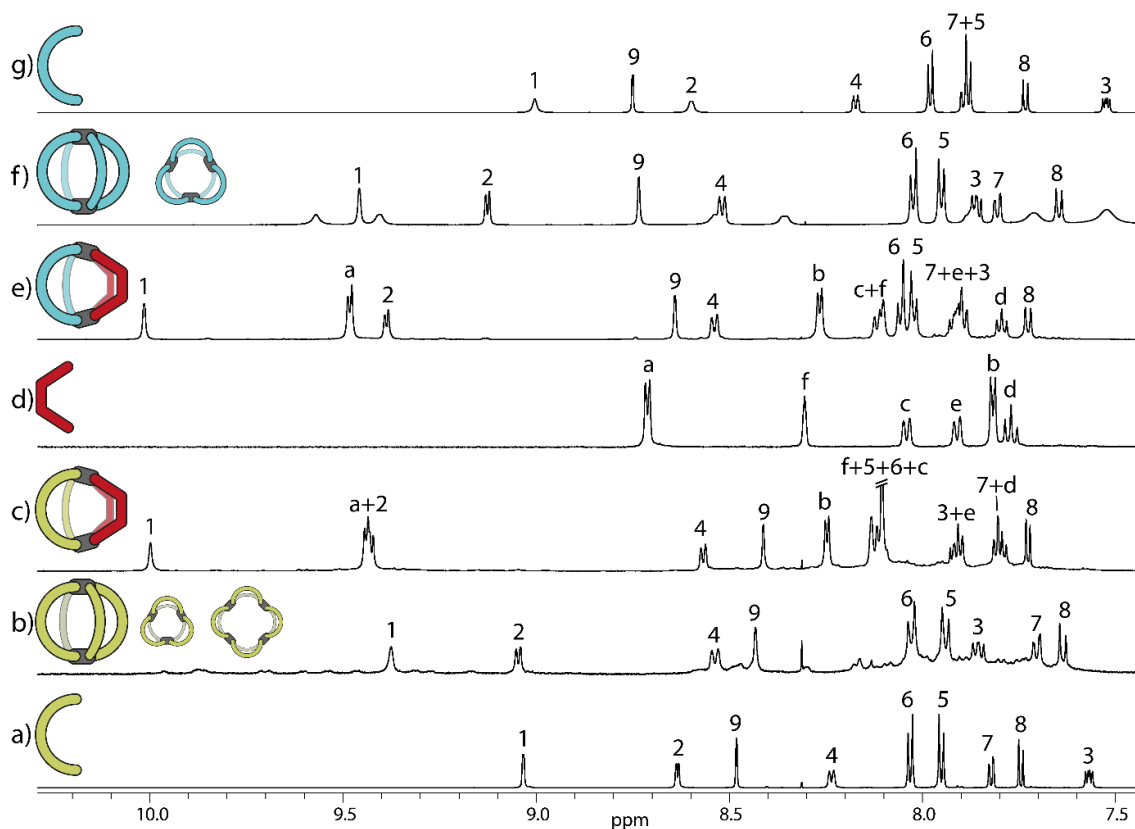
Figure 100: Partial ^{1}H NMR spectra of a) ligand L^{F2} (700 MHz), b) homoleptic Pd$_2$L$^{F2}_4$ cage and the Pd$_n$L$^{F2}_{2n}$ (n=3-5) rings formed upon addition of 0.55 equiv. Pd(II) cations to ligand L^{F2} (600 MHz), c) heteroleptic Pd$_2$L$^{F2}_2$L$^{IR}_2$ (700 MHz), d) ligand L^{IR} (500 MHz),), e) heteroleptic Pd$_2$L$^{C2}_2$L$^{IR}_2$ (600 MHz), f) homoleptic Pd$_2$L$^{C2}_4$ cage and Pd$_3$L$^{C2}_6$ ring formed upon addition of 0.55 equiv. Pd(II) cations to ligand L^{C2} (600 MHz) and g) ligand L^{C2} (700 MHz) in DMSO-d_6 at T = 298 K (bottom to top).

As evident from Figure 100, neither ligand nor homoleptic assemblies can be found in the spectra of both heteroleptic assemblies $Pd_2L^{F2}_2L^{IR}_2$ (Figure 100, c)) and $Pd_2L^{C2}_2L^{IR}_2$ (Figure 100, e)). For each heteroleptic system, 15 proton signals in the aromatic region could be identified and assigned based on 1D and 2D NMR analysis. The signal count matches the sum of six aromatic signals derived from L^{IR} and nine signals from L^{F2}, respectively L^{C2}. Proton signals around the coordination sphere experience downfield shifting upon Pd(II) coordination, which is more pronounced in the heteroleptic environment as compared to the homoleptic Pd_2L_4 cages. With the signal of proton H^1 shifting from $\delta = 9.03$ ppm in L^{F2} to $\delta = 10.00$ ppm in the heteroleptic $Pd_2L^{F2}_2L^{IR}_2$ assembly and the signal of H^2 going from $\delta = 8.63$ ppm to $\delta = 9.43$ ppm, while $\Delta\delta = 0.73$ ppm for the signal of H^a, all proton signals close to the donor-nitrogen sport a downfield shift $\Delta\delta \geq 0.6$ ppm. Furthermore, the signals of the inner protons of the final cages, H^9 and H^f experience upfield shifting compared to the situation in the free ligands (H^9 from $\delta = 8.48$ ppm to $\delta = 8.41$ ppm; H^f from $\delta = 8.30$ ppm to $\delta = 8.10$ ppm), which is congruent with the behavior previously observed for central-cavity proton signals.

The shifts for $Pd_2L^{C2}_2L^{IR}_2$ (Figure 100, e)) closely resemble those of $Pd_2L^{F2}_2L^{IR}_2$ (Figure 100, c)) and will thus not be discussed in further detail. The only proton signal that shows a significant difference is the one assigned to the inner proton H^9 of L^{F2} ($\delta = 8.41$ ppm), respectively L^{C2} ($\delta = 8.64$ ppm). While it shows an upfield shift in both heteroleptic assemblies as compared to the homoleptic ones and the free ligands, the difference in proton shift from one heteroleptic assembly to the other equals $\Delta\delta = 0.23$ ppm. This difference however, is already portrayed in the spectrum of the ligands and the absolute difference from ligand to heteroleptic assembly is $\Delta\delta = 0.07$ ppm for $Pd_2L^{F2}_2L^{IR}_2$ and $\Delta\delta = 0.11$ ppm for $Pd_2L^{C2}_2L^{IR}_2$ making the observed effect neglectable and attributable to the structure of the backbone, with carbazole holding less electron density than fluorenone, thus providing increased deshielding of the attached protons.

With the observed shifts for $Pd_2L^{F2}_2L^{IR}_2$ and $Pd_2L^{C2}_2L^{IR}_2$ being very closely related, it can be assumed that the resulting structures of both coordination events are related to the point of almost being congruent. Another indication for this is the shift of proton H^f, attached to the DPP-backbone of L^{IR} and being located farthest away from the coordination site of the ligand. The signal shifts by $\Delta\delta = 0.2$ ppm in both cases, showing that this specific proton experiences basically the same change in chemical environment, despite the counter-ligand being different.

^{1}H DOSY NMR of both species were measured, yielding hydrodynamic radii of $r_H = 12.155 \pm 0.005$ Å for the fluorenone-containing $Pd_2L^{F2}_2L^{IR}_2$ (Figure 137, experimental part), which has no aliphatic chains attached to the L^{F2} ligand but only to

L^{IR} (total number of hexyl-chains x = 4), and r_H = 13.185 ± 0.013 Å for $Pd_2L^{C2}{}_2L^{IR}{}_2$ (Figure 146, experimental part), in which both ligands carry hexyl-chains attached to their backbones, making the total number of hexyl-chains the system possesses x = 6, which leads to the observed increase in hydrodynamic radius. NOE analysis showed no contacts of the aliphatic chains of one ligand to the inner protons of the counter ligand, which indicates no folding of the chains inside the cavity. This observation is backed up by the increase in spatial extent when more chains are introduced into the system. The size of both heteroleptic assemblies matches well with previously observed dimensions, making it reasonable to assume the formation of cages with a palladium nuclearity of n = 2. However, to provide further information on nuclearity and assembly composition, ESI-MS of both assemblies has been measured (Figure 101).
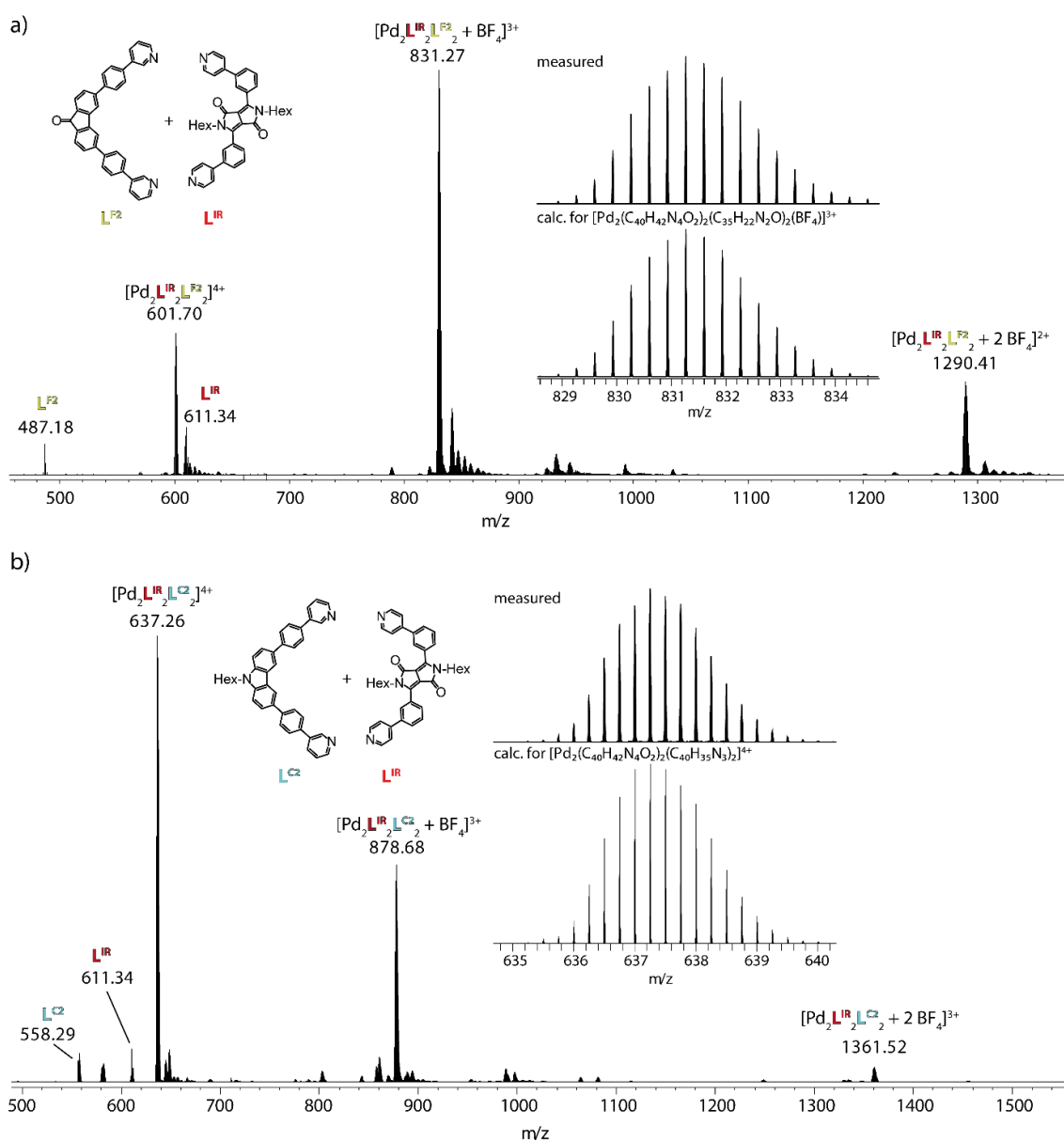
Figure 101: ESI-MS spectrum of a) heteroleptic $[Pd_2L^{F2}_2L^{IR}_2 + xBF_4]^{(4-x)+}$ (x = 0-2) and b) heteroleptic $[Pd_2L^{C2}_2L^{IR}_2 + xBF_4]^{(4-x)+}$ (x = 0-2). The measured and calculated isotopic patterns of the highest peak are shown in the inset.

Both heteroleptic assemblies can be unambiguously described based on their ESI-MS measurements, yielding values of m/z = 601.7014 (4+), 831.2705 (3+) and 1290.4078 (2+) for $[Pd_2L^{F2}_2L^{IR}_2 + nBF_4]^{(4-n)+}$ (n = 0-2) with $[Pd_2L^{F2}_2L^{IR}_2 + nBF_4]^{(3+)}$ having the highest abundance, respectively m/z = 637.2570 (4+), 878.6768 (3+) and 1361.5188 (2+) for $[Pd_2L^{C2}_2L^{IR}_2 + nBF_4]^{(4-n)+}$ (n = 0-2) with the anion-devoid 4+ species being most abundant. The given ESI-MS results confirm the previously made claim, that the 1:2:2 mixture of Pd(II) cations with L^{IR} and L^{F2}, respectively L^{C2}, forms binuclear heteroleptic coordination cages.

Based on the bite angle of L^{F2}/L^{C2}, which is slightly > 0°, and the one of L^{IR}, which is > 90°, a *trans*-topology of the assemblies has been ruled out due to an overabundance

109

of strain building up. DFT models with a *cis*-arrangement of the two complementary ligands have been calculated to visualize the spatial extent of the cages in special regard to the formed cavity (Figure 102).
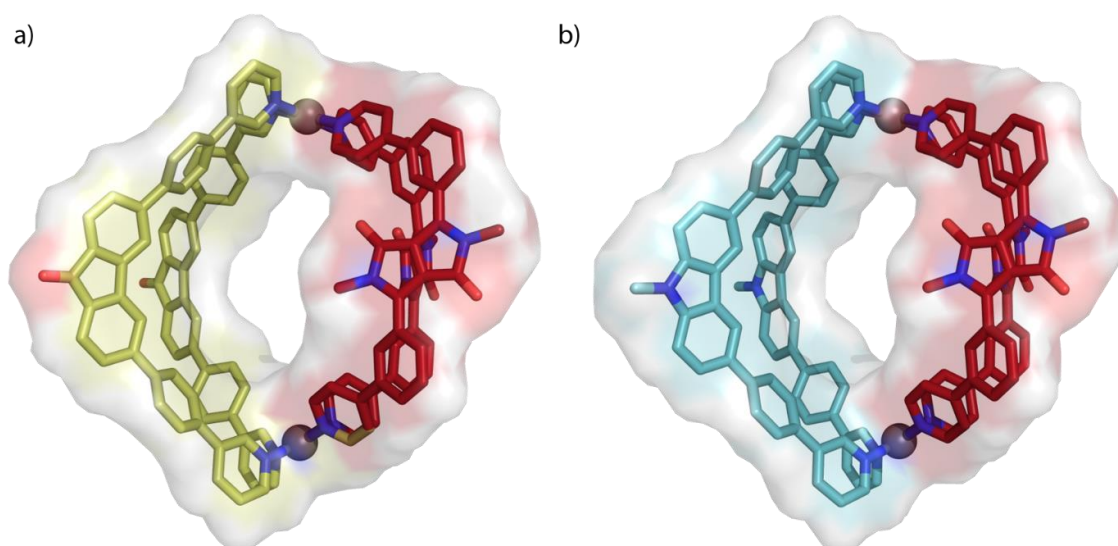
Figure 102: Model of a) heteroleptic Pd$_2$**L**^{F2}$_2$**L**^{IR}$_2$ and b) heteroleptic Pd$_2$**L**^{C2}$_2$**L**^{IR}$_2$ (sticks overlaid with surface representation). Hydrogens and chains are omitted for clarity. Calculated on DFT theory level.

Figure 102 shows the *in silico* models of Pd$_2$**L**^{F2}$_2$**L**^{IR}$_2$ (Figure 102, a)) and Pd$_2$**L**^{C2}$_2$**L**^{IR}$_2$ (Figure 102, b)) represented sideways to visualize the spatial extent of the cages and the orientation of the ligands in a 3D environment. The models themselves are almost congruent to one another, which is in good accordance with the analyzed NMR data with the Pd-Pd distance for Pd$_2$**L**^{F2}$_2$**L**^{IR}$_2$ amounting to $d = 14.6$ Å, while it is only slightly increased for Pd$_2$**L**^{C2}$_2$**L**^{IR}$_2$ being $d = 14.7$ Å. This slight increase in size can be associated to the backbone change from fluorenone to carbazole, with carbazole containing the smaller nitrogen atom instead of a carbon atom at the same position, leading to an overall slight angle increase of the backbone and, in succession the bite angle of the ligand. While the ligands themselves are quite rigid due to aromatic phenylene-linkers being incorporated instead of more flexible alkynes, the outcome of the coordination event proved to be the same for both systems, suggesting at least a little leeway and adaptivity to form the heteroleptic structure. The overall structure suggests little conformational freedom at least compared to previously described systems containing alkyne-linkers. While the orientation of the hexyl-chains attached to the diketopyrrolopyrrole could suggest them pointing to the inside of the cavity, the NOE cross peak of H^9 with any of the hexyl-chain atoms is devoid in both systems (Figure 135 and Figure 144, experimental part), thus suggesting no inside folding of the chains, leaving the cavity to be a void space. The Pd-Pd distance is relatively high compared to previously described systems (14.0 Å for Pd$_2$**L**^{A1}$_2$**L**^{P2}$_2$) and the distance of H^9 to the carbonyl-group of the

opposing DPP backbone is measured to be 12.1 Å (closest H^9), respectively 12.7 Å (diagonally opposing H^9) in $Pd_2L^{F2}{}_2L^{IR}{}_2$ and 12.0 Å, respectively 12.7 Å in $Pd_2L^{C2}{}_2L^{IR}{}_2$. These measurements can be used to estimate the size of the formed cavity. The increased size of the aforementioned as compared to previous systems will prove to be valuable later on in applied host-guest chemistry with a sterically more demanding guest than naphthyl-bis-sulfonate. A further asset of the systems are the phenylene-linkers which could provide stabilization of host-guest interaction based on π-π stacking.

As the heteroleptic cage formation in this chapter is used to bring two chromophores close to one another and analyze their interaction with each other, the photophysical properties of the system were measured. The chromophores did not lose their emissive properties in both heteroleptic cages, as well as the homoleptic assemblies, with the emission of L^{IR} being the most predominant one in its homoleptic, as well as heteroleptic environment. A comparison of absorption, emission and excitation spectra of the individual species, especially considering the Pd(II) assemblies, is shown in Figure 103.
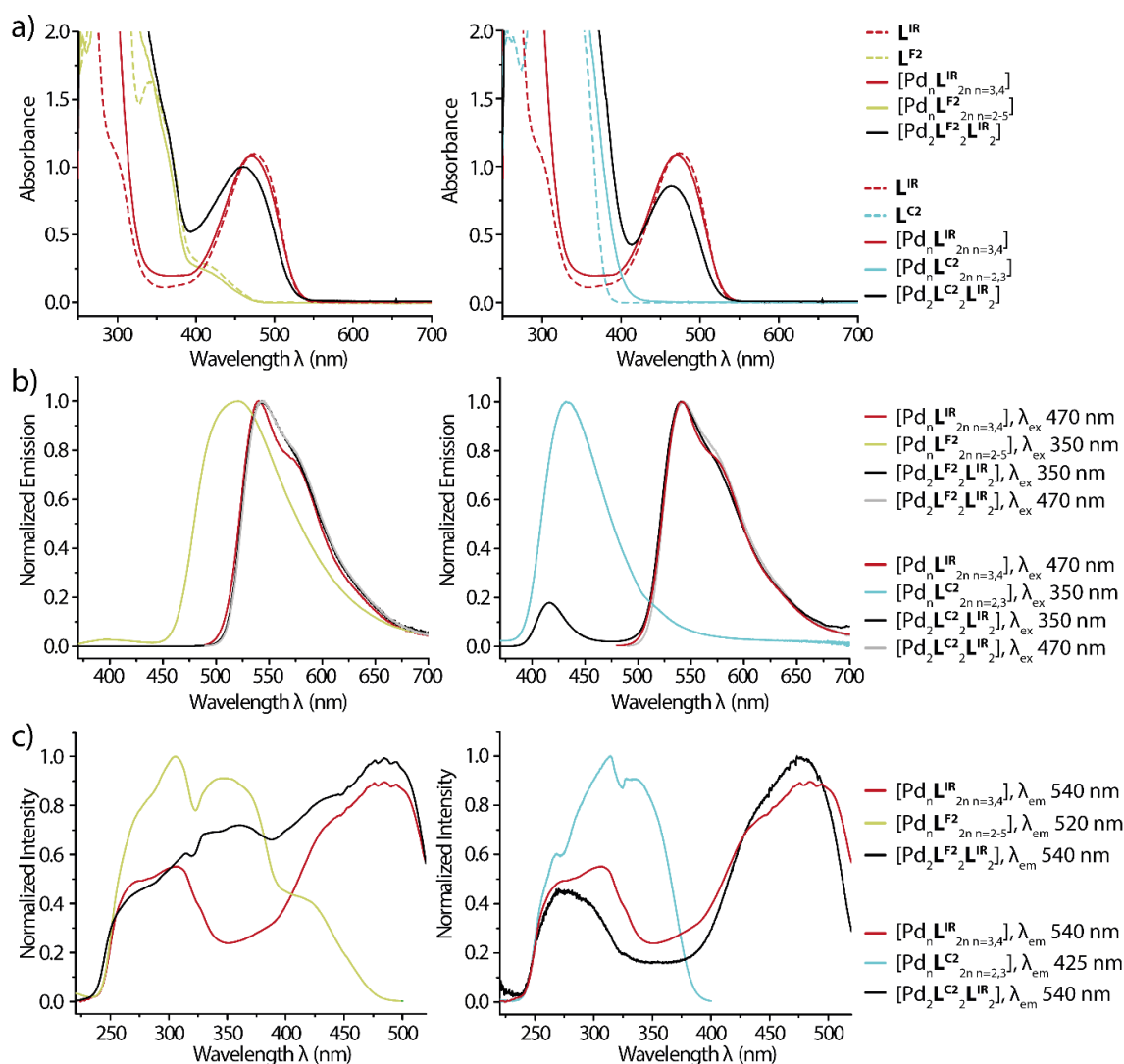
Figure 103: a) UV-Vis absorption spectra, b) emission spectra and c) excitation spectra of ligands, corresponding homoleptic assemblies and heteroleptic cages. All spectra have been recorded on solutions of 0.35 mM in chromophore concentration in DMSO at 25 °C with cuvettes of 0.2 cm optical path.

Figure 103 a) shows the absorption spectra of the fluorenone- (left), respectively the carbazole-based system (right). While the homoleptic assemblies show little change when comparing ligand and Pd(II) assembly in the range, with no evident changes aside from the local maximum L^{F2} shows at $\lambda = 343$ nm disappearing. The difference between the spectra of the homoleptic $Pd_nL^{IR}_{2n}$ (n = 3,4) and $Pd_nL^{F2}_{2n}$ (n = 2-5), respectively $Pd_nL^{C2}_{2n}$ (n = 2,3), is more imminent as especially the local maximum associated to the DPP chromophore, that was previously found at $\lambda = 470$ nm, showed a hypsochromic shift when it was incorporated in the heteroleptic assemblies $Pd_2L^{F2}_2L^{IR}_2$ and $Pd_2L^{C2}_2L^{IR}_2$. This shift was more pronounced in the fluorenone-based system $Pd_2L^{F2}_2L^{IR}_2$ amounting to $\Delta\lambda = 10$ nm, while it was only 5 nm in case of $Pd_2L^{C2}_2L^{IR}_2$. While this change in absorption from homoleptic to heteroleptic assemblies already indicates the two ligands interacting in a way, it gets more evident when comparing the emission spectra (Figure

103, b)). The emission of homoleptic $Pd_nL^{IR}_{2n}$ (n = 3,4) can be detected at λ = 540 nm, while homoleptic $Pd_nL^{F2}_{2n}$ (n = 2-5) emits at λ = 520 nm. Upon excitation of heteroleptic $Pd_2L^{F2}_2L^{IR}_2$ at λ = 350 or 470 nm however, the emission associated to L^{F2} cannot be observed, but only the one of the other chromophore L^{IR}. This is not the case for the control system $Pd_2L^{C2}_2L^{IR}_2$, in which the emission associated with L^{C2} at λ = 434 nm prevails, however is shifted hypsochromically to λ = 417 nm. Knowing the chromophores maintain the emissive properties upon Pd(II) coordination, albeit suffering in terms of emission intensity, the observation of the emission of L^{F2} missing from the emission spectrum of the heteroleptic cage poses the question of energy transfer. A comparison of the excitation spectra of the homoleptic and heteroleptic assemblies (Figure 103, c)) proved that suspicion to be correct since the intensity of the excitation spectrum of homoleptic $Pd_nL^{IR}_{2n}$ (n = 3,4) has a local minimum at λ_{ex} = 350 nm, while the heteroleptic cage $Pd_2L^{F2}_2L^{IR}_2$ sports a local maximum at this specific wavelength, similar to homoleptic $Pd_nL^{F2}_{2n}$ (n = 2-5). This is not the case for heteroleptic $Pd_2L^{C2}_2L^{IR}_2$, which shows lower intensity in the excitation spectrum of the heteroleptic cage as compared to the ones of both homoleptic species. This observation coupled with the missing emission of the fluorenone-based chromophore leads to the conclusion, that L^{F2} acts as a donor-chromophore for non-radiative energy transfer to the acceptor-chromophore L^{IR}. This effect is known as Förster-resonance energy transfer (FRET) and it requires the emission wavelength of one chromophore to overlap with the excitation wavelength of the other, which is given in the herein described case. The overlap is however not perfect since the emission wavelength of L^{F2} is λ = 520 nm with the optimal excitation wavelength of L^{IR} being λ = 485 nm. Due to the emission of the donor chromophore L^{F2} being quite broad, the optimal excitation wavelength of the acceptor chromophore L^{IR} is still covered.

3.3.3 Host-Guest Chemistry

As previously discussed, the increase in linker length led to an overall increase in Pd-Pd distance as compared to systems reported in earlier chapters. This allows the incorporation of bigger, more complex guest molecules, such as *(R)*-1,1'-Binaphthyl-2,2'-disulfonate (*(R)*-BINSO), a chiral bis-sulfonate. The introduction of chirality into this system in addition to the reported FRET effect due to the combination of two complementary chromophores in one heteroleptic assembly will be analyzed in the following part.
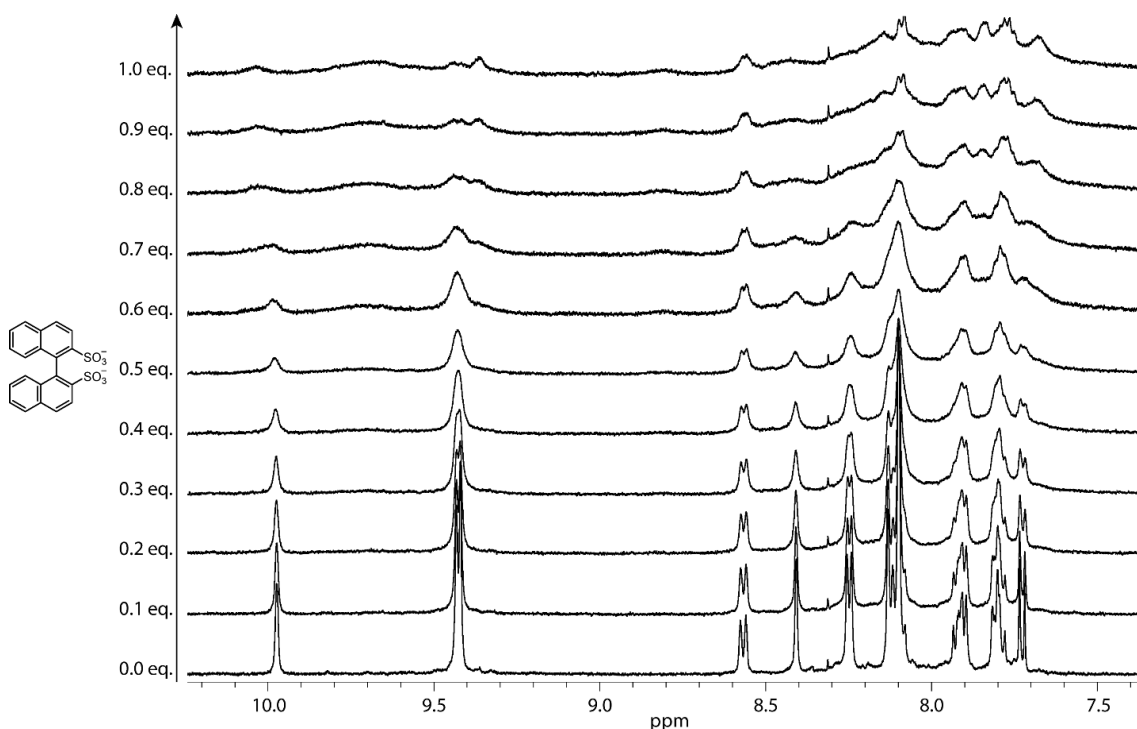
Figure 104: Partial ^{1}H NMR spectra (500 MHz, 298K, DMSO-d_6) of the titration of Pd$_2$**L**$^{F2}_2$**L**$^{IR}_2$ with **G** (15 mM solution in DMSO-d_6).

As Figure 104 depicts, the ^{1}H signals of Pd$_2$**L**$^{F2}_2$**L**$^{IR}_2$ broaden immediately after addition of the guest. A shift of the signals can only be assumed and the determination of a binding constant is impossible with the data at hand. However, the broadening does indicate an interaction between cage and guest, as otherwise sharp signals of both would be observable.

To verify the proposed interaction of the cage with the chiral guest, variable temperature (VT) NMR was measured at 75 °C to investigate the system further and see if signals would sharpen as molecular movement is accelerated. Thus, the individual species, Pd$_2$**L**$^{F2}_2$**L**$^{IR}_2$ and Pd$_2$**L**$^{C2}_2$**L**$^{IR}_2$, as well as the 1:1 mixture of the aforementioned with the guest, *(R)*-BINSO, and the guest individually were subjected to ^{1}H NMR measurement at T = 348.15 K. The aromatic region of the resulting spectra is shown in Figure 105.
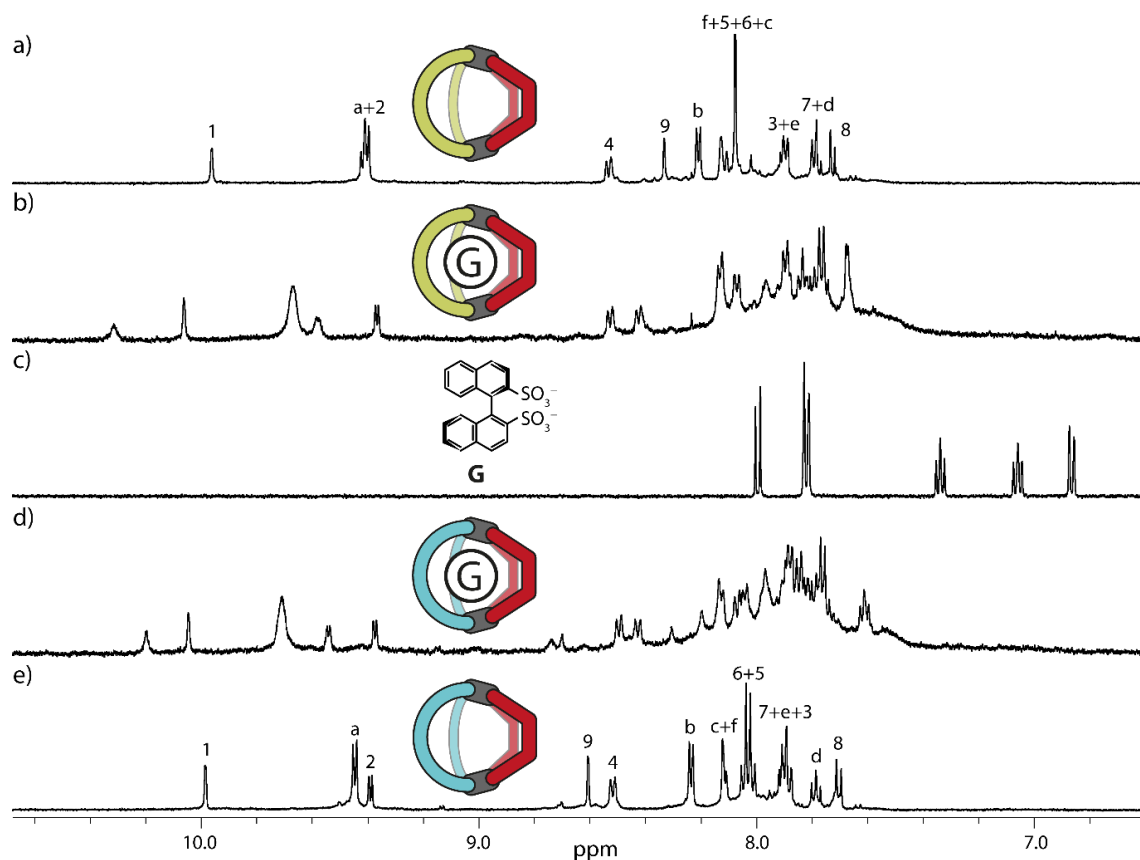
Figure 105: Partial ^{1}H NMR spectra (500 MHz, 348 K, DMSO-d_6) of a) $Pd_2L^{F2}{}_2L^{IR}{}_2$, b) $Pd_2L^{F2}{}_2L^{IR}{}_2$ with 1 equiv. of **G**, c) **G**, d) $Pd_2L^{C2}{}_2L^{IR}{}_2$ with 1 equiv. of **G** and e) $Pd_2L^{C2}{}_2L^{IR}{}_2$.

The VT experiments show a definite change from the empty host molecules $Pd_2L^{F2}{}_2L^{IR}{}_2$ (Figure 105 a)) and $Pd_2L^{C2}{}_2L^{IR}{}_2$ (Figure 105 e)) to the spectra after the addition of 1 equiv. **G**. The empty host cannot be detected anymore, neither can the free guest **G** (Figure 105 c)). The spectra of the 1:1 mixtures of **G** and the individual heteroleptic host molecules are shown in (Figure 105 b)) for **G** + $Pd_2L^{F2}{}_2L^{IR}{}_2$ and d) for **G** + $Pd_2L^{C2}{}_2L^{IR}{}_2$. Both spectra show similarities regarding their signal distribution, which is to be expected considering their close structural relation. What is most intriguing is, that proton signals of the host molecules show splitting upon addition of the chiral guest due to the desymmetrization of the complex, which indicates quite tight and snuck binding of **G** inside the host molecules. While the interaction of a bis-anion with a 4+ charged coordination assembly is not surprising, the question was, whether the guest binds inside the cavity or associates outside of the assembly. Since the complex was stable even with prolonged heating, VT ^{1}H DOSY NMR spectra of both host-guest mixtures were measured. The signal-to-noise ratio was insufficient to give an accurate value with error but a dimension. Both ^{1}H DOSY experiments showed a singular species with diffusion coefficients of $D = 2.296 \cdot 10^{-10}$ m$^2\cdot$s^{-1} for **G** + $Pd_2L^{F2}{}_2L^{IR}{}_2$ (Figure 151, experimental part) and $D = 2.148 \cdot 10^{-10}$ m$^2\cdot$s^{-1} for **G** + $Pd_2L^{C2}{}_2L^{IR}{}_2$ (Figure 154, experimental part) at

T = 348.15 K. Calculating the hydrodynamic radius of the species based on these values resulted in r_H = 12.76 Å for **G** + Pd$_2$**L**$^{F2}_2$**L**$^{IR}_2$ and r_H = 13.64 Å for **G** + Pd$_2$**L**$^{C2}_2$**L**$^{IR}_2$. Both values are indeed higher than the ones measured for the empty cages (r_H = 12.16 Å for Pd$_2$**L**$^{F2}_2$**L**$^{IR}_2$; r_H = 13.19 Å for Pd$_2$**L**$^{C2}_2$**L**$^{IR}_2$), however just slightly (Δr_H < 0.6 Å). While this amounts to a 5 % increase in hydrodynamic radius for the fluorenone-based Pd$_2$**L**$^{F2}_2$**L**$^{IR}_2$ system and 4 % for the carbazole-based Pd$_2$**L**$^{C2}_2$**L**$^{IR}_2$ system, the overall increase would be larger if a guest with the spatial dimensions of *(R)*-BINSO would associate outside of the assembly, especially considering the distance of the sulfur atom to the farthest hydrogen atom of the corresponding naphthyl-ring already measuring to approximately 8 Å. Even if the guest would fit snuck inside the interspaces of the ligands, it would yield to an overall stronger increase in spatial extent of the complex, since the consideration of the 3D structure of **G** is of the essence. The increase in hydrodynamic radius for the host-guest complexes as compared to the free hosts can be reasoned with two possible explanations. One would be the overall increase of the hydrodynamic radius at elevated temperatures already in the free host due to more extensive movement of the hexyl-chains in the vicinity of the assembly. While the viscosity of the outer solvent is considered in the calculation of r_H, a change of r_H in the free host cannot be ruled out since the ^{1}H DOSY spectrum of the free hosts has only been measured at room temperature. To verify this claim, ^{1}H DOSY experiments of the empty hosts at T = 348 K could be measured. Second would be an overall structural change of the host to adapt to bind the guest, leading to a slight increase in r_H in the process. Following this reasoning, it can be assumed that the spectra represent [**G**@Pd$_2$**L**$^{F2}_2$**L**$^{IR}_2$] and [**G**@Pd$_2$**L**$^{C2}_2$**L**$^{IR}_2$]. However, further analytic techniques have been applied to support this claim, namely ESI-MS experiments and ion-mobility measurements, and *in silico* methods.

ESI-MS spectra of all homoleptic species with **G** and of 1:1 mixtures of the heteroleptic assemblies and **G** have been analyzed. The ESI-MS spectra of a) [**G**@Pd$_2$**L**$^{F2}_2$**L**$^{IR}_2$] and b) [**G**@Pd$_2$**L**$^{C2}_2$**L**$^{IR}_2$] are shown in Figure 106.
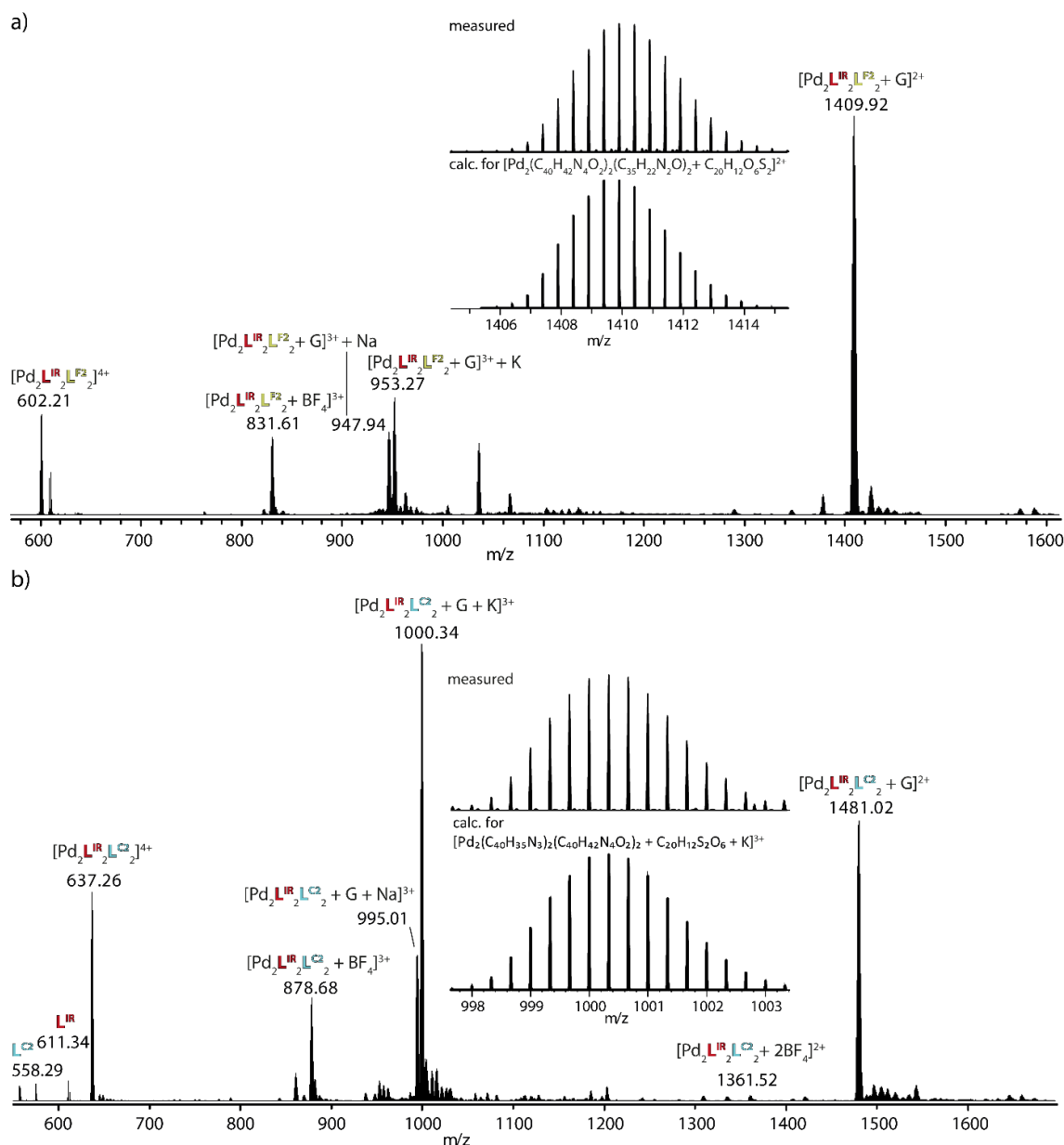
Figure 106: ESI-MS spectrum of a) a 1:1 mixture of heteroleptic $Pd_2L^{F2}_2L^{IR}_2$ after the addition of 1 equiv. **G** yielding species of the $[Pd_2L^{F2}_2L^{IR}_2 + xG + yBF_4 + zNa/K]^{(4-2x-y+z)+}$ ($x = 0,1$; $y = 0-2$; $z = 0,1$) type and b) a 1:1 mixture of heteroleptic $Pd_2L^{C2}_2L^{IR}_2$ after the addition of 1 equiv. **G** yielding species of the $[Pd_2L^{C2}_2L^{IR}_2 + xG + yBF_4 + zNa/K]^{(4-2x-y+z)+}$ ($x = 0,1$; $y = 0-2$; $z = 0,1$) type. The measured and calculated isotopic patterns of the highest peak are shown in the inset.

As evident from Figure 106, the main species detected in the mass spectrum are host-guest complexes, with small amounts of free host at $m/z = 602.2098$ for $Pd_2L^{F2}_2L^{IR}_2$ and $m/z = 637.2584$ for $Pd_2L^{C2}_2L^{IR}_2$. While the host-guest complex is the most abundant species detected for the fluorenone-based system $[G + Pd_2L^{F2}_2L^{IR}_2]^{2+}$ (Figure 106, a)) at $m/z = 1409.9167$, it can even be detected in form of sodium- or potassium-adducts ($m/z = 947.9443$ for $[Na + G + Pd_2L^{F2}_2L^{IR}_2]^{3+}$; $m/z = 953.2692$ for $[K + G + Pd_2L^{F2}_2L^{IR}_2]^{3+}$). While potassium is inherently in solution due to it being the counter cation of the guest, the presence of sodium is likely a contamination from the

117

spectrometer. A similar species distribution can be observed for the ESI-MS spectra of the 1:1 mixture of $Pd_2L^{C2}_2L^{IR}_2$ and the guest **G** (Figure 106, b). However in this case, the potassium-adduct $[K + G + Pd_2L^{F2}_2L^{IR}_2]^{3+}$ is the most abundant species at $m/z = 1000.3348$ while also $[G + Pd_2L^{F2}_2L^{IR}_2]^{2+}$ and $[Na + G + Pd_2L^{F2}_2L^{IR}_2]^{3+}$ are prominent peaks. The abundance of the species $[Pd_2L^{F/C2}_2L^{IR}_2 + 2BF_4]^{2+}$ is neglectable for both cases, leaving the **HG** complex being the predominant 2+ species in both cases. Finding **G** to associate strongly to the heteroleptic host molecules is a good indication, however it does not yield any information, on whether the guest is associated to the outside of the assembly and the interaction is purely derived from electromagnetic attractive forces, or whether it is bound in the inside of the cavity. While the latter has been proposed based on the results of the VT NMR experiments, ion-mobility measurements were performed to verify and strengthen the argument based on another dataset measured in the gas phase.
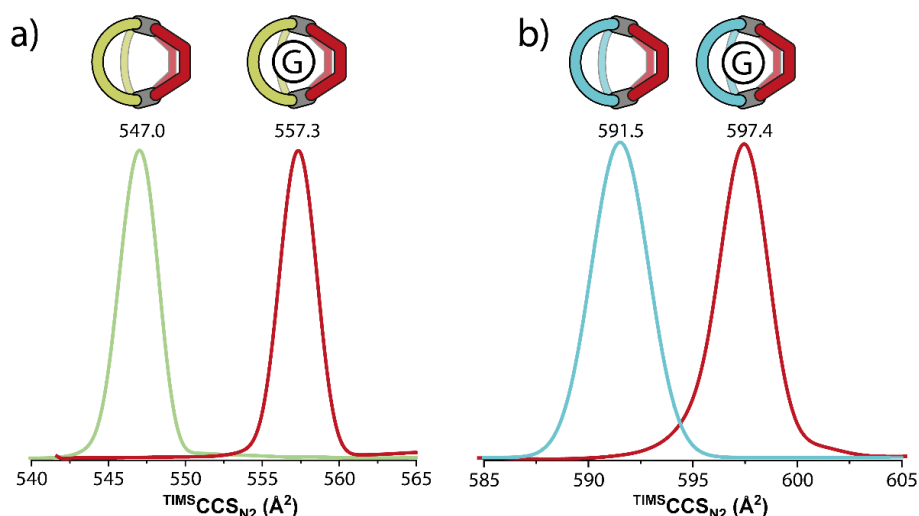
Figure 107: Superposition of the mobilograms obtained by trapped ion mobility ESI-TOF mass spectrometry of a) $[Pd_2L^{F2}_2L^{IR}_2 + 2BF_4]^{2+}$ and $[G@Pd_2L^{F2}_2L^{IR}_2]^{2+}$ and b) $[Pd_2L^{C2}_2L^{IR}_2 + 2BF_4]^{2+}$ and $[G@Pd_2L^{C2}_2L^{IR}_2]^{2+}$.

Figure 107 gives the results of the ion mobility measurements of the 2+ species of both hosts, $Pd_2L^{F2}_2L^{IR}_2$ and $Pd_2L^{C2}_2L^{IR}_2$ each with either 2 BF_4^- counter anions or the guest **G**. This is of utmost importance, as only two mobilities of species with the same charge can be reasonably compared. The determined CCS values for $Pd_2L^{F2}_2L^{IR}_2$ (Figure 107, a)) were 547.0 Å^2 without the guest and 557.3 Å^2 with the guest, respectively, subsequently yielding radii (see chapter 3.1 for calculation) in the gas phase of $r_G = 11.38$ Å for $[Pd_2L^{F2}_2L^{IR}_2 + 2BF_4]^{2+}$ and $r_G = 11.50$ Å for $[G@Pd_2L^{F2}_2L^{IR}_2]^{2+}$. This amounts to an overall 1.1 % increase in spatial extent in the gas phase for the fluorenone-based system. Similar results were obtained for its carbazole-based

analogue $Pd_2L^{C2}{}_2L^{IR}{}_2$, with determined CCS values amounting to 591.5 $Å^2$ for the empty host with 2 BF_4^- anions and 597.4 $Å^2$ for $[\mathbf{G}@Pd_2L^{C2}{}_2L^{IR}{}_2]^{2+}$. Calculated radii of the individual species based on the measured CCS values were $r_G = 11.90$ Å for $[Pd_2L^{C2}{}_2L^{IR}{}_2 + 2BF_4]^{2+}$ and $r_G = 11.97$ Å for $[\mathbf{G}@Pd_2L^{C2}{}_2L^{IR}{}_2]^{2+}$. The overall size increase for this system is 1%. The size increase in both systems from free host to $[\mathbf{G}@\mathbf{H}]$ complex is neglectable small and the results are in good accordance with the estimated values derived from solution via VT ^{1}H DOSY NMR spectroscopy. PLATZEK et al. discussed a similar problem of in- vs. outside binding in 2022 and found the increase in tCCS being much higher when simulating outside binding as compared to a minimal increase in tCCS with inside binding,[65] thus leaving to conclude an increase of merely 1% to be inside binding of **G** in our case. *In silico* structures of both host-guest complexes were calculated on DFT theory level for visualization purposes and to evaluate the fit of **G** in the respective host molecules $Pd_2L^{F2}{}_2L^{IR}{}_2$ and $Pd_2L^{C2}{}_2L^{IR}{}_2$.
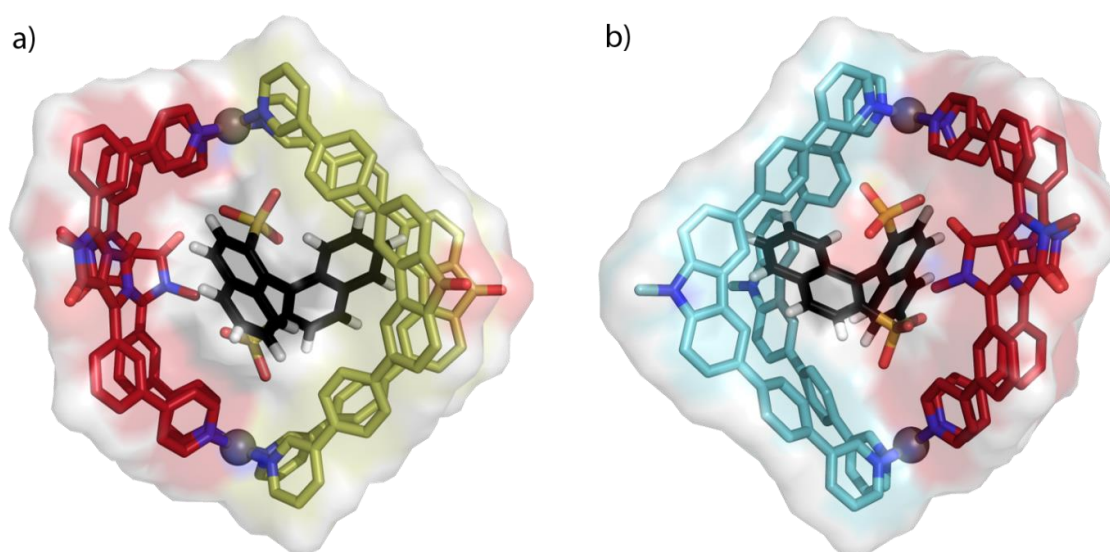
Figure 108: *In silico* Model of a) $[\mathbf{G}@Pd_2L^{F2}{}_2L^{IR}{}_2]$ and b) $[\mathbf{G}@Pd_2L^{C2}{}_2L^{IR}{}_2]$ (sticks overlaid with surface representation). Hydrogens and chains are omitted for clarity in the respective cage structures. Calculated on DFT theory level.

Figure 108 shows a) $[\mathbf{G}@Pd_2L^{F2}{}_2L^{IR}{}_2]$ and b) $[\mathbf{G}@Pd_2L^{C2}{}_2L^{IR}{}_2]$. Since the cavity of both molecules is structurally very similar, $[\mathbf{G}@Pd_2L^{F2}{}_2L^{IR}{}_2]$ is shown from one side with $[\mathbf{G}@Pd_2L^{C2}{}_2L^{IR}{}_2]$ being turned around its y-axis by 180°. The sulfonate groups are oriented towards the Pd(II) centers of the respective assemblies with the shortest Pd-O distance ranging from $d = 3.4$ Å in $Pd_2L^{F2}{}_2L^{IR}{}_2$ to $d = 3.8$ Å in $Pd_2L^{C2}{}_2L^{IR}{}_2$. The structures visualize how tight the guest fits into the hosts as there is barely any vacant space and the guest has to twist by a substantial amount with one naphthyl group standing perpendicular to the other in and angle of approximately 90°. This extremely tight fit

explains the splitting signals in the ^{1}H NMR spectra at elevated temperatures ($T = 348$ K) as an interaction of a chiral guest that is that close to the enveloping ligands leads to a desymmetrization of the host-guest complex as a whole. The interaction of the guest further leads to a minor contraction of the assemblies, reducing the Pd-Pd distance from $d = 14.6$ Å to $d = 14.2$ Å in Pd$_2$L$^{F2}_2$L$^{IR}_2$ and from $d = 14.7$ Å to $d = 14.6$ Å in Pd$_2$L$^{C2}_2$L$^{IR}_2$. This could come to place due to the attractive electrostatic interaction with the guest inside the cavity. Most interestingly is the introduction of a chiral guest molecule on the photophysical properties of the assemblies, especially for the FRET system Pd$_2$L$^{F2}_2$L$^{IR}_2$.
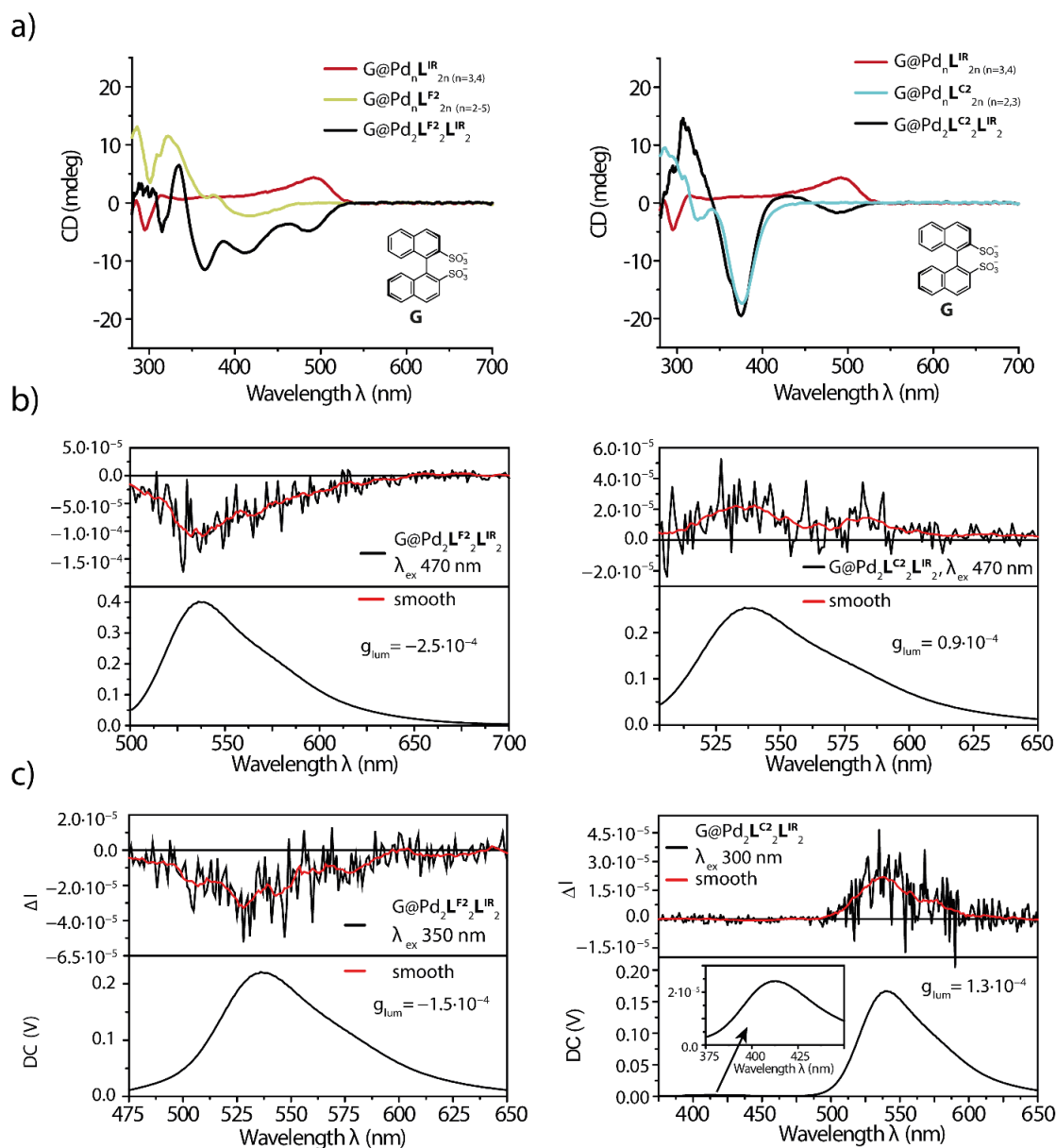
Figure 109: a) CD and b) CPL spectra as stacking of emission and 2ΔI (DMSO at 25 °C) of heteroleptic host-guest complexes [**G**@Pd$_2$L$^{F2}_2$L$^{IR}_2$] (0.35 mM) (left) and [**G**@Pd$_2$L$^{C2}_2$L$^{IR}_2$] (0.35 mM) (right) excited at $\lambda = 470$ nm and c) the aforementioned excited at the respective maxima observed for the complementary ligands ($\lambda_{ex} = 350$ nm for [**G**@Pd$_2$L$^{F2}_2$L$^{IR}_2$] (left); $\lambda_{ex} = 300$ nm for [**G**@Pd$_2$L$^{C2}_2$L$^{IR}_2$] (right)). A zoom-in of the residual emission from the carbazole-derivative is shown in the inset; smoothed ΔI spectra added for clarity (red lines); λ_{ex} and g_{lum} values are shown in the inset.

Figure 109 a) shows the CD spectra of the host-guest complexes of $Pd_2L^{F2}_2L^{IR}_2$, respectively $Pd_2L^{C2}_2L^{IR}_2$ (both black), with **G** compared to the spectra derived from adding **G** to the homoleptic assemblies (red: $Pd_nL^{IR}_{2n}$ (n = 3,4); yellow $Pd_nL^{F2}_{2n}$ (n = 2-5); teal: $Pd_nL^{C2}_{2n}$ (n = 2,3)). The heteroleptic assemblies [**G**@$Pd_2L^{F2}_2L^{IR}_2$] and [**G**@$Pd_2L^{C2}_2L^{IR}_2$]. show transitions that are a combination of the ones observed for the homoleptic HG complexes, however for some transitions a change of sign can be observed. The transition associated to the DPP ligand L^{IR} always changes sign from positive in homoleptic **G** + $Pd_nL^{IR}_{2n}$ (n = 3,4) to negative in both heteroleptic host-guest complexes. Further changes of sign can be observed for transitions at λ = 320 nm going from positive sign in **G** + $Pd_nL^{F2}_{2n}$ (n = 2-5) to negative in [**G**@$Pd_2L^{F2}_2L^{IR}_2$] while the shoulder directly next to this band at λ = 335 nm maintains its positive sign. A local minimum in the CD spectrum of **G** + $Pd_nL^{F2}_{2n}$ (n = 2-5) can be found at λ = 365 nm, which is presented in the heteroleptic host-guest complex as an absolute minimum. Another band at λ = 415 nm associated to the fluorenone-based chromophore ligand L^{F2} does not change its sign but is well more pronounced in the heteroleptic assembly. The behavior of the CD signals of **G** + $Pd_nL^{C2}_{2n}$ (n = 2,3) as compared to [**G**@$Pd_2L^{C2}_2L^{IR}_2$] as a change in sign can be observed at λ = 320 nm though in this case is changes from negative sign in the homoleptic environment to a positive one in the heteroleptic complex. A local maximum of the CD spectrum of **G** + $Pd_nL^{C2}_{2n}$ (n = 2,3) at λ = 340 nm can no longer be observed in the heteroleptic host-guest complex, whereas the absolute minimum in both curves is located at λ = 375 nm, even with comparable intensity. As for absolute values, the CD signal of [**G**@$Pd_2L^{C2}_2L^{IR}_2$] has a maximum of −19.5 mdeg at λ = 375 nm, whereas the one of [**G**@$Pd_2L^{F2}_2L^{IR}_2$] reaches its peak CD signal of −11.5 mdeg at λ = 365 nm. However, the difference of the heteroleptic host-guest complexes to their homoleptic counter parts is strongest for [**G**@$Pd_2L^{F2}_2L^{IR}_2$]. A direct comparison of the species has to be carefully evaluated, considering that each of the homoleptic assemblies measured is a mixture of assemblies with different nuclearities.

Finding the guest inducing chirality onto the systems, circular polarized luminescence (CPL) was measured, as both systems maintained the fluorescence of their respective chromophores, with special regard to the FRET induced from L^{F2} to L^{IR} in $Pd_2L^{F2}_2L^{IR}_2$. Figure 109 b) shows the detected CPL at λ = 470 nm, the local maximum in the absorption spectrum of L^{IR}, while Figure 109 c) shows the aforementioned at the excitation maxima of the respective chromophore partner (λ = 350 nm for L^{F2} and λ = 300 nm for L^{C2}; taken from the excitation spectra of the host-guest complexes, see Figure 157, experimental part). A CPL signal could be detected in all four cases, however the measured g_{lum} values and their sign differed quite significantly. While

[**G**@Pd$_2$**L**$^{F2}_2$**L**$^{IR}_2$] yielded negative g_{lum} values of $-2.5 \cdot 10^{-4}$ when directly exciting the DPP chromophore in **L**^{IR} ($\lambda = 470$ nm) and $-1.5 \cdot 10^{-4}$ when exciting the FRET partner ligand **L**^{F2}. This decrease by 40% in g_{lum} value is in accordance with the intensities observed in the excitation spectra of the host-guest complex [**G**@Pd$_2$**L**$^{F2}_2$**L**$^{IR}_2$], the overall value however is relatively low compared to other recently published systems.[67,68] A comparison of the observed signs of the g_{lum} with the homoleptic host-guest mixtures showed that a negative sign could only be observed for **G** + Pd$_n$**L**$^{F2}_{2n}$ (n = 2-5), while it was positive for **G** + Pd$_n$**L**$^{IR}_{2n}$ (n = 3,4) and **G** + Pd$_n$**L**$^{C2}_{2n}$ (n = 2,3). The positive sign is maintained in the heteroleptic assembly [**G**@Pd$_2$**L**$^{C2}_2$**L**$^{IR}_2$], which yielded g_{lum} values of $0.9 \cdot 10^{-4}$ when directly exciting the DPP chromophore in **L**^{IR} ($\lambda = 470$ nm) and $1.3 \cdot 10^{-4}$ when exciting counter-ligand **L**^{C2} at $\lambda = 300$ nm. Thus, while the g_{lum} value of [**G**@Pd$_2$**L**$^{F2}_2$**L**$^{IR}_2$] is increased when exciting the DPP chromophore directly as compared to exciting **L**^{F2}, it is decreased when doing the same in [**G**@Pd$_2$**L**$^{C2}_2$**L**$^{IR}_2$] with the additional mention, that upon chromophore excitation in the latter, the emission of **L**^{C2} can still be detected at $\lambda = 415$ nm (Figure 109, c), right spectrum, inset). A comparison of the absolute g_{lum} values must however be viewed cautiously, since the spectra are evidently quite noisy due to low signal intensity, thus making the values less reliable. The significant difference in photophysical properties of the host-guest complexes, with [**G**@Pd$_2$**L**$^{F2}_2$**L**$^{IR}_2$] showing negative values for g_{lum} and [**G**@Pd$_2$**L**$^{C2}_2$**L**$^{IR}_2$] sporting positive ones, shows that despite being structurally closely related, the electric and magnetic dipole moments differ quite a lot.

The herein reported results are a multi-step analysis of the step-by-step introduction of additional properties into a newly proposed system utilizing the heteroleptic cage as a means to bring two different functional ligands in close proximity to one another followed by the use of the cavity of the formed cage to incorporate a chiral guest molecule.

It has been shown that heteroleptic cage formation can be used to bring two chromophore-based ligands, **L**^{F2} and **L**^{IR}, with complementary photophysical properties in close proximity to one another, that upon excitation of the fluorenone-based ligand **L**^{F2}, the emission of the other is enabled, effectively displaying FRET within the confines of a heteroleptic coordination cage. A control system was synthesized based on another ligand **L**^{C2}, that carries the same structural properties as **L**^{F2} in terms of binding angle and linker constitution, but has its backbone replaced by a carbazole heterocyclic system, that no longer emits at a wavelength complementary to **L**^{IR}. While both combinations yield heteroleptic cages of the Pd$_2$**L**$^A_2$**L**$^B_2$ type, which were investigated using 1D and 2D NMR- and ESI-MS analysis, as well as *in silico* studies, only the system containing complementary chromophores, Pd$_2$**L**$^{F2}_2$**L**$^{IR}_2$, showed detectable FRET.

The next step was the utilization of the cavity the formed assemblies possessed, to bind a guest molecule and add another property to the system, namely chirality. The chiral guest molecule (*R*)-1,1'-Binaphthyl-2,2'-disulfonate ((*R*)-BINSO) has been added to both assemblies in a 1:1 fashion and the host-guest complexes [**G**@Pd$_2$**L**$^{F2}_2$**L**$^{IR}_2$] and [**G**@Pd$_2$**L**$^{F2}_2$**L**$^{IR}_2$], as well as the homoleptic host-guest mixtures **G** + Pd$_n$**L**$^{IR}_{2n}$ (n = 3,4), **G** + Pd$_n$**L**$^{F2}_{2n}$ (n = 2-5) and **G** + Pd$_n$**L**$^{C2}_{2n}$ (n = 2,3) have been analyzed. The system enabled not only the detection of chirality transfer from guest to host in the ground state yielding detectable CD signals for all host-guest complexes, but furthermore in their excited state by means of measuring CPL. The final step was the detection of the CPL emission of **L**^{IR} when exciting **L**^{F2}, thus realizing chirality transfer from the guest to its host molecule combined with FRET.

All Measurements regarding the photophysical properties (UV/Vis, fluorescence and CD) of the herein described systems have been performed by DR. I. REGENI, who also synthesized ligand **L**^{IR}. CPL measurements have been performed by DR. J. TESSAROLO.

3.3.4 Experimental part

3.3.4.1 Ligand Synthesis
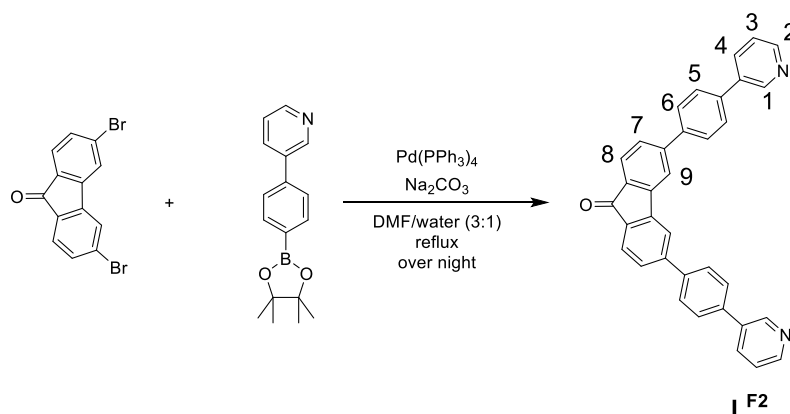
Scheme 9: Synthesis of ligand **L^{F2}**.

3,6-dibromo-9H-fluoren-9-one (250 mg, 0.74 mmol, 1 equiv.), 3-(4-(4,4,5,5-tetramethyl-1,3,2-dioxaborolan-2-yl)phenyl)pyridine (500 mg, 1.78 mmol, 2.4 equiv.), Na$_2$CO$_3$ (235 mg, 2.22 mmol, 3 equiv.) and Pd(PPh$_3$)$_4$ (25.6 mg, 0.022 mmol, 0.03 equiv.) were suspended in a mixture of DMF/H$_2$O (3:1, 12 ml). The mixture was degassed three times using the *Freeze-Pump-Thaw*-method, heated to reflux and stirred overnight. After cooling down to room temperature, the reaction mixture was extracted with chloroform. The organic phase was washed consecutively with water and then brine. It was dried over MgSO$_4$, filtered and the solvent was removed under reduced pressure. The crude product was purified by column chromatography (SiO$_2$; CHCl$_3$/methanol; 0 to 10 %) yielding a yellow powder that was further purified by GPC. The yield of the final product was 87 mg (0.179 mmol, 24%).

^{1}H NMR (700 MHz, 298 K, DMSO-d_6) δ 9.03 (d, ^4J = 2.0 Hz, 2H, H^1), 8.63 (dd, ^3J = 4.7, ^4J = 1.05 Hz, 2H, H^2), 8.48 (s, 2H, H^9), 8.24 (d, ^3J = 7.9 Hz, 2H, H^4), 8.03 (d, ^3J = 8.3 Hz, 4H, H^6), 7.95 (d, ^3J = 8.3 Hz, 4H, H^5), 7.82 (d, ^3J = 7.7, ^4J = 1.05 Hz, 2H, H^7), 7.75 (d, ^3J = 7.7 Hz, 2H, H^8), 7.57 (d, ^3J = 7.7, 4.7 Hz, 2H, H^3) ppm.

^{13}C NMR (176 MHz, 298 K, DMSO-d_6) δ 192.16 (C$_{XVI}$), 148.42 (C$_{II}$), 147.35 (C$_I$), 146.06 (C$_X$), 144.65 (C$_{XIV}$), 138.66 (C$_{IX}$), 137.15 (C$_{VI}$), 134.94 (C$_V$), 134.57 (C$_{IV}$), 132.93 (C$_{XIII}$), 127.78 (C$_{VIII}$), 127.67 (C$_{XI}$), 127.53 (C$_{VII}$), 124.46 (C$_{XII}$), 124.10 (C$_{III}$), 119.90 (C$_{XV}$) ppm.

HR ESI-MS:

measured for [C$_{35}$H$_{22}$N$_2$O+H]$^+$:   487.1784

calculated: 487.1805
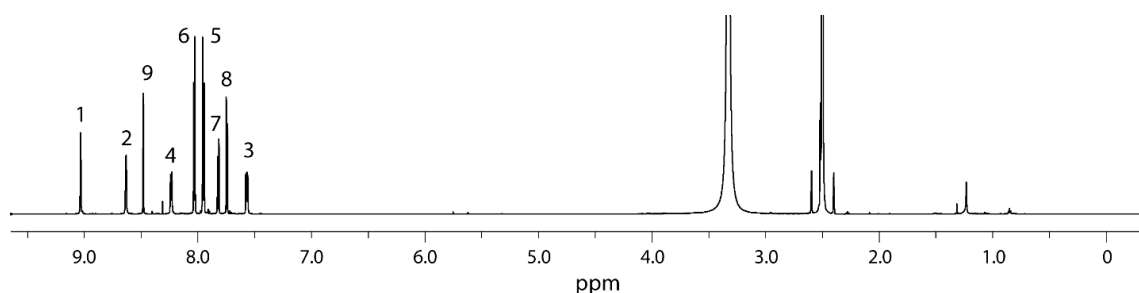
Figure 110: ^{1}H NMR spectrum (700 MHz, 298 K, DMSO-d_6) of **L^{F2}**.
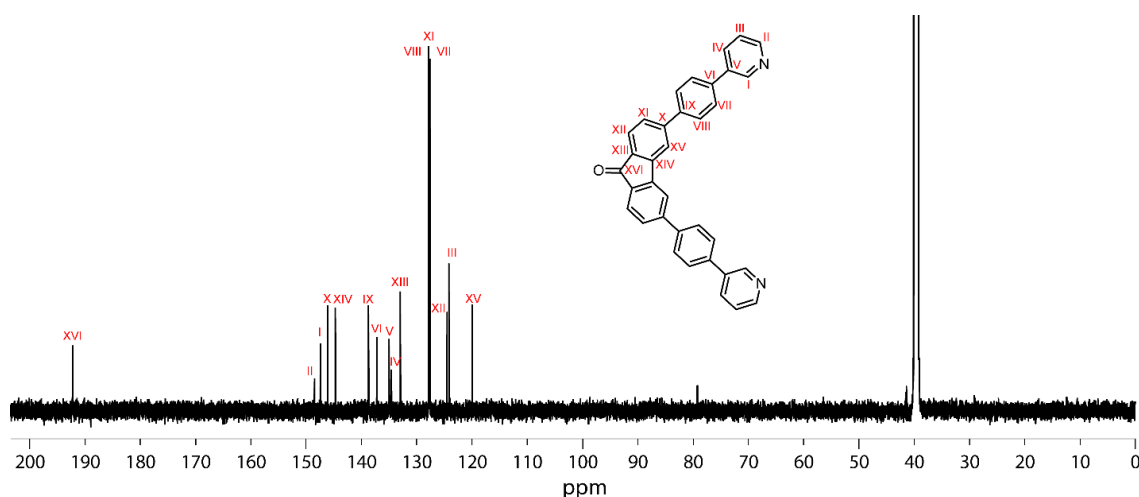
Figure 111: ^{13}C NMR spectrum (176 MHz, 298 K, DMSO-d_6) of **L^{F2}**.
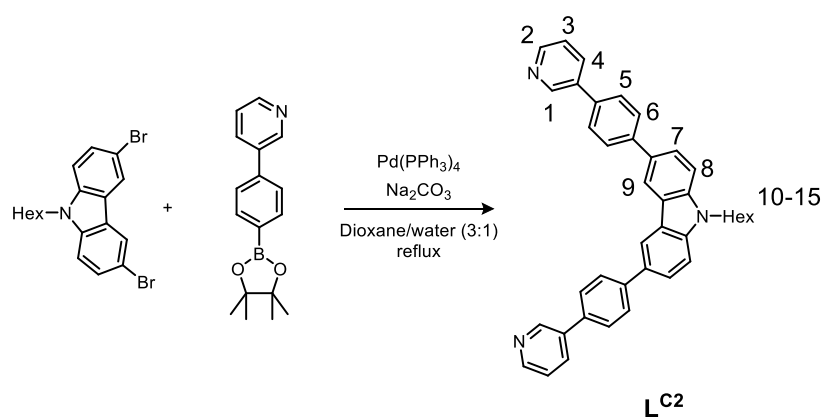
Scheme 10: Synthesis of ligand **L^{C2}**.

3,6-dibromo-9-hexyl-9H-carbazole (500 mg, 1.22 mmol, 1 equiv.), 3-(4-(4,4,5,5-tetramethyl-1,3,2-dioxaborolan-2-yl)phenyl)pyridine (1.03 g, 3.67 mmol, 3 equiv.) Na$_2$CO$_3$ (388.55 mg, 3.67 mmol, 3 equiv.) and Pd(PPh$_3$)$_4$ (42.36 mg, 0.037 mmol, 0.03 equiv.) were suspended in a mixture of dioxane/H$_2$O (3:1, 25 mL). The mixture was degassed three times using the *Freeze-Pump-Thaw*-method, heated to reflux and stirred over night. After cooling down to room temperature, the reaction mixture was extracted with chloroform. The organic phase was washed consecutively with water and then brine.

It was dried over $MgSO_4$, filtered and the solvent was removed under reduced pressure. The crude product was purified by column chromatography (SiO_2; acetone/pentane; 50 % to 75 %) yielding a light beige powder that was further purified by GPC. The yield of the final product was 285 mg (0.511 mmol, 42 %).

3,6-dibromo-9-hexyl-9H-carbazole has been synthesized as previously reported.[117]

^{1}H NMR (700 MHz, 298 K, DMSO-d_6) δ 9.00 (s, 2H, H^1), 8.75 (d, ^4J = 1.7 Hz, 2H, H^9), 8.60 (d, ^4J = 2.65 Hz, 2H, H^2), 8.17 (dt, ^3J = 8.0 Hz , ^4J = 1.7 Hz, 2H, H^4), 7.98 (d, ^3J = 8.3 Hz, 4H, H^6), 7.86 – 7.90 (m, 6H, H^5 + H^7) , 7.73 (d, ^3J = 8.5 Hz, 2H, H^8), 7.52 (dd, ^3J = 7.8, 4.7 Hz, 2H, H^3) , 4.47 (t, ^3J = 7.05 Hz, 2H, H^{10}), 1.83 (q, ^3J = 7.5 Hz, 2H, H^{11}), 1.38-1.21 (m, 6H, H$^{12-14}$), 0.83 (t, ^3J = 7.2 Hz, 3H, H^{15}) ppm.

^{13}C NMR (176 MHz, 298 K, DMSO-d_6) δ 148.39 (C$_{II}$), 147.53 (C$_I$), 140.72 (C$_{XIII}$), 140.26 (C$_{IX}$), 135.21 (C$_V$), 135.03 (C$_{VI}$), 133.88 (C$_{IV}$), 130.36 (C$_X$), 127.33 (C$_{VIII}$), 127.23 (C$_{VII}$), 124.80 (C$_{XI}$), 123.93 (C$_{III}$), 123.03 (C$_{XIV}$), 118.81 (C$_{XV}$), 109.97 (C$_{XII}$), 41.91 (C$_{XVI}$), 31.00 (C$_{XVII}$), 28.59 (C$_{XVIII}$), 26.15 (C$_{XIX}$), 22.02 (C$_{XX}$), 13.87 (C$_{XXI}$) ppm.

<u>HR ESI-MS:</u>

measured for $[C_{40}H_{35}N_3+H]^+$:   558.2869

calculated: 558.2904
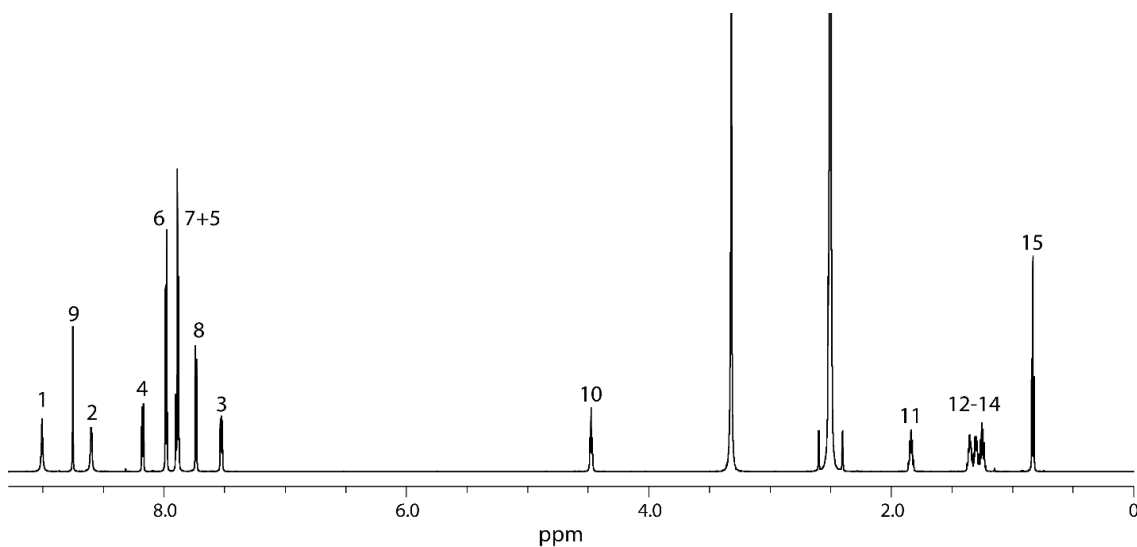
Figure 112: ^{1}H NMR spectrum (700 MHz, 298 K, DMSO-d_6) of **L^{C2}**.
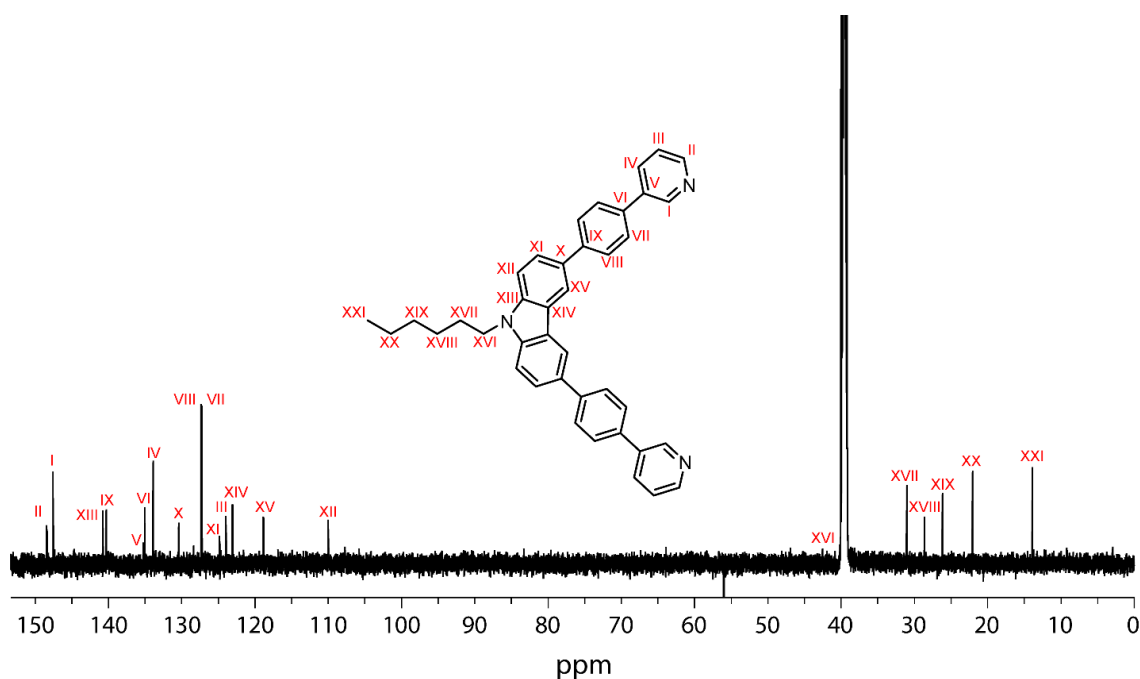
Figure 113: ^{13}C NMR spectrum (176 MHz, 298 K, DMSO-d_6) of L^{C2}.

3.3.4.2 Synthesis and Characterization of Homoleptic Assemblies

Pd$_3$L$^{IR}_6$ + Pd$_4$L$^{IR}_8$
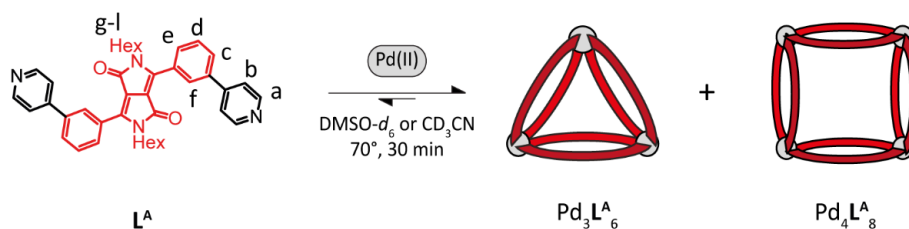
Scheme 11: Formation of Pd$_3$L$^{IR}_6$ + Pd$_4$L$^{IR}_8$ rings upon addition of 0.5 equiv. Pd(II) cations to ligand L^{IR}. The assembly has been described by Dr. Irene Regeni in her thesis.[69]

Pd$_n$L$^{F2}_{2n}$ (n = 2-5)
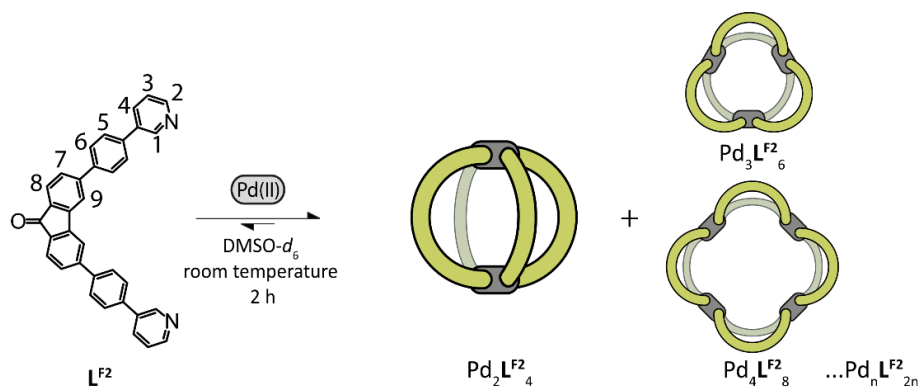
Scheme 12: Formation of the Pd$_2$L$^{F2}_4$ cage and the Pd$_n$L$^{F2}_{2n}$ $_{n=3-5}$ rings upon addition of 0.55 equiv. Pd(II) cations to ligand L^{F2}.

A mixture of ligand **L^{F2}** (540 µL of a 3.11 mM solution in DMSO-d_6) and [Pd(CH$_3$CN)$_4$](BF$_4$)$_2$ (60 µL of a 15 mM solution in DMSO-d_6) was left to rest at room temperature for 2 h to afford a mixture of Pd$_2$**L^{F2}**$_4$ and Pd$_n$**L^{F2}**$_{2n\ n=3-5}$.
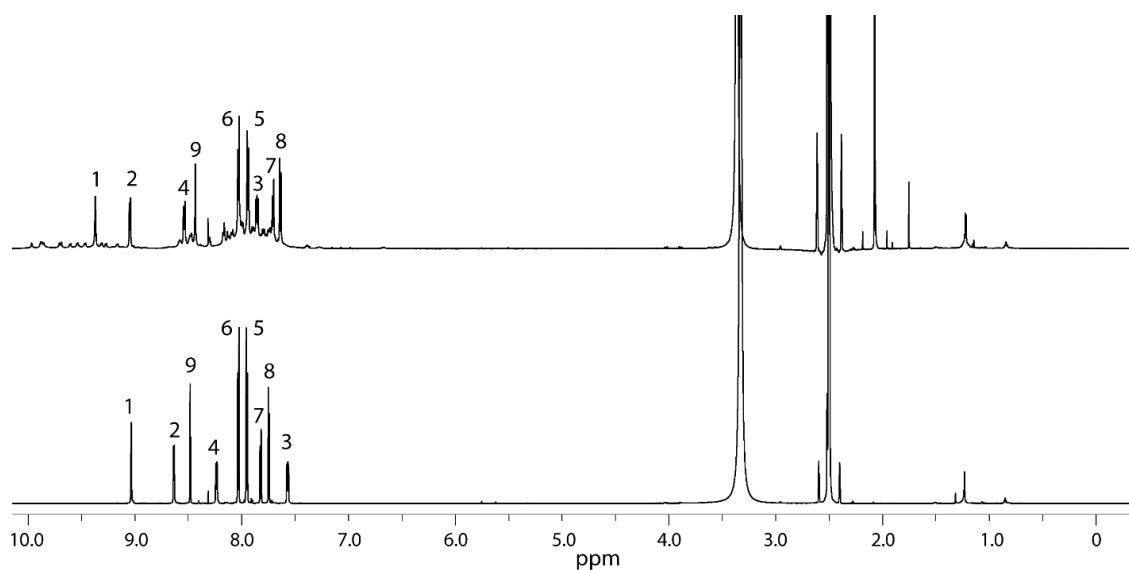
Figure 114: Stacked ^{1}H NMR spectra of Ligand **L^{F2}** (bottom; 700 MHz, 298 K, DMSO-d_6) and ligand **L^{F2}** upon addition of 0.55 equiv. Pd(II) to yield a mixture of Pd$_2$**L^{F2}**$_4$ and Pd$_n$**L^{F2}**$_{2n\ n=3-5}$ (top; 600 MHz, 298K, DMSO-d_6).
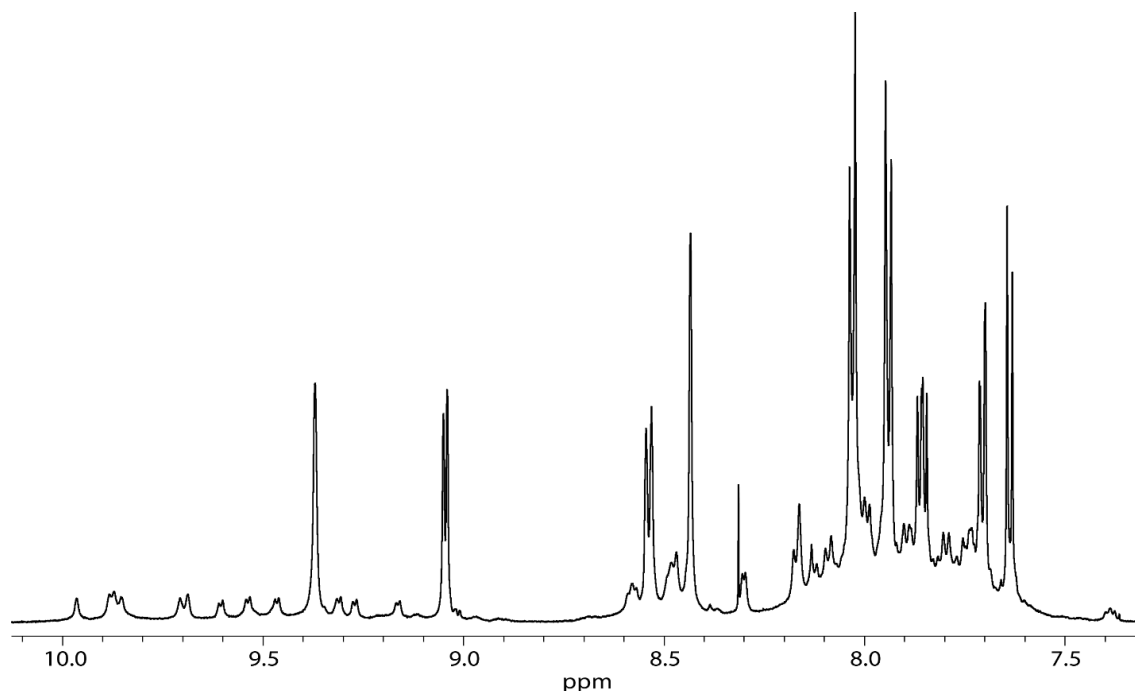
Figure 115: Partial ^{1}H NMR spectrum (600 MHz, 298K, DMSO-d_6) of the mixture formed from **L^{F2}** after the addition of 0.55 equiv. Pd(II).

^{1}H NMR (600 MHz, 298 K, DMSO-d_6) Pd$_2$**L^{F2}**$_4$ δ 9.37 (s, 8H, H^1), 9.05 (d, ^3J = 5.75 Hz, 8H, H^2), 8.54 (d, ^3J = 8.05 Hz, 8H, H^4), 8.44 (s, 8H, H^9), 8.03 (d, ^3J = 8.4 Hz, 16H, H^6), 7.94 (d, ^3J = 8.4 Hz, 16H, H^5), 7.86 (dd, ^3J = 8.05, 5.85 Hz, 8H, H^3), 7.71 (dd, ^3J = 7.85 Hz, 1.05 Hz, 8H, H^7), 7.64 (d, ^3J = 7.75 Hz, 8H, H^8) ppm.

128
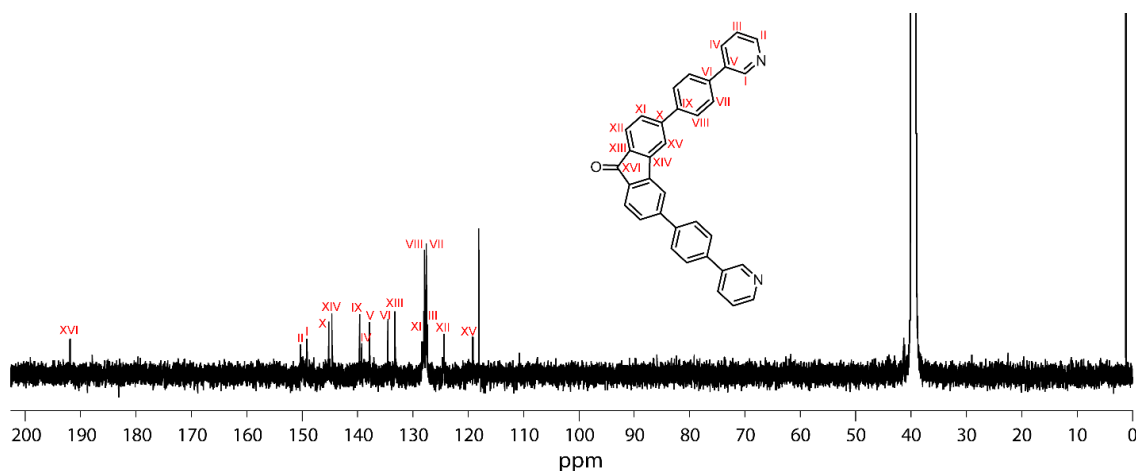
Figure 116: ^{13}C NMR spectrum (151 MHz, 298 K, DMSO-d_6) of Pd$_2$**L^{F2}**$_4$ (lb = 2.5 Hz). The other Pd(II)-species were not resolved due to their low respective concentration.

^{13}C NMR (151 MHz, 298 K, DMSO-d_6) Pd$_2$**L^{F2}**$_4$ $δ$ 191.88 (C$_{XVI}$), 150.25 (C$_{II}$), 149.09 (C$_I$), 145.16 (C$_X$), 144.59 (C$_{XIV}$), 139.60 (C$_{IX}$), 139.19 (C$_{IV}$), 137.78 (C$_V$), 134.47 (C$_{VI}$), 133.19 (C$_{XIII}$), 128.00 (C$_{XI}$), 127.85 (C$_{VIII}$), 127.56 (C$_{VII}$), 127.35 (C$_{III}$), 124.37 (C$_{XII}$), 119.14 (C$_{XV}$) ppm.
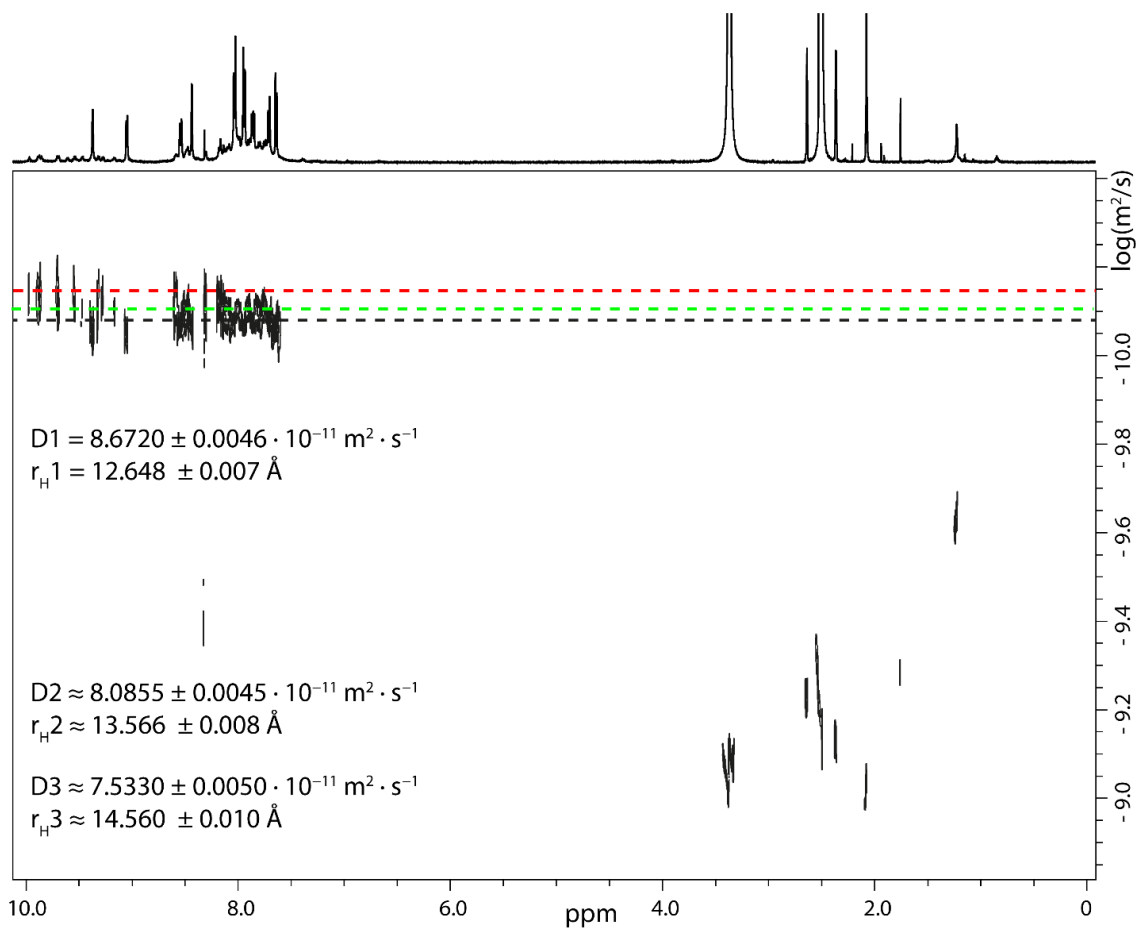
Figure 117: ^{1}H DOSY NMR spectrum (500 MHz, 298K, DMSO-d_6) of the mixture of Pd$_2$**L^{F2}**$_4$ and Pd$_n$**L^{F2}**$_{2n}$ $_{n=3-5}$ formed upon Pd(II) addition to ligand **L^{F2}**. Hydrodynamic radii of D2 and D3 could only be estimated due to lack of non-overlapping signals (see Table 6).

Table 6: Signals taken for the calculation of r_H of the multi-species mixture ligand $\mathbf{L^{F2}}$ forms upon Pd(II) addition. Radii assigned to different species are indicated by color.

Signal	Region [ppm]	D [m$^2 \cdot$ s^{-1}]	SD	Species
1	10.005 to 9.944	$8.03 \cdot 10^{-11}$	$4.92 \cdot 10^{-3}$	2
2	9.918 to 9.827	$7.42 \cdot 10^{-11}$	$5.69 \cdot 10^{-3}$	3
3	9.744 to 9.678	$7.51 \cdot 10^{-11}$	$5.38 \cdot 10^{-3}$	3
4	9.414 to 9.350	$8.78 \cdot 10^{-11}$	$4.15 \cdot 10^{-3}$	1
5	9.341 to 9.252	$7.68 \cdot 10^{-11}$	$5.31 \cdot 10^{-3}$	3
6	9.194 to 9.143	$8.14 \cdot 10^{-11}$	$4.03 \cdot 10^{-3}$	2
7	9.090 to 9.032	$8.87 \cdot 10^{-11}$	$4.09 \cdot 10^{-3}$	1
8	8.570 to 8.518	$8.54 \cdot 10^{-11}$	$4.29 \cdot 10^{-3}$	1
9	8.463 to 8.414	$8.52 \cdot 10^{-11}$	$4.08 \cdot 10^{-3}$	1
10	8.317 to 8.282	$7.52 \cdot 10^{-11}$	$3.51 \cdot 10^{-3}$	3
11	8.206 to 8.151	$7.53 \cdot 10^{-11}$	$5.20 \cdot 10^{-3}$	3
12	7.683 to 7.596	$8.65 \cdot 10^{-11}$	$6.51 \cdot 10^{-3}$	1

The signals chosen for the determination of the hydrodynamic radius are given in Table 6. It is noted that, due to low signal intensity and small dataset, the diffusion coefficients and thus hydrodynamic radius of species 2 and 3 could only be estimated. We opted to assign signals 1 and 6 (green) to another species due to their measured diffusion coefficients being vastly different from the signals assigned to species 3 (red, signals 2, 3, 5, 10 and 11).
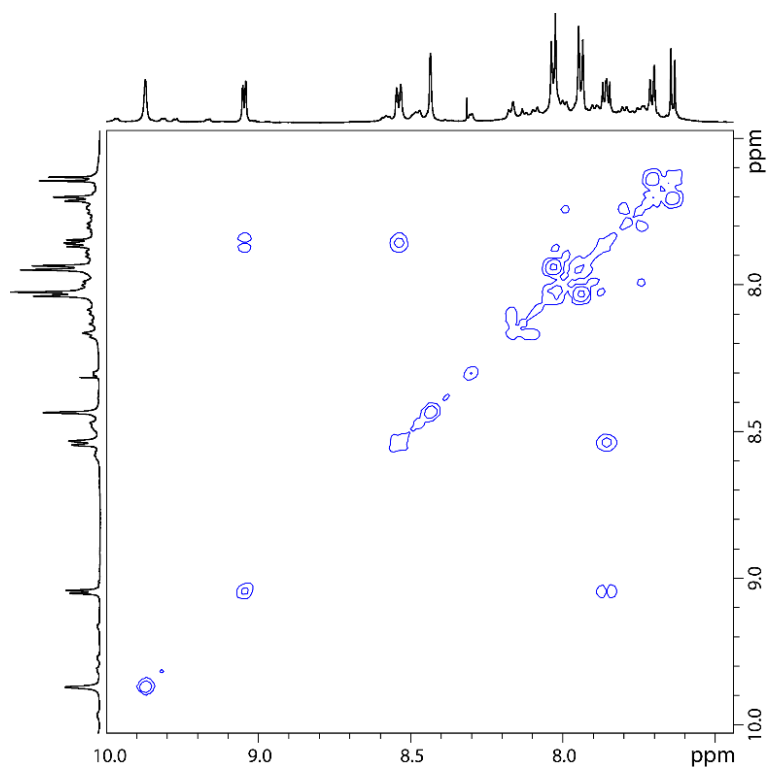
Figure 118: Partial ^{1}H-^{1}H COSY NMR spectrum (600 MHz, 298K, DMSO-d_6) of the mixture of Pd$_2$**L**$^{F2}_4$ and Pd$_n$**L**$^{F2}_{2n, n=3-5}$ formed upon Pd(II) addition to ligand **L**^{F2}. Peak intensity is set to show the ^{1}H-^{1}H COSY contacts of the main species Pd$_2$**L**$^{F2}_4$.
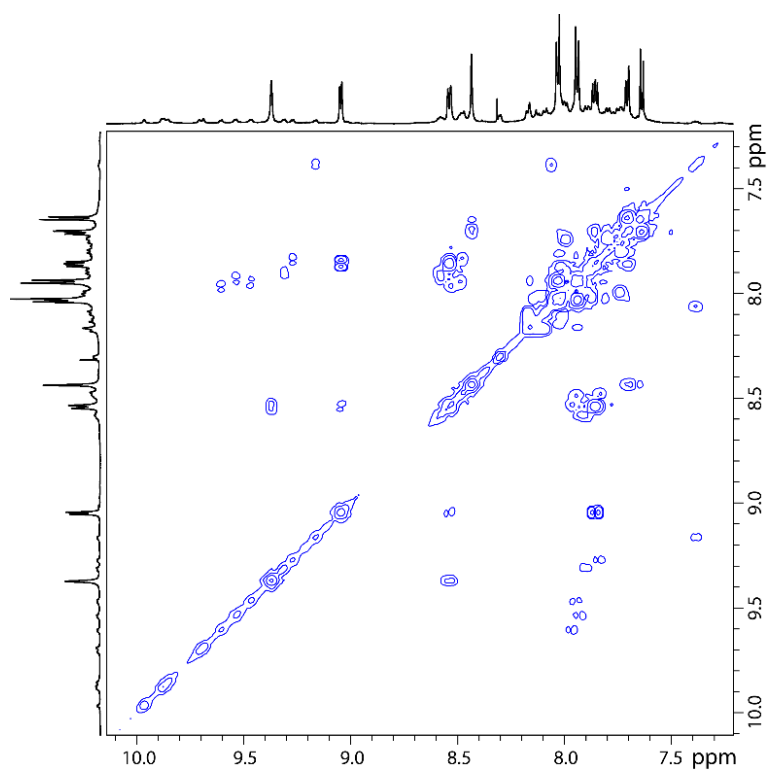
Figure 119: Partial ^{1}H-^{1}H COSY NMR spectrum (600 MHz, 298K, DMSO-d_6) of the mixture of Pd$_2$**L**$^{F2}_4$ and Pd$_n$**L**$^{F2}_{2n \, n=3-5}$ formed upon Pd(II) addition to ligand **L**^{F2}. Peak intensity is set to show the ^{1}H-^{1}H COSY contacts of the subspecies Pd$_n$**L**$^{F2}_{2n \, n=3-5}$.
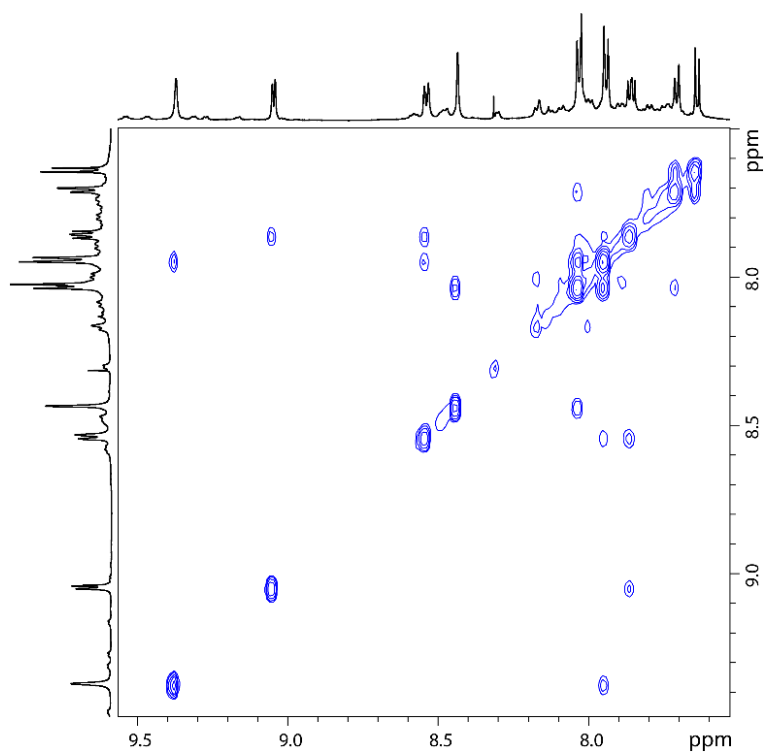
Figure 120: Partial ^{1}H-^{1}H NOESY NMR spectrum (600 MHz, 298K, DMSO-d_6) of the mixture of Pd$_2$**L**$^{F2}_4$ and Pd$_n$**L**$^{F2}_{2n\ n=3-5}$ formed upon Pd(II) addition to ligand **L**^{F2}. Peak intensity is set to show the ^{1}H-^{1}H NOESY contacts of the main species Pd$_2$**L**$^{F2}_4$.
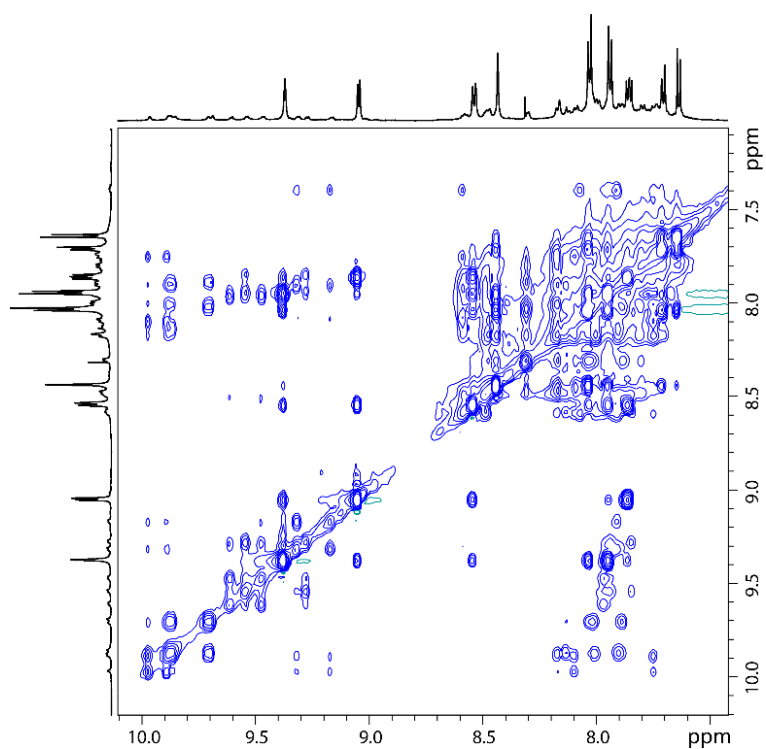
Figure 121: Partial ^{1}H-^{1}H NOESY NMR spectrum (600 MHz, 298K, DMSO-d_6) of the mixture of Pd$_2$**L**$^{F2}_4$ and Pd$_n$**L**$^{F2}_{2n\ n=3-5}$ formed upon Pd(II) addition to ligand **L**^{F2}. Peak intensity is set to show the ^{1}H-^{1}H NOESY contacts of the subspecies Pd$_n$**L**$^{F2}_{2n\ n=3-5}$.
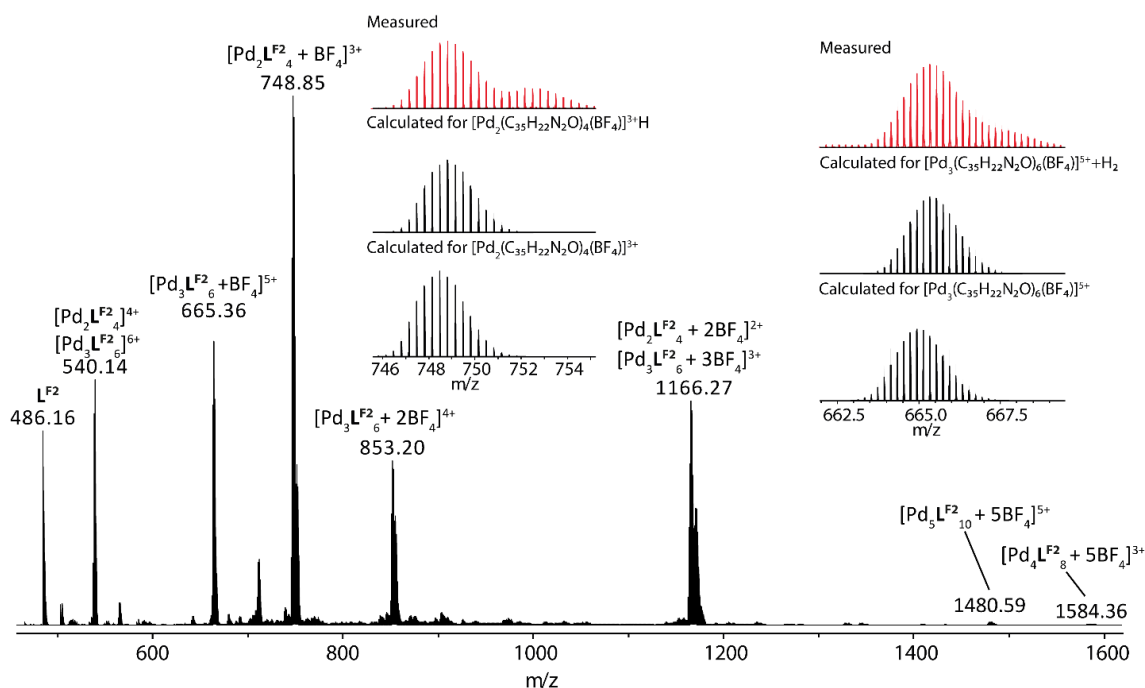
Figure 122: ESI-MS spectrum of the mixture of $Pd_2L^{F2}_4$ and $Pd_nL^{F2}_{2n\ n=3-5}$ formed upon Pd(II) addition (0.55 equiv.) to ligand L^{F2}. Main species detected were $[Pd_2L^{F2}_4 + xBF_4]^{(4-x)}$ (x = 2-4) and $[Pd_3L^{F2}_6 + xBF_4]^{(6-x)}$ (x = 3-6). The observed and calculated isotopic patterns of the main species are shown in the inset. Species with higher nuclearity could be detected only with a high number of counter anions (see Figure 123).
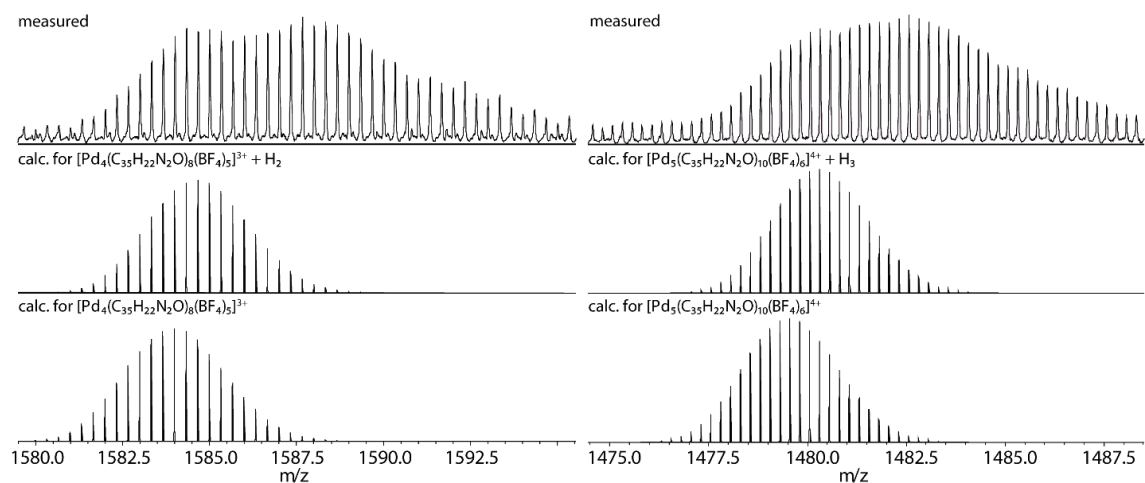
Figure 123: Partial ESI-MS spectrum of the mixture of $Pd_2L^{F2}_4$ and $Pd_nL^{F2}_{2n\ n=3-5}$ formed upon Pd(II) addition to ligand L^{F2}. The depicted regions show species of higher nuclearity, namely $[Pd_4L^{F2}_8 + 5BF_4]^{3+}$ and $[Pd_5L^{F2}_{10} + 6BF_4]^{4+}$.
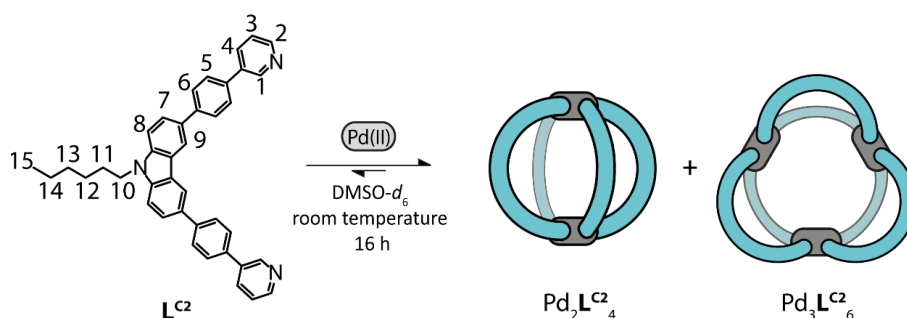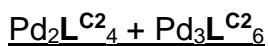
Scheme 13: Formation of the Pd$_2$**L**^{C2}$_4$ cage and Pd$_3$**L**^{C2}$_6$ ring upon addition of 0.55 equiv. Pd(II) cations to ligand **L**^{C2}.

A mixture of ligand **L**^{C2} (540 µL of a 3.11 mM solution in DMSO-d_6) and [Pd(CH$_3$CN)$_4$](BF$_4$)$_2$ (60 µL of a 15 mM solution in DMSO-d_6) was left to rest at room temperature overnight to afford a mixture of Pd$_2$**L**^{C2}$_4$ and Pd$_3$**L**^{C2}$_6$.
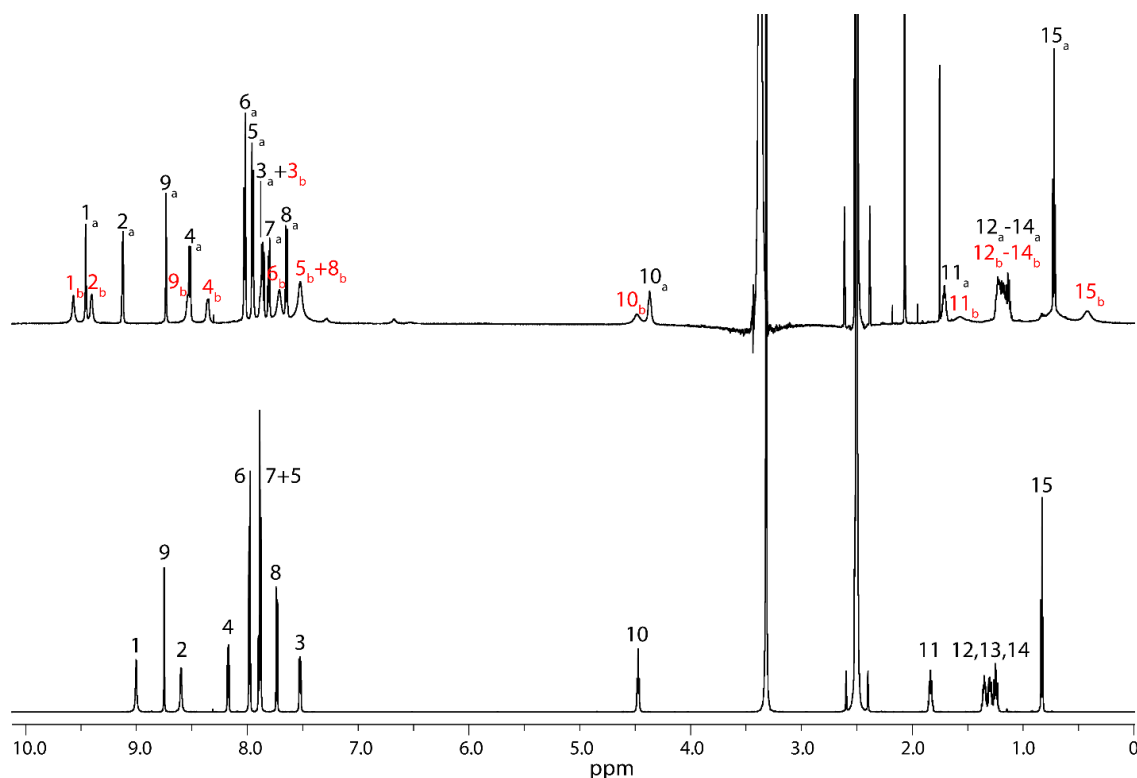
Figure 124: Stacked ^{1}H NMR spectra of Ligand L^{C2} (bottom; 700 MHz, 298 K, DMSO-d_6) and ligand L^{C2} upon addition of 0.55 equiv. Pd(II) to yield a mixture of Pd$_2$L^{C2}$_4$ and Pd$_3$L^{C2}$_6$ (top; 600 MHz, 298K, DMSO-d_6).

^{1}H NMR (600 MHz, 298 K, DMSO-d_6) Pd$_2$**L**^{C2}$_4$ δ 9.46 (s, 8H, H^{1a}), 9.13 (d, ^3J = 5.70 Hz, 8H, H^{2a}), 8.73 (d, ^4J = 1.15 Hz, 8H, H^{9a}), 8,52 (d, ^3J = 8.15 Hz, 8H, H^{4a}), 8.02 (d, ^3J = 8.40 Hz, 16H, H^{6a}), 7.95 (d, ^3J = 8.40 Hz, 16H, H^{5a}), 7.86 (dd, ^3J = 8.40 Hz, 5.95 Hz 8H, H^{3a}), 7.81 (dd, ^3J = 8.75 Hz, ^4J = 1.30 Hz, 8H, H^{7a}), 7.65 (d, ^3J = 8.85 Hz, 8H, H^{8a}), 4.37 (broad

s, 8H, H^{10a}), 1.71 (quint, ^3J = 6.80 Hz, 8H, H^{11a}), 1.09 – 1.27 (m, overlapping w. H^{12-14b} of the Pd$_3$**L^{C2}**$_6$ species, H^{12-14a}), 0.72 (t, ^3J = 7.15 Hz, 12H, H^{15a}) ppm.

^{1}H NMR (600 MHz, 298 K, DMSO-d_6) Pd$_3$**L^{C2}**$_6$ $δ$ 9.57 (broad s, 12H, H^{1b}), 9.40 (broad s, 12H, H^{2b}), 8.54 (broad, overlapping w. H^{4a}, H^{9b}), 8.36 (d, ^3J = 6.2 Hz, 12H, H^{4b}), 7.88 (broad, overlapping w. H^{3a}, H^{3b}), 7.71 (broad, 24H, H^{6b}), 7.52 (broad, 36H, H^{5+8b}), 4.48 (broad, 12H, H^{10b}) ,1.57 (broad, 12H, H^{11b}), 1.09 – 1.27 (m, overlapping w. H^{12-14a} of the first species, H^{12-14b}), 0.42 (broad, 18H, H^{15b}) ppm. Proton H^{7b} is not resolved due to severe broadening.
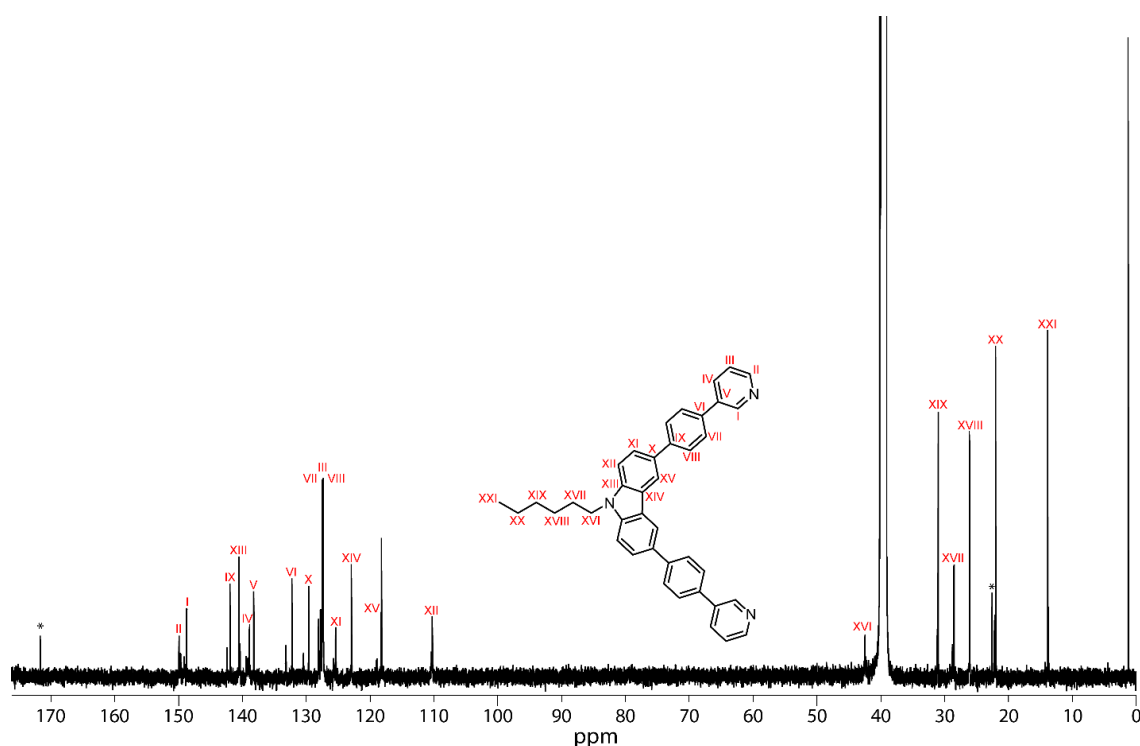
Figure 125: ^{13}C NMR spectrum (151 MHz, 298 K, DMSO-d_6) of the mixture of Pd$_2$**L^{C2}**$_4$ and Pd$_3$**L^{C2}**$_6$ (lb = 2.5 Hz).

Main species Pd$_2$**L^{C2}**$_4$: ^{13}C NMR (151 MHz, 298 K, DMSO-d_6) $δ$ 149.84 (C$_{IIb}$), 148.66 (C$_{Ib}$), 141.86 (C$_{IXb}$), 140.48 (C$_{XIIIb}$), 138.81 (C$_{IVb}$), 138.15 (C$_{Vb}$), 132.17 (C$_{VIb}$), 129.54 (C$_{Xb}$), 127.45 (C$_{VIIb}$), 127.38 (C$_{IIIb}$), 127.27 (C$_{VIIIb}$), 125.32 (C$_{XIb}$), 122.87 (C$_{XIVb}$), 118.21 (C$_{XVb}$), 110.19 (C$_{XIIb}$), 42.43 (C$_{XVIb}$), 30.95 (C$_{XIXb}$), 28.48 (C$_{XVIIb}$), 26.06 (C$_{XVIIIb}$), 21.97 (C$_{XXb}$), 13.81 (C$_{XXIb}$) ppm.

Second species Pd$_3$**L^{C2}**$_6$: ^{13}C NMR (151 MHz, 298 K, DMSO-d_6) $δ$ 149.60, 149.05, 142.32, 140.32, 139.32, 139.05, 133.13, 130.37, 128.00, 127.69, 125.63, 122.83, 118.85, 110.33, 31.09, 28.74, 22.13, 13.70 ppm.

A ^{13}C assignment of Pd$_3$**L^{C2}**$_6$ was not possible due to insufficient signal intensity in the 2D spectra. Three ^{13}C signals could not be resolved due to low signal intensity or signal overlap.
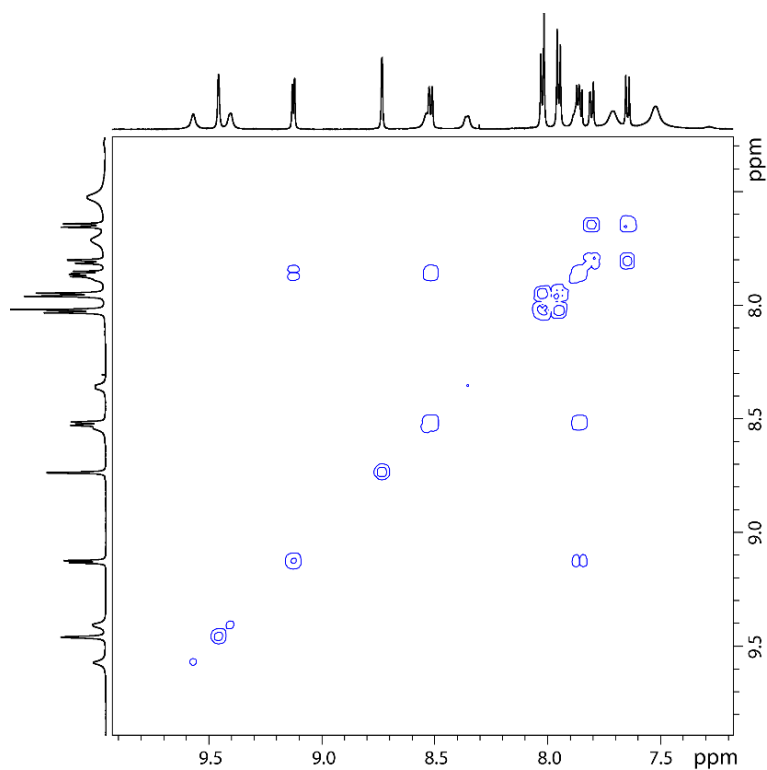
Figure 126: Partial ^{1}H-^{1}H COSY NMR spectrum (600 MHz, 298K, DMSO-d_6) of the mixture of Pd$_2$**L^{C2}**$_4$ and Pd$_3$**L^{C2}**$_6$ formed upon Pd(II) addition to ligand **L^{C2}**. Peak intensity is set to show the ^{1}H-^{1}H COSY contacts of the main species Pd$_2$**L^{C2}**$_4$.
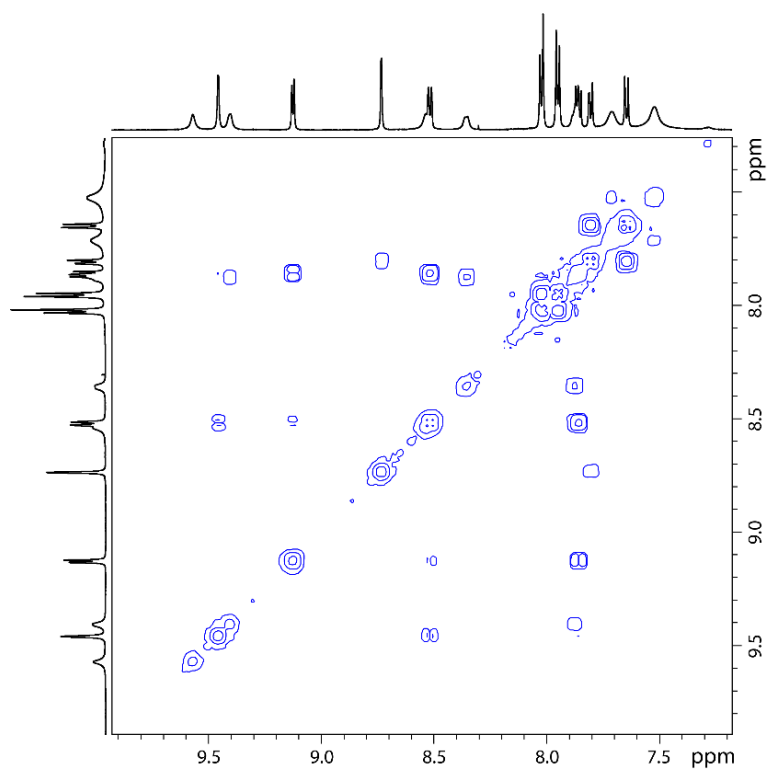
Figure 127: Partial ^{1}H-^{1}H COSY NMR spectrum (600 MHz, 298K, DMSO-d_6) of the mixture of Pd$_2$**L^{C2}**$_4$ and Pd$_3$**L^{C2}**$_6$ formed upon Pd(II) addition to ligand **L^{C2}**. The peaks intensity is set to show the ^{1}H-^{1}H COSY contacts of both species.
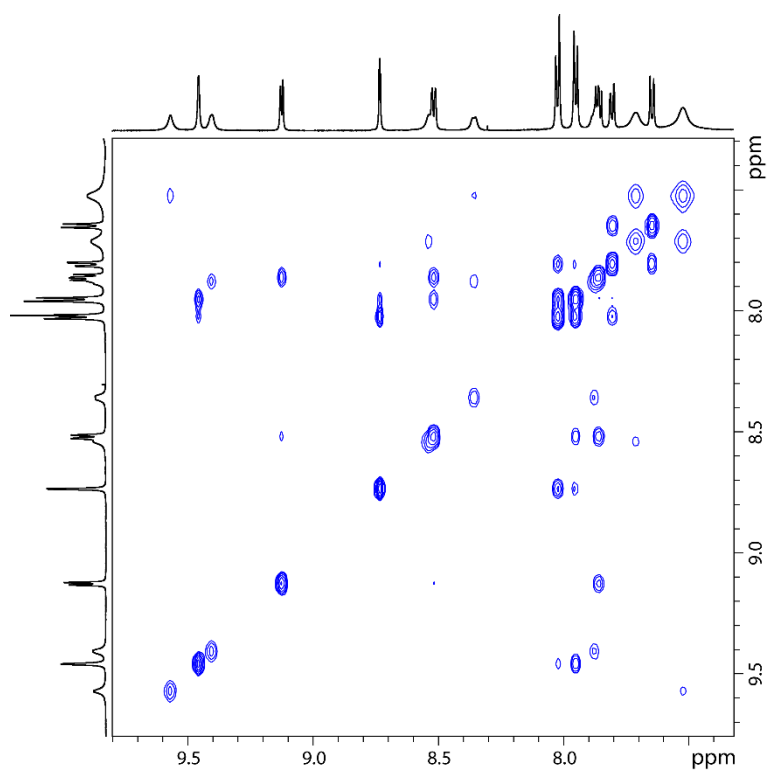
Figure 128: Partial ^{1}H-^{1}H NOESY NMR spectrum (600 MHz, 298K, DMSO-d_6) of the mixture of Pd$_2$**L^{C2}**$_4$ and Pd$_3$**L^{C2}**$_6$ formed upon Pd(II) addition to ligand **L^{C2}**. Peak intensity is set to show all ^{1}H-^{1}H NOESY contacts.
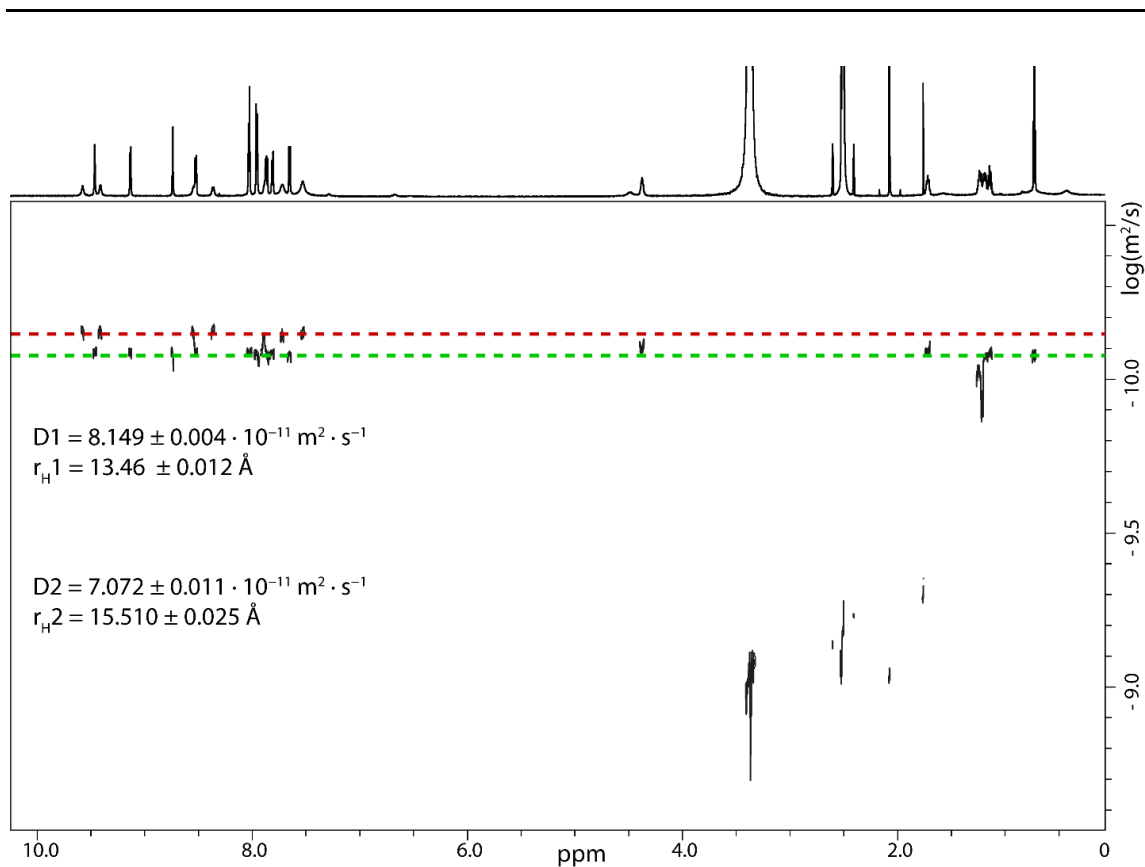
Figure 129: ^{1}H DOSY NMR spectrum (700 MHz, 298K, DMSO-d_6) of the mixture of $Pd_2L^{C2}{}_4$ and $Pd_3L^{C2}{}_6$ formed upon Pd(II) addition to ligand L^{C2}.

$D1 = 8.149 \pm 0.004 \cdot 10^{-11}\,m^2 \cdot s^{-1}$
$r_H1 = 13.46 \pm 0.012\,Å$

$D2 = 7.072 \pm 0.011 \cdot 10^{-11}\,m^2 \cdot s^{-1}$
$r_H2 = 15.510 \pm 0.025\,Å$
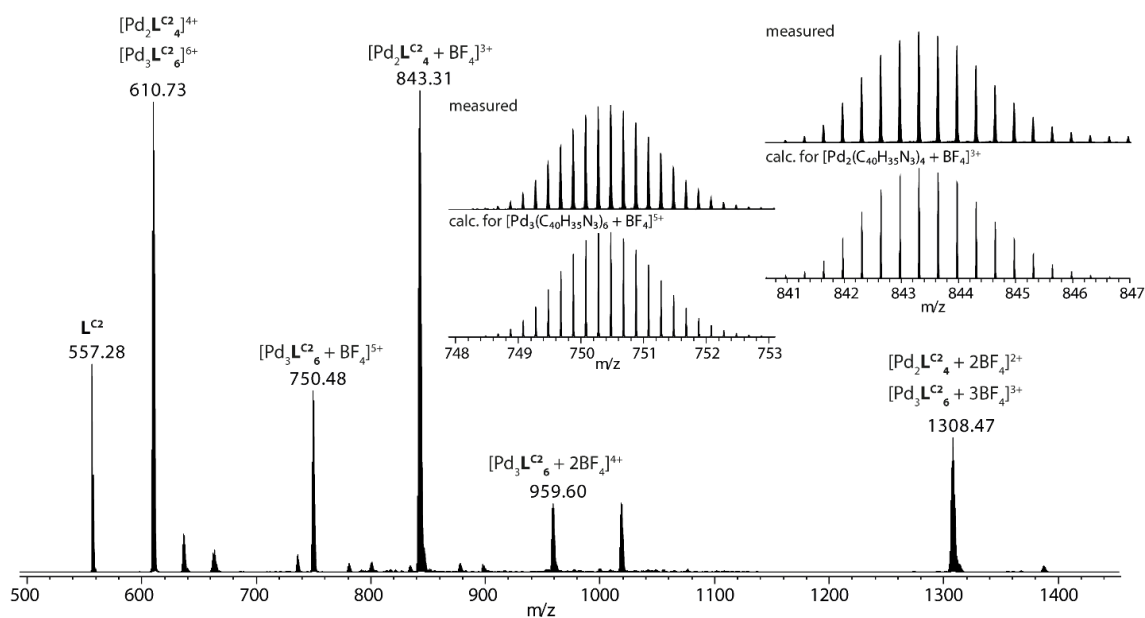
Figure 130: ESI-MS spectrum of the mixture of $Pd_2L^{C2}{}_4$ and $Pd_3L^{C2}{}_6$ formed upon Pd(II) addition (0.55 equiv.) to ligand L^{C2}. The main species detected are $[Pd_2L^{C2}{}_4 + xBF_4]^{(4-x)}$ (x = 2-4) and $[Pd_3L^{C2}{}_6 + xBF_4^-]^{(6-x)}$ (x = 3-6). The observed and calculated isotopic patterns of the main species are shown in the inset.

3.3.4.3 Synthesis and Characterization of Heteroleptic Assemblies

$\underline{Pd_2L^{IR}{}_2L^{F2}{}_2}$

A mixture of ligand L^{F2} (270 µL of a 3.11 mM solution in DMSO-d_6), ligand L^{IR} (270 µL of a 3.11 mM solution in DMSO-d_6) and [Pd(CH$_3$CN)$_4$](BF$_4$)$_2$ (60 µL of a 15 mM solution in DMSO-d_6) was left to rest at room temperature overnight to afford the heteroleptic coordination cage $Pd_2L^{F2}{}_2L^{IR}{}_2$.
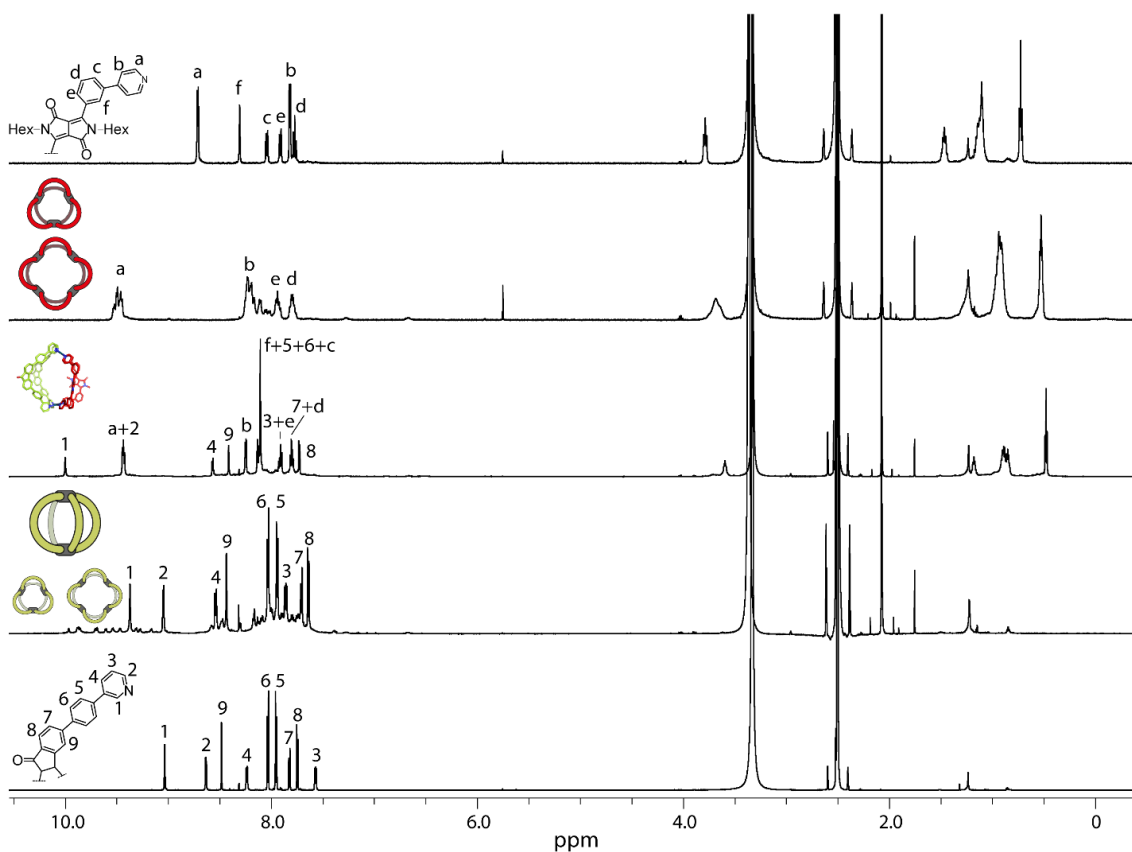
Figure 131: Full stacked ^{1}H NMR spectra of (bottom to top) ligand L^{F2} (700 MHz, 298 K, DMSO-d_6), the mixture of Pd$_n$L$^{F2}{}_{2n\ n=2-5}$ (600 MHz, 298 K, DMSO-d_6) formed upon addition of 0.55 equiv. Pd(II) to ligand L^{F2}, the heteroleptic assembly Pd$_2$L$^{F2}{}_2$L$^{IR}{}_2$ (700 MHz, 298 K, DMSO d_6), ligand L^{IR} upon addition of 0.5 equiv. Pd(II) yielding the mixture of Pd$_n$L$^{IR}{}_{2n\ n=3,4}$ (500 MHz, 298 K, DMSO-d_6) and ligand L^{IR} (500 MHz, 298 K, DMSO-d_6).
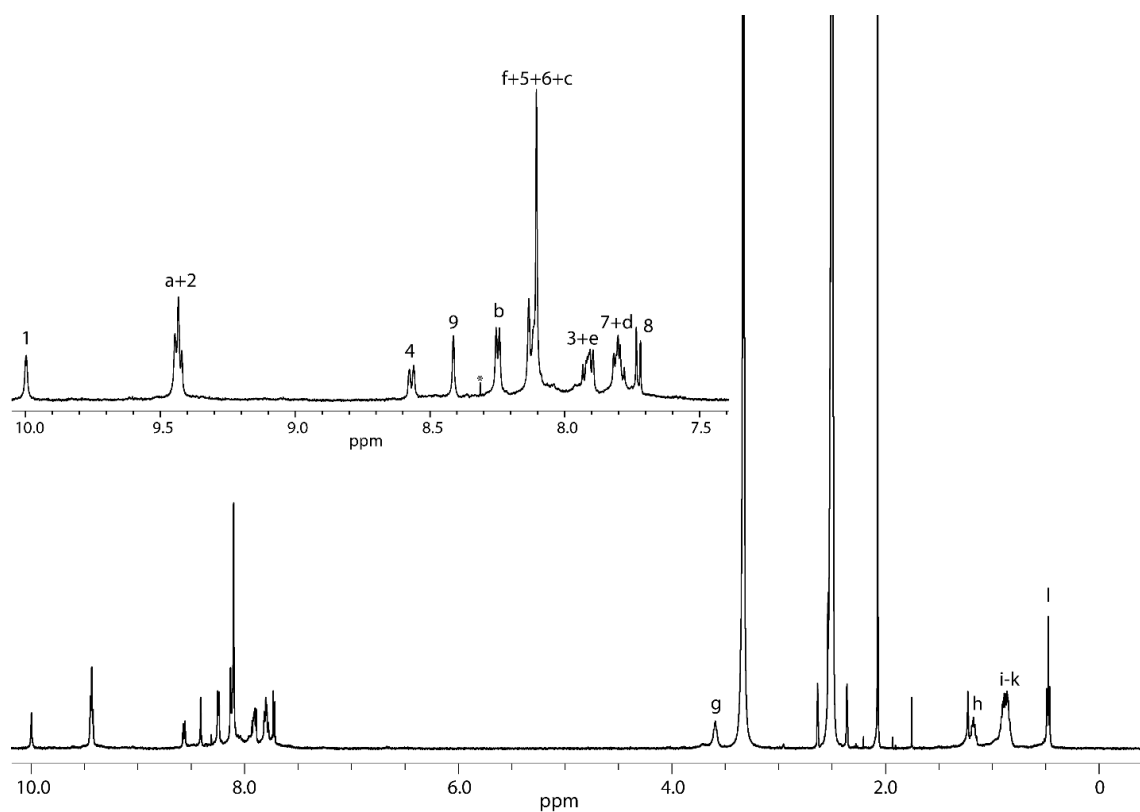
Figure 132: Full ^{1}H NMR spectrum (500 MHz, 298 K, DMSO-d_6) of Pd$_2$L$^{F2}_2$L$^{IR}_2$.

^{1}H NMR (700 MHz, 298 K, DMSO-d_6) δ 10.00 (s, 4H, H^1), 9.41-9.46 (m, 12H, H^2+H^a), 8.57 (d, ^3J = 8.15 Hz, 4H, H^4), 8.41 (s, 4H, H^9), 8.25 (d, ^3J = 6.7 Hz, 4H, H^b), 8.08-8.15 (m, 24H, H^5, H^6, H^c + H^f), 7.89-7.93 (m, 8H, H^3 + H^e), 7.77-7.83 (m, 8H, H7 + H^d), 7.73 (d, ^3J = 7.65 Hz, 4H, H^8), 3.59 (t, ^3J = 7.25 Hz 8H, H^g), 1.14-1.21 (m, 8 H, H^h), 0.81-0.94 (m, 24H, H^{i-k}), 0.48 (t, ^3J = 7.25 Hz, 12H, H^l) ppm.
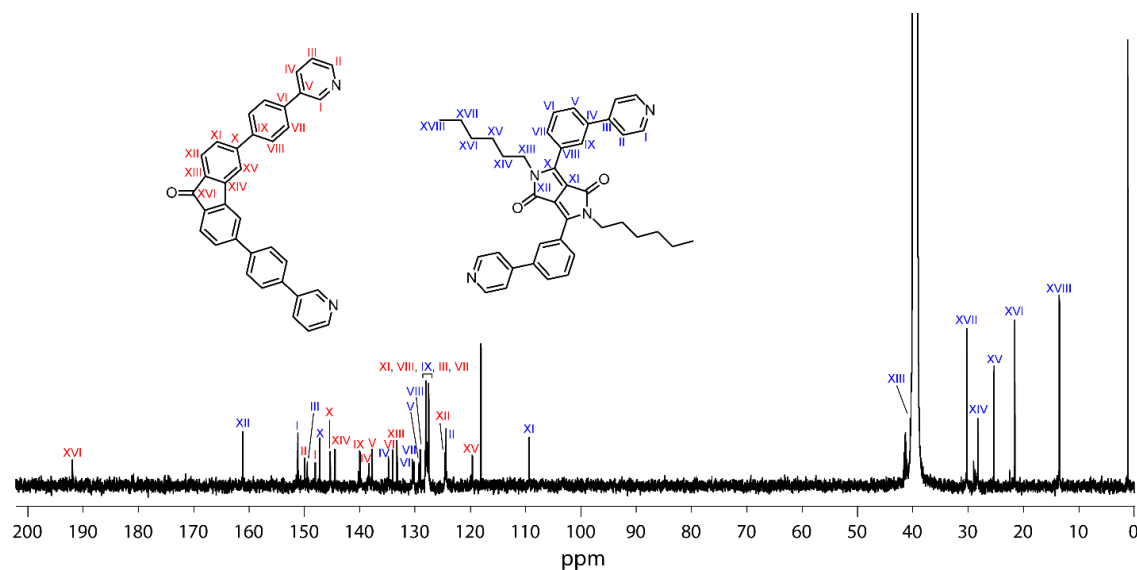
Figure 133: ^{13}C NMR spectrum (176 MHz, 298 K, DMSO-d_6) of Pd$_2$**L$^{F2}_2$L^{IR}**$_2$ (lb = 2.5 Hz).

^{13}C NMR (176 MHz, 298 K, DMSO-d_6): δ 191.94 (C_{XVIb}), 161.09 (C_{XIIa}), 151.15 (C_{Ia}), 149.93 (C_{IIb}), 149.44 (C_{IIIa}), 148.01 (C_{Ib}), 147.20 (C_{Xa}), 145.32 (C_{Xb}), 144.45 (C_{XIVb}), 139.96 (C_{IXb}), 138.30 (C_{IVb}), 137.74 (C_{Vb}), 134.78 (C_{IVa}), 134.01 (C_{VIb}), 133.24 (C_{XIIIb}), 130.47 (C_{VIa}), 130.18 (C_{VIIa}), 129.25 (C_{Va}), 129.05 (C_{VIIIa}), 128.13 (C_{XIb}), 128.00 (C_{VIIIb}), 127.81 (C_{IXa}), 127.68 (C_{IIIb}), 127.51 (C_{VIIb}), 124.59 (C_{XIIb}), 124.37 (C_{IIa}), 119.61 (C_{XVb}), 109.38 (C_{XIa}), 40.15 (C_{XIIIa}), 30.22 (C_{XVIIa}), 28.22 (C_{XIVa}), 25.29 (C_{XVa}), 21.55 (C_{XVIa}), 13.49 (C_{XVIIIa}) ppm.
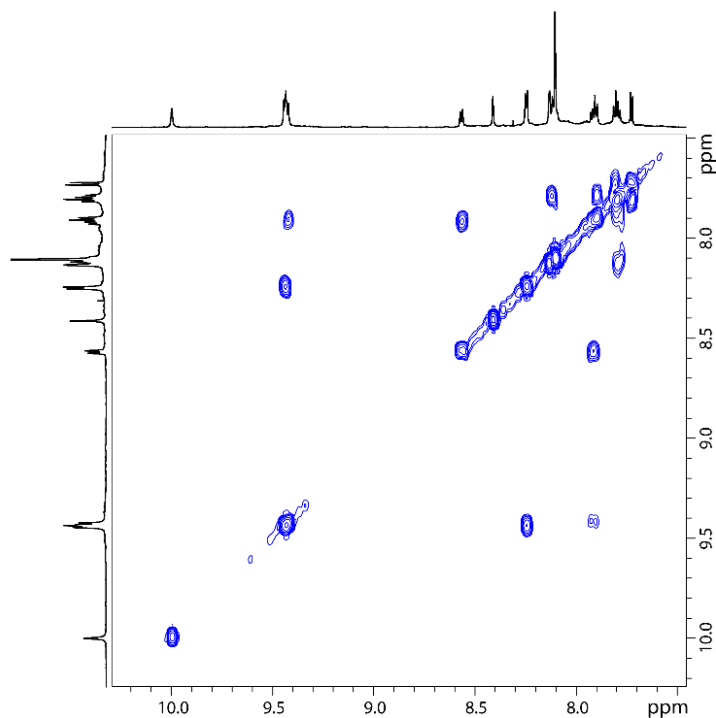
Figure 134: Partial ^{1}H-^{1}H COSY NMR spectrum (700 MHz, 298K, DMSO-d_6) of Pd$_2$**L**$^{F2}_2$**L**$^{IR}_2$.
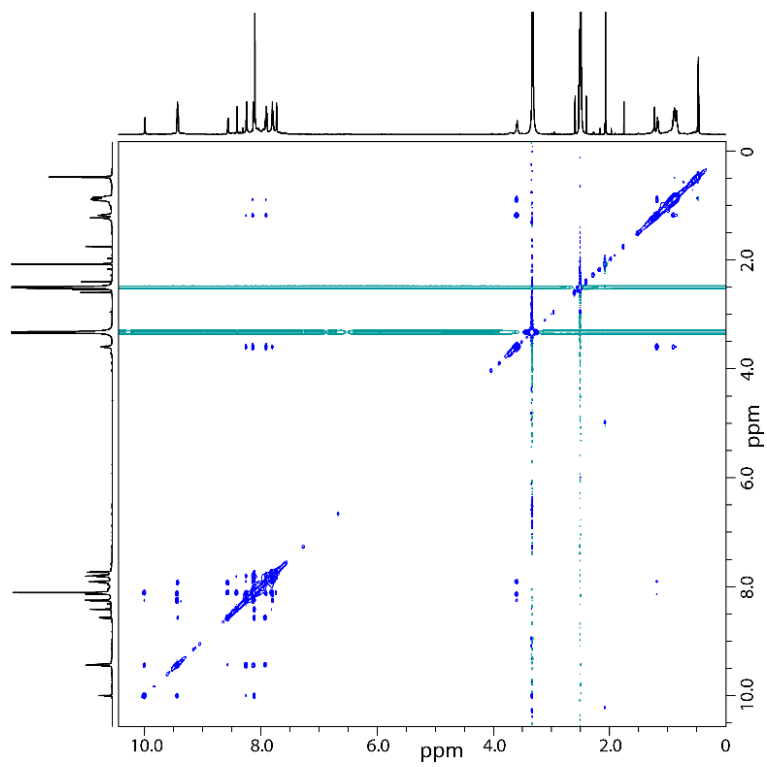
Figure 135: Full ^{1}H-^{1}H NOESY NMR spectrum (700 MHz, 298K, DMSO-d_6) of Pd$_2$**L^{F2}**$_2$**L^{IR}**$_2$.
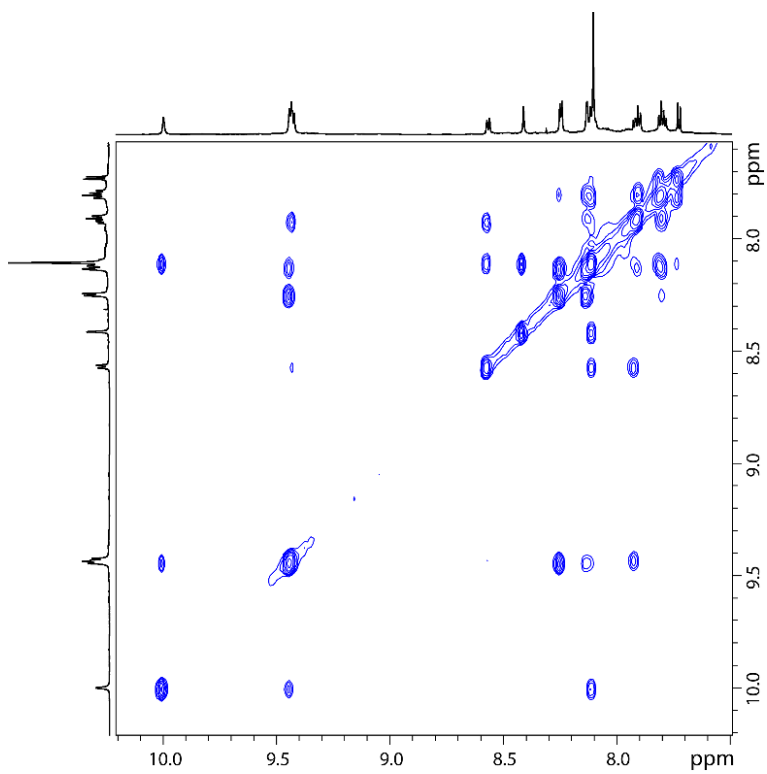
Figure 136: Partial ^{1}H-^{1}H NOESY NMR spectrum (700 MHz, 298K, DMSO-d_6) of Pd$_2$**L^{F2}**$_2$**L^{IR}**$_2$.

$$D = 9.024 \pm 0.004 \cdot 10^{-11} \, m^2 \cdot s^{-1}$$
$$r_H = 12.155 \pm 0.005 \, \text{Å}$$
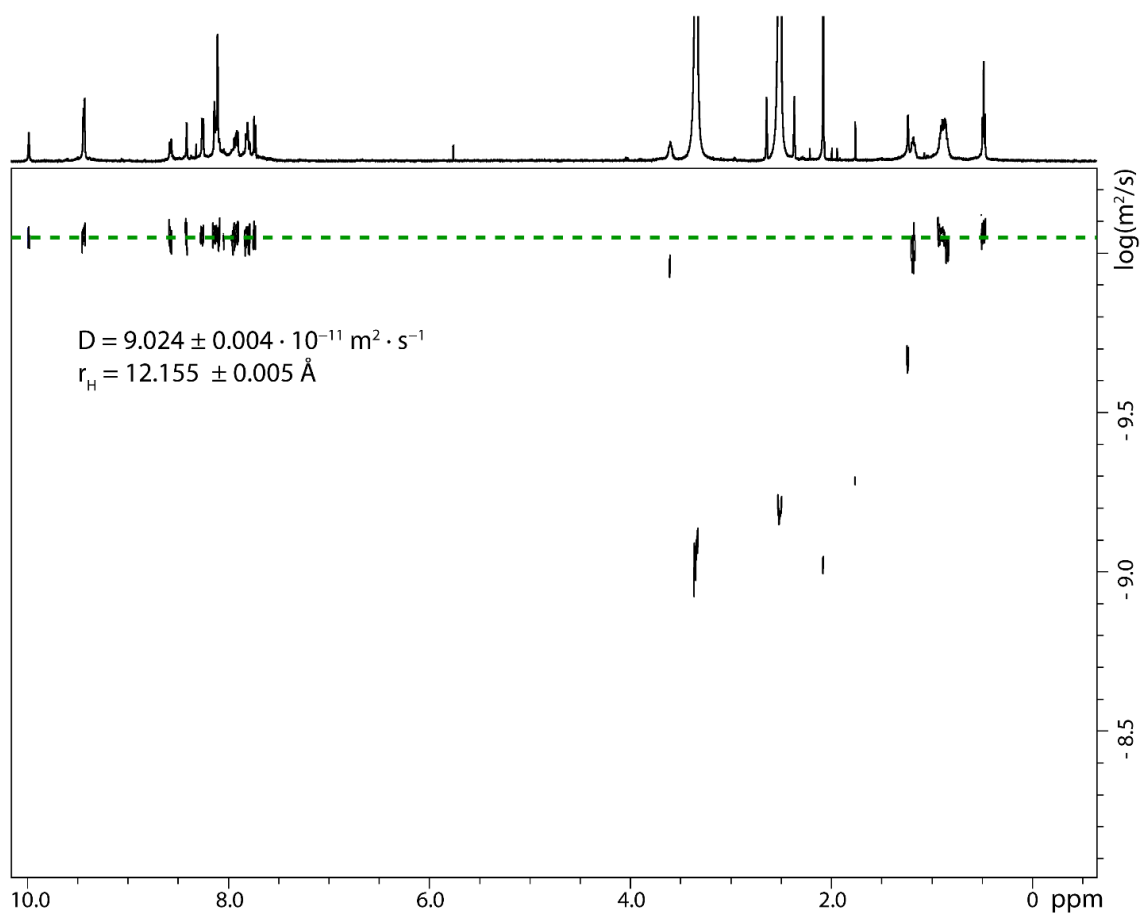
Figure 137: ^{1}H DOSY NMR spectrum (500 MHz, 298K, DMSO-d_6) of Pd$_2$L$^{F2}_2$L$^{IR}_2$.
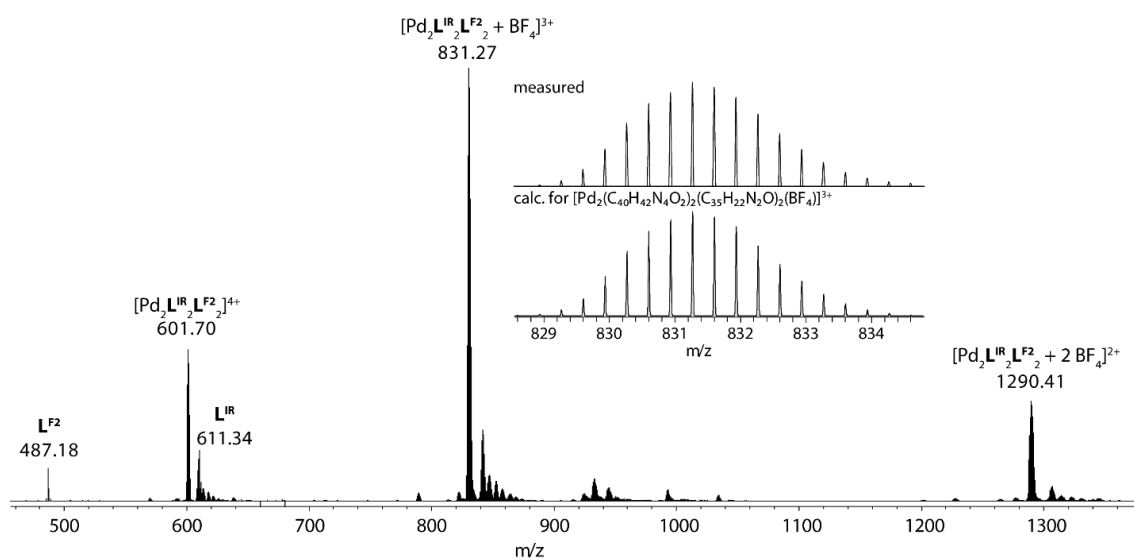
Figure 138: ESI-MS spectrum of [Pd$_2$L$^{F2}_2$L$^{IR}_2$ + xBF$_4$]$^{(4-x)+}$ (x = 0-2). The observed and calculated isotopic patterns are shown in the inset.

143
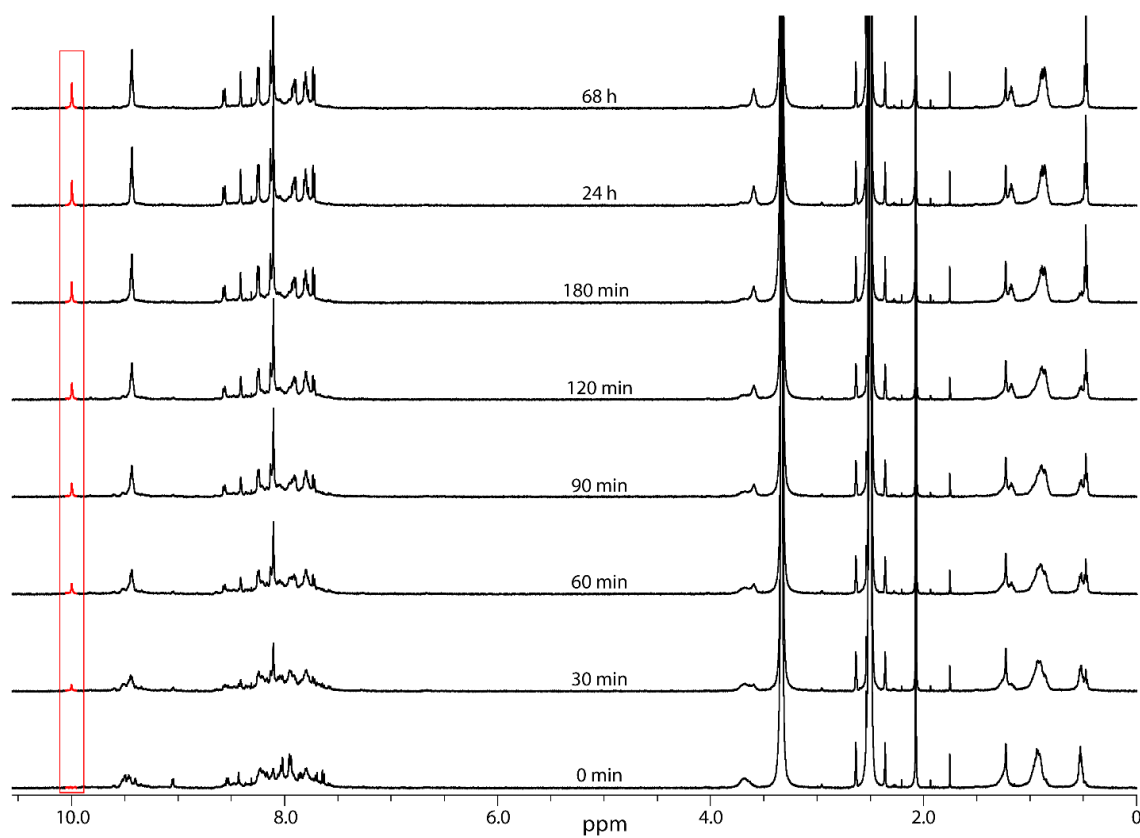
Figure 139: Selected full ^{1}H NMR Spectra (500 MHz, 298 K, DMSO-d_6) of the cage-to-cage transformation from a 1:1 mixture of Pd$_n$L$^{F2}_{2n}$ $_{n=2-5}$ and the mixture of Pd$_n$L$^{IR}_{2n}$ $_{n=3,4}$ to clean Pd$_2$L$^{F2}_2$L$^{IR}_2$. Transformation kinetics were evaluated at 298 K using well defined signal 1 (marked in red). The transformation was monitored over the course of three days.

Pd$_2$L$^{IR}_2$L$^{C2}_2$

A mixture of ligand **L^{C2}** (270 µL of a 3.11 mM solution in DMSO-d_6), ligand **L^{IR}** (270 µL of a 3.11 mM solution in DMSO-d_6) and [Pd(CH$_3$CN)$_4$](BF$_4$)$_2$ (60 µL of a 15 mM solution in DMSO-d_6) was heated for 30 minutes to afford the heteroleptic coordination cage Pd$_2$**L$^{C2}_2$L$^{IR}_2$**.
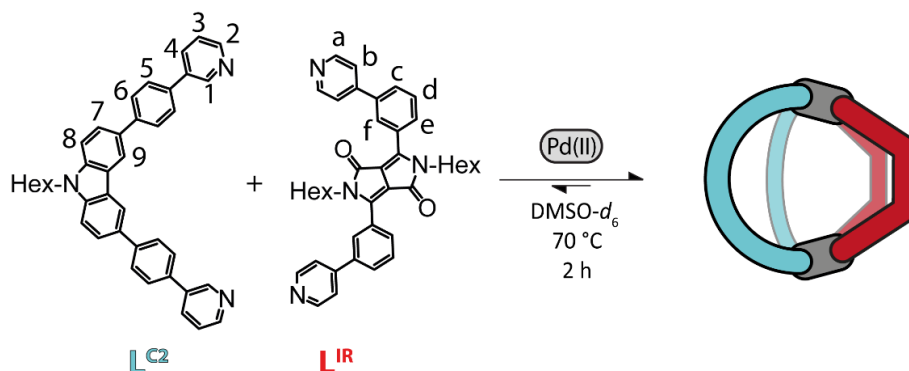
Scheme 14: Formation of Pd$_2$**L$^{C2}_2$L$^{IR}_2$** with consecutive proton labels.
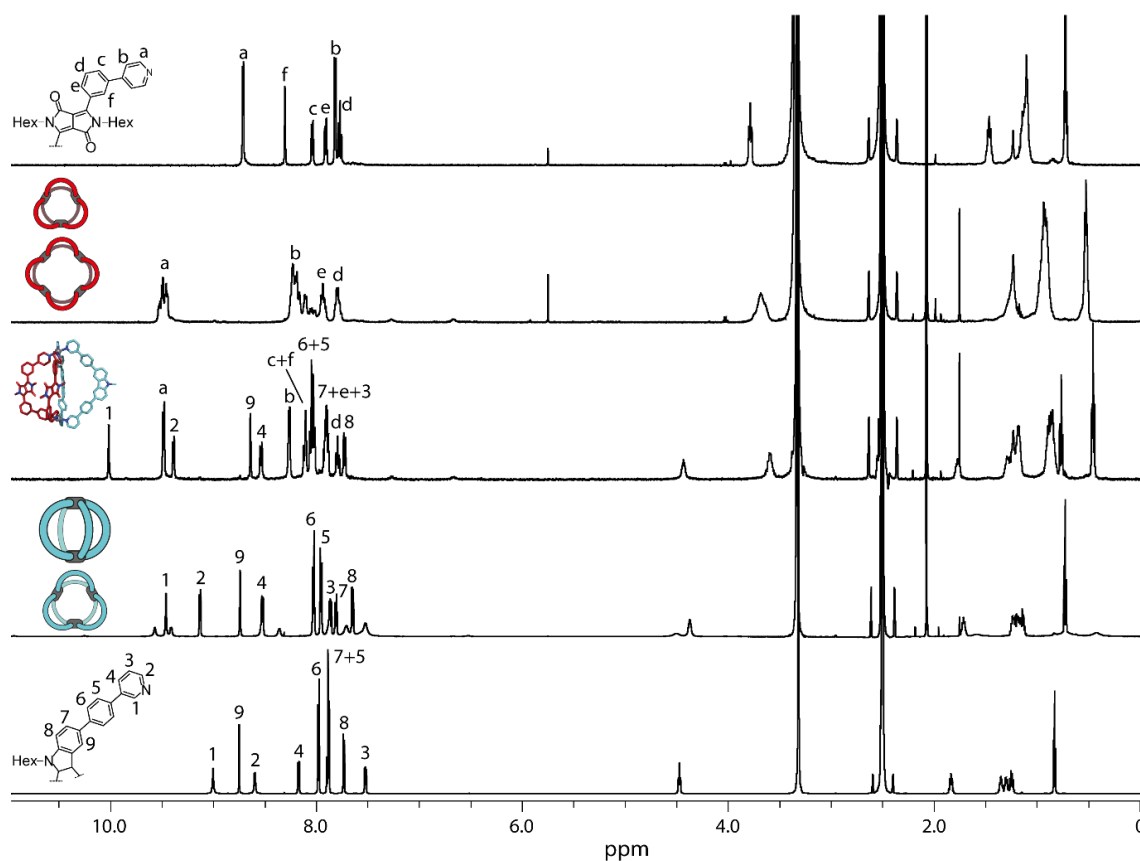
Figure 140: Full stacked ^{1}H NMR spectra of (bottom to top) ligand **L^{C2}** (700 MHz, 298 K, DMSO-d_6), the mixture of Pd$_2$**L$^{C2}_4$** and Pd$_3$**L$^{C2}_6$** (600 MHz, 298 K, DMSO-d_6) formed upon addition of 0.55 equiv. Pd(II) to ligand **L^{C2}**, the heteroleptic assembly Pd$_2$**L$^{C2}_2$L$^{IR}_2$** (600 MHz, 298 K, DMSO-d_6), ligand **L^{IR}** upon addition of 0.5 equiv. Pd(II) yielding the mixture of Pd$_3$**L$^{IR}_6$** and Pd$_4$**L$^{IR}_8$** (500 MHz, 298 K, DMSO-d_6) and ligand **L^{IR}** (500 MHz, 298 K, DMSO-d_6).
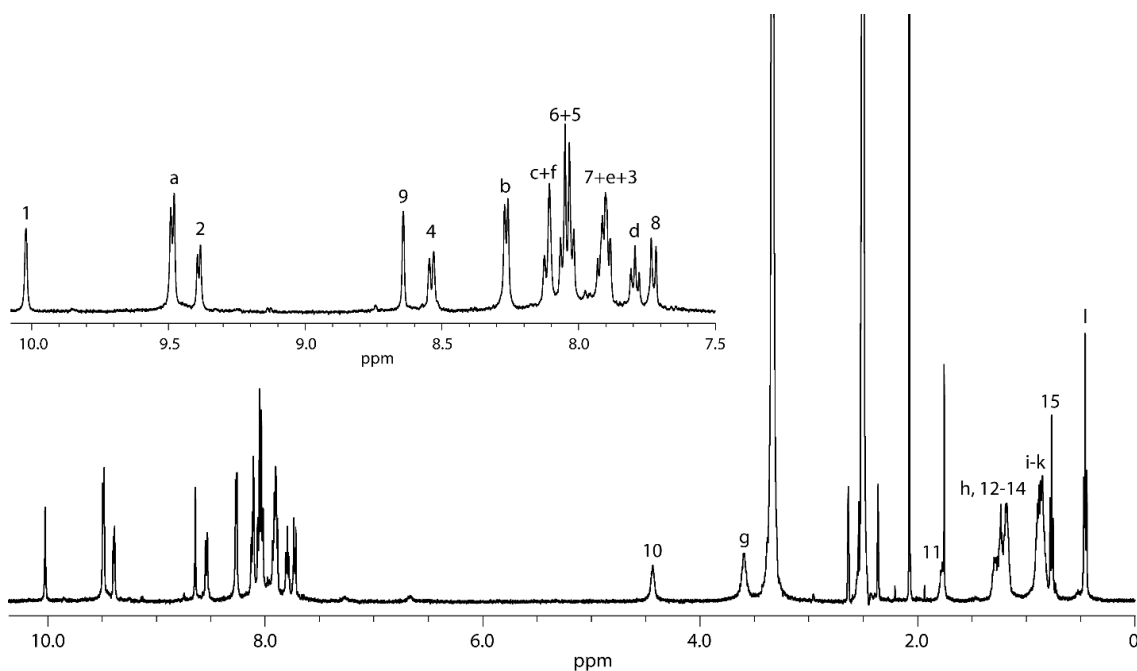
Figure 141: Full ^{1}H NMR spectrum (600 MHz, 298 K, DMSO-d_6) of Pd$_2$**L^{C2}**$_2$**L^{IR}**$_2$.

^{1}H NMR (600 MHz, 298 K, DMSO-d_6) δ 10.01 (s, 4H, H^1), 9.48 (d, ^3J = 6.4 Hz, 8H, H^a), 9.39 (d, ^3J = 5.5 Hz, 4H, H^2), 8.64 (d, ^4J = 1.05 Hz, 4H, H^9), 8.54 (d, ^3J = 8.1 Hz, 4H, H^4), 8.27 (d, ^3J = 6.6 Hz, 8H, H^b), 8.14-8.09 (m, 8H, H^c + H^f), 8.06 (d, ^3J = 8.5 Hz, 8H, H^6), 8.02 (d, ^3J = 8.5 Hz, 8H, H^5), 7.94-7.87 (m, 12H, H3, H^7, H^e), 7.80 (t, ^3J = 7.7 Hz, 4H, H^d), 7.73 (d, ^3J = 8.7 Hz, 4H, H^8), 4.43 (s, 4H, H^{10}), 3.59 (m, 8H, H^9), 1.81-1.73 (m, 4H, H^{11}), 1.33-1.13 (m, 20H, Hh + H$^{12-14}$), 0.93-0.79 (m, 24H,H^{i-k}), 0.77 (t, ^3J = 7.2 Hz, 6H, H^{15}), 0.46 (t, ^3J = 7.2 Hz, 12H, H^l) ppm.
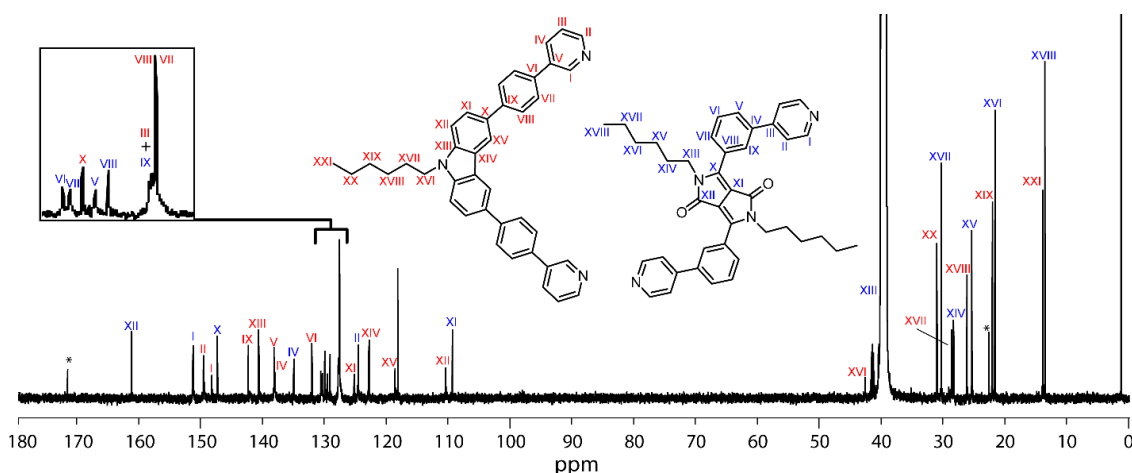
Figure 142: Full ^{13}C NMR spectrum (151 MHz, 298 K, DMSO-d_6) of Pd$_2$**L^{C2}**$_2$**L^{IR}**$_2$.

^{13}C NMR (151 MHz, 298 K, DMSO-d_6): δ 161.08 (C$_{XIIa}$), 151.16 (C$_{Ia}$), 149.42 (C$_{IIb}$), 148.13 (C$_{Ib}$), 147.22 (C$_{Xa}$), 142.21 (C$_{IXb}$), 140.54 (C$_{XIIIb}$), 138.08 (C$_{Vb}$), 137.91 (C$_{IVb}$), 134.87 (C$_{IVa}$), 131.95 (C$_{VIb}$), 130.51 (C$_{VIa}$), 130.26 (C$_{VIIa}$), 129.87 (C$_{Xb}$), 129.43 (C$_{Va}$), 129.02

(C_{VIIIa}), 127.68 (C_{IXa}), 127.60 (C_{Vb}), 127.54 (C_{IIIb}), 127.50 (C_{VIIIb}), 127.48 (C_{VIIb}), 125.10 (C_{XIb}), 124.47 (C_{IIa}), 122.72 (C_{XIVb}), 118.52 (C_{XVb}), 110.34 (C_{XIIb}), 109.24 (C_{XIa}), 42.52 (C_{XVIb}), 40.31 (C_{XIIIa}), 30.93 (C_{XIXb}), 30.23 (C_{XVIIa}), 28.53 (C_{XVIIb}), 28.24 (C_{XIVa}), 26.07 (C_{XVIIIb}), 25.30 (C_{XVa}), 21.97 (C_{XXb}), 21.56 (C_{XVIa}), 13.81 (C_{XXIb}), 13.49 (C_{XVIIIa}) ppm.
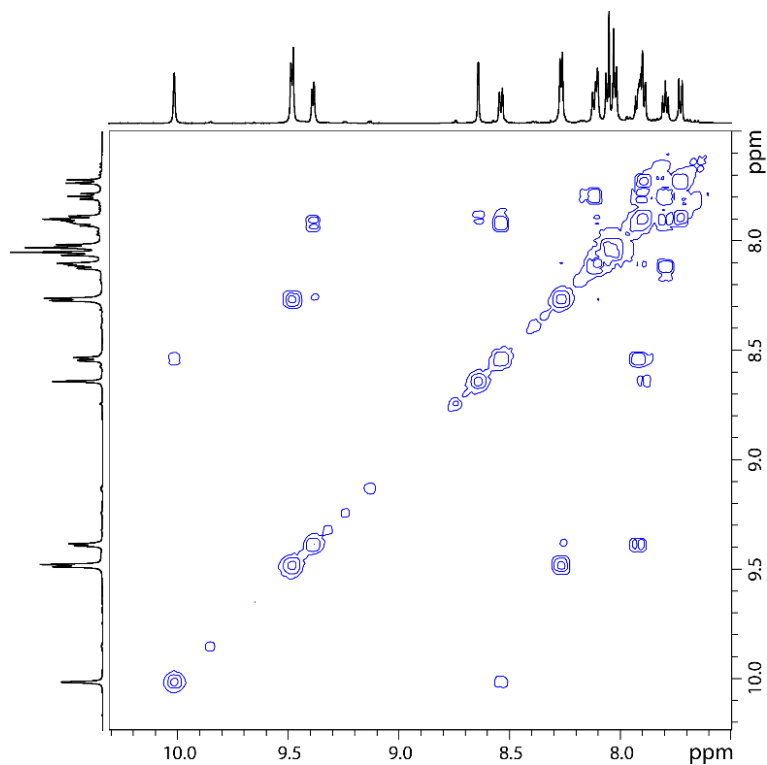
Figure 143: Partial ^{1}H-^{1}H COSY NMR spectrum (600 MHz, 298K, DMSO-d_6) of $Pd_2\mathbf{L^{C2}}_2\mathbf{L^{IR}}_2$.
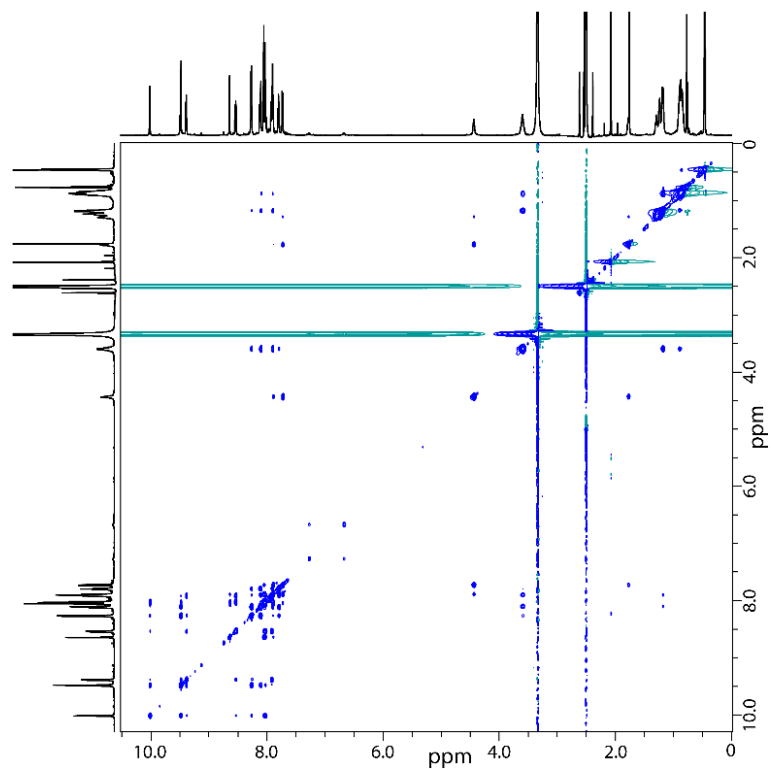
Figure 144: Full ^{1}H-^{1}H NOESY NMR spectrum (600 MHz, 298K, DMSO-d_6) of Pd$_2$**L^{C2}**$_2$**L^{IR}**$_2$.
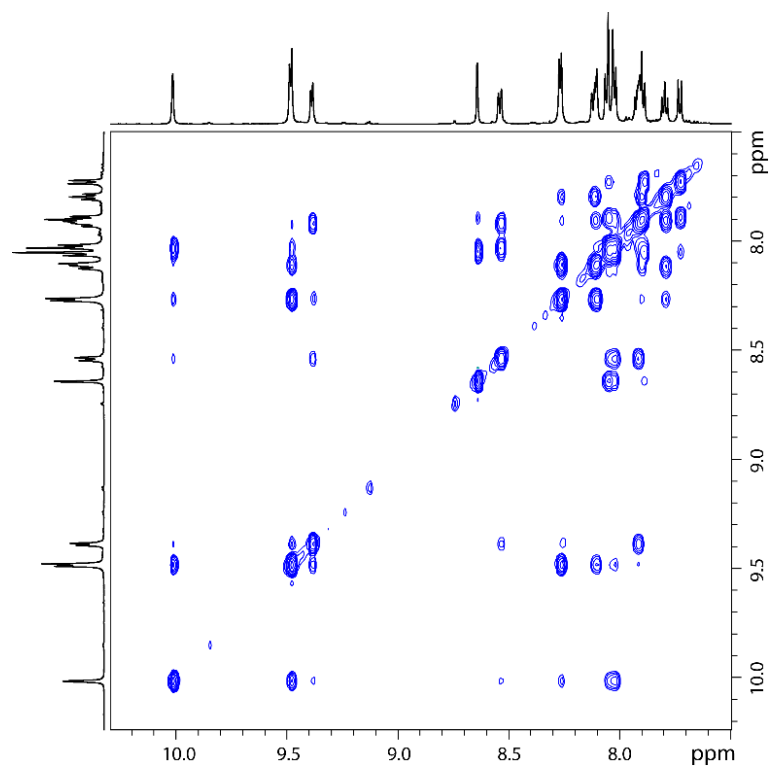
Figure 145: Partial ^{1}H-^{1}H NOESY NMR spectrum (600 MHz, 298K, DMSO-d_6) of Pd$_2$**L^{C2}**$_2$**L^{IR}**$_2$.
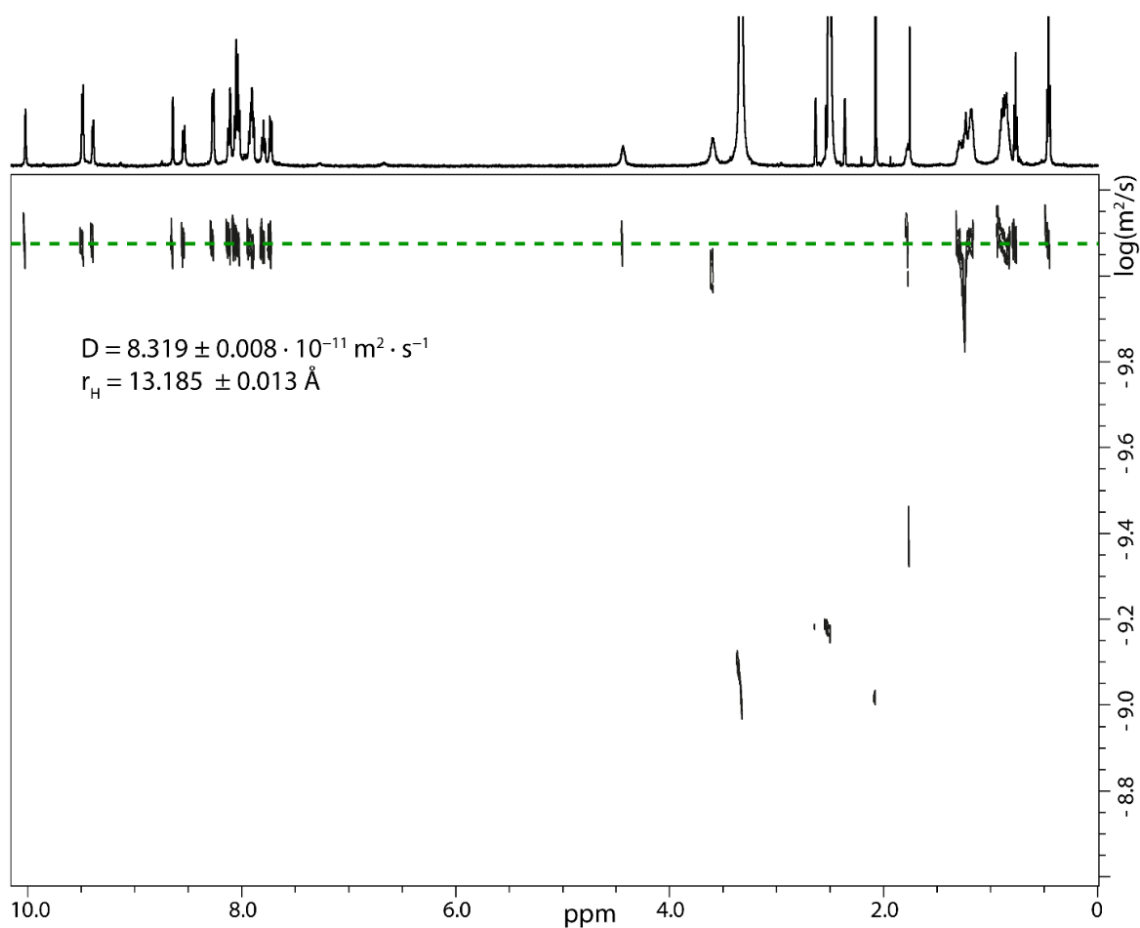
Figure 146: ^{1}H DOSY NMR spectrum (500 MHz, 298K, DMSO-d_6) of Pd$_2$**L**$^{C2}_2$**L**$^{IR}_2$.

$D = 8.319 \pm 0.008 \cdot 10^{-11}$ m$^2 \cdot$ s^{-1}
$r_H = 13.185 \pm 0.013$ Å
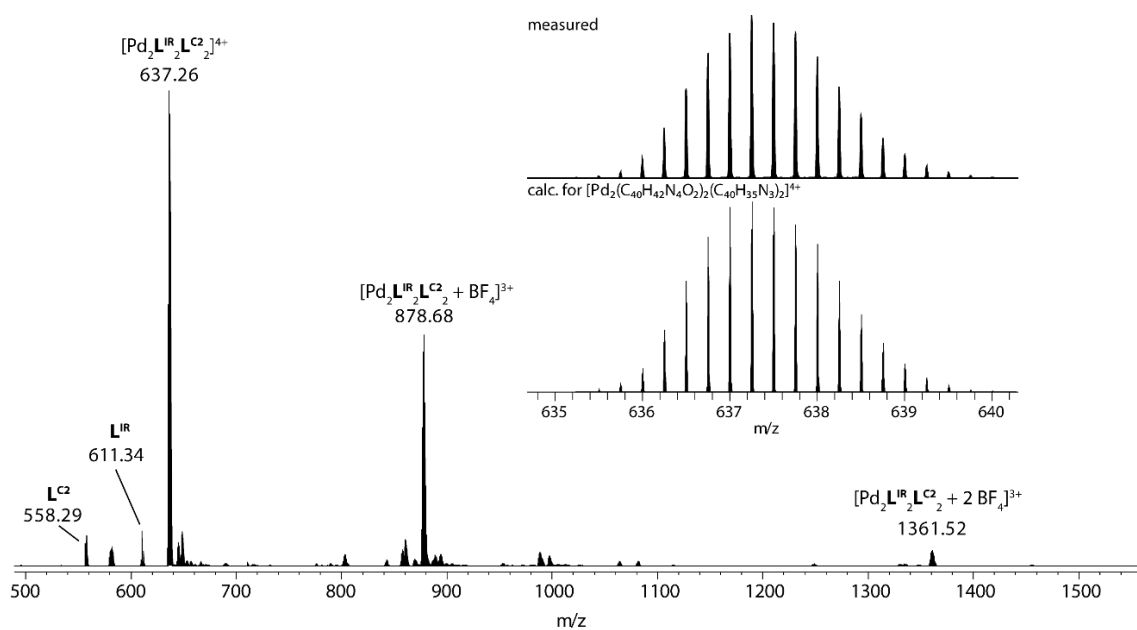
Figure 147: ESI-MS spectrum of [Pd$_2$**L**$^{C2}_2$**L**$^{IR}_2$ + xBF$_4$]$^{(4-x)+}$ (x = 0-2). The observed and calculated isotopic patterns are shown in the inset.

3.3.4.4 Host-Guest Chemistry with Dipotassium (*R*)-1,1'-Binaphthyl-2,2'-disulfonate (**G**)

Figure 148: ESI-MS spectrum of $[Pd_3\mathbf{L^{IR}}_6+xBF_4]^{(6-x)+}$ with x=1-3 and $[Pd_4\mathbf{L^{IR}}_8+xBF_4]^{(8-x)+}$ with x=2-4 after the addition of 1 equiv. of **G** to $Pd_n\mathbf{L^{IR}}_{2n\ n=3,4}$. The observed and calculated isotopic pattern of $[\mathbf{G}@Pd_3\mathbf{L^{IR}}_6]^{4+}$ is shown in the inset.

Figure 149: ESI-MS spectrum of the mixture of $\mathbf{G}@Pd_2\mathbf{L^{F2}}_4$ and $\mathbf{G}@Pd_3\mathbf{L^{F2}}_6$ formed upon addition of 1 equiv. of **G** to the mixture of $Pd_n\mathbf{L^{F2}}_{2n\ n=2-5}$. The observed and calculated isotopic patterns of $[\mathbf{G}@Pd_2\mathbf{L^{F2}}_4]^{2+}$ and $[\mathbf{G}@Pd_3\mathbf{L^{F2}}_6]^{4+}$ are shown in the inset.

Figure 150: ESI-MS spectrum of the mixture of **G**@Pd$_2$**L^{C2}**$_4$ and **G**@Pd$_3$**L^{C2}**$_6$ formed upon addition of 1 equiv. of **G** to the mixture of Pd$_n$**L^{C2}**$_{2n}$ $_{n=2,3}$. The observed and calculated isotopic patterns of [**G**@Pd$_3$**L^{C2}**$_6$]$^{4+}$ are shown in the inset.
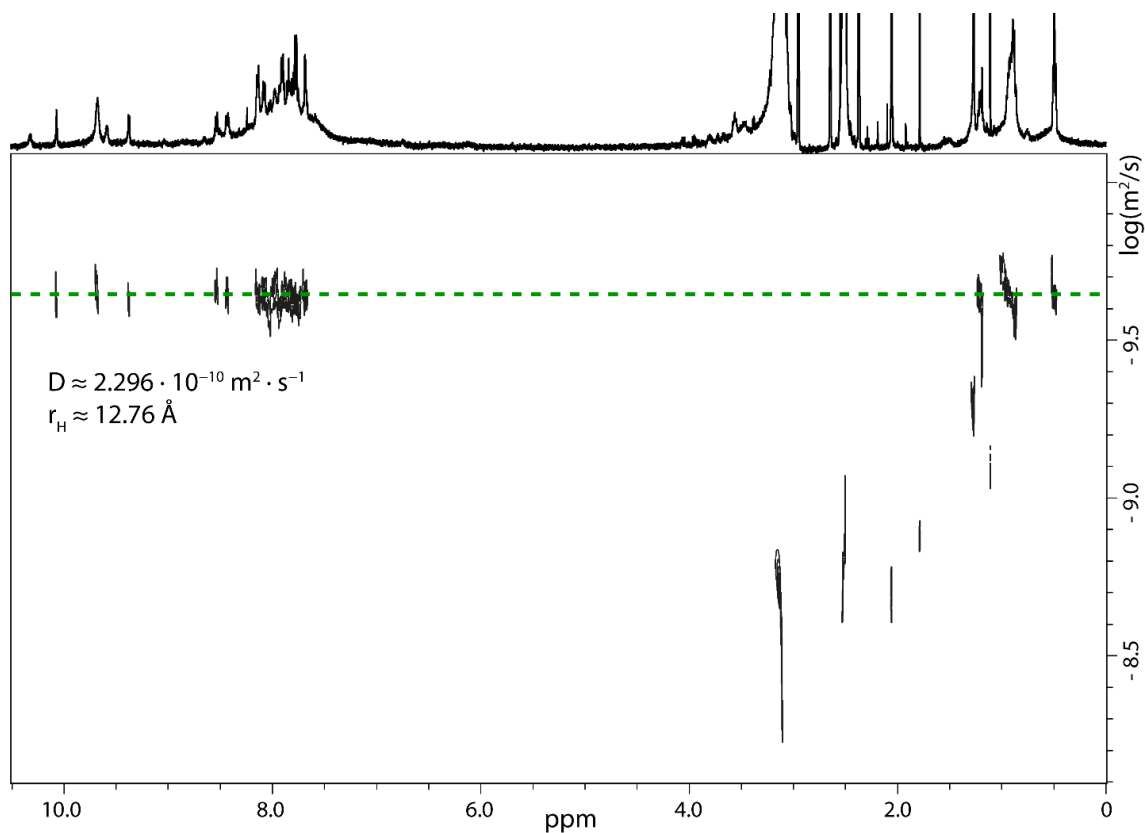
Figure 151: High temperature ^{1}H DOSY NMR spectrum (500 MHz, 348K, DMSO-d_6) of Pd$_2$**L^{F2}**$_2$**L^{IR}**$_2$ with 1 equiv. of **G**.
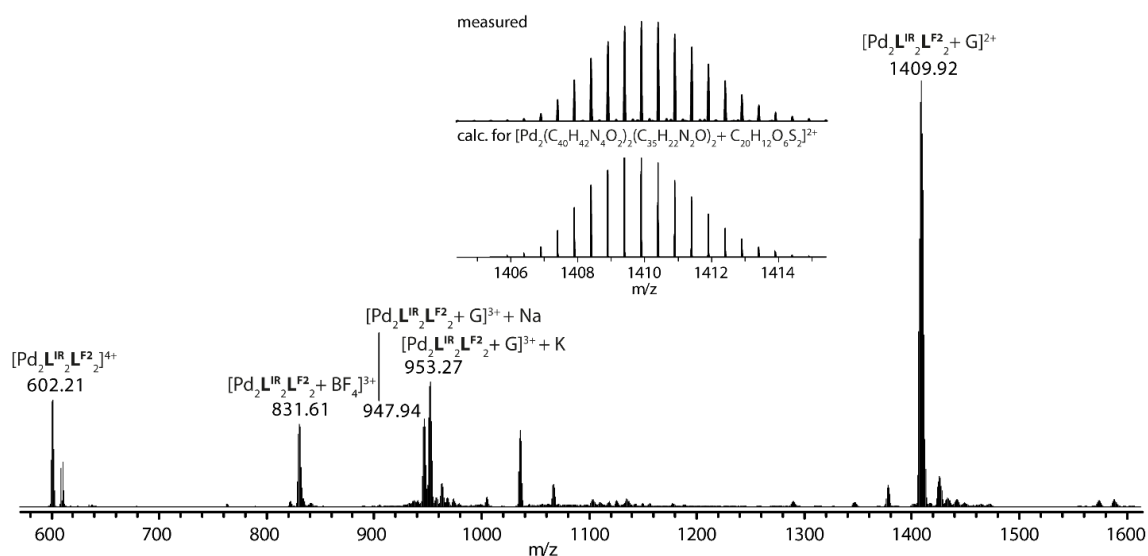
Figure 152: ESI-MS spectrum of $[Pd_2\mathbf{L^{F2}}_2\mathbf{L^{IR}}_2 + xBF_4]^{(4-x)+}$ + 1 equiv. of **G**. The observed and calculated isotopic pattern of $[G@Pd_2\mathbf{L^{IR}}_2\mathbf{L^{F2}}_2]^{2+}$ are shown in the inset.
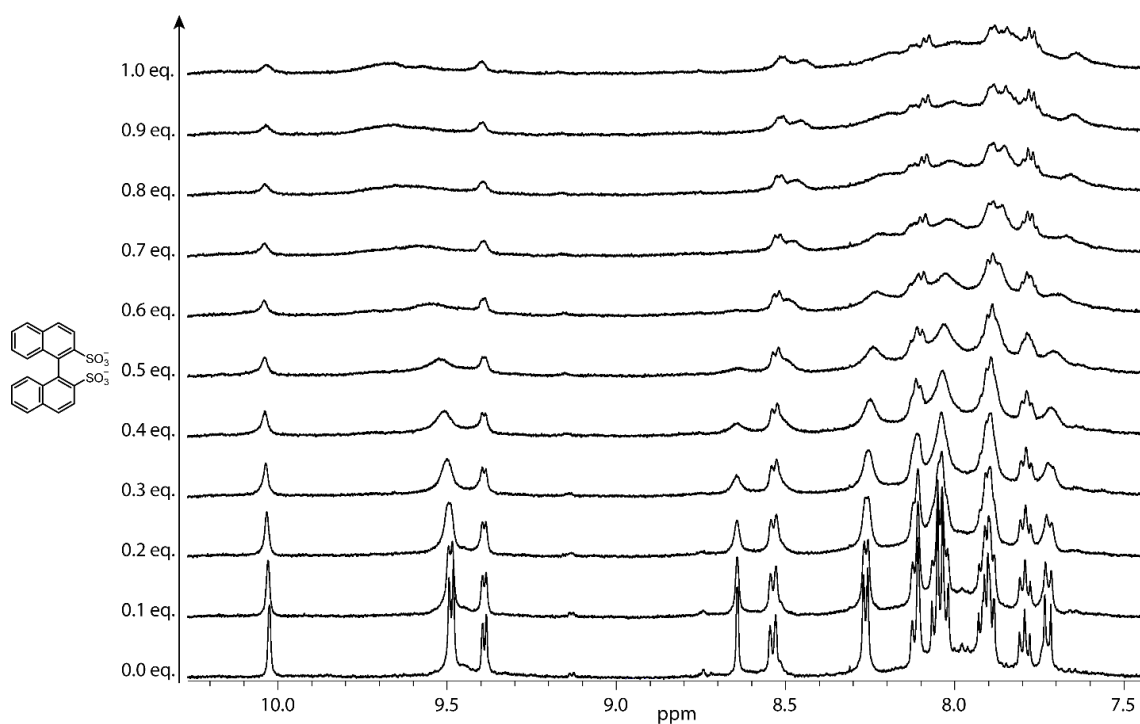
Figure 153: ^{1}H NMR titration (500 MHz, 298K, DMSO-d_6) of $Pd_2\mathbf{L^{C2}}_2\mathbf{L^{IR}}_2$ with **G** (15 mM in DMSO-d_6).
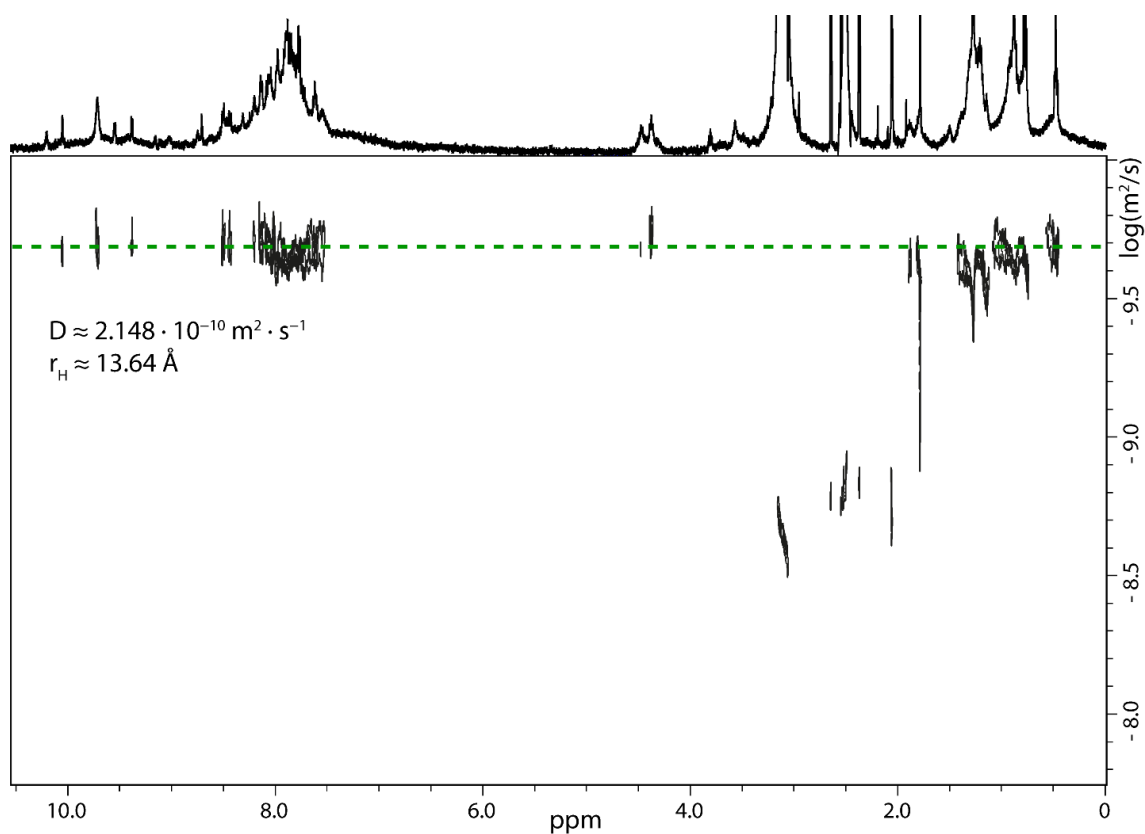
Figure 154: High temperature ^{1}H DOSY NMR spectrum (500 MHz, 348K, DMSO-d_6) of Pd$_2$L$^{C2}_2$L$^{IR}_2$ with 1 equiv. of **G**.
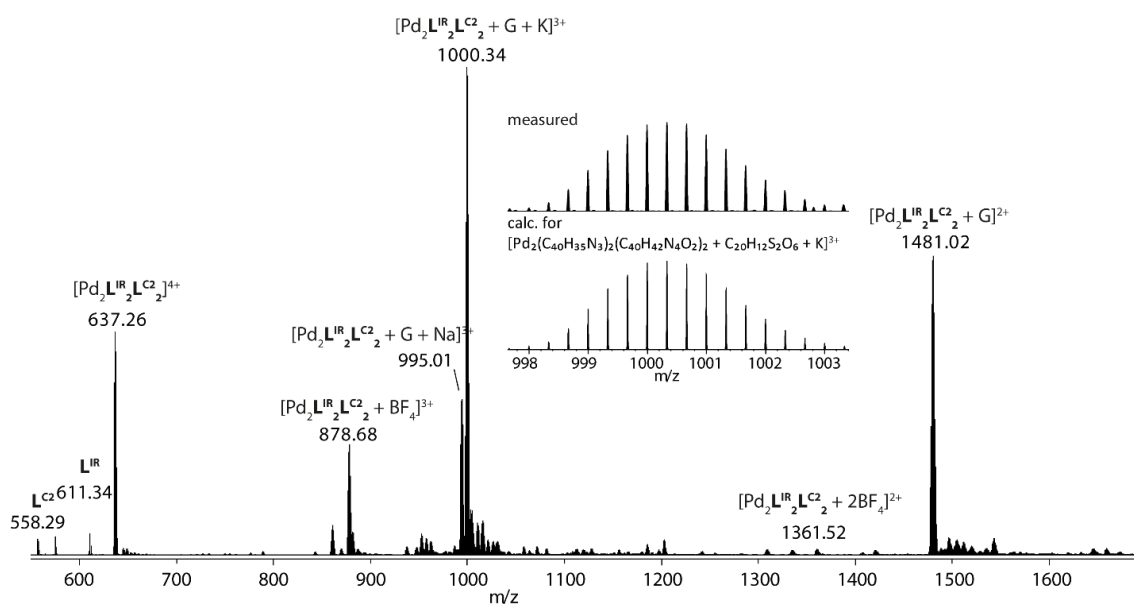
Figure 155: ESI-MS spectrum of [Pd$_2$L$^{C2}_2$L$^{IR}_2$ + xBF$_4$]$^{(4-x)+}$ + 1 equiv. of **G**. The observed and calculated isotopic pattern of [G@Pd$_2$L$^{IR}_2$L$^{C2}_2$]$^{2+}$ are shown in the inset.
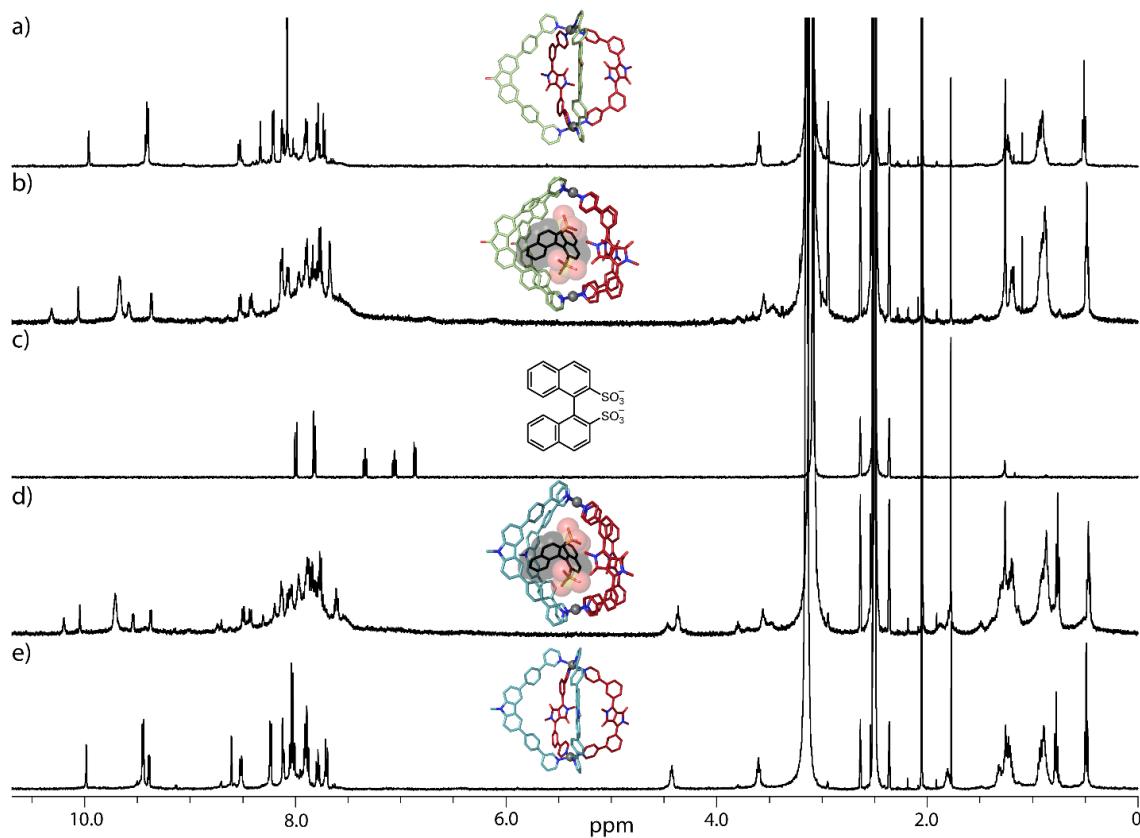
Figure 156: Stacked ^{1}H NMR spectra (500 MHz, 348 K, DMSO-d_6) of a) Pd$_2$**L**$^{F2}_2$**L**$^{IR}_2$, b) Pd$_2$**L**$^{F2}_2$**L**$^{IR}_2$ with 1 equiv. of **G**, c) **G**, d) Pd$_2$**L**$^{C2}_2$**L**$^{IR}_2$ with 1 equiv. of **G** and e) Pd$_2$**L**$^{C2}_2$**L**$^{IR}_2$. For proton-assignment see Figure 105.

3.3.4.5 Optical Properties
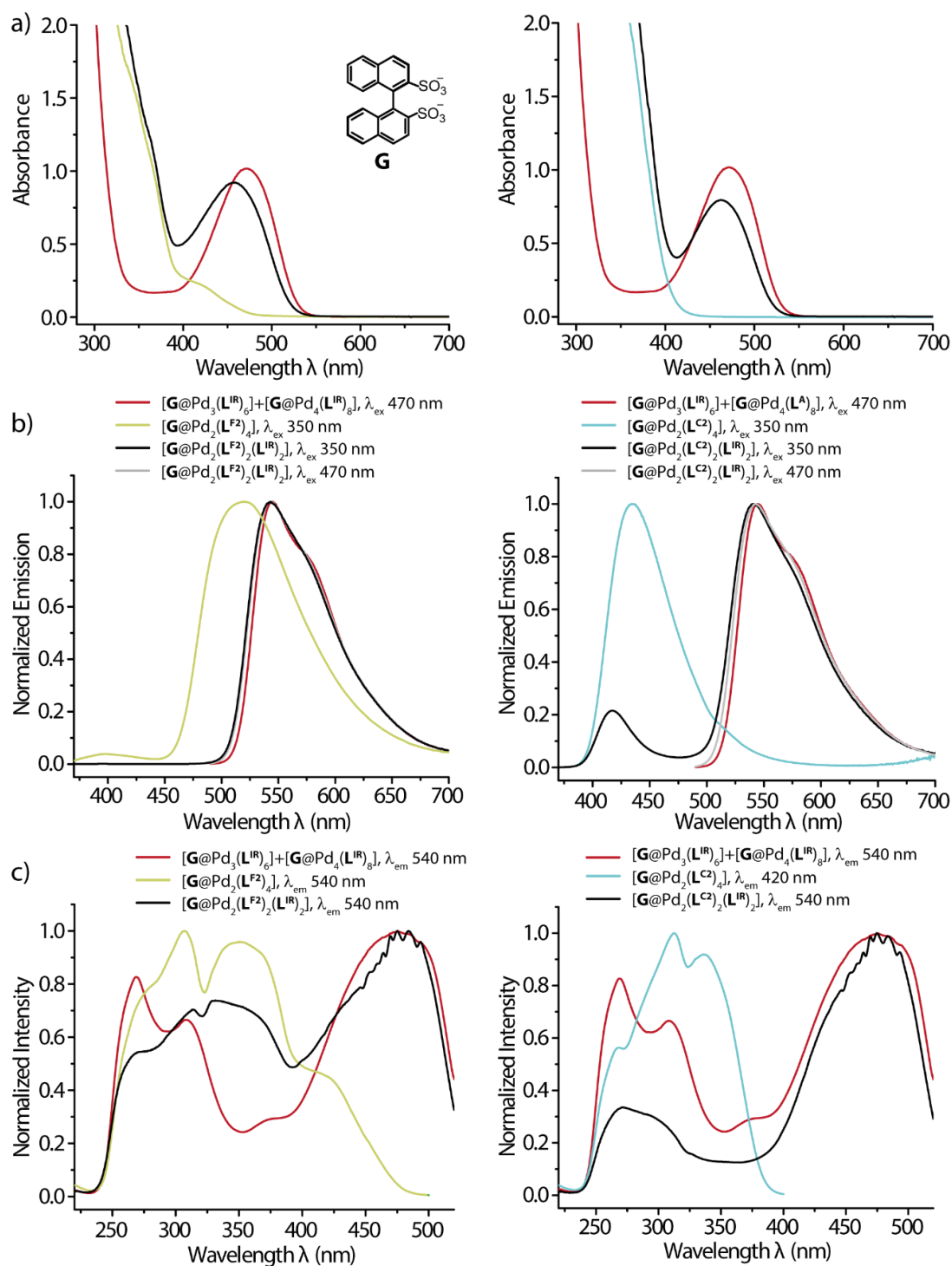
Figure 157: a) UV-Vis absorption spectra b) normalized emission spectra and c) excitation spectra in DMSO at 25 °C of host-guest complexes developed in this work. Solutions 0.35 mM in chromophore concentration for the assemblies and 0.18 mM of guest **G**.
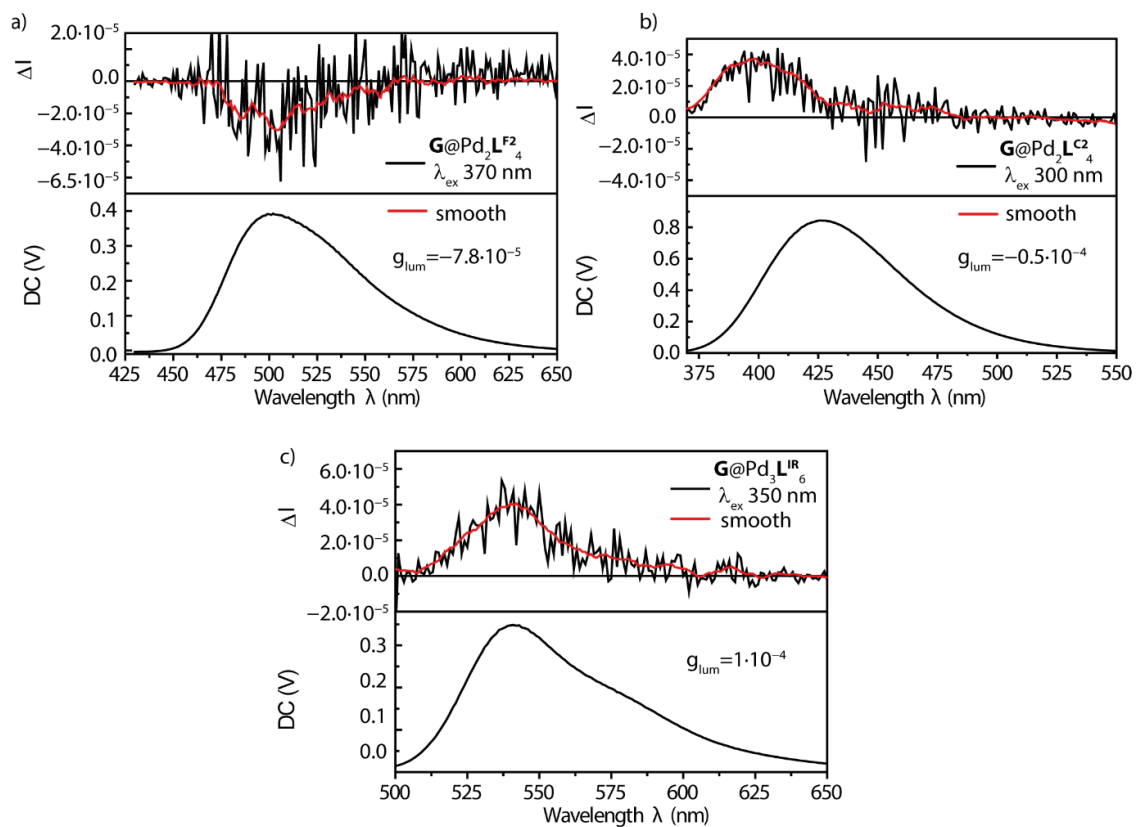
Figure 158: CPL spectra as stacking of emission and 2ΔI (DMSO at 25 °C) of homoleptic host-guest complexes a) [**G**@Pd$_n$**L^{F2}**$_{2n}$; n=2-4] (0.7 mM), b) [**G**@Pd$_n$**L^{C2}**$_{2n}$; n=2,3] (0.35 mM) and c) [**G**@Pd$_n$**L^{IR}**$_{2n}$; n=3,4] (0.7 mM); smoothed ΔI spectra added for clarity (red lines); λ$_{exc}$ and g$_{lum}$ values are given in the inset.

3.4 Unique Fluorescent Open Structures - UFOS

3.4.1 Introduction: Heteroleptic Pd(II)-based $Pd_nL^A_xL^B_y$ coordination cages with n > 2

Where heteroleptic Pd(II)-based coordination cages of the $Pd_2L^A_2L^B_2$ type are commonly found in literature with a wide range of properties and applications, heteroleptic $Pd(II)_n$ assemblies with n > 2 are scarce since clean nuclearity control is increasingly difficult in higher ordered assemblies. The careful balance between entropic and enthalpic gain and penalty is essential and oftentimes solvent and counter anion effects play a major role (e.g. in the homoleptic assemblies of aforementioned L^{P1})[57], thus yielding mixtures in one medium and clean assemblies in another.
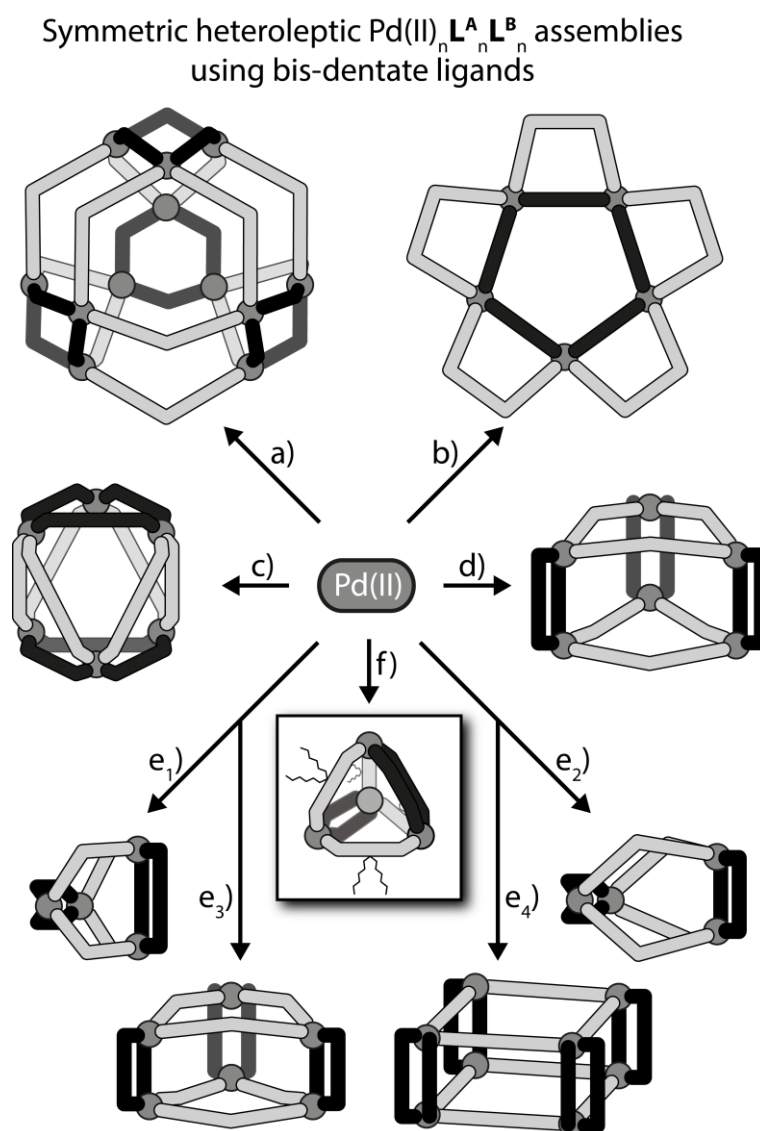
Figure 159: Heteroleptic coordination assemblies with $Pd_nL^A_nL^B_n$ composition.[51,87–89,157,158]

While binuclear Pd(II) assemblies are far more commonly described in literature, as described in chapter 3.3, there are examples of heteroleptic assemblies of higher nuclearity as summarized in Figure 159.

In 2014, FUJITA and coworkers showed the distinct formation of a cantellated (and pseudocantellated) $Pd_{12}L^A_{12}L^B_{12}$ tetrahedron from two ligands with the same phenyl-based backbone but different linker lengths (Figure 159, a))[87]. While previous studies showed, that both ligands form homoleptic $Pd_{12}L_{24}$ cuboctahedral spheres, *when* combined with $Pd(NO_3)_2$ separately[159], a 1:1:1 combination led to the formation of one distinct, heteroleptic species. A star-shaped, pentanuclear $Pd_5L^A_5L^B_5$ complex has been reported by CHAND and coworkers[157] from a non-chelating bidentate 1,4-phenylenebis-(methylene) diisonicotinate ligand and a rigid 4,4′-bipyridine ligand forming a singular, flat structure (Figure 159, b)). It is noted, that this example is the only heteroleptic assembly with a 1:1:1 component ratio that has an odd-numbered nuclearity. $Pd_6L^A_6L^B_6$ assemblies have been reported by MUKHERJEE and coworkers (Figure 159, d)[158] and Severin and coworkers (Figure 159, c)[88] and e_3)[89]. Both groups used small rigid ligands carrying meta-substituted pyridines as dative bond donors on one side, and ones equipped with para-substituted pyridines to enforce entropic penalty on the system on the other. Severin and coworkers could furthermore show the clean formation of two $Pd_4L^A_4L^B_4$ assemblies and a $Pd_8L^A_8L^B_8$ structure based on the same approach in 2022 (Figure 159, e1), e2) and e4))[89]. While the short, meta-pyridine functionalized ligand L^A was consistent within all four structures, the slight alteration of the bite angle of the second, para-pyridine-donned ligand led to changes in assembly nuclearity with a bite angle of α = 120° yielding tetranuclear complexes, α = 149° resulting in the formation of the aforementioned hexanuclear $Pd_6L^A_6L^B_6$ complex and α = 180° leading to the self-assembly of an octanuclear box shaped structure. Elongation of the para-pyridine functionalized donor-ligands and thus size increase of the final structure was possible in case of the tetranuclear assembly, not however for the octanuclear one, where elongation of the α = 180° ligand led to the formation of a mixture of $Pd_6L^A_6L^B_6$ and $Pd_8L^A_8L^B_8$. The elongation in the latter case was done by introducing alkyne linkers, which does lead to an increase in ligand flexibility (as described in chapter 3.2) thus enabling the system to adapt to smaller structures. The last example of a heteroleptic $Pd_nL^A_nL^B_n$ coordination cage with n > 2 has been shown by CLEVER and coworkers being a heteroleptic $Pd_4L^A_4L^B_4$ tetrahedron (Figure 159, f))[51]. While ligand L^A is based upon a fluorenone-backbone equipped with meta-pyridine donor groups, ligand L^B sports a sterically demanding 9,9-dihexyl-9H-fluorene backbone while carrying the same meta-pyridine donors. Both ligands are rigid and while L^A forms a mixture of $Pd_3L^A_6$, $Pd_4L^A_8$

and minor $Pd_6L^A_{12}$, L^B forms a clean octahedral structure $Pd_6L^B_{12}$ due to its high steric demand. The 1:1 combination of both ligands however, led to a compromise between entropy, driving the formation of the smallest possible assembly, and an enthalpic penalty derived from steric hinderance. The result is the aforementioned $Pd_4L^A_4L^B_4$ tetrahedron where the double-bridged sides are occupied by L^A and the single-bridged ones by sterically demanding L^B.

It is notable, that all of the herein reported examples show a *cis* ligand arrangement in the heteroleptic assemblies and sport at least one very rigid ligand.

Symmetric heteroleptic $Pd_nL^A_nL^B_n$ assemblies with odd-numbered nuclearity, especially with n = 3, however, have, to the best of my knowledge, not yet been described in literature. While n = 3 is commonly found in homoleptic assemblies, it is rarely found in heteroleptic structures, though a few examples are given in Figure 160.
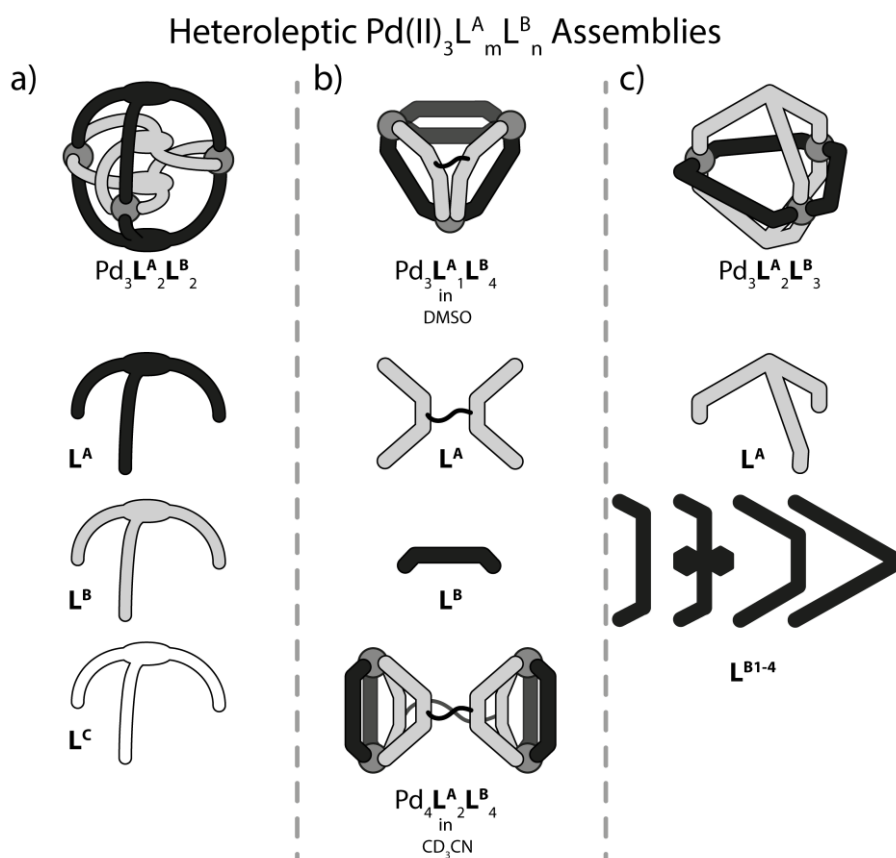
Figure 160: Heterolpetic trinuclear $Pd_3L^A_mL^B_n$ assemblies.[63,160,161]

JUNG and coworkers described the formation of a heteroleptic four-layered trinuclear Pd(II) assembly in 2016 using flexible tris-dentate ligands and a two-step complex formation approach (Figure 160, a))[160]. The first step consisted of the combination of K_2PdCl_4 and L^B forming an intertwined stacked dimer in a plane with three Pd(II) atoms which each still having two Cl^- ligands attached. Successive use of $Ag(NO_3)_2$ led to

precipitation of AgCl and vacant coordination sites at the palladium being occupied by two molecules of L^A coordinating as tripod-ligands from top and below, yielding *trans*-coordinated $Pd_3L^A_2L^B_2$. Depending on the stoichiometry, additional complexes of the same type can be formed using the ligands L^A, L^B and L^C, namely $Pd_3L^A_3L^B$, $Pd_3L^AL^B_2L^C$ and $Pd_3L^B_2L^C_2$. CLEVER and coworkers presented, among other things, a $Pd_3L^AL^B_4$ system based on a flexible linked tetradentate ligand L^A and a rigid ligand L^B (Figure 160, b)[63] in 2021. The system forms due to the backbone-bridging of L^A and prevalent entropic penalty and it has a high susceptibility to solvent changes, thus forming only in DMSO, while the same ligand combination forms $Pd_4L^A_2L^B_4$ assemblies in CD_3CN. While ligand L^A coordinates to one out of three Pd(II) centers of the trinuclear assembly in a *cis*-conformation, it is debatable if this wording can apply since, strictly speaking, it is the exact same ligand occupying two coordination sites at the same Pd(II) atom. Furthermore, the other two Pd(II) centers are coordinated by three L^B and only one donor site of L^A. Finally, PRESTON and coworkers presented the formation of a total of four heteroleptic cages formed by a tripod ligand L^A, based on triphenyl-adamantane, and four different bis-dentate ligands L^{B1-4}, each having a bite angle of 60°, forming *trans*-coordinated $Pd_3L^A_2L^{B1-4}_3$ upon Pd(II) addition (Figure 160, c))[161].

It is particular, that opposed to the symmetric $Pd_nL^A_nL^B_n$ assemblies described before (Figure 159), where the Pd(II):L^A:L^B ratio is 1:1:1 and the ligands are, without exception, coordinated to Pd(II) in *cis*-conformation, the shown trinuclear assemblies have their ligands coordinating to Pd(II) in *trans*-conformation, dictated by the structure of utilized tripod ligands. To the best of my knowledge, no $Pd_nL^A_nL^B_n$ assembly with $n = 3$ using exclusively bis-monodentate ligands has been reported in the literature yet.

As evident from almost all of these examples, the incorporation of at least one ligand carrying meta-substituted pyridines as dative bond donors is essential for the formation of heteroleptic coordination assemblies of higher nuclearity. This chapter will follow this strategy, using small, rigid, para-pyridine functionalized ligands with simple backbones and the previously described ligand L^{F2}, which is very prone to form heteroleptic coordination assemblies due to its overall rigidity and structure (see chapter 3.3).

3.4.2 Novel $Pd(II)_nL^A_nL^B_n$ Assemblies with $n = 3$ or 4

While the presented literature does show a few trinuclear Pd(II)-based heteroleptic coordination cages[63,160,161], the exact stoichiometry of 1:1:1 (Pd(II):L^A:L^B) has, to the best of my knowledge, not yet been shown and is therefore unprecedented. The following chapter analyzes five Pd(II)-based coordination cages of the $Pd_3L^A_3L^B_3$ type, giving

structural insight and highlighting different functions incorporated into the system. Furthermore, an analysis of the boundaries of this system is carried out whereby the effect of electrostatic repulsive groups, steric bulk and an increase in donor angle are analyzed.
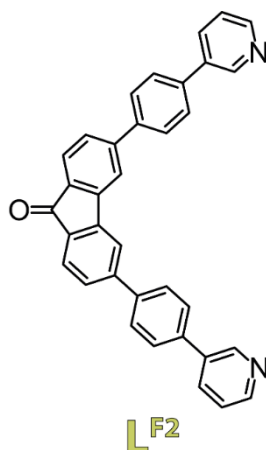
Scheme 15: Structure of ligand L^{F2}.
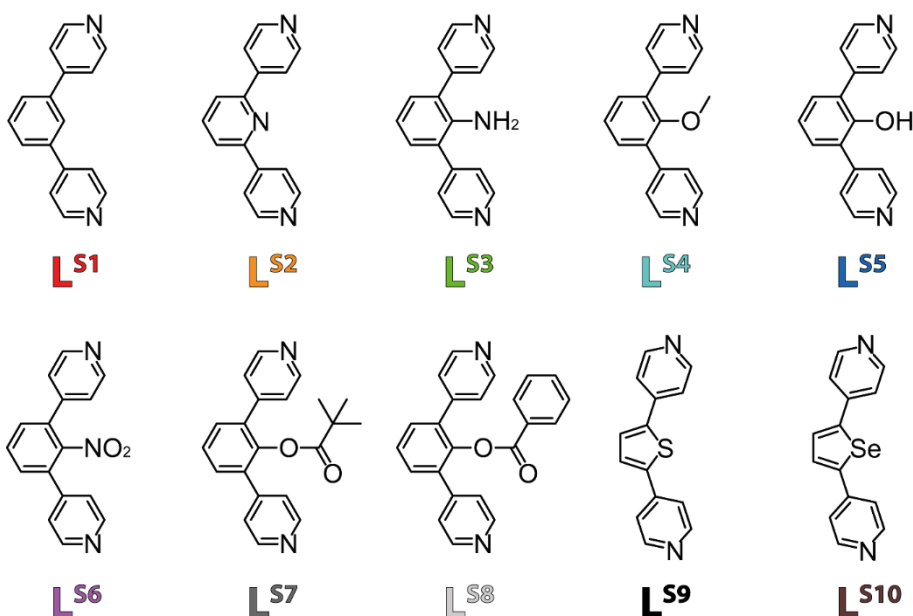
Scheme 16: Structure of ligands L^{S1-10}.

The fundamental system consists of the previously reported L^{F2} ligand (Scheme 15), a fluorenone-based ligand in which the meta-pyridine donor group is connected to the backbone by a rigid phenyl-linker. Ligand L^{F2} has been shown to form mixtures of $Pd_n L^{F2}{}_{2n}$ homoleptic assemblies upon Pd(II) addition in the previous chapter. The utilized counter ligands (L^{S1-5}, Scheme 16, first row) are short ligands based upon a phenyl-backbone or phenyl derivatives equipped with para-pyridine donor groups of which some (L^{S1} and L^{S2}) have been reported to form large spheres or truncated structures of higher nuclearity upon Pd(II) coordination before[162,163].

Thus, both homoleptic species formed by the utilized ligands are thermodynamically disfavored, which is highly desired in heteroleptic coordination cage formation. Furthermore, the rigidity of each of these ligands does not allow any adaptivity by for example bending of alkynes as described before (chapter 3.2) and the systems have to adapt to the least strained, yet entropically favored structure.

Combined in a 1:1 manner with 0.55 equiv. tetrakis(acetonitrile)Pd(II)triflate ($[Pd(CH_3CN)_4](OTf)_2$), the clean formation of $Pd_3L^{F2}_3L^{S1-5}_3$ could be observed. All five systems will be analyzed meticulously in this chapter.

Additionally, a structural analysis of these coordination systems was carried out as to analyze the systematics and limits of $Pd_3L^A_3L^B_3$ formation. Ligands L^{S6-10} (Scheme 16, second row) were synthesized, characterized and combined with L^{F2} and Pd(II) cations in a 1:1:1 manner. While ligands L^{S6-8} still sport a phenyl-derivative backbone, L^{S9} and L^{S10} were prepared with five membered heterocyclic backbones and are based on thiophene (L^{S9}) and selenophene (L^{S10}), respectively. All short ligands (L^{S1-10}) are equipped with para-pyridine donor groups and were prepared using standard SUZUKI coupling reactions and, in case of L^{S7} and L^{S8}, condensations of L^{S5} with the corresponding acid chlorides. A combination of ligands L^{S6} and ligands L^{S8-10} with L^{F2} in a 1:1 stoichiometry and addition of 0.55 equiv. Pd(II) cations yielded clean structures of nuclearity n = 4.

Most interestingly, ligand L^{F2} maintains its fluorescent properties in all of these systems, yet its fluorescence is subjected to certain changes depending on the utilized counter ligand.

An analysis of each individual combination of L^{F2} with the respective counter ligand L^{S1-10} is conducted in the following chapter (K. E. Ebbert et al. Manuscript in preparation).

3.4.2.1 Pd$_3$L$^{F2}_3$L$^{S1}_3$

270 µl of a 3.11 mM solution of L^{F2} in DMSO-d_6 were combined with 270 µl of a 3.11 mM solution of L^{S1} in DMSO-d_6 with 60 µl of a 15 mM solution of [Pd(CH$_3$CN)$_4$](OTf)$_2$ in a 5 mm standard NMR tube and either heated to 70°C for 5 minutes or let to rest at room temperature for 2 h to afford Pd$_3$L$^{F2}_3$L$^{S1}_3$ (Scheme 17).
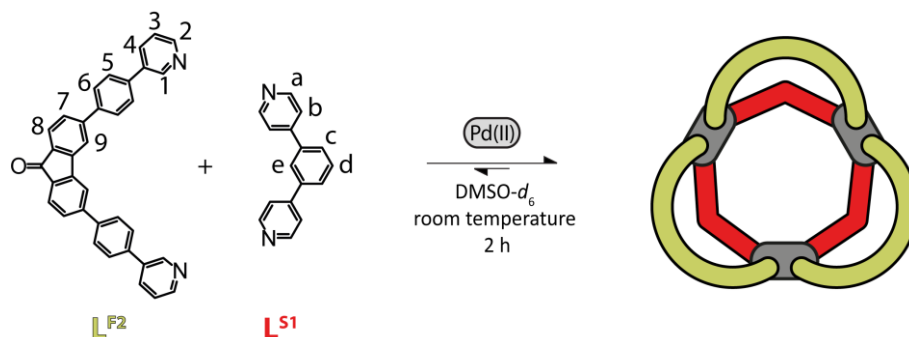
Scheme 17: Formation of Pd$_3$L$^{F2}_3$L$^{S1}_3$ with consecutive proton labels.

Figure 161 depicts the aromatic region of the ^{1}H NMR spectra of ligand L^{F2} (Figure 161, a)), the homoleptic mixture L^{F2} forms upon addition of Pd(II) cations (Figure 161, a)), the heteroleptic assembly (Figure 161, c)) and ligand L^{S1} (Figure 161, d)). The ^{1}H NMR spectra of the homoleptic Pd$_{12}$L$^{S1}_{24}$ sphere L^{S1} forms upon Pd(II) addition[162] is shown in Figure 254 in the experimental part and is omitted here for clarity.
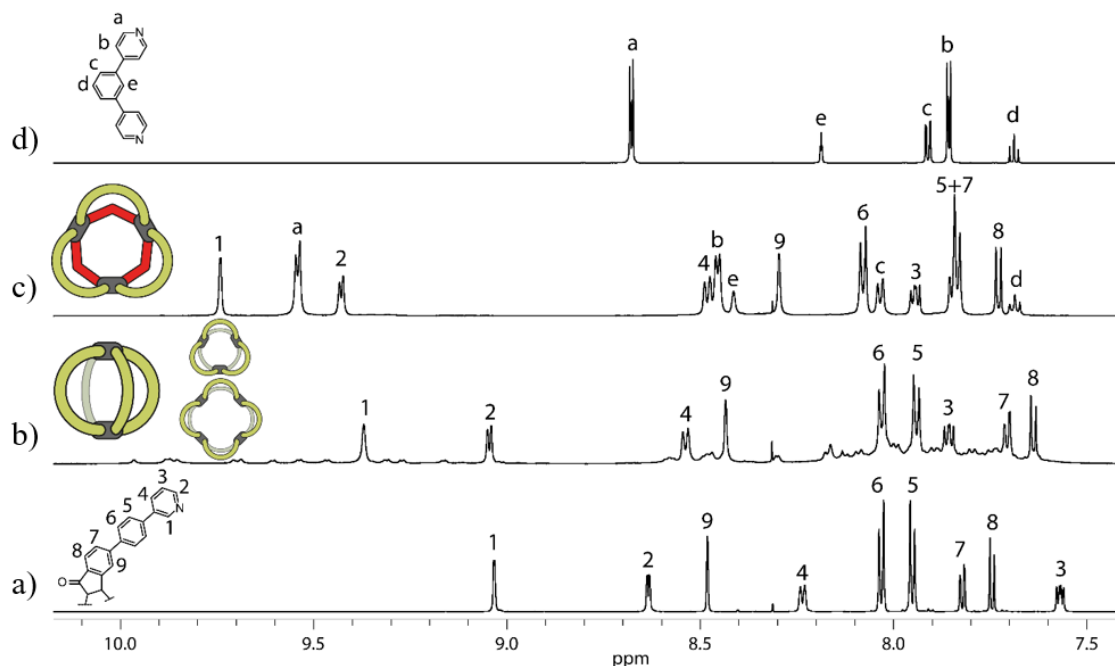
Figure 161: Partial ^{1}H NMR spectra of a) ligand L^{F2} (700 MHz, 298 K) b) homoleptic Pd$_2$L$^{F2}_4$ cage (major species) and the Pd$_n$L$^{F2}_{2n}$ (n=3-5) rings formed upon addition of 0.55 equiv. Pd(II) cations to ligand L^{F2} (600 MHz, 298 K) c) heteroleptic Pd$_3$L$^{F2}_3$L$^{S1}_3$ (600 MHz, 298 K) d) ligand L^{S1} (700 MHz, 298 K) in DMSO-d$_6$.

As evident from Figure 161 c), the spectrum shows no traces of free ligand L^{F2} nor L^{S1}. Furthermore, the homoleptic assembly of L^{F2} cannot be detected. 14 proton signals could be detected in the aromatic region of the spectrum, which could be assigned to the corresponding protons using 2D NMR techniques. Proton signals assigned to H^1, H^2, H^a and H^b are subjected to a significant downfield shift upon $[Pd(CH_3CN)_4](OTf)_2$ addition while the signal of proton H^9, that is oriented to the inside of the assembly shifts to the upfield, likely due to shielding effects. Strong NOE contacts of protons H^1 to H^a and weaker contacts of proton H^2 to H^a (Figure 257, experimental part) attest the structural closeness of the two ligands in the assembly. While the stoichiometry of the assembly was initially unclear, as the combination of these two ligands aimed at the formation of a typical $Pd_2L^{F2}_2L^{S1}_2$ coordination cage, the hydrodynamic radius obtained from the ^1H DOSY spectrum attributed to 14.78 Å (Figure 258, experimental part), which is well above the scale typically applying to Pd_2L_4 assemblies (see e.g. previous chapters) and also notably higher than the hydrodynamic radius previously reported for the heteroleptic $Pd_2L^{F2}_2L^{IR}_2$ cage (Figure 137, $r_H = 12.16$ Å). Considering that $Pd_2L^{F2}_2L^{IR}_2$ no less contains hexyl chains attached to L^{IR}, whose presence usually leads to an increase in hydrodynamic radius, yet still is substantially smaller than the measured r_H for the assembly formed by L^{F2} and L^{S1} in the presence of Pd(II) cations, it was reasonable to assume a species of higher nuclearity has been formed. Default procedure to find out the stoichiometry of an assembly is ESI-MS spectrometry. This however was unsuccessful in the first instance and yielded mainly free ligand and just very small peaks, that could be attributed to $[Pd_3L^{F2}_3L^{S1}_3 + nCF_3SO_3]^{(6-n)+}$. Since the assembly was formed in DMSO and the MS sample had to be diluted with CH_3CN with a factor of at least 10, it is reasonable to assume, that the loss of its solvent shell in combination with the standard ESI-MS conditions led to the disintegration of the assembly. While ESI is already a relatively mild source for MS measurements, the utilization of Cryo-Spray-Ionization mass spectrometry (CSI-MS), an even more moderate ionization procedure avoiding harsh ionization temperatures, proved to be the solution for this problem. Figure 162 shows the CSI-MS spectrum of the assembly obtained under optimized conditions.
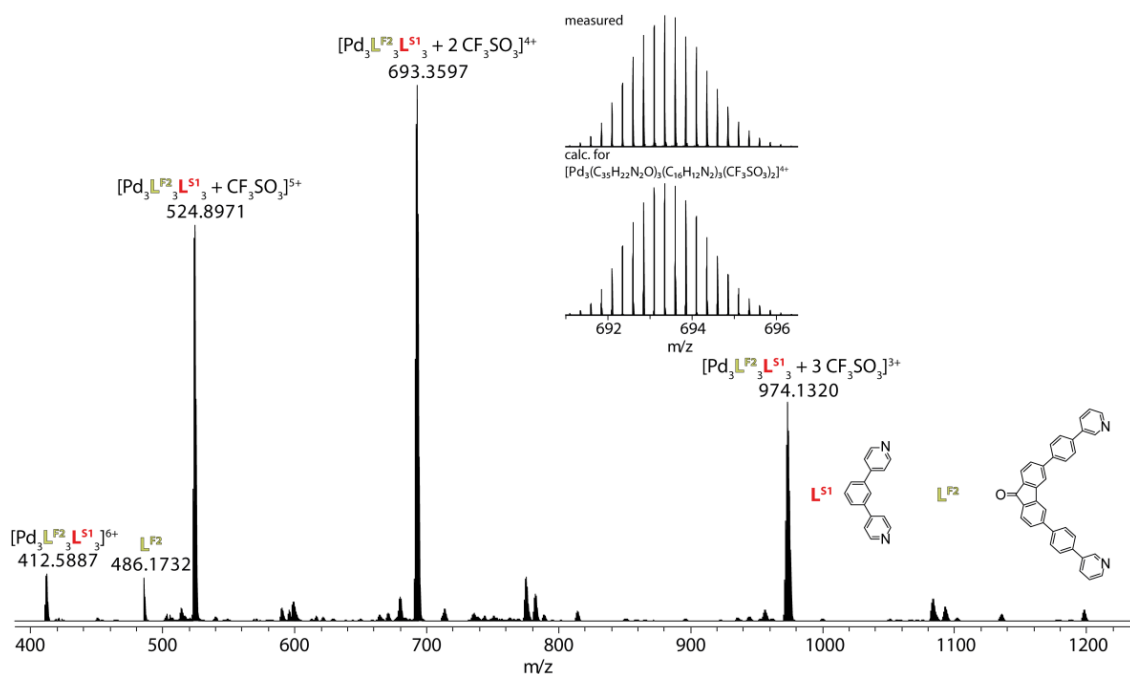
Figure 162: CSI-MS spectrum of heteroleptic $[Pd_3L^{F2}_3L^{S1}_3 + xCF_3SO_3]^{(6-x)+}$ (x = 0-3). The measured and calculated isotopic patterns of the highest peak are shown in the inset.

An analysis of the CSI-MS spectrum proved indeed the formation of a species of higher nuclearity, namely $Pd_3L^{F2}_3L^{S1}_3$. The spectrum shows the species $[Pd_3L^{F2}_3L^{S1}_3 + nCF_3SO_3]^{(6-n)+}$ (n = 0-3) with the 4+ species being the most prominent peak. The inset shows the matching measured (top) and simulated (bottom) isotopic patterns of $[Pd_3L^{F2}_3L^{S1}_3 + 2CF_3SO_3]^{4+}$, further proving the successful assembly of a coordination species with a nuclearity of three and a 1:1:1 ($Pd:L^1:L^2$) ratio of its sub-components.

In case of supramolecular structures, visualization is a crucial and helpful means to further analyze and understand the structure, thus a calculated model using semi-empirical calculations on a PM6 theory level has been created. It was straightforward to place the Pd(II)-atoms, since three Pd(II)-centers can only form a two-dimensional triangle. Furthermore, NMR data suggested a highly symmetric structure and the limited flexibility of the ligands allowing only one possible spatial arrangement of the components where the short L^{S1} ligand with a 120° binding angle bridges the square-planar Pd(II)-centers, forming a small 3-ring, while the larger L^{F2} ligand attaches to the vacant coordination sites via its meta-pyridine donor moieties forming a second, outside ring. A trans-coordination environment can be ruled out for this assembly, since the small L^{S1} ligand would force the system into entropically disfavored structures with higher nuclearity due to its large binding angle. Thus, the result of these considerations is depicted below in Figure 163.
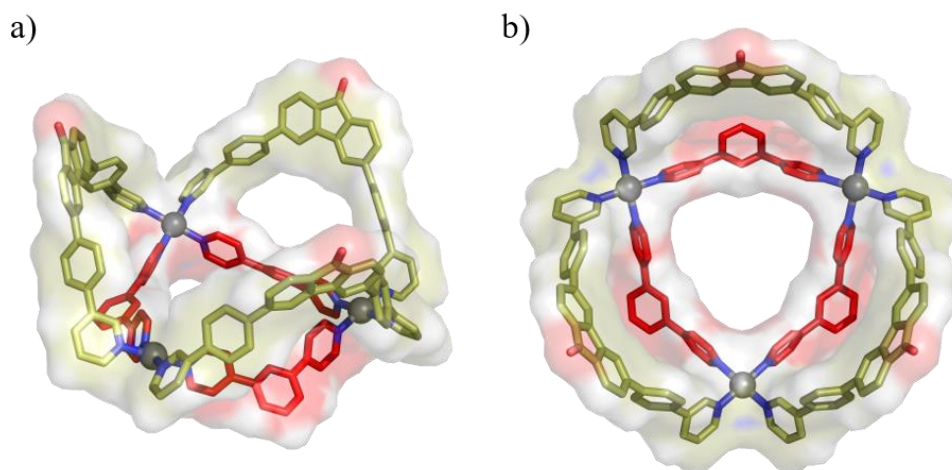
Figure 163: Model of heteroleptic Pd$_3$L$^{F2}_3$L$^{S1}_3$ (sticks overlaid with surface representation) a) side view b) top view. Hydrogens are omitted for clarity. Calculated on semi-empirical PM6 theory level.

Figure 159 depicts the model heteroleptic Pd$_3$L$^{F2}_3$L$^{S1}_3$ assembly with ligand L^{F2} colored in yellow and L^{S1} in red, while the Pd-centers are held in grey. Heteroatoms are colored according to common standard. The three components form a bowl-like structure when combined in a 1:1:1 manner with L^{S1} in the center ring and L^{F2} forming the outer ring. While bowl-like structures in supramolecular Pd(II)-coordination chemistry are usually coordinative unsaturated[71,75–77] and thus contain residual solvent molecules, often acetonitrile, coordinated to the vacant Pd(II)-coordination sites, this structure adapts a bowl-shaped form while avoiding this matter.

A crystal structure obtained by slow vapor diffusion of toluene into 100 µl of Pd$_3$L$^{F2}_3$L$^{S1}_3$ in DMSO-d_6 proved the considerations taken from *in silico* structure modeling right and provided two different conformations of the 3-ring in the unit cell (Figure 164).
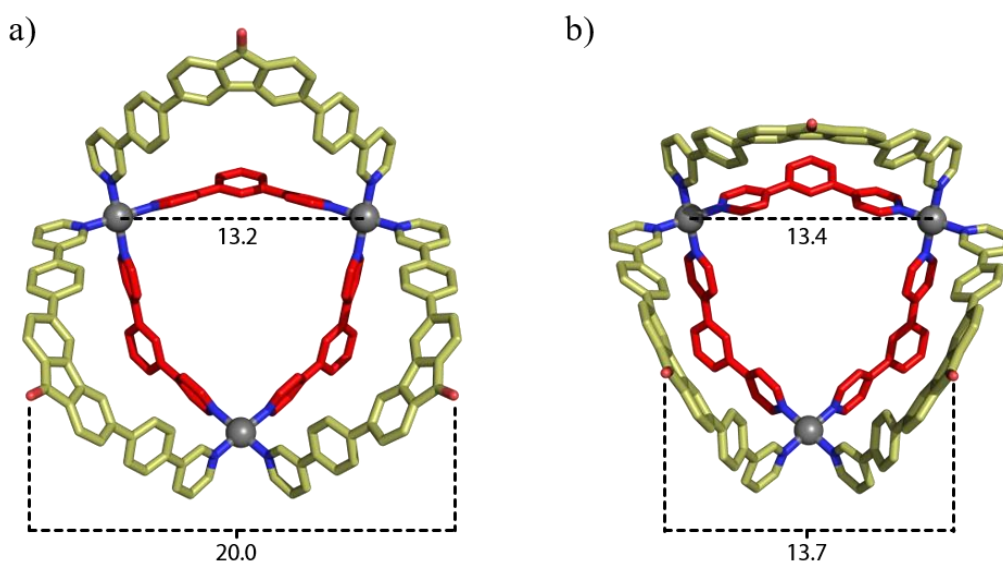
Figure 164: Preliminary X-ray structure of Pd$_3$L$^{F2}_3$L$^{S1}_3$ obtained by slow vapor diffusion of toluene into a 0.46 mM solution of Pd$_3$L$^{F2}_3$L$^{S1}_3$ in DMSO-d_6. Depicted are the two conformers found in the unit cell. Measurements are given in Å.

While the structure depicted in Figure 164 a) resembles the PM6 model very closely, ligand L^{F2} in structure b) is pointing out of the Pd_3-plane in an almost perpendicular manner. This shows the structure having at least some degree of conformational freedom despite the rigidity of the utilized ligands. While the Pd-Pd distance attributes to 13.2 Å in case of conformation a), respectively 13.4 Å for conformer b) and is thus relatively similar, the carbonyl distance differs substantially with it being 20.0 Å for conformer a) and 13.7 Å in case of conformer b). This conformational freedom could be exploited in host-guest experiments given that a suitable guest matching the size of the bowl can be found.

As mentioned before, the fluorenone-based ligand L^{F2} maintains its fluorescent properties to some extent upon coordination to Pd(II), in stark contrast to most other ligands, which usually loose this property. The optical properties of the assembly (see Figure 165) were determined at 0.07 mM chromophore concentration for absorption measurements and 0.14 mM for fluorescence spectroscopy. To verify the integrity of the structure at this concentration, additional absorption measurements were performed with undiluted sample in an ultrathin 0.1 mm cuvette. The absorption is compared to an equimolar amount of ligand, respectively homoleptic assembly. Since it is highly unlikely that the sphere formed by L^{S1} is intact due to dilution and no confirmation experiments run, to ensure the integrity of this high-nuclearity assembly, the species will just be referred to "L^{S1} + 0.55 equiv. Pd(II)". The homoleptic mixture L^{F2} forms upon Pd(II) addition is treated as aforesaid since especially the species of higher nuclearity (n = 4,5) are likely to disassemble upon dilution.
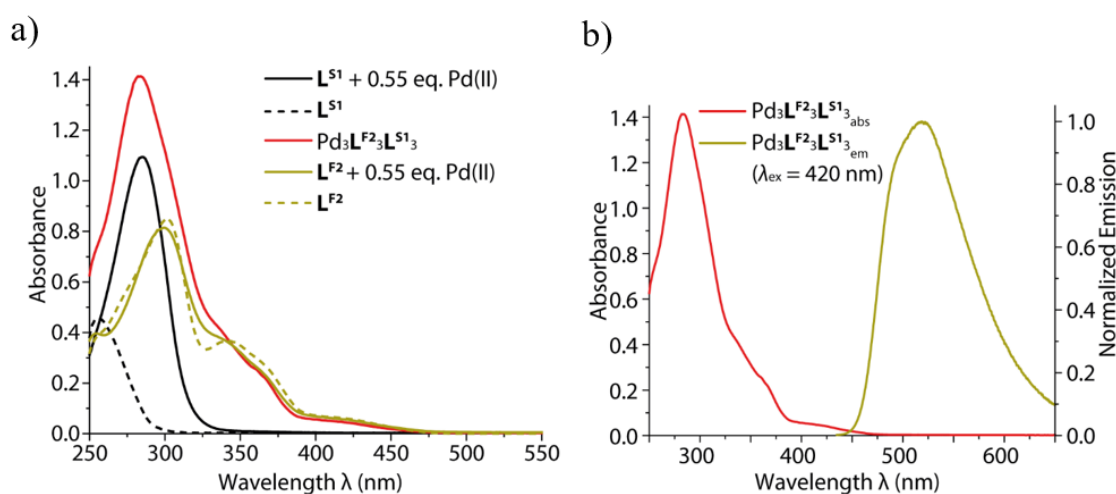
Figure 165: a) UV/VIS spectra of L^{S1}, L^{S1} upon addition of 0.55 equiv. Pd(II), heteroleptic $Pd_3L^{F2}{}_3L^{S1}{}_3$, L^{F2} and L^{F2} upon addition of 0.55 equiv. Pd(II), b) absorbance and normalized emission of heteroleptic $Pd_3L^{F2}{}_3L^{S1}{}_3$.

While ligand L^{S1} and the latter after addition of 0.55 equiv. Pd(II) show no detectable absorption beyond 350 nm given also by their colorless appearance, ligand L^{F2} and both,

its homoleptic assemblies and the heteroleptic $Pd_3L^{F2}_3L^{S1}_3$, absorb even beyond 450 nm. The ligand L^{F2} shows two absorption maxima, one at $\lambda = 302$ nm and the other at $\lambda = 342$ nm. The second maximum converts into a shoulder upon Pd-coordination while the first undergoes a slight hypsochromic shift to $\lambda = 299$ nm. In contrast to this, the absorption maximum of the heteroleptic assembly is found at $\lambda = 284$ nm with shoulders at $\lambda = 335$ nm, $\lambda = 365$ nm and $\lambda = 420$ nm. The same shoulders can be found for the homoleptic L^{F2} assemblies, thus leaving the conclusion that they stem from L^{F2} in the assembly. Upon irradiation of $Pd_3L^{F2}_3L^{S1}_3$ at $\lambda = 420$ nm, the emission of the species can be detected with a maximum at $\lambda = 520$ nm. While the quantum yield of the ligand L^{F2} is 13.4%, it drops substantially in the heteroleptic assembly to 1.1%. It is however higher than in the homoleptic mixture L^{F2} forms coordination to Pd(II) (0.8%).

A comparison of the quantum yields of all heteroleptic assemblies with the nuclearity of n = 3 can be found in Table 8 in the summary chapter 3.4.2.7.

While the successful formation of a symmetric $Pd_3L^{F2}_3L^{S1}_3$ species could be shown with the short ligand L^{S1} sporting the most basic phenyl backbone, the structural scope was further analyzed using phenyl derivatives and pyridine as backbones implemented in the short ligand. While pyridine as a backbone adds another coordination site to the system and shrinks the binding angle, phenyl derivatives with different functional groups change the electronic properties and steric demand of the ligand.

3.4.2.2 $Pd_3L^{F2}_3L^{S2}_3$ – Vacant Coordination Sites

270 μl of a 3.11 mM solution of L^{F2} in DMSO-d_6 were combined with 270 μl of a 3.11 mM solution of L^{S2} in DMSO-d_6 with 60 μl of a 15 mM solution of $[Pd(CH_3CN)_4](OTf)_2$ in a 5 mm standard NMR tube and either heated to 70°C for 5 minutes or let to rest at room temperature for 2h to afford $Pd_3L^{F2}_3L^{S2}_3$ (Scheme 18).
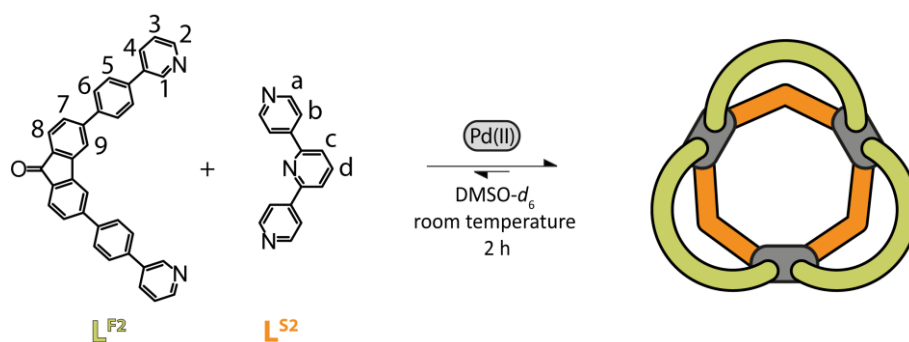
Scheme 18: Formation of $Pd_3L^{F2}_3L^{S2}_3$ with consecutive proton labels.

As small changes in the binding angles of the utilized ligands can have major effects on the outcome of a coordination event,[39] a short ligand L^{S2} was synthesized, its binding angle being decreased by 8° in comparison to L^{S1} (L^{S1}: 120°; L^{S2}:112°). The resulting ligand L^{S2} and its behavior upon Pd(II) coordination have been described previously in the literature.[163] While L^{S1} forms a $Pd_{12}L^{S1}_{24}$ sphere, the minor change from carbon (120°) to nitrogen (112°) in the backbone changes the outcome of the homoleptic coordination cage formation gravely, with the result being a mixture of spheric $Pd_8L^{S2}_{16}$ and $Pd_9L^{S2}_{18}$.[163] While it has to be taken into consideration, that FUJITA et al. used $[Pd(CH_3CN)_4](BF_4)_2$ instead of $[Pd(CH_3CN)_4](OTf)_2$ the outcome of the homoleptic coordination event proved to be comparable showing very similar shifts and two sets of signals in the ^{1}H NMR spectrum (Figure 261, experimental part) deeming the effect of the counter anion neglectable in this case.
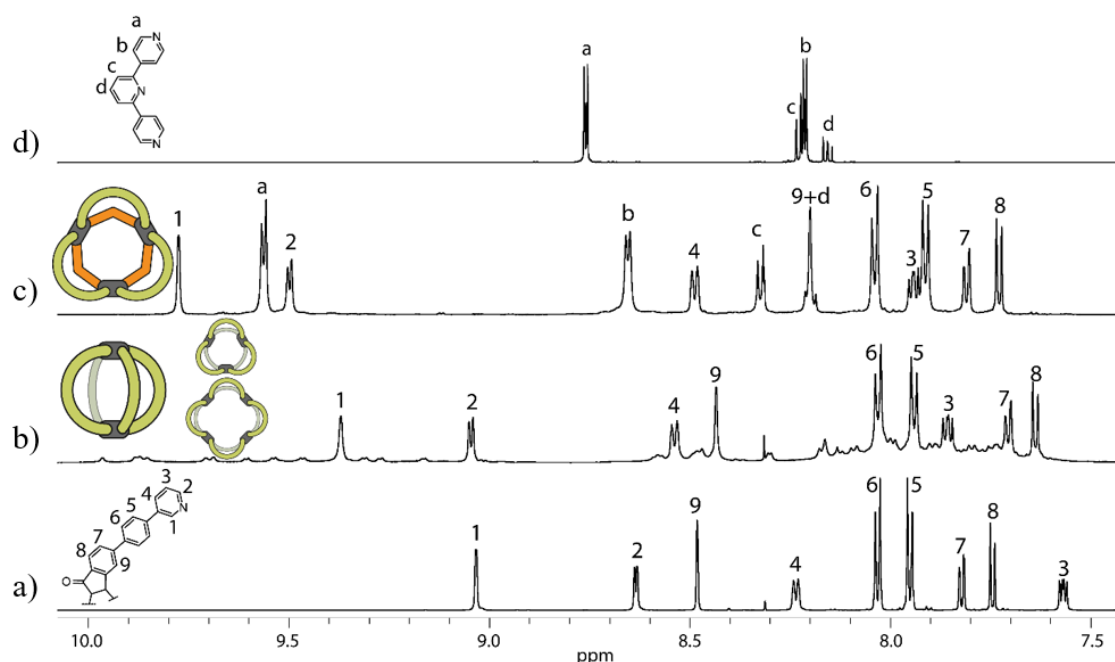
Figure 166: Partial ^{1}H NMR spectra of a) ligand L^{F2} (700 MHz, 298 K) b) homoleptic $Pd_2L^{F2}_4$ cage and the $Pd_nL^{F2}_{2n}$ (n=3-5) rings formed upon addition of 0.55 equiv. Pd(II) cations to ligand L^{F2} (600 MHz, 298 K) c) heteroleptic $Pd_3L^{F2}_3L^{S2}_3$ (600 MHz, 298 K) d) ligand L^{S2} (700 MHz, 298 K) in DMSO-d_6.

An effect of the decrease in binding angle could not be observed for the heteroleptic assembly formation with L^{F2}. The ^{1}H NMR spectrum of the heteroleptic assembly formed from a 1:1:1: mixture of L^{F2}, L^{S2} and $Pd[CH_3CN]_4(OTf)_2$ shows neither signals of residual ligands, nor homoleptic assemblies (for comparison with the mixture of $Pd_8L^{S2}_{16}$ and $Pd_9L^{S2}_{18}$ see Figure 261, experimental part). The ^{1}H spectrum (Figure 166, c)) shows 13 distinguishable signals in the aromatic region, which is in accordance with the number of protons derived from the two ligands L^{F2} and L^{S2}. The signals assigned to protons H^1, H^2, H^a and H^b show a substantial downfield shift while the one of proton H^9 shifts into the

upfield. This behavior is similar to the shifts shown for Pd$_3$L$^{F2}_3$L$^{S1}_3$ (see Figure 161). An ^{1}H DOSY experiment showed only one species being present with a hydrodynamic radius of r_H = 14.57 Å (Figure 266, experimental part).

CSI-MS measurements showed a clean spectrum of [Pd$_3$L$^{F2}_3$L$^{S2}_3$ + nCF$_3$SO$_3$]$^{(6-n)+}$ (n = 0-3) with the 5+ species at m/z = 525.4941 being the most abundant further supporting the claim. Species with extra Pd-cations attached to the structure could not be detected (Figure 267, experimental part).

The presented data from NMR and CSI-MS studies allows the conclusion, that the decrease in binding angle and implementation of a vacant coordination side does not lead to any major differences in the outcome of the coordination event compared to assembly formation with L^{S1}. An *in silico* model based on these deductions is shown in Figure 167.
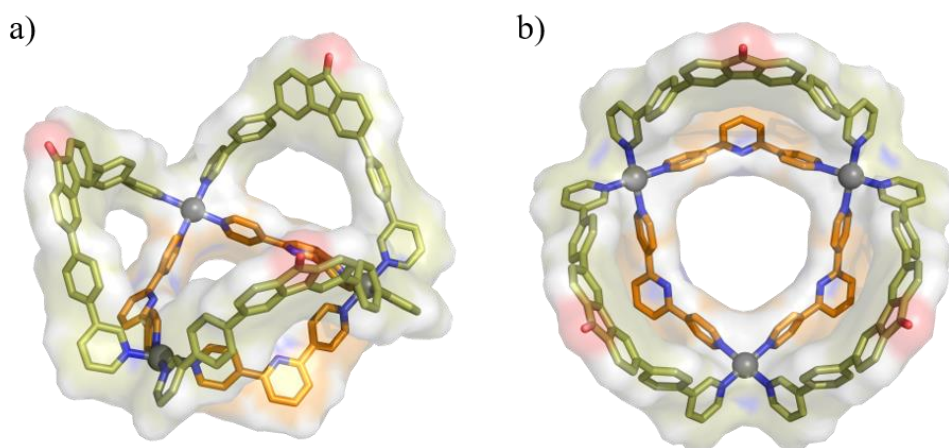
Figure 167: Model of heteroleptic Pd$_3$L$^{F2}_3$L$^{S2}_3$ (sticks overlaid with surface representation) a) side view b) top view. Hydrogens are omitted for clarity. Calculated on semi-empirical PM6 theory level.

The model further emphasized the structural closeness to the assembly formed with L^{S1}. The vacant pyridine coordination sites point into the middle of the central 3-ring. While accessing this position is certainly more sterically demanding than that of the para-pyridine nitrogen atoms, the possibility for further metal coordination using e.g. Ag(I) as shown by FUJITA et al. is certainly given.[40]
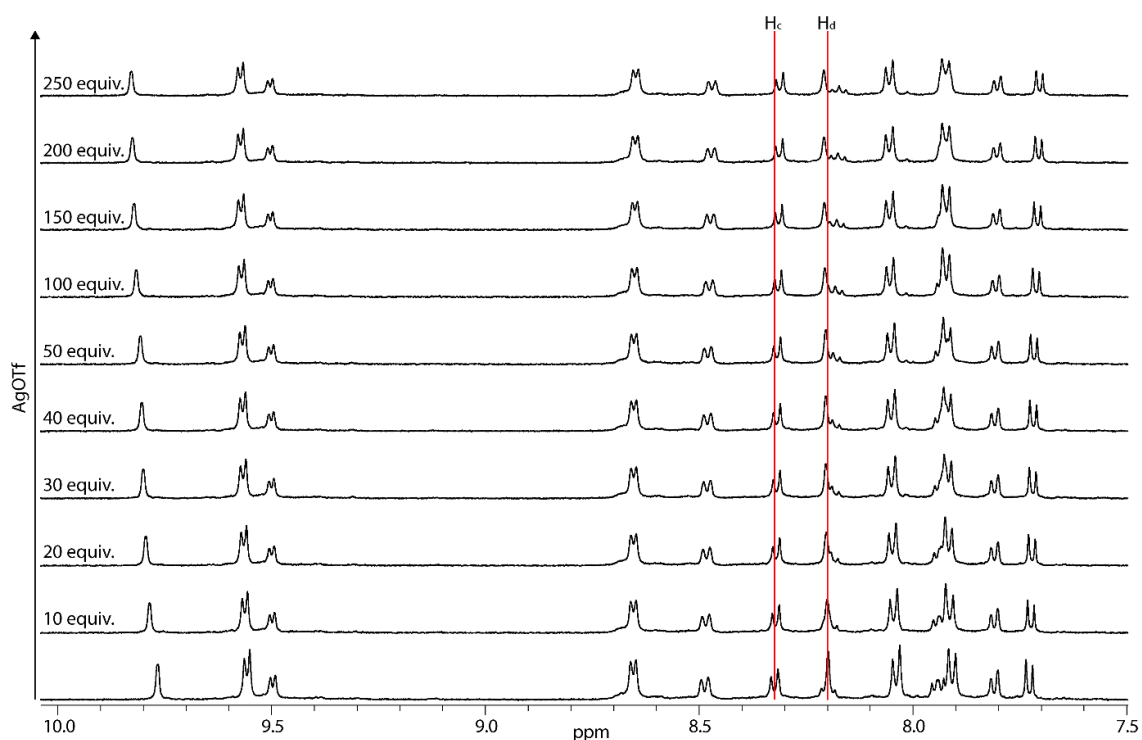
Figure 168: Partial ^{1}H NMR titration (500 MHz, 298 K, DMSO-d_6) of Pd$_3$L$^{F2}_3$L$^{S2}_3$ with AgOTf.

While the ^{1}H NMR titration with AgOTf showed proton signals shifting (see Figure 168), they shift by no means to the same extent as described by FUJITA et al.[40] Especially protons H^c and H^d attached to the central pyridine ring, and thus presumably most affected by a coordination event at the herein mentioned, shift by 0.02 and 0.01 ppm, respectively, indicating no coordination of the central pyridine to silver. The shifts of the other protons could be attributed to the general increase in ion density in solution. This lack of coordination of silver to the vacant pyridine-site can however be attributed to the solvent system, since DMSO has been shown to disturb silver coordination to pyridine as it is a decently strong coordinating solvent itself with a content of only 15% already resulting in detachment of the silver ions from the central pyridine position.[40]

Most fortunately, single crystals suitable for X-ray diffraction could be obtained by slow vapor diffusion of either benzene or toluene into a 0.46 mM solution of Pd$_3$L$^{F2}_3$L$^{S2}_3$ in DMSO-d_6.
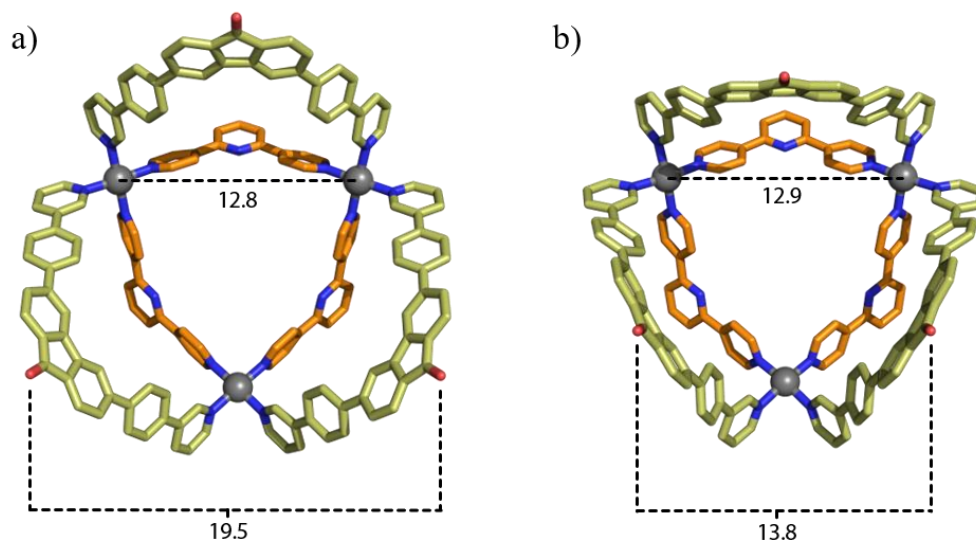
Figure 169: Preliminary X-ray structure of $Pd_3L^{F2}_3L^{S2}_3$ obtained by slow vapor diffusion of toluene into a 0.46 mM solution of $Pd_3L^{F2}_3L^{S2}_3$ in DMSO-d_6. Depicted are the two conformers found in the unit cell. Measurements are given in Å.

As evident from the preliminary X-ray structure (Figure 169), no additional electron density could be detected at the pyridine backbone of L^{S2} even though the solution is setup to contain a 10% excess of Pd(II). The solid-state behavior of $Pd_3L^{F2}_3L^{S2}_3$ is congruent with that of $Pd_3L^{F2}_3L^{S1}_3$ showing two different conformers in the unit cell. The Pd-Pd distance is decreased in comparison to $Pd_3L^{F2}_3L^{S1}_3$, from 13.2 Å, respectively 13.4 Å to 12.8 Å, respectively 12.9 Å. This behavior can be attributed to the decrease in binding angle of L^{S2} (112°) compared to L^{S1} (120°). The carbonyl distance is slightly decreased for conformer a) from 20.0 Å ($Pd_3L^{F2}_3L^{S1}_3$) to 19.5 Å ($Pd_3L^{F2}_3L^{S2}_3$) and almost unchanged for conformer b) (13.7 Å ($Pd_3L^{F2}_3L^{S1}_3$) to 13.8 Å ($Pd_3L^{F2}_3L^{S2}_3$)). This second structure confirms the claim of a certain degree of conformational freedom the system exhibits, sporting an open and a contracted form.

While the change from phenyl- to pyridine backbone does not introduce a substantial change in structure, an effect on its photophysical properties (see Figure 170) is expected due to the different electronic properties of the systems.
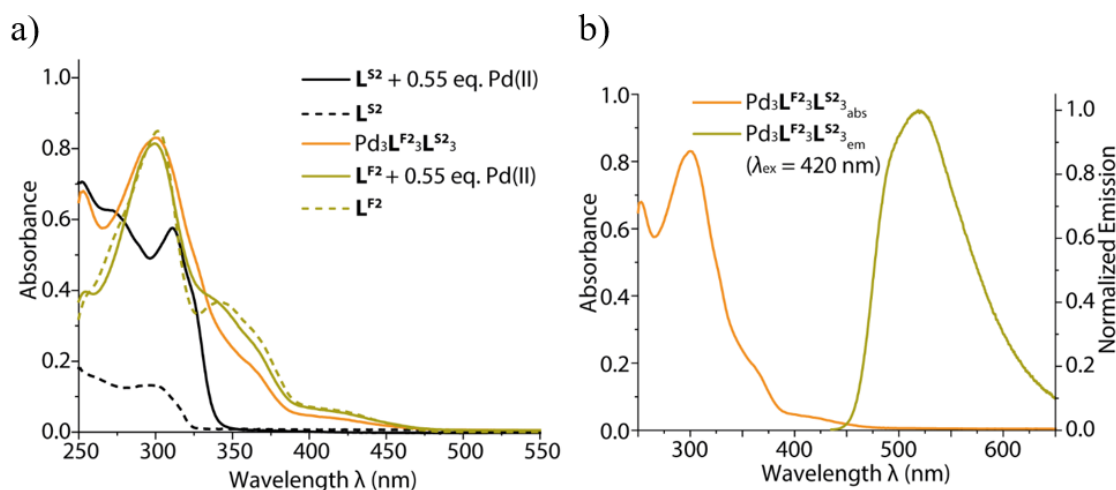
Figure 170: a) UV/VIS spectra of L^{S2}, L^{S2} upon addition of 0.55 equiv. Pd(II), heteroleptic Pd$_3$L$^{F2}_3$L$^{S2}_3$, L^{F2} and L^{F2} upon addition of 0.55 equiv. Pd(II), b) absorbance and normalized emission of heteroleptic Pd$_3$L$^{F2}_3$L$^{S2}_3$.

As proposed, L^{S2} shows different absorption behavior than L^{S1}. While L^{S1} showed an absorption maximum at $\lambda = 257$ nm which shifted to 285 nm upon Pd(II) addition, L^{S2} shows an absorption maximum at 299 nm and a shoulder at 263 nm. Upon Pd(II) addition the spectrum shows maxima at $\lambda = 253$, 272 and 311 nm. The heteroleptic assembly Pd$_3$L$^{F2}_3$L$^{S2}_3$ shows absorption maxima at $\lambda = 253$ and 300 nm which shows a bathochromic shift by 17 nm compared to the heteroleptic assembly formed with the phenyl-based L^{S1}. The shoulders of the absorption curve are congruent with the measurement of Pd$_3$L$^{F2}_3$L$^{S1}_3$ found at $\lambda = 365$ and 420 nm. Excitation at 420 nm results in the assembly emitting at $\lambda = 520$ nm. While the emission occurs at the same wavelength, it is notably weaker with a quantum yield of only 0.84%. This effect could be attributed to the lower electron density in L^{S2} compared to L^{S1}. While the fluorescence stems from the counter ligand L^{F2}, it is diminished by a substantial amount upon Pd-coordination, thus leading to the conclusion that non-radiative processes lead to this decay. Substitution of Pd(II) with Pt(II) as a central metal could solve this issue, however previous experience within the CLEVER group has proven the formation of heteroleptic Pt(II)-assemblies to be quite challenging.

The formation of the second Pd$_3$L$^{F2}_3$L$^{SX}_3$ assembly does not only show the structural flexibility of the approach but also the potential of tuning its properties with the right L^S counter ligand.

3.4.2.3 Pd$_3$L$^{F2}_3$L$^{S3}_3$ – Functional Groups and H-Bond Donors

While the effect of changing the backbone from phenyl to pyridine did not affect the outcome of the final coordination structure, but only its photophysical properties, a wider backbone scope was investigated starting with aniline.

270 µl of a 3.11 mM solution of **L^{F2}** in DMSO-d_6 were combined with 270 µl of a 3.11 mM solution of **L^{S3}** in DMSO-d_6 with 60 µl of a 15 mM solution of [Pd(CH$_3$CN)$_4$](OTf)$_2$ in a 5 mm standard NMR tube and either heated to 70°C for 5 minutes or let to rest at room temperature for 2h to afford Pd$_3$L$^{F2}_3$L$^{S3}_3$ (Scheme 19).
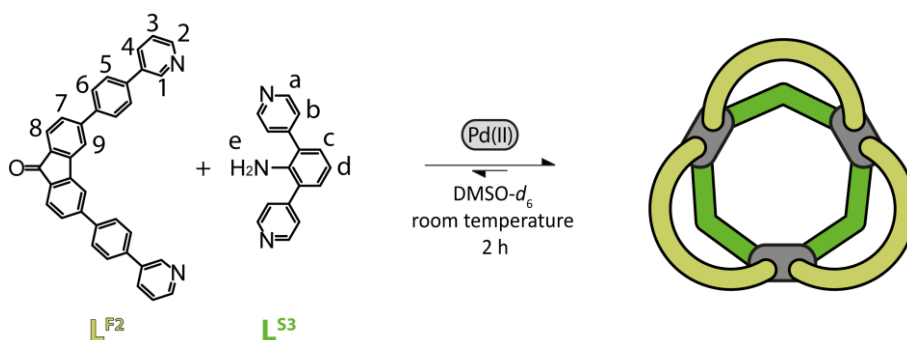
Scheme 19: Formation of Pd$_3$L$^{F2}_3$L$^{S3}_3$ with consecutive proton labels.
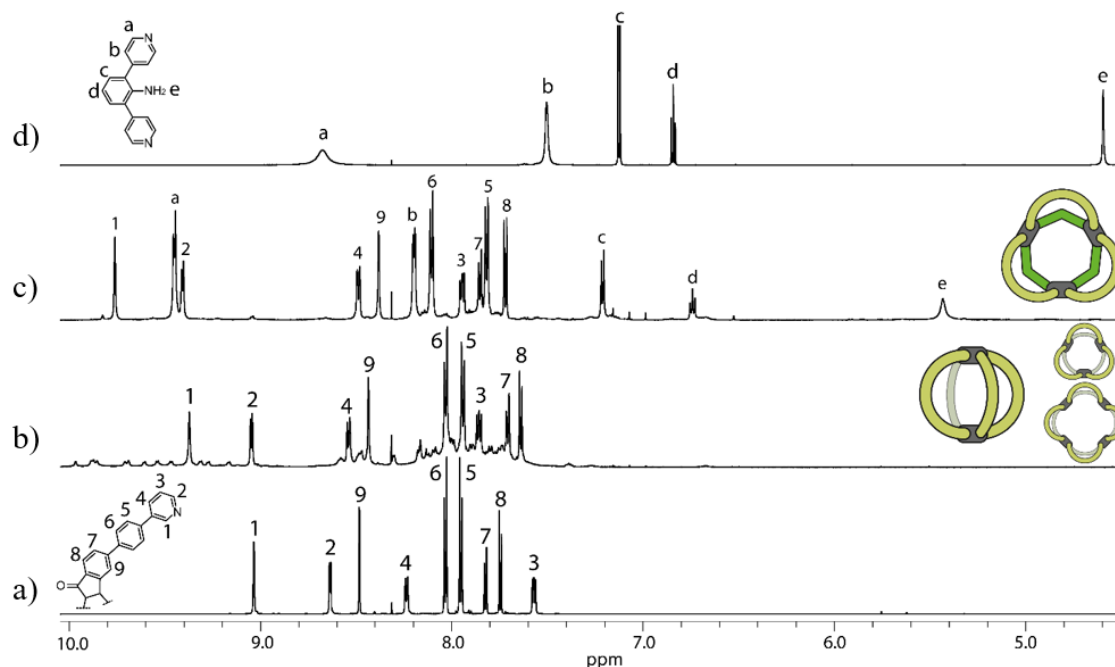
Figure 171: Partial ^{1}H NMR spectra of a) ligand **L^{F2}** (700 MHz, 298 K) b) homoleptic Pd$_2$L$^{F2}_4$ cage and the Pd$_n$L$^{F2}_{2n}$ (n=3-5) rings formed upon addition of 0.55 equiv. Pd(II) cations to ligand **L^{F2}** (600 MHz, 298 K) c) heteroleptic Pd$_3$L$^{F2}_3$L$^{S3}_3$ (600 MHz, 298 K) d) ligand **L^{S3}** (700 MHz, 298 K) in DMSO-d_6.

The combination of Pd(II), **L^{F2}** and **L^{S3}** in a 1:1:1 manner led to the formation of a distinct species in the ^{1}H NMR spectrum (Figure 171, c)) with 13 signals in the aromatic region and an additional signal at δ = 5.43 ppm. The shift of protons H^1, H^2, H^a and H^b is

comparable to the two previous systems showing a substantial downfield shift compared to the free ligands. Contrariwise, the signals attributed to protons H^c and H^d of L^{S3} experience far less downfield shift compared to the two previous systems (L^{S1} and L^{S2}), H^d even shifting to the upfield. A comparison with the homoleptic assembly formed by Pd(II) and L^{S3} could not be performed in a reasonable manner since the spectrum showed substantial broadening and the signal to noise ratio decreased vastly (Figure 270, experimental part) yielding no definite conclusion regarding the homoleptic species, which, to the best of my knowledge, has not been described in the literature yet. The shift of protons H^c and H^d upfield by $\Delta\delta = 0.8$ ppm, respectively $\Delta\delta = 0.95$ ppm in comparison to $Pd_3L^{F2}_3L^{S1}_3$ is likely attributed to the functional group, as this trend can also be observed for the ligands themselves, thus leaving the conclusion that an electronic effect of the functional group leads to increased shielding of these protons. The signal of utmost interest in the system is however the aniline -NH_2 signal found at $\delta = 4.59$ ppm in the free ligand and shifted to $\delta = 5.43$ ppm in the assembly. This downfield shift can be explained with the decrease of electron density in the central ring of the aniline upon coordination of L^{S3} to Pd(II) leading to deshielding of H^e. The measured hydrodynamic radius of the assembly was $r_H = 14.34$ Å (Figure 275, experimental part) being in good accordance with the radii measured for the two previously described assemblies. The CSI-MS spectrum showed peaks at $m/z = 420.0943$ (6+), 533.9038 (5+), 704.6183 (4+) and 989.1434 (3+) with the 5+-peak being the most abundant species. All peaks could be assigned to the heteroleptic $Pd_3L^{F2}_3L^{S3}_3$ assembly with the respective amount of triflate counter anions (Figure 276, experimental part). While the protonation or deprotonation of the NH_2-group has been considered a possibility, the mass analysis did not show either.
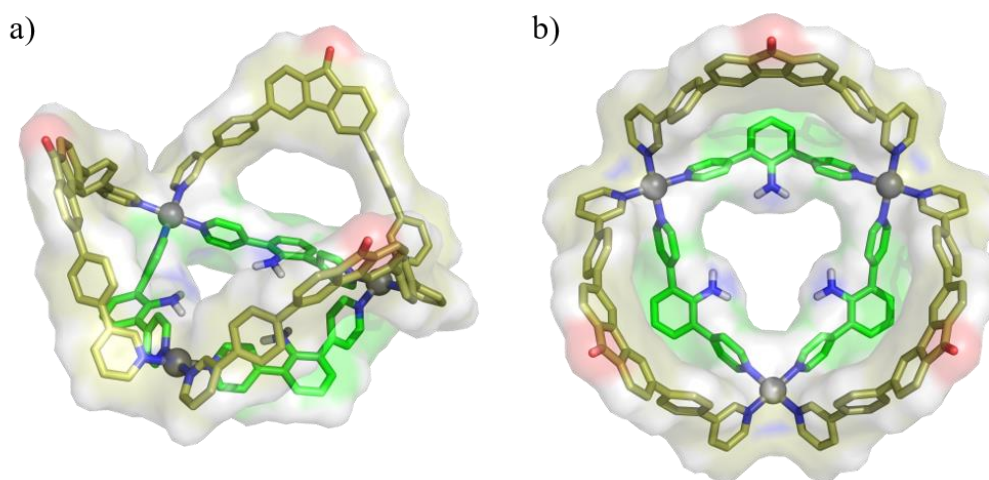
Figure 172: Model of heteroleptic $Pd_3L^{F2}_3L^{S3}_3$ (sticks overlaid with surface representation) a) side view b) top view. Non-polar hydrogens are omitted for clarity. Calculated on semi-empirical PM6 theory level.

A model calculated on PM6 theory level based on NMR and CSI-MS data, as well as the previously shown structures of $Pd_3L^{F2}_3L^{S1}_3$ and $Pd_3L^{F2}_3L^{S2}_3$, visualizes the orientation of the -NH_2 groups, which point to the inside of the central 3-ring. NOE contacts of proton H^e to protons H^a and H^b are prominent though also a weak contact to proton H^c could be observed (Figure 274, experimental part) which is accountable to the free rotation of the -NH_2 group. The analysis yields a structure with an abundance of hydrogen bond donors pointing to the central cavity, yet it is noted that no contact to residual H_2O in the utilized DMSO-d_6 has been detected. While hydrogen bonding is diminished by the presence of competing DMSO, the potential to find a suitable H-bond acceptor for this system is amplified by the high local concentration of H-bond donors in the central ring, which would lead to increased stabilization.
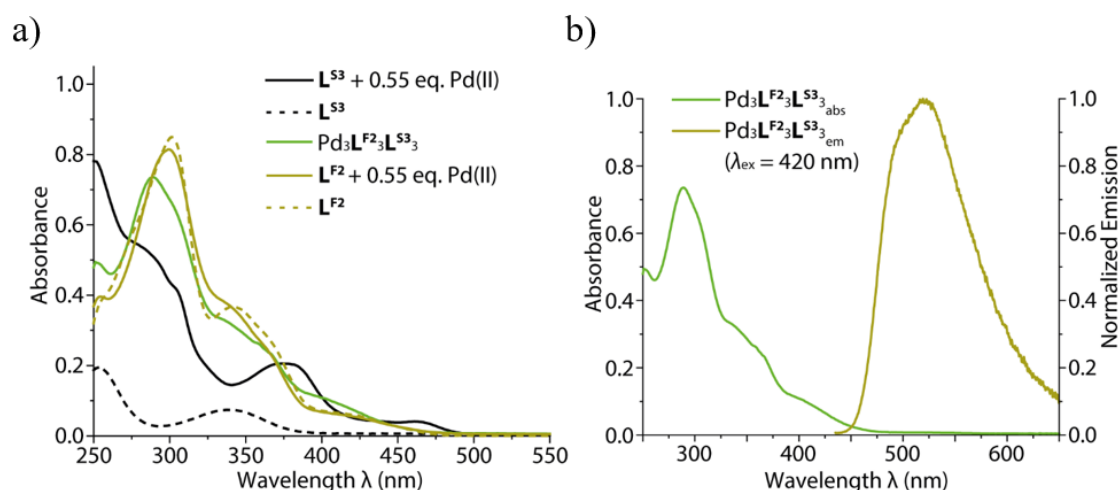
Figure 173: a) UV/VIS spectra of L^{S3}, L^{S3} upon addition of 0.55 equiv. Pd(II), heteroleptic $Pd_3L^{F2}_3L^{S3}_3$, L^{F2} and L^{F2} upon addition of 0.55 equiv. Pd(II), b) absorbance and normalized emission of heteroleptic $Pd_3L^{F2}_3L^{S3}_3$.

Since the electronic properties of the short ligand were altered, the observed photophysical properties changed (see Figure 173). While ligand L^{S3} exhibits absorption maxima at $\lambda = 254$ nm and 342 nm, the combination of latter and 0.55 equiv. Pd(II) shows absorption maxima at $\lambda = 252$ nm, 377 nm and 465 nm with two shoulders at 290 nm and 305 nm. The heteroleptic assembly $Pd_3L^{F2}_3L^{S3}_3$ shows an absorption maximum at $\lambda = 298$ nm, exhibiting a bathochromic shift compared to the assembly containing the phenyl based L^{S1}, $Pd_3L^{F2}_3L^{S1}_3$ and a hypsochromic shift compared to homoleptic L^{F2}, respectively ligand L^{F2} ($\lambda = 300$ nm, respectively $\lambda = 302$ nm). Further notable aspects of the spectrum are shoulders at $\lambda = 365$ nm and 420 nm which were previously attributed to the contribution of L^{F2} in the heteroleptic assembly. Upon irradiation at $\lambda = 420$ nm a weak fluorescence at $\lambda = 520$ nm could be detected with a quantum yield of 0.26%. This substantial decrease in fluorescence intensity could be explained with an abundance of non-radiative pathways due to e.g. hydrogen bonding

interactions which might exhibit exchange kinetics too fast to be detected in the NMR (see NOESY) yet well in the time range of radiative processes. Since dry DMSO is hard to come by, costly and extremely hygroscopic once opened, the explanation could be verified measuring the fluorescence intensity with increasing water content.

While the potential in sensing via hydrogen-bonding interactions has been proposed for this system, an application of $Pd_3L^{F2}_3L^{S3}_3$ as a catalyst in hydrazone formation as described in Scheme 20 would be most interesting especially if the coordination assembly exhibits higher catalytic potential compared to the native ligand.
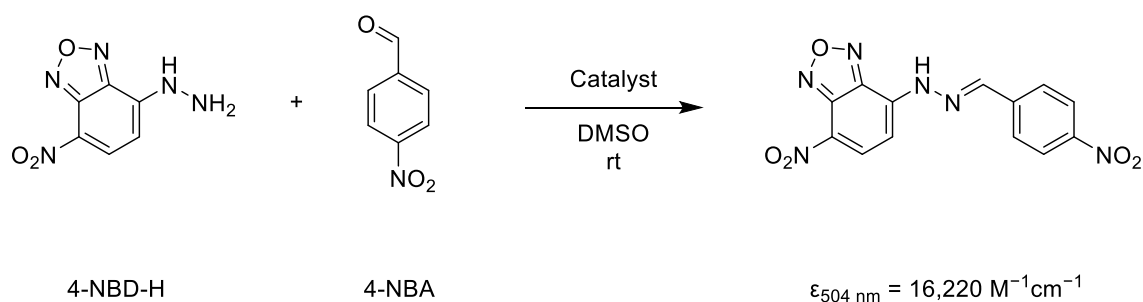
Scheme 20: Proposed scheme of the amine catalyzed reaction of 4-Hydrazino-7-nitro-2,1,3-benzoxadiazole hydrazine (4-NBD-H) with 4-nitrobenzaldehyde (4-NBA).

Since aniline itself is known to be an organocatalyst[164] for the herein mentioned reaction[165], it would be intriguing to find a difference in reaction rate, more specifically whether it would be increased due to stronger N-H bond polarization or decreased due to steric effects. Furthermore, the systems fluorescence should be monitored over the course of the reaction as changes could yield valuable information about the progress of the reaction as well as the integrity of the assembly.

While a coordination cage incorporating aniline is certainly an interesting and promising kickoff for further studies involving hydrogen bonding or catalysis, it is noted that this assembly does seem to be less stable than the previously mentioned two, thus utmost care regarding assembly integrity has to be exercised when performing further studies.

3.4.2.4 Pd$_3$L$^{F2}_3$L$^{S4}_3$ – Moderate Steric Bulk

The next ligand analyzed herein is based upon an anisole backbone. It has been synthesized in a similar manner as the previous ligands L^{S1-3} by Dr. Robin Rudolf.[166] The methoxy-group of the final ligand does possess a certain steric demand and its effect on assembly formation will be analyzed in this part.

270 µl of a 3.11 mM solution of L^{F2} in DMSO-d_6 were combined with 270 µl of a 3.11 mM solution of L^{S4} in DMSO-d_6 with 60 µl of a 15 mM solution of [Pd(CH$_3$CN)$_4$](OTf)$_2$ in a 5 mm standard NMR tube and either heated to 70°C for 5 minutes or let to rest at room temperature for 2h to afford Pd$_3$L$^{F2}_3$L$^{S4}_3$ (Scheme 21).
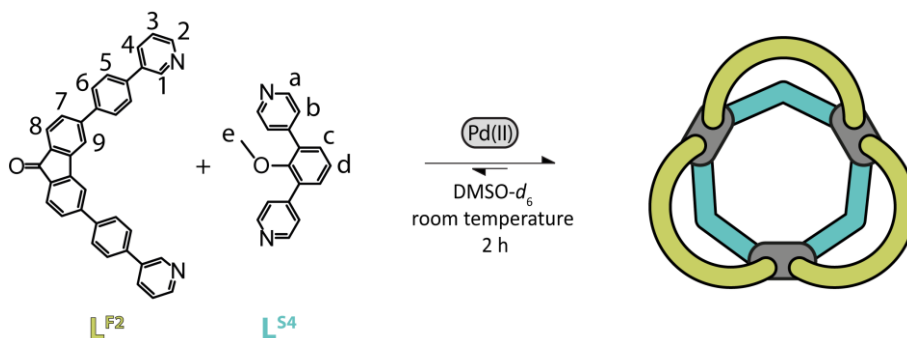
Scheme 21: Formation of Pd$_3$L$^{F2}_3$L$^{S4}_3$ with consecutive proton labels.
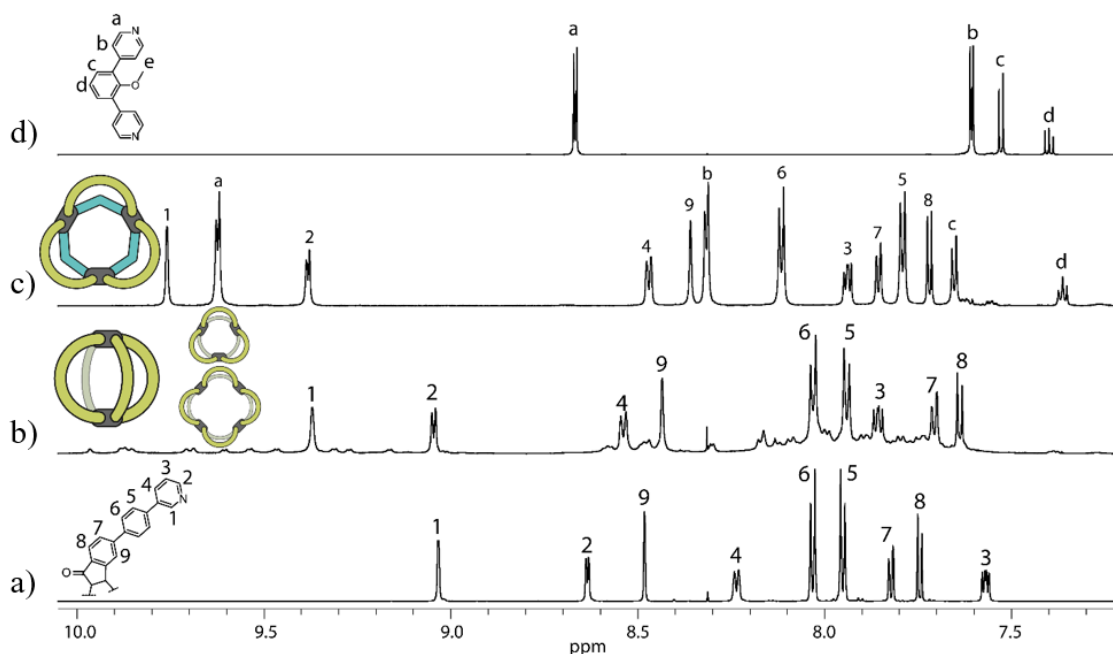
Figure 174: Partial ^{1}H NMR spectra of a) ligand L^{F2} (700 MHz, 298 K) b) homoleptic Pd$_2$L$^{F2}_4$ cage and the Pd$_n$L$^{F2}_{2n}$ (n=3-5) rings formed upon addition of 0.55 equiv. Pd(II) cations to ligand L^{F2} (600 MHz, 298 K) c) heteroleptic Pd$_3$L$^{F2}_3$L$^{S4}_3$ (700 MHz, 298 K) d) ligand L^{S4} (700 MHz, 298 K) in DMSO-d_6.

Upon combination of ligands L^{F2} and L^{S4} with 0.55 equiv. Pd(II) a distinct new species could be detected in the ^1H NMR spectrum (Figure 174, c)) sporting 13 signals in the aromatic region and an additional signal at $\delta = 2.94$ ppm in the aliphatic region. The integration ratio suggested a 1:1 stoichiometry of the ligands in the assembly. Consistent with the systems previously described, signals of the protons around the coordination sphere (H^a, H^b, H^1 and H^2) show a substantial downfield shift in contrast to the free ligands. In contrast, the signal of proton H^e attributed to the $-OCH_3$ group shows an upfield shift of $\Delta\delta = 0.22$ ppm compared to the ligand which can be explained with increased shielding of the herein named protons by the assembly. The shifts of the signals attributed to protons H^c and H^d are comparable to the first assembly formed with L^{S1}. A spectrum of ligand L^{S4} upon addition of 0.55 equiv. Pd(II) was measured and can be found in Figure 278 in the experimental part showing that no distinct species is identifiable, hence it is likely forming a mixture of species of higher nuclearity. The clean assembly depicted in Figure 174 c) has a hydrodynamic radius $r_H = 14.26$ Å (Figure 283, experimental part) which is in the range of the previously reported radii of this type of assemblies, leaving to conclude that the methoxy-group is not bulky enough to disturb heteroleptic assembly formation. CSI-MS analysis confirms the formation of $Pd_3L^{F2}_3L^{S4}_3$ with detected peaks at $m/z = 427.5944$ (6+), 542.9041 (5+), 716.1187 (4+) and 1004.1437 (3+) matching with the simulated m/z values for $[Pd_3L^{F2}_3L^{S4}_3 + xCF_3SO_3]^{(6-x)+}$ (x = 0-3) with the peak at $m/z = 716.1187$ attributed to $[Pd_3L^{F2}_3L^{S4}_3 + 2CF_3SO_3]^{4+}$ being the most abundant species (Figure 284, experimental part).

a)   b)
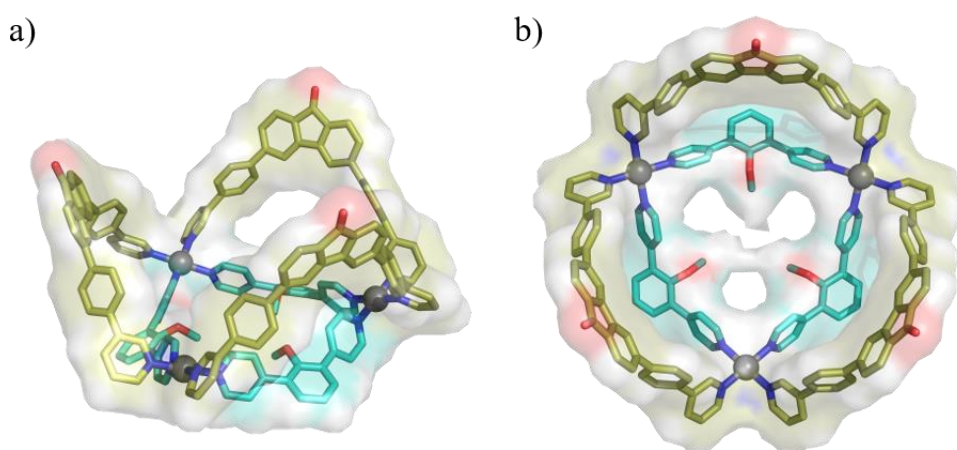
Figure 175: Model of heteroleptic $Pd_3L^{F2}_3L^{S4}_3$ (sticks overlaid with surface representation) a) side view b) top view. Hydrogens are omitted for clarity. Calculated on semi-empirical PM6 theory level.

The *in silico* model (PM6 theory level) visualizes the increased steric demand of the methoxy-group in contrast to the previously reported ligands L^{S1-3}. While the $-OCH_3$ group does not seem all too sterically demanding, the omitted hydrogen atoms have to be taken into consideration leading to the central ring being almost closed off in the

surface representation. ^{1}H DOSY data yielded the lowest r_H for this structure within the systems reported in this chapter until here, suggesting the methoxy-groups pointing inside the central ring. However, given the lack of steric hindrance by protons H^b of the pyridine rings, free rotation of the -OCH$_3$ group is likely.

While the change from aniline to anisole backbone does not alter the outcome of the coordination even in terms of nuclearity, the alteration of electronic properties changes the optical properties.
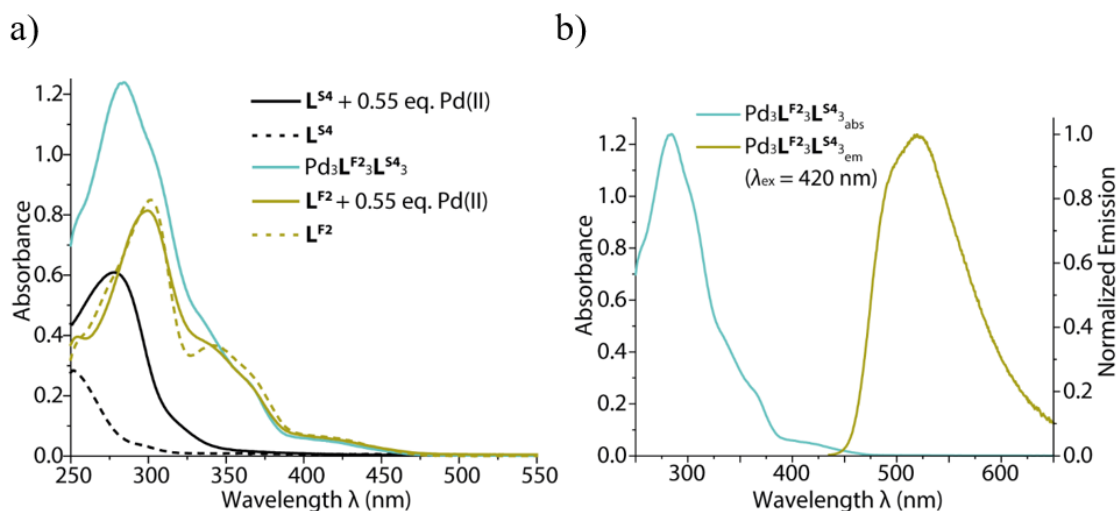
Figure 176: a) UV/VIS spectra of **L^{S4}**, **L^{S4}** upon addition of 0.55 equiv. Pd(II), heteroleptic Pd$_3$**L$^{F2}_3$L$^{S4}_3$**, **L^{F2}** and **L^{F2}** upon addition of 0.55 equiv. Pd(II), b) absorbance and normalized emission of heteroleptic Pd$_3$**L$^{F2}_3$L$^{S4}_3$**.

While ligand **L^{S4}** shows an absorption maximum at $\lambda = 252$ nm, the latter after addition of Pd(II) exhibits a maximum at $\lambda = 279$ nm. The heteroleptic assembly Pd$_3$**L$^{F2}_3$L$^{S4}_3$** shows very similar absorption properties as the assembly with the phenyl-based ligand **L^{S1}**, Pd$_3$**L$^{F2}_3$L$^{S1}_3$**. The absorption maximum is located at $\lambda = 284$ nm with shoulders at $\lambda = 335$ nm, $\lambda = 365$ nm and $\lambda = 420$ nm, which are the exact values that have been recorded for Pd$_3$**L$^{F2}_3$L$^{S1}_3$**, albeit the intensity is slightly higher. Upon excitation at $\lambda = 420$ nm, an emission at $\lambda = 520$ nm with a quantum yield of 1.12% could be measured, being slightly higher than the quantum yield of 1.10% measured for Pd$_3$**L$^{F2}_3$L$^{S1}_3$**. Since the deviation is very small, this might as well be attributed to a statistical or concentration derived error. The similarities the heteroleptic assemblies of **L^{S1}** and **L^{S4}** show within their photophysical properties despite their different chemical structure are most interesting and their behavior in host-guest studies will be evaluated in the second part of this chapter.

3.4.2.5 Pd$_3$L$^{F2}_3$L$^{S5}_3$ – Introducing an Acidic OH-Group

The next ligand analyzed herein is based upon a phenol backbone and has also been synthesized by Dr. Robin Rudolf in the scope of his thesis.[166] Phenol itself is known to be slightly acidic in water with a pK_a value of 10 [167], which is a property that is likely to persist in the formed ligand. Moreover, this effect could be further increased within the ligand upon coordination to palladium due to electron density relocating into the dative bond, which supposing has a similar (yet weaker) effect as electron-withdrawing groups directly attached to the phenol-backbone. A comparison can be made with e.g. *para*-nitrophenol ($pK_a = 7.23$ (H$_2$O); $pK_a = 11.0$ (DMSO)), 2,6-dinitrophenol ($pK_a = 3.74$ (H$_2$O); $pK_a = 4.82$ (DMSO)) or 2,4,6-trinitrophenol ($pK_a = 0.43$ (H$_2$O); $pK_a = -0.3$ (DMSO))[167], in all of which the acidity is increasingly stronger, the more electron-withdrawing nitro-groups are attached to the central ring. As evident from the given examples, the general trend in pK_a value applies for DMSO as a solvent system too, however the absolute pK_a values differ, as e.g. OLMSTEAD et al. showed the pK_a of phenol in DMSO being approximately 18.[168] There are multiple examples on successful implementation of OH-groups into metal-based coordination cages[36,52,166,169,170] with this chapter adding another example in form of a heteroleptic Pd$_3$L$^A_3$L$^B_3$ assembly.

270 µl of a 3.11 mM solution of L^{F2} in DMSO-d_6 were combined with 270 µl of a 3.11 mM solution of L^{S5} in DMSO-d_6 with 60 µl of a 15 mM solution of [Pd(CH$_3$CN)$_4$](OTf)$_2$ in a 5 mm standard NMR tube and either heated to 70°C for 5 minutes or let to rest at room temperature for 2h to afford Pd$_3$L$^{F2}_3$L$^{S5}_3$ (Scheme 22).
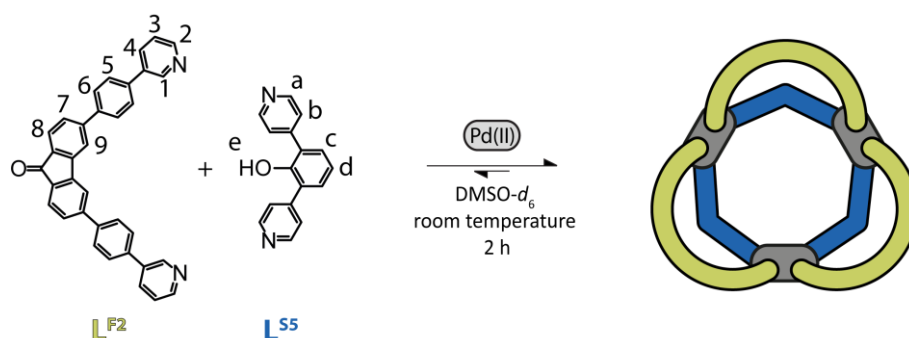
Scheme 22: Formation of Pd$_3$L$^{F2}_3$L$^{S5}_3$ with consecutive proton labels.
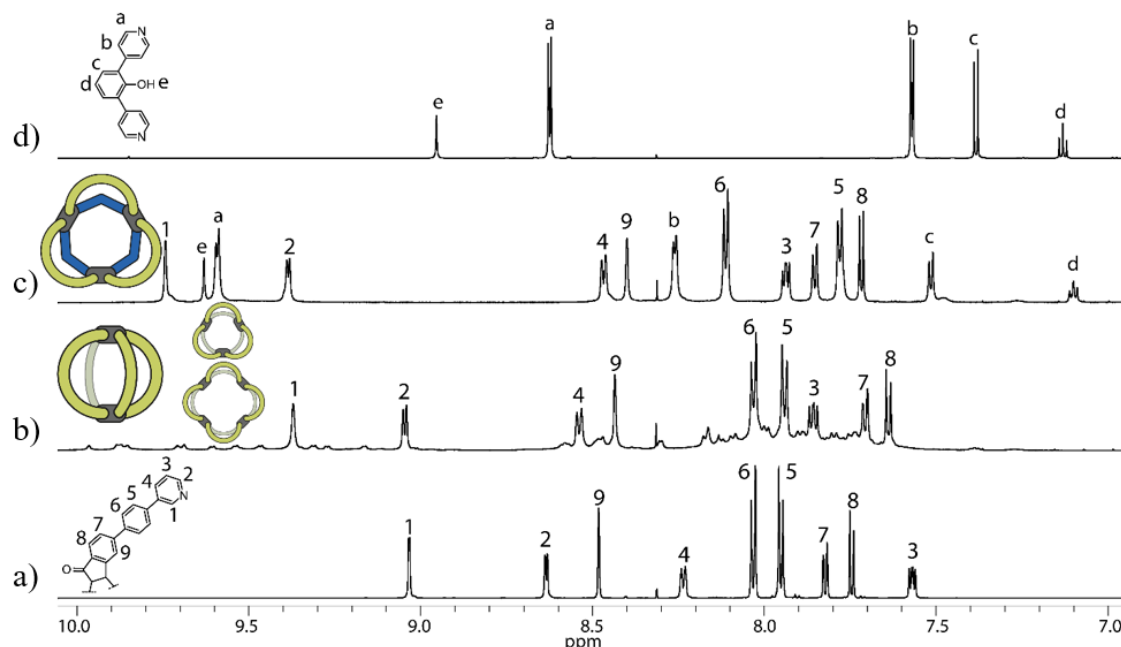
Figure 177: Partial ^{1}H NMR spectra of a) ligand $\mathbf{L^{F2}}$ (700 MHz, 298 K) b) homoleptic $Pd_2\mathbf{L^{F2}}_4$ cage and the $Pd_n\mathbf{L^{F2}}_{2n}$ (n=3-5) rings formed upon addition of 0.55 equiv. Pd(II) cations to ligand $\mathbf{L^{F2}}$ (600 MHz, 298 K) c) heteroleptic $Pd_3\mathbf{L^{F2}}_3\mathbf{L^{S5}}_3$ (700 MHz, 298 K) d) ligand $\mathbf{L^{S5}}$ (700 MHz, 298 K) in DMSO-d_6.

The 1:1:1 combination of $\mathbf{L^{F2}}$, $\mathbf{L^{S5}}$ and Pd(II) cations led to the formation of a distinct, singular species in the ^{1}H NMR spectrum (Figure 177, c)) displaying 14 signals in the aromatic region with their integration matching the formation of a 1:1 ligand ratio in the final assembly. Signals attributed to protons H^a, H^b, H^1 and H^2 shift downfield in comparison to the free ligands. Signals attributed to protons c and d are less upfield shifted than the ones of $\mathbf{L^{S3}}$ but still more compared to ligands $\mathbf{L^{S1}}$ and $\mathbf{L^{S2}}$. The signal assigned to the OH-proton H^e amounts to only 85% of the expected integration value compared to other ligands, though this is expected for an exchangeable proton in a medium containing a certain amount of water. The signal is shifted by $\Delta\delta = 0.68$ ppm compared to the free ligand indicating less shielding due to assembly formation resulting in stronger bond polarization. The measured hydrodynamic radius $r_H = 14.14$ Å (Figure 292, experimental part) is the smallest radius measured for the so far reported assemblies based on $\mathbf{L^{F2}}$ and the short ligands $\mathbf{L^{S1-5}}$, yet it suggests the formation of an assembly with a nuclearity of n = 3, like the four previously reported ones. A notable feat for this system is a NOE contact of the OH-proton H^e to residual water (Figure 290, experimental part), which is usually present in DMSO if it is not meticulously dried and kept under dry conditions. This NOE contact indicates water strongly associated to the assembly with its exchange kinetics being slow compared to the NMR timescale yielding this cross peak.

While ligand L^{S5} or its analogue with an additional alkyne linker have been synthesized before[171,172], it does not seem to form $Pd_{12}L_{24}$ coordination spheres like e.g. its phenyl-based analogue with the same donor angle (Figure 286, experimental part) and a distinct answer to its homoleptic assembly under these conditions cannot be given. Implementation into heteroleptic coordination cages however, has been shown by Dr. Robin Rudolf.[166] To confirm the formation of $Pd_3L^{F2}_3L^{S5}_3$, a CSI-MS spectrum has been recorded (Figure 178). As it is more complex, than the previously reported ones ($Pd_3L^{F2}_3L^{S1-4}_3$) it will be discussed in more detail.
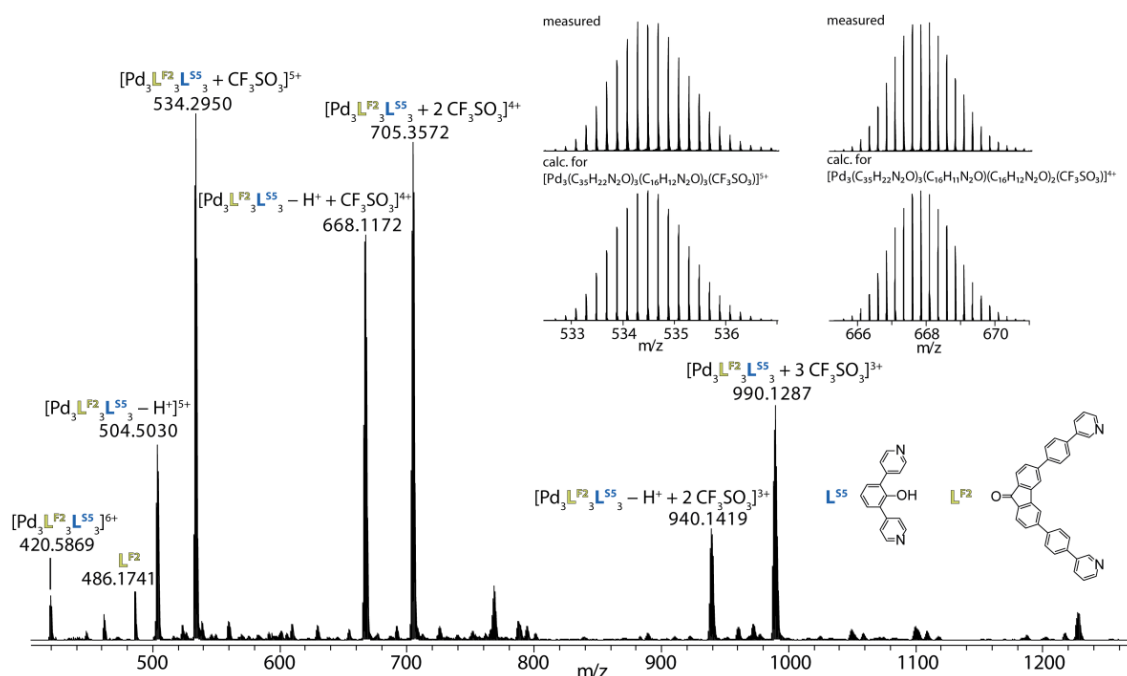
Figure 178: CSI-MS spectrum of heteroleptic $[Pd_3L^{F2}_3L^{S5}_3 + xCF_3SO_3]^{(6-x)+}$ (x = 0-3). The measured and calculated isotopic patterns of the highest peak of the native species and the deprotonated $[Pd_3L^{F2}_3L^{S5}_3 - H + CF_3SO_3]^{4+}$ are shown in the inset.

Whereas the previous CSI-MS spectra of this structure family have shown clean peak distributions according to the respective m/z values with each charge yielding one distinct peak, the CSI-MS analysis of the assembly formed with L^{S5} showed two peaks for each charge state aside from $z = +6$. While the peak with the higher intensity could be assigned to $[Pd_3L^{F2}_3L^{S5}_3 + xCF_3SO_3]^{(6-x)+}$ (x = 0-3), so the respective assembly with triflate counter anions, the second peak to each charge state could be assigned to $[Pd_3L^{F2}_3L^{S5}_3 - yH + xCF_3SO_3]^{(6-y-x)+}$ (x = 0-3; y = 0, 1). This observation undermines the previously stated increased acidity of the OH proton, as one OH-group is prone to deprotonation even under mild CSI conditions. Yet it cannot be fully ruled out to be an effect stemming from the unique conditions during MS measurement. It is noted that the CSI-MS spectrum of $Pd_3L^{F2}_3L^{S3}_3$ has been checked for similar traces of which none could be detected (Figure 276, experimental part).
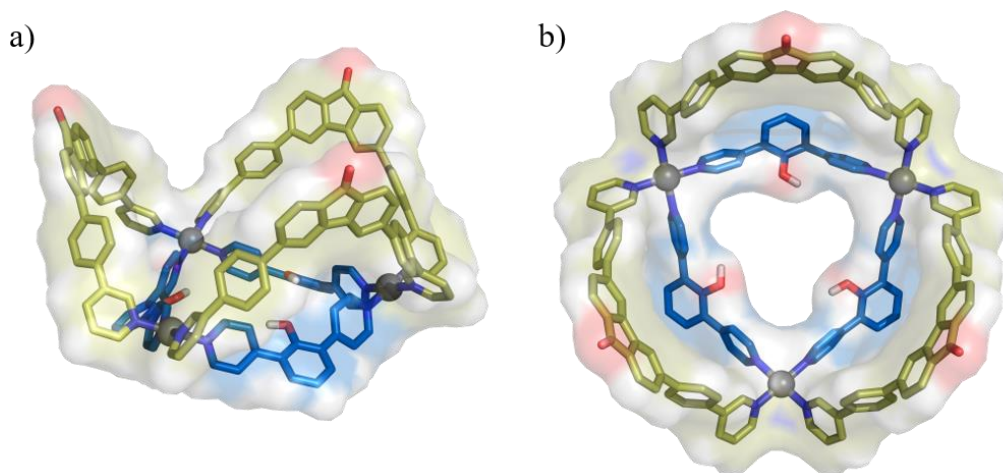
Figure 179: Model of heteroleptic Pd$_3$L$^{F2}_3$L$^{S5}_3$ (sticks overlaid with surface representation) a) side view b) top view. Non-polar hydrogens are omitted for clarity. Calculated on semi-empirical PM6 theory level.

Again, an *in silico* model (PM6 theory level) of the assembly based upon analytical data is provided (Figure 285-143, experimental part). The oxygen-atoms are 7.5 Å apart, while the hydrogen atoms of the phenol-backbone are likely to exhibit free rotation, their distance to opposing OH-groups possibly alternating between 6.0 to 6.8 Å. While the average hydrogen bond distance for H···O within water molecules in bulk water is between $d = 1.2$ Å and 3.2 Å[173] the spanning of a water molecule between two of the three phenol moieties is entirely possible, whereas the orientation cannot be determined based on the available data. It is however likely, that it is fluxionally exchanging between all three OH-moieties. Furthermore, the deprotonation of one of the phenol moieties has to be taken into consideration, as it is not known whether the water molecule is associated via its hydrogen- or oxygen part (or both).

With strong hydrogen bonding capacity like this, the possibility of binding neutral, H-bonding guest molecules is given and should be pursued in future experiments. Furthermore, the stronger polarization of the O···H bond could be exploited, leading to an increase in acidity and future use in protonation dependent catalysis applications.

The photophysical properties of this assembly proved to be most intriguing since the solution differed from the previously reported assembly solutions for Pd$_3$L$^{F2}_3$L$^{S1-4}_3$, which all formed yellow solutions, by yielding a solution of moderate to deep orange color. This effect has already been reported by Dr. Robin Rudolf with a similar ligand sporting a phenol-backbone,[166] yet it seems to be enhanced in this particular case, as it is already observed at room temperature without any additional heating, as opposed to previously reported only upon heating the assembly to 70°C.
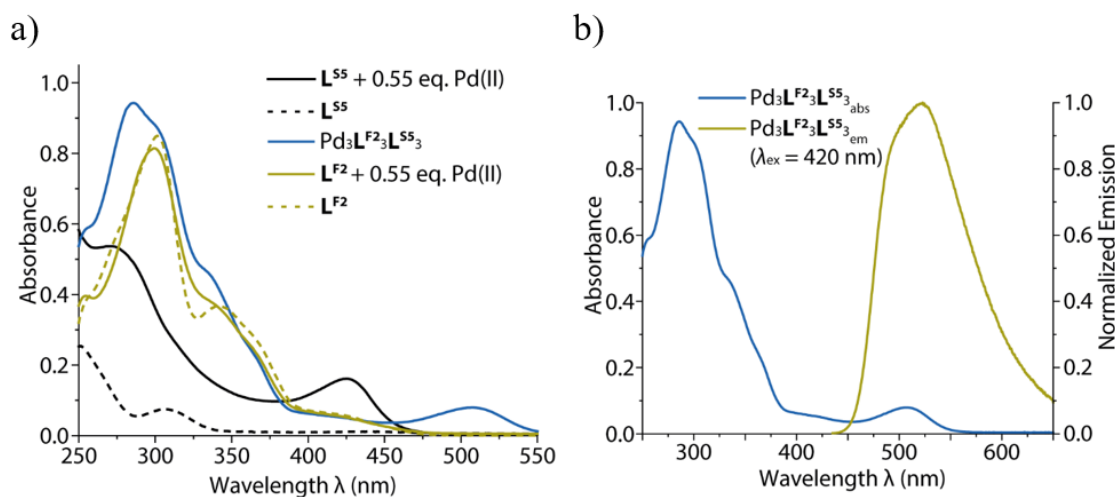
Figure 180: a) UV/VIS spectra of L^{S5}, L^{S5} upon addition of 0.55 equiv. Pd(II), heteroleptic $Pd_3L^{F2}_3L^{S5}_3$, L^{F2} and L^{F2} upon addition of 0.55 equiv. Pd(II), b) absorbance and normalized emission of heteroleptic $Pd_3L^{F2}_3L^{S5}_3$.

While the assembly formed with L^{S4}, $Pd_3L^{F2}_3L^{S4}_3$, did not show substantially different behavior in the absorption measurements compared to its phenyl-based analogue $Pd_3L^{F2}_3L^{S1}_3$, L^{S5} and the formed assemblies exhibit different photophysical properties. The absorption maximum at $\lambda = 284$ nm is shifted slightly bathochromic by 2 nm to $\lambda = 286$ nm. The shoulders in the absorption spectrum at $\lambda = 302$, respectively 338 nm and 365 nm are more pronounced showing a hyperchromic shift compared to the analogues with L^{S1} or L^{S4}, while the shoulder at $\lambda = 420$ nm is only slightly elevated. The most prominent difference however, is an additional absorption maximum at $\lambda = 508$ nm, explaining the orange color of the solution. This additional maximum can also be detected for the two-component mixture of L^{S5} with Pd(II), though at a lower wavelength $\lambda = 426$ nm, indicating the effect stemming from L^{S5}. This claim is further supported by the observation, that neither $Pd_3L^{F2}_3L^{S1}_3$ nor $Pd_3L^{F2}_3L^{S4}_3$ sport similar behavior in their absorption spectra (Figure 165, Figure 176). Excitation of $Pd_3L^{F2}_3L^{S5}_3$ at $\lambda = 420$ nm resulted in subsequent emission at $\lambda = 520$ nm with a quantum yield of 0.92%, which is lower than the one measured for the analogues $Pd_3L^{F2}_3L^{S1}_3$ (1.10%) nor $Pd_3L^{F2}_3L^{S4}_3$. (1.12%), yet not as quenched as for $Pd_3L^{F2}_3L^{S3}_3$ (0.26%). This observation suggests, that hydrogen bonding dynamics lead to fluorescence decay yielding non-radiative relaxation pathways.

Since deprotonation of the phenol OH-group has been observed in the CSI-MS spectrum, and the connection between an additional absorption maximum at $\lambda = 508$ nm and deprotonation of the functional group has already been shown by Dr. Robin Rudolf[166], the behavior of the system upon acid, respectively base addition has been analyzed. The acid chosen was HNO_3, since nitrate is a common counter anion to

coordination cages and should not disturb the assembly. The base chosen was KOH, K^+ being a counterion to guest molecules commonly used (see chapter 3.3) and found to not disturb cage formation. Since KOH is not readily soluble in DMSO, the solution was setup in H_2O. Since the final amount of H_2O did not exceed a few µl, the effect on the assembly was deemed neglectable, yet further analysis of the influence of the water content tolerated by this system was implemented (Figure 184).

It is noted that, while absorption measurements have been usually performed applying a 1:20 dilution factor, pH and host-guest experiments have been performed at a dilution of only 1:10 to rule out disassembly of the systems. The full spectrum of the following pH titration can be found in the experimental part (Figure 294, experimental part).

a)

b)
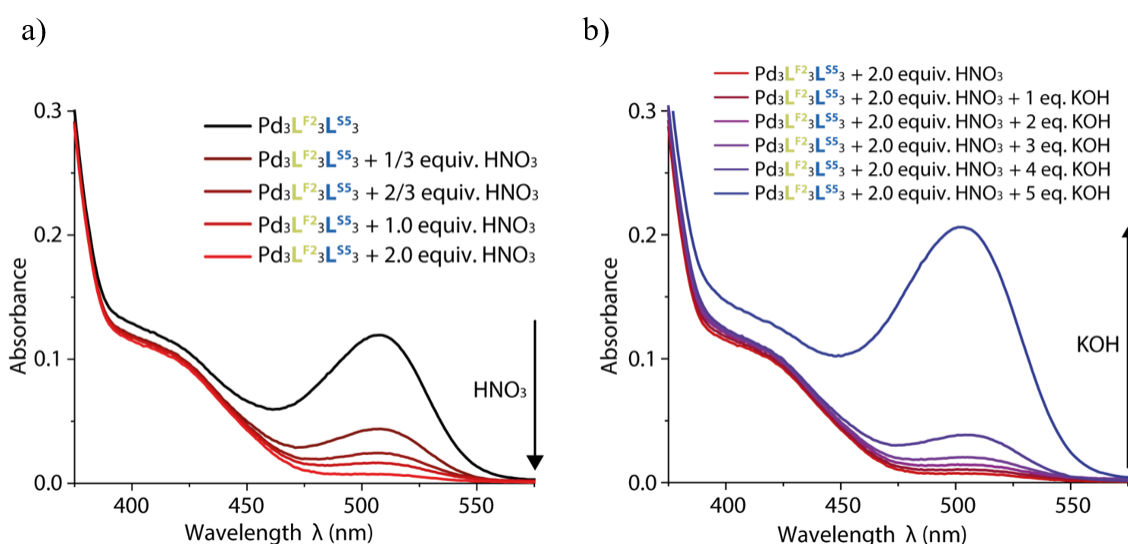
Figure 181: UV/VIS spectra of $Pd_3L^{F2}_3L^{S5}_3$ upon a) addition of HNO_3 (17.5 mM in DMSO-d_6) and b) subsequent addition of KOH (17.5 mM in H_2O).

While the addition of HNO_3 does not result in a shift of the maximum at $\lambda = 284$ nm, the absorption maximum at $\lambda = 508$ nm shows a substantial decrease upon acid addition reaching almost 0 upon addition of 2 equiv.. Subsequent base addition leads to reappearance and following hyperchromic shift of the band, yet also a slight hypsochromic shift by 5 nm could be observed resulting in a local absorption maximum at $\lambda = 503$ nm. Furthermore, the absorption maximum at $\lambda = 284$ nm was subjected to a bathochromic shift to approximately $\lambda = 290$ nm (accuracy is not given due to A > 1) and the shoulder at $\lambda = 338$ nm exhibits a hypochromic shift upon base addition. The observed shifts could be due to the increase of water content or a structural change, possible a second deprotonation event. The isosbestic point of the titration is at $\lambda = 360$ nm (Figure 294, experimental part). Since the curves maintained their overall shape over the course of the measurement, the integrity of the structure can be assumed. Furthermore, none of the homoleptic assemblies, nor the free ligands exhibit an

absorption maximum beyond 500 nm, thus leaving the conclusion that this is exclusive to the deprotonation of the OH-group in this coordination environment. To confirm these results, a titration with purely water as a control experiment is needed.

This particular property could be utilized as means to determine pK_a values for organic molecules in DMSO. While there are protocols for this kind of analysis,[174,175] the coordination assembly forms fast and clean and is, in its primary form, already deprotonated to some extent, thus the effect of base and acid addition can be studied without previous preparations. Furthermore, the result can be observed via a simple optical readout in the decrease or increase of a single local maximum in the absorption spectrum. To establish a valid protocol for pK_a determination in DMSO, effects from the water content of the used DMSO and other error factors have to be either ruled out or quantified and taken into consideration.

As a first attempt to utilize the system in the proposed way, one equivalent of each nucleobase was added to a solution of $Pd_3L^{F2}_3L^{S5}_3$ while the absorption (1:10 dilution) was measured before and after addition of the respective nucleobase.
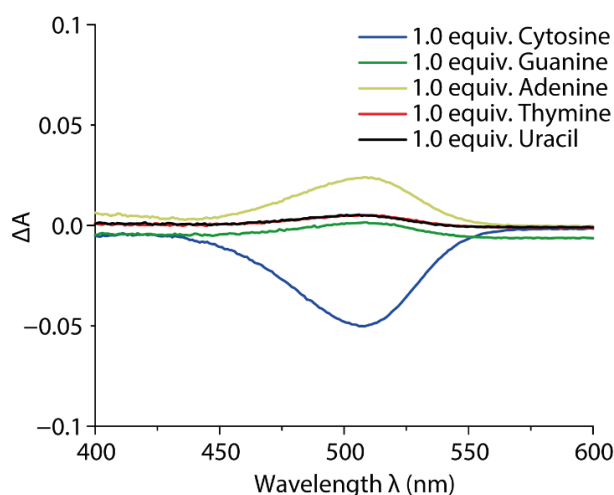
Figure 182: Difference in absorption of the native $Pd_3L^{F2}_3L^{S5}_3$ species and the same sample after addition of 1 equiv. of nucleobase.

As Figure 182 shows, ΔA at λ_{508nm} differs from zero, thus an effect of the addition on the protonation status of $Pd_3L^{F2}_3L^{S5}_3$ can be assumed. While there is a very minimal effect ($\Delta A < 0.006$) for guanine, thymine and uracil, more significant changes could be observed for cytosine ($\Delta A = -0.05$) and adenine ($\Delta A = 0.024$). Whereas $\Delta A > 0$ for adenine, guanine, thymine and uracil indicating further deprotonation of the $Pd_3L^{F2}_3L^{S5}_3$ assembly (thus, the nucleobases reacting as Brønsted bases), it is $\Delta A < 0$ for cytosine which would suggest an increase in protonation of the assembly, whereas cytosine would react as a Brønsted acid. This observation, alongside with the different dimension ΔA for

cytosine and adenine however cannot be explained with known *pKa* values found in literature.[176,177]

As the presented reference data does not give any coherent conclusions, further experiments and investigation is required.

The susceptibility of $Pd_3L^{F2}_3L^{S5}_3$ to acid, respectively base addition, has additionally been followed by ^1H NMR titration.
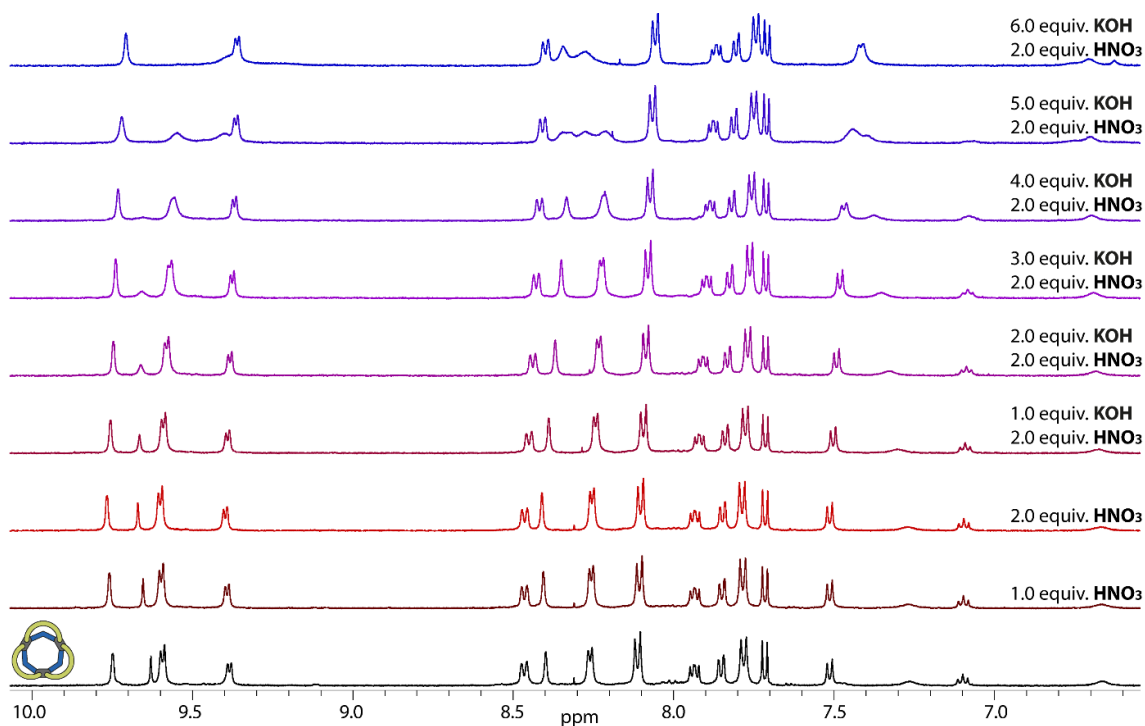
Figure 183: Partial ^1H NMR spectra (500 MHz, 298 K, DMSO-d_6) of heteroleptic $Pd_3L^{F2}_3L^{S5}_3$ upon addition of first HNO_3 (17.5 mM in DMSO-d_6) and then KOH (17.5 mM in H_2O).

Figure 183 shows that the assembly is stable in between the addition of up to 2 equiv. HNO_3 (17.5 mM in DMSO-d_6) followed by up to 6 equiv. KOH (17.5 mM in D_2O). In addition to the previously reported visible shift in color, shifts of protons around the OH-group and the coordination sphere can be observed upon acid addition. Protons H^1, H^2, H^a and H^e shift downfield upon addition of one, respectively two equivalents of HNO_3. Additionally, proton H^9 also shows a downfield shift as opposed to proton H^4, which is located out of vicinity of the OH group. Proton H^9 being affected by acid addition could either be explained by the OH group pointing towards H^9 or a protonation of the carbonyl functional group of ligand L^{F2}. A protonation there however would affect proton H^8 and its shift is entirely unaltered. Upon KOH addition, a shift of all signals to the upfield can be observed. This however, can be attributed to the increase in D_2O content, thus the effect of the base itself cannot be deduced from the shift of the signals. Repetition of the experiment with a different base, which is soluble in DMSO could yield proper insight into

base-related behavior of the system. While the shift itself cannot be used to determine the base's effect on the assembly, the shape of the signals and the integration values of specifically the OH proton H^e do allow an interpretation to some extent. Considering the shape of the signals first, all signals of $\mathbf{L^{S5}}$ broaden upon addition of KOH. Furthermore, broadening of the signal attributed to proton H^9 can be observed. Since it is safe to assume, that at least one water molecule is present inside the assembly, evidenced from the NOE cross peak to H_2O, (Figure 290, experimental part), the broadening might stem from the rapid dynamics of forming hydrogen bonds. Since KOH is added in D_2O medium, the water content increases by a substantial amount with each addition of base making an interaction at the more and more deprotonated phenol-backbones even more likely. Furthermore, $-O^-$ is a more potent H-bond acceptor compared to -OH. VT measurements could verify this claim as speeding up the exchange kinetics could lead to sharpening of the signals in question. Further information can be derived from the integral value of the phenol OH proton H^e (Table 7).

Table 7: Relative integral values of the signal attributed to the OH-function of $Pd_3\mathbf{L^{F2}}_3\mathbf{L^{S5}}_3$ after given acid (HNO_3) and base (KOH) addition. The value at 2 equiv. HNO_3 and 0 equiv. KOH has been assigned to be 100%. Due to the signal diminishing and broadening, no values can be given for 5, respectively 6 equiv. KOH.

Integral Value (%)	HNO$_3$ (equiv.)	KOH (equiv.)
100	2	0
96	2	1
42	2	2
36	2	3
17	2	4
n.a.	2	5
n.a.	2	6

After adding 2 equiv. HNO_3 to the solution of $Pd_3\mathbf{L^{F2}}_3\mathbf{L^{S5}}_3$, it turns yellow. This change could be attributed to the protonation of the partly deprotonated OH-groups. Thus, the integral value of H^e was set to 100% after addition of 2 equiv. HNO_3 deeming the assembly fully protonated (100%). The integral value increased from 91% in the complex after setup to 100%, yet CSI-MS measurement would solidify the stated assumption further.

A most peculiar situation can be observed at 2 equiv. HNO_3 and 5 equiv. KOH addition (Figure 183). While the addition of KOH lead to H^e no longer being detectable, broadening of the signals corresponding to $\mathbf{L^{S5}}$ and proton H^9 of $\mathbf{L^{F2}}$ as described before, at 5 equiv. KOH an approximate 1:1 splitting of the herein mentioned signals can be

observed in addition to broadening. The effect is gone after the addition of one more equivalent of base, thus leaving to conclude the effect being due to different protonation states present in the system at the same time. Furthermore, the shift of the split signals resembles the situation after 4 equiv., respectively 6 equiv. KOH addition, leaving to conclude that two out of three OH-groups are deprotonated after 4 equiv. KOH and three out of three after 6 equiv. with the situation at 5 equiv. base addition being an intermediate state. The splitting of H^9 suggests its close proximity to the deprotonated OH-group as it is the only signal of ligand $\mathbf{L^{F2}}$ that splits. VT measurements and additional pH dependent MS studies could yield further information to the protonation, respectively deprotonation status of the assembly.

While the integrity of the $Pd_3\mathbf{L^{F2}}_3\mathbf{L^{S5}}_3$ assembly and its charge states under basic conditions should be further confirmed by CSI-MS analysis, ^{1}H NMR analysis suggests not only its integrity but also the formation of an assembly carrying positive charges at the Pd(II) centers and negative charges in form of phenolate backbones. Since charged groups in a molecule increase its general polarity and thus water solubility, the effect of water on the deprotonated system was tested. Therefore, two different conditions were chosen, altering the KOH content in the system (5 equiv., respectively 10 equiv. KOH addition before water addition; Figure 404, experimental part). It is noted, that the increase in water content led to a decrease in assembly concentration, thus possibly affecting the general stability.
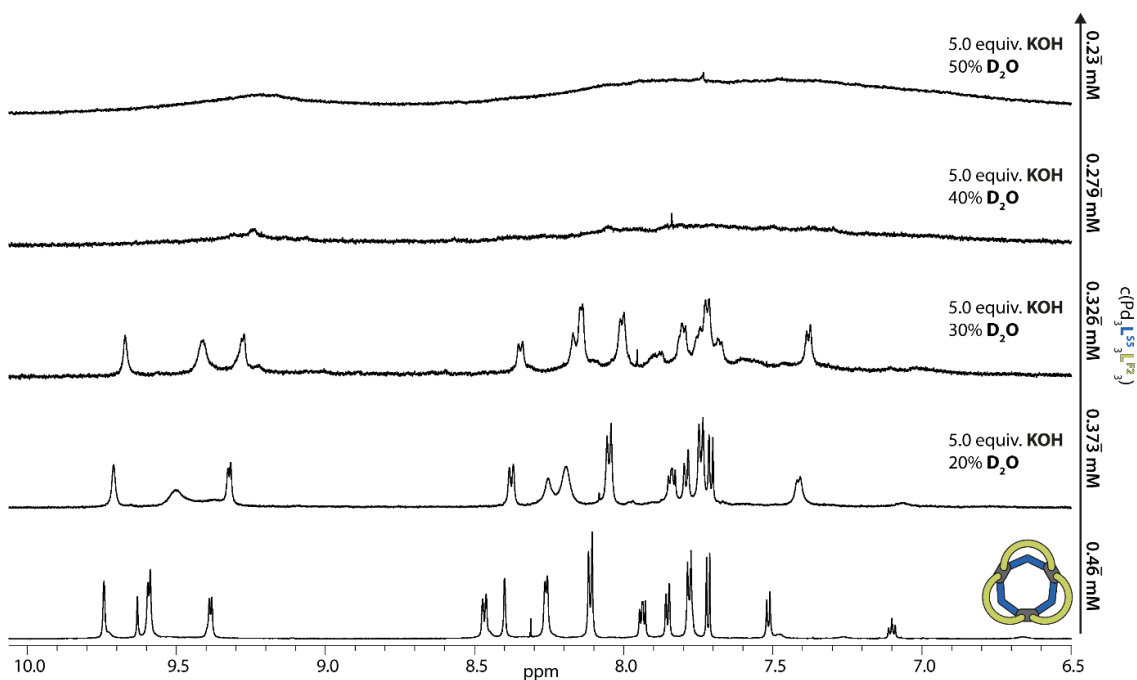
Figure 184: Partial ^{1}H NMR spectra (500 MHz, 298 K, DMSO-d$_6$) of $Pd_3\mathbf{L^{F2}}_3\mathbf{L^{S5}}_3$ after addition of 5 equiv. KOH (17.5 mM in D$_2$O) and increasing dilution and D$_2$O content.

While the system tolerates both, 5 and 10 equiv. KOH (for 10 equiv. see Figure 404, experimental part) and a D_2O content of 20%, the signal-to-noise ratio decreases notably starting from 30% D_2O addition. This effect is stronger for the system with 10 equiv. KOH, where also new signals start appearing. However, this effect could also be attributed to the dilution of the system and the addition of more Pd(II) could stabilize the assembly. While long term stability has not been analyzed, it is striking that the system, carrying mostly aromatic structural features in its ligands tolerates this amount of water. Increasing the water content above 30% lead to the assembly being no longer detectable, likely due to colloidal aggregation.

While deprotonated Pd$_3$**L$^{F2}_3$L$^{S5}_3$** merely tolerates a water content of 20%, the general observation that introduction of a zwitterion can increase water-solubility, founded the idea to introduce a novel pyridine-donor group that will be described in the following interlude.

3.4.2.6 Interlude – Tackling Water-Solubility

As addressing water solubility is a mayor key point in coordination chemistry, since water is a "clean" solvent and uptake of hydrophobic guests would be amplified in water-soluble coordination cages due to the hydrophobic effect, an accessible and relatively easy method for the introduction of this property into standard organic ligands, as used by many research groups, is herein proposed.
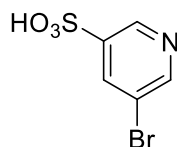
Scheme 23: Structure of 5-bromopyridine-3-sulfonic acid, a commercially available small building block and proposed donor group for water-soluble Pd(II) coordination assemblies.

As MAL et al. already showed, the introduction of sulfonate groups into the backbone of an organic ligand led to it being water soluble.[178] This approach however is very limited in respect to the accessible structures, as the backbone carrying the functional groups responsible for its water solubility cannot be replaced or easily modified. SIVALINGAM et al. recently published a strategy for synthesis of a water soluble Pd(II) coordination cage using multiple polyethylene glycol chains (PEG-chains) attached to the backbone of the ligand.[179] Herein proposed is a modified pyridine donor group directly carrying the sulfonate group (Scheme 23). Since the building block is already equipped with a bromine-residue, it can readily be utilized in standard cross-coupling reactions allowing it to be introduced into basically any meta-pyridine-based donor ligand system with minimal extra effort. It is noted, that this approach is limited to coordination cages based

upon meta-pyridine donor groups, as the repulsive effect (steric and electrostatic) of the sulfonates would likely be too strong in case of para-pyridines and, as an even more pressing reason, the building block not being commercially available.

To analyze the feasibility of the proposed approach, a model-ligand L^{AQ} was synthesized. While the donor angle of L^{AQ} is a very good fit for a homoleptic Pd_2L_4 assembly, the sulfonate group could pose two problems. First, as an electron withdrawing group it is likely to weaken the coordination bond due to electron density being withdrawn from the donor pyridine and second, a strong accumulation of negatively charged groups relatively close to one another could lead to electrostatic repulsion thus preventing the formation of the cage.
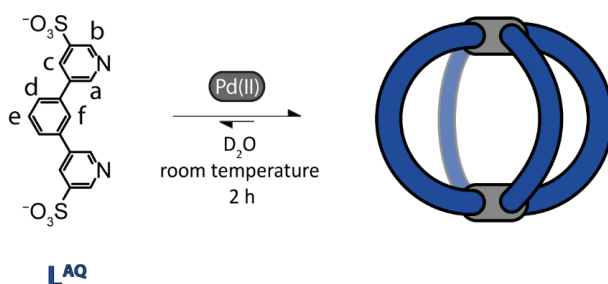
Scheme 24: Formation of $Pd_2L^{AQ}_4$ with consecutive proton labels.
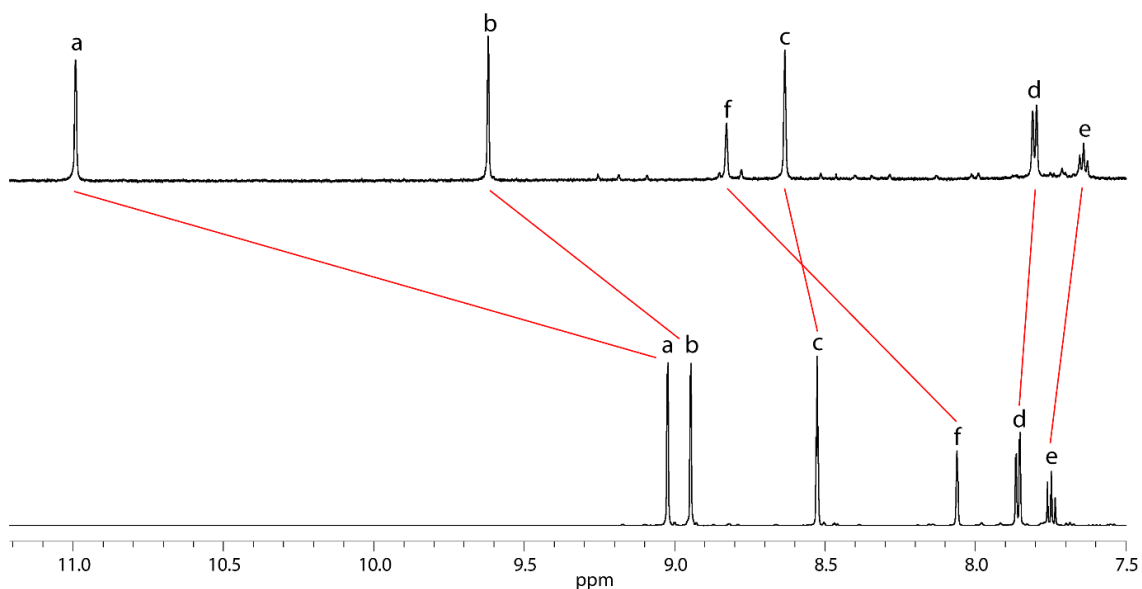
Figure 185: ^{1}H NMR stack of ligand L^{AQ} (600 MHz, 298 K, D$_2$O, bottom) and the corresponding cage $Pd_2L^{AQ}_4$ (600 MHz, 298 K, D$_2$O, top) with proton assignment.

540 µl of a 3.11 mM solution of L^{AQ}+2K in D$_2$O and 60 µl of [Pd(CH$_3$CN)$_4$]OTf$_2$ solution (15 mM in D$_2$O) were combined to form $Pd_2L^{AQ}_4$. As evident from Figure 185, the protons signals of L^{AQ} shift upon addition of Pd(II) cations with the downfield shifts of protons H^a, H^b and H^f being the most pronounced. While the signal of proton H^a is uncommonly strong downfield shifted, this was to be expected hence the previously mentioned

electron withdrawing sulfonate group and even more electron density getting withdrawn by the dative bond leading to strong deshielding of the protons involved. While a strong downfield shift of the signals of the protons around the donor site is a first indication of complex formation, additional analytic procedures are needed to verify the formation of a coordination assembly and furthermore give information about e.g. its nuclearity. Since ESI-MS analysis proved to be difficult and no clean spectrum could be obtained but only one peak at $m/z = 925.8251$ assignable to $[Pd_2L^{AQ}_4+K_2]^{2-}$ was identified (Figure 411, experimental part), ^1H DOSY NMR spectra of ligand L^{AQ} and potential coordination cage $Pd_2L^{AQ}_4$ were measured and the hydrodynamic radii of both species were compared (Figure 186).
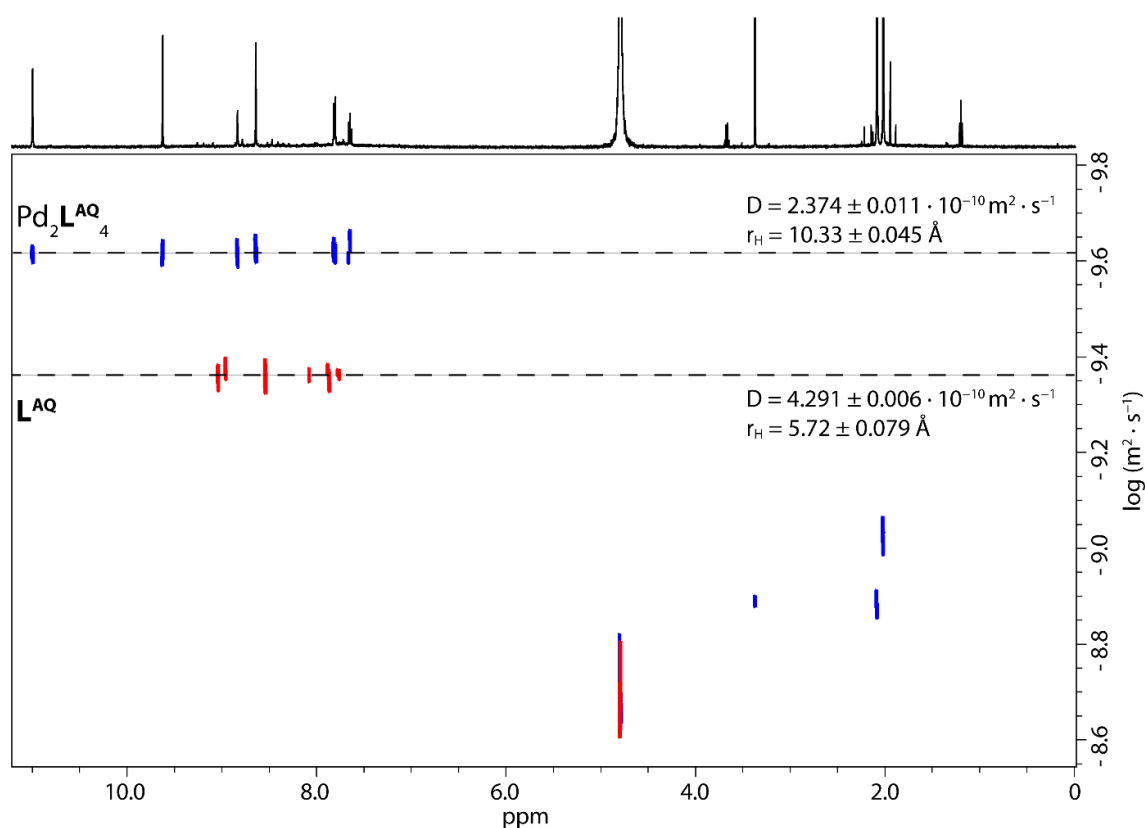
Figure 186: Overlay of the ^1H DOSY NMR spectra (500 MHz, 298 K, D_2O) of L^{AQ} and $Pd_2L^{AQ}_4$. Values for diffusion coefficients and resulting hydrodynamic radius are given.

While L^{AQ} has a hydrodynamic radius of $r_H = 5.72$ Å, the species formed upon Pd(II) addition is significantly larger, with a hydrodynamic radius $r_H = 10.33$ Å. Comparison with other Pd(II) assemblies of similar ligands allows to conclude the formation of a binuclear complex of the Pd_2L_4 type and thus the successful synthesis of a water-soluble coordination cage utilizing this novel pyridine donor group.
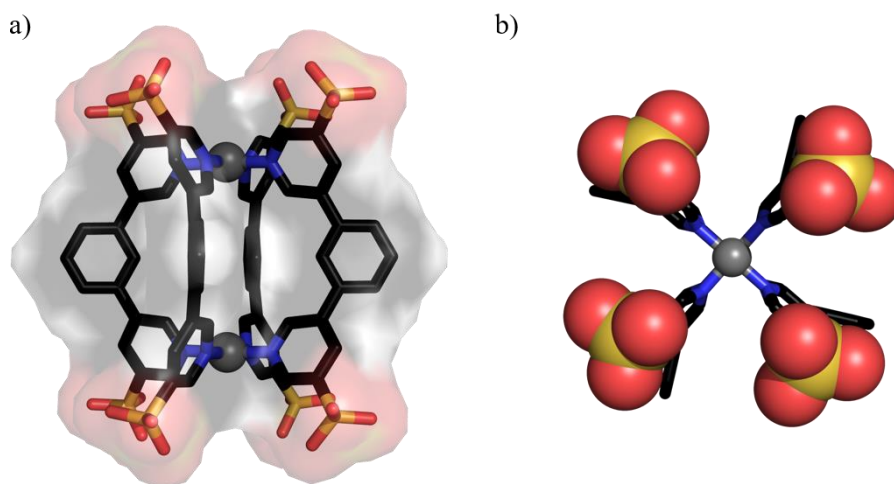
Figure 187: *In silico* model of Pd$_2$**L**$^{AQ}_4$ a) side view (sticks overlaid with surface representation) b) top view with sphere representation for sulfonate groups. Hydrogens are omitted for clarity. Structure optimized with GFN0-xTB.

Figure 187 shows an *in silico* model of the cage including its surface representation (Figure 187, a) and a spherical representation of the sulfonate-groups (Figure 187, b) to emphasize on their steric demand and distance in the assembly. As evident from the model, the negatively charged groups are sufficiently distanced as also the delocalization of the negative charge over the three oxygen-atoms has to be taken into consideration. The overall charge of the assembly would be 4−, while the inner cavity will have a high local positive charge due to the Pd(II) centers. This made ESI-MS analysis difficult, as previously mentioned, since negative and positive counterions alike can associate to the cage.

Implementing this novel approach into the previously discussed Pd$_3$**L**$^{F2}_3$**L**$^{S5}_3$ assembly, to use it in heteroleptic assemblies, could yield a zwitterionic supramolecular assembly, that is formally neutral but carries high local charges thus enabling water-solubility.
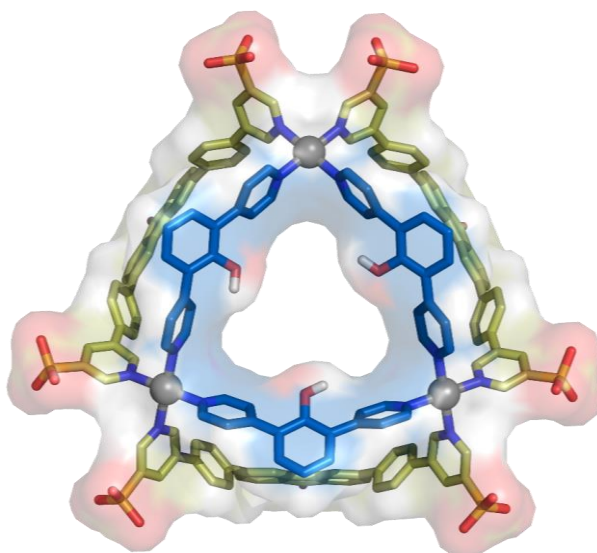
Figure 188: Proposed structure of a water-soluble modification of Pd$_3$**L**^{F2}$_3$**L**^{S5}$_3$ equipped with sulfonate-groups attached to its donor sites (calculated on PM6 theory level).

The above depicted modified version of **L**^{F2} can be readily accessed with the previously mentioned building block (Scheme 23) and 3,6-dibromo-9H-fluoren-9-one in a two-step synthesis with consecutive SUZUKI-coupling reactions using 1,4-bis(4,4,5,5-tetramethyl-1,3,2-dioxaborolan-2-yl)benzene as depicted in Scheme 25.
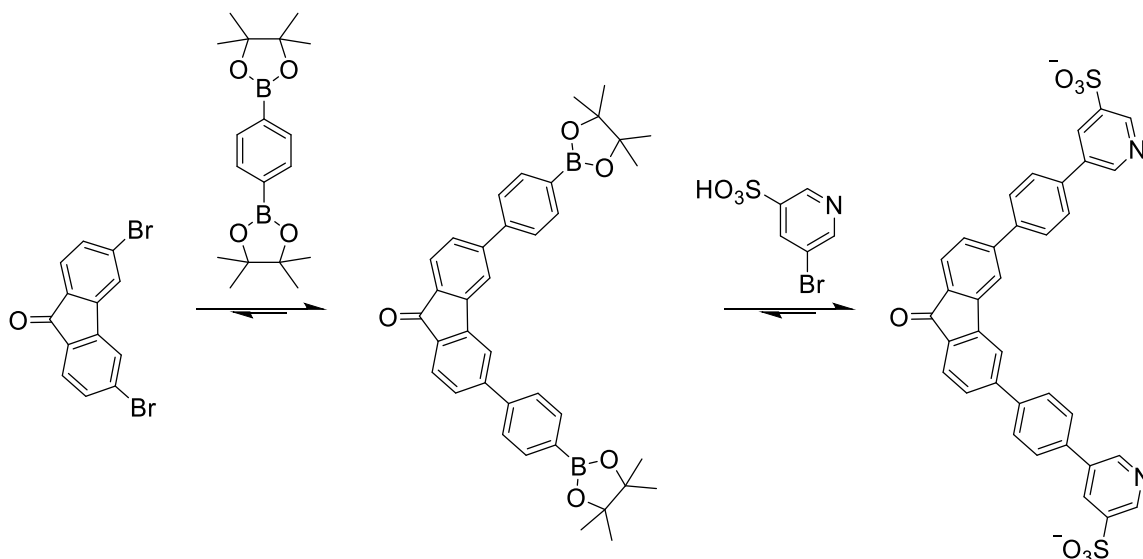
Scheme 25: Proposed reaction for the synthesis of a modified **L**^{F2} carrying sulfonate groups directly attached to the pyridine-donor groups as to access water solubility.

Step one can be worked up according to regular workup procedures including column chromatography and successive GPC separation. A clean educt is highly recommended before proceeding with step two. Depending on the base used for the last cross-coupling, the counter cation of the ligand can be altered appropriately.

While the final product of the self-assembly process of **L**^{FAQ} and **L**^{S5} would be a neutral molecule, deprotonation of the phenol-groups as shown before can increase the negative

charge of the molecule thus making it accessible for ESI-MS measurement. While the workup of the synthesized ligands will differ depending on the backbone, the use of this novel donor group could help to access water solubility with formerly unpolar ligands.

3.4.2.7 Summary: $Pd_3L^{F2}_3L^{S1-5}_3$

In summary, a novel $Pd_3L^A_3L^B_3$ topology has been achieved forming an open structured molecular assembly while maintaining the fluorescent properties of ligand L^A, adding the implementation of functional groups with ligand L^B. The system tolerates multiple functional groups as for example introduction of primary amines (L^{S3}) which are a relatively rare occurrence in supramolecular assemblies. The two preliminary X-ray structures obtained (Figure 164 and Figure 169) show, that the system has a certain degree of conformational freedom despite consisting of very rigid ligands. Coordination to Pd(II) altered the properties of the ligands, e.g. L^{S5}, carrying an -OH group, shows an increased acidity in the assembly as opposed to the free ligand. While ligand L^{F2} maintains its fluorescent properties in all five assemblies, there are differences in the corresponding quantum yield (Figure 189 and Table 8).
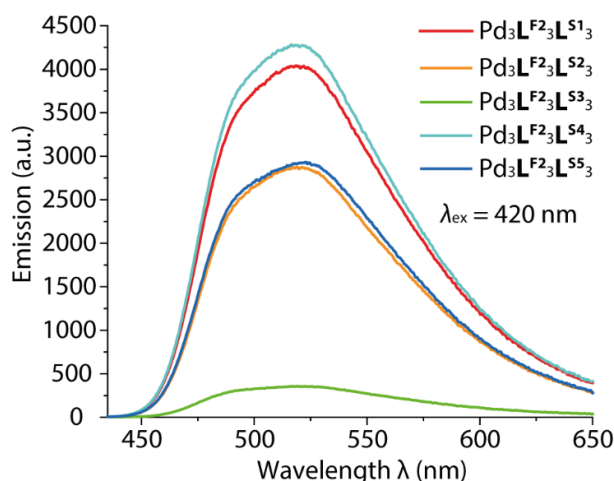
Figure 189: Absolute emission measured of $Pd_3L^{F2}_3L^{S1-5}_3$. Measurement parameters were kept constant throughout the test series (λ_{ex} = 420 nm; $c_{chromophore}$ = 0.14 mM).

While the fluorescence of L^{F2} in $Pd_3L^{F2}_3L^{S3}_3$ is mostly quenched, likely due to non-radiative H-bonding processes of the primary amine with the solvent DMSO and residual water present in the latter mentioned, $Pd_3L^{F2}_3L^{S1}_3$ and $Pd_3L^{F2}_3L^{S4}_3$ display even higher fluorescence quantum yield than the homoleptic assembly $Pd_nL^{F2}_{2n}$ (n = 2-5) L^{F2} forms upon Pd(II) addition (Table 8). Herein, the system provides not only the possibility of a fluorescence readout, but directly supplies a system ($Pd_3L^{F2}_3L^{S1}_3$ or $Pd_3L^{F2}_3L^{S4}_3$) to run control experiments in future applications as e.g. catalysis studies ($Pd_3L^{F2}_3L^{S3}_3$) or pK_a sensing ($Pd_3L^{F2}_3L^{S5}_3$).

Table 8: Measured quantum yields (λ_{ex} = 420 nm; $c_{chromophore}$ = 0.14 mM) for ligand $\mathbf{L^{F2}}$, the corresponding homolpetic $Pd_n\mathbf{L^{F2}}_{2n}$ (n = 2-5) mixture it forms upon Pd(II) addition and heteroleptic $Pd_3\mathbf{L^{F2}}_3\mathbf{L^{S1-5}}_3$.

Structure	Quantum Yield (%)
$\mathbf{L^{F2}}$	13.406
$Pd_n\mathbf{L^{F2}}_{2n}$ (n = 2-5)	0.824
$Pd_3\mathbf{L^{F2}}_3\mathbf{L^{S1}}_3$	1.102
$Pd_3\mathbf{L^{F2}}_3\mathbf{L^{S2}}_3$	0.835
$Pd_3\mathbf{L^{F2}}_3\mathbf{L^{S3}}_3$	0.256
$Pd_3\mathbf{L^{F2}}_3\mathbf{L^{S4}}_3$	1.122
$Pd_3\mathbf{L^{F2}}_3\mathbf{L^{S5}}_3$	0.920

As shown in the previous chapter, $\mathbf{L^{F2}}$ is able to provide as a FRET partner in an appropriate system and with a huge open cavity present in these new kind of molecules, host-to-guest FRET could be realized. Furthermore, the bowl-like structure provides enough space for multi-guest encapsulation while having no vacant coordination sites to weaken the structure or interfere with its guest molecules. The combination of a fluorescent ligand and an easily functionable ligand provides a versatile system in which the appropriate counter ligand can be chosen depending on the desired application. Further structural elucidation of the systematics heteroleptic cages based on the rigid $\mathbf{L^{F2}}$ ligand and a short counter ligand $\mathbf{L^S}$ will be described in the following part, as of means to determine the boundaries of the system regarding ligand $\mathbf{L^S}$.

3.4.3 Structural Analysis – Accessing Structures of Higher Nuclearity

3.4.3.1 $Pd_4\mathbf{L^{F2}}_4\mathbf{L^{S6}}_4$ – Electrostatic Repulsion

While ligands $\mathbf{L^{S1-5}}$ combined with $\mathbf{L^{F2}}$ in a 1:1 fashion with 0.55 equiv. Pd(II) yielded clean $Pd_3\mathbf{L^A}_3\mathbf{L^B}_3$ assemblies, the effect of further functional groups and ligand backbones will be studied in this part. The first ligand to be elucidated was $\mathbf{L^{S6}}$, based on a nitrobenzene backbone, which has also been synthesized by Dr. Robin Rudolf in the scope of his PhD thesis[166]. While its size does not deviate substantially from $\mathbf{L^{S3}}$ (aniline backbone), its electronic properties differ vastly.

270 µl of a 3.11 mM solution of $\mathbf{L^{F2}}$ in DMSO-d_6 were combined with 270 µl of a 3.11 mM solution of $\mathbf{L^{S6}}$ in DMSO-d_6 with 60 µl of a 15 mM solution of $[Pd(CH_3CN)_4](OTf)_2$ in a 5 mm standard NMR tube and either heated to 70°C for 5 minutes or let to rest at room temperature for 2h to afford a clean spectrum of a new species $Pd_4\mathbf{L^{F2}}_4\mathbf{L^{S6}}_4$ (Scheme 26).
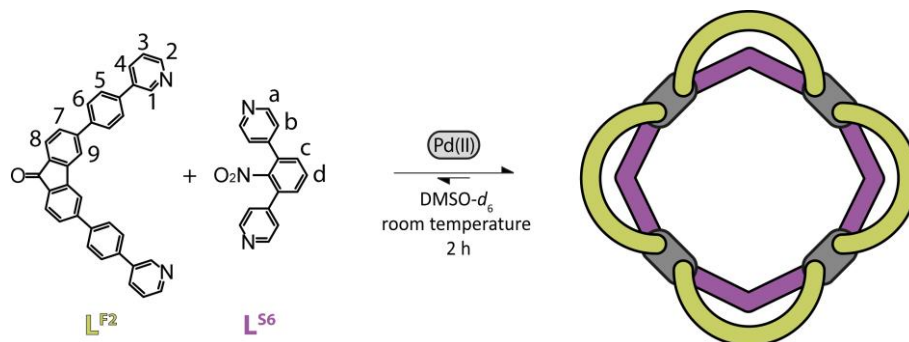
Scheme 26: Formation of $Pd_4L^{F2}_4L^{S6}_4$ with consecutive proton labels.

As Scheme 26 already suggests, L^{F2} combined with L^{S6} in a 1:1:1 manner with Pd(II) cations does no longer form a trinuclear complex, but a tetranuclear one. This information however could not be directly deduced from the ^{1}H NMR spectrum (Figure 190, c)) as it shows clean assembly formation with signal shifts not too different from the previously reported systems.
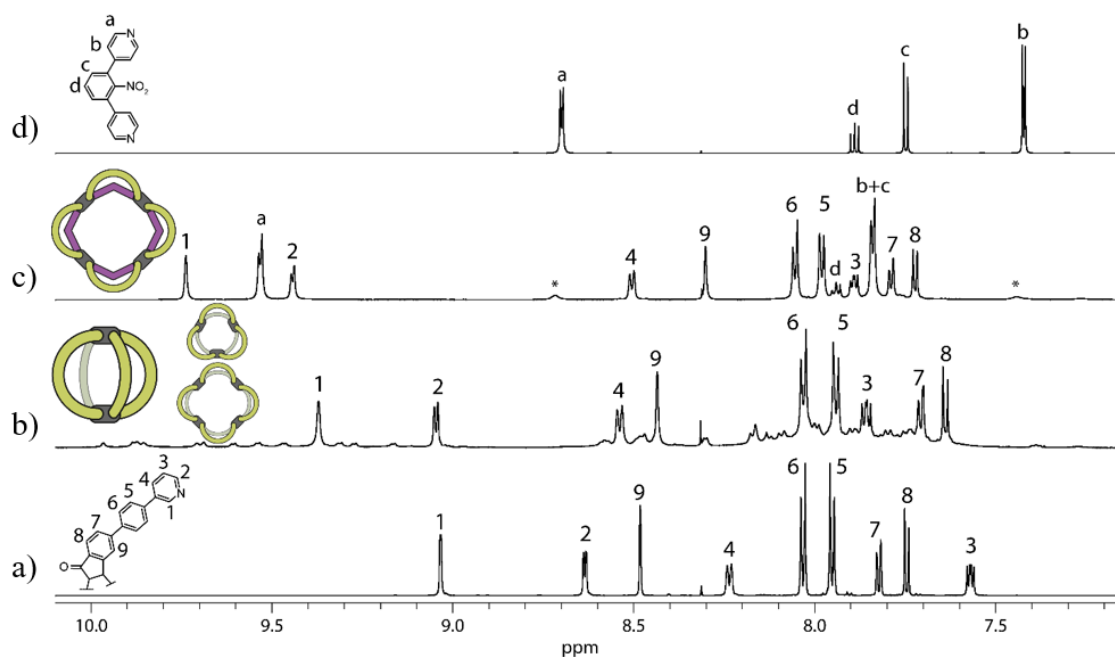
Figure 190: Partial ^{1}H NMR spectra of a) ligand L^{F2} (700 MHz, 298 K) b) homoleptic $Pd_2L^{F2}_4$ cage and the $Pd_nL^{F2}_{2n}$ (n=3-5) rings formed upon addition of 0.55 equiv. Pd(II) cations to ligand L^{F2} (600 MHz, 298 K) c) heteroleptic $Pd_4L^{F2}_4L^{S6}_4$ (700 MHz, 298 K) d) ligand L^{S6} (700 MHz, 298 K) in DMSO-d_6.

The spectrum shows 12 distinguishable signals while 13 were to be expected. 2D NMR experiments (Figure 299 and Figure 300, experimental part) however showed an overlap of the signals corresponding to protons H^b and H^c, this information also matching with the integral value of the signal relative to the others. Further two broad signals at $\delta = 7.44$ and $\delta = 8.72$ ppm were observed, which were not attributed to the assembly (Figure 299 to Figure 301, experimental part). Prolonged heating of the solution lead to an increase in intensity of these signals and, upon reaching a certain level, disassembly of

$Pd_4L^{F2}_4L^{S6}_4$. Since the effect could also be observed for the homoleptic mixture of 2:1 L^{S6} and $[Pd(CH_3CN)_4](OTf)_2$ (Figure 296, experimental part), it is safe to assume that this effect stems from the nitro-group bearing ligand L^{S6}, whereas up until now no conclusive explanation for the effect could be found. Protons H^1, H^a and H^b show a substantial downfield shift while proton H^9 shifts into the upfield. As stated before, this behavior shares great resemblance with the previously mentioned systems $Pd_3L^{F2}_3L^{S1-5}_3$. While an ^1H DOSY experiment presented only one species, the hydrodynamic radius derived from the measurement was notably high, equaling to $r_H = 16.57$ Å (Figure 301, experimental part), that being approximately 2 Å more than obtained for the previous five systems ($r_H = 14.14$-14.78 Å). A CSI-MS measurement proved the existence of only tetranuclear species as no trinuclear complexes could be found.
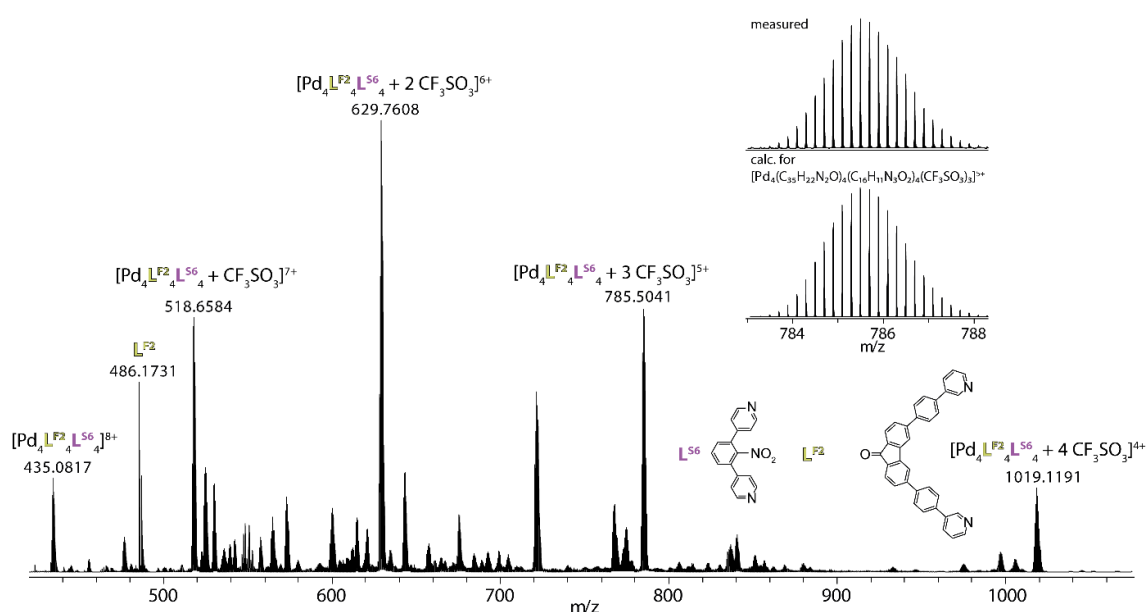
Figure 191: CSI-MS spectrum of heteroleptic $[Pd_4L^{F2}_4L^{S6}_4 + xCF_3SO_3]^{(8-x)+}$ (x = 0-4). The measured and calculated isotopic patterns of the highest peak are shown in the inset.

Detected peaks at m/z = 435.0817 (8+), 518.6584 (7+), 629.7608 (6+), 785.5041 (5+), 1019.1191 (4+) could all be assigned to the tetranuclear complex with the chemical composition of $[\mathbf{Pd_4L^{F2}_4L^{S6}_4} + xCF_3SO_3]^{(8-x)}$ (x = 0-4). While the applied measurement parameters were similar, the mass spectrum turned out to be much noisier. The assembly seems to be less stable without its solvent shell, which could stem from its size and thus lower overall concentration upon sample preparation or repulsive effects in the central ring caused by the nitro-groups. With both, ^1H DOSY NMR and CSI-MS data, being in agreement, it is safe to assume the exclusive formation of a tetranuclear assembly with the composition $Pd_4L^{F2}_4L^{S6}_4$.

The 1:1:1 combination of L^{F2}, L^{S3} (aniline-backbone) and Pd(II) yields heteroleptic $Pd_3L^{F2}_3L^{S3}_3$, the same combination with L^{S6} (nitrobenzene-backbone) yields $Pd_4L^{F2}_4L^{S6}_4$.

While there certainly is a size difference in these functional groups, thus yielding an increase in steric demand, it should not exceed that of the methoxy-group present by L^{S4}, which still forms a trinuclear complex with L^{F2} upon Pd(II) addition. While rotation of the methoxy-group has to be taken into consideration, it is quite limited due to the tipping of the short ligands backbone towards the center of the assembly. Deeming the steric effect of the nitro-group neglectable leaves electrostatic repulsion as a possible explanation for the change from trinuclear to tetranuclear complex. Simple *in silico* models (PM6 theory level) were calculated for both, $Pd_3L^{F2}_3L^{S6}_3$ and $Pd_4L^{F2}_4L^{S6}_4$ (Figure 192).
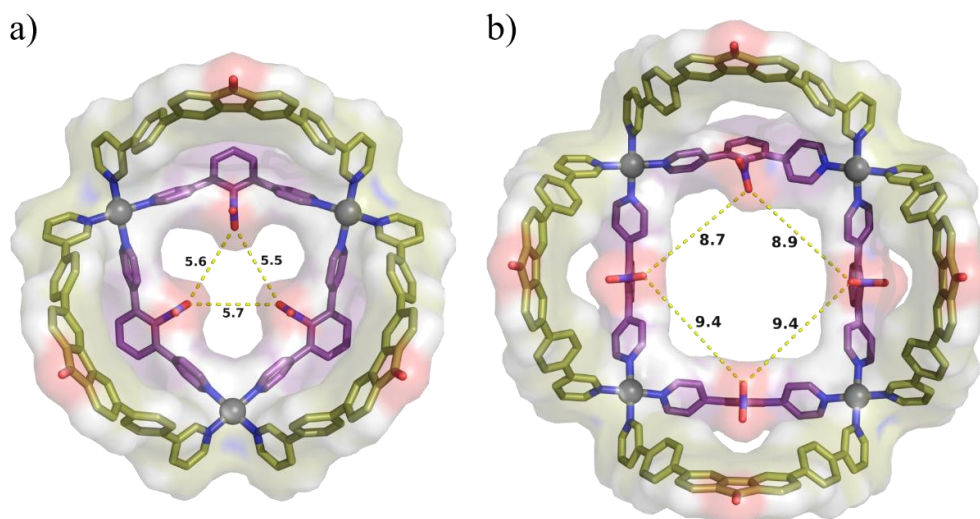
Figure 192: Model of heteroleptic $Pd_3L^{F2}_3L^{S6}_3$ and $Pd_4L^{F2}_4L^{S6}_4$ (sticks overlaid with surface representation) a) side view b) top view. Hydrogens are omitted for clarity. The closest distances (given in Å) between nitro-groups is given for both structures. Calculated on semi-empirical PM6 theory level.

While the amino-group in L^{S3} carries partial charges, the nitro-groups of L^{S6} carry formal charges where the nitrogen atom is formally charged positive and the negative charge is delocalized over the two oxygen atoms yielding a neutral over all charge for the functional group. To analyze the effect, that the nitro-groups have on one another dependent on whether a tri- or tetranuclear assembly is formed, COULOMB's Law can be employed.

$$|F| = k_e \frac{|q_1 \times q_2|}{r^2}$$

(1)

F is the electrostatic force between two point-charges q_1 and q_2, while k_e is the COULOMB constant ($k_e \approx 8.988 \cdot 10^9$ N·m²·C⁻²). With both charged partners involved being chemically equivalent, it can be assumed $q_1 = q_2$ and with k_e being constant, F is entirely dependent on r, so the distance between the two charged oxygens. With $r \approx 5.6$ Å in the 3-ring, while $r \approx 9.1$ Å in the 4-ring (averaged over all measurements) the value for F in the tetranuclear environment is smaller by a notable factor of 2.64 as compared to the

trinuclear environment. Considering the measured data, the repulsive force in the trinuclear assembly seems too high and the system relaxes into the next best thermodynamically stable structure, that being $Pd_4L^{F2}_4L^{S6}_4$.

This consideration can also be applied to the fully deprotonated $Pd_3L^{F2}_3L^{S5}_3$, which would carry three -O⁻ groups pointing into the central ring. The average distance of the oxygen-atoms in this case would be $d \approx 7.5$ Å in the trinuclear complex, which seems to be tolerated by the system (see chapter 3.4.2.5), though CSI-MS studies are required to verify the nuclearity of the deprotonated system, ruling out a quick reorganization from trinuclear to tetranuclear assembly. A comparison of these two systems in terms of factors however, cannot be readily made since the functional groups are different and thus carry different values for q.

To visualize the effect herein described, electrostatic potential maps for $Pd_3L^{F2}_3L^{S6}_3$ and $Pd_4L^{F2}_4L^{S6}_4$ have been calculated (GFN0-xTB,[180] Figure 193).
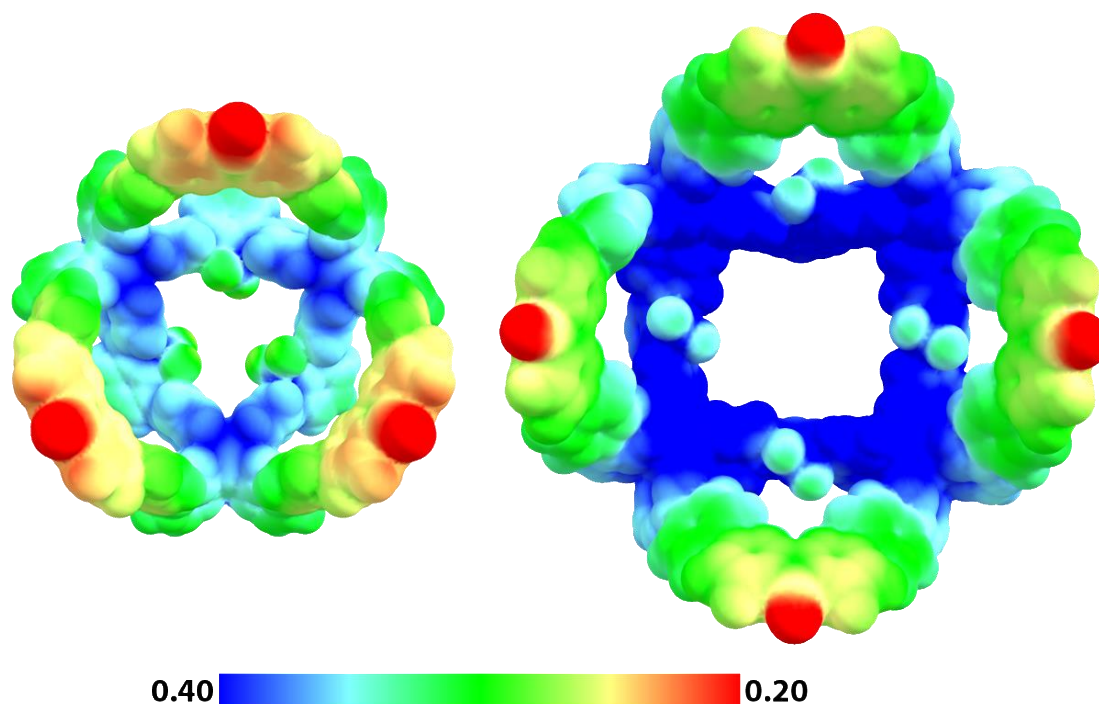
Figure 193: Electropotential maps of heteroleptic $Pd_3L^{F2}_3L^{S6}_3$ (left) and $Pd_4L^{F2}_4L^{S6}_4$ (right). *In silico* models were optimized using GFN0-xTB.[180] The same scale applies to both molecules.

The accurate calculation verifies the simple assumption previously made based on COULOMB's law considering solely the distance of the repulsive groups. Figure 193 shows the calculated COULOMB potential for the whole molecule for both, $Pd_3L^{F2}_3L^{S6}_3$ and $Pd_4L^{F2}_4L^{S6}_4$. While the potential is inheritly positive over the entire molecule, which is not surprising considering it being hexa- or octacationic, differences from trinuclear to tetranuclear complex are imminent with $Pd_4L^{F2}_4L^{S6}_4$ showing a stronger positive potential

throughout its structure with the overall charge affecting the whole structure. The region of interest however are the nitro-groups pointing inside the central ring. Changes in the calculated COULOMB potential of the nitro-groups in both structures are difficult to assign to their proximity since the effect of the overall charge might be overpowering in respect to their scope. However, combined with the approximation based on COULOMB's law discussed earlier, a feasible explanation for the difference in nuclearity has been proposed making electrostatic repulsion being a valid explanation for the observed nuclearity change.

While the nuclearity of the complex differed from the previously reported $Pd_3L^{F2}_3L^{S1-5}_3$ assemblies, the fluorescence derived from L^{F2} could still be observed, thus the photophysical properties of the complex were measured.
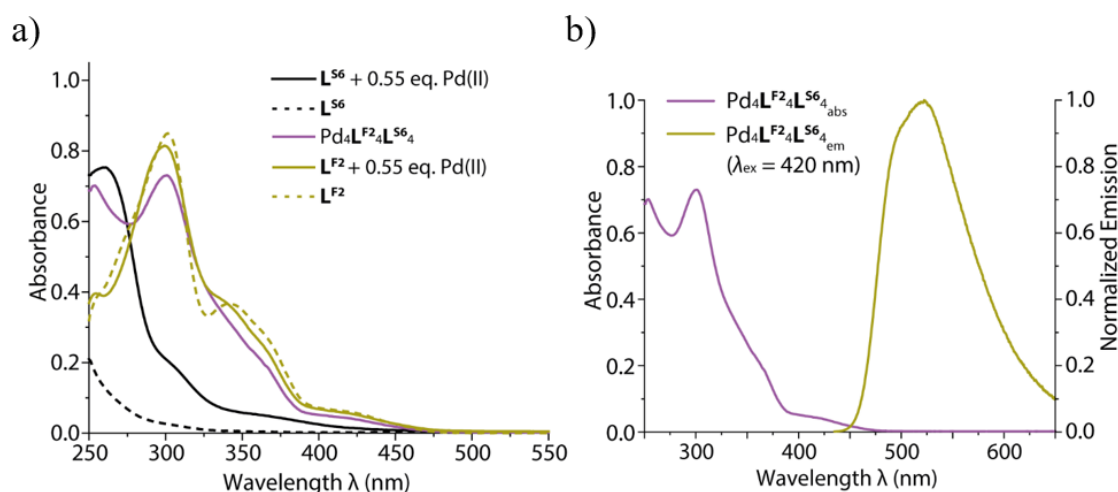
Figure 194: a) UV/VIS spectra of L^{S6}, L^{S6} upon addition of 0.55 equiv. Pd(II), heteroleptic $Pd_4L^{F2}_4L^{S6}_4$, L^{F2} and L^{F2} upon addition of 0.55 equiv. Pd(II), b) absorbance and normalized emission of heteroleptic $Pd_4L^{F2}_4L^{S6}_4$.

Ligand L^{S6} does not show an absorption maximum above $\lambda = 250$ nm, after Pd(II) addition a maximum at $\lambda = 260$ nm and shoulders at $\lambda = 305$ nm and $\lambda = 365$ nm are observed. Heteroleptic $Pd_4L^{F2}_4L^{S6}_4$ bears semblance with the absorption behavior of $Pd_3L^{F2}_3L^{S2}_3$ as it shares the absorption maximum at $\lambda = 300$ nm with a slightly less intense local absorption maximum at $\lambda = 253$ nm. The local minimum in-between these differs however, attributing to $\lambda = 277$ nm for $Pd_4L^{F2}_4L^{S6}_4$ while measuring $\lambda = 266$ nm for $Pd_3L^{F2}_3L^{S2}_3$. The shoulders at $\lambda = 365$ and 420 nm are congruent with $Pd_3L^{F2}_3L^{S2}_3$, albeit slightly more pronounced for $Pd_4L^{F2}_4L^{S6}_4$. Upon exitation at $\lambda = 420$ nm the sample emitted at $\lambda = 520$ nm. Determination of quantum yields did not include tetranuclear complexes, as the set was not completed at that time and their integrity upon dilution has to be fully confirmed beforehand.

The observation that electrostatic repulsion of functional groups inside the central ring of these systems can lead to an increase in nuclearity, while the heteroleptic assembly is still the preferred outcome, begs the question, what structural systematics the systems follows. Therefore, the effect of steric bulk was analyzed utilizing ligands L^{S7} and L^{S8}.

3.4.3.2 L^{S7} and L^{S8} – Introducing Steric Bulk

Ligand L^{S7} can be readily synthesized from L^{S5} by condensation of pivaloyl chloride followed up by extracting the ligand with chloroform and chromatographic purification.

To setup the assembly, 270 µl of a 3.11 mM solution of L^{F2} in DMSO-d_6 were combined with 270 µl of a 3.11 mM solution of L^{S7} in DMSO-d_6 with 60 µl of a 15 mM solution of $[Pd(CH_3CN)_4](OTf)_2$ in a 5 mm standard NMR tube and either heated to 70°C for 2h to afford a mixture of $Pd_3L^{F2}_3L^{S7}_3$ and $Pd_4L^{F2}_4L^{S7}_4$ (Scheme 27). To perform the experiment with utmost care and rule out concentration inaccuracies, the ligand ratio was adjusted pre Pd(II) addition.
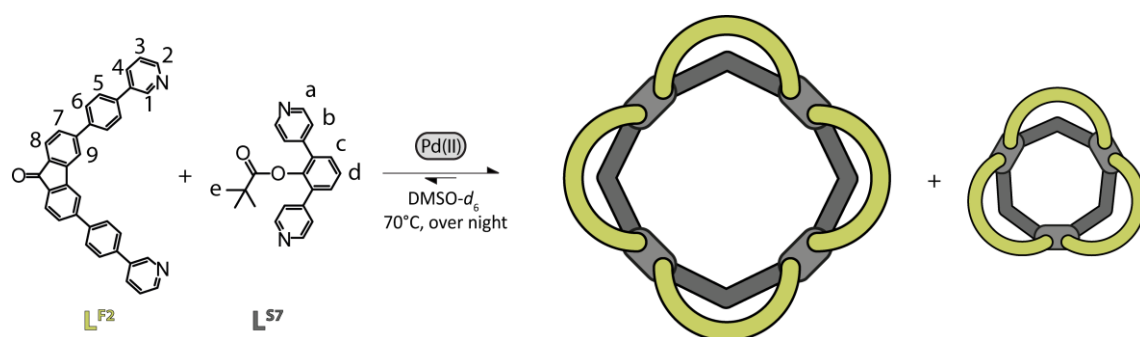
Scheme 27: Formation of the mixture of $Pd_3L^{F2}_3L^{S7}_3$ and $Pd_4L^{F2}_4L^{S7}_4$ with consecutive proton labels.

Figure 195 depicts the aromatic region of the ^{1}H NMR spectra of ligand L^{F2} (Figure 195, a)), the homoleptic mixture L^{F2} forms upon addition of Pd(II) cations (Figure 195, a)), the 1:1:1 mixture of L^{F2}, L^{S7} and Pd(II) cations after heating to 70°C for 2h (Figure 195, c)) and ligand L^{S7} (Figure 195, d)). A spectrum of the homoleptic assembly L^{S7} forms upon Pd(II) addition has not been recorded.
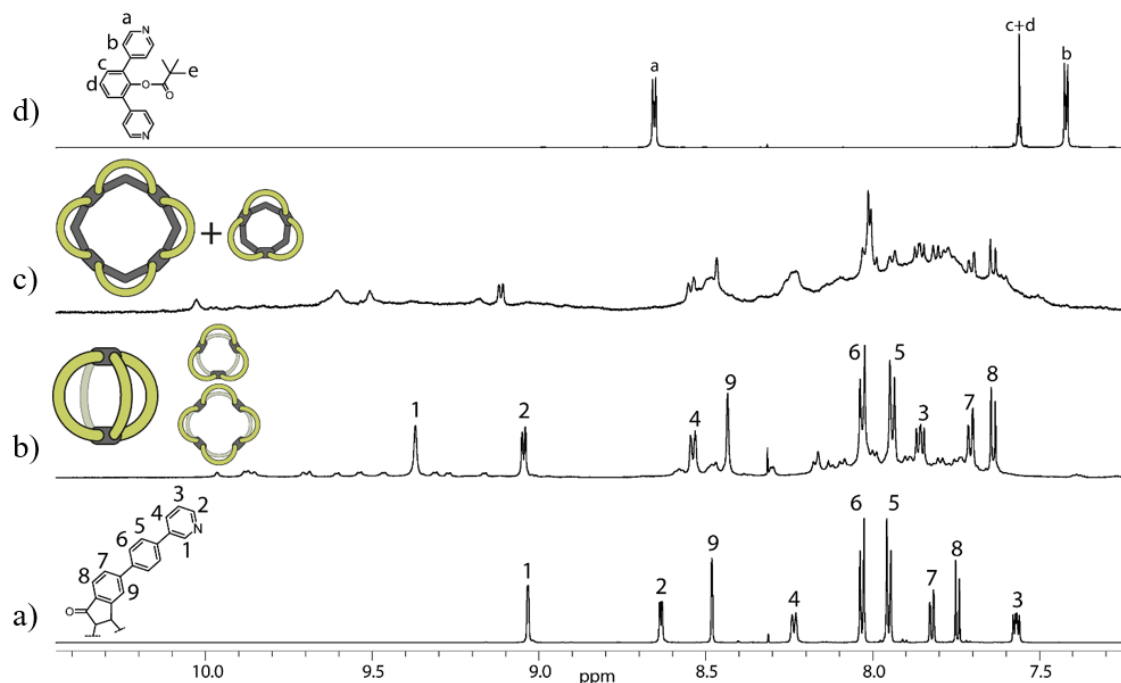
Figure 195: Partial ^{1}H NMR spectra of a) ligand $\mathbf{L^{F2}}$ (700 MHz, 298 K) b) homoleptic $Pd_2L^{F2}_4$ cage and the $Pd_nL^{F2}_{2n}$ (n=3-5) rings formed upon addition of 0.55 equiv. Pd(II) cations to ligand $\mathbf{L^{F2}}$ (600 MHz, 298 K) c) mixture of heteroleptic $Pd_3L^{F2}_3L^{S7}_3$ and $Pd_4L^{F2}_4L^{S7}_4$ (500 MHz, 298 K) d) ligand $\mathbf{L^{S7}}$ (600 MHz, 298 K) in DMSO-d_6.

As evident from Figure 195 c), the spectrum shows neither traces of free ligand $\mathbf{L^{F2}}$, nor its assembly upon Pd(II) addition, nor $\mathbf{L^{S7}}$. However, the spectrum recorded shows broad signals in the downfield with one mayor species formed but smaller signals indicating the formation of subspecies. Further information regarding the sample could be derived from an ESI-MS measurement. Since no clean structure was formed, no cumbersome CSI-MS measurements were performed.
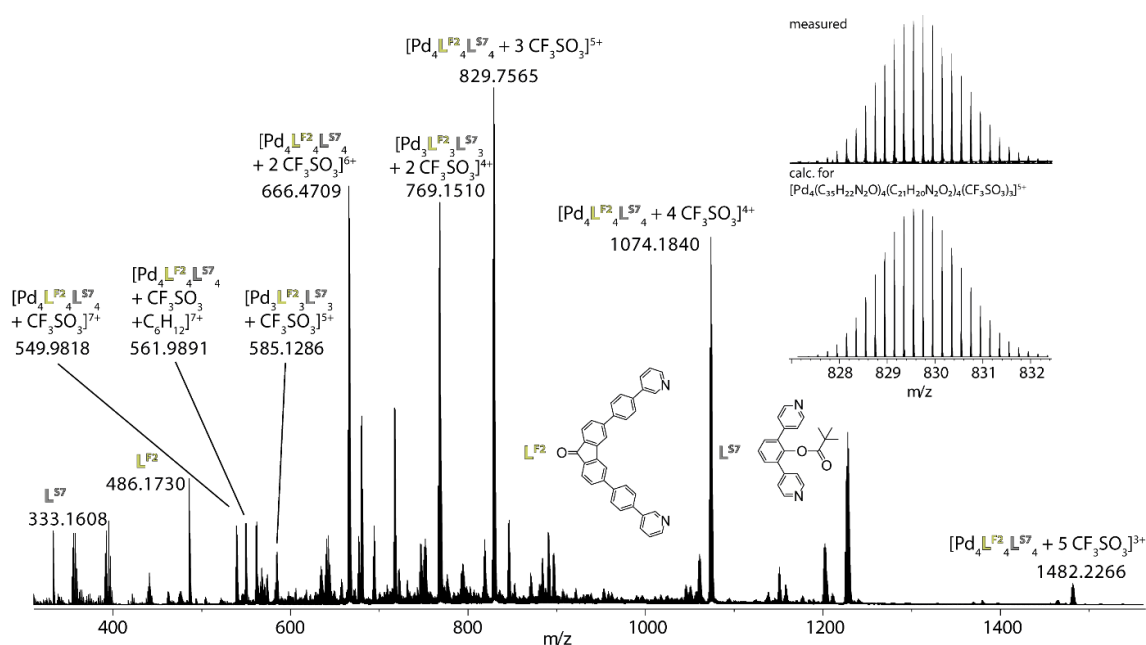
Figure 196: ESI-MS spectrum of the mixture of heteroleptic $[Pd_3L^{F2}_3L^{S7}_3 + xCF_3SO_3]^{(6-x)+}$ (x = 1-2) $[Pd_4L^{F2}_4L^{S7}_4 + xCF_3SO_3]^{(8-x)+}$ (x = 1-5). The measured and calculated isotopic patterns of the highest peak are shown in the inset.

The ESI-MS measurement (Figure 196) confirms the formation of a mixture of $Pd_3L^{F2}_3L^{S7}_3$ and $Pd_4L^{F2}_4L^{S7}_4$ with the latter being the more abundant species. Peaks at m/z = 585.1286 (5+) and 769.1510 (4+) could be assigned to the trinuclear complex, while detected peaks at m/z = 549.9891 (7+), 666.4709 (6+), 829.7565 (5+), 1074.1840 (4+) and 1482.2266 (3+) stemmed from the presence of the tetranuclear complex with chemical formula $[Pd_4L^{F2}_4L^{S7}_4 + xCF_3SO_3]^{(8-x)}$ (x = 0-5). While the steric demand of a pivaloyl-group attached to the short ligand does seem to force an increase in nuclearity, it does not seem to be quite enough to form a clean, tetranuclear assembly.

In silico models have been calculated (PM6 theory level) to visualize the steric demand of a pivaloyl-residue attached to the inside of the small ligand in both, trinuclear and tetranuclear complexes.
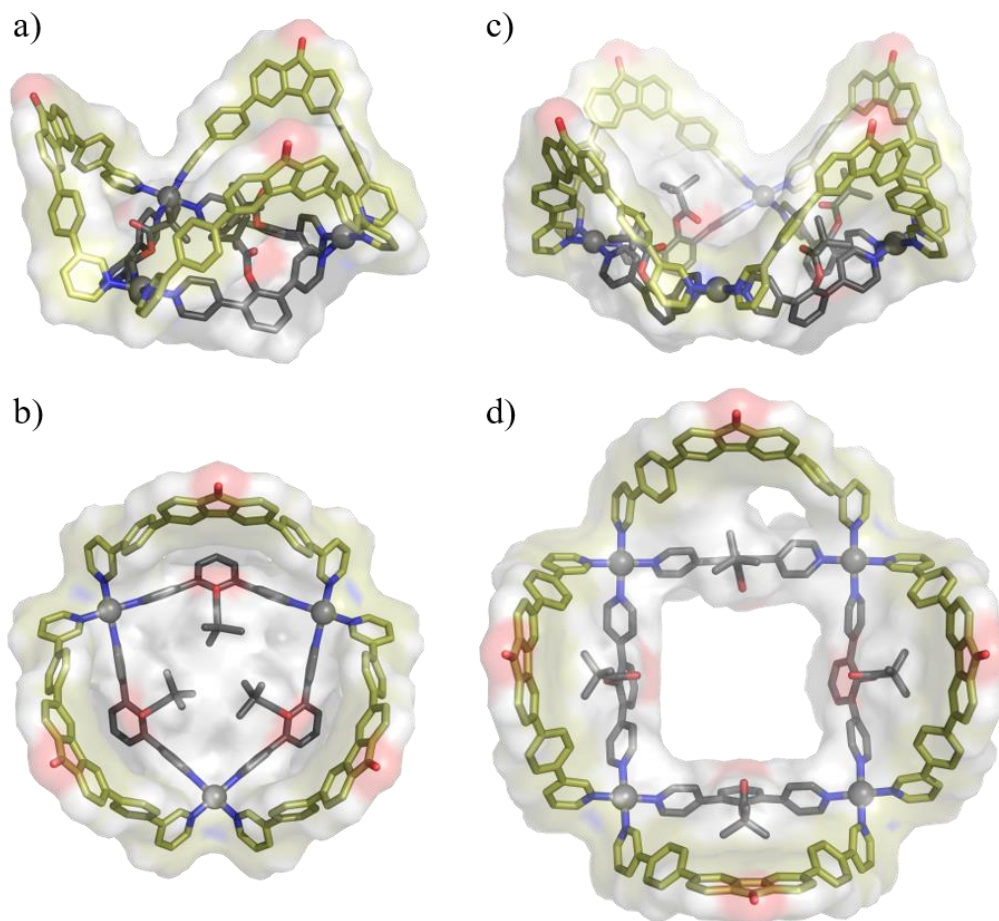
Figure 197: Model of heteroleptic $Pd_3L^{F2}_3L^{S7}_3$ and $Pd_4L^{F2}_4L^{S7}_4$ (sticks overlaid with surface representation) a) side view of $Pd_3L^{F2}_3L^{S7}_3$, b) top view of $Pd_3L^{F2}_3L^{S7}_3$, c) side view of $Pd_4L^{F2}_4L^{S7}_4$, d) top view of $Pd_4L^{F2}_4L^{S7}_4$. Hydrogens are omitted for clarity. Calculated on semi-empirical PM6 theory level.

While the pivaloyl-moiety is pointing almost perpendicular to L^{F2} in the tetranuclear assembly (Figure 197, c, d), it is forced into a more horizontal orientation in the trinuclear assembly due to the bent plane given by the longer ligand L^{F2} (Figure 197, b). In contrast to the *in silico* structure of $Pd_4L^{F2}_4L^{S7}_4$, indicating no steric conflict, the inner ring of $Pd_3L^{F2}_3L^{S7}_3$ is sterically overcrowded which might be an explanation for the reluctance of the system to form $Pd_3L^{F2}_3L^{S7}_3$, even if it would be entropically favored. While the trinuclear assembly does form, as evident from the ESI-MS experiment, it is not thermodynamically favored as the main species is the tetranuclear $Pd_4L^{F2}_4L^{S7}_4$ assembly.

Since a pivaloyl-residue was not sterically demanding enough to force the system fully into a tetranuclear environment, benzoyl chloride was condensed with L^{S5} to form L^{S8}, a phenyl-based ligand with an internal benzoate group attached to its central ring.

270 µl of a 3.11 mM solution of L^{F2} in DMSO-d_6 were combined with 270 µl of a 3.11 mM solution of L^{S8} in DMSO-d_6 with 60 µl of a 15 mM solution of $[Pd(CH_3CN)_4](OTf)_2$ in a

206

5 mm standard NMR tube and heated to 70°C for 2h to afford clean $Pd_4L^{F2}{}_4L^{S8}{}_4$ (Scheme 28). To perform the experiment with utmost care, and rule out concentration inaccuracies, the ligand ratio was adjusted pre Pd(II) addition.
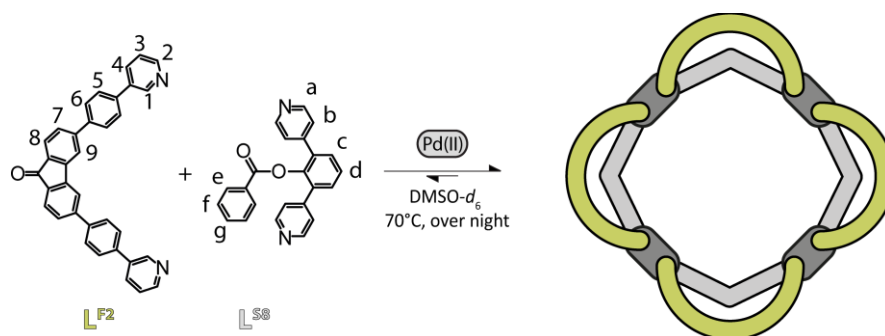
Scheme 28: Formation of $Pd_4L^{F2}{}_4L^{S8}{}_4$ with consecutive proton labels.

A comparison of the aromatic region of the ^1H NMR spectra of ligand L^{F2} (Figure 198, a)), the homoleptic mixture L^{F2} forms upon addition of Pd(II) cations (Figure 198, b)), the 1:1:1 mixture of L^{F2}, L^{S8} and Pd(II) cations after heating to 70°C for 2h (Figure 198, c)) and ligand L^{S8} (Figure 198, d)) shows the clean formation of one distinct species formed from ligands L^{F2}, L^{S8} and Pd(II) cations.
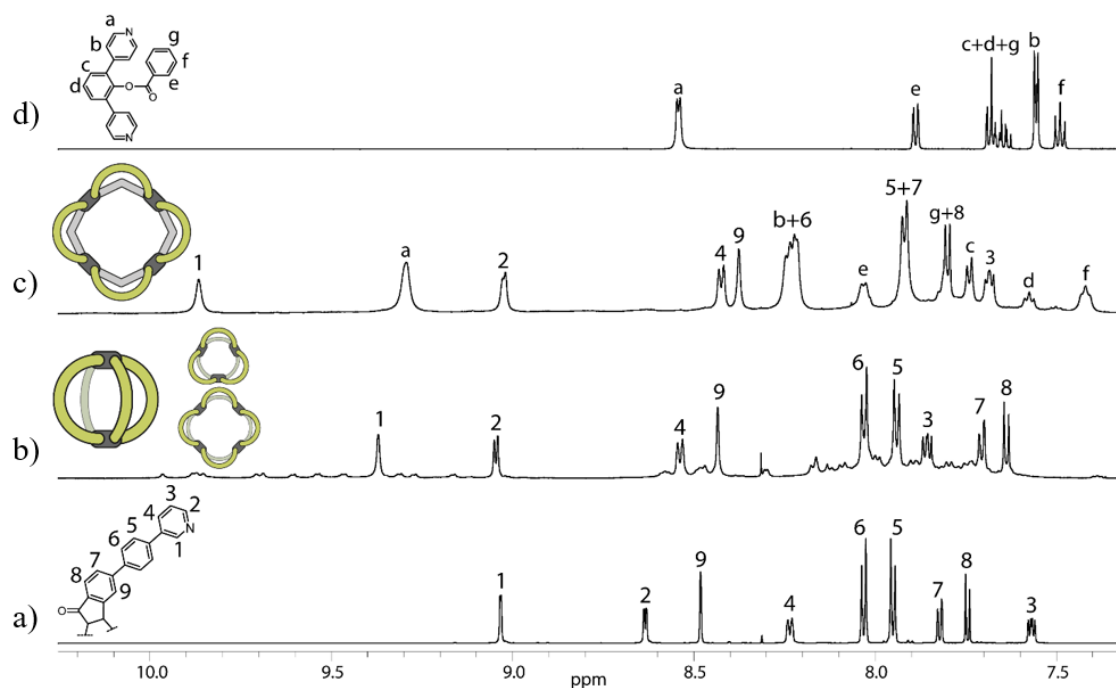
Figure 198: Partial ^1H NMR spectra of a) ligand L^{F2} (700 MHz, 298 K) b) homoleptic $Pd_2L^{F2}{}_4$ cage and the $Pd_nL^{F2}{}_{2n}$ (n=3-5) rings formed upon addition of 0.55 equiv. Pd(II) cations to ligand L^{F2} (600 MHz, 298 K) c) heteroleptic $Pd_4L^{F2}{}_4L^{S8}{}_4$ (600 MHz, 298 K) d) ligand L^{S8} (600 MHz, 298 K) in DMSO-d_6.

The newly formed species (Figure 198, c) showed 13 distinguishable signals with 2D experiments providing information on three of these 13 signals being in fact two signals overlapping with one another resulting in a total signal count of 16 (Figure 310 and Figure

311, experimental part). The integration ratio suggested a 1:1 stoichiometry of the ligands in the assembly. The signals of protons H^1, H^a, H^2 and H^b, situated around the coordination sphere, shift to the downfield upon Pd(II) coordination as compared to the free ligands. The signal shift of protons H^e, H^f and H^g, located at the benzoate moiety cannot be readily interpreted as multiple effects play a role, such as Pd(II) coordination and the change of chemical environment in general. A spectrum of the homoleptic assembly $\mathbf{L^{S8}}$ forms upon Pd(II) addition has not been recorded, though it can be assumed, that a $Pd_{12}\mathbf{L^{S8}}_{24}$ sphere would be formed, even with the included bulk, as shown by FUJITA et al. on multiple occasions.[40,159,162,181,182] Comparison with $\mathbf{L^{F2}}$ and its corresponding Pd(II) assemblies showed that neither is present in Figure 198c). The measured hydrodynamic radius $r_H = 15.49$ Å (Figure 312, experimental part) is larger compared to the previously reported trinuclear complexes $Pd_3\mathbf{L^{F2}}_3\mathbf{L^{S1-5}}_3$ ($r_H = 14.14$-14.78 Å) but smaller than the one of $Pd_4\mathbf{L^{F2}}_4\mathbf{L^{S6}}_4$ ($r_H = 16.57$ Å) not yet allowing a safe conclusion for its nuclearity. Thus, a CSI-MS spectrum was recorded (Figure 199).
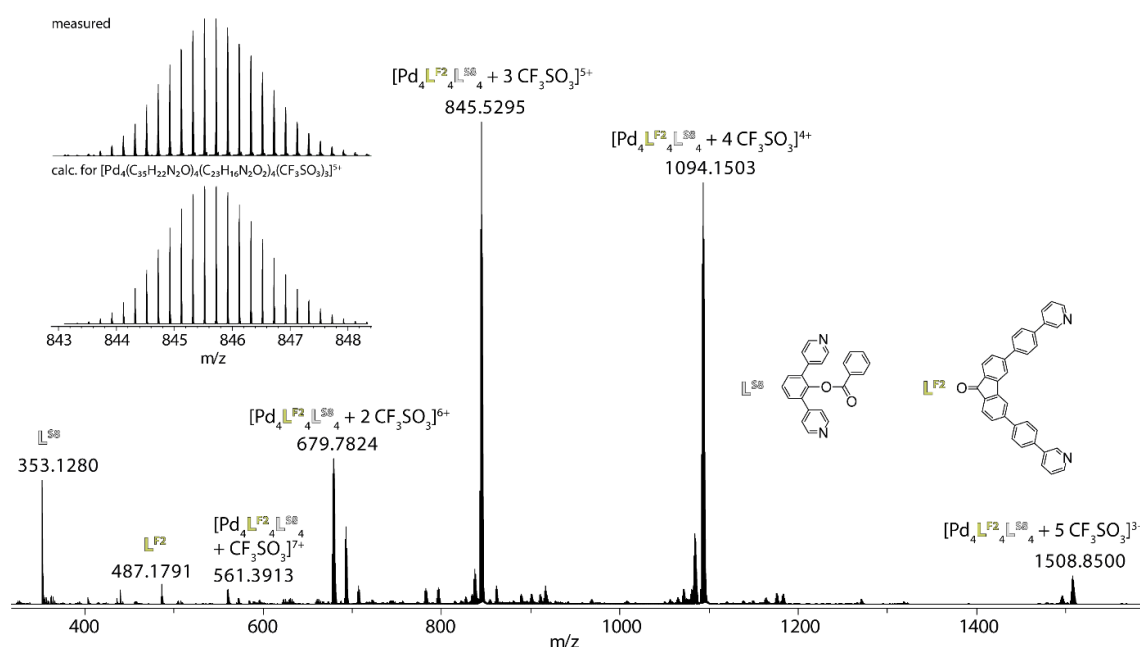
Figure 199: CSI-MS spectrum of heteroleptic $[Pd_4\mathbf{L^{F2}}_4\mathbf{L^{S8}}_4 + xCF_3SO_3]^{(8-x)+}$ (x = 1-5). The measured and calculated isotopic pattern of the highest peak are shown in the inset.

CSI-MS analysis yielded peaks assignable to the 1:1:1 assembly of ligand $\mathbf{L^{F2}}$, $\mathbf{L^{S8}}$ and Pd(II) at $m/z = 561.3913$ (7+), 679.7824 (6+), 845.5295 (5+), 1094.1503 (4+) and 1508.8500 (3+), all assignable to the tetranuclear complex $[Pd_4\mathbf{L^{F2}}_4\mathbf{L^{S8}}_4 + xCF_3SO_3]^{(8-x)+}$ (x = 1-5) with the 5+ species being the most abundant.

While CSI-MS confirmed the same nuclearity for the palladium-assemblies formed from $\mathbf{L^{F2}}$ and $\mathbf{L^{S6}}$, respectively $\mathbf{L^{S8}}$, the difference in their hydrodynamic radii of >1 Å, with the

Pd$_4$**L**$^{F2}_4$**L**$^{S8}_4$ assembly being smaller even though carrying a more sterically demanding group as compared to **L**^{S6} (-NO$_2$), poses the question as to why that is.

A closer look at the collected data led to a peculiarity in the ^{1}H NOESY spectrum.
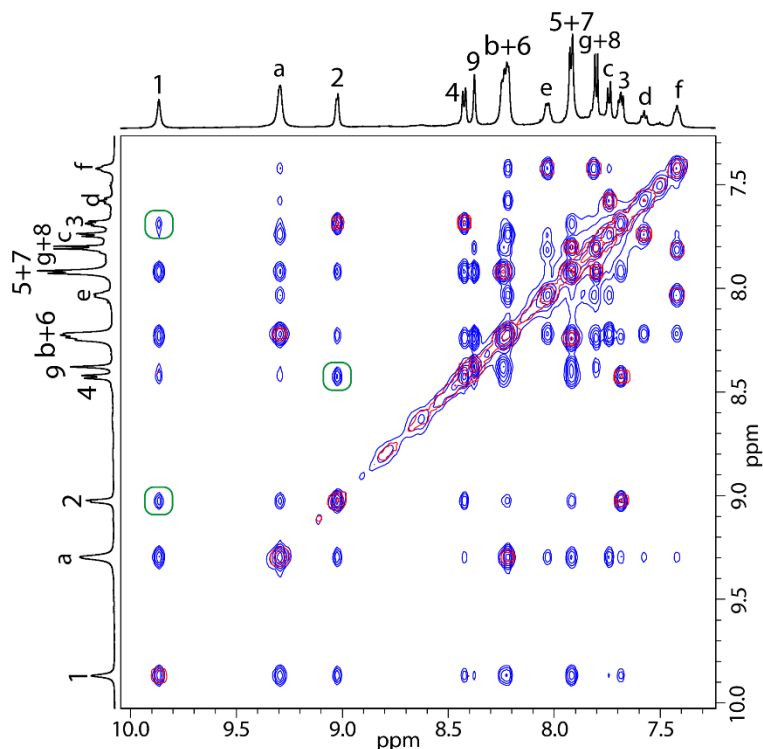
Figure 200: Aromatic region of the overlayed ^{1}H-^{1}H NOESY (blue) and ^{1}H-^{1}H COSY (red) spectra of heteroleptic Pd$_4$**L**$^{F2}_4$**L**$^{S8}_4$ with proton assignment and highlighted NOE signals from one **L**^{F2} to its neighboring counterpart (green).

The NOE of signals assigned to proton H^1 and H^2 of ligand **L**^{F2} is very weak in the trinuclear assemblies due to them being relatively far apart (d = 4.4-4.5 Å for Pd$_3$**L**$^{F2}_3$**L**$^{S1}_3$, measurement taken from preliminary X-ray structure, Figure 164). Furthermore, these protons point into opposite directions, thus not showing any NOE for the same ligand molecule. The NOE cross peak of the signals of H^1 and H^2 in this structure however is very pronounced, the same effect being observable for the cross peak from signals H^2 to H^4 and even H^1 to H^3 (Figure 200, green boxes). While the change from trinuclear to tetranuclear complex does alter the distance of the ligands and thus the distance of these protons, a comparison with the ^{1}H-^{1}H NOESY spectrum of Pd$_4$**L**$^{F2}_4$**L**$^{S6}_4$ (Figure 300) showed that the NOE is significantly weaker as that for Pd$_4$**L**$^{F2}_4$**L**$^{S8}_4$. As the intensity of the NOE cross peak is directly proportional to the distance of the corresponding protons[183–185] this observation leaves the conclusion that a different orientation of neighboring ligands **L**^{F2} applies. While the orientation of **L**^{F2} is fixed in trinuclear complexes, which was also shown by X-ray analysis, the ligand can adapt two different orientations in tetranuclear complexes resulting in either an all-up structure with the same coordination environment as already observed for the trinuclear complexes or a *trans-*

saddle-shaped structure with inverted coordination sites. An *in silico* model (PM6 theory level) was calculated for both cases for better visualization and rough distance estimation (Figure 201).
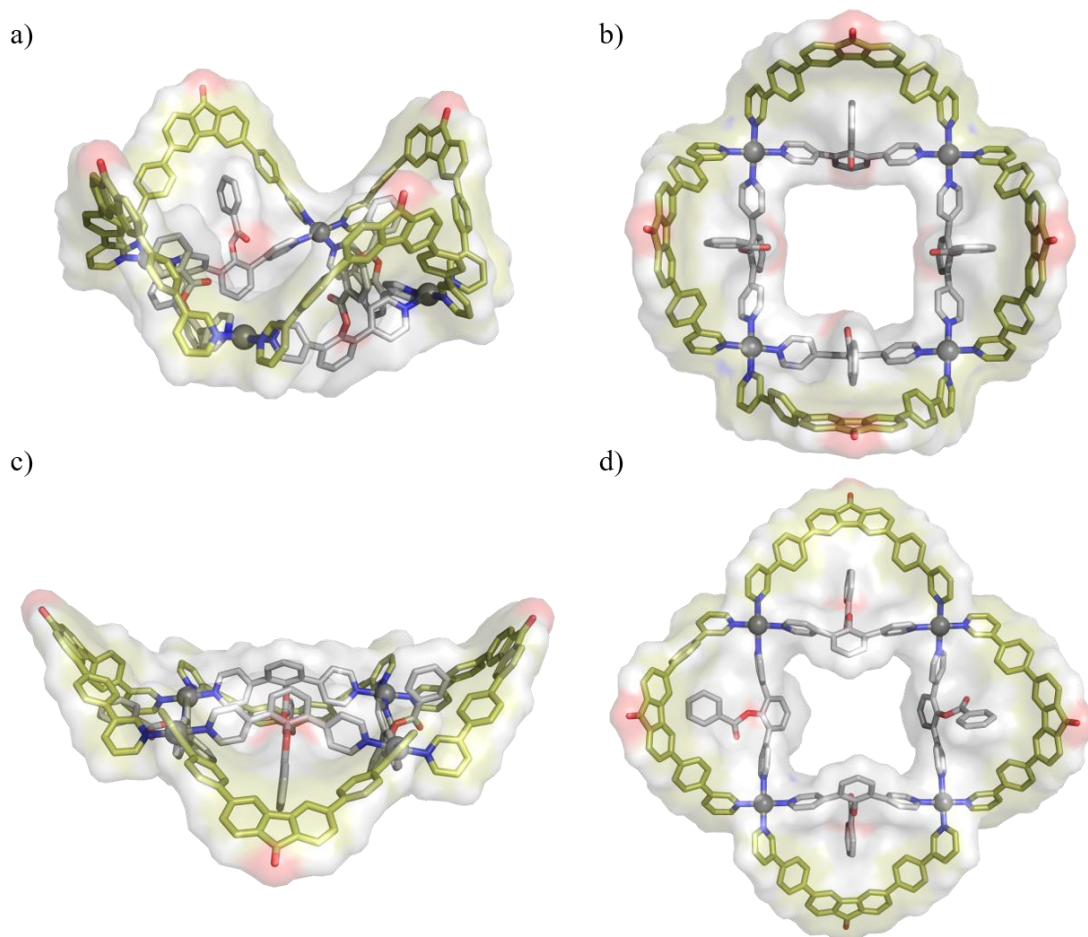
Figure 201: Compared models of heteroleptic $Pd_4L^{F2}_4L^{S8}_4$ in bowl respectively saddle conformation (sticks overlaid with surface representation) a) side view bowl conformation b) top view bowl conformation c) side view saddle conformation d) top view saddle conformation. Hydrogens are omitted for clarity. Calculated on semi-empirical PM6 theory level.

Figure 201 a) and b) show the calculated model for the all-up structure, while c) and d) depict the saddle-conformation with an up-down-up-down motif. While the difference is not easily seen from the top (Figure 201, b and d) it is very imminent from the side view. The bowl-like conformation seems more spatially condensed and the benzoyl-groups have very limited freedom of motion since they are both locked by the set orientation of the backbone and the steric hinderance imposed by the other benzoate-groups. While there is a NOE contact between proton H^g of L^{F2} and H^g of the benzoate-group of L^{S8} it is way weaker than the distance in the models would suggest (saddle: 3.6-4.6 Å; bowl: 3.7-4.1 Å) thus leaving to conclude the group exhibiting a certain degree of freedom being able to rotate out of the proximity to L^{F2}, therefore yielding a NOE peak averaged over all possible distances. Efforts have been made to analyze NOE distances in flexible molecules, though this would require more data acquisition and *in silico* studies in this

210

case.[183] Though presented data suggests the structure taking on a saddle conformation instead of forming a bowl-like structure like Pd$_4$L$^{F2}_4$L$^{S6}_4$, this does not explain the difference in hydrodynamic radius (>1 Å). A possible explanation could derive from the chemical structure of the molecules themselves, since the degree of solvent interaction will be quite different, thus yielding a difference in r_H. This claim could be verified by IMS measurements, as the radius deducted from these excludes the solvent shell. Furthermore, while L^{S8}, compared to L^{S6}, is the ligand with a higher spatial extent, the benzoate-group has the capability of π-stacking to other parts of the assembly (e.g. L^{F2}). This could possibly lead to the assembled structure Pd$_4$L$^{F2}_4$L$^{S8}_4$ taking up a more condensed form as opposed to the nitro-group carrying Pd$_4$L$^{F2}_4$L$^{S6}_4$ bowl. Another aspect of Pd$_4$L$^{F2}_4$L$^{S8}_4$ preferring a saddle-conformation over the formation of a bowl could be the dipole-moments, which are oriented in one direction in a bowl, while being opposed to one another in a saddle, making the saddle energetically more favorable. To finally answer the question, as to why L^{S6} forms a bowl-like structure with L^{F2} and L^{S8} forms a saddle, further *in silico* studies will be needed to provide valuable insight on entropic and enthalpic contributions.

While the structure of Pd$_4$L$^{F2}_4$L$^{S8}_4$ does seem to differ from the previously discussed systems, its photophysical properties are vastly similar to them (Figure 202).
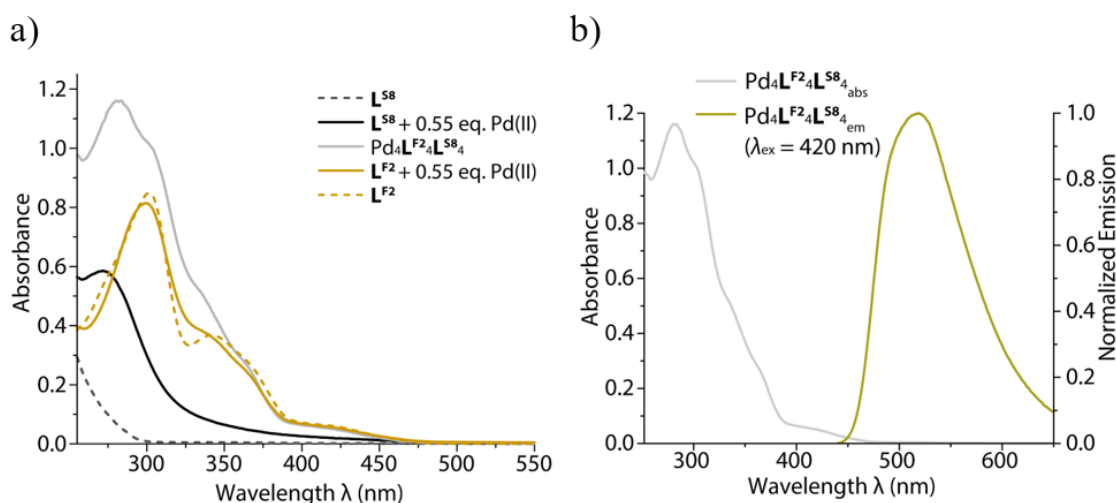
Figure 202: a) UV/VIS spectra of L^{S8}, L^{S8} upon addition of 0.55 equiv. Pd(II), heteroleptic Pd$_4$L$^{F2}_4$L$^{S8}_4$, L^{F2} and L^{F2} upon addition of 0.55 equiv. Pd(II), b) absorbance and normalized emission of heteroleptic Pd$_4$L$^{F2}_4$L$^{S8}_4$.

The heteroleptic assembly exhibits an absorption maximum at λ = 282 nm with shoulders at λ = 304 nm, 335 nm, 365 nm and 420 nm which is in good accordance with the photophysical properties of the previously reported structures Pd$_3$L$^{F2}_3$L$^{S1-5}_3$ and Pd$_4$L$^{F2}_4$L$^{S6}_4$. The shoulder at 304 nm is notable since it is only pronounced in systems containing a short ligand based on the phenol-backbone like L^{S4}, L^{S5} and L^{S8} and the

aniline-based ligand L^{S3} (albeit weaker). The strongest expression of this shoulder can be found for $Pd_3L^{F2}_3L^{S5}_3$ and the system at hand, $Pd_4L^{F2}_4L^{S8}_4$. Upon excitation at $\lambda = 420$ nm, the assembly emitted light with a maximum at $\lambda = 520$ nm (Figure 202, b)).

The easy modification of L^{S5} with different acyl chlorides in combination with the system adapting to a potential increase in steric demand simply by increasing its nuclearity, opens up the possibility to introduce a variety of functional groups and can be used to introduce e.g. chiral groups.

Electrochemical repulsion (L^{S6}) and the introduction of bulk (L^{S7}/L^{S8}) led to an increase in nuclearity of the heteroleptic assemblies L^{F2} forms with Pd(II) and a shorter counter ligand L^S but the standard approach on increasing nuclearity in Pd(II) systems, being bite angle increase,[41–44,162] has been neglected up until now.

3.4.3.3 L^{S9} and L^{S10} – Bite Angle Increase

To complete the structural study on these assemblies, ligands L^{S9}, based on thiophene, and L^{S10}, based on selenophene were synthesized, sporting bite angles of 149°[42], respectively 152°[43]. While L^{S9} has been shown to form $M_{24}L_{48}$ spheres upon Pd(II) coordination, the switch from sulfur to selenium in L^{S10} increases the bite angle of the ligand by only 3°, yet leading to the formation of an $M_{30}L_{60}$ sphere. The combination of both ligands with L^{F2} and Pd(II) in a 1:1:1 ratio will be analyzed in the following part (Scheme 29).
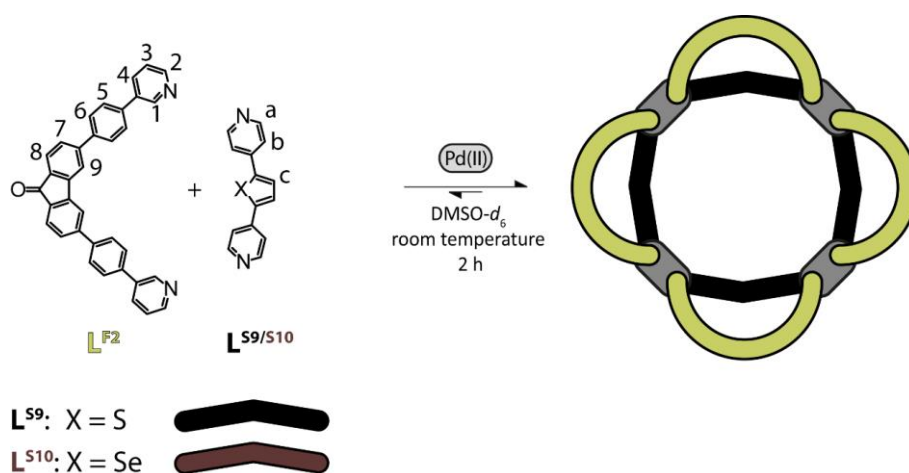
Scheme 29: Formation of $Pd_4L^{F2}_4L^{S9}_4$, respectively $Pd_4L^{F2}_4L^{S10}_4$ with consecutive proton labels.

The combination of either 270 µl of a 3.11 mM solution of L^{S9} or L^{S10} with 270 µl L^{F2} in DMSO-d_6 followed up by the addition of 60 µL of a 15 mM solution of (Pd[CH$_3$CN]$_4$)OTf$_2$ in DMSO-d_6 in a standard 5 mm NMR tube led to the formation of $Pd_4L^{F2}_4L^{S9}_4$, respectively $Pd_4L^{F2}_4L^{S10}_4$ (Figure 203).
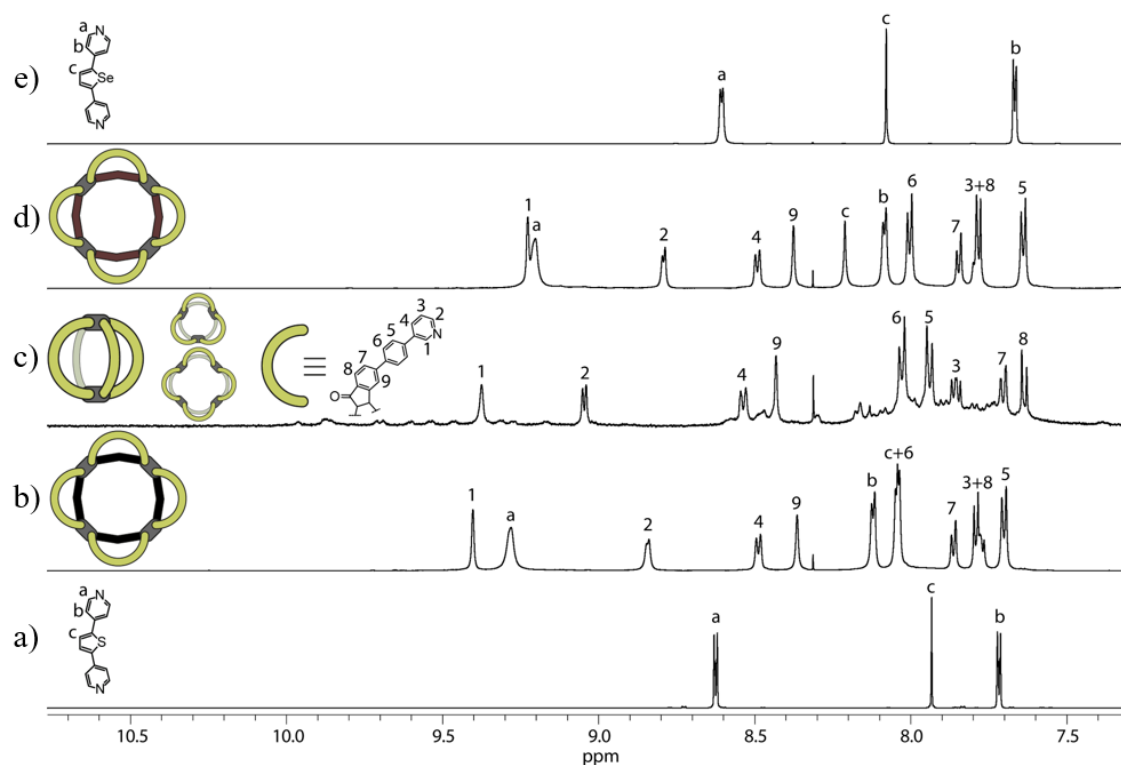
Figure 203: Partial ^{1}H NMR spectra of a) ligand $\mathbf{L^{S9}}$ (600 MHz, 298 K) b) heteroleptic $Pd_4\mathbf{L^{F2}}_4\mathbf{L^{S9}}_4$ (600 MHz, 298 K) c) homoleptic $Pd_2\mathbf{L^{F2}}_4$ cage and the $Pd_n\mathbf{L^{F2}}_{2n}$ (n=3-5) rings formed upon addition of 0.55 equiv. Pd(II) cations to ligand $\mathbf{L^{F2}}$ (600 MHz, 298 K) d) heteroleptic $Pd_4\mathbf{L^{F2}}_4\mathbf{L^{S10}}_4$ (600 MHz, 298 K) and e) ligand $\mathbf{L^{S10}}$ (600 MHz, 298 K) in DMSO-d_6.

As evident from Figure 203 b), respectively d), both combinations led to the formation of one distinct species. While the ^{1}H NMR of the 1:1:1 combination of $\mathbf{L^{F2}}$, Pd(II) and $\mathbf{L^{S9}}$ yielded 10 differentiable signals (Figure 203, b), the one with $\mathbf{L^{S10}}$ instead of $\mathbf{L^{S9}}$ yielded 11 signals (Figure 203, d). Neither homoleptic species, nor residual ligand could be detected and 2D NMR experiments (Figure 318 to Figure 320 and Figure 328 to Figure 330, experimental part) allowed the assignment of all 13 protons to the newly formed species. As observed already for other assemblies, proton signals H^a, H^b, H^1 and H^2 shift downfield upon Pd(II) coordination. It is noted however, that the shift of especially proton H^1 is not as pronounced as in the previously reported systems. While it shifted to $\delta = 9.87$ ppm in the previously reported $Pd_4\mathbf{L^{F2}}_4\mathbf{L^{S8}}_4$, the shift for $Pd_4\mathbf{L^{F2}}_4\mathbf{L^{S9}}_4$ is at $\delta = 9.40$ ppm and at $\delta = 9.23$ ppm for $Pd_4\mathbf{L^{F2}}_4\mathbf{L^{S10}}_4$. A similar trend can be described for the other protons around the coordination sphere (H^a, H^b and H^2). The less pronounced downfield shift can be attributed to the heavier atoms sulfur ($\mathbf{L^{S9}}$) and selenium ($\mathbf{L^{S10}}$) present in the short counter ligands, whose presence leads to increased shielding, thus influencing the proton chemical shifts. The effect is stronger for $\mathbf{L^{S10}}$ carrying the heavier selenium atom in its backbone. The measured hydrodynamic radii were $r_H = 17.01$ Å for $Pd_4\mathbf{L^{F2}}_4\mathbf{L^{S9}}_4$ (Figure 321, experimental part) and $r_H = 17.77$ Å for $Pd_4\mathbf{L^{F2}}_4\mathbf{L^{S10}}_4$ (Figure 332, experimental part), thus being higher than the previously reported values found for

Pd$_4$L$^{F2}_4$L$^{S6}_4$ (r_H = 16.57 Å) and for Pd$_4$L$^{F2}_4$L$^{S8}_4$ (r_H = 15.49 Å). This increase in spatial extent does make sense considering the angle change in the small ligands L^{S9} and L^{S10} leading to an increase in central ring size and consequently an effect on the coordination angle of L^{F2}. While the hydrodynamic radius could thus suggest the formation of a tetranuclear structure as described before for the structures of Pd$_4$L$^{F2}_4$L$^{S6}_4$ and Pd$_4$L$^{F2}_4$L$^{S8}_4$, final certainty can be deduced from MS analysis (Figure 204).
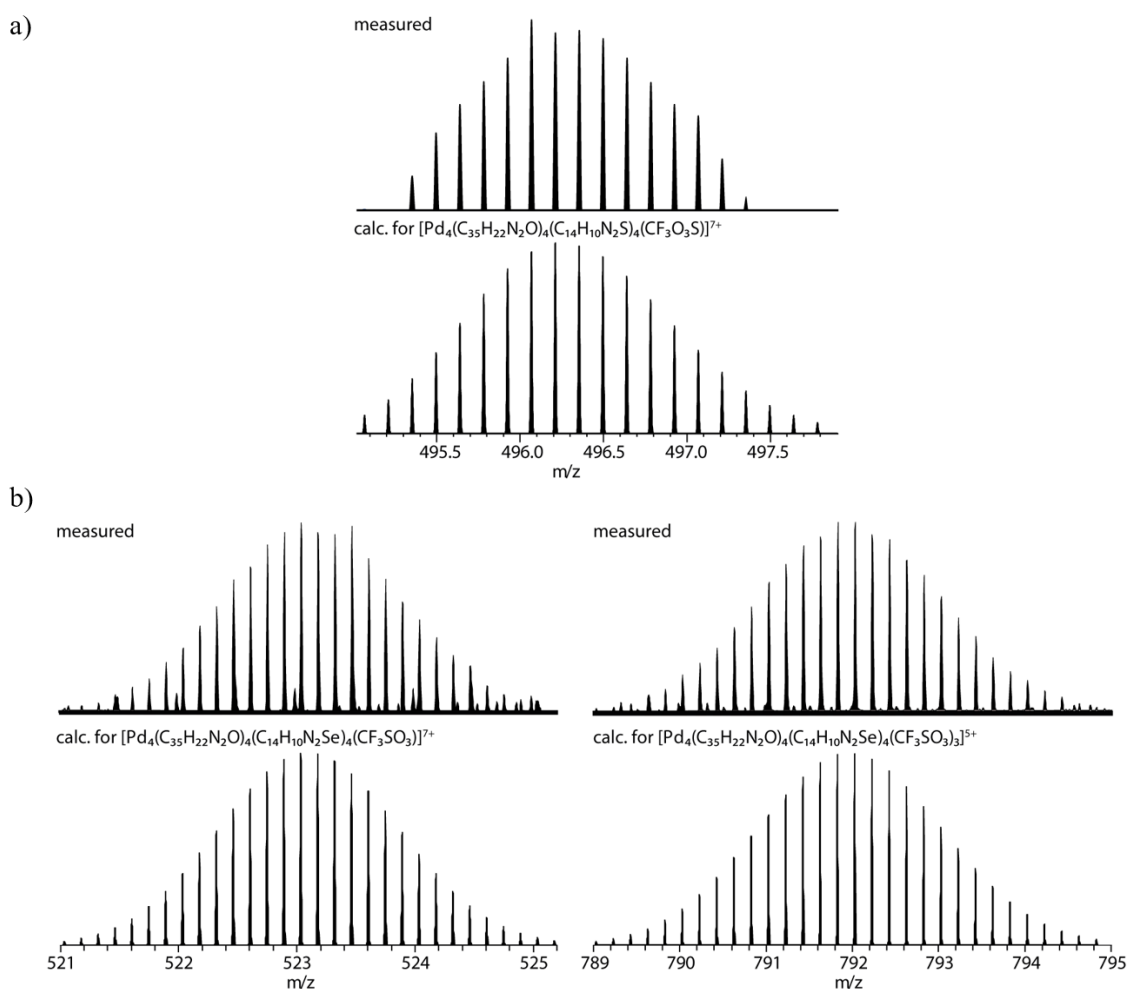
Figure 204: a) CSI-MS spectrum of heteroleptic [Pd$_4$L$^{F2}_4$L$^{S9}_4$ + CF$_3$SO$_3$]$^{7+}$. Only the measured and calculated isotopic pattern of the 7+ species is shown since only fragmented assembly could be detected otherwise. b) ESI-MS spectrum of heteroleptic [Pd$_4$L$^{F2}_4$L$^{S10}_4$ + CF$_3$SO$_3$]$^{7+}$ and [Pd$_4$L$^{F2}_4$L$^{S10}_4$ + 3 CF$_3$SO$_3$]$^{5+}$. Only the measured and calculated isotopic patterns of the 7+ and 5+ species is shown since only fragmented assembly could be detected otherwise.

Obtaining a proper MS spectrum however, proved to be difficult since the structures of both assemblies tended to fragment under ESI but also CSI-MS conditions. While this can be attributed to their flat topologies and thus potential need to maintain their solvent shell as of means of stability, it consequently led to extremely convoluted spectra in which fragments of the assembly and only small peaks of fully assembled complex could be detected (Figure 204). However, neither trinuclear, nor pentanuclear complexes could be found thus leaving to conclude the formation of tetranuclear Pd$_4$L$^{F2}_4$L$^{S9}_4$, respectively

Pd$_4$**L^{F2}**$_4$**L^{S10}**$_4$. While the MS analysis on its own would not be convincing, combined with very clear results from NMR, especially ^{1}H DOSY analysis, it is sufficient to assign a nuclearity of n = 4 to the obtained assemblies. *In silico* models of both structures were computed on a PM6 theory level for visualization purposes.
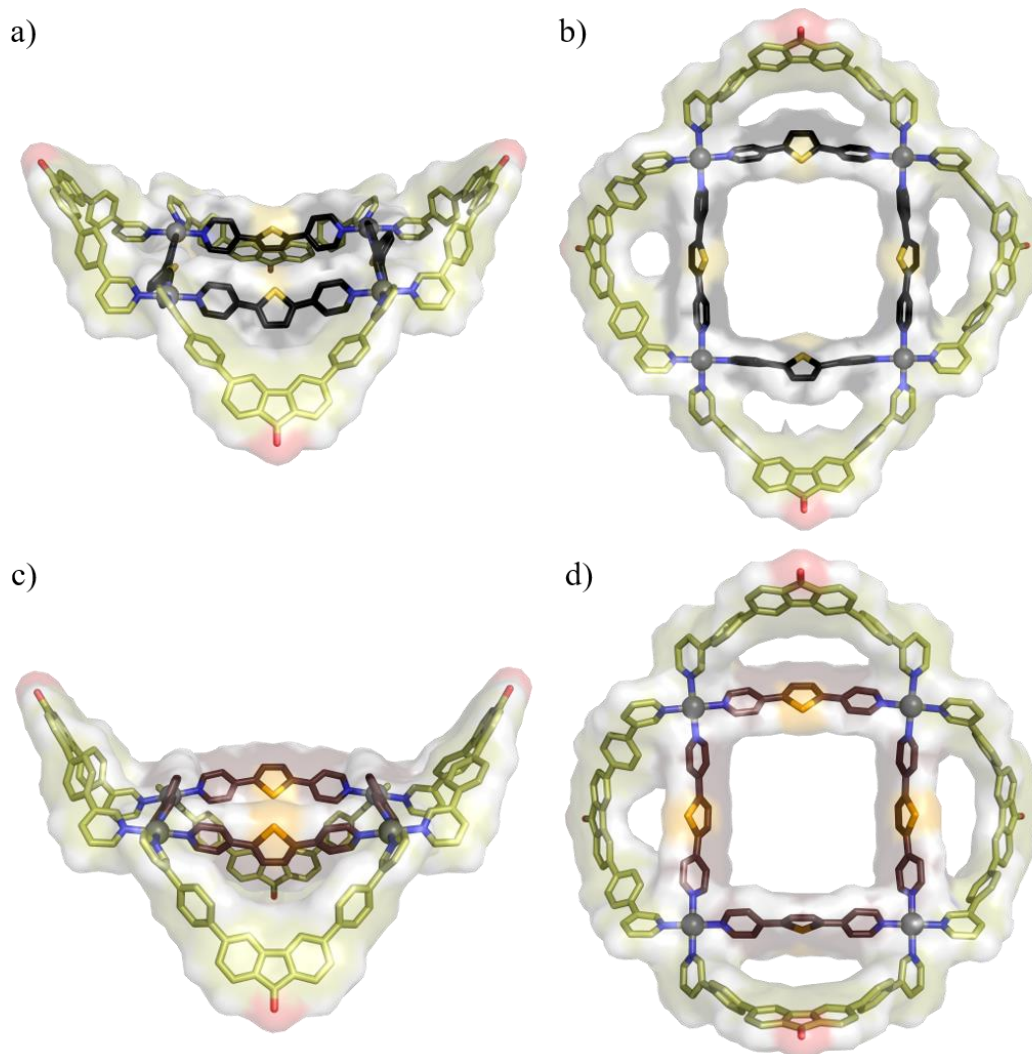
Figure 205: Models of heteroleptic Pd$_4$**L^{F2}**$_4$**L^{S9}**$_4$ (sticks overlaid with surface representation) a) side view b) top view and Pd$_4$**L^{F2}**$_4$**L^{S10}**$_4$ (sticks overlaid with surface representation) c) side view d) top view. Hydrogens are omitted for clarity. Calculated on semi-empirical PM6 theory level.

Figure 205 shows the computed models of Pd$_4$**L^{F2}**$_4$**L^{S9}**$_4$ (Figure 205, a and b), respectively Pd$_4$**L^{F2}**$_4$**L^{S10}**$_4$ (Figure 205, c and d), each from the side and the top. Their depiction in the saddle conformation is supported by analytical data and will be discussed later in this chapter in a comparison with the other tetranuclear complexes. As evident from both *in silico* models, the central, tetranuclear ring is almost planar while the longer ligand **L^{F2}** is arranged around it in an up-down-up-down fashion, thus yielding the saddle conformation for both assemblies. It is noted, that the short ligands **L$^{S9/10}$** did not maintain a preset up-down conformation, instead one ligand underwent a backbone rotation

yielding a three-up one-down topology best seen in Figure 205 b) and d). It is likely that free rotation of the backbones is possible due to the obtuse bite angles and the protons on the five-membered rings posing less steric hinderance to obstruct the beforementioned. Calculations on a higher theory level, followed up by MD calculations could yield a satisfactory answer to this uncertainty.
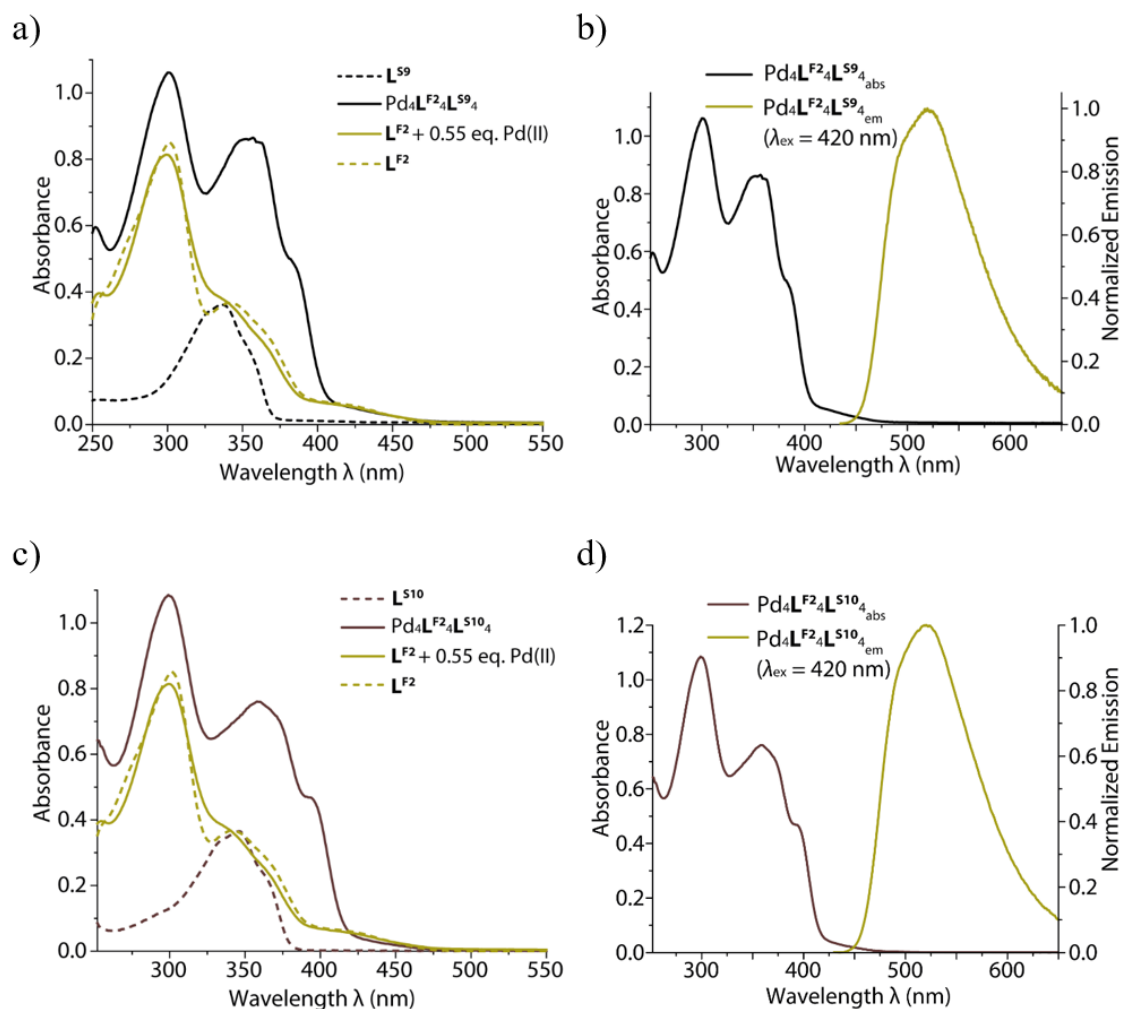
Figure 206: a) UV/VIS spectra of L^{S9}, heteroleptic $Pd_4L^{F2}_4L^{S9}_4$, L^{F2} and L^{F2} upon addition of 0.55 equiv. Pd(II), b) absorbance and normalized emission of heteroleptic $Pd_4L^{F2}_4L^{S9}_4$, c) UV/VIS spectra of L^{S10}, heteroleptic $Pd_4L^{F2}_4L^{S10}_4$, L^{F2} and L^{F2} upon addition of 0.55 equiv. Pd(II), d) absorbance and normalized emission of heteroleptic $Pd_4L^{F2}_4L^{S10}_4$.

The photophysical properties of both, $Pd_4L^{F2}_4L^{S9}_4$ (Figure 206, a and b) and $Pd_4L^{F2}_4L^{S10}_4$ (Figure 206, c and d) differ vastly from those of the structures with small ligands L^{S} based on phenyl-backbones. Whereas the aforementioned usually presented one distinct absorption maximum with additional shoulders, the spectra for $Pd_4L^{F2}_4L^{S9}_4$ and $Pd_4L^{F2}_4L^{S10}_4$ show additional local maxima. While the curve characteristics of the absorption spectra of the two species have similar shape, the values for the wavelength at which the corresponding transition occurs differs (Table 9).

Table 9: Absorption characteristics for $Pd_4L^{F2}_4L^{S9}_4$ and $Pd_4L^{F2}_4L^{S10}_4$.

	A_{max}	local A_{max}	Shoulder1	Shoulder2	Shoulder3
$Pd_4L^{F2}_4L^{S9}_4$	301 nm	355 nm	n.a.	385 nm	420 nm
$Pd_4L^{F2}_4L^{S10}_4$	299 nm	360 nm	375 nm	395 nm	440 nm

The wavelengths for the absorption maximum A_{max} are quite similar to each other for both species, differing by only a few nanometers. From here on however, the values for $Pd_4L^{F2}_4L^{S10}_4$ are bathochromically shifted as compared to $Pd_4L^{F2}_4L^{S9}_4$. The second local maximum at $\lambda = 355$ nm (respectively $\lambda = 355$ nm for $Pd_4L^{F2}_4L^{S10}_4$) is not present in any of the other species leaving to conclude its association to the introduced heteroatoms sulfur and selenium. The bathochromic shift for selenium-species as compared to the ones containing sulfur can already be seen in the absorption of the ligands L^{S9} ($\lambda_{max} = 337$ nm) and L^{S10} ($\lambda_{max} = 346$ nm). This effect is observable for all other absorption values measured for $Pd_4L^{F2}_4L^{S10}_4$ which are shifted to the bathochromic region between $\Delta\lambda = 5\text{-}20$ nm as compared to the values measured for $Pd_4L^{F2}_4L^{S9}_4$. The emission of both species when excited at $\lambda_{ex} = 420$ nm shows a maximum at $\lambda_{em} = 520$ nm, which is in accordance with all previously reported species containing L^{F2} as their emitting species.

3.4.3.4 Summary $Pd_nL^{F2}_nL^{S6\text{-}10}_n$ (n = 4)

To summarize, three strategies for increasing the nuclearity from trinuclear to tetranuclear complexes have been shown with the only variable being the short counter ligand L^{SX}. The ligand was altered in respect of its electrostatic properties, steric demand by introducing bulky residues and bite angle. Figure 207 summarizes the previously discussed strategies.
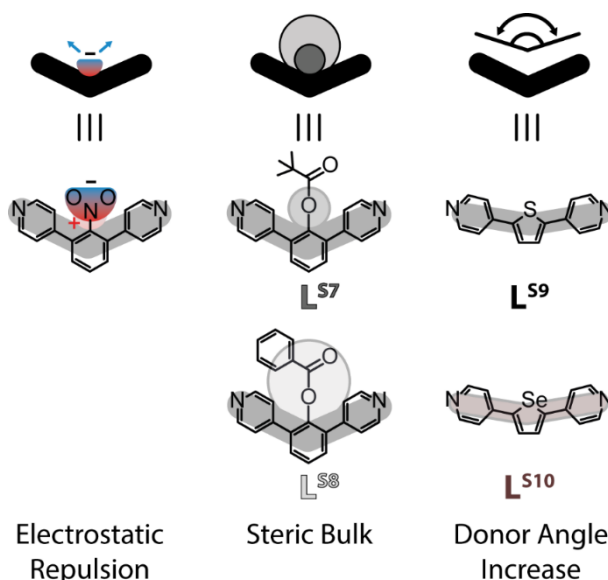
Figure 207: Schematic representation of the established strategies allowing the transition from previously established trinuclear complexes $Pd_2L^{F2}_3L^{S1-5}_3$ to tetranuclear structures.

While the outer ligand L^{F2} and the metal ion Pd(II) have not been altered, a relatively small change in the short ligands had significant effect on the outcome of the final assembly. The increase in nuclearity for L^{S6}, based on nitrobenzene, was initially unexpected, yet can be readily explained by means of Coulombs Law, this observation induced the closer look into the systematic behavior of the assemblies and the response of the system to slight alterations of L^S. The introduction of bulk in form of a pivaloyl-group (L^{S7}) did not quite pose enough steric demand to force the system into a clean increase in nuclearity, while a benzoyl-group (L^{S8}) was sufficient to form clean $Pd_4L^{F2}_4L^{S8}_4$. Changing the bite angle of L^S by altering the central six-membered ring to a five-membered one using thiophene-, respectively selenophene ($L^{S9/10}$) as backbones, led to the clean formation of tetranuclear assemblies in both cases with only the size differing slightly. The size, deduced from the hydrodynamic radius r_H, posed to be an extremely valuable source of information on these assemblies as they often fragmented under MS conditions, even using cryo-spray ionization techniques. ^{1}H NMR spectra of the aromatic region of all four clean tetranuclear assemblies are shown in Figure 208, together with the corresponding ^{1}H DOSY trace, diffusion coefficient D and hydrodynamic radius r_H.
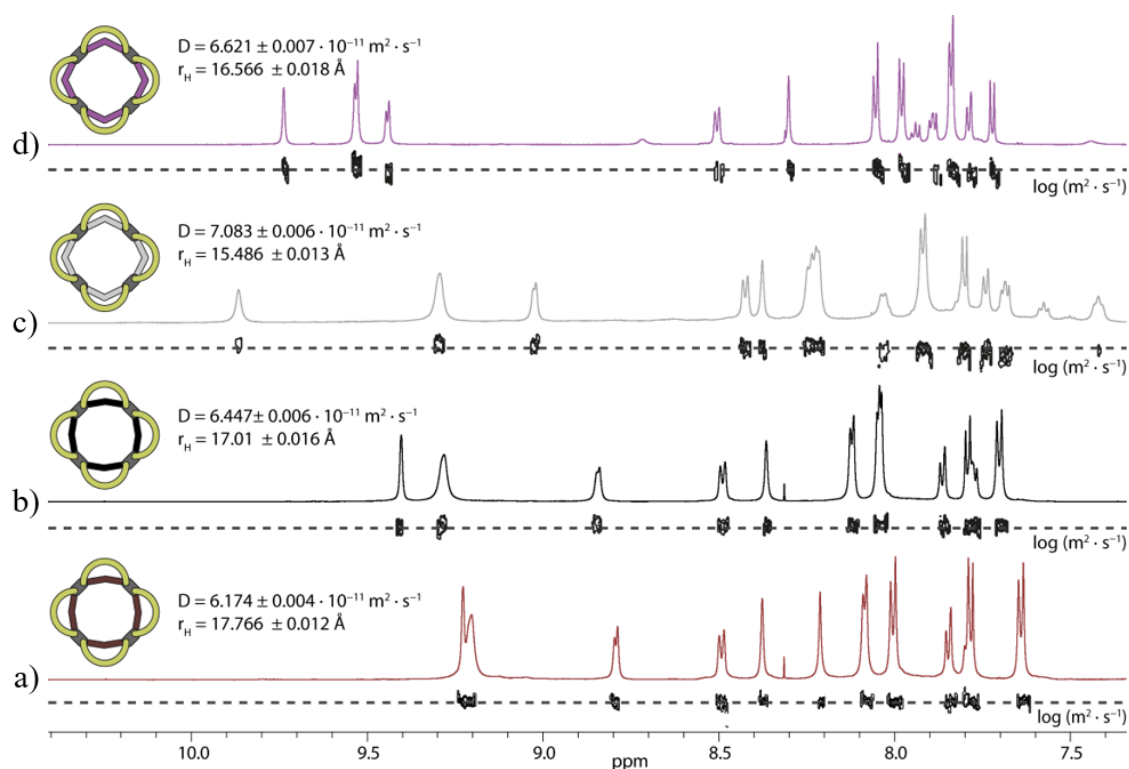
Figure 208: Partial ^{1}H NMR spectra (600 MHz, 298 K, DMSO-d_6) and corresponding ^{1}H DOSY NMR spectra (500 MHz, 298 K, DMSO-d_6) of a) $Pd_4L^{F2}_4L^{S10}_4$, b) $Pd_4L^{F2}_4L^{S9}_4$, c) $Pd_4L^{F2}_4L^{S8}_4$ and d) $Pd_4L^{F2}_4L^{S6}_4$. Diffusion coefficient D and hydrodynamic radius r_H are given.

While all measured hydrodynamic radii were substantially larger than the ones measured for the trinuclear complexes (r_H = 14.14-14.78 Å), it was most curious that the structure with the highest atom count and introduced bulk proved to be the smallest of the tetranuclear complexes with a hydrodynamic radius of r_H = 15.49 Å (Figure 208, b)). As already discussed in the corresponding sub-chapter it is even more curious considering the structure taking on a saddle conformation as opposed to a bowl one. While trinuclear complexes of the $Pd_3L^A_3L^B_3$ type can only adapt one conformation in the reported cases, since the ligand donor angles and length, combined with square-planar coordinated Pd(II), dictate the outcome of the self-assembly, this is not the case for tetranuclear complexes, as briefly mentioned already. It is still set, that the smaller ligand L^S occupies the central ring with the larger ligand L^{F2} occupying the outer positions, however L^{F2} can adopt two different orientations in tetranuclear complexes, all pointing up, resulting in a bowl conformation and up-down-up-down, resulting in a structure akin to a saddle. While this option was initially neglected in the analysis of $Pd_4L^{F2}_4L^{S6}_4$, the unusually high abundance of NOE cross peaks, or more the intensity of the aforementioned, for the structures $Pd_4L^{F2}_4L^{S8-10}_4$ seemed irregular. Most notably were the cross peaks between signals attributed to protons in-between which a cross peak of this intensity was not expected, e.g. H^1-H^2, H^1-H^3 and H^2-H^4. Consequently, an in-depth structural analysis

based on the NOE contact of protons H^1-H^a (taken as reference intensity) and H^1-H^2 was performed (Figure 209).
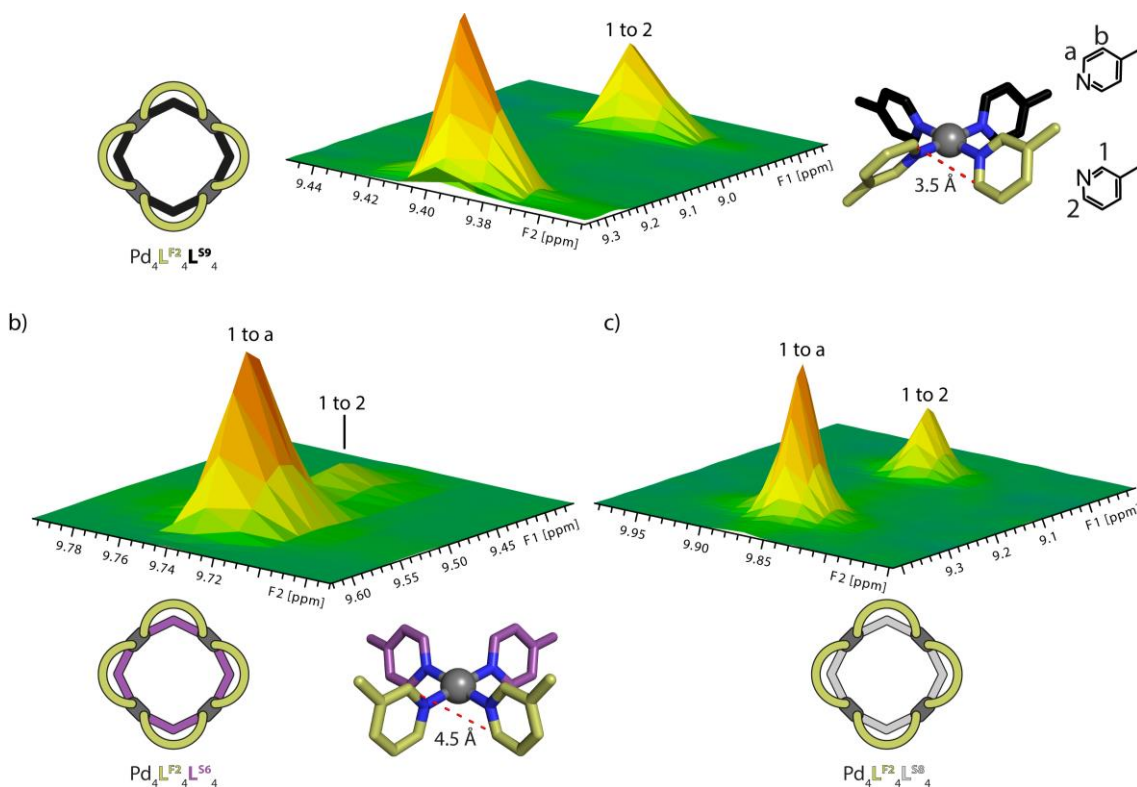
Figure 209: Comparision of the NOE cross peaks of the signals of protons H^1 and H^2 in respect to the intensity of the contakt of protons H^1 and H^a for a) $Pd_4\mathbf{L^{F2}}_4\mathbf{L^{S9}}_4$, b) $Pd_4\mathbf{L^{F2}}_4\mathbf{L^{S6}}_4$ and c) $Pd_4\mathbf{L^{F2}}_4\mathbf{L^{S8}}_4$. Intenisty is given by color (orange: high intensity, green: low intensity). The coordination environment of both possible conformations, bowl and saddle, is presented as a cutout from the *in silico* model with the measured distance of H^1-H^2 given (PM6 theory level).

The cross peak chosen as a reference distance marker was the one between the signals of H^1 and H^a, since it was deemed relatively constant even considering potential rotation of the para-pyridine donors of $\mathbf{L^{SX}}$. The contact analyzed in respect to its intensity was the cross peak between signals of H^1 and H^2, which would not yield any NOE contact while in the same ligand molecule, thus this contact can only be measured if two ligand molecules come in close proximity to each other, like upon coordination to Pd(II) in a *cis* conformation. The analysis is purely qualitative, no integral values of the respective cross peaks were determined. Due to signal overlap, $Pd_4\mathbf{L^{F2}}_4\mathbf{L^{S10}}_4$ is not shown though it is noted that is shows the same cross peaks as $Pd_4\mathbf{L^{F2}}_4\mathbf{L^{S9}}_4$ (Figure 323, experimental part). Figure 209 shows the 3D plots of the NOE cross peak intensity of the cross peaks assigned to the signal contacts of H^1-H^a and H^1-H^2 for the three tetranuclear structures $Pd_4\mathbf{L^{F2}}_4\mathbf{L^{S6}}_4$ (Figure 209, b), $Pd_4\mathbf{L^{F2}}_4\mathbf{L^{S8}}_4$ (Figure 209, c) and $Pd_4\mathbf{L^{F2}}_4\mathbf{L^{S9}}_4$ (Figure 209, a). The analyzed cross peaks were chosen exemplary due to the compared signals being situated conveniently next to each other. As evident from Figure 209, the intensity of the compared cross peaks differs notably from $Pd_4\mathbf{L^{F2}}_4\mathbf{L^{S6}}_4$ (Figure 209, b) to the other two

220

plots derived from $Pd_4L^{F2}_4L^{S9}_4$, respectively $Pd_4L^{F2}_4L^{S8}_4$ (Figure 209, a, c). It is significantly weaker and its intensity is comparable to the one found for this contact in the trinuclear assemblies. While the contact between H^1 and H^2 can be observed also there, it is extremely weak and close to being no longer differentiable from the noise of the spectrum. The distance of these protons in $Pd_3L^{F2}_3L^{S1}_3$ ranges between 4.4-4.5 Å, derived from the X-ray structure, matching the distance of the corresponding protons in the *in silico* structure of $Pd_4L^{F2}_4L^{S6}_4$ extremely well. While a certain conformational freedom has to be taken into consideration, the change would be likely in the picometer range and not affect the NOE cross peak intensity by the observed magnitude, especially considering that it would be the average of all adaptable distances in a flexible molecule, thus being even lower.

Contrary to the very low intensity observed for the trinuclear complexes and $Pd_4L^{F2}_4L^{S6}_4$, the intensity of the cross peak assigned to the contact between H^1 and H^2 is quite pronounced for $Pd_4L^{F2}_4L^{S8}_4$, $Pd_4L^{F2}_4L^{S9}_4$ and $Pd_4L^{F2}_4L^{S10}_4$. As evident from Figure 209 a) and c) the intensity of the contact H^1-H^2 relative to the one of H^1 to H^a is approximately 50% of its value which matches the rough distance of d = 3.5 Å of the corresponding protons in the *in silico* structure. The ratio is a little lower for $Pd_4L^{F2}_4L^{S8}_4$ which could be due to a steeper angle of ligand L^{F2} resulting in a distance increase, however the similarity of the NOE pattern for $Pd_4L^{F2}_4L^{S9}_4$ (Figure 209, a) and $Pd_4L^{F2}_4L^{S8}_4$ (Figure 209, c) suggests a very close structural relationship in between the two structures, which is different from the one of the previously reported trinuclear complexes and $Pd_4L^{F2}_4L^{S6}_4$ (Figure 209, b). With the molecular structure of all assemblies being quite rigid and the data at hand, it can be concluded that a tetranuclear complex based on a nitrobenzene-backbone (L^{S6}) adopts a bowl-conformation with all counter ligands L^{F2} pointing in one direction, while the tetranuclear assemblies $Pd_4L^{F2}_4L^{S8-10}_4$ sport a saddle conformation with the ligands altering between pointing up or down. As to why the assembly formed from Pd(II), L^{F2} and L^{S8} adopts a saddle conformation instead of a bowl like the one formed with L^{S6}, an educated guess can be made based upon the nature of the driving force that induces the switch from trinuclear to tetranuclear assembly. While this change is based on COULOMB repulsion for $Pd_4L^{F2}_4L^{S6}_4$ which is relieved by a substantial amount going from trinuclear to tetranuclear complex (chapter 3.4.3.1) the steric bulk provided by the benzoate-group in L^{S8} is a little harder to interpret. The *in silico* structure shows the benzoate-group taking up a conformation pointing directly to the backbone of L^{F2} in both, bowl and saddle structure (Figure 201), while the NOE intensity of the corresponding contact H^g-H^9 provides the information, that the group can very well swing out of this conformation. This flexibility might be the reason for the topological change

from bowl to saddle as in the bowl conformation, the inside of the structure would be quite cramped having four benzoate-residues pointing to the center of the molecule. Furthermore, the aforementioned dipole moments are opposed to one another in the saddle conformation, making it enthalpically more favored. Furthermore, if a saddle conformation is adapted, the benzoate-group is less constrained, which would be favorable in terms of entropy. To verify this claim, MD simulations, as well as energy calculations based on DFT optimized structures should be performed.

3.4.4 Summary: Structural Discussion

To summarize, nine novel, heteroleptic assemblies based upon Pd(II), L^{F2} and a short counter ligand L^{SX} have been characterized and each one has been analyzed by 1D and 2D NMR techniques, mass spectrometry and *in silico* structure. Furthermore, the photophysical properties of all nine clean complexes were analyzed regarding absorption and emission. A novel heteroleptic topology, $Pd_3L^A_3L^B_3$ has been achieved, in which the short ligand L^{S1-5} can carry a variety of different functional groups, while the counter ligand L^{F2} maintains its fluorescent properties upon Pd(II) coordination providing photophysical readout potential. The resulting structure can be described as bowl-like with no vacant coordination sites. Quantum yields were determined for all trinuclear complexes finding that $Pd_3L^{F2}_3L^{S4}_3$ carrying a methoxy-group on its smaller ligand has the highest measured QY within the array of analyzed structures. Additionally, the scope of short ligands L^{S6-10} has been introduced to elucidate the structural impact of a) electrostatic repulsion (L^{S6}), b) steric bulk ($L^{S7/8}$) and c) bite angle increase ($L^{S9/10}$) on the outcome of the coordination event. Each of these alterations led to an increase in nuclearity from trinuclear complex to a tetranuclear one. A detailed analysis of the tetranuclear structures was performed regarding the orientation of the ligands using 3D NOE analysis with the intensity of the signals posing as the third dimension. A summary of all structures, their nuclearity and hydrodynamic radii in given in Table 10.

Table 10: Summary of ligand combinations used in this project, formed structure upon Pd(II) addition, nuclearity and measured hydrodynamic radius. Since L^{S7} did not form a clean structure with L^{F2}, the hydrodynamic radius was not be determined.

L^{F2} +Pd+	L^{S1}	L^{S2}	L^{S3}	L^{S4}	L^{S5}	L^{S6}	L^{S7}	L^{S8}	L^{S9}	L^{S10}
Structure	UFO	UFO	UFO	UFO	UFO	UFO	UFO	Saddle	Saddle	Saddle
Nuclearity	3	3	3	3	3	4	3+4	4	4	4
r_H (Å)	14.78	14.57	14.34	14.26	14.14	16.57	n.a.	15.49	17.01	17.77

3.4.5 Host-Guest Chemistry

3.4.5.1 Host-Guest Chemistry – Chiral Guests (**G**)

After thorough structural analysis of these novel supramolecular assemblies, an attempt was made to study the host-guest chemistry of the trinuclear complexes $Pd_3L^{F2}{}_3L^{S1-5}{}_3$. As they are inherently open, bowl-like structures without vacant coordination sites, size and geometry of potential guest molecules are subject to way less restrictions. This chapter will contain experiments with two different types of guest molecules. One type will be chiral guest molecules, subsequently referred to as "**G**", while the other type addresses dyes, referred to as "**D**".

The chiral molecules chosen for guest studies were (*R*)-1,1'-Binaphthyl-2,2'-disulfonate (*(R)*-BINSO, **G¹**), (*S*)-1,1'-Binaphthyl-2,2'-phosphate (*(S)*-BINPhos, **G²**) and (*R*)-camphorsulfonate (*(R)*-CSA, **G³**) with their structures shown in Scheme 30.
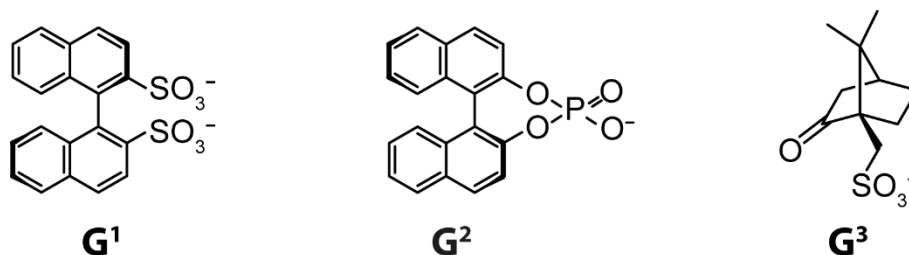
Scheme 30: Chemical structure of the chiral guests **G¹⁻³** used as guests for $Pd_3L^{F2}{}_3L^{S1-5}{}_3$.

A 0.467 mM solution of $Pd_3L^{F2}{}_3L^{S1}{}_3$ has been setup as described before and a 17.5 mM solution of **G¹** has been added in steps of 0.2 equiv.
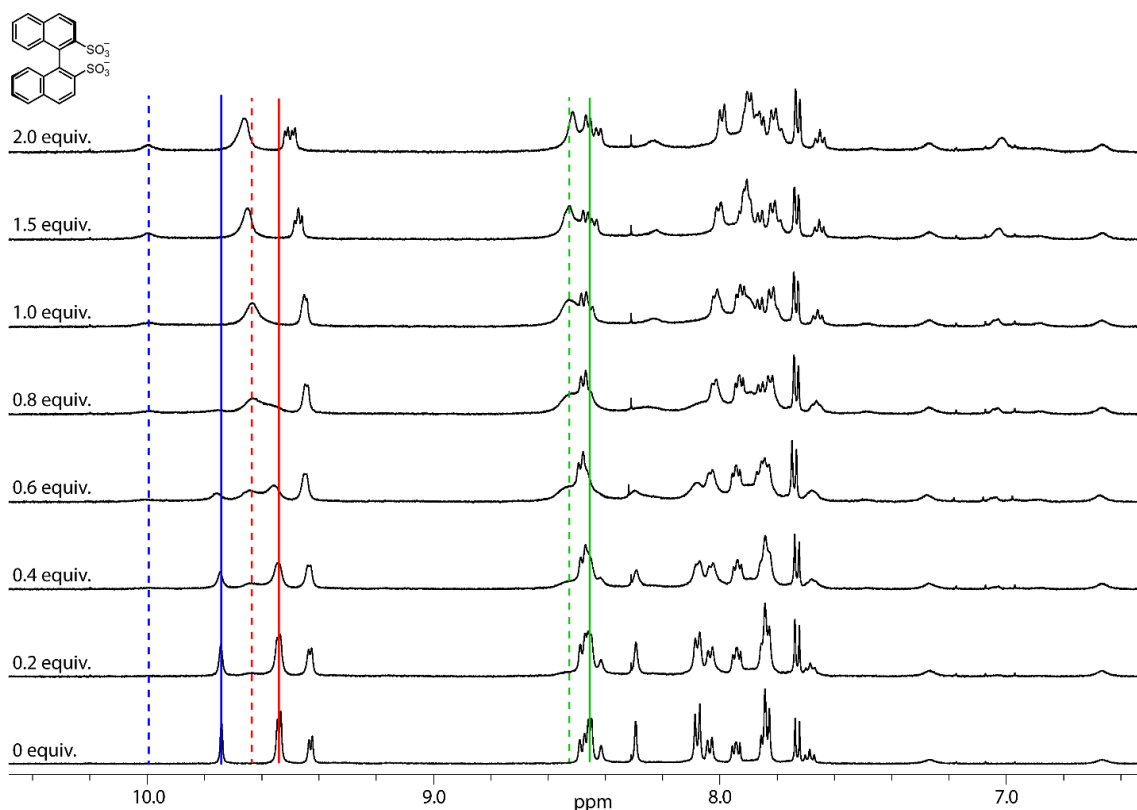
Figure 210: Partial ^{1}H NMR spectra (500 MHz, 298 K, DMSO-d_6) of the titration of (*R*)-BINSO (**G^1**) to Pd$_3$**L^{F2}**$_3$**L^{S1}**$_3$. Splitting proton signals are marked by color (solid line: original location of the signal; dashed line: newly emerging signal).

As evident from Figure 210, the signals shift slightly, but also splitting and broadening of signals close to the Pd(II) coordination site is observed (H^1, H^a and H^b), while other proton signals broaden and shift (e.g. H^9). The original position of the splitting signals is indicated by solid lines, the newly emerging signals corresponding to the aforementioned with dashed lines in the same color. Due to this intricate mixed behavior of splitting and shifting protons, neither binding mode nor binding constant could be determined.

To verify binding of **G^1** to Pd$_3$**L^{F2}**$_3$**L^{S1}**$_3$ and obtain information on the number of **G^1** associating to the host, CSI-MS was measured. The obtained spectrum is shown in Figure 211.
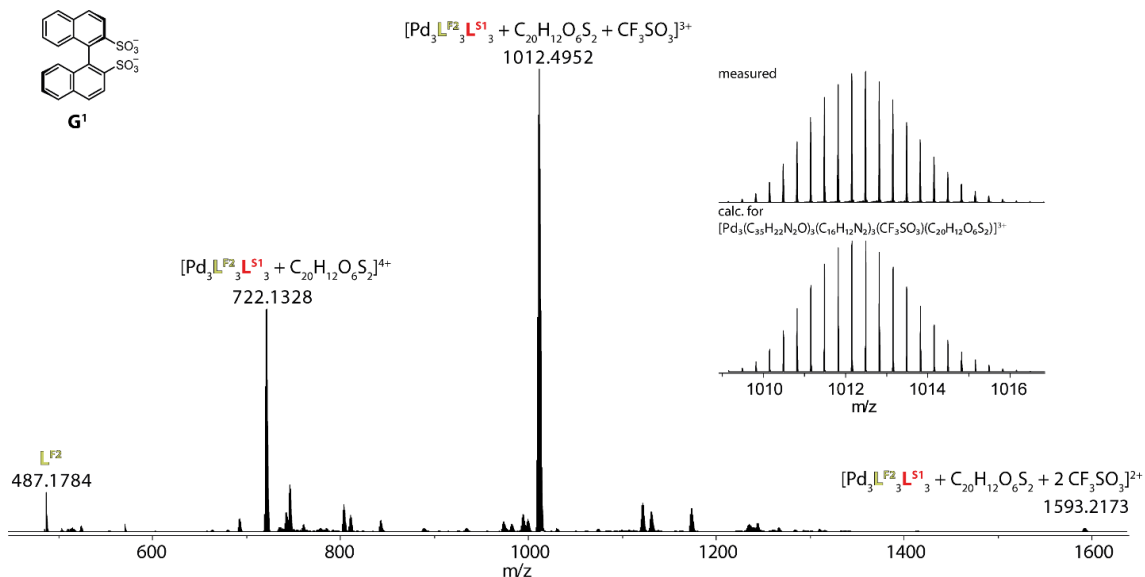
Figure 211: CSI-MS spectrum of Pd$_3$**L**$^{F2}_3$**L**$^{S1}_3$ after the addition of 1 equiv. **G**^{1}. The measured and calculated isotopic pattern of the highest peak are shown in the inset.

The CSI MS spectrum depicted in Figure 211 shows peaks at m/z = 722.1328 (4+), 1012.4952 (3+) and 1593.2173 (2+). All of the aforementioned peaks are assignable to a species of the chemical composition [Pd$_3$**L**$^{F2}_3$**L**$^{S1}_3$ + **G**^{1} + xCF$_3$SO$_3$]$^{(6-2-x)+}$ (x = 0-2) with the z =3+ species being most abundant. The association of 2 **G**^{1} to the host complex has not been detected. While this would be inherently possible, since the molecule still carries a 4+ charge after binding 1 equiv. **G**^{1}, inside binding of 2 **G**^{1} is highly unlikely due to steric reasons.

After confirming binding of **G**^{1} to Pd$_3$**L**$^{F2}_3$**L**$^{S1}_3$, is was reasonable to assume similar behavior for the structural related compounds Pd$_3$**L**$^{F2}_3$**L**$^{S2-5}_3$. Thus, circular dichroism measurements were performed on the whole set of new trinuclear assemblies Pd$_3$**L**$^{F2}_3$**L**$^{S1-5}_3$ without additional NMR and MS analysis. The measured spectra are shown in Figure 212.
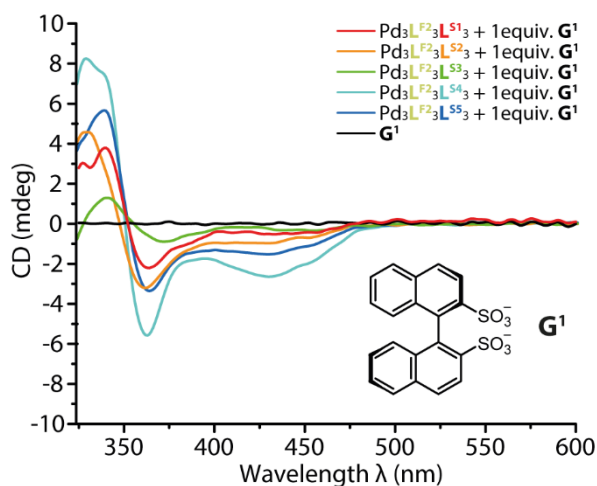
Figure 212: Circular dichroism measurement of $Pd_3L^{F2}_3L^{S1-5}_3$ after addition of 1 equiv. (*R*)-BINSO (G^1). CD of the guest is shown in black.

As evident from Figure 212, the phenyl-based $Pd_3L^{F2}_3L^{S1}_3$ (red) is not showing the strongest chiral readout out of the five analyzed structures. While all structures do show chiral induction from G^1 to the assembly, strong differences in intensity of this effect are observed depending on counter ligand L^{S1-5}. The assembly formed by the small ligand based on aniline, $Pd_3L^{F2}_3L^{S3}_3$ (green), shows the weakest response for all analyzed assemblies, while the assembly $Pd_3L^{F2}_3L^{S4}_3$, based on methoxy-functionalized L^{S4}, shows the strongest chiral induction after addition of G^1. Apart from the intensity of the chiral induction, the trend is consistent within all five assemblies, a positive CD response in the UV region until approximately $\lambda = 360$ nm followed by a change to negative CD response from there on.

After finding that $Pd_3L^{F2}_3L^{S4}_3$ showed the most intense CD response upon G^1 addition, its binding has been characterized via ^{1}H NMR titration and ESI-MS. Interestingly, the ^{1}H NMR titration showed G^1 having fast exchange kinetics with the host molecule $Pd_3L^{F2}_3L^{S4}_3$ (Figure 348, experimental part), as opposed to slow exchange with $Pd_3L^{F2}_3L^{S1}_3$. A binding constant K of G^1 to $Pd_3L^{F2}_3L^{S4}_3$ has been determined to be $K = 139.19 \pm 6.53$ M^{-1}. While the MS spectrum does look way more convoluted than the one for [G^1@ $Pd_3L^{F2}_3L^{S1}_3$] (Figure 352, experimental part), it is noted that it was measured using mild ESI conditions as opposed to cryo-spray ionization, thus higher energies might lead to disassembly or loss of host-guest interaction.

Since ligand L^{F2} maintains its fluorescent properties in the formed assemblies even upon Pd(II) coordination and all systems showing a response in the CD measurement with G^1, the assemblies $Pd_3L^{F2}_3L^{S1-5}_3$ with each 1 equiv. G^1 were analyzed in respect to circular polarized luminescence.
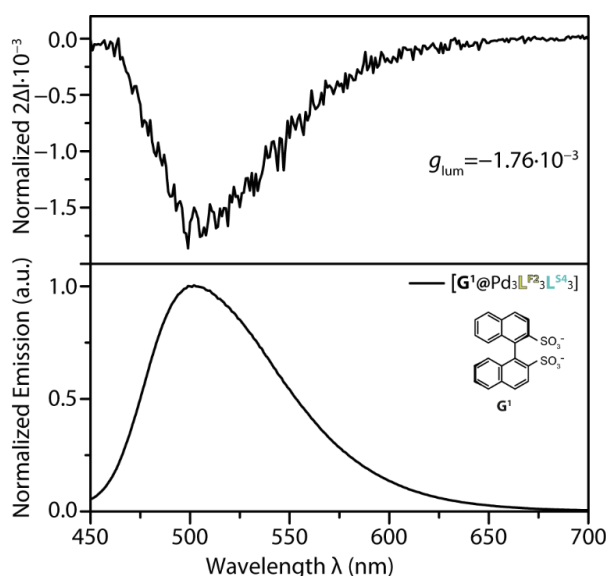
Figure 213: Normalized emission and CPL signal of $Pd_3L^{F2}_3L^{S4}_3$ after addition of 1 equiv. $\mathbf{G^1}$. Exited at $\lambda = 365$ nm.

As evident from Figure 213, $Pd_3\mathbf{L^{F2}}_3\mathbf{L^{S4}}_3$ shows a strong CPL response with an emission maximum at $\lambda = 502$ nm in the presence of 1 equiv. $\mathbf{G^1}$ with a g_{lum} value of $-1.76\cdot10^{-3}$, which is relatively high if compared to other luminescent Pd(II) systems which themselves are pretty scarce.[48,51,67,68]

Wu et al. reported a guest induced increase of g_{lum} by factor 4 in a $Pd_2\mathbf{L^{A/B}}_2\mathbf{L^{P/M}}_2$ system containing a fluorescent ligand $\mathbf{L^A}$, respectively $\mathbf{L^B}$, and a helicene-based ligand $\mathbf{L^M}$, respectively $\mathbf{L^P}$. The strongest measured values for g_{lum} were $3.5\cdot10^{-3}$ for $[\mathbf{G}@Pd_2\mathbf{A}_2(\mathbf{M/P})_2]$ and $1.5\cdot10^{-3}$ for $[\mathbf{G}@Pd_2\mathbf{B}_2(\mathbf{M/P})_2]$ with the initial g_{lum} values without guest being $>1.0\cdot10^{-3}$. They concluded the increase in overall g_{lum} values was due to a decrease in structural flexibility and thus non-radiative pathways, however warned not to neglect the electronic influence of the negatively charged guest.[67] Another publication using the same emitting ligand $\mathbf{L^A}$ with a chiral, cyclohexane-based counter-ligand $\mathbf{L^B}$ highlighted g_{lum} values of $2.5\cdot10^{-3}$.[68]

While the g_{lum} values obtained for the aforementioned systems are higher than the ones found here for $[\mathbf{G^1}@Pd_3\mathbf{L^{F2}}_3\mathbf{L^{S4}}_3]$, it has to be considered, that the chirality in the aforementioned systems stems from the incorporated ligands $\mathbf{L^M}$, respectively $\mathbf{L^P}$, or $\mathbf{L^B}$ and not from a chiral guest. Chirality transfer from the chiral guest molecule $\mathbf{G^1}$ to a luminescent coordination assembly with the same luminophore $\mathbf{L^{F2}}$ has previously been shown to yield far lower g_{lum} values (see chapter 3.3) of $-1.5\cdot10^{-4}$ with $\lambda_{ex} = 350$ nm. While the excitation wavelength is not exactly the same, it is in close range and it can be assumed that the g_{lum} values will not be affected to such a mayor extent.

The other systems [G^1@Pd$_3$L$^{F2}_3$L$^{S1}_3$], [G^1@Pd$_3$L$^{F2}_3$L$^{S2}_3$], [G^1@Pd$_3$L$^{F2}_3$L$^{S3}_3$] and [G^1@Pd$_3$L$^{F2}_3$L$^{S5}_3$] were also analyzed in regard to their CPL response under the same conditions as [G^1@Pd$_3$L$^{F2}_3$L$^{S4}_3$]. The resulting g_{lum} values are given in Table 11.

Table 11: g_{lum} values measured for Pd$_3$L$^{F2}_3$L$^{S1-5}_3$ after the addition of 1 equiv. G^1.

	[G^1@Pd$_3$L$^{F2}_3$L$^{S1}_3$]	[G^1@Pd$_3$L$^{F2}_3$L$^{S2}_3$]	[G^1@Pd$_3$L$^{F2}_3$L$^{S3}_3$]	[G^1@Pd$_3$L$^{F2}_3$L$^{S4}_3$]	[G^1@Pd$_3$L$^{F2}_3$L$^{S5}_3$]
g_{lum}	$-6.64 \cdot 10^{-4}$	$-6.08 \cdot 10^{-4}$	n.a.[a]	$-1.76 \cdot 10^{-3}$	$-9.67 \cdot 10^{-4}$

[a]signal-to-noise ratio of the spectrum did not allow the determination of accurate values

While the systems with short ligands L^S based on phenyl- or pyridine backbones (Pd$_3$L$^{F2}_3$L$^{S1}_3$ or Pd$_3$L$^{F2}_3$L$^{S2}_3$) show relatively weak g_{lum} values, the ones based on phenol, and especially anisole show values of $g_{lum} \geq -1.0 \cdot 10^{-3}$. Pd$_3L^{F2}_3L^{S3}_3$ with its short ligand being based on aniline, does not yield any exploitable results which could be either due to disassembly during the measurement or a generally weak response to G^1. The strong response from Pd$_3$L$^{F2}_3$L$^{S4}_3$ and Pd$_3$L$^{F2}_3$L$^{S5}_3$ could either stem from the crowded inner pocket of the bowl-shaped molecules due to the functional groups, which would further explain the stronger response of Pd$_3$L$^{F2}_3$L$^{S4}_3$ to G^1, however an electronic effect of the electron withdrawing oxygen moiety cannot fully be ruled out. Due to the two naphthyl rings of G^1 only being linked by a single bond, a certain degree of freedom of rotation around the C7-C11 bond is granted and the guest can adjust itself inside the host while its negatively charged sulfonate groups will likely be oriented towards the Pd(II) centers of the host.

Analysis of the system's interaction with G^2 was performed analogous to the previously described procedures.
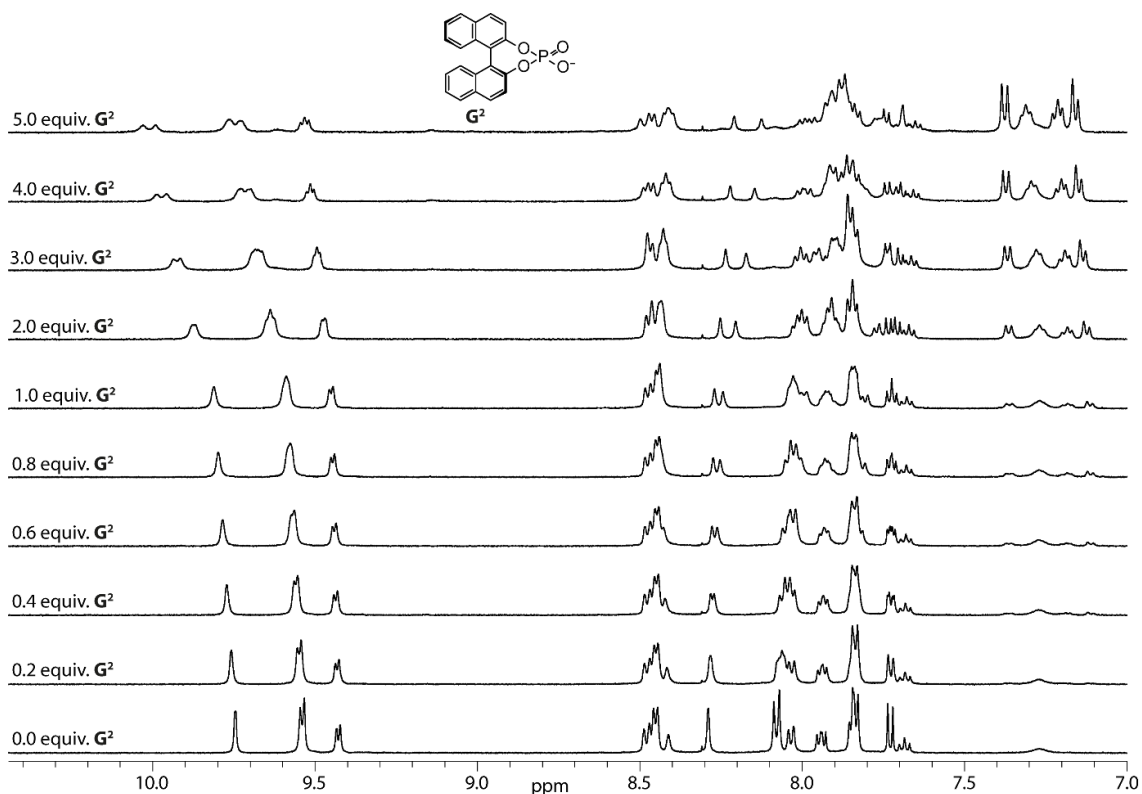
Figure 214: Partial ^{1}H NMR spectra (500 MHz, 298 K, DMSO-d_6) of the titration of (S)-BINPHOS (G^2) to $Pd_3L^{F2}_3L^{S1}_3$.

A binding constant of $K = 85.9 \pm 0.96$ M^{-1} could be determined for the association of G^2 to $Pd_3L^{F2}_3L^{S1}_3$ (Figure 214). As already observed for G^1, broadening of inwards pointing protons H^1 and H^a until 1 equiv. G^2 is observed. It is noted, that the signal broadening is by far not as pronounced as for G^1. Afterwards, in addition to further shifting of the proton signals, splitting was observed. The signals associated to proton H^9, directly located at the fluorenone-backbone of ligand L^{F2}, shows splitting immediately after guest addition. The proton signals stemming from G^2 are shifted as compared to the ones of the free guest molecule (Figure 361 and Figure 362, experimental part). The ESI MS spectrum of the host-guest mixture (Figure 363, experimental part) shows fragmentation, likely due to reasons discussed previously.

After the binding of G^2 to the host was confirmed by ^{1}H NMR and MS techniques, CD spectra of the five host-guest complexes $[G^2@ Pd_3L^{F2}_3L^{S1-5}_3]$ were measured (Figure 215).
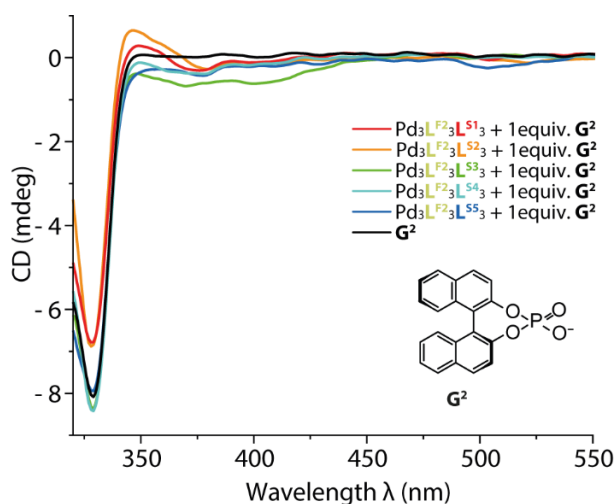
Figure 215: Circular dichroism measurement of $Pd_3L^{F2}_3L^{S1-5}_3$ after addition of 1 equiv. G^2. CD of the guest is shown in black.

As evident from the measured spectra as compared to free G^2, the change in CD signal is, if at all, minimal. For host molecules $Pd_3L^{F2}_3L^{S3-5}_3$, the spectrum does not show a positive CD signal at all, while for $Pd_3L^{F2}_3L^{S1/2}_3$, a small positive CD signal (CD (mdeg) < 1) is observable. All structures show a minimal response in between $\lambda = 350 - 430$ nm with $Pd_3L^{F2}_3L^{S5}_3$, having the phenol-based L^{S5} incorporated in its structure, sporting another CD band at $\lambda = 505$ nm. This band is, as previously discussed, attributed to the deprotonation of the phenol and has not been observed with G^1, thus leaving to conclude that (*S*)-BINPHOS (G^2), as a weak base, has the ability to deprotonate $Pd_3L^{F2}_3L^{S5}_3$ in dilution.

While $Pd_3L^{F2}_3L^{S3}_3$, containing aniline-based L^{S3}, showed the weakest CD response for G^1, is shows the strongest response for G^2 with an amplitude of −0.68 mdeg at $\lambda = 380$ nm. This effect could be due to hydrogen bonding of the -NH_2 protons to the oxygen molecules of the phosphate and thus increased chiral induction due to increased conformational stability of the guest inside the host. With results from ^1H NMR titration experiments suggesting inside binding of G^2, there is little to no chirality transfer to the analyzed host molecules. Looking into the differences in structure of the two guests leads to two possible reasons for the lack of response in case of G^2. First, G^2 is only a mono-anion as compared to G^1 carrying two negative charges. This could lead to increased attractive forces and stronger binding of G^1 to the hexacationic hosts in addition to a different spatial orientation of G^2 in its hosts. Second would be the decreased conformational freedom of G^2 due to the rotation around the single bond connecting C^7 and C^{11} being constraint by the phosphate group, while this rotation in G^1 is only limited by steric effects and the two naphthalene-residues can potentially even sit orthogonal to

each other. Since the strongest CPL effect for G^1 was measured with $Pd_3L^{F2}_3L^{S4}_3$, the experiment was repeated using G^2 but no significant CPL could be detected.

To analyze the effect of the charge and size of the chiral guest molecule, the binding of (R)-camphorsulfonate ((R)-CSA, G^3), a small, monoanionic guest, was analyzed following the previously established procedures.

A 0.467 mM solution of $Pd_3L^{F2}_3L^{S1}_3$ has been prepared and a 17.5 mM solution of G^3 has been added in steps of 0.1 equiv. until the addition of 1 equiv. total, followed by 0.5 equiv. steps until 4.0 equiv. of G^3 in respect to the host have been added (Figure 216).
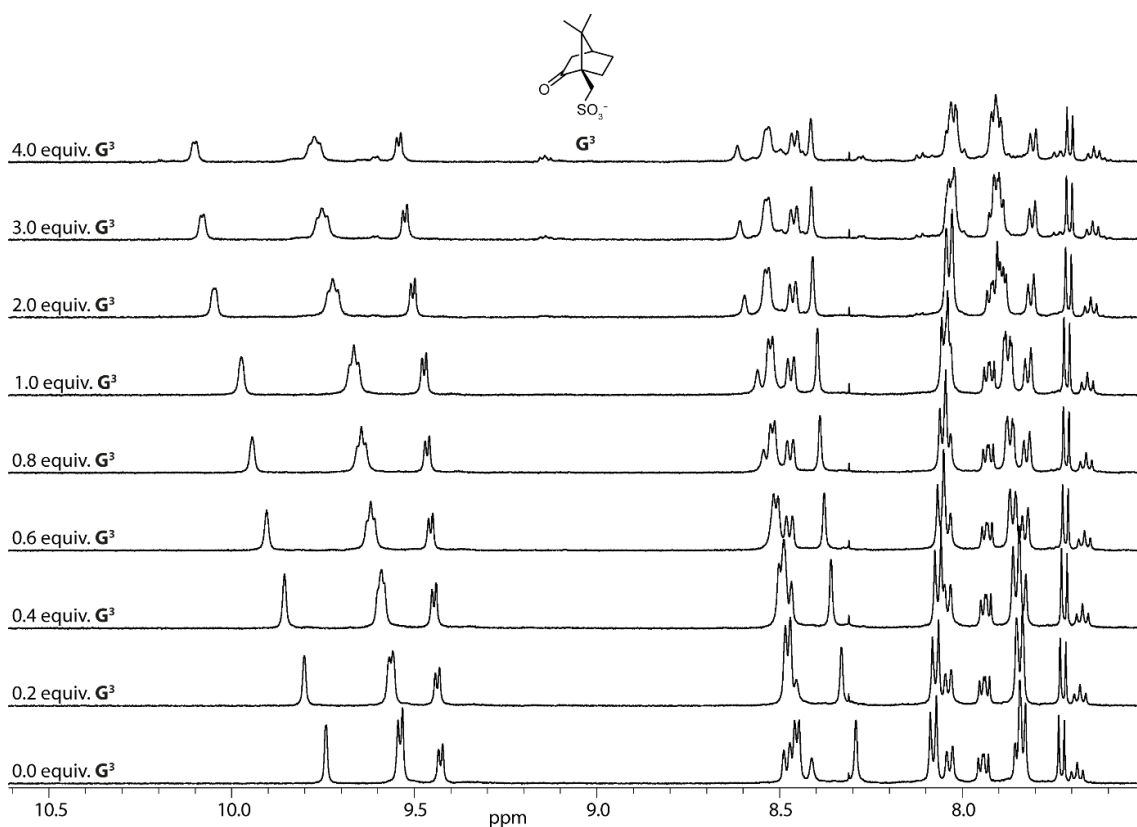
Figure 216: Partial ^{1}H NMR spectra (500 MHz, 298 K, DMSO-d_6) of the titration of (R)-Camphorsulfonate (G^3) to $Pd_3L^{F2}_3L^{S1}_3$.

While signal broadening has been observed after the addition of G^1, proton signals broaden only by a small margin upon addition of G^3. Inwards pointing protons like H^1, H^a, H^9 and H^e shift downfield and the signals of H^1 and H^a show splitting, which is far less pronounced as the splitting observed in the ^{1}H NMR titration of $Pd_3L^{F2}_3L^{S1}_3$ with G^2. A binding constant of $K = 8472.8 \pm 963.8$ M^{-1} could be determined, which is extremely high for guest binding in DMSO, as e.g. a recent study in our group showed binding constants of guest molecules to Pd(II)-based hosts amounting to just up to $K = 2062 \pm 31$ M^{-1}.[65]

To further characterize the system, an ESI MS spectrum of a 1:1 mixture of $Pd_3L^{F2}_3L^{S1}_3$ and G^3 was measured (Figure 367, experimental part). The spectrum shows the most

abundant species being $Pd_3L^{F2}_3L^{S1}_3 + 2G^3$. While binding of G^3 to the host has been confirmed in the NMR experiment, MS analysis would suggest two guest molecules associating to the host. It is however unclear from this measurement, as to where the guest molecules are located and the binding isotherms from the ^1H NMR titration strongly suggest only one guest molecule binding inside the host's cavity, as evident from the curve's scope (Figure 217), thus leaving the second guest molecule observed in the MS measurement simply being a counter anion.
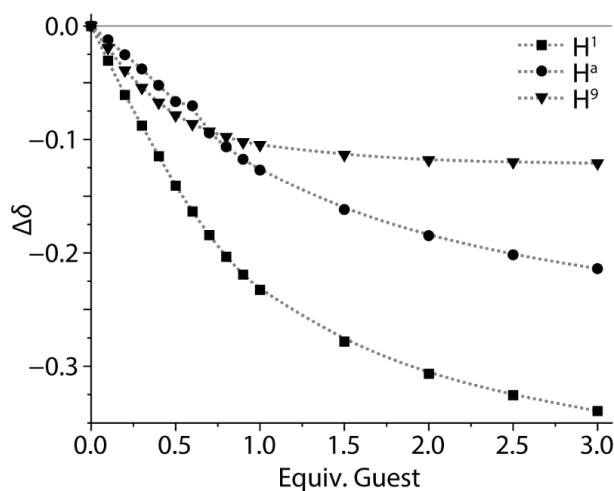
Figure 217: $\Delta\delta$ of proton signals H^1, H^a and H^9 of $Pd_3L^{F2}_3L^{S1}_3$ upon consecutive addition of G^3. Proton signal H^e was not included due to signal overlap.

After having confirmed the binding motif of G^3 to the model host, all five species were analyzed in regard to potential chirality transfer from G^3 to $Pd_3L^{F2}_3L^{S1-5}_3$ (Figure 218).
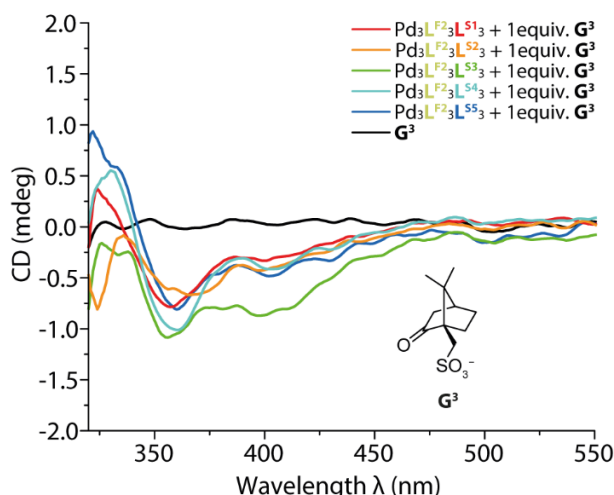
Figure 218: Circular dichroism measurement of $Pd_3L^{F2}_3L^{S1-5}_3$ after addition of 1 equiv. G^3. CD of the guest is shown in black.

Figure 218 shows the CD spectra of G^3 compared to the 1:1 mixtures of G^3 and $Pd_3L^{F2}_3L^{S1-5}_3$. All species do indeed show chiral induction from the guest, though the effect of G^3 on all systems does not exceed ± 1.1 mdeg, which is likely attributed to the small size of G^3 as compared to the hosts. And while $Pd_3L^{F2}_3L^{S4}_3$, with increased steric

232

demand inside its cavity due to the methoxy-residues, had the strongest CD response with (*R*)-BINSO (**G**^{1}) and the aniline-based Pd$_3$**L**$^{F2}_3$**L**$^{S3}_3$ showed the weakest, the effect does seem to be reversed in case of **G**^{3}. Albeit all structures respond to guest addition with an extremely weak CD signal, Pd$_3$**L**$^{F2}_3$**L**$^{S3}_3$ does show the strongest response, especially in the region from λ = 350 – 450 nm. Noteworthy is also, that the phenol-based Pd$_3$**L**$^{F2}_3$**L**$^{S5}_3$ sports the highest positive chiral induction being 0.94 mdeg. Both structures have hydrogen bond donors incorporated in their cavity, leaving to suggest an elevated effect of the small, monoanionic, chiral guest based on hydrogen bonding interactions. As already observed for **G**^{2}, no CPL could be detected when combining Pd$_3$**L**$^{F2}_3$**L**$^{S4}_3$ with 1 equiv. **G**^{3} (Figure 369, experimental part). This result is in good accordance with the weak CD response and is likely attributed to the size of the guest.

To summarize, the analysis of the three guest molecules **G**$^{1-3}$ shows the effect of a) the charge and b) the size of the guest molecule on the corresponding CD readout with the host molecules Pd$_3$**L**$^{F2}_3$**L**$^{S1-5}_3$. While the sterically demanding, dianionic (*R*)-BINSO (**G**^{1}) yields the strongest CD response with a sterically crowded host molecule (Pd$_3$**L**$^{F2}_3$**L**$^{S4}_3$), the monoanionic guest molecules (*S*)-BINPHOS (**G**^{2}) and (*R*)-CSA (**G**^{3}) show elevated, though still extremely weak, CD output when hydrogen bond donors are involved.

3.4.5.2 Host-Guest Chemistry – Dye-based Guest Molecules (D)

Considering the size and structure of the $Pd_3L^{F2}_3L^S_3$ assemblies, being open, bowl-like molecules, an array of bis-sulfonate-based azo dyes (**D**[1-4]), both with linear and unilateral charge distribution, and rhodamine-based "Texas Red" (**D**[5]) were chosen as potential guest molecules to study their interaction with the new assemblies (Scheme 31). Chosen azo dyes were "Sunset Yellow FCF" (**D**[1]), "Allura Red AC" (**D**[2]), "Azorubine" (**D**[3]) and "Naphthol Blue Black" (**D**[4]). While all of these dyes are inherent bis-sulfonates, their color and positioning of the sulfonate groups differs vastly. In addition to that, **D**[5] is known for its emissive properties and could thus be used to analyze host-to-guest FRET, as opposed to host internal FRET from one ligand to another as described in the previous chapter 3.3.
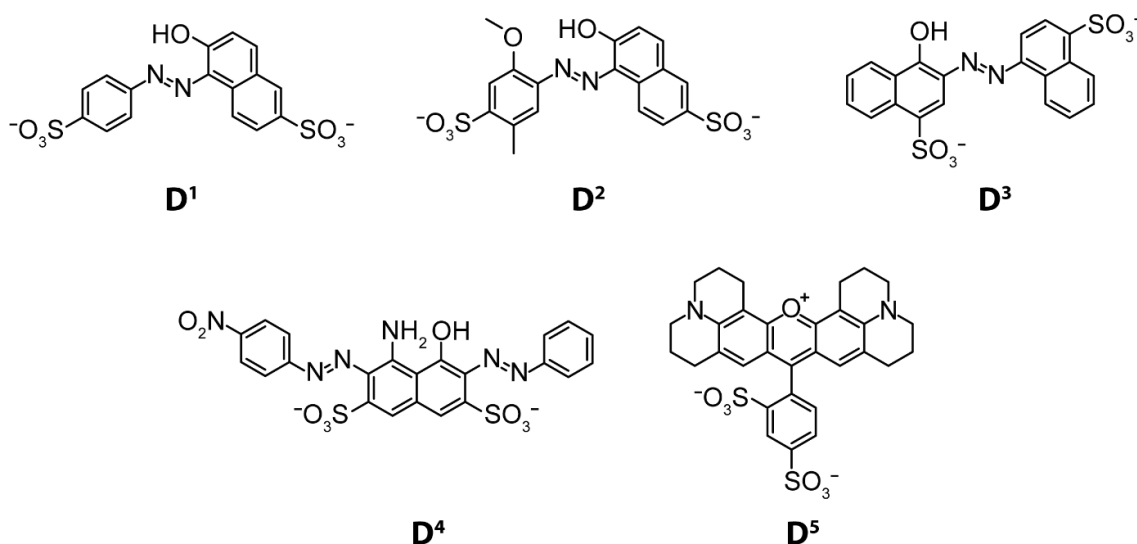
Scheme 31: Chemical structure of the dyes **D**[1-5] used as guest molecules for $Pd_3L^{F2}_3L^{S1}_3$.

To study the basic interaction of the new structural motif, all host-guest experiments were carried out using $Pd_3L^{F2}_3L^{S1}_3$ thus the effect of functional groups and bulk is not covered. Experiments were carried out using ^{1}H NMR and UV/VIS titrations supported by CSI-MS studies. While **D**[1] and **D**[2] carry close structural similarity with an almost linear connection of the two sulfonate groups, **D**[3] possesses increased steric demand and a slightly different orientation of the aforementioned groups. **D**[4] and **D**[5] pose sulfonate groups attached to the same aromatic system within the molecule, be it naphthalene (**D**[4]) or phenyl (**D**[5]), thus yielding a higher local concentration of negative charges. While it can be assumed, that all of these dianions will interact with $Pd_3L^{F2}_3L^{S1}_3$, being hexacationic, differences in their respective binding motifs will be analyzed and correlated with the given structure of dye molecule **D**[1-5].

3.4.5.2.1 Linear dyes **D^1** (SunsetYellow) and **D^2** (AlluraRed)

The initial assembly formation followed the protocol established for these assemblies and previously described. All ^{1}H NMR titration experiments were carried out in a 5 mm standard NMR tube with an assembly concentration of 0.46 mM and a final volume of 600 µl. A 17.5 mM solution of disodium 6-hydroxy-5-[(4-sulfophenyl)azo]-2-naphthalenesulfonate was prepared and added in steps of 1.6 µl, equaling 0.1 equiv. in respect to the Pd$_3$L$^{F2}_3$L$^{S1}_3$ assembly, until reaching 1.0 equiv. **D^1**. From this point on, 0.5 equiv. were added until reaching 2.0 equiv. in total guest addition (Figure 219).
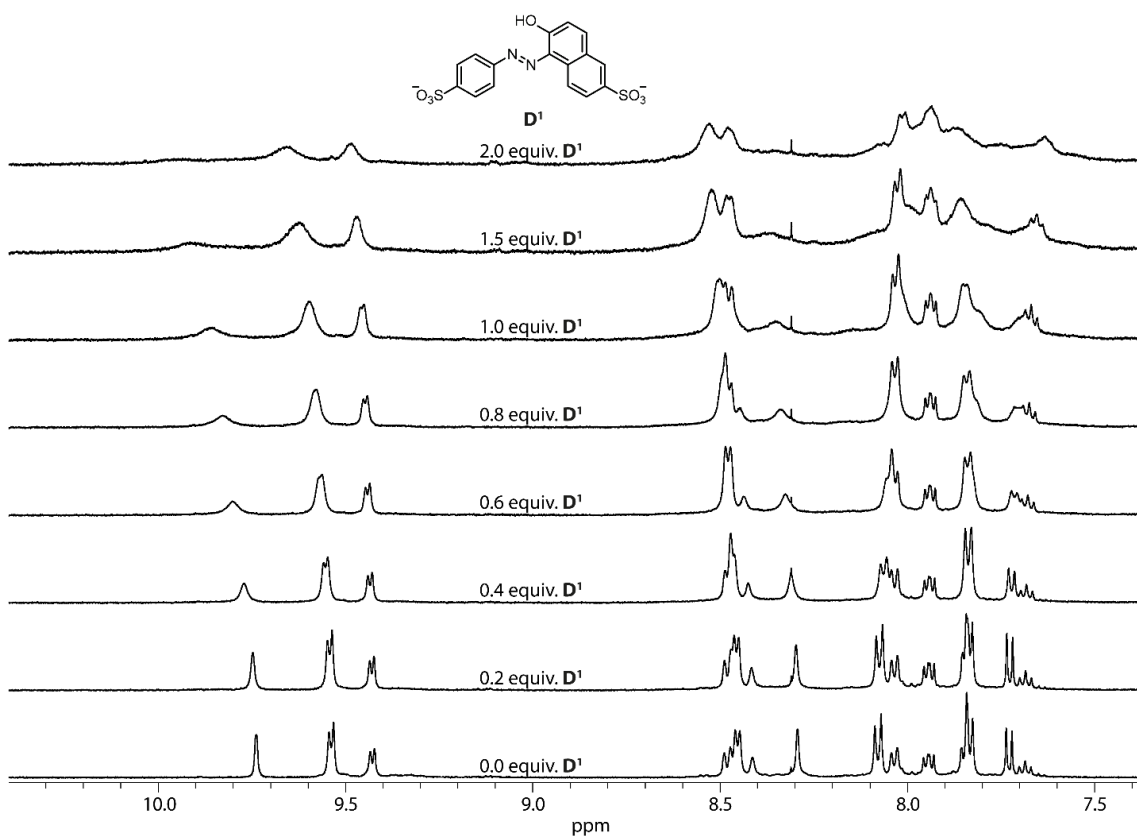
Figure 219: Partial ^{1}H NMR spectra (500 MHz, 298 K, DMSO-d_6) of the titration of **D^1** to Pd$_3$L$^{F2}_3$L$^{S1}_3$.

Upon addition of **D^1**, the proton signals of the Pd$_3$L$^{F2}_3$L$^{S1}_3$ assembly broaden, especially **H^1**, which broadens up to the point of no longer being distinguishable from the spectral noise after addition of 2.0 equiv. **D^1** (Figure 219). In addition to that, a downfield shift is observable for most signals. Due to this intense broadening and signal overlap (e.g. for H^9), a binding constant was not determined. A further observation upon titrating **D^1** to Pd$_3$L$^{F2}_3$L$^{S1}_3$ was the decrease in signal-to-noise ratio of the spectrum while keeping the measurement parameters constant. Since no precipitation could be observed, the formation of a bigger structure can be suggested.

It is noted, that a comparison of the spectra of the free host, host-guest mixture and of the free dyes in DMSO-d_6 is shown in the experimental part associated to each individual titration. As the concentration of the dyes is very low and the proton signals broaden upon interaction with the host, a clear assignment in the mixture cannot readily be given (Figure 372and Figure 373, experimental part).

A CSI-MS spectrum of a 1:1 mixture of **D^1** and Pd$_3$**L$^{F2}_3$L$^{S1}_3$** was measured to obtain further information on the present binding motif (Figure 220).
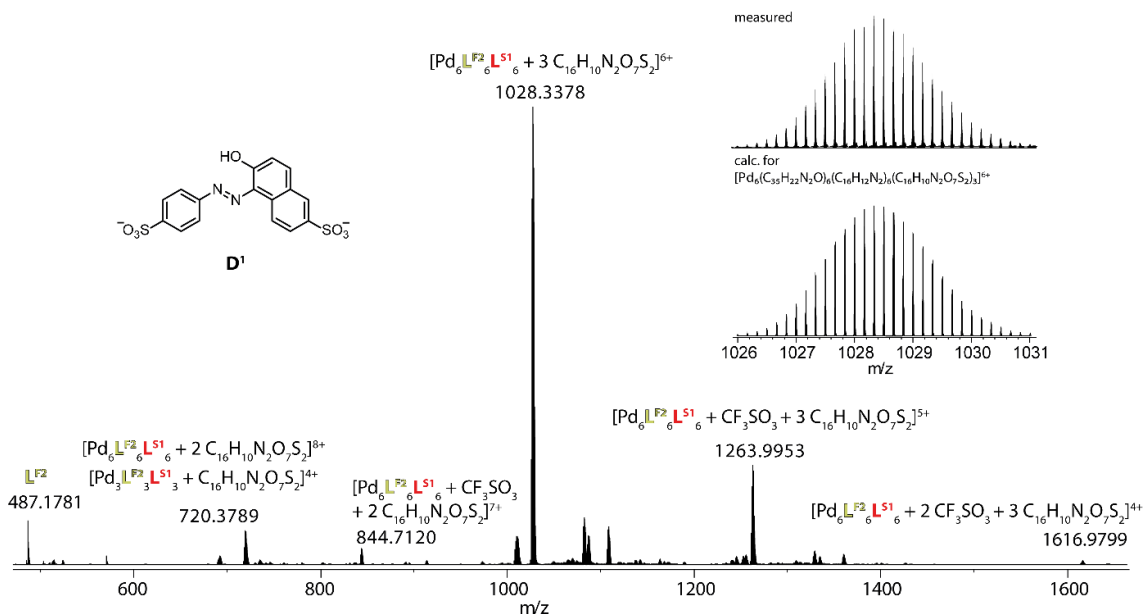
Figure 220: CSI-MS spectrum of Pd$_3$**L$^{F2}_3$L$^{S1}_3$** after the addition of 1 equiv. **D^1**. The measured and calculated isotopic pattern of the highest peak are shown in the inset.

Figure 220 shows the CSI MS spectrum of Pd$_3$**L$^{F2}_3$L$^{S1}_3$** after addition of 1 equiv. **D^1**. All dominant peaks could be assigned to the species [Pd$_6$**L$^{F2}_6$L$^{S1}_6$** + x**D^1** + y CF$_3SO_3$]$^{(12-2x-y)+}$ (x = 2,3 , y = 0-2). Additionally, a very small intensity peak of [Pd$_3$**L$^{F2}_3$L$^{S1}_3$** + **D^1**]$^{4+}$ overlapping with [Pd$_6$**L$^{F2}_6$L$^{S1}_6$** + 2**D^1**]$^{8+}$ was found. The inset shows the isotopic pattern of the hexacationic species providing a very clean gaussian distribution typically observed for Pd(II)$_n$ complexes with n ≥ 2. Furthermore, the continuity of the distribution shows, that it is unlikely that two peaks of species with the same *m/z* value (e.g. 6+ and 3+ species) overlap since this would only be given if both species have the same absolute intensity. While [3**G**@2**H**] is the predominant species formed, the spectrum would likely show even less peaks associated to incomplete complexes (n$_{guest}$ < 3) if the correct stoichiometry (1 equiv. host, 1.5 equiv. guest) would have been used. This assumption could be confirmed by remeasuring the host-guest mixture with adjusted ratio. The formation of a higher ordered species like this would further explain the intense broadening and signal-to-noise decrease observed in the ^{1}H NMR spectrum (Figure 220). A high temperature ^{1}H DOSY NMR experiment could provide information regarding

the size of the host-guest complex, though this would only be feasible if the signals sharpen significantly at higher temperatures.

During NMR and MS analysis, a color change of the solution containing both, $Pd_3L^{F2}_3L^{S1}_3$ and D^1 was observed, thus UV/VIS spectroscopy was measured (Figure 221). To observe the color change during the measurement, the assembly was titrated into a solution of the dye, which was deemed a reverse titration as compared to the usual protocol. Measurements were performed at a concentration of 0.046 mM (final assembly and initial dye concentration) to prevent disassembly.
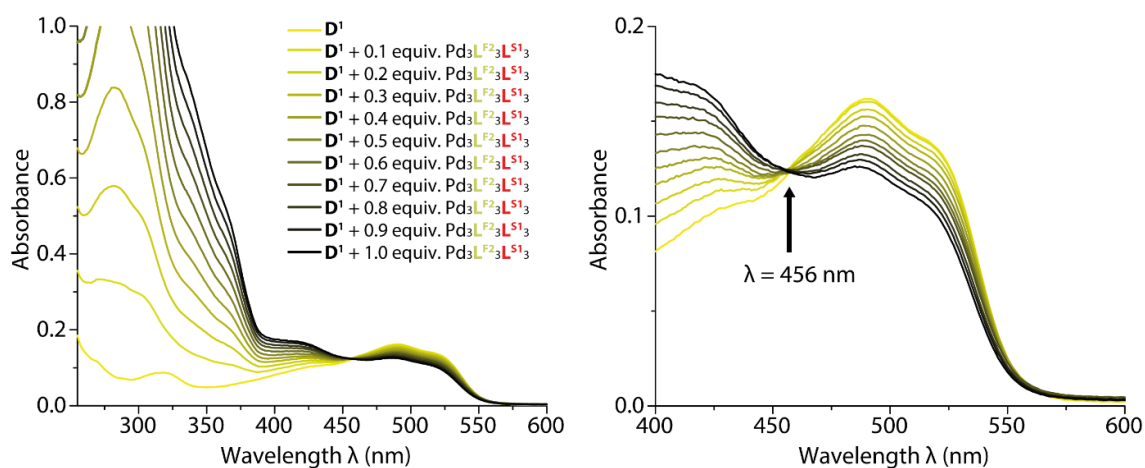
Figure 221: UV/VIS spectra of the reverse titration of $Pd_3L^{F2}_3L^{S1}_3$ to D^1. Left: Wavelength coverage from 255-600 nm; right: Wavelength coverage from 400-600 nm with annotated isosbestic point.

During the reverse titration of the assembly to D^1, a slight hypsochromic and a hypochromic shift of the characteristic absorption band of D^1 at 490 nm was observed. No precipitation was observed. The single isosbestic point of the titration was at $\lambda = 456$ nm.

While it could be argued, that the observed binding motif is a measurement artifact and only is present as a result of CSI-MS conditions, the same results could be obtained with D^2 sharing close structural similarity to D^1 (Scheme 31), especially in respect to the orientation of the sulfonate groups. The ^{1}H NMR titration (Figure 376 to Figure 379, experimental part) shows similar shifts and signal-to-noise ration decrease while again, no precipitation could be observed. CSI-MS yielded a very clean spectrum with species of the $[Pd_6L^{F2}_6L^{S1}_6 + xD^2 + y\ CF_3SO_3]^{(12-2x-y)+}$ (x = 2,3 , y = 0-2) type (Figure 380, experimental part) and the photophysical behavior correlated nicely, with showing hypsochromic and hypochromic shifts of the initial dye absorption band at $\lambda = 515$ nm to $\lambda = 510$ nm. The titration showed a single isosbestic point at $\lambda = 465$ nm (Figure 381, experimental part).

As both dyes, **D^1** and **D^2**, show consistent behavior in all analytic techniques used, the possibility of the observations being an artifact is neglectable. Crystallization of the mixture has been attempted with both counter solvents known to crystallize the host molecule Pd$_3$**L^{F2}**$_3$**L^{S1}**$_3$ well, benzene and toluene. In case of Pd$_3$**L^{F2}**$_3$**L^{S1}**$_3$ + **D^1**, blackish green hexagonal crystals could be observed, yet did not diffract or were twinned. Repetition with an accurate host-guest ratio and a lower initial concentration of the mother liquor is advised to get better results.

Furthermore, the bridging experiments of two Pd$_3$**L^{F2}**$_3$**L^{S1}**$_3$ structures could be performed using simple, linear bissulfonate guests as e.g. the one used in chapter 3.2.

3.4.5.2.2 Bulky linear dye D^3 (Azorubin)

While D^1 and D^2 shared close structural similarity, the sulfonate groups in D^3 are both attached to the first aromatic ring of naphthalenes, thus making its environment sterically more demanding. Furthermore, rotation around single bonds will not yield steric relief inside a potential host molecule, as discussed for D^1 and D^2. A 17.5 mM solution of disodium 4-hydroxy-3-[(1E)-2-(4-sulfonatonaphthalen-1-yl)diazen-1-yl]naphthalene-1-sulfonate was prepared in DMSO-d_6 and added to a freshly prepared solution of 600 μl of $Pd_3L^{F2}_3L^{S1}_3$ in DMSO-d_6 in a standard 5 mm NMR tube. The addition followed 1.6 μl steps, equaling 0.1 equiv., until reaching 1 equiv. and then 0.5 equiv. steps (8 μl) until 2 equiv. in total were added (Figure 222).
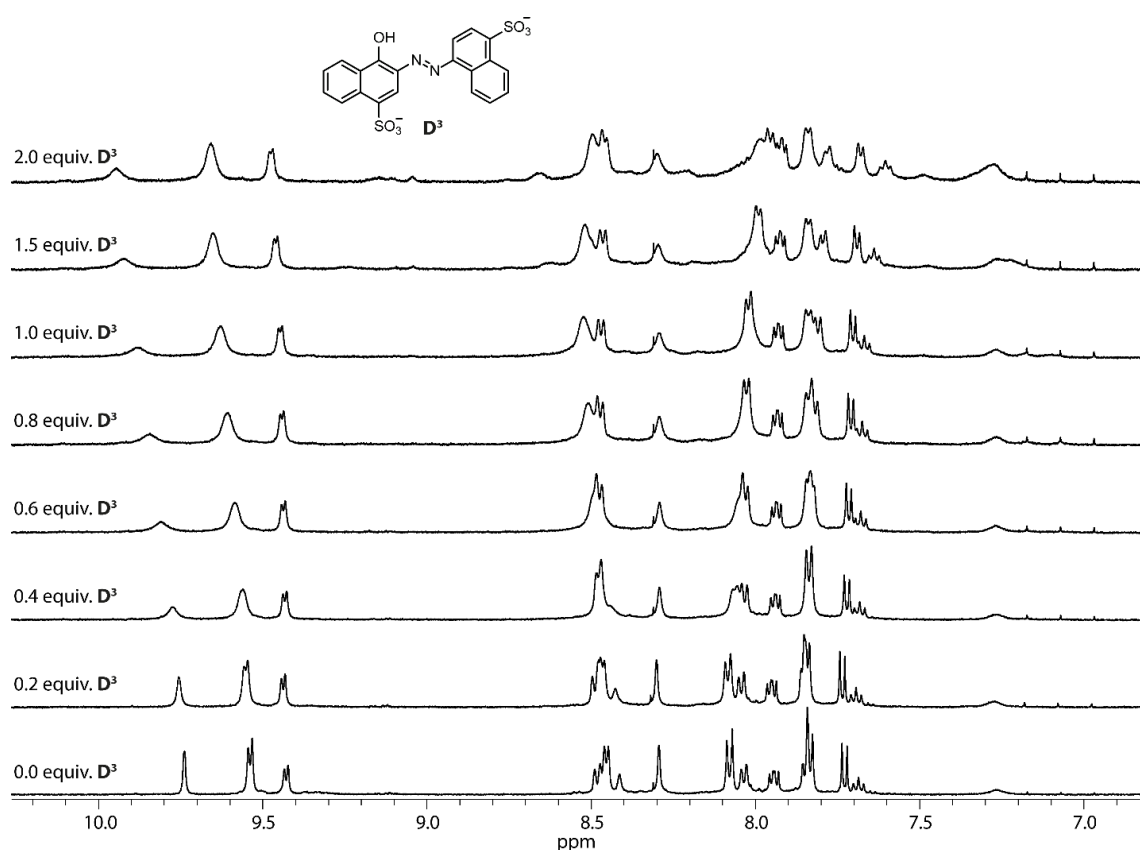
Figure 222: Partial ^{1}H NMR spectra (500 MHz, 298 K, DMSO-d_6) of the titration of D^3 to $Pd_3L^{F2}_3L^{S1}_3$.

Figure 222 shows the ^{1}H NMR titration of D^3 to $Pd_3L^{F2}_3L^{S1}_3$. Upon addition of the guest, signals broaden though not nearly as much as previously reported for D^1 and D^2. Furthermore, the signal-to-noise ratio remains relatively good, decreasing only by a small margin. The signal of proton H^1 remains observable and shifts downfield, as well as proton H^a. Plotting $\Delta\delta$ of both aforementioned proton signals against the added equivalents of D^3 yielded the plot depicted in Figure 223.
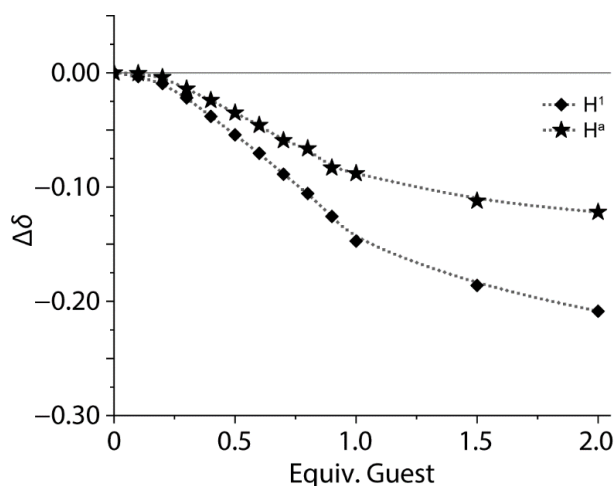
Figure 223: Δδ of protons Hᵃ and H¹ of Pd₃L^F2₃L^S1₃ upon consecutive addition of **D³**.

As evident from the sigmoidal course Δδ, **D³** does not associate to Pd₃L^F2₃L^S1₃ in a 1:1 manner, which would result in a hyperbolic curve in this plot, but instead would fit a [1**G**@2**H**] stoichiometry. This suggests the increased steric demand around the sulfonate-groups resulting from the naphthyl rings is no longer allowing three guest molecules to link two hosts, but only one bis-sulfonate guest fitting inside the space. Binding constants derived from fitting the obtained data of the titration are $K_1 = 40106 \, M^{-1} \pm 11 \, \%$ and $K_2 = 1045 \, M^{-1} \pm 7 \, \%$. To further confirm this observation, CSI-MS was measured using the same conditions as previously for [3**D**^{1/2}@2 Pd₃L^F2₃L^S1₃] (Figure 224).
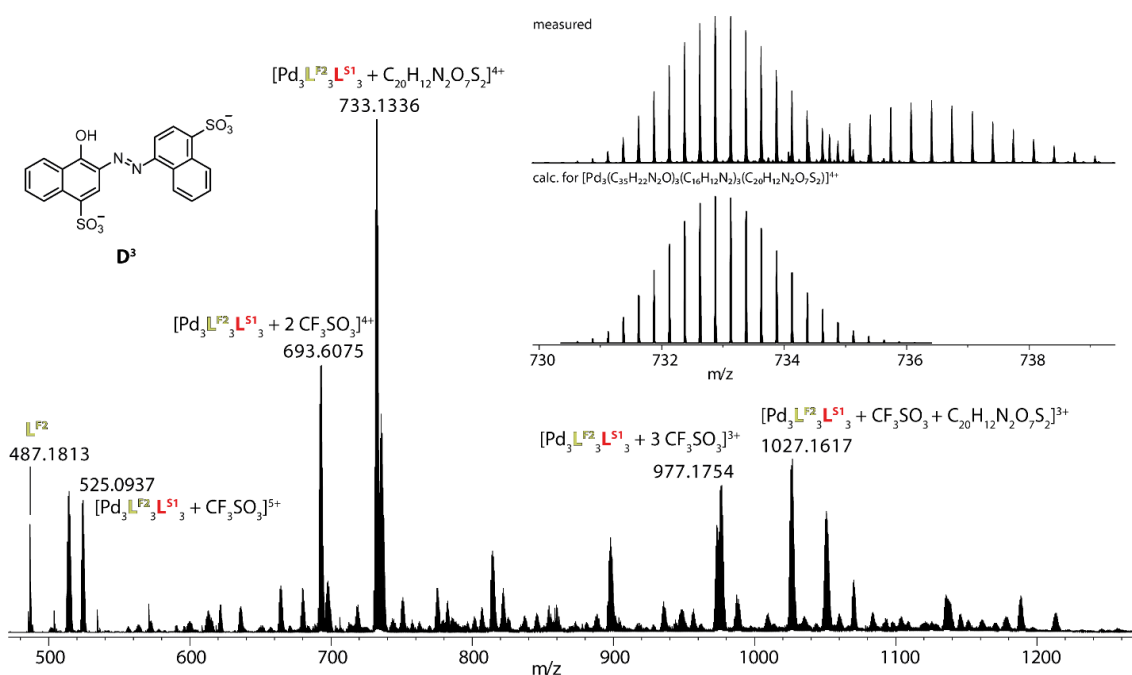
Figure 224: CSI-MS spectrum of Pd₃L^F2₃L^S1₃ after the addition of 1 equiv. **D³**. The measured and calculated isotopic pattern of the highest peak are shown in the inset.

240

The obtained CSI-MS spectrum showed fragmented species and $[Pd_3L^{F2}_3L^{S1}_3 + xD^3 + y\,CF_3SO_3]^{(6-2x-y)+}$ ($x = 0,\textbf{1}$, $y = 0\text{-}3$) with a lot of free $Pd_3L^{F2}_3L^{S1}_3$ host. Upon closer inspection of the spectrum in respect to a [1**G**@2**H**] complex, species of the type $[Pd_6L^{F2}_6L^{S1}_6 + 1D^3 + y\,CF_3SO_3 + z\,SO(CD_3)_2]^{(12-2-y)+}$ ($y = 4;5$, $z = 5$) were found as shown in Figure 225. While finding and identifying one peak can happen by chance, a second one with the exact same inherent composition (aside from the anions) but different charge proves a pattern and verifies the existence of the species in question.
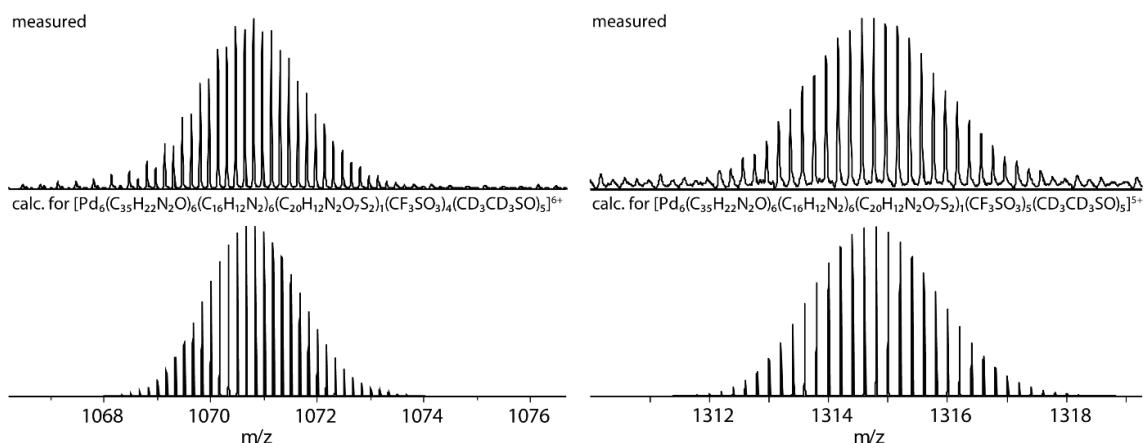
Figure 225: Measured and calculated isotopic patterns of $[Pd_6L^{F2}_6L^{S1}_6 + 1D^3 + y\,CF_3SO_3 + z\,SO(CD_3)_2]^{(12-2-y)+}$ ($y = 4;5$, $z = 5$).

No species with $z \neq 5$ were found and the species were more prominent in the CSI measurement as opposed to an ESI one. While it is unusual that solvent molecules are detected alongside supramolecular complexes in mass spectrometry, it is not entirely impossible if they are confined in a closed space like e.g. in a cavity or between two bowl-shaped molecules bridged by an anion. As mass spectrometry is an invasive analytic method, fragmentation of species can never be ruled out with dilution and ionization straining the weakly associated molecules especially considering host-guest chemistry. The reason as to why $[Pd_6L^{F2}_6L^{S1}_6 + xD^{1/2} + y\,CF_3SO_3]^{(12-2x-y)+}$ ($x = 2,\textbf{3}$, $y = 0\text{-}2$) forming a [3**G**@2**H**] complex could be observed so cleanly in a CSI-MS measurement is likely due to the sum of attractive forces keeping the complex intact. These forces are significantly weaker when only one guest is linking two hosts, thus the complex tends to fall apart under MS conditions. The result can be verified by setting up the experiment in non-deuterated DMSO. If the same peaks arise with $SO(CH_3)_2$ instead of $SO(CD_3)_2$, the complex formed encapsulates five additional DMSO molecules.^{1}H DOSY NMR analysis to verify the formation of a higher ordered host-guest species is likely not feasible, due to the system undergoing fast exchange kinetics.

While a difference in binding motif as opposed to the [3**G**@2**H**] stoichiometry observed for **D**[1] and **D**[2] is clear by considering the results from ^{1}H NMR titration, binding isotherms

and ESI-MS results, a reverse UV/VIS titration was done to further analyze the binding of D^3 to $Pd_3L^{F2}_3L^{S1}_3$ (Figure 226).
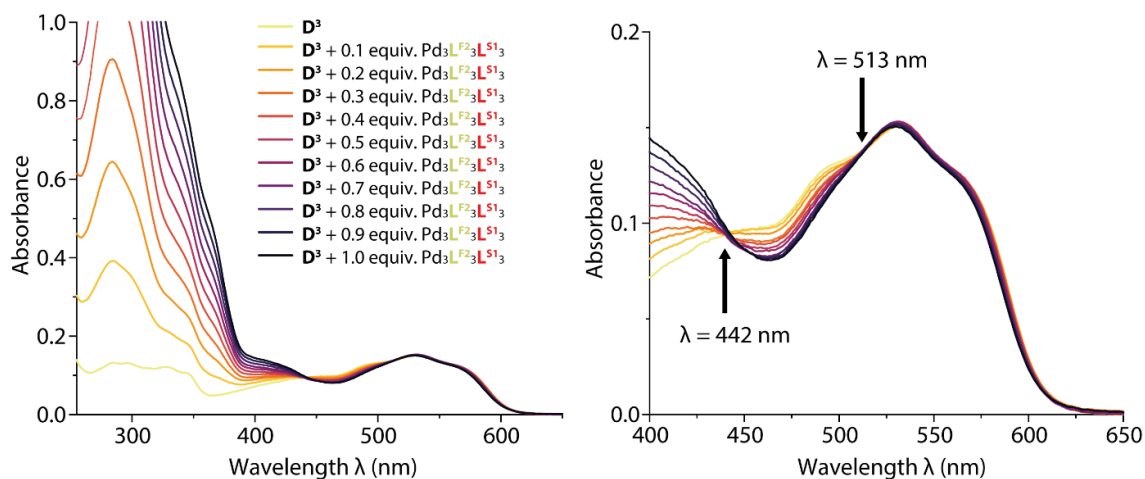
Figure 226: UV/VIS spectra of the reverse titration of $Pd_3L^{F2}_3L^{S1}_3$ to D^3. Left: Wavelength coverage from 255-600 nm; right: Wavelength coverage from 400-600 nm with annotated isosbestic points.

The addition of $Pd_3L^{F2}_3L^{S1}_3$ to D^3 led to no color change evident in the absorption band of the dye with an absorption maximum at $\lambda = 532$ nm staying almost unaltered upon addition of the assembly. The titration showed two isosbestic points, one at $\lambda = 442$ nm and the second at $\lambda = 513$ nm. A slight hypochromic shift is observable until 0.6 equiv. $Pd_3L^{F2}_3L^{S1}_3$ in respect to the dye were added. No significant further change could be observed for the following additions up until 1 equiv. This observation solidifies the assumption that a [1G@2H] complex is formed. Small inaccuracies regarding stoichiometry could stem from an insufficient purity of the dye or dilution effects.

The additional information on the binding taken from the UV/VIS experiment solidified the hypothesis, that D^3 forms a [1G@2H] with $Pd_3L^{F2}_3L^{S1}_3$. This observation should be considered, when attempting to crystallize the mixture and for further experimentation.

3.4.5.2.3 Bulky dye D^4 (NaptholBlueBlack)

While the sulfonate groups were attached to different aromatic systems and sides of the diazene inside the azo dyes for D^{1-3}, naphthol blue black (D^4) is a dye carrying both sulfonate groups attached to its central naphthyl ring system. This geometric orientation should not enable linking two $Pd_3L^{F2}{}_3L^{S1}{}_3$ host molecules together but instead form a 1:1 complex. Sodium 4-amino-5-hydroxy-3-((E)-(4-nitrophenyl)diazenyl)-6-((E)-phenyldiazenyl)naphthalene-2,7-disulfonate (D^4) was solubilized in DMSO-d_6, the concentration amounting to 17.5 mM. It was then titrated in 0.1 equiv steps (1.6 µl) to 600 µl of a 0.467 mM solution of $Pd_3L^{F2}{}_3L^{S1}{}_3$ in DMSO-d_6 in a standard 5 mm NMR tube until 1 equiv. was added, then followed by 8 µl steps until reaching a total of 2 equiv. guest added in respect to the assembly (Figure 227).
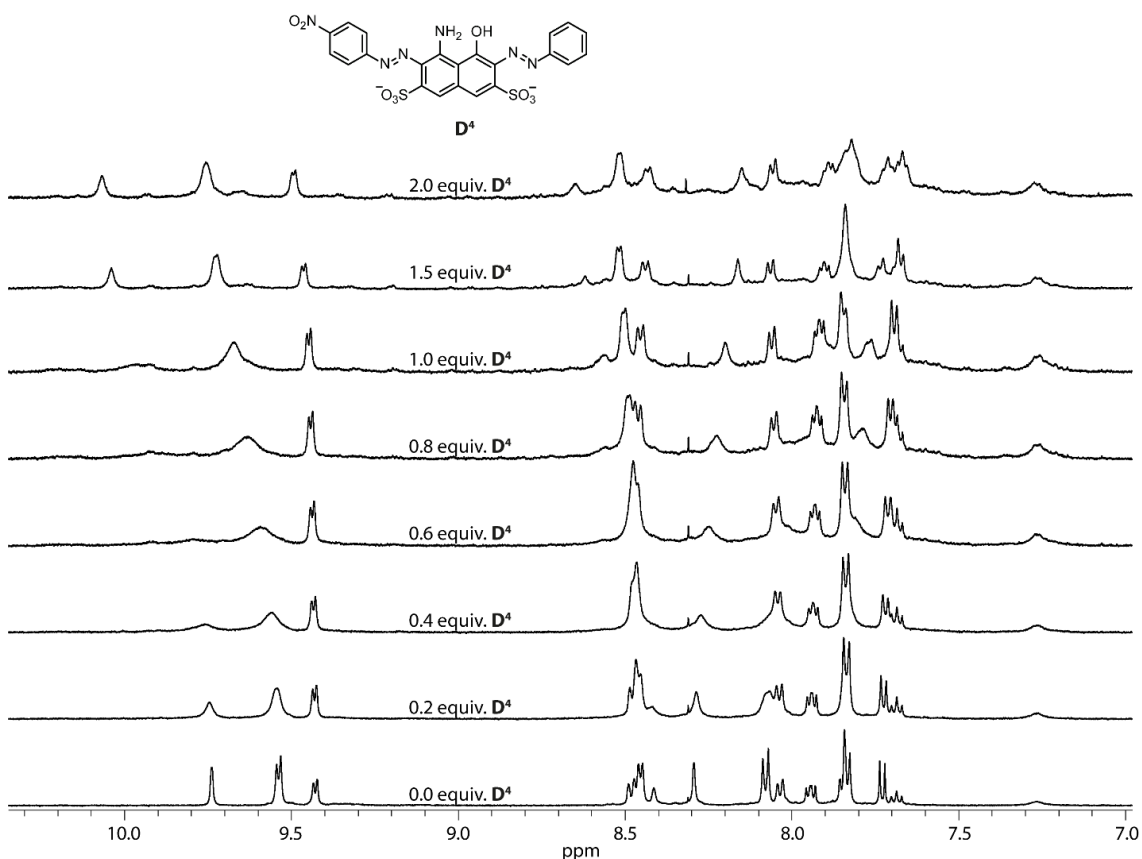
Figure 227: Partial ^{1}H NMR spectra (500 MHz, 298 K, DMSO-d_6) of the titration of D^4 to $Pd_3L^{F2}{}_3L^{S1}{}_3$.

Upon addition of D^4, the proton signals of H^1 and H^a broaden immediately with the one of H^1 broadening even to a point where it is hard to distinguish from the noise of the spectrum. After reaching 1.0 equiv. guest however, the signals sharpen again suggesting fast exchange kinetics leading to broadening and, upon full occupation of all host molecules with one guest molecule, re-sharpening of the signals. It is notable, that proton H^2, pointing outside of the assembly's center, does not broaden, even maintaining its

243

splitting pattern until 1 equiv. **D⁴** was added. A binding constant of **D⁴** to $Pd_3L^{F2}_3L^{S1}_3$ based on the shift of protons H^a, H^2 and H^9 amounted to $K_1 = 175\ M^{-1} \pm 6\%$. The 1:1 mixture of **D⁴** and $Pd_3L^{F2}_3L^{S1}_3$ was subjected to CSI-MS measurement to confirm the presumed stoichiometry (Figure 228).
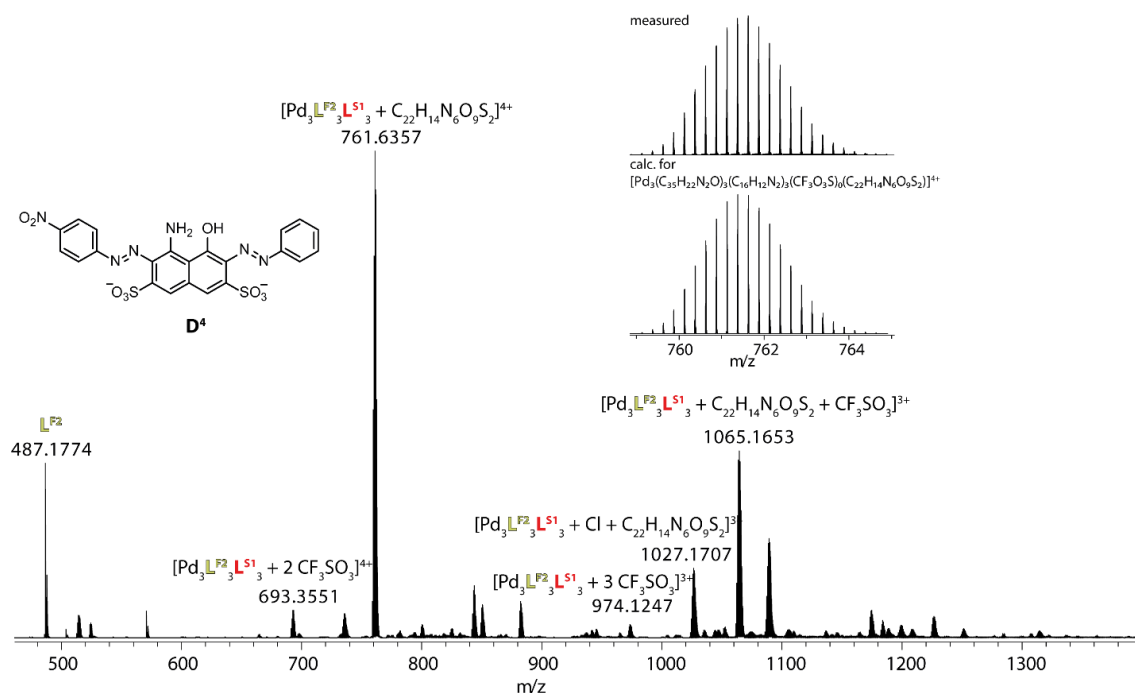
Figure 228: CSI-MS spectrum of $Pd_3L^{F2}_3L^{S1}_3$ after the addition of 1 equiv. **D⁴**. The measured and calculated isotopic pattern of the highest peak are shown in the inset.

In stark contrast to the MS spectrum of **D³** combined with $Pd_3L^{F2}_3L^{S1}_3$, the combination with **D⁴** yields a cleaner spectrum with less unidentifiable species or fragments. The predominant species is $[D^4@Pd_3L^{F2}_3L^{S1}_3]$, supporting the claim of a 1:1 complex formation. Species without **D⁴** are extremely low in intensity and the isotopic pattern shows no underlying second species.

The binding was further analyzed via reverse UV/VIS titration as already established previously (Figure 229).
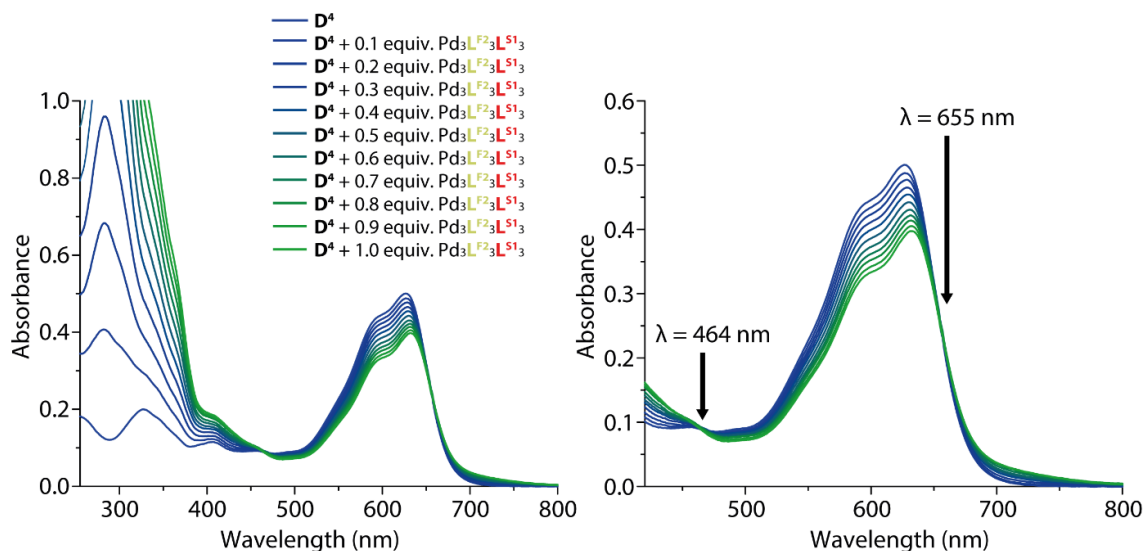
Figure 229: UV/VIS spectra of the reverse titration of Pd$_3$L$^{F2}_3$L$^{S1}_3$ to D^4. Left: Wavelength coverage from 255-800 nm; right: Wavelength coverage from 425-800 nm with annotated isosbestic points.

Upon addition of D^4 to Pd$_3$L$^{F2}_3$L$^{S1}_3$ in the ^{1}H NMR titration, a visible color change from the blue guest stock solution to a teal solution containing both, host and guest, was observed. The absorption maximum of D^4 shifts bathochromic and hypochromic from $\lambda = 627$ nm to $\lambda = 633$ nm and the isosbestic points of the titration were $\lambda = 464$ nm and $\lambda = 655$ nm. As opposed to D^1 and D^2, which shifted in the hypsochromic region or D^3, which showed only hypochromic shifting upon addition of Pd$_3$L$^{F2}_3$L$^{S1}_3$, D^4 is the first of the analyzed dye molecules, whose absorption undergoes a bathochromic shift upon host interaction.

3.4.5.2.4 Fluorescent dye D^5 (Sulforhodamine101)

Up until now, bis-sulfonate azo dyes showed different photophysical behavior upon interaction with Pd$_3$L$^{F2}_3$L$^{S1}_3$ depending on the formed complex stoichiometry. To confirm this claim and to analyze the potential of the host molecule, containing the fluorescent ligand L^{F2}, to act as a FRET donor as already previously established (chapter 3.3), a sulforhodamine-based dye D^5 (sulforhodamine 101) was analyzed in respect to its interaction with Pd$_3$L$^{F2}_3$L$^{S1}_3$. The sulfonate groups of D^5 are attached to the same phenyl moiety, thus no cross linking of two host molecules is to be expected and D^5 will likely form a 1:1 complex with Pd$_3$L$^{F2}_3$L$^{S1}_3$.

Sulforhodamine 101 (D^5) was solubilized in DMSO-d_6 to achieve a 17.5 mM stock solution. It was titrated to Pd$_3$L$^{F2}_3$L$^{S1}_3$ in a standard 5 mm NMR tube with conditions previously stated for the titrations of D$^{1-4}$ (Figure 230). Since a certain acid tolerance could already be shown for Pd$_3$L$^{F2}_3$L$^{S5}_3$ (see 3.4.2.5), D^5 was used unaltered, in its sulfonic acid form, though deprotonation is highly likely in solution.
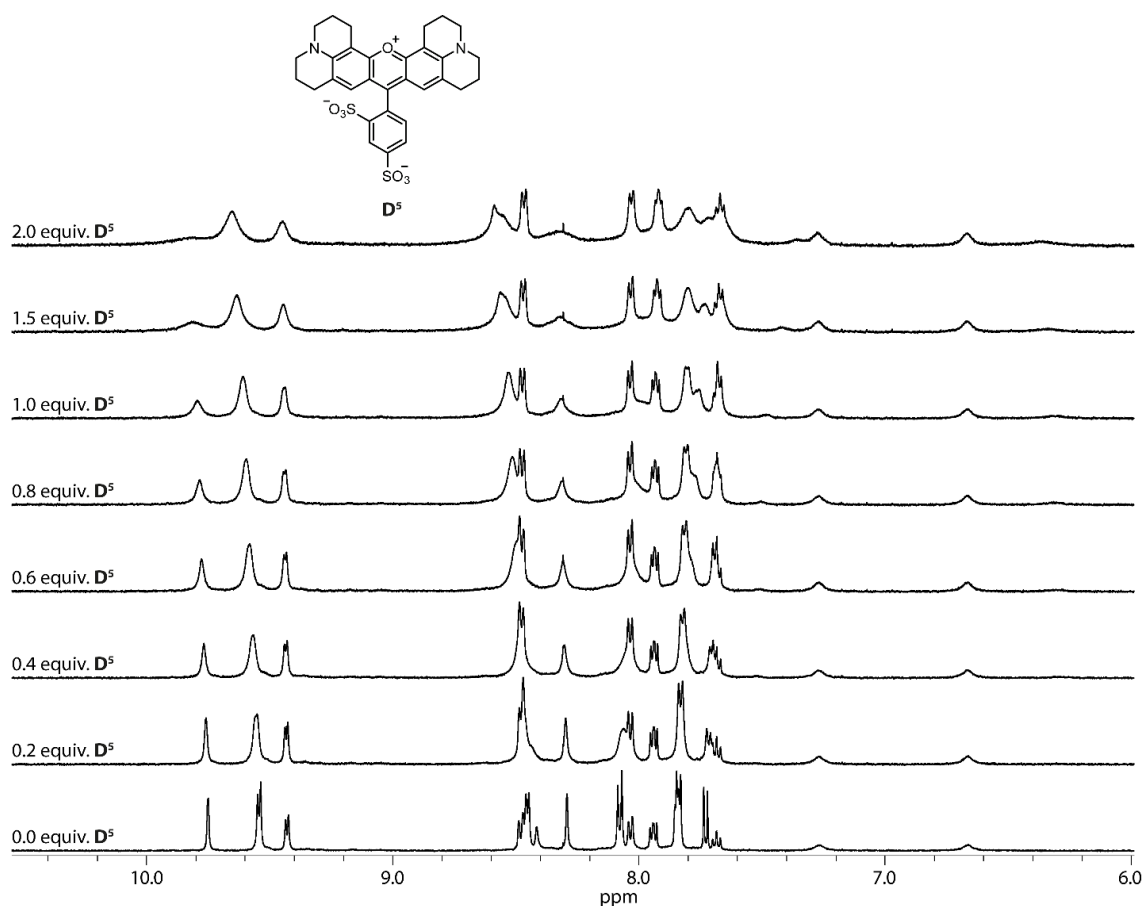
Figure 230: Partial ^{1}H NMR spectra (500 MHz, 298 K, DMSO-d_6) of the titration of **D^5** to Pd$_3$**L$^{F2}_3$L$^{S1}_3$**.

Proton signals of protons pointing to the inside of the assembly, like H^1, H^a and H^9 broadened substantially upon addition of **D^5** (Figure 230). Furthermore, all of the aforementioned signals show a downfield shift, H^1 shifting from $\delta = 9.75$ ppm to $\delta = 9.82$ ppm, H^a from $\delta = 9.54$ ppm to $\delta = 9.65$ ppm and H^9 shifting from $\delta = 8.29$ ppm to $\delta = 8.33$ ppm. The binding constant for [**D^5**@ Pd$_3$**L$^{F2}_3$L$^{S1}_3$**] was determined and amounted to K$_1 = 607$ M^{-1} $\pm$ 15% with the binding isotherms following a hyperbolic course supporting the claim of a 1:1 binding.

An ESI-MS spectrum of the 1:1 mixture of Pd$_3$**L$^{F2}_3$L$^{S1}_3$** and **D^5** was measured (Figure 231).
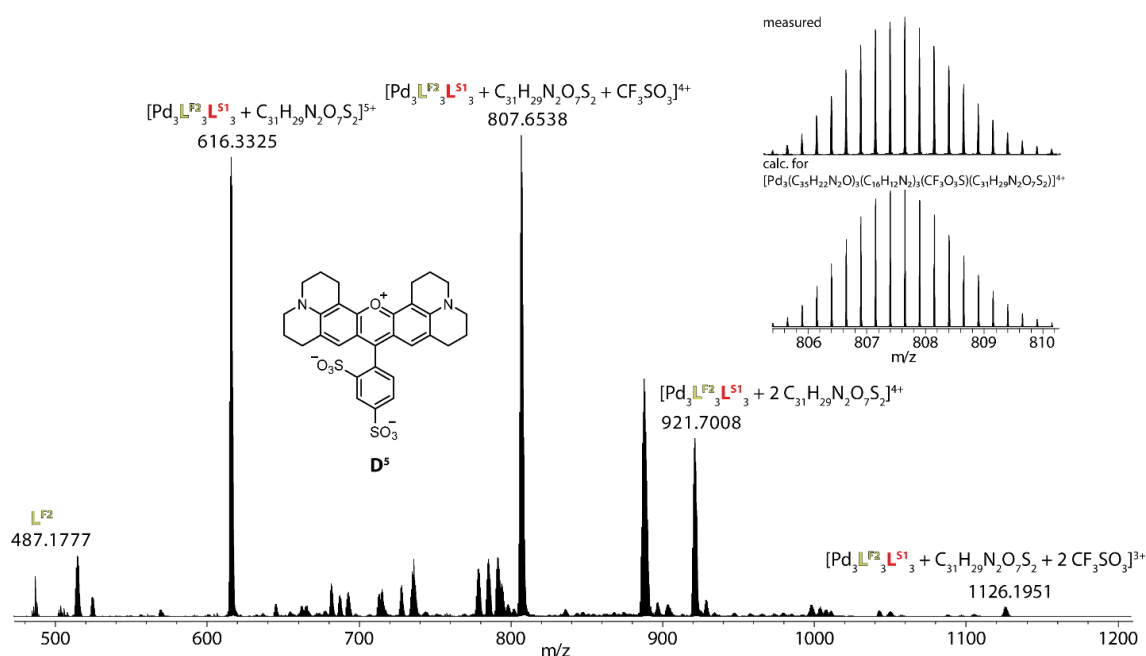
Figure 231: ESI-MS spectrum of Pd$_3$L$^{F2}_3$L$^{S1}_3$ after the addition of 1 equiv. **D^5**. The measured and calculated isotopic pattern of the highest peak are shown in the inset.

The assumed 1:1 binding was confirmed by ESI-MS measurement, yielding a clean spectrum with predominantly [Pd$_3$L$^{F2}_3$L$^{S1}_3$ + **D^5** + xCF$_3$SO$_3$]$^{(6-1-x)+}$ species (Figure 231). Empty Pd$_3$L$^{F2}_3$L$^{S1}_3$ could be detected with peaks having extremely low intensity as even Cl$^-$ adducts of the host-guest complex were more abundant. While a peak with the composition of [Pd$_3$L$^{F2}_3$L$^{S1}_3$ + 2**D^5**]$^{4+}$ could be detected, outside binding of the second **D^5** molecule was assumed based on the steric demand of **D^5**. This claim can be verified using ion-mobility measurements if necessary.

A reverse UV/VIS titration of Pd$_3$L$^{F2}_3$L$^{S1}_3$ to **D^5** was performed (Figure 232) as a color change of **D^5** from pink to a more reddish-pink hue was observed.
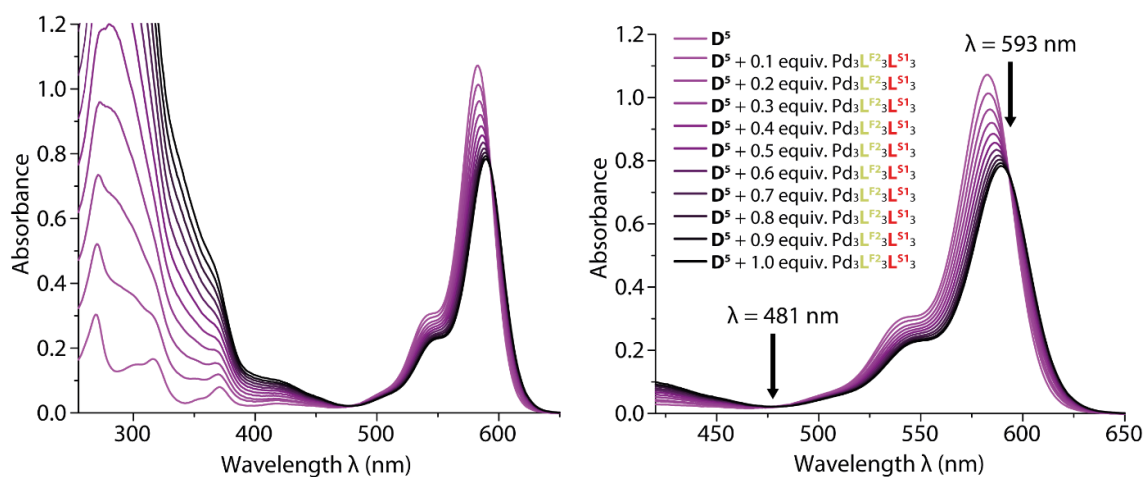
Figure 232: UV/VIS spectra of the reverse titration of Pd$_3$L$^{F2}_3$L$^{S1}_3$ to **D^5**. Left: Wavelength coverage from 255-650 nm; right: Wavelength coverage from 385-650 nm with annotated isosbestic points.

The titration showed two isosbestic points, one at $\lambda = 481$ nm and one at $\lambda = 593$ nm. Consistent with the behavior already shown in the titration of $Pd_3L^{F2}_3L^{S1}_3$ to D^4, the absorption of D^5 showed bathochromic and hypochromic shift from $\lambda = 583$ nm, with only the dye in DMSO, to $\lambda = 590$ nm after addition of 1 equiv. $Pd_3L^{F2}_3L^{S1}_3$. Whereas this behavior does seem to be a common observation in 1:1 binding of the complex to a dye, more data is needed to verify that claim.

Upon addition of $Pd_3L^{F2}_3L^{S1}_3$ to D^5 or vice versa, reduced emission of D^5 was observed as compared to free D^5 (Figure 233).
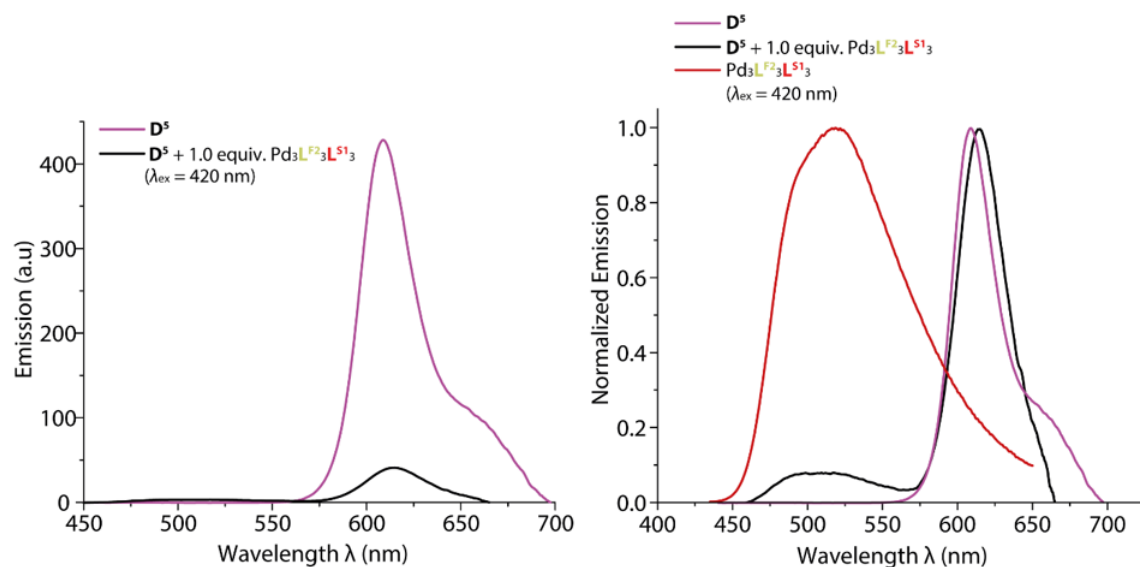
Figure 233: a) Absolute emission of D^5 and D^5 after addition of 1 equiv. $Pd_3L^{F2}_3L^{S1}_3$ and b) normalized emission of D^5 and D^5 after addition of 1 equiv. $Pd_3L^{F2}_3L^{S1}_3$ compared to just $Pd_3L^{F2}_3L^{S1}_3$.

The measured absolute emission of both, free D^5 and $[D^5@Pd_3L^{F2}_3L^{S1}_3]$, after excitation at $\lambda = 420$ nm is shown in Figure 233, left. Upon formation of the host-guest complex, the emission of D^5 diminishes below 10% (9.55%) of its initial value in the free dye. Furthermore, λ_{max_em} shifts bathochromic from $\lambda = 609$ nm to $\lambda = 615$ nm (Figure 233, right). The shoulder after $\lambda = 650$ nm in the emission of the free dye D^5 is less pronounced in the emission spectrum of the host-guest complex (Figure 233, right, black) where it is almost no longer detectable. The incorporation of D^5 in $Pd_3L^{F2}_3L^{S1}_3$ leads to the dye absorbing and emitting light at lower energy levels indicated by the bathochromic shift in both, absorption and emission maximum, thus an axial shift of the Stoke's shift of the dye ensues. However, it is also accompanied by a vast decrease in emission intensity, suggesting the systems access to new, non-radiative pathways. This observation solidifies the binding of D^5 to $Pd_3L^{F2}_3L^{S1}_3$.

Since the emission of $Pd_3L^{F2}_3L^{S1}_3$ (Figure 233, right, red) is still observed in the emission spectrum of the host-guest complex, host-to-guest FRET cannot be readily confirmed, nor ruled out and more experiments are required.

An attempt to grow crystals of the host-guest complex from a1:1 mixture of D^5 and $Pd_3L^{F2}_3L^{S1}_3$ ($c_{complex}$ = 0.467 mM) was successful and pink, hexagonal crystals were obtained (Figure 234).
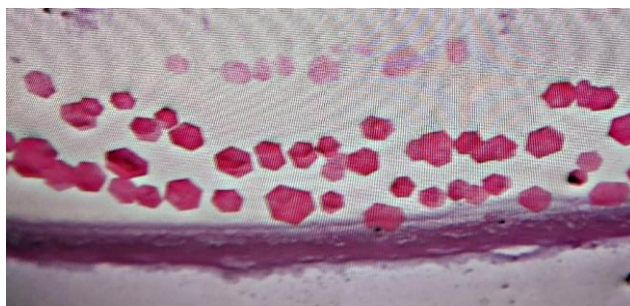
Figure 234: Photo taken of crystals grown from $Pd_3L^{F2}_3L^{S1}_3$ after the addition of 1 equiv. D^5 by slow vapor diffusion of toluene into the mother liquor.

Crystals were picked for subjection to synchrotron radiation, though no structure could be resolved from the selected crystals. Figure 234 however shows the attainability of crystals that are very likely to be host-guest complex, as the shape matches the crystals of which the x-ray structures of $Pd_3L^{F2}_3L^{S1}_3$ and $Pd_3L^{F2}_3L^{S2}_3$ were obtained from and the color matches the absorption of the guest D^5. The approach seems to be promising and should be pursued further.

3.4.5.2.5 Summary: Dye Binding

In summary, binding of common azo dyes D^{1-4} and sulforhodamine 101 (D^5) to $Pd_3L^{F2}_3L^{S1}_3$ yielded different binding topologies based on the orientation of the sulfonate groups in the respective guest molecules. Three different binding motifs could be observed and were discussed in detail in respect to the stoichiometry of the host-guest complex and its photophysical behavior. The results are summarized in Table 12.

Table 12: Summary for the observed and characterized binding of D^{1-5} at $Pd_3L^{F2}_3L^{S1}_3$ deduced from NMR, MS and UV/VIS data.

	D^1/D^2	D^3	D^4/D^5
Binding motif			
Stoichiometry (H:G)	2:3	2:1	1:1
UV/VIS behavior	Hypsochromic + hypochromic	hypochromic	Bathochromic + hypochromic
No. of isosbestic points	1	2	2

D^1 and D^2, being able to freely rotate one of their two sulfonate groups in a way that the molecule takes up an almost linear form as viewed from one sulfonate to the other, forms an unusual 2:3 (3G@2H) complex with seemingly three bis-sulfonate dyes bridging two $Pd_3L^{F2}{}_3L^{S1}{}_3$ host molecules. The dominant absorption band of the dye underwent a hypsochromic and hypochromic shift upon addition of the host complex.

As opposed to this, D^4 and D^5, having their sulfonate groups oriented in one direction and close to one another, for 1:1 host-guest complexes with $Pd_3L^{F2}{}_3L^{S1}{}_3$. In this case, the absorption shifts bathochromic and hypochromic, thus showing the exact opposite behavior as described for the 3G@2H complexes D^1 and D^2 form.

D^3 has sulfonates attached to different ring systems in the azo dye but was not able to form a linear connection between both through free rotation around single bonds. ^{1}H NMR titration experiments showed a 1:2 (1G@2H) binding stoichiometry from the binding isotherms which was challenging to confirm by CSI MS due to fragmentation of the potential host-guest complex. However, smaller peaks assignable to $[Pd_6L^{F2}{}_6L^{S1}{}_6 + 1D^3 + y\ CF_3SO_3 + z\ SO(CD_3)_2]^{(12-2-y)+}$ (y = 4;5, z = 5) were found. UV/VIS experiments further supported the claim, since only a hypochromic shift upon addition of up to 0.6 equiv. $Pd_3L^{F2}{}_3L^{S1}{}_3$ in respect to the dye was observed. No more change in the absorption of the dye could be detected upon further host addition.

Unfortunately, the postulated host-guest stoichiometries could not be verified by means of DOSY NMR due to substantial signal broadening and low signal to noise-ratio.

It is noted, that hypochromic shifts observed in these experiments should be corrected by a titration with only DMSO to rule out dilution effects.

While more experiments with additional guest molecules are needed to verify the observed systematic behavior, the $Pd_3L^{F2}{}_3L^{S1}{}_3$ host molecule seems to induce vastly different photophysical behavior of its guest molecules depending on the formed host-guest stoichiometry.

3.4.6 Chapter Summary and Outlook

The herein reported system consisting of equimolar amounts of Pd(II) cations, a rigid, fluorescent ligand L^{F2} and an array of different short, rigid ligands L^{S1-10} yielded nine novel heteroleptic assemblies of which five, namely $Pd_3L^{F2}_3L^{S1-5}_3$, show a yet unprecedented nuclearity n = 3 for symmetric, heteroleptic Pd(II) structures. These unique, fluorescent, open structures provide a bowl-shaped topology without the drawback of open coordination sites. The system tolerates a wide array of functional groups in the central ring, including primary amines and alcohols. The effect of the coordination to Pd(II) on these functional groups attached to the ligands central phenyl-backbone has been proposed to enhance interesting properties like hydrogen bonding capability and acidity (-OH, L^{S5}) and organocatalytic potential (-NH$_2$, L^{S3}) of the provided assemblies as compared to the free ligands.

Furthermore, the effect of changes in the properties of the short ligand L^S have been analyzed in regard of electrochemical repulsion, steric repulsion and bite angle increase. Interestingly, electrochemical repulsion (L^{S6}) led to an increase in nuclearity while maintaining the bowl-topology, while the incorporation of steric bulk (L^{S8}) and ligand bite angle increase ($L^{S9/10}$) led to the formation of saddle-shaped $Pd_4L^{F2}_4L^{S8-10}_4$ assemblies.

Overall the system is structurally very well understood and the combination of varying functional groups and a fluorescent counter-ligand could prove to be a valuable asset in further analysis regarding guest binding and catalytic potential.

Since the system provided open structures without vulnerable free coordination sites at the Pd(II) centers, host guest chemistry with two types of guests was explored, namely chiral guest molecules G^{1-3} and large sized organic dye molecules D^{1-5}. While binding of G^{1-3} could be shown for all three guests, the chiral induction proved to be most efficient for a combination of (R)-BINSO (G^1) and $Pd_3L^{F2}_3L^{S4}_3$, carrying methoxy-groups in the central ring spanned by the small ligand. Chirality transfer from G^1 to the host molecule was not only observed for the ground state (CD) but also for the excited state yielding a relatively high g_{lum} value of $1.7 \cdot 10^{-3}$ after the addition of only 1 equiv. G^1. While comparable (and higher) values have been reported for Pd(II)-based coordination cages, the chirality is often incorporated into the cage structure and does not derive from the guest.[67,68]

While a g_{lum} value of $1.7 \cdot 10^{-3}$ is already a relatively high value for Pd(II)-based coordination cages, we were able to obtain a value of $g_{lum} = 1.0 \cdot 10^{-3}$ for $Pd_4L^{F2}_4L^{S8}_4$ after

the addition of 1 equiv. G^1 (Figure *235*, a)) and g_{lum} = 2.7·10^{-3} for Pd$_4$L$^{F2}_4$L$^{S8}_4$ after the addition of 2 equiv. G^1 (Figure 235, b)).
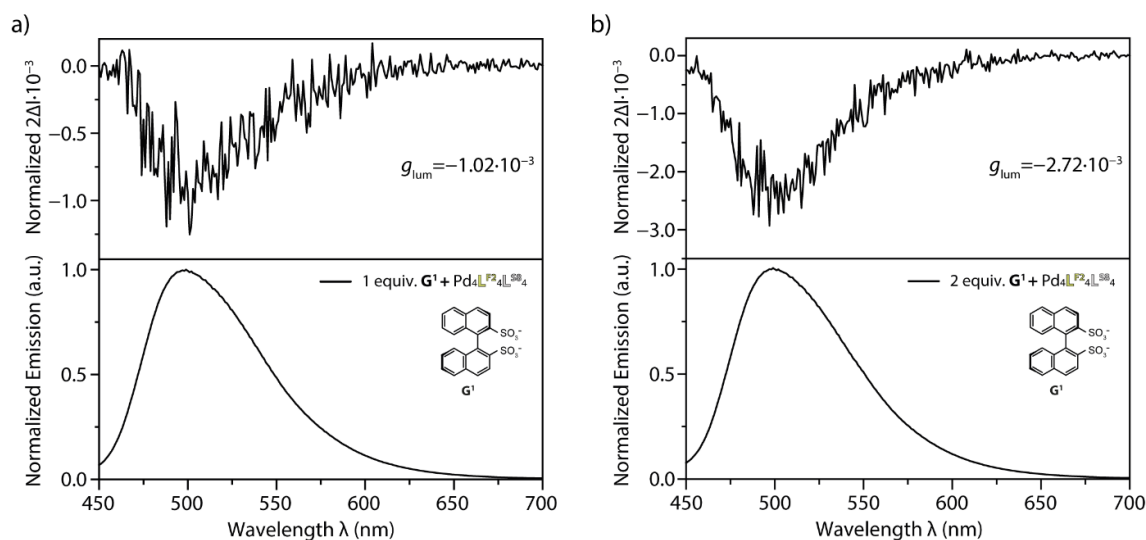
Figure 235: Normalized emission and CPL signal of Pd$_4$L$^{F2}_4$L$^{S8}_4$ after addition of a) 1 equiv. G^1 and b) 2 equiv. G^1. Exited at λ = 365 nm.

Aside from the measured CPL data depicted in Figure 235, no data on this combination is available and it is highly unclear how the host-guest complex looks like since NOE distance analysis for Pd$_4$L$^{F2}_4$L$^{S8}_4$ led to the conclusion of it forming a saddle topology with no defined cavity. However, the assembly still carries an 8+ charge while G^1 is twice negatively charged and with the sterically demanding benzoate residues providing an aromatic system eligible for π-stacking, proposed binding of G^1 from top and bottom of the assembly is not entirely unreasonable. These conjectures have to be confirmed applying further analytic techniques such as 1D and 2D NMR studies and CSI-MS analysis to access information regarding the number of guest molecules G^1 that associate to Pd$_4$L$^{F2}_4$L$^{S8}_4$, since the effect might not indicate binding of [2G^1@ Pd$_4$L$^{F2}_4$L$^{S8}_4$], but only stem from the increased concentration of G^1. Yet the herein described host molecules provide the possibility to analyze the effect of charge and steric effects on CPL readout.

The second group of guest molecules analyzed were organic azo-dyes and sulforhodamine 101. Treatment of Pd$_3$L$^{F2}_3$L$^{S1}_3$ (host, **H**) with five different organic bis-sulfonate dyes **D**$^{1-5}$ of varying sulfonate-group orientation, yielded three different binding behaviors for [**D**@**H**], namely [3**D**@2 **H**] for **D**^{1} and **D**^{2}, [1**D**@2 **H**] for **D**^{3} and [1**D**@ **H**] in case of **D**^{4} and **D**^{5}. Binding to the host altered the photophysical properties of the dye and was highly dependent on the binding motif where [3**D**@2**H**] led to a hypsochromic shift, [1**D**@2**H**] only showing a hypochromic shift and [1**D**@1**H**] led to bathochromic shifting of the maximum absorption band of the dye in the visible range.

With the strong potential for photophysical readout and a large cavity, the possibility of multi-guest incorporation and thus guest-to-host-to-guest chirality transfer was explored. It is noted, that results are preliminary and have to be further verified. Co-encapsulation of G^1 and D^5 was attempted using $Pd_3L^{F2}_3L^{S4}_3$, since it showed the highest CD and CPL response upon addition of only the chiral guest G^1. CD spectra for only G^1 (black), $[G^1@Pd_3L^{F2}_3L^{S4}_3]$ (teal)and $[G^1@Pd_3L^{F2}_3L^{S4}_3]$ + 1 equiv. D^5 (purple) are shown in Figure 236 below.
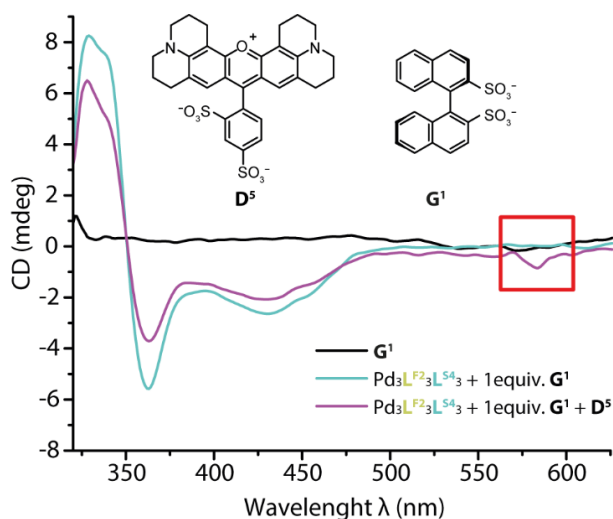
Figure 236: Circular dichroism measurement of $Pd_3L^{F2}_3L^{S4}$ after addition of 1 equiv. G^1 (teal) and successive addition of 1 equiv. D^5 (purple). CD of only G^1 is shown in black; a CD signal at $\lambda = 583$ nm is highlighted in a red box.

While the overall CD response of $[G^1@Pd_3L^{F2}_3L^{S4}_3]$ is diminished upon addition of D^5, a small amplitude at $\lambda = 583$ nm (Figure 236, red box) is detectable. With D^5 carrying no inherent chiral information this effect could be due to chirality transfer from G^1 to $Pd_3L^{F2}_3L^{S4}_3$ and the to D^5. However, association of G^1 to D^5 is not ruled out since D^5 does carry a formal positive charge that is delocalized within the chromophores heterocyclic system, thus, a necessary control experiment with only G^1 and D^5 is needed. While $Pd_3L^{F2}_3L^{S4}_3$ could be too small to host two guest molecules, the experiment could be performed with a larger sized host molecule such as $Pd_4L^{F2}_4L^{S6}_4$, which still sports a bowl-topology, though repulsion from the nitro-groups could prove to be problematic, or $Pd_4L^{F2}_4L^{S8}_4$, which yields inherently good CPL response with G^1, however the structural topology and binding motif have to be elucidated.

3.4.7 Experimental Part

3.4.7.1 Organic Synthesis (if applicable)

Synthesis of 1,3-di(pyridin-4-yl)benzene (L^{S1})
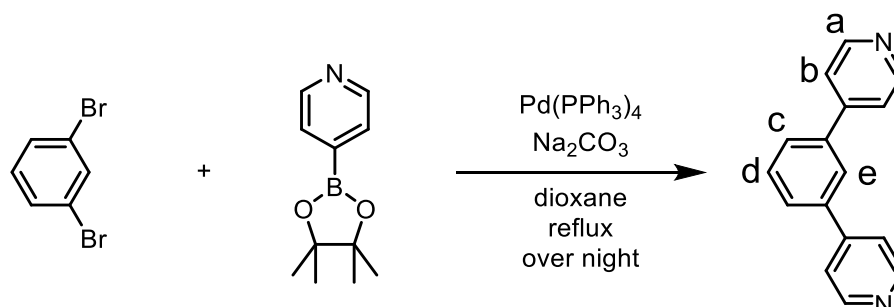
Scheme 32: Synthesis of **L**^{S1} with proton assignment.

1,3-dibromobenzene (500 mg, 2.12 mmol, 1 equiv.), 4-(4,4,5,5-tetramethyl-1,3,2-dioxaborolan-2-yl)pyridine (1.3 g, 6.36 mmol, 3 equiv.), Na$_2$CO$_3$ (674 mg, 6.36 mmol, 3 equiv.) and Pd(PPh$_3$)$_4$ (73.5 mg, 0.064 mmol, 0.03 equiv.) were suspended in a mixture of dioxane/H$_2$O (4:1; 25 ml). The mixture was degassed three times using the *Freeze-Pump-Thaw*-method, heated to reflux and stirred overnight. After cooling down to room temperature, the reaction mixture was extracted with DCM. The organic phase was washed consecutively with water and then brine. It was dried over MgSO$_4$, filtered and the solvent was removed under reduced pressure. The crude product was purified by column chromatography (pure acetone) yielding a white powder that was further purified by GPC. The yield of the final product was 347 mg (1.49 mmol, 70%).
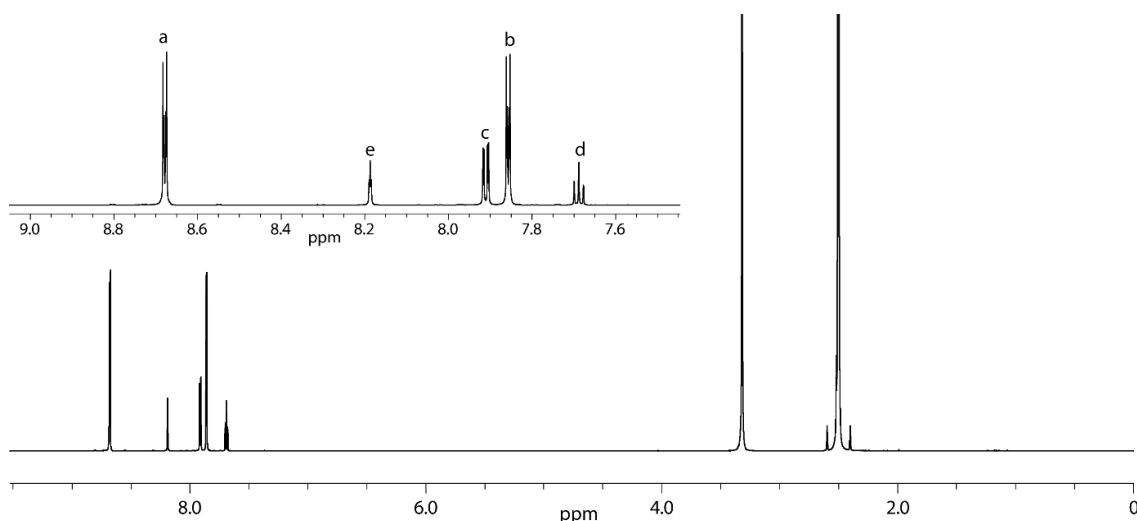
Figure 237: ^{1}H NMR spectrum (700 MHz, 298 K, DMSO-d_6) of **L**^{S1}. A zoom into the aromatic region including proton assignment is shown in the inset.

^{1}H NMR (700 MHz, 298 K, DMSO-d_6) $δ$ 8.68 (dd, ^3J = 6.1, ^4J = 1.65 Hz, 4H, H^a), 8.19 (t, ^4J = 1.7 Hz 1H, H^e), 7.91 (dd, ^3J = 7.8, ^4J = 1.7 Hz, 2H, H^c), 7.86 (dd, ^3J = 6.1, ^4J = 1.65 Hz, 4H, H^b), 7.69 (t, ^3J = 7.7, 1H, H^d) ppm.
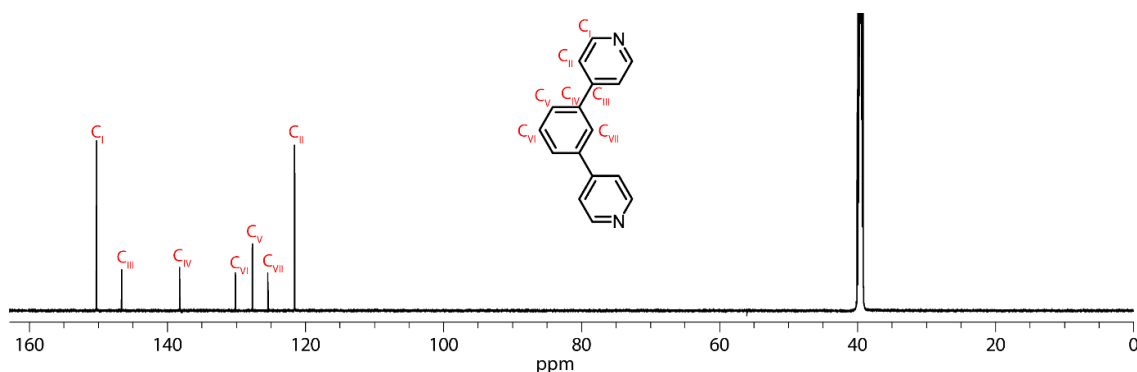
Figure 238: ^{13}C NMR spectrum (176 MHz, 298 K, DMSO-d_6) of **L^{S1}** including carbon assignment.

^{13}C{^{1}H} NMR (176 MHz, 298 K, DMSO-d_6) $δ$ 150.24 (C$_I$), 146.60 (C$_{III}$), 138.20 (C$_{IV}$), 130.12 (C$_{VI}$), 127.65 (C$_V$), 125.40 (C$_{VII}$), 121.53 (C$_{II}$) ppm.

HR ESI-MS:

measured for [C$_{16}$H$_{12}$N$_2$+H]$^+$: 233.1137

calculated: 233.1073

Synthesis of 4,2':6',4''-terpyridine (L^{S2})
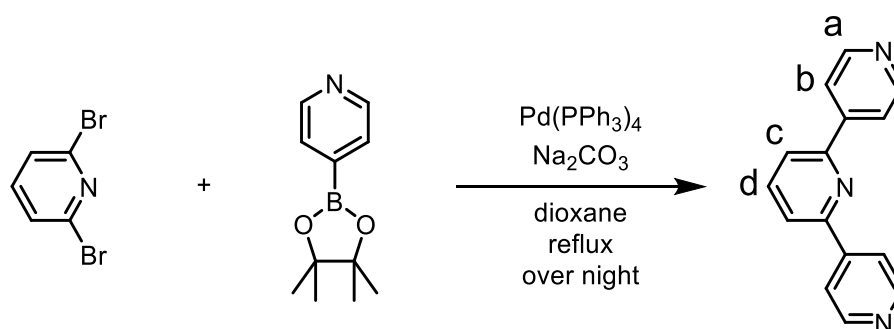
Scheme 33: Synthesis of **L^{S2}** with proton assignment.

2,6-dibromopyridine (500 mg, 2.11 mmol, 1 equiv.), 4-(4,4,5,5-tetramethyl-1,3,2-dioxaborolan-2-yl)pyridine (1.3 g, 6.33 mmol, 3 equiv.), Na$_2$CO$_3$ (671 mg, 6.33 mmol, 3 equiv.) and Pd(PPh$_3$)$_4$ (73.2 mg, 0.063 mmol, 0.03 equiv.) were suspended in a mixture of dioxane/H$_2$O (4:1; 25 ml). The mixture was degassed three times using the *Freeze-Pump-Thaw*-method, heated to reflux and stirred overnight. After cooling down to room temperature, the reaction mixture was extracted with DCM. The organic phase was washed consecutively with water and then brine. It was dried over MgSO$_4$, filtered and the solvent was removed under reduced pressure. The crude product was purified by

column chromatography (pure acetone) yielding a white crystalline powder that was further purified by GPC. The yield of the final product was 293 mg (1.26 mmol, 60%).
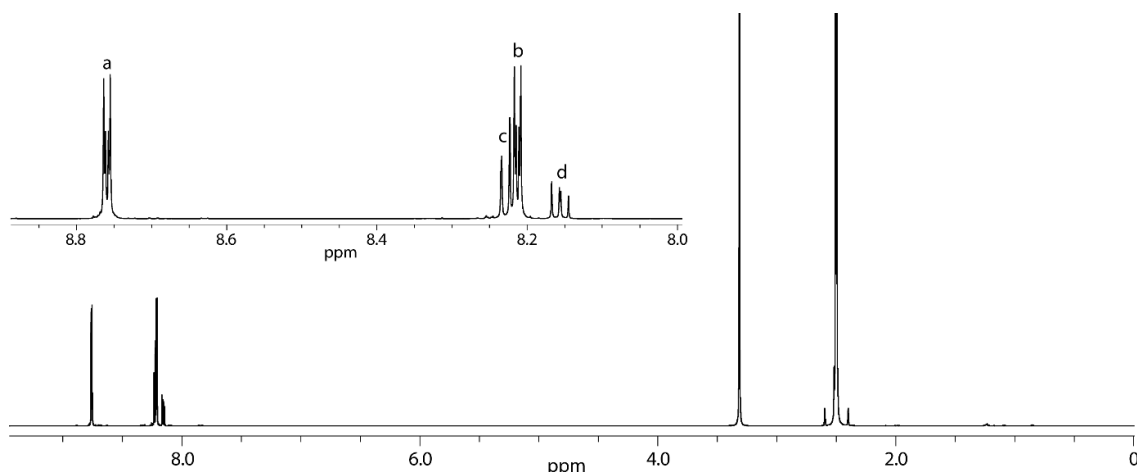
Figure 239: ^{1}H NMR spectrum (700 MHz, 298 K, DMSO-d_6) of **L^{S2}**. A zoom into the aromatic region including proton assignment is shown in the inset.

^{1}H NMR (700 MHz, 298 K, DMSO-d_6) δ 8.76 (dd, $^3J = 6.1$, $^4J = 1.65$ Hz, 4H, H^a), 8.23 (d, $^3J = 7.8$, 2H, H^c), 8.21 (dd, $^3J = 6.15$, $^4J = 1.65$ Hz, 4H, H^b), 8.16 (t, $^3J = 7.8$, 1H, H^d) ppm.
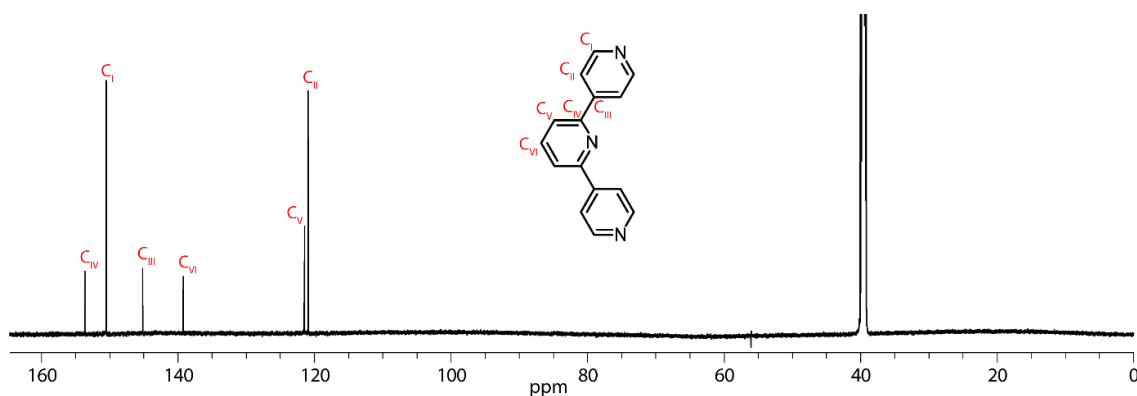
Figure 240: ^{13}C NMR spectrum (176 MHz, 298 K, DMSO-d_6) of **L^{S2}** including carbon assignment.

^{13}C{^{1}H} NMR (176 MHz, 298 K, DMSO-d_6) δ 153.56 (C$_{IV}$), 150.45 (C$_I$), 145.13 (C$_{III}$), 139.19 (C$_{VI}$), 121.43 (C$_V$), 120.87 (C$_{II}$) ppm.

HR ESI-MS:

measured for [C$_{15}$H$_{11}$N$_3$+H]$^+$:   234.1092

calculated: 234.1026

Synthesis of 2,6-di(pyridin-4-yl)aniline (L^{S3})
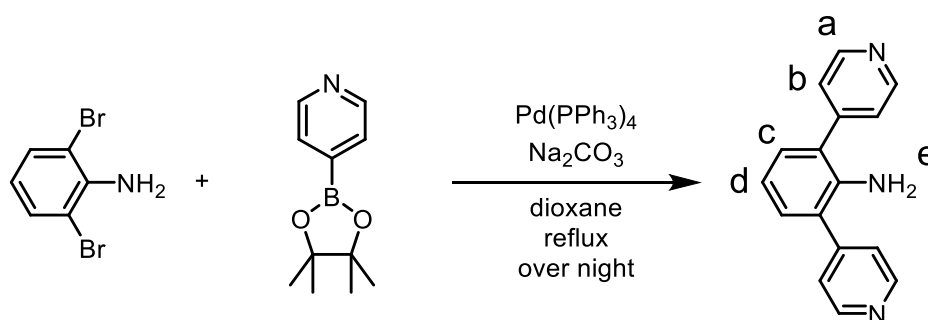
Scheme 34: Synthesis of **L^{S3}** with proton assignment.

2,6-dibromoaniline (400 mg, 1.59 mmol, 1 equiv.), 4-(4,4,5,5-tetramethyl-1,3,2-dioxaborolan-2-yl)pyridine (980.7 mg, 4.78 mmol, 3 equiv.), Na$_2$CO$_3$ (507 mg, 4.78 mmol, 3 equiv.) and Pd(PPh$_3$)$_4$ (55.3 mg, 0.048 mmol, 0.03 equiv.) were suspended in a mixture of dioxane/H$_2$O (4:1; 20 ml). The mixture was degassed three times using the *Freeze-Pump-Thaw*-method, heated to reflux and stirred overnight. After cooling down to room temperature, the reaction mixture was extracted with DCM. The organic phase was washed consecutively with water and then brine. It was dried over Na$_2$SO$_4$, filtered and the solvent was removed under reduced pressure. The crude product was purified by column chromatography (pure acetone) yielding a light brown powder that was further purified by GPC. The yield of the final product was 207 mg (0.837 mmol, 53%).
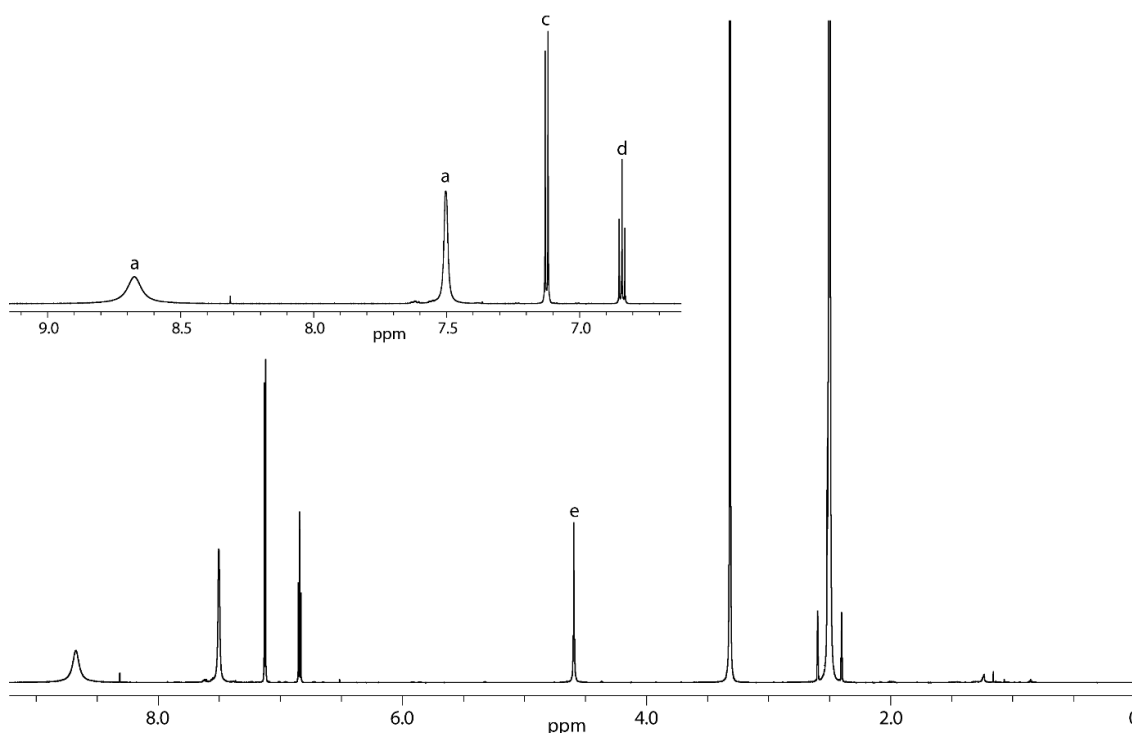
Figure 241: ^{1}H NMR spectrum (700 MHz, 298 K, DMSO-d_6) of **L^{S3}**. A zoom into the aromatic region including proton assignment is shown in the inset.

^{1}H NMR (700 MHz, 298 K, DMSO-d_6) δ 8.67 (s (br), 4H, H^a), 7.50 (s, 4H, H^b), 7.12 (d, ^3J = 7.5 Hz, 2H, H^c), 6.84 (t, ^3J = 7.6 Hz, 1H, H^d), 4.59 (s, 2H, H^e) ppm.
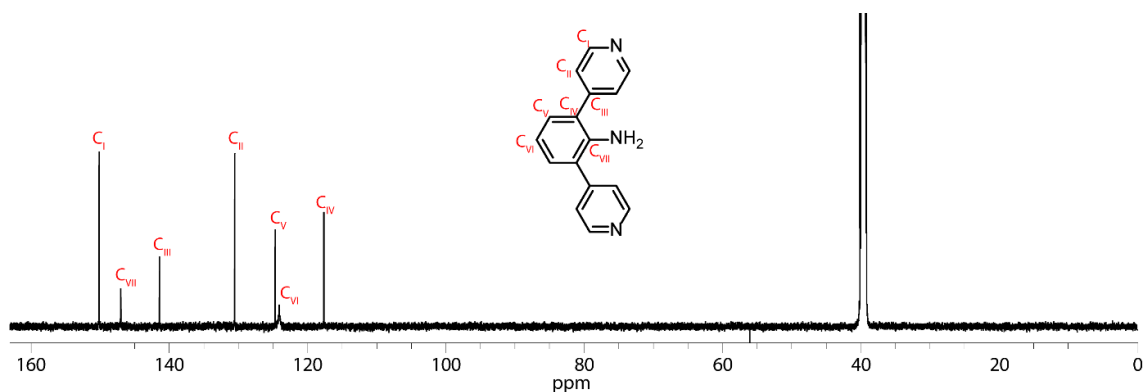
Figure 242: ^{13}C NMR spectrum (176 MHz, 298 K, DMSO-d_6) of **L^{S3}** including carbon assignment.

^{13}C{^{1}H} NMR (176 MHz, 298 K, DMSO-d_6) δ 150.11 (C$_I$), 146.97 (C$_{VII}$), 141.37 (C$_{III}$), 130.48 (C$_{II}$), 124.65 (C$_V$), 124.05 (C$_{VI}$), 117.59 (C$_{IV}$) ppm.

HR ESI-MS:

measured for [C$_{16}$H$_{12}$N$_3$+H]$^+$:   248.1246

calculated: 248.1182

Synthesis of 2,6-di(pyridin-4-yl)phenyl pivalate (L^{S7})
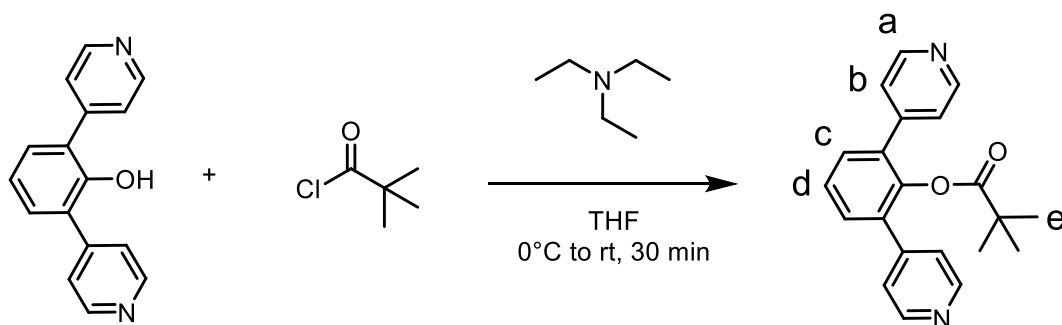
Scheme 35: Synthesis of **L^{S7}** with proton assignment.

2,6-di(pyridin-4-yl)phenol (10 mg, 40.3 µmol, 1 equiv.) and triethylamine (11.2 µl, 80.6 µmol, 2 equiv.) were suspended in dry THF on ice. Pivaloyl chloride (5.46 µl, 40.3 µmol, 1.1 equiv.) was added and the reaction mixture was stirred for 30 minutes until reaching room temperature. The reaction mixture was extracted with DCM and the organic phase was washed consecutively with water and then brine. It was dried over Na$_2$SO$_4$, filtered and the solvent was removed under reduced pressure. The crude product was directly purified by GPC. The yield of the final product was 7 mg (21 µmol, 52%).
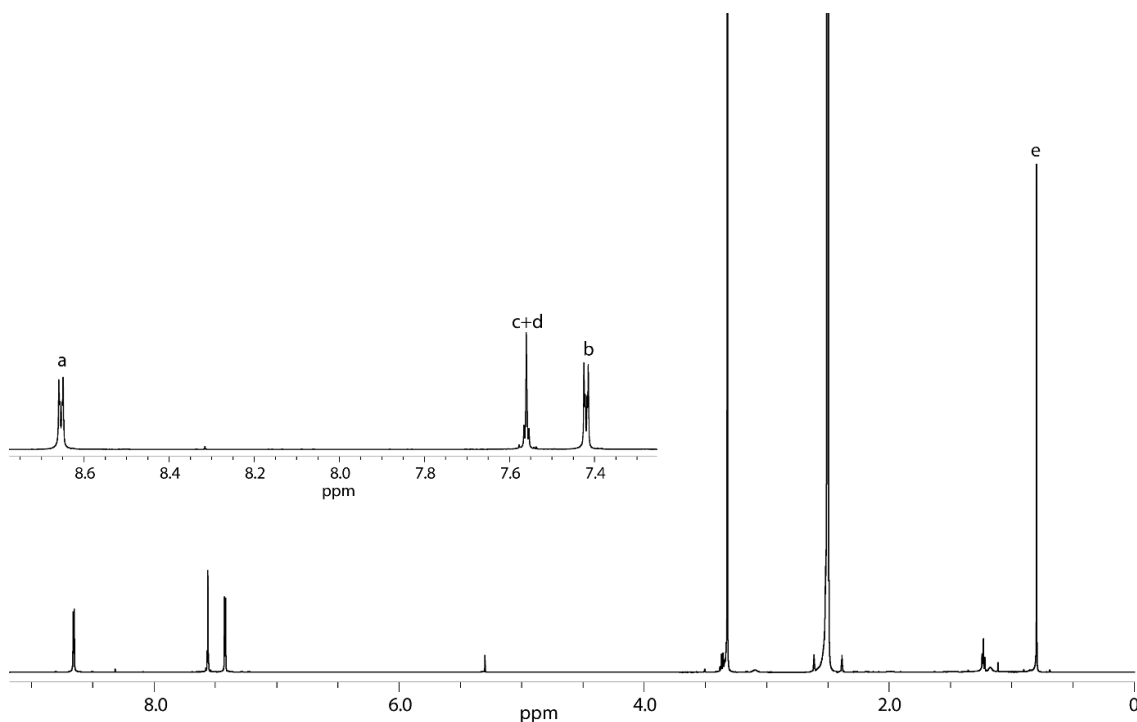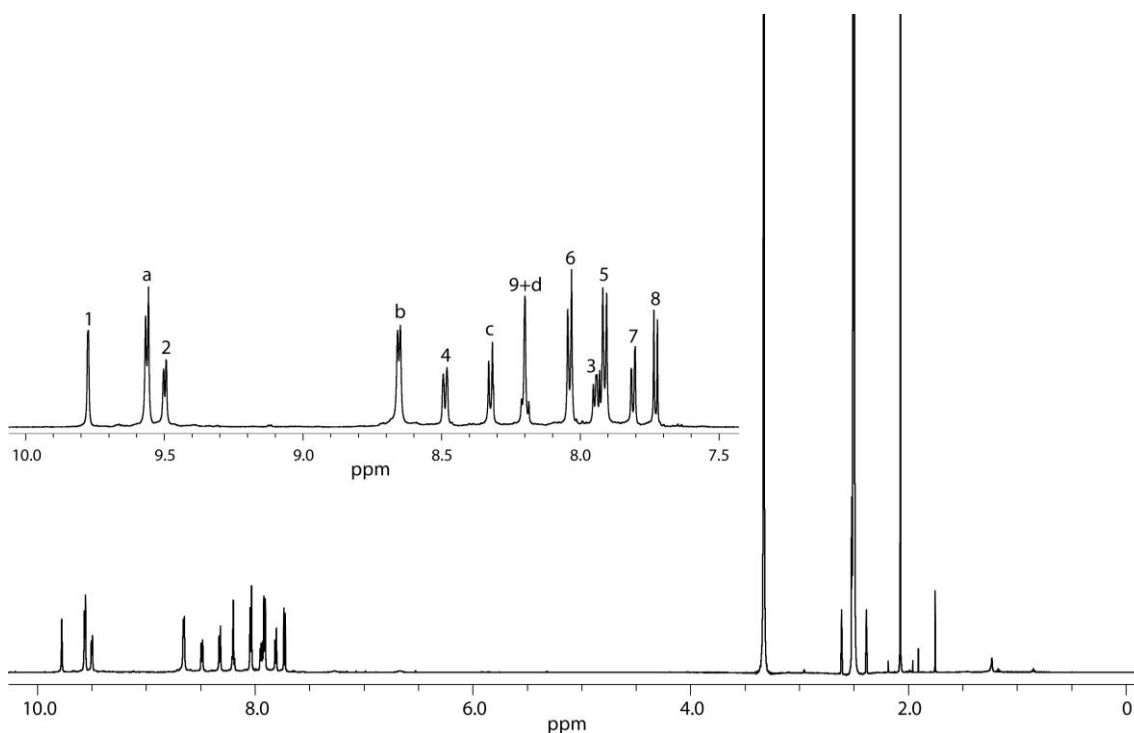
Figure 243: ^{1}H NMR spectrum (600 MHz, 298 K, DMSO-d_6) of **L**^{S7}. A zoom into the aromatic region including proton assignment is shown in the inset.

^{1}H NMR (600 MHz, 298 K, DMSO-d_6) δ 8.65 (dd, ^3J = 6.0, ^4J = 1.55 Hz, 4H, H^a), 7.55 – 7.57 (m, 3H, H^c+H^d), 7.42 (dd, ^3J = 6.0 Hz, ^4J = 1.55 Hz, 4H, H^b), 0.8 (s, 9H, H^e) ppm.
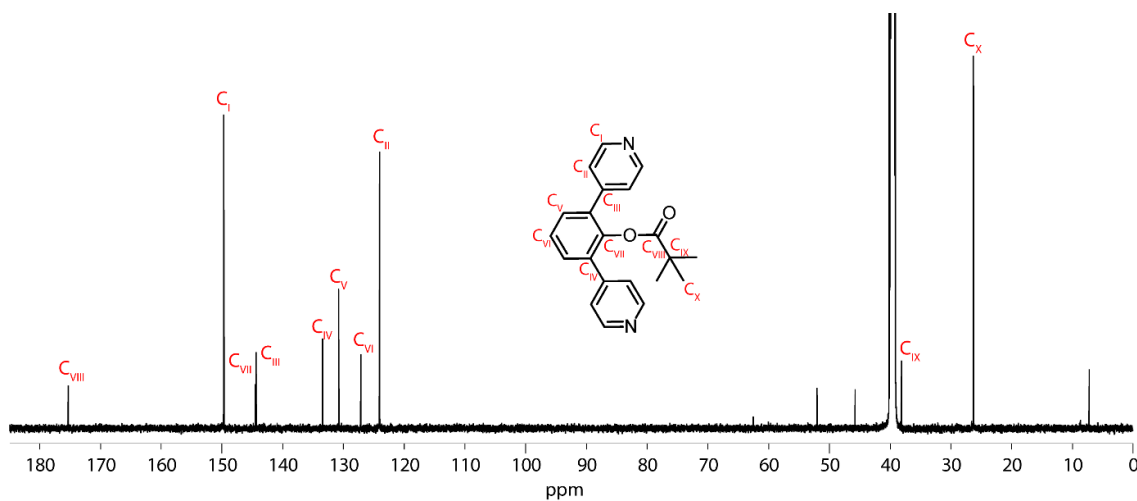
Figure 244: ^{13}C NMR spectrum (151 MHz, 298 K, DMSO-d_6) of **L**^{S7} including carbon assignment.

^{13}C{^{1}H} NMR (151 MHz, 298 K, DMSO-d_6) δ 175.71 (C$_{VIII}$), 150.11 (C$_I$), 144.92 (C$_{VII}$), 144.79 (C$_{III}$), 133.85 (C$_{IV}$), 131.20 (C$_V$), 127.57 (C$_{VI}$), 124.47(C$_{II}$), 38.56 (C$_{IX}$), 26.71 (C$_X$) ppm.

HR ESI-MS:

measured for [C$_{21}$H$_{21}$N$_2$O$_2$+H]$^+$:   333.1608

calculated: 333.1603

Synthesis of 2,6-di(pyridin-4-yl)phenyl benzoate (L^S8)
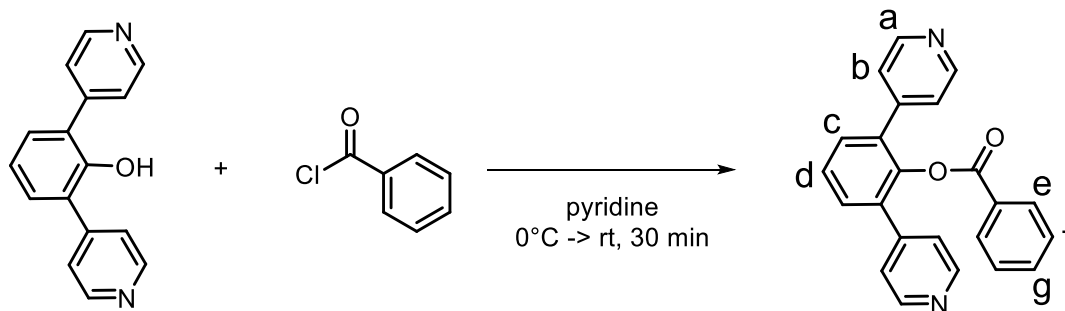
Scheme 36: Synthesis of **L^S8** with proton assignment.

2,6-di(pyridin-4-yl)phenol (10 mg, 40.3 µmol, 1 equiv.) was suspended in dry pyridine on ice. Benzoyl chloride (5.57 µl, 48.3 µmol, 1.2 equiv.) was added and the reaction mixture was stirred for 60 minutes until reaching room temperature. The reaction mixture was extracted with DCM and the organic phase was washed consecutively with water and then brine. It was dried over Na_2SO_4, filtered and the solvent was removed under reduced pressure. The crude product was directly purified by GPC. The yield of the final product was 9.8 mg (27.8 µmol, 69%).
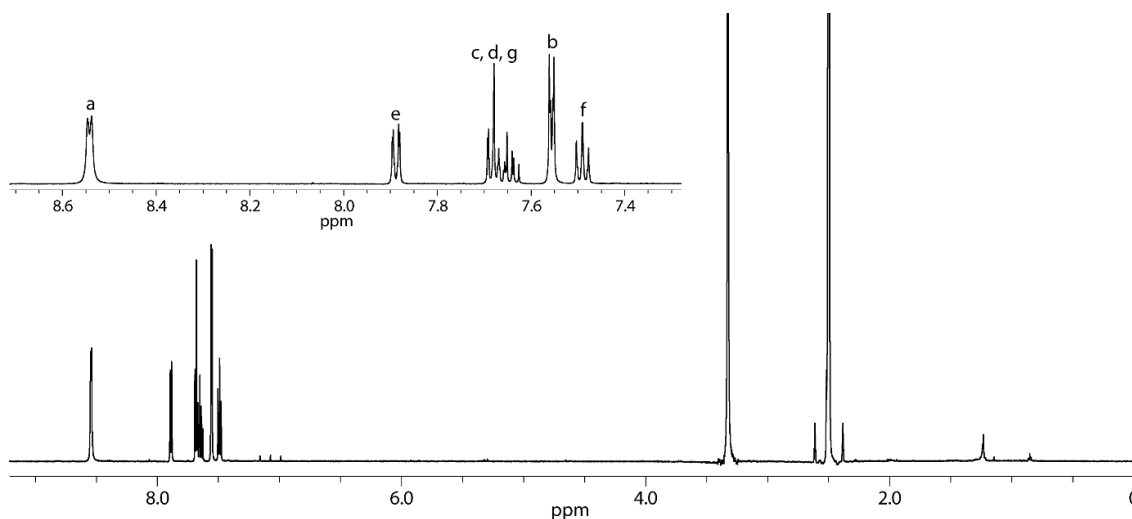
Figure 245: ^{1}H NMR spectrum (600 MHz, 298 K, DMSO-d_6) of **L^S8**. A zoom into the aromatic region including proton assignment is shown in the inset.

^{1}H NMR (600 MHz, 298 K, DMSO-d_6) δ 8.54 (d, $^3J = 5.45$, 4H, H^a), 7.89 (m, 4H, H^e), 7.62 – 7.70 (m, 4H, H^c, H^d, H^g), 7.56 (dd, $^3J = 6.1$, $^4J = 1.55$ Hz, 4H, H^b), 7.49 (dd, dd, $^3J = 8.5$, $^3J = 7.6$ Hz, 4H, H^f) ppm.
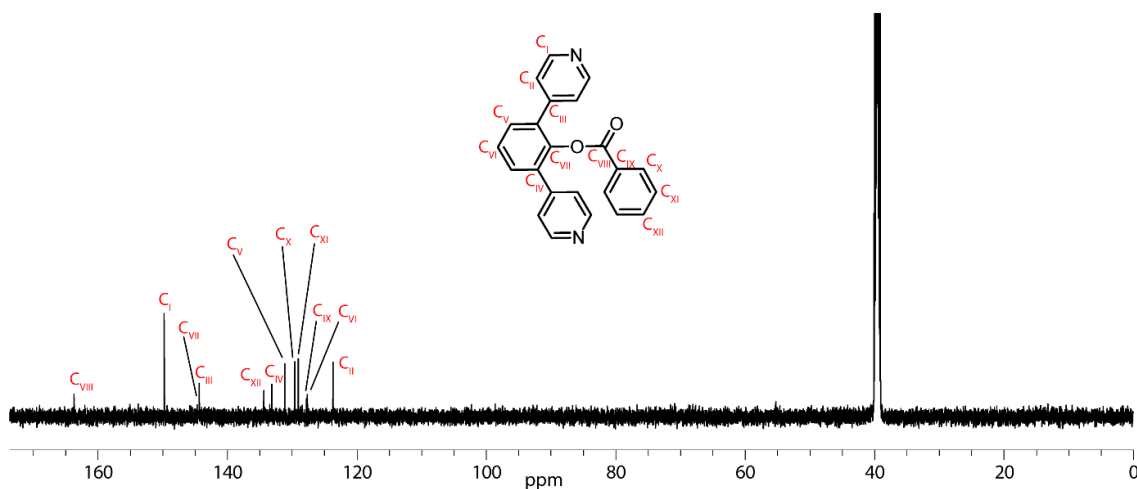
Figure 246: ^{13}C NMR spectrum (151 MHz, 298 K, DMSO-d_6) of $\textbf{L}^{\textbf{S8}}$ including carbon assignment.

^{13}C{^{1}H} NMR (151 MHz, 298 K, DMSO-d_6) δ 163.65 (C$_{VIII}$), 149.73 (C$_I$), 144.63 (C$_{VII}$), 144.31 (C$_{III}$), 134.35 (C$_{XII}$), 133.12 (C$_{IV}$), 131.09 (C$_V$), 129.56 (C$_X$), 129.01 (C$_{XI}$), 127.73 (C$_{IX}$), 127.60 (C$_{VI}$), 123.63(C$_{II}$) ppm.

HR ESI-MS:

measured for [C$_{23}$H$_{16}$N$_2$O$_2$+H]$^+$:   353.1280

calculated: 353.1290

Synthesis of 2,5-di(pyridin-4-yl)thiophene (L^{S9})
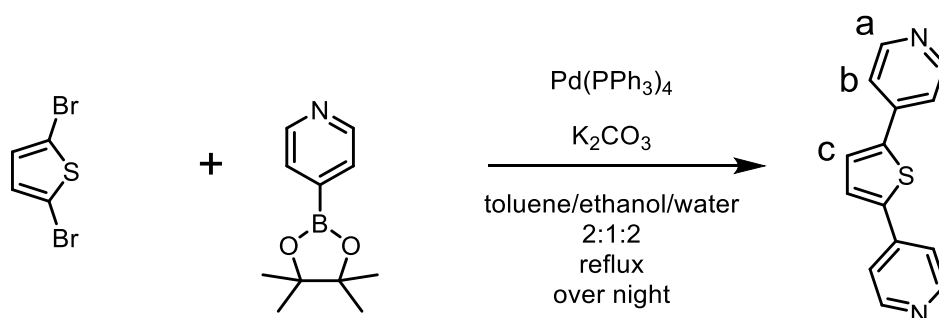
Scheme 37: Synthesis of $\textbf{L}^{\textbf{S9}}$ with proton assignment.

2,5-dibromothiophene (100 mg, 0.48 mmol, 1 equiv.), 4-(4,4,5,5-tetramethyl-1,3,2-dioxaborolan-2-yl)pyridine (295.4 mg, 1.44 mmol, 3 equiv.), K$_2$CO$_3$ (199 mg, 1.44 mmol, 3 equiv.) and Pd(PPh$_3$)$_4$ (27.7 mg, 0.024 mmol, 0.05 equiv.) were suspended in a mixture of toluene/ethanol/H$_2$O (2:1:2; 15 ml). The mixture was degassed three times using the *Freeze-Pump-Thaw*-method, heated to reflux and stirred overnight. After cooling down to room temperature, the reaction mixture was extracted with DCM. The organic phase was washed consecutively with water and then brine. It was dried over MgSO$_4$, filtered

and the solvent was removed under reduced pressure. The crude product was directly purified by GPC. The yield of the final product was 132 mg (0.36 mmol, 75%).
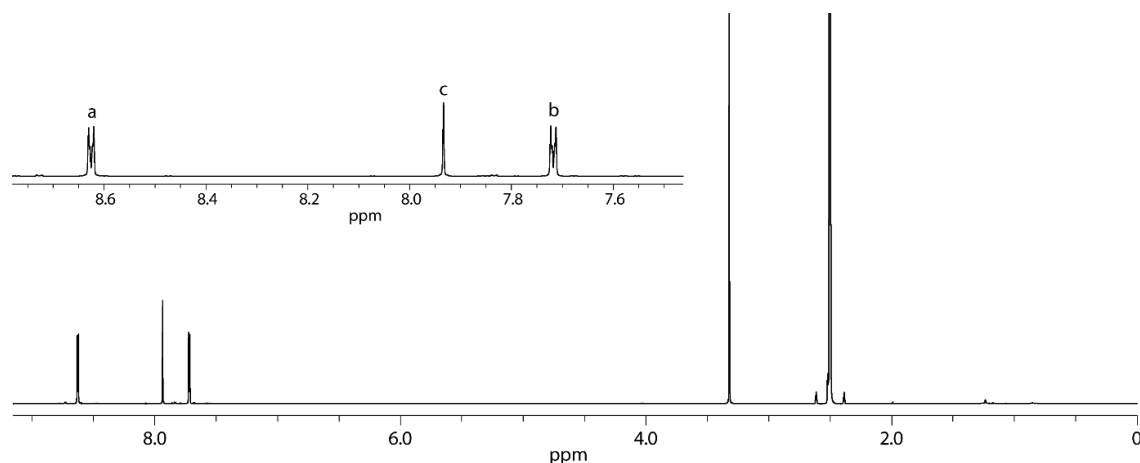
Figure 247: ^{1}H NMR spectrum (600 MHz, 298 K, DMSO-d_6) of $\mathbf{L^{S9}}$. A zoom into the aromatic region including proton assignment is shown in the inset.

^{1}H NMR (600 MHz, 298 K, DMSO-d_6) δ 8.63 (dd, $^3J = 6.2$, $^4J = 1.6$ Hz, 4H, H^a), 7.93 (s, 2H, H^c), 7.72 (dd, $^3J = 6.2$, $^4J = 1.6$ Hz, 4H, H^b) ppm.
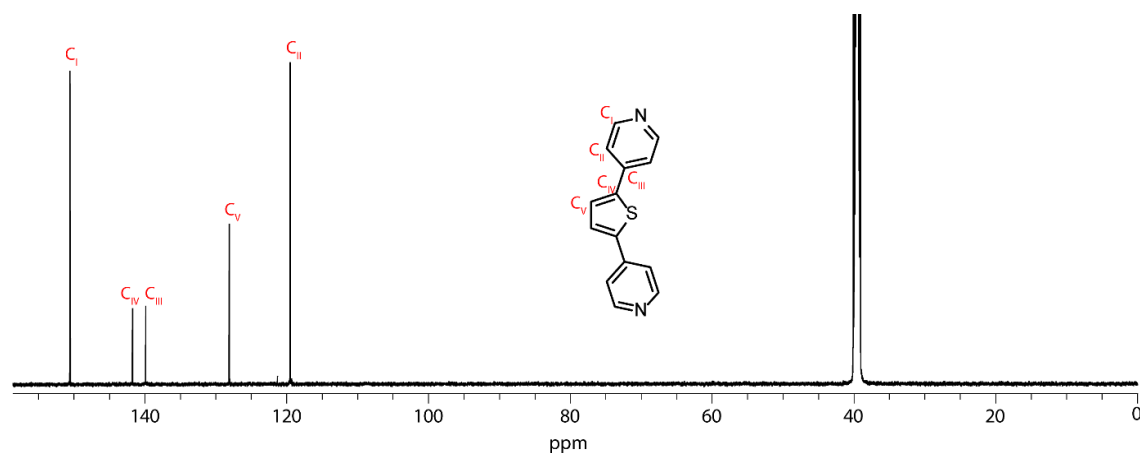
Figure 248: ^{13}C NMR spectrum (151 MHz, 298 K, DMSO-d_6) of $\mathbf{L^{S9}}$ including carbon assignment.

^{13}C{^{1}H} NMR (151 MHz, 298 K, DMSO-d_6) δ 150.54 (C$_I$), 141.73 (C$_{IV}$), 139.86 (C$_{III}$), 128.08 (C$_V$), 119.49 (C$_{II}$) ppm.

HR ESI-MS:

measured for [C$_{14}$H$_{10}$N$_2$S+H]$^+$:   238.0558

calculated: 238.0565

Synthesis of 2,5-di(pyridin-4-yl)selenophene (L^{S10})
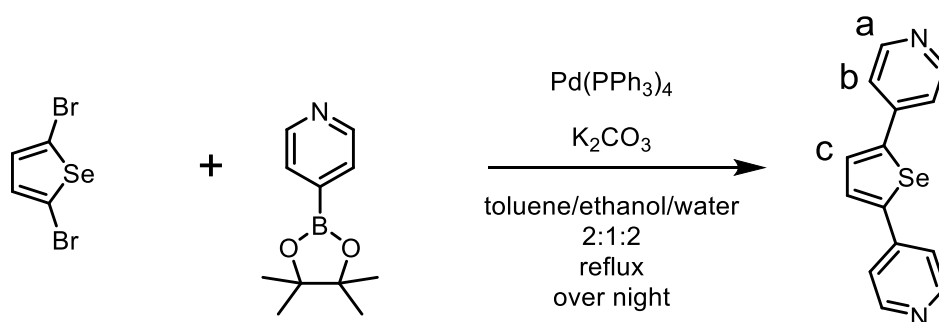
Scheme 38: Synthesis of **L^{S10}** with proton assignment.

2,5-dibromoselenophene (200 mg, 0.69 mmol, 1 equiv.), 4-(4,4,5,5-tetramethyl-1,3,2-dioxaborolan-2-yl)pyridine (426.0 mg, 2.08 mmol, 3 equiv.), K_2CO_3 (287 mg, 2.08 mmol, 3 equiv.) and Pd(PPh$_3$)$_4$ (40 mg, 0.035 mmol, 0.05 equiv.) were suspended in a mixture of toluene/ethanol/H$_2$O (2:1:2; 20 ml). The mixture was degassed two times using the *Freeze-Pump-Thaw*-method, heated to reflux and stirred overnight. After cooling down to room temperature, the reaction mixture was extracted with DCM. The organic phase was washed consecutively with water and then brine. It was dried over MgSO$_4$, filtered and the solvent was removed under reduced pressure. The crude product was directly purified by GPC. The yield of the final product was 144 mg (0.505 mmol, 73%).
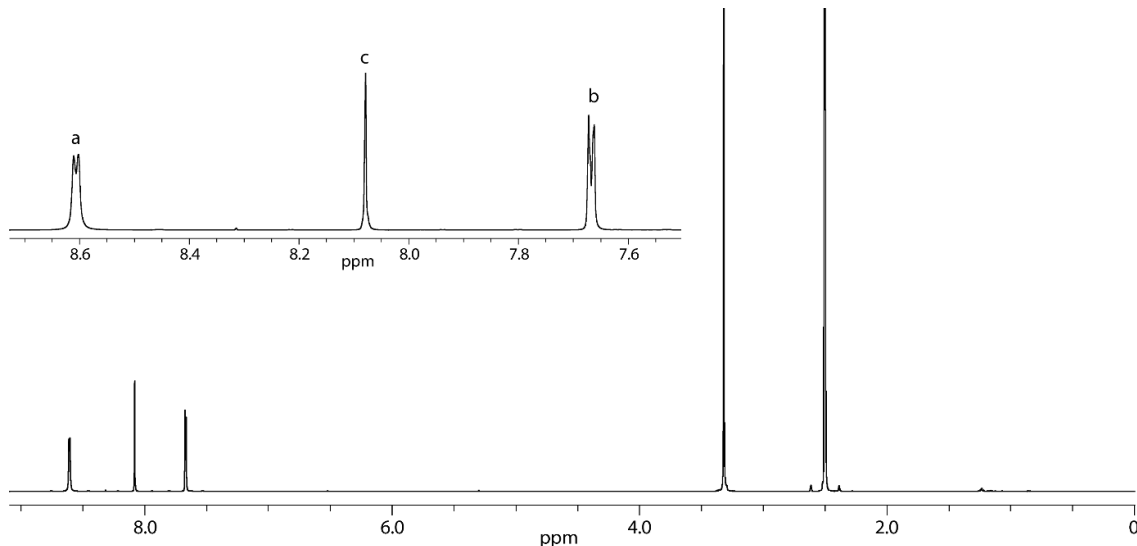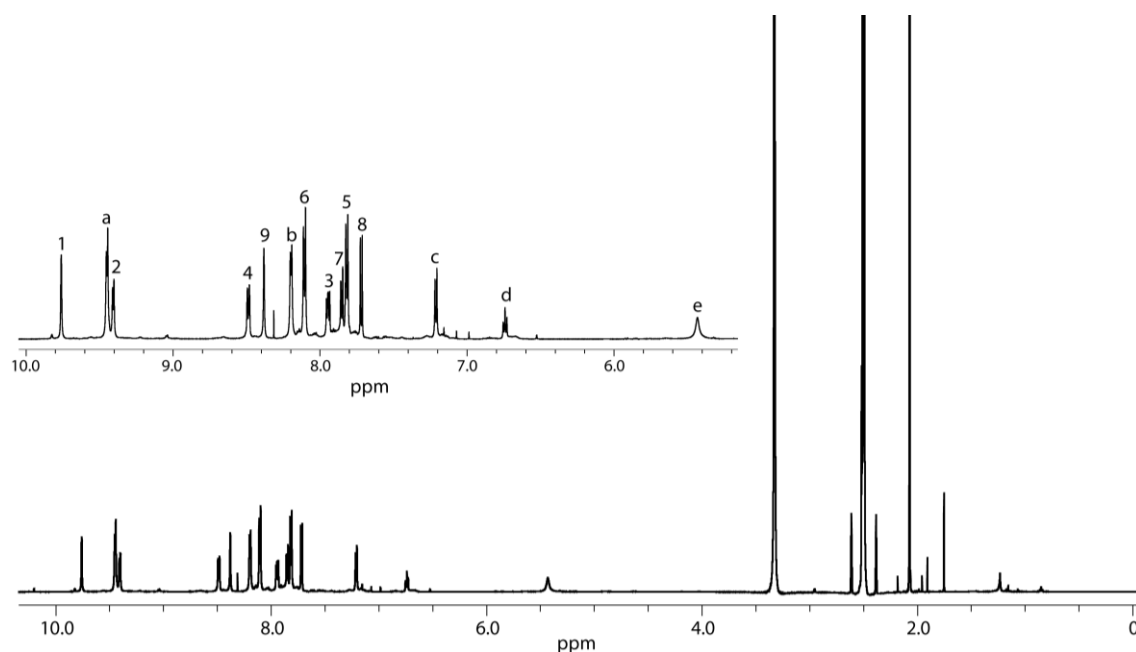

Figure 249: ^{1}H NMR spectrum (600 MHz, 298 K, DMSO-d_6) of L^{S10}. A zoom into the aromatic region including proton assignment is shown in the inset.

^{1}H NMR (600 MHz, 298 K, DMSO-d_6) δ 8.61 (d, ^3J = 5.1 Hz, 4H, H^a), 8.08 (s, 2H, H^c), 7.67 (dd, ^3J = 5.9, ^4J = 1.6 Hz, 4H, H^b) ppm.
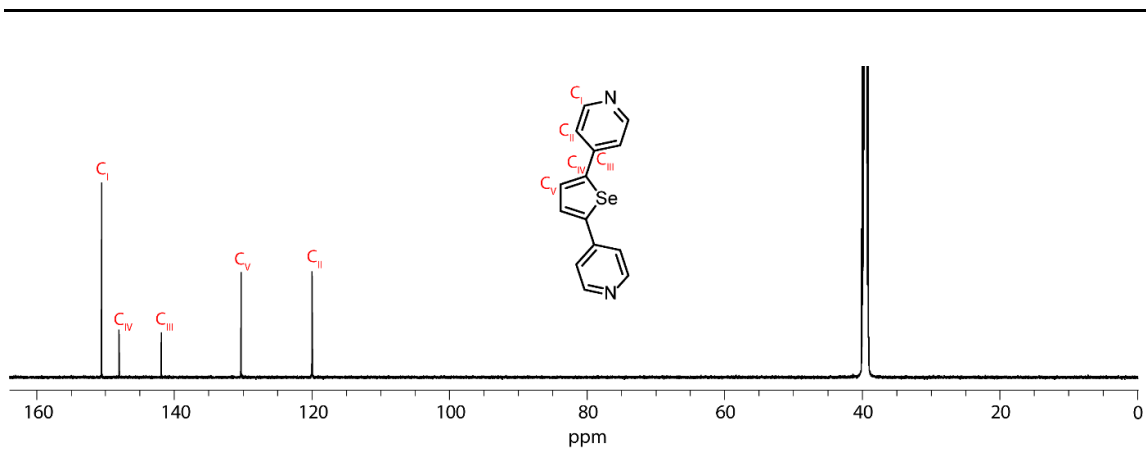
Figure 250: ^{13}C NMR spectrum (151 MHz, 298 K, DMSO-d_6) of **L^{S10}** including carbon assignment.

^{13}C{^{1}H} NMR (151 MHz, 298 K, DMSO-d_6) δ 150.52 (C$_I$), 147.99 (C$_{IV}$), 141.83 (C$_{III}$), 130.25 (C$_V$), 119.94 (C$_{II}$) ppm.
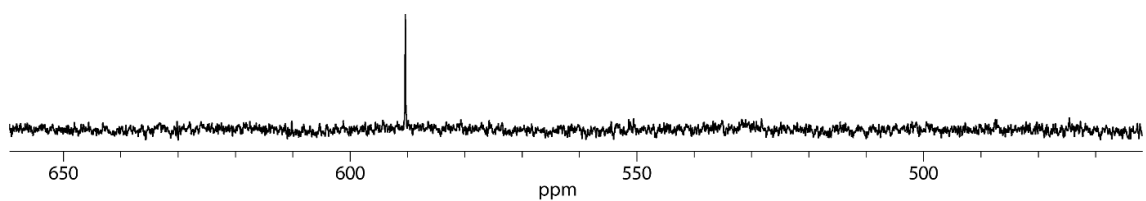
Figure 251: ^{77}Se NMR spectrum (115 MHz, 298 K, DMSO-d_6) of **L^{S10}**.

^{77}Se{^{1}H} (114.5 MHz, 298 K, DMSO-d_6) δ 590.32 ppm.

HR ESI-MS:

measured for [C$_{14}$H$_{10}$N$_2$Se+H]$^+$:   286.0038

calculated: 286.0004

3.4.7.2 Assembly Characterization

All ^{13}C spectra reported here contain additional signals attributed to CH_3CN (δ 1.16 and 118.09 ppm), the triflate anion ($CF_3SO_3^-$; δ 123.87, 121.74, 119.60, 117.47 ppm), both stemming from the utilized Pd source ($Pd[CH_3CN]_4OTf_2$), and acetic acid (δ 22.51 and 171.42 ppm). Shifts may vary slightly.

3.4.7.2.1 $Pd_3L^{F2}_3L^{S1}_3$

A mixture of ligand L^{F2} (270 µL of a 3.11 mM solution in DMSO-d_6), L^{S1} (270 µL of a 3.11 mM solution in DMSO-d_6), and $[Pd(CH_3CN)_4](OTf)_2$ (60 µL of a 15 mM solution in DMSO-d_6) was left to rest at room temperature for 2 h to afford clean $Pd_3L^{F2}_3L^{S1}_3$.
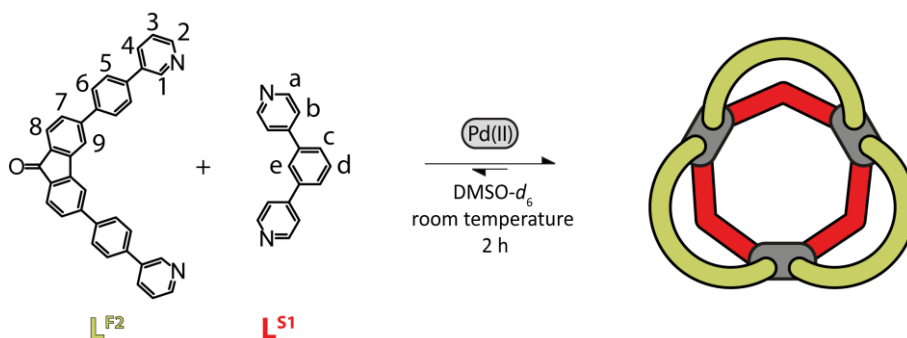
Scheme 39: Formation of $Pd_3L^{F2}_3L^{S1}_3$ with consecutive proton labels.
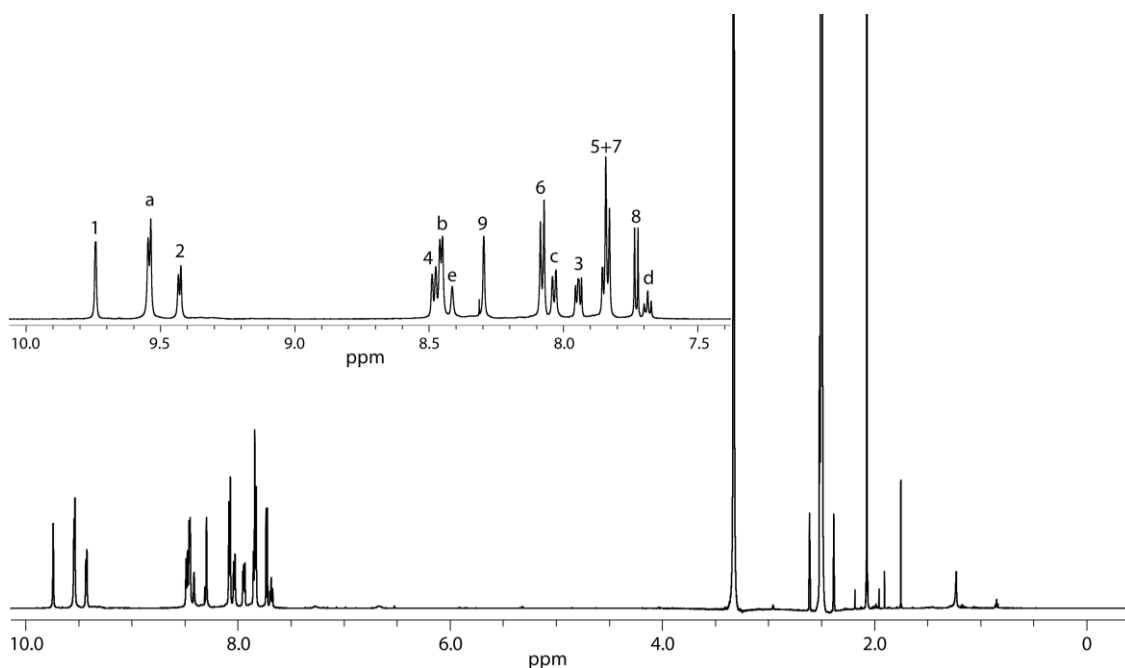
Figure 252: ^1H NMR spectrum (600 MHz, 298 K, DMSO-d_6) of $Pd_3L^{F2}_3L^{S1}_3$. A zoom into the aromatic region including proton assignment is shown in the inset.

^{1}H (600 MHz, 298 K, DMSO-d_6) δ 9.74 (d, ^5J = 1.05 Hz, 6H, H^1), 9.54 (d, ^3J = 6.1 Hz, 12H, H^a), 9.43 (d, ^3J = 5.6 Hz, 6H, H^2), 8.48 (d, ^3J = 8.2 Hz, 6H, H^4), 8.46 (d, ^3J = 6.1 Hz, 12H, H^b), 8.41 (s, 3H, H^e), 8.30 (s, 6H, H^9), 8.08 (d, ^3J = 8.3 Hz, 12H, H^6), 8.03 (d, ^3J = 7.9 Hz, 6H, H^c), 7.94 (dd, ^3J = 8.3, 5.7 Hz, 6H, H^3), 7.81-7.87 (m, 18H, H^5+H^7), 7.73 (d, ^3J = 7.7 Hz, 6H, H^8), 7.69 (t, ^3J = 7.9 Hz, 3H, H^d) ppm.
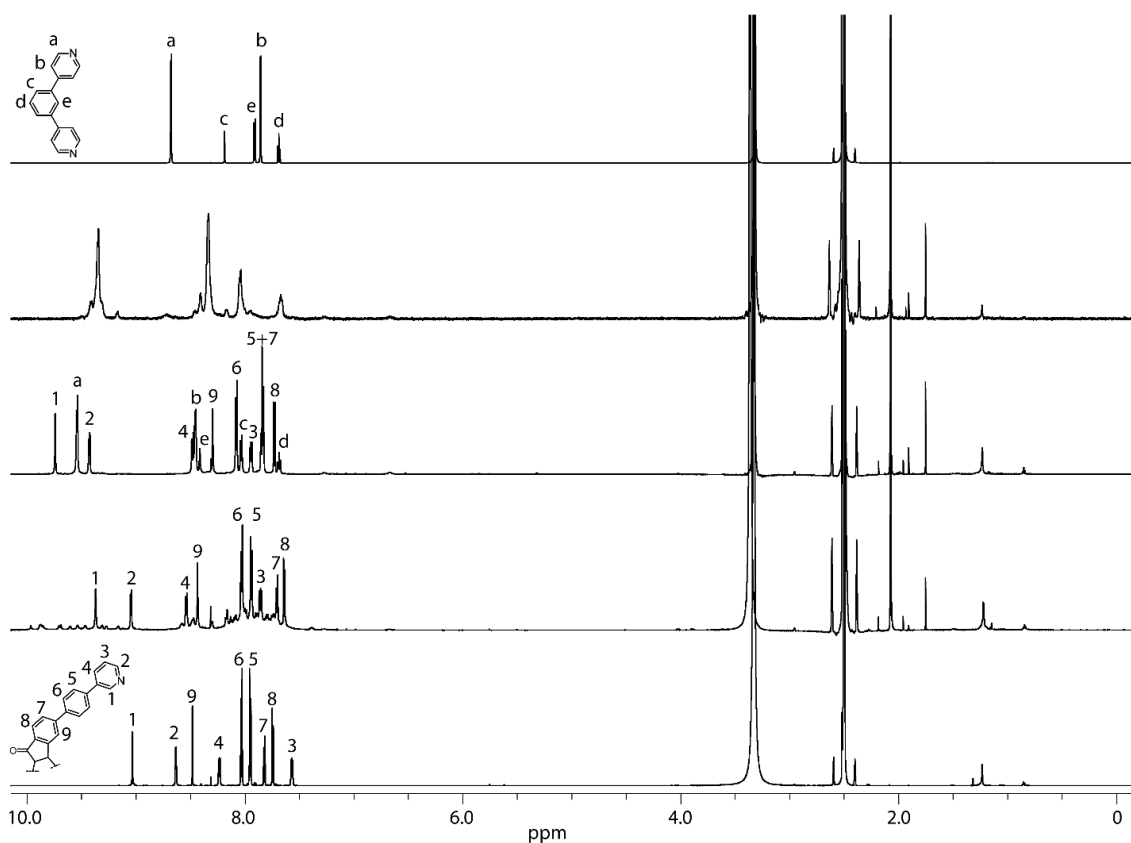
Figure 253: Full ^{1}H NMR spectra (298 K, DMSO-d_6)of ligand **L^{F2}** (700 MHz); homoleptic Pd$_2$**L^{F2}**$_4$ cage and the Pd$_n$**L^{F2}**$_{2n}$ (n=3-5) rings formed upon addition of 0.55 equiv. Pd(II) cations to ligand **L^{F2}** (600 MHz); heteroleptic Pd$_3$**L^{F2}**$_3$**L^{S1}**$_3$ (600 MHz); ligand **L^{S1}** upon addition of 0.55 equiv. Pd(II) cations (500 MHz); ligand **L^{S1}** (700 MHz)(listed bottom to top).
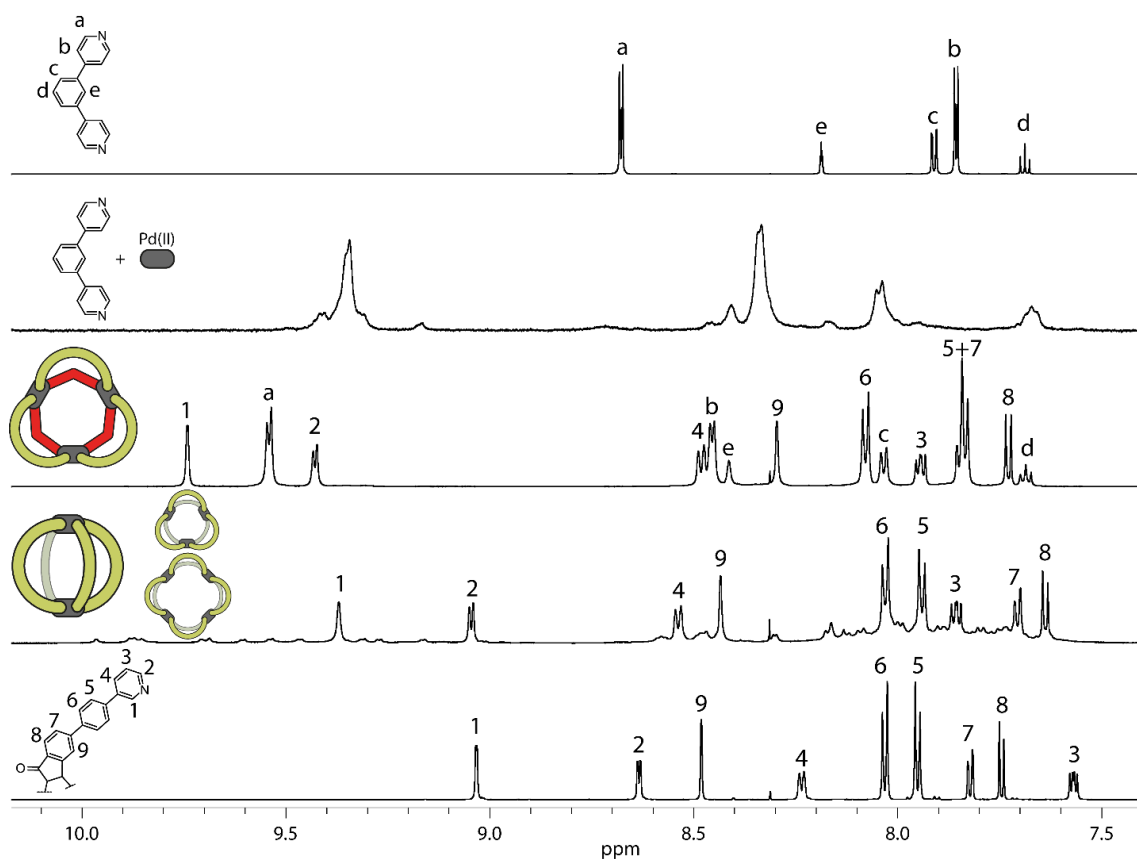
Figure 254: Partial ^{1}H NMR spectra (298 K, DMSO-d_6)of ligand L^{F2} (700 MHz); homoleptic $Pd_2L^{F2}_4$ cage and the $Pd_nL^{F2}_{2n}$ (n=3-5) rings formed upon addition of 0.55 equiv. Pd(II) cations to ligand L^{F2} (600 MHz); heteroleptic $Pd_3L^{F2}_3L^{S1}_3$ (600 MHz); ligand L^{S1} upon addition of 0.55 equiv. Pd(II) cations (500 MHz); ligand L^{S1} (700 MHz)(listed bottom to top).
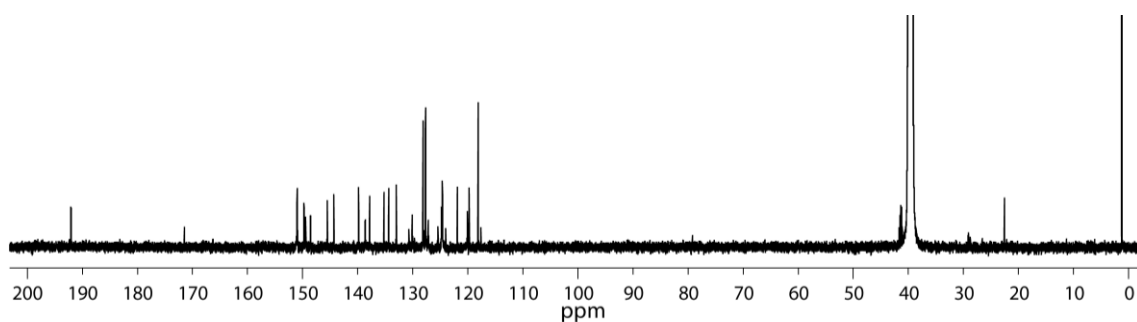
Figure 255: ^{13}C NMR spectrum (151 MHz, 298 K, DMSO-d_6) of $Pd_3L^{F2}_3L^{S1}_3$.

^{13}C{^{1}H} (151 MHz, 298 K, DMSO-d_6) δ 192.0, 150.9, 149.7, 149.4, 148.5, 145.5, 144.3, 139.8, 138.6, 137.8, 135.2, 134.3, 133.0, 130.7, 130.1, 128.1, 127.6, 127.2, 125.4, 124.8, 124.6, 120.0 ppm.
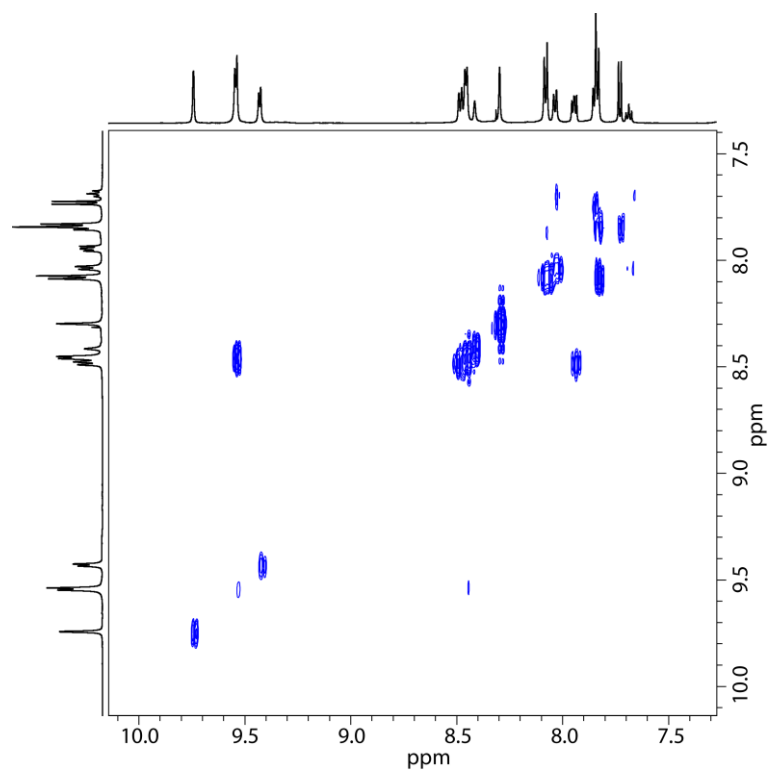
Figure 256: Partial ^{1}H-^{1}H COSY NMR spectrum (600 MHz, 298 K, DMSO-d_6) of Pd$_3$**L**$^{F2}_3$**L**$^{S1}_3$.
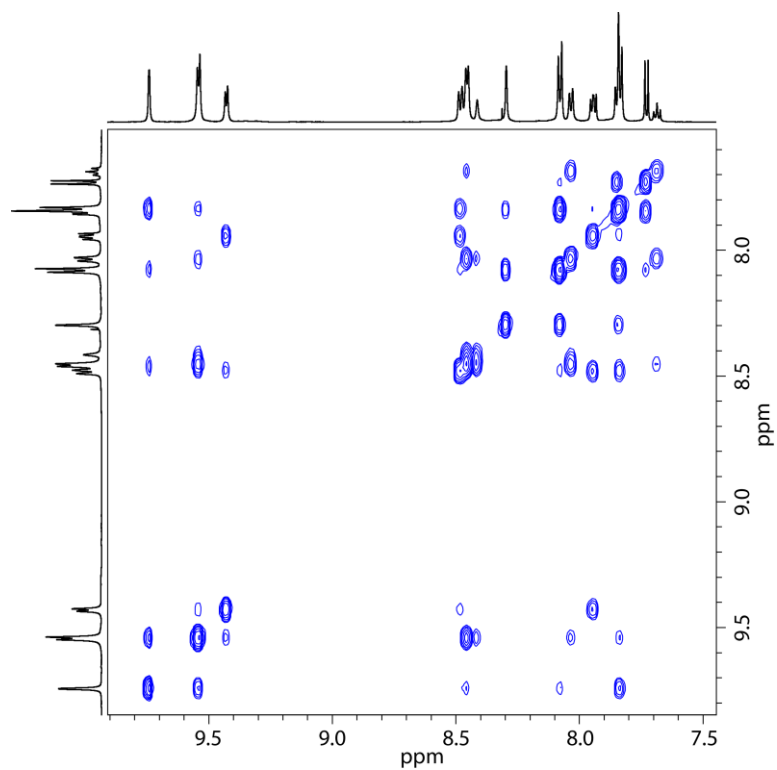
Figure 257: Partial ^{1}H-^{1}H NOESY NMR spectrum (600 MHz, 298 K, DMSO-d_6) of Pd$_3$**L**$^{F2}_3$**L**$^{S1}_3$.
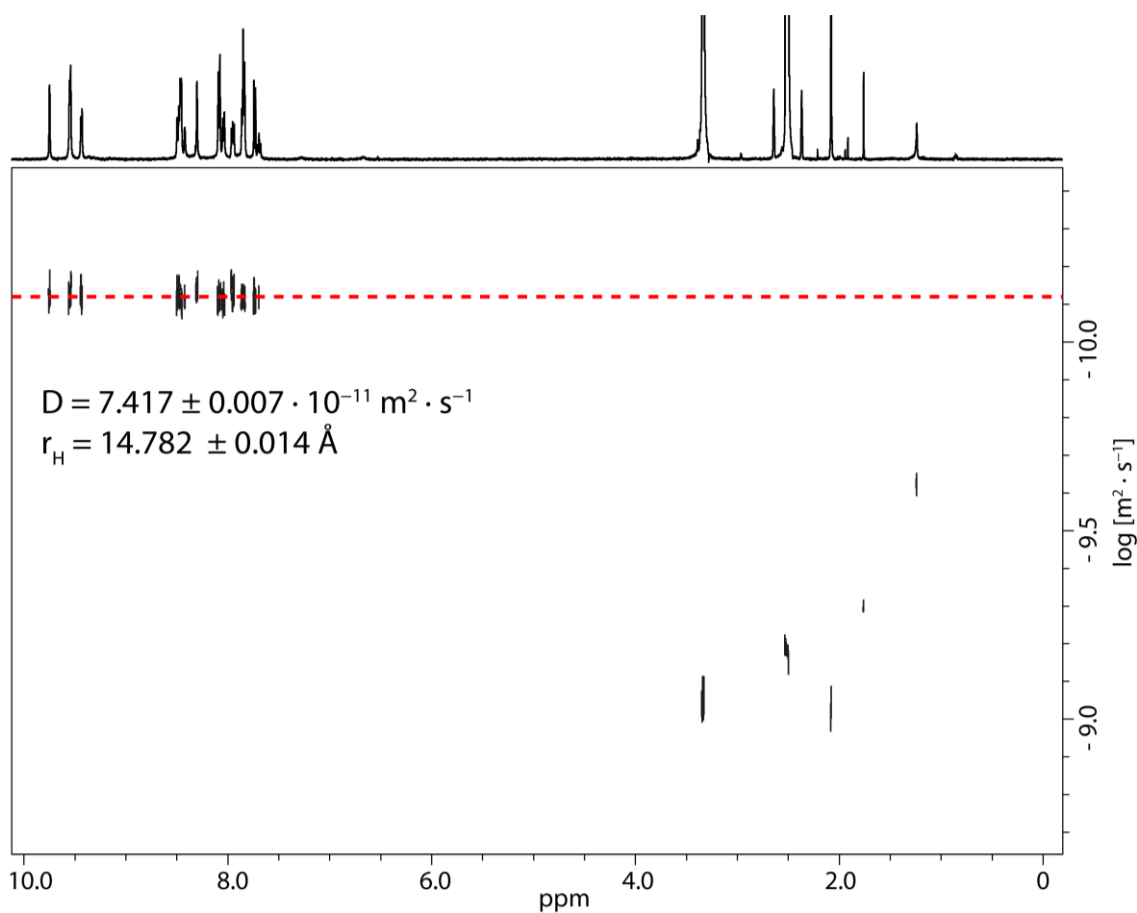
Figure 258: ^{1}H DOSY NMR spectrum (500 MHz, 298 K, DMSO-d_6) of Pd$_3$**L^{F2}**$_3$**L^{S1}**$_3$. Values for diffusion coefficient and resulting hydrodynamic radius are given.
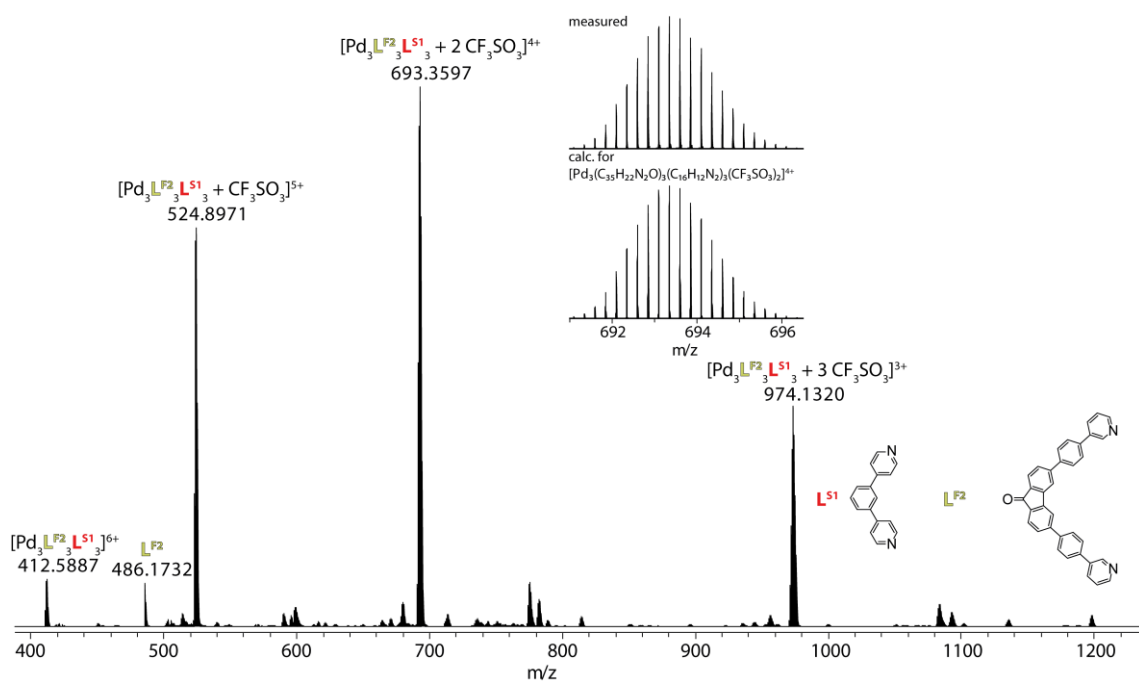
Figure 259: CSI-MS spectrum of Pd$_3$**L^{F2}**$_3$**L^{S1}**$_3$. Peaks could be assigned to [Pd$_3$**L^{F2}**$_3$**L^{S1}**$_3$ + xCF$_3$SO$_3$]$^{(6-x)}$ (x = 0-3). The observed and calculated isotopic patterns are shown in the inset.

3.4.7.2.2 Pd$_3$**L**$^{F2}_3$**L**$^{S2}_3$

A mixture of ligand **L**^{F2} (270 µL of a 3.11 mM solution in DMSO-d_6), **L**^{S2} (270 µL of a 3.11 mM solution in DMSO-d_6), and [Pd(CH$_3$CN)$_4$](OTf)$_2$ (60 µL of a 15 mM solution in DMSO-d_6) was left to rest at room temperature for 2 h to afford clean Pd$_3$**L**$^{F2}_3$**L**$^{S2}_3$.
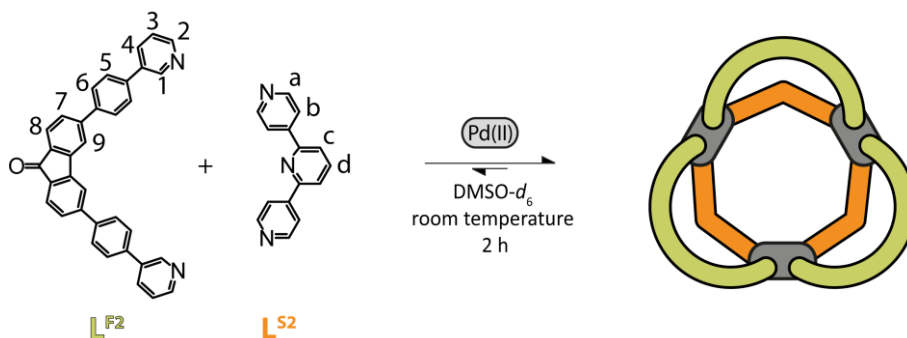
Scheme 40: Formation of Pd$_3$**L**$^{F2}_3$**L**$^{S2}_3$ with consecutive proton labels.

Figure 260: ^{1}H NMR spectrum (600 MHz, 298 K, DMSO-d_6) of Pd$_3$**L**$^{F2}_3$**L**$^{S2}_3$. A zoom into the aromatic region including proton assignment is shown in the inset.

^{1}H (600 MHz, 298 K, DMSO-d_6) δ 9.78 (d, ^5J = 0.9 Hz, 6H, H^1), 9.56 (d, ^3J = 6.2 Hz, 12H, H^a), 9.50 (d, ^3J = 5.7 Hz, 6H, H^2), 8.65 (d, ^3J = 6.2 Hz, 12H, H^b), 8.49 (d, ^3J = 8.1 Hz, 6H, H^4), 8.32 (d, ^3J = 7.9 Hz, 6H, H^c), 8.18-8.22 (m, 9H, H^9+H^d), 8.04 (d, ^3J = 8.5 Hz, 12H, H^6), 7.94 (dd, ^3J = 8.2, 5.8 Hz, 6H, H^3), 7.91 (d, ^3J = 8.5 Hz, 12H, H^5), 7.81 (dd, ^3J = 7.6 Hz, ^5J = 0.9 Hz, 6H, H^7), 7.73 (d, ^3J = 7.8 Hz, 6H, H^8) ppm.
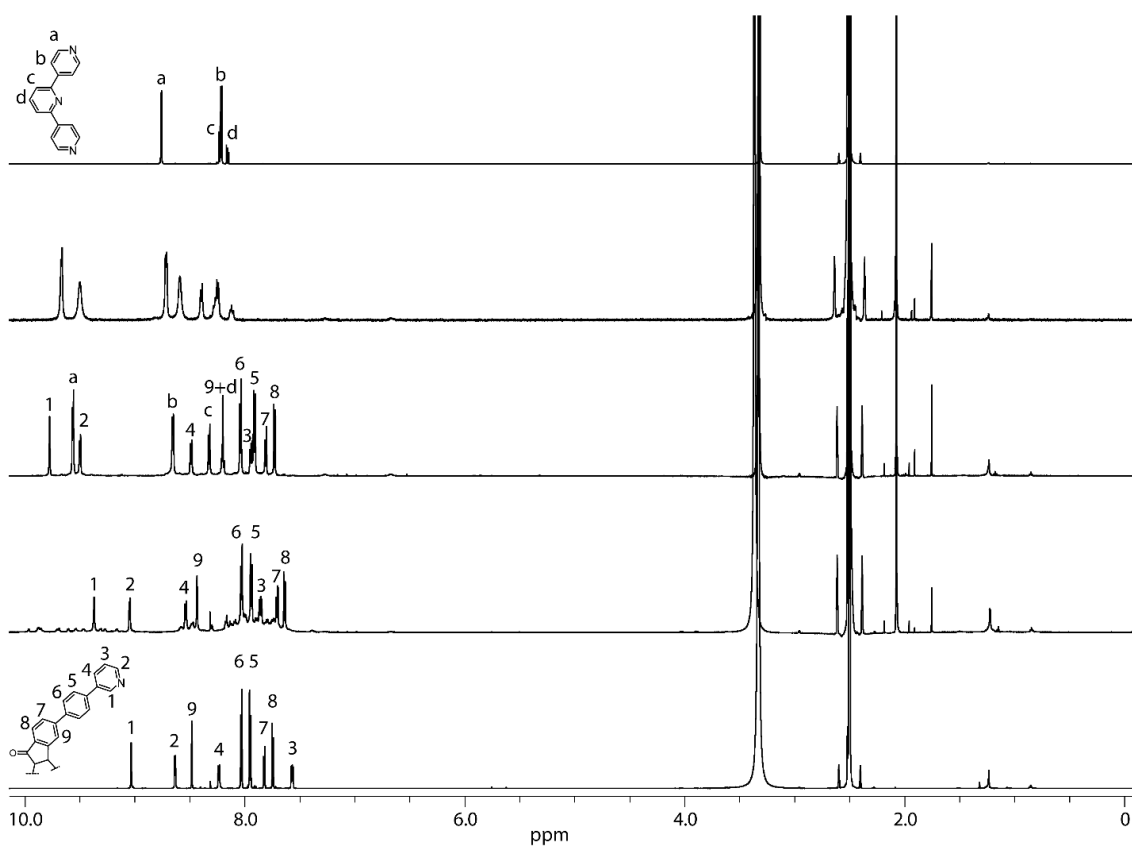
Figure 261: Full ^{1}H NMR spectra (298 K, DMSO-d_6)of ligand $\mathbf{L^{F2}}$ (700 MHz); homoleptic Pd$_2\mathbf{L^{F2}}_4$ cage and the Pd$_n\mathbf{L^{F2}}_{2n}$ (n=3-5) rings formed upon addition of 0.55 equiv. Pd(II) cations to ligand $\mathbf{L^{F2}}$ (600 MHz); heteroleptic Pd$_3\mathbf{L^{F2}}_3\mathbf{L^{S2}}_3$ (600 MHz); ligand $\mathbf{L^{S2}}$ upon addition of 0.55 equiv. Pd(II) cations (600 MHz);[163] ligand $\mathbf{L^{S2}}$ (700 MHz)(listed bottom to top).
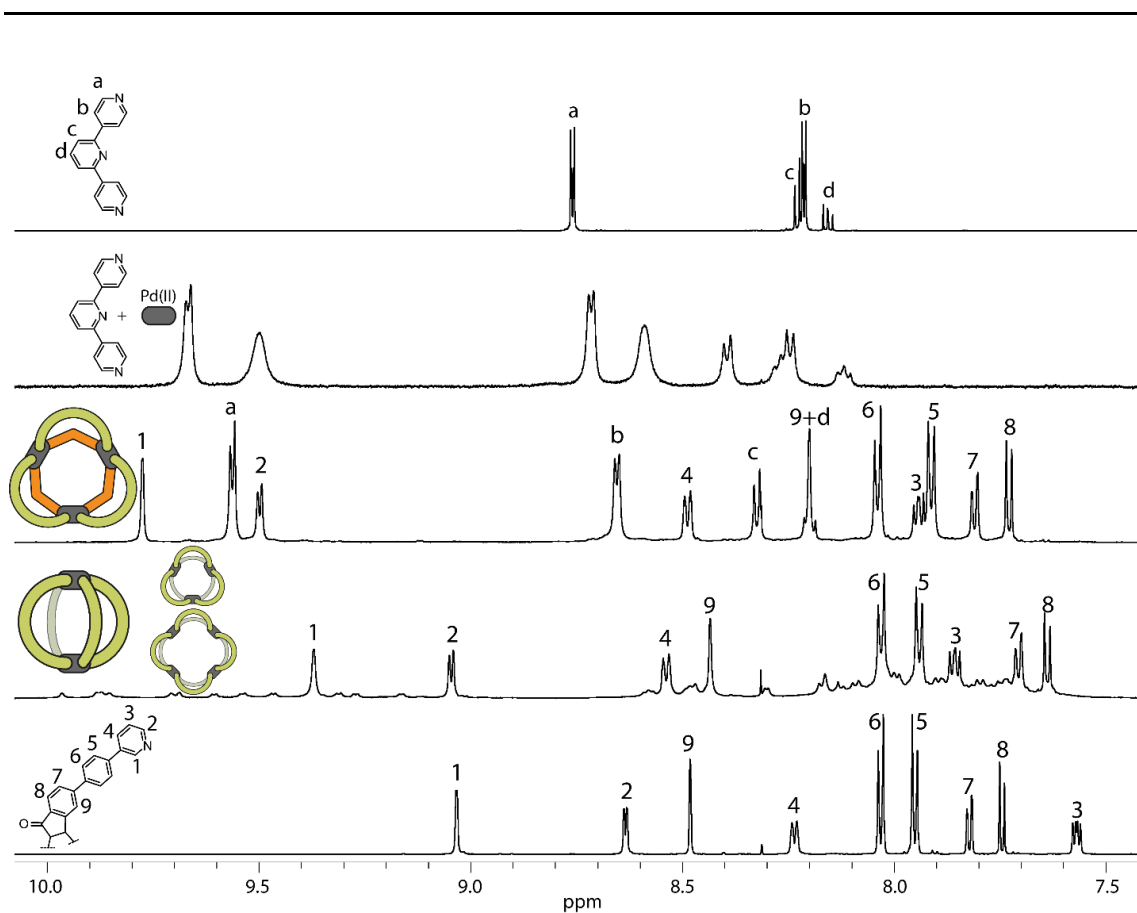
Figure 262: Partial ^{1}H NMR spectra (298 K, DMSO-d_6)of ligand $\mathbf{L^{F2}}$ (700 MHz); homoleptic Pd$_2\mathbf{L^{F2}}_4$ cage and the Pd$_n\mathbf{L^{F2}}_{2n}$ (n=3-5) rings formed upon addition of 0.55 equiv. Pd(II) cations to ligand $\mathbf{L^{F2}}$ (600 MHz); heteroleptic Pd$_3\mathbf{L^{F2}}_3\mathbf{L^{S2}}_3$ (600 MHz); ligand $\mathbf{L^{S2}}$ upon addition of 0.55 equiv. Pd(II) cations (600 MHz); ligand $\mathbf{L^{S2}}$ (700 MHz)(listed bottom to top).
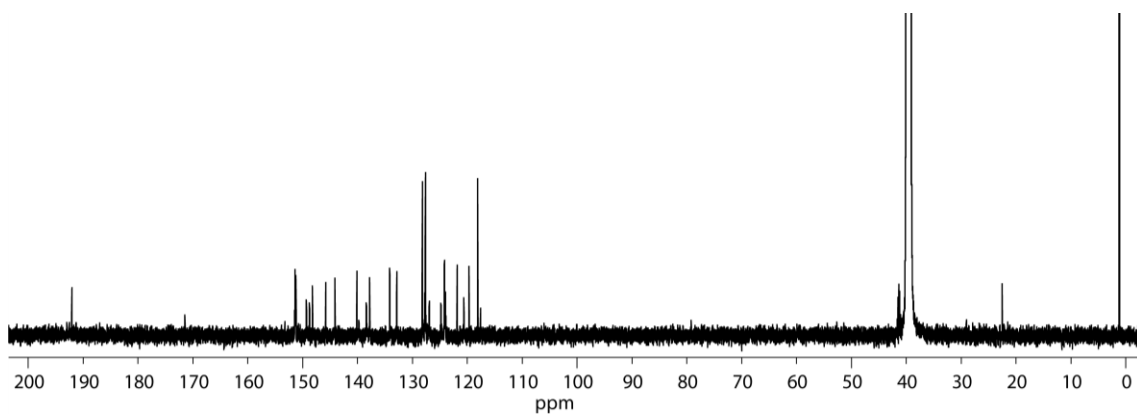
Figure 263: ^{13}C NMR spectrum (151 MHz, 298 K, DMSO-d_6) of Pd$_3\mathbf{L^{F2}}_3\mathbf{L^{S2}}_3$.

^{13}C{^{1}H} (151 MHz, 298 K, DMSO-d_6) δ 192.0, 151.4, 151.2, 149.3, 148.8, 148.2, 145.8, 144.1, 140.1, 138.4, 137.8, 134.1, 132.8, 128.2, 127.7, 127.6, 126.9, 124.8, 124.1, 124.0, 120.6 ppm.
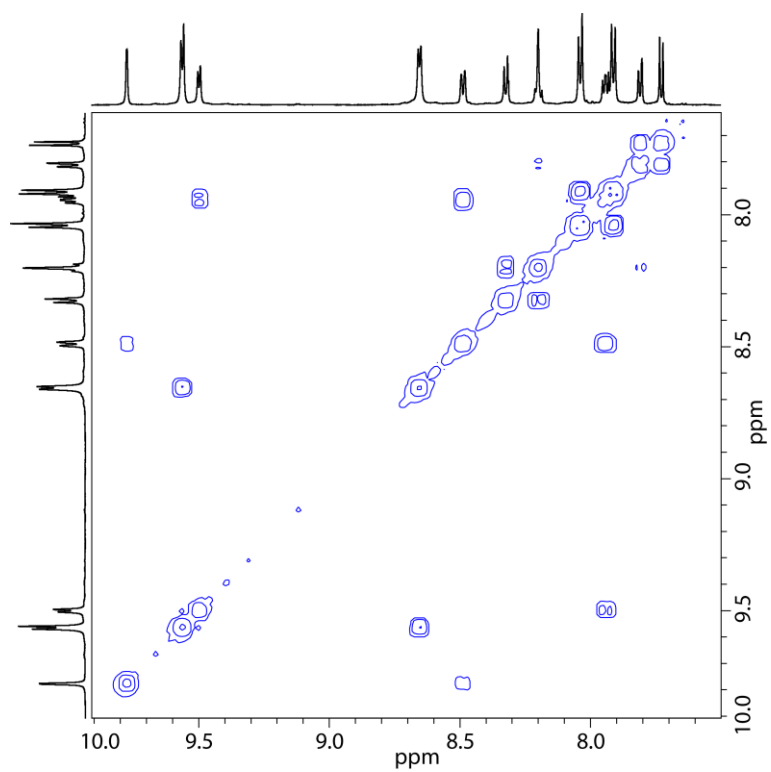
Figure 264: Partial ^{1}H-^{1}H COSY NMR spectrum (600 MHz, 298 K, DMSO-d_6) of Pd$_3$**L**$^{\textbf{F2}}{}_3$**L**$^{\textbf{S2}}{}_3$.
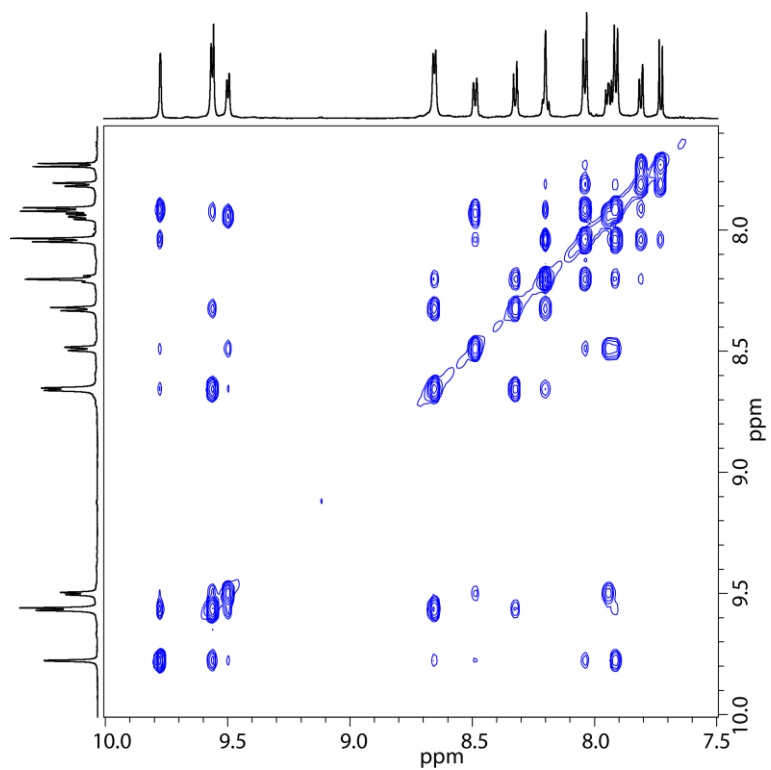
Figure 265: Partial ^{1}H-^{1}H NOESY NMR spectrum (600 MHz, 298 K, DMSO-d_6) of Pd$_3$**L**$^{\textbf{F2}}{}_3$**L**$^{\textbf{S2}}{}_3$.
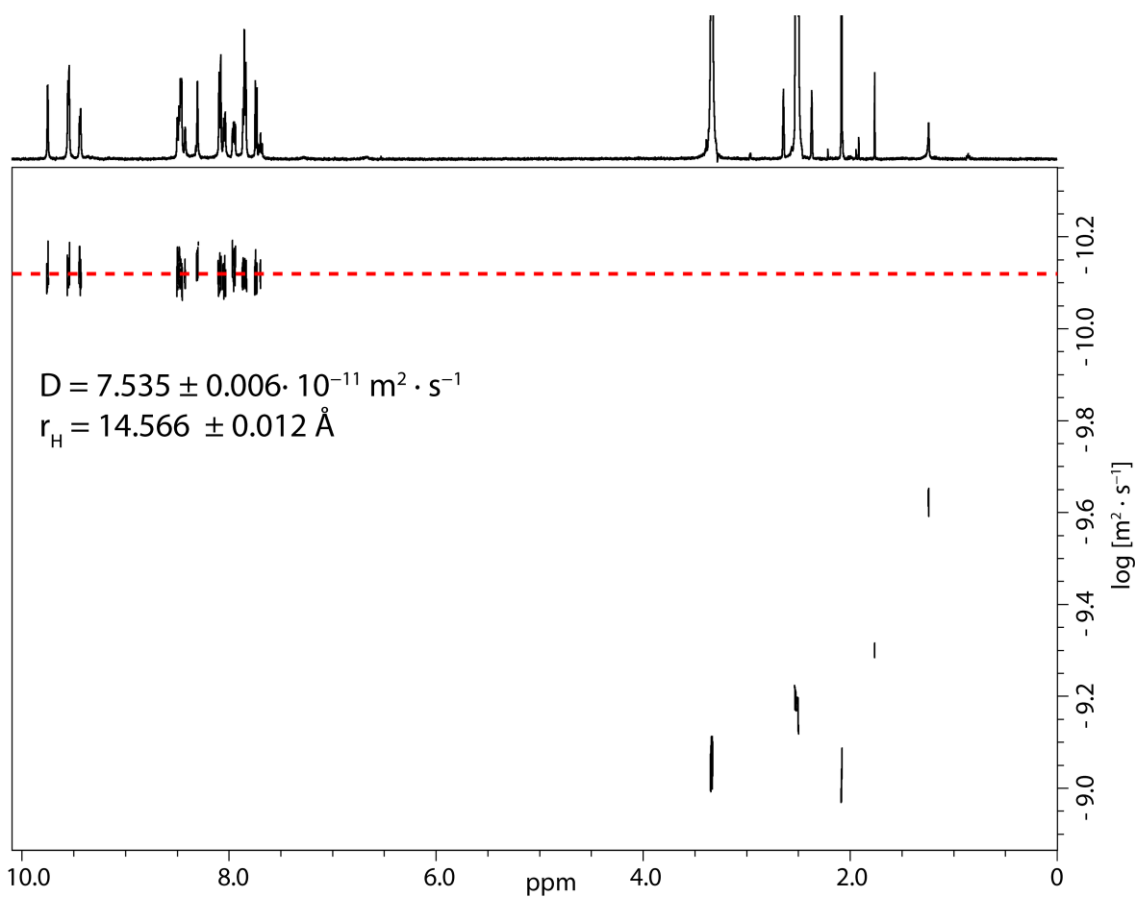
Figure 266: ^{1}H DOSY NMR spectrum (500 MHz, 298 K, DMSO-d_6) of Pd$_3$**L^{F2}**$_3$**L^{S2}**$_3$. Values for diffusion coefficient and resulting hydrodynamic radius are given.

D = 7.535 ± 0.006· 10^{-11} m^2 · s^{-1}
r$_H$ = 14.566 ± 0.012 Å
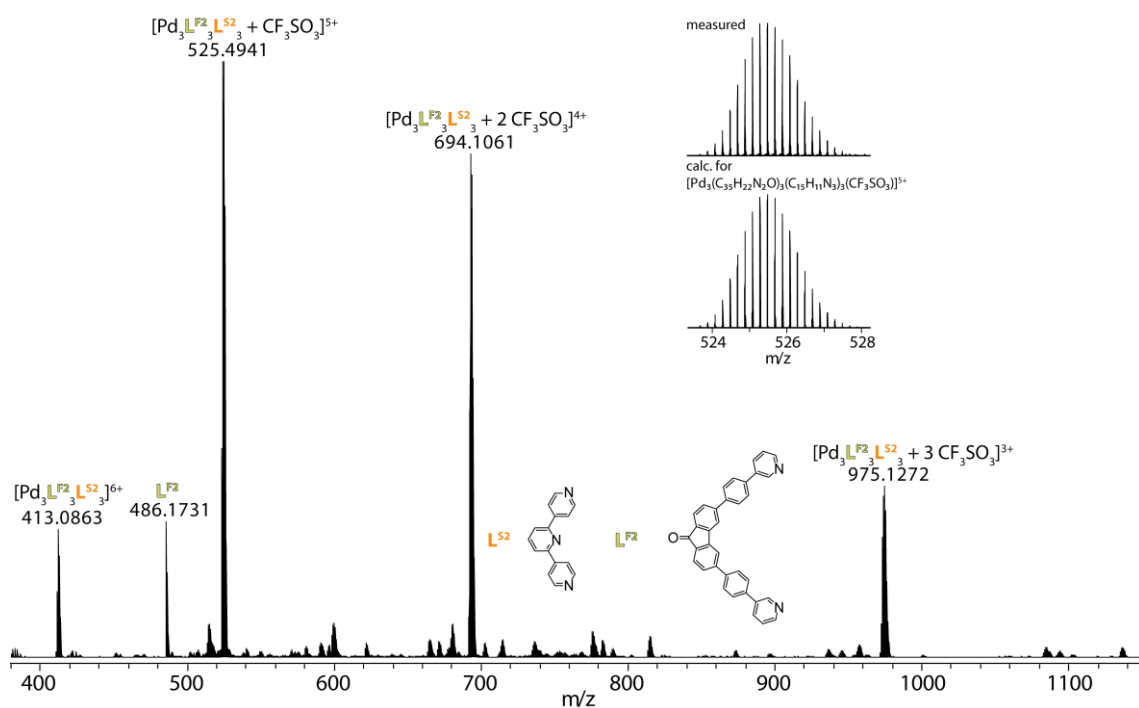
Figure 267: CSI-MS spectrum of Pd$_3$**L^{F2}**$_3$**L^{S2}**$_3$. Peaks could be assigned to [Pd$_3$**L^{F2}**$_3$**L^{S2}**$_3$ + xCF$_3$SO$_3$]$^{(6-x)}$ (x = 0-3). The observed and calculated isotopic patterns are shown in the inset.
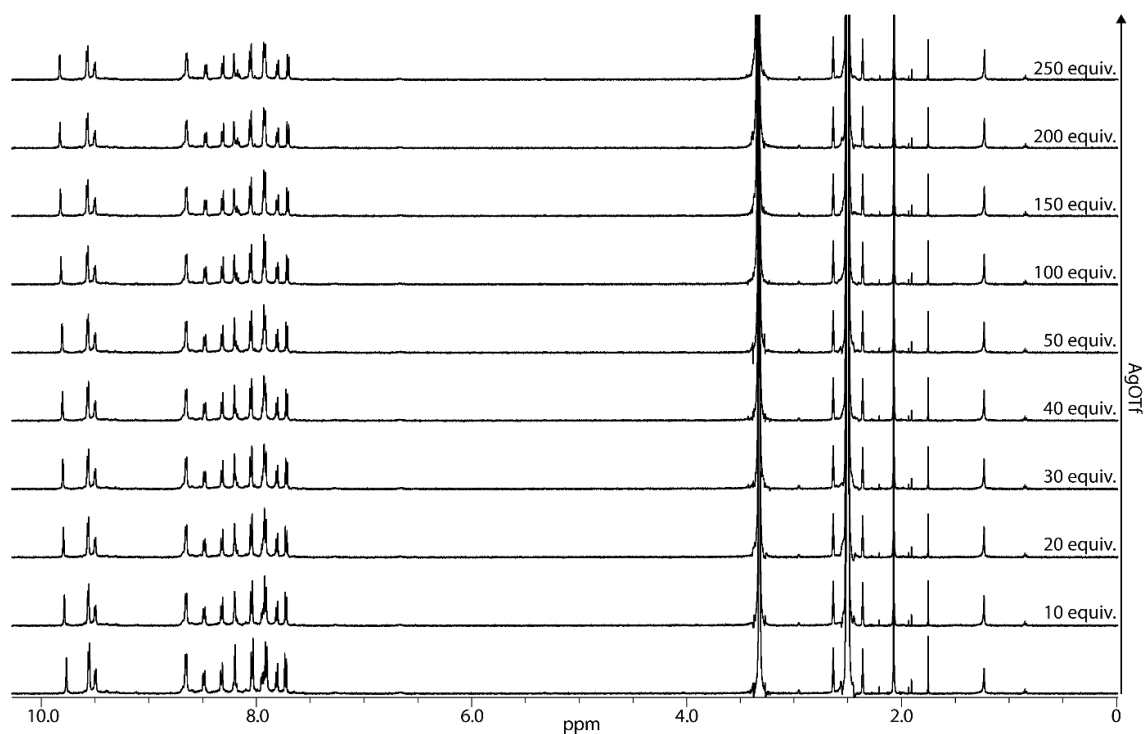
Figure 268: Full ^{1}H NMR titration (500 MHz, 298 K, DMSO-d_6) of Pd$_3$L$^{F2}_3$L$^{S2}_3$ with AgOTf.

3.4.7.2.3 Pd$_3$L$^{F2}_3$L$^{S3}_3$

A mixture of ligand **L^{F2}** (270 µL of a 3.11 mM solution in DMSO-d_6), **L^{S3}** (270 µL of a 3.11 mM solution in DMSO-d_6), and [Pd(CH$_3$CN)$_4$](OTf)$_2$ (60 µL of a 15 mM solution in DMSO-d_6) was left to rest at room temperature for 2 h to afford clean Pd$_3$L$^{F2}_3$L$^{S3}_3$.
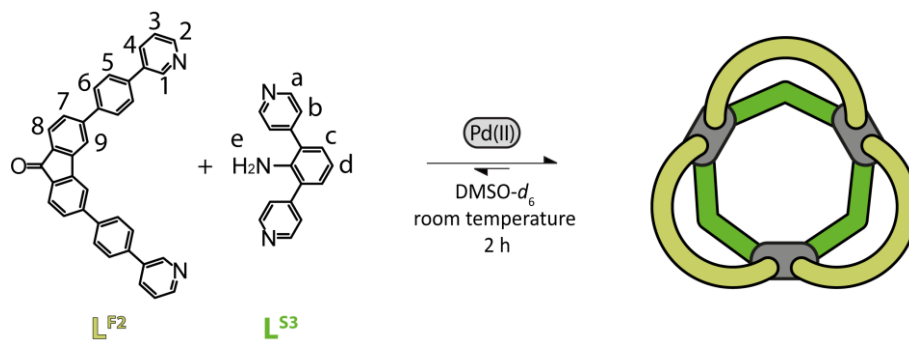
Scheme 41: Formation of Pd$_3$L$^{F2}_3$L$^{S3}_3$ with consecutive proton labels.

Figure 269: ^{1}H NMR spectrum (600 MHz, 298 K, DMSO-d_6) of Pd$_3$**L**$^{F2}_3$**L**$^{S3}_3$. A zoom into the aromatic region including proton assignment is shown in the inset.

^{1}H (600 MHz, 298 K, DMSO-d_6) δ 9.76 (s, 6H, H^1), 9.45 (d, ^3J = 6.0 Hz, 12H, H^a), 9.41 (d, ^3J = 5.7 Hz, 6H, H^2), 8.48 (d, ^3J = 8.1 Hz, 6H, H^4), 8.38 (s, 6H, H^9), 8.20 (d, ^3J = 6.0 Hz, 12H, H^b), 8.11 (d, ^3J = 8.4 Hz, 12H, H^6), 7.94 (dd, ^3J = 8.4, 5.7 Hz, 6H, H^3), 7.85 (dd, ^3J = 7.7 Hz, ^5J = 1.0 Hz, 6H, H^7), 7.82 (d, ^3J = 8.3 Hz, 12H, H^5), 7.72 (d, ^3J = 7.7 Hz, 6H, H^8), 7.21 (d, ^3J = 7.7 Hz, 6H, H^c), 6.74 (t, ^3J = 7.7 Hz, 3H, H^d), 5.43 (s (br), 6H, H^e) ppm.
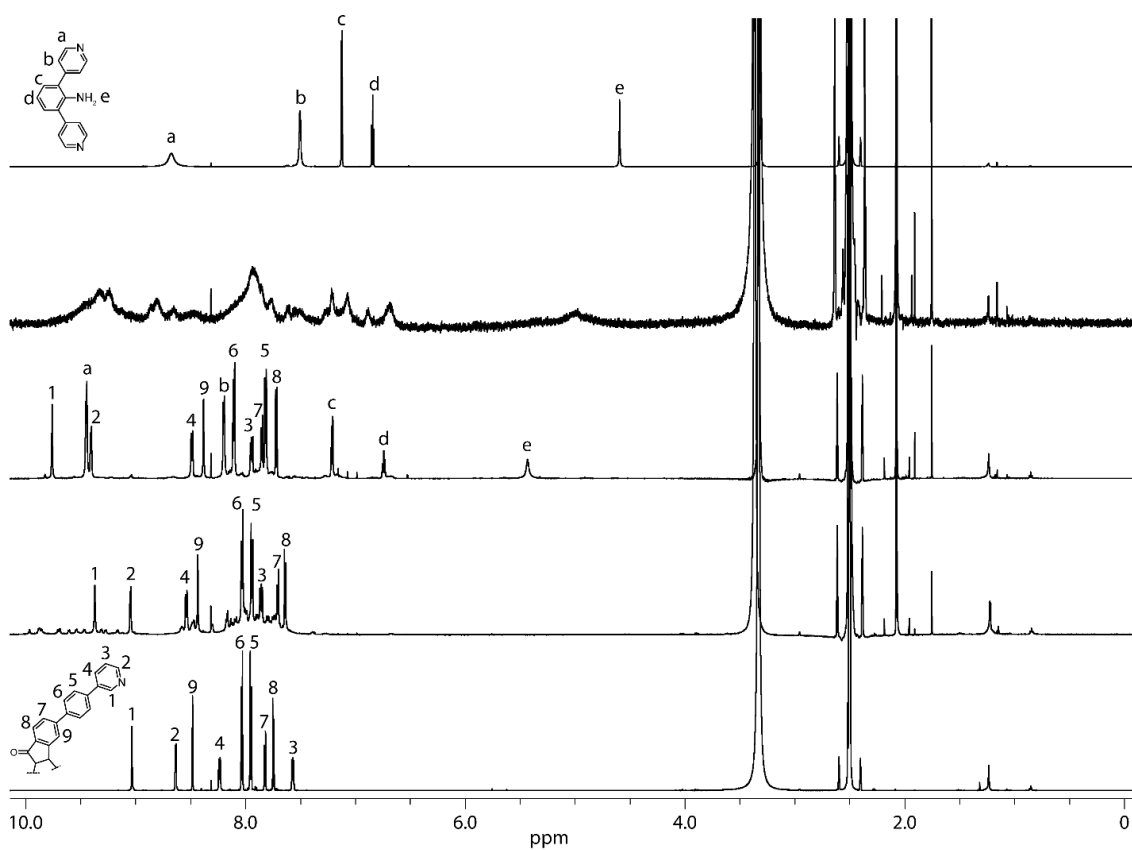
Figure 270: Full ^{1}H NMR spectra (298 K, DMSO-d_6)of ligand $\mathbf{L^{F2}}$ (700 MHz); homoleptic $Pd_2\mathbf{L^{F2}}_4$ cage and the $Pd_n\mathbf{L^{F2}}_{2n}$ (n=3-5) rings formed upon addition of 0.55 equiv. Pd(II) cations to ligand $\mathbf{L^{F2}}$ (600 MHz); heteroleptic $Pd_3\mathbf{L^{F2}}_3\mathbf{L^{S3}}_3$ (600 MHz); ligand $\mathbf{L^{S3}}$ upon addition of 0.55 equiv. Pd(II) cations (500 MHz); ligand $\mathbf{L^{S3}}$ (700 MHz)(listed bottom to top).
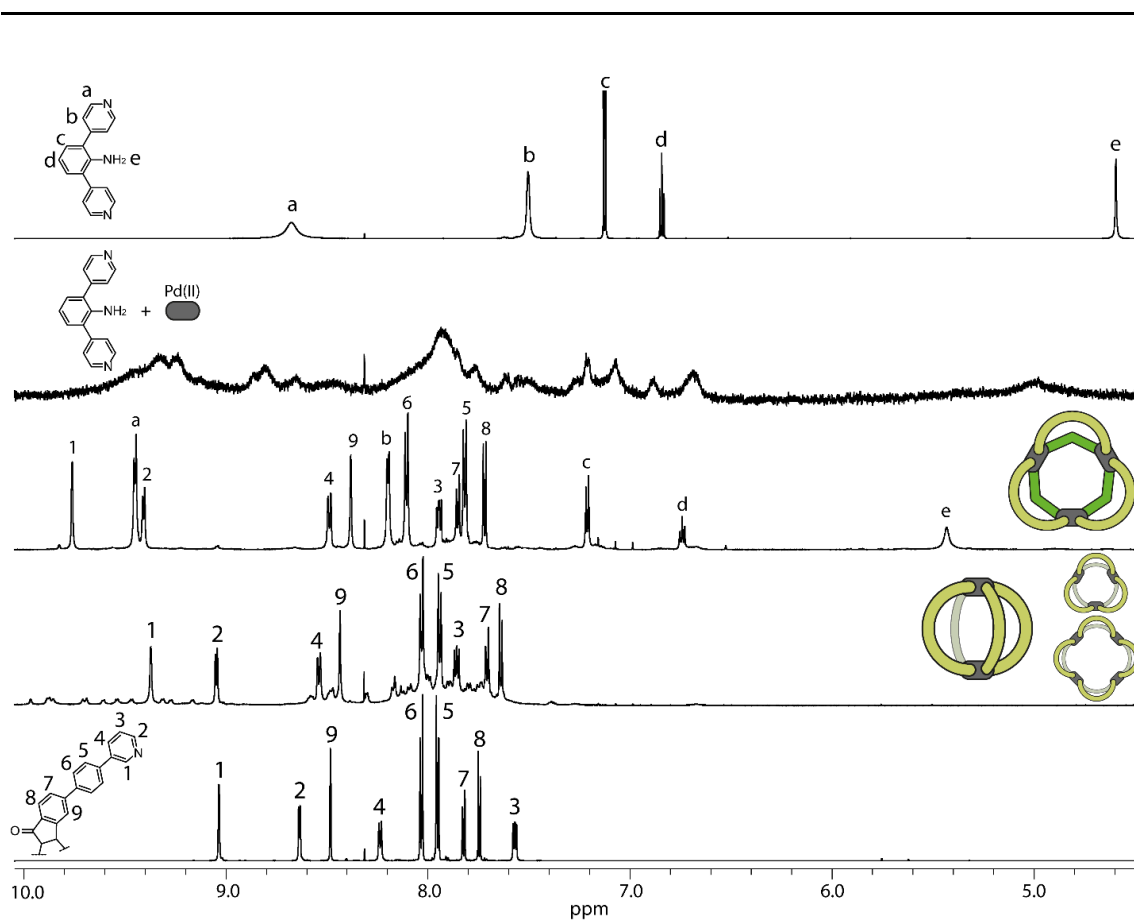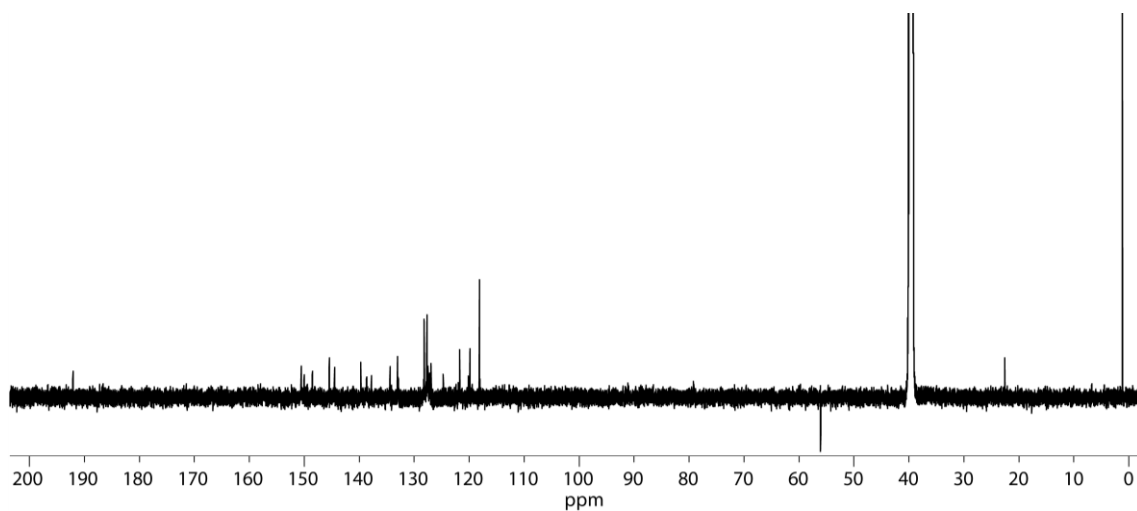
Figure 271: Partial ^{1}H NMR spectra (298 K, DMSO-d_6)of ligand $\mathbf{L^{F2}}$ (700 MHz); homoleptic Pd$_2$$\mathbf{L^{F2}}_4$ cage and the Pd$_n$$\mathbf{L^{F2}}_{2n}$ (n=3-5) rings formed upon addition of 0.55 equiv. Pd(II) cations to ligand $\mathbf{L^{F2}}$ (600 MHz); heteroleptic Pd$_3$$\mathbf{L^{F2}}_3$$\mathbf{L^{S3}}_3$ (600 MHz); ligand $\mathbf{L^{S3}}$ upon addition of 0.55 equiv. Pd(II) cations (500 MHz); ligand $\mathbf{L^{S3}}$ (700 MHz)(listed bottom to top).
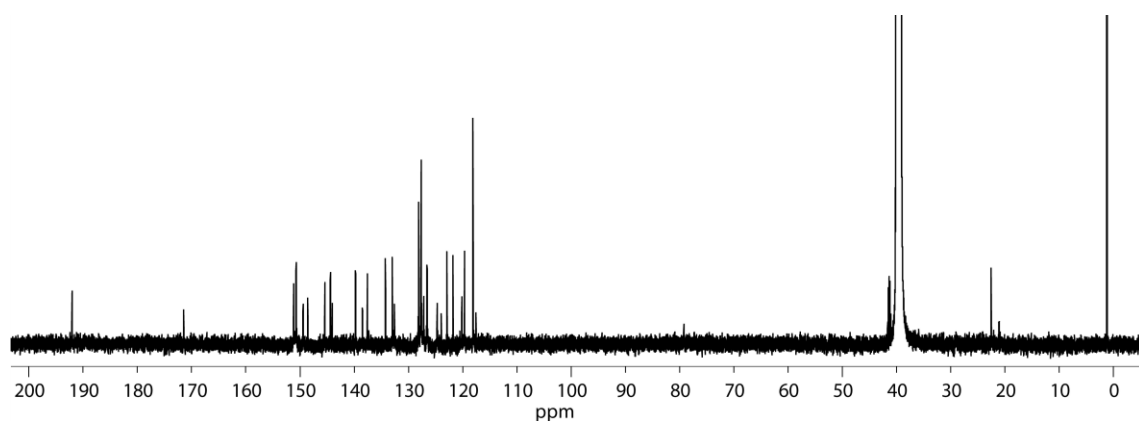
Figure 272: ^{13}C NMR spectrum (151 MHz, 298 K, DMSO-d_6) of Pd$_3$$\mathbf{L^{F2}}_3$$\mathbf{L^{S3}}_3$.

^{13}C{^{1}H} (151 MHz, 298 K, DMSO-d_6) δ 192.0, 151.2, 150.7, 149.2, 148.6, 145.4, 144.4, 144.0, 139.8, 138.5, 137.6, 134.2, 133.0, 132.6, 128.1, 127.6, 127.2, 126.6, 124.7, 123.9, 122.9, 120.1 ppm.

278
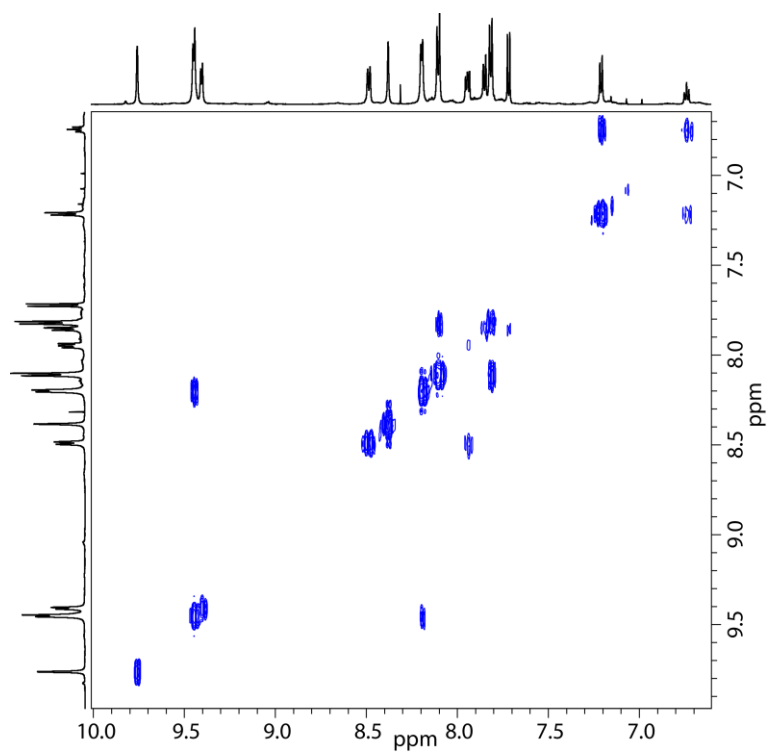
Figure 273: Partial ^{1}H-^{1}H COSY NMR spectrum (600 MHz, 298 K, DMSO-d_6) of Pd$_3$**L^{F2}**$_3$**L^{S3}**$_3$.
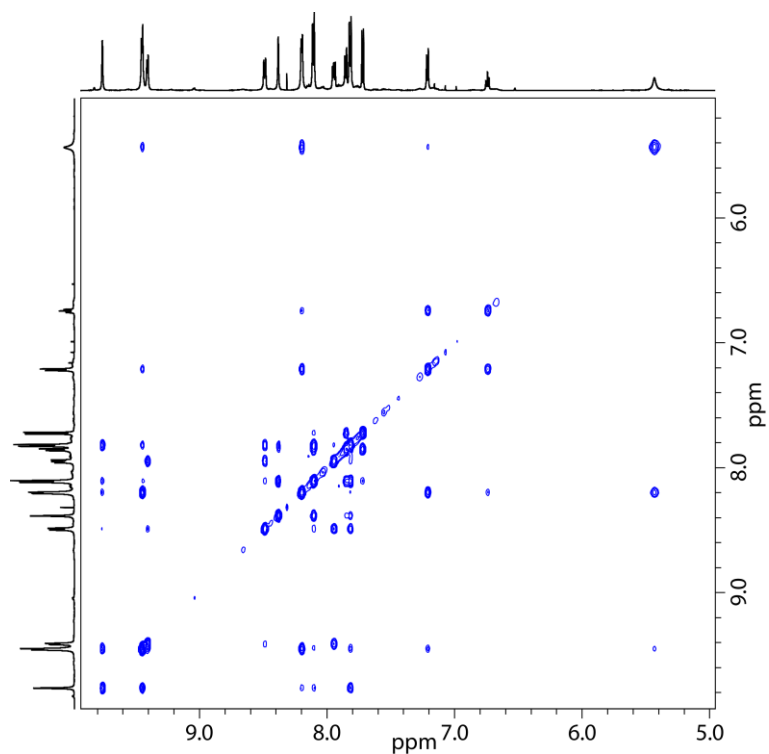
Figure 274: Partial ^{1}H-^{1}H NOESY NMR spectrum (600 MHz, 298 K, DMSO-d_6) of Pd$_3$**L^{F2}**$_3$**L^{S3}**$_3$.
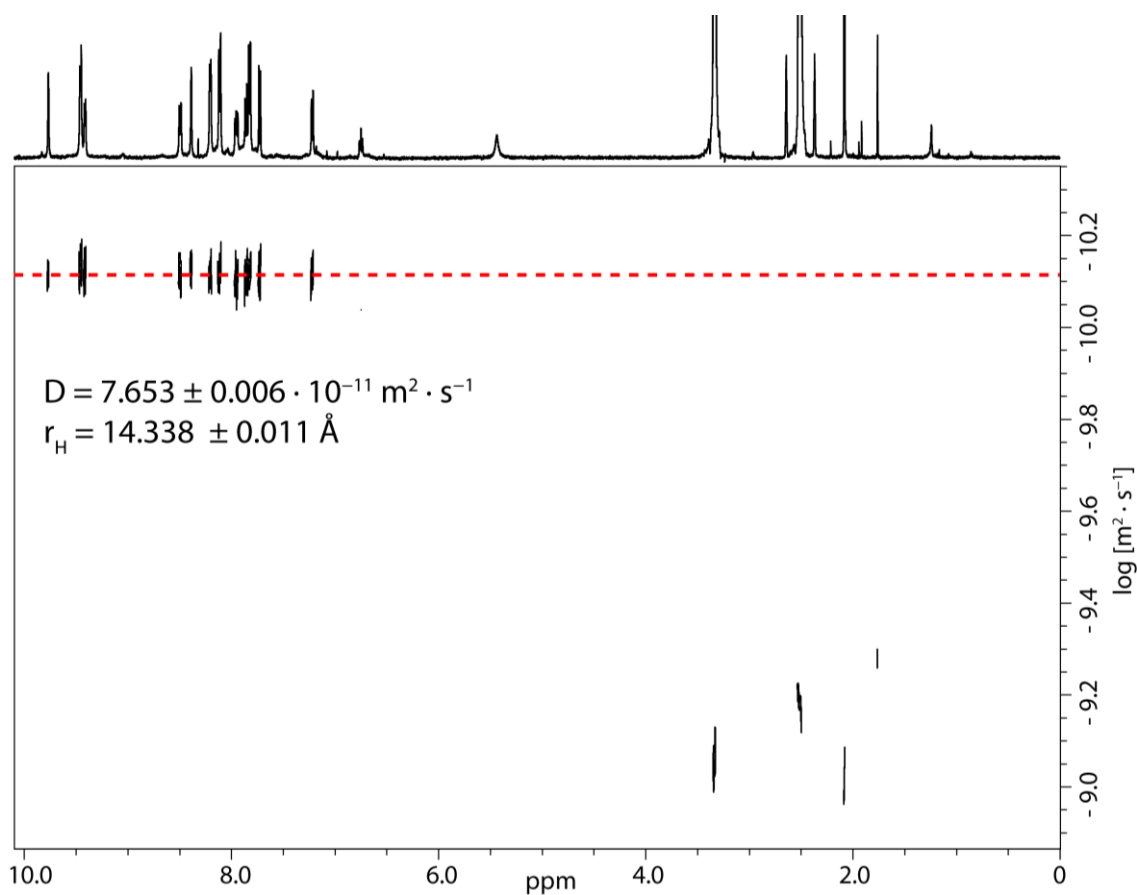
Figure 275: ^1H DOSY NMR spectrum (500 MHz, 298 K, DMSO-d_6) of Pd$_3$**L^{F2}**$_3$**L^{S3}**$_3$. Values for diffusion coefficient and resulting hydrodynamic radius are given.
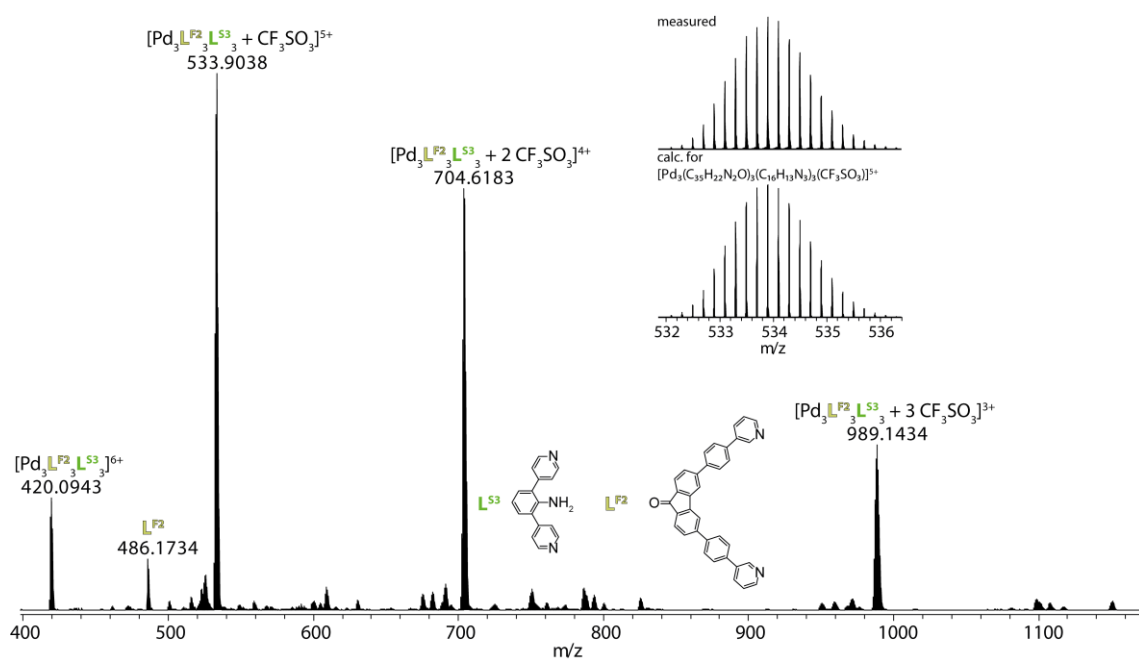
Figure 276: CSI-MS spectrum of Pd$_3$**L^{F2}**$_3$**L^{S3}**$_3$. Peaks could be assigned to [Pd$_3$**L^{F2}**$_3$**L^{S3}**$_3$ + xCF$_3$SO$_3$]$^{(6-x)}$ (x = 0-3). The observed and calculated isotopic patterns are shown in the inset.

3.4.7.2.4 Pd₃**L**^{F2}₃**L**^{S4}₃

3.4.7.2.4 Pd$_3$**L**$^{F2}_3$**L**$^{S4}_3$

A mixture of ligand **L**^{F2} (270 µL of a 3.11 mM solution in DMSO-d_6), **L**^{S4} (270 µL of a 3.11 mM solution in DMSO-d_6), and [Pd(CH$_3$CN)$_4$](OTf)$_2$ (60 µL of a 15 mM solution in DMSO-d_6) was left to rest at room temperature for 2 h to afford clean Pd$_3$**L**$^{F2}_3$**L**$^{S4}_3$.
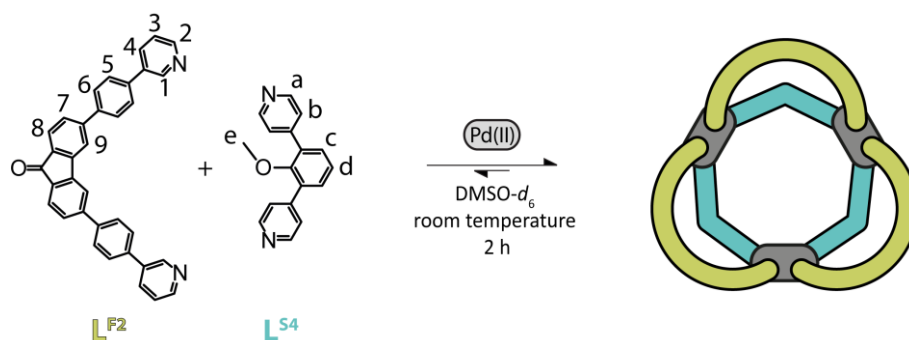
Scheme 42: Formation of Pd$_3$**L**$^{F2}_3$**L**$^{S4}_3$ with consecutive proton labels.
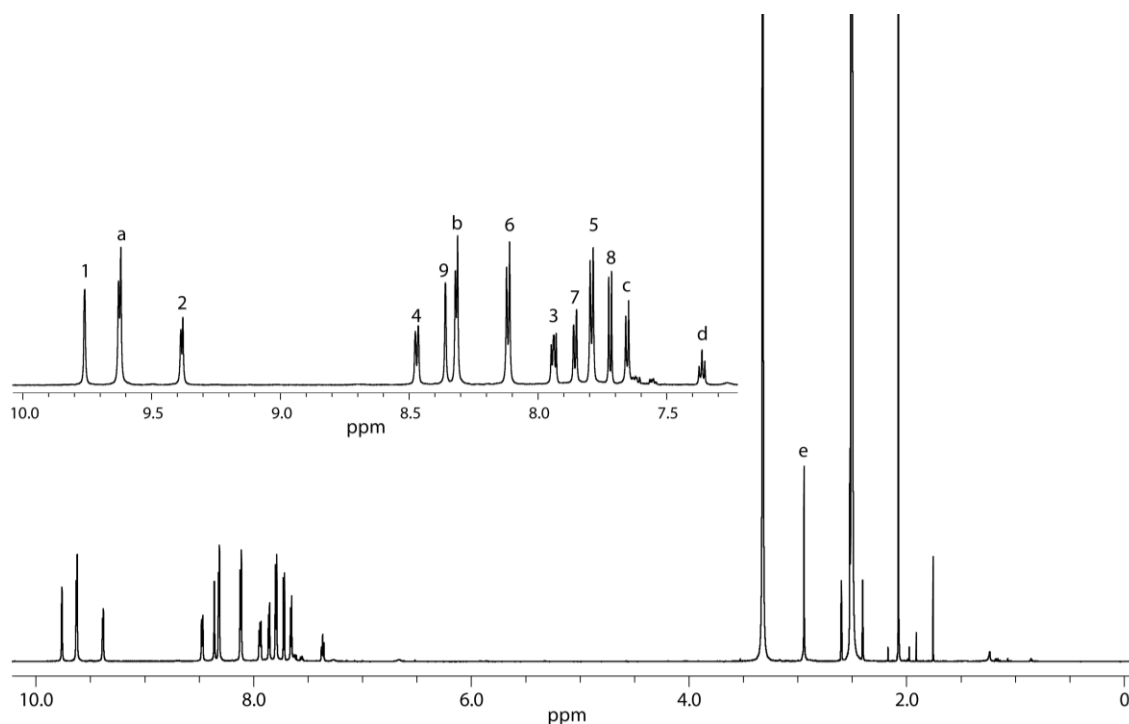
Figure 277: ^{1}H NMR spectrum (700 MHz, 298 K, DMSO-d_6) of Pd$_3$**L**$^{F2}_3$**L**$^{S4}_3$. A zoom into the aromatic region including proton assignment is shown in the inset.

^{1}H (700 MHz, 298 K, DMSO-d_6) δ 9.76 (s, 6H, H^1), 9.62 (d, ^3J = 6.2 Hz, 12H, H^a), 9.38 (d, ^3J = 5.6 Hz, 6H, H^2), 8.47 (d, ^3J = 8.1 Hz, 6H, H^4), 8.36 (s, 6H, H^9), 8.32 (d, ^3J = 6.2 Hz, 12H, H^b), 8.12 (d, ^3J = 8.2 Hz, 12H, H^6), 7.94 (dd, ^3J = 8.1, 5.8 Hz, 6H, H^3), 7.85 (dd, ^3J = 7.8 Hz, ^5J = 0.8 Hz, 6H, H^7), 7.79 (d, ^3J = 8.2 Hz, 12H, H^5), 7.72 (d, ^3J = 7.8 Hz, 6H, H^8), 7.65 (d, ^3J = 7.8 Hz, 6H, H^c), 7.36 (t, ^3J = 7.8 Hz, 3H, H^d), 2.94 (s, 9H, H^e) ppm.
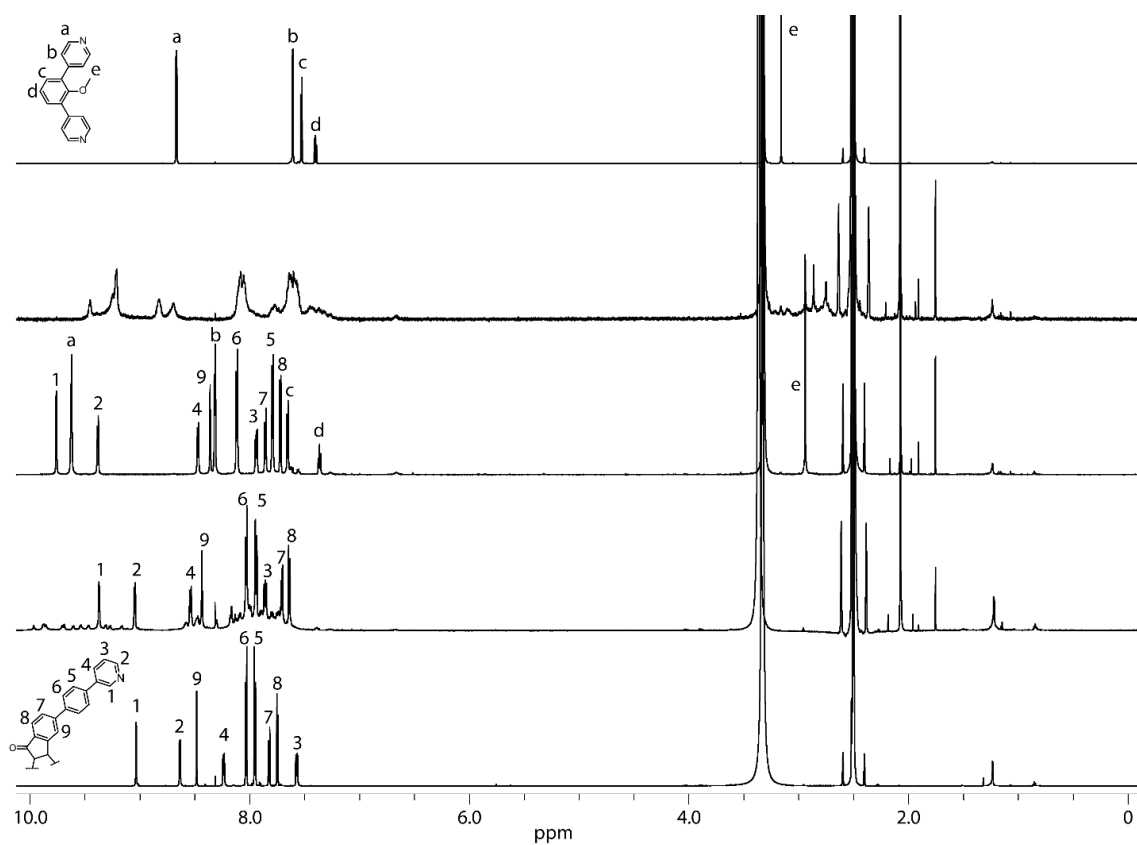
Figure 278: Full ^{1}H NMR spectra (298 K, DMSO-d_6)of ligand L^{F2} (700 MHz); homoleptic Pd$_2$L$^{F2}_4$ cage and the Pd$_n$L$^{F2}_{2n}$ (n=3-5) rings formed upon addition of 0.55 equiv. Pd(II) cations to ligand L^{F2} (600 MHz); heteroleptic Pd$_3$L$^{F2}_3$L$^{S4}_3$ (700 MHz); ligand L^{S4} upon addition of 0.55 equiv. Pd(II) cations (500 MHz); ligand L^{S4} (700 MHz)(listed bottom to top).
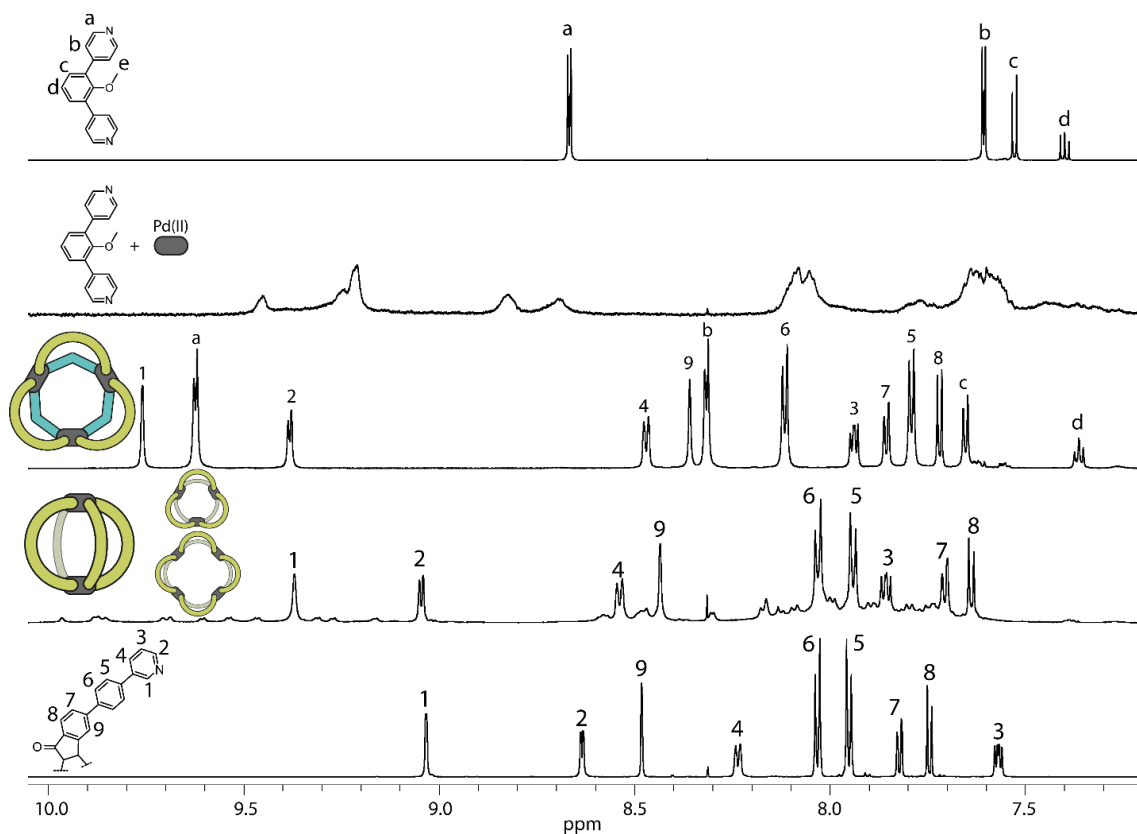
Figure 279: Partial ^{1}H NMR spectra (298 K, DMSO-d_6)of ligand L^{F2} (700 MHz); homoleptic $Pd_2L^{F2}_4$ cage and the $Pd_nL^{F2}_{2n}$ (n=3-5) rings formed upon addition of 0.55 equiv. Pd(II) cations to ligand L^{F2} (600 MHz); heteroleptic $Pd_3L^{F2}_3L^{S4}_3$ (700 MHz); ligand L^{S4} upon addition of 0.55 equiv. Pd(II) cations (500 MHz); ligand L^{S4} (700 MHz)(listed bottom to top).
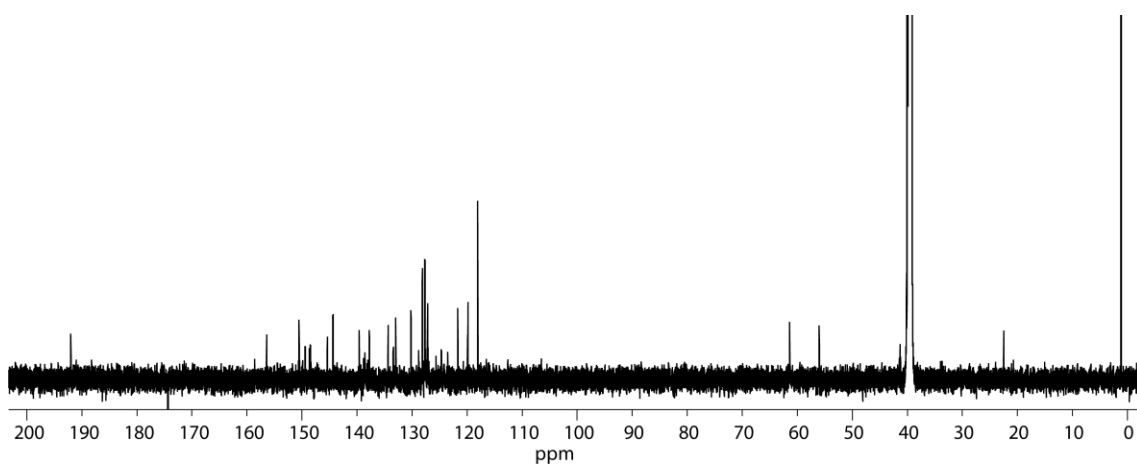

Figure 280: ^{13}C NMR spectrum (176 MHz, 298 K, DMSO-d_6) of $Pd_3L^{F2}_3L^{S4}_3$.

^{13}C{^{1}H} (176 MHz, 298 K, DMSO-d_6) δ 192.0, 156.4, 150.6, 149.4, 148.7, 148.5, 145.4, 144.4, 139.6, 138.6, 137.8, 134.4, 133.4, 133.0, 130.2, 128.1, 127.7, 127.6, 127.2, 127.1, 125.7, 124.7, 119.9, 61.4 ppm.
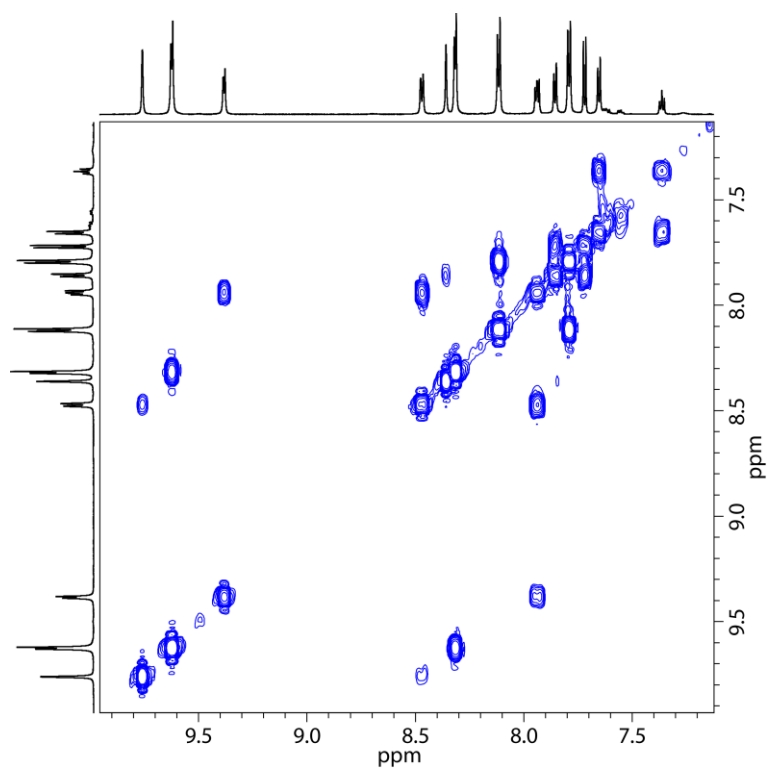
Figure 281: Partial ^{1}H-^{1}H COSY NMR spectrum (700 MHz, 298 K, DMSO-d_6) of Pd$_3$**L**$^{F2}_3$**L**$^{S4}_3$.
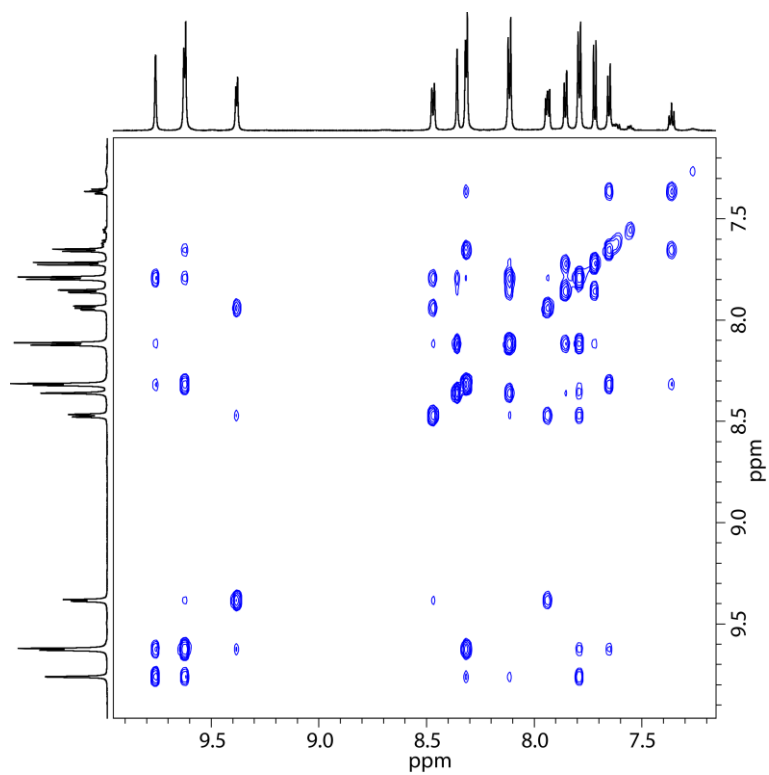
Figure 282: Partial ^{1}H-^{1}H NOESY NMR spectrum (700 MHz, 298 K, DMSO-d_6) of Pd$_3$**L**$^{F2}_3$**L**$^{S4}_3$.
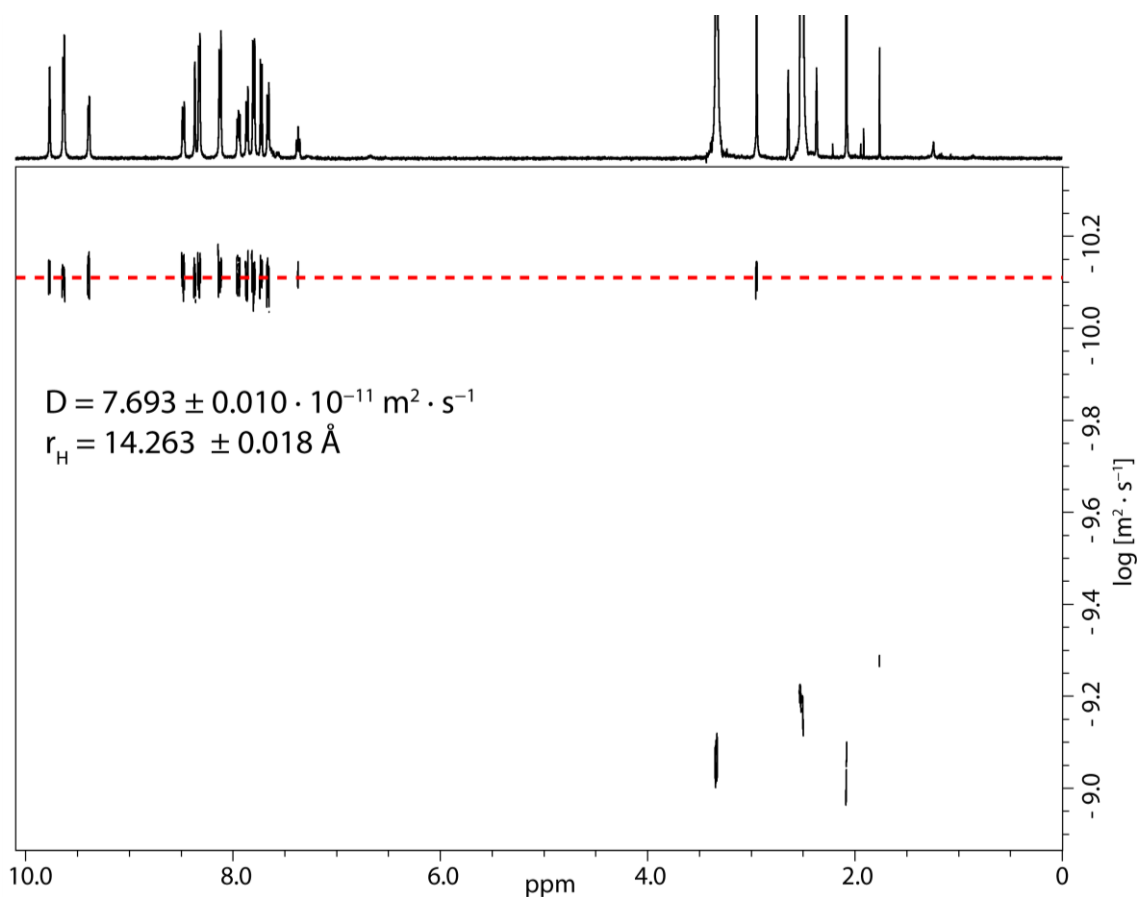
Figure 283: ^{1}H DOSY NMR spectrum (500 MHz, 298 K, DMSO-d_6) of Pd$_3$**L**$^{F2}_3$**L**$^{S4}_3$. Values for diffusion coefficient and resulting hydrodynamic radius are given.
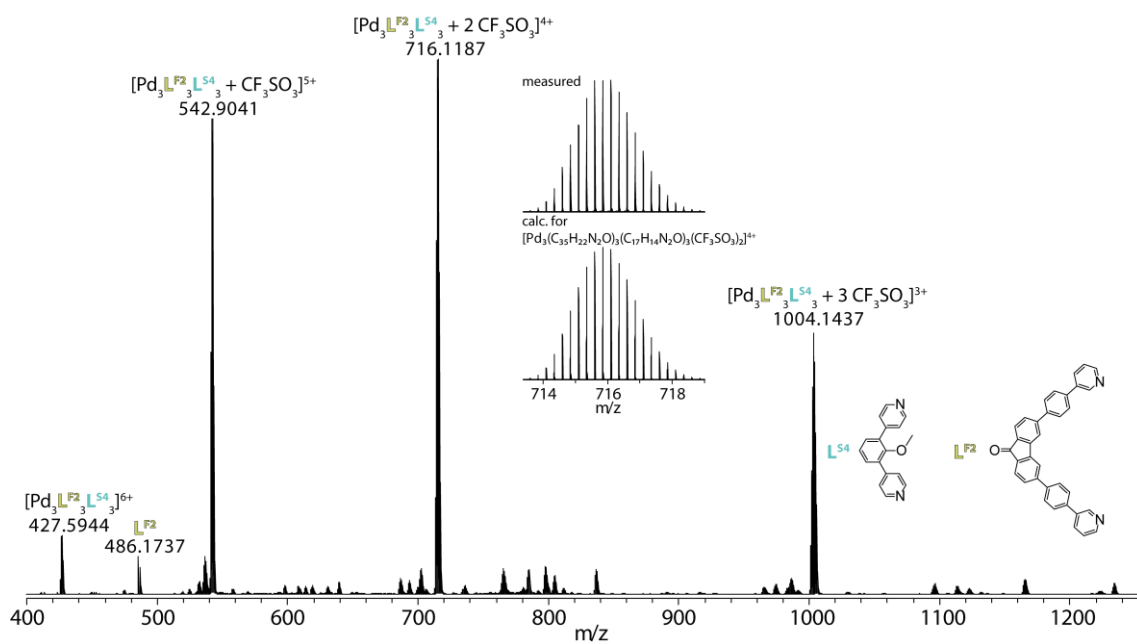
Figure 284: CSI-MS spectrum of Pd$_3$**L**$^{F2}_3$**L**$^{S4}_3$. Peaks could be assigned to [Pd$_3$**L**$^{F2}_3$**L**$^{S4}_3$ + xCF$_3$SO$_3$]$^{(6-x)}$ (x = 0-3). The observed and calculated isotopic patterns are shown in the inset.

3.4.7.2.5 Pd₃L^F2₃L^S5₃

A mixture of ligand **L^F2** (270 µL of a 3.11 mM solution in DMSO-d_6), **L^S5** (270 µL of a 3.11 mM solution in DMSO-d_6), and [Pd(CH₃CN)₄](OTf)₂ (60 µL of a 15 mM solution in DMSO-d_6) was left to rest at room temperature for 2 h to afford clean Pd₃L^F2₃L^S5₃.
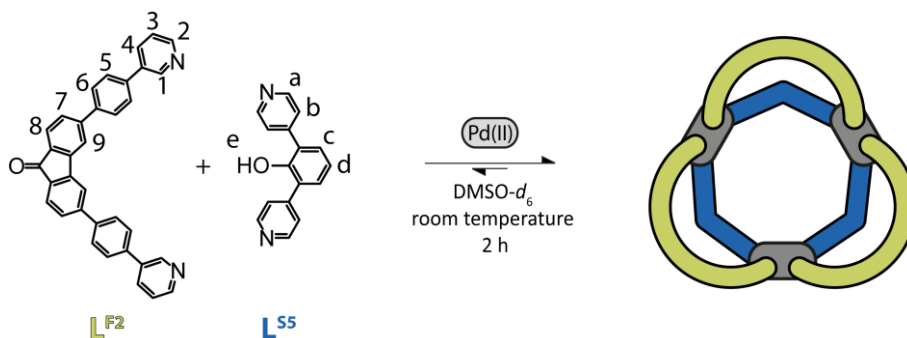
Scheme 43: Formation of Pd₃L^F2₃L^S5₃ with consecutive proton labels.
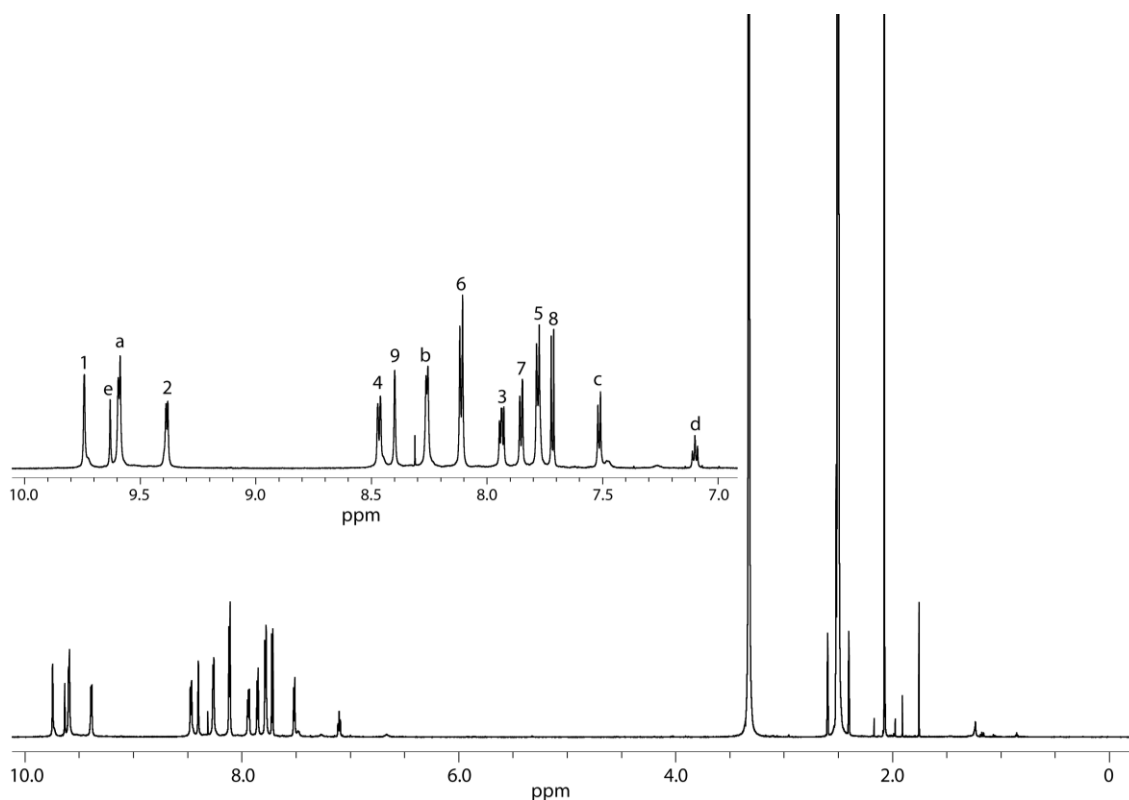
Figure 285: ¹H NMR spectrum (700 MHz, 298 K, DMSO-d_6) of Pd₃L^F2₃L^S5₃. A zoom into the aromatic region including proton assignment is shown in the inset.

¹H (700 MHz, 298 K, DMSO-d_6) δ 9.74 (s, 6H, H¹), 9.63 (s, 3H, Hᵉ), 9.59 (d, ^3J = 6.0 Hz, 12H, Hᵃ), 9.39 (d, ^3J = 5.6 Hz, 6H, H²), 8.47 (d, ^3J = 8.2 Hz, 6H, H⁴), 8.40 (s, 6H, H⁹), 8.26 (d, ^3J = 5.7 Hz, 12H, Hᵇ), 8.11 (d, ^3J = 8.3 Hz, 12H, H⁶), 7.94 (dd, ^3J = 8.2, 5.7 Hz, 6H, H³), 7.85 (d, ^3J = 7.8 Hz, 6H, H⁷), 7.78 (d, ^3J = 8.2 Hz, 12H, H⁵), 7.72 (d, ^3J = 7.8 Hz, 6H, H⁸), 7.51 (d, ^3J = 7.8 Hz, 6H, Hᶜ), 7.10 (t, ^3J = 7.8 Hz, 3H, Hᵈ) ppm.
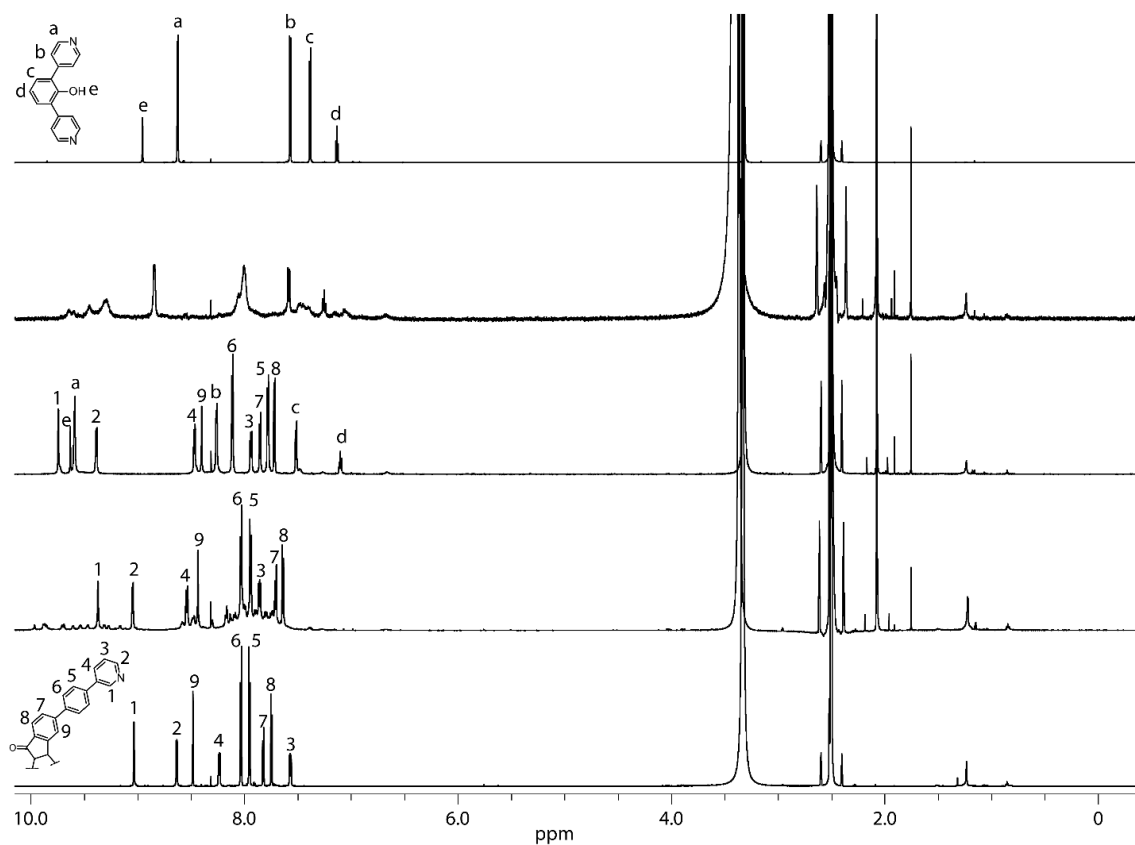
Figure 286: Full ¹H NMR spectra (298 K, DMSO-d_6)of ligand L^{F2} (700 MHz); homoleptic $Pd_2L^{F2}_4$ cage and the $Pd_nL^{F2}_{2n}$ (n=3-5) rings formed upon addition of 0.55 equiv. Pd(II) cations to ligand L^{F2} (600 MHz); heteroleptic $Pd_3L^{F2}_3L^{S5}_3$ (700 MHz); ligand L^{S5} upon addition of 0.55 equiv. Pd(II) cations (500 MHz); ligand L^{S5} (700 MHz)(listed bottom to top).
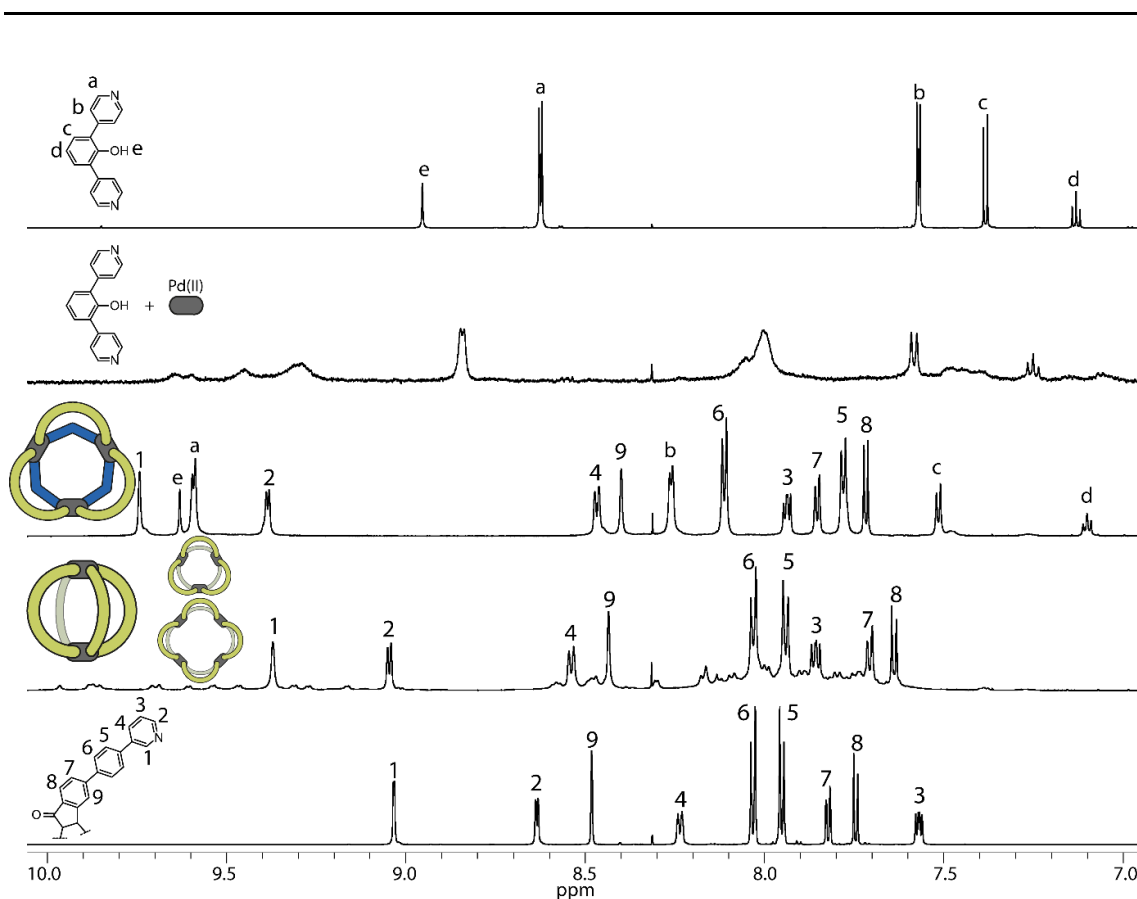
Figure 287: Partial ^{1}H NMR spectra (298 K, DMSO-d_6)of ligand $\mathbf{L^{F2}}$ (700 MHz); homoleptic Pd$_2$L$^{F2}_4$ cage and the Pd$_n$L$^{F2}_{2n}$ (n=3-5) rings formed upon addition of 0.55 equiv. Pd(II) cations to ligand $\mathbf{L^{F2}}$ (600 MHz); heteroleptic Pd$_3$L$^{F2}_3$L$^{S5}_3$ (700 MHz); ligand $\mathbf{L^{S5}}$ upon addition of 0.55 equiv. Pd(II) cations (500 MHz); ligand $\mathbf{L^{S5}}$ (700 MHz)(listed bottom to top).

Figure 288: ^{13}C NMR spectrum (176 MHz, 298 K, DMSO-d_6) of Pd$_3$L$^{F2}_3$L$^{S5}_3$.

^{13}C{^{1}H} (176 MHz, 298 K, DMSO-d_6) δ 192.0, 152.3, 150.5, 150.0, 149.4, 148.5, 145.4, 144.4, 139.7, 138.6, 137.7, 134.3, 133.0, 132.9, 128.2, 127.6, 127.6, 127.4, 127.1, 126.9, 124.7, 121.9, 120.1 ppm.

288
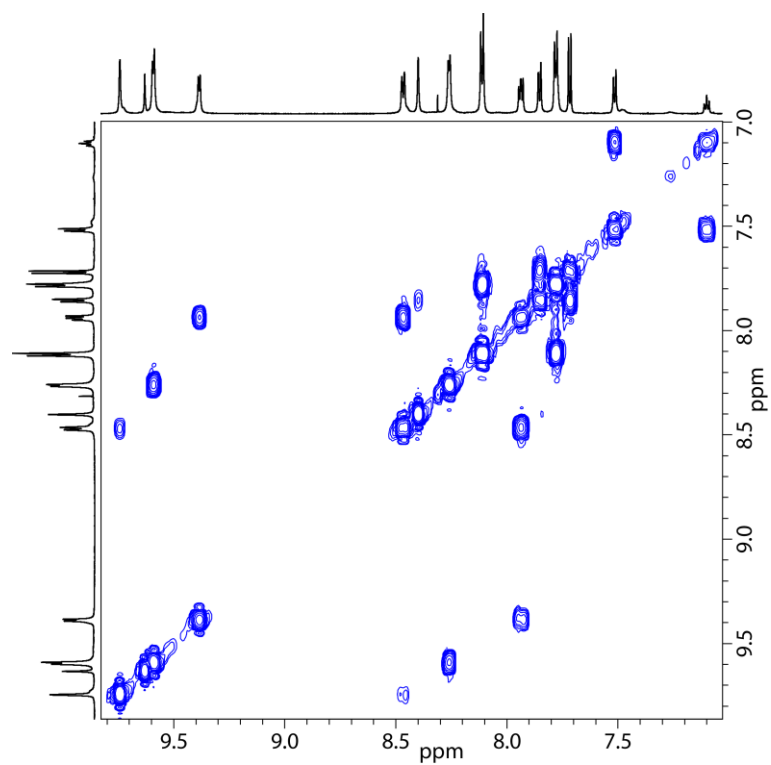
Figure 289: Partial ^{1}H-^{1}H COSY NMR spectrum (700 MHz, 298 K, DMSO-d_6) of Pd$_3$**L^{F2}**$_3$**L^{S5}**$_3$.
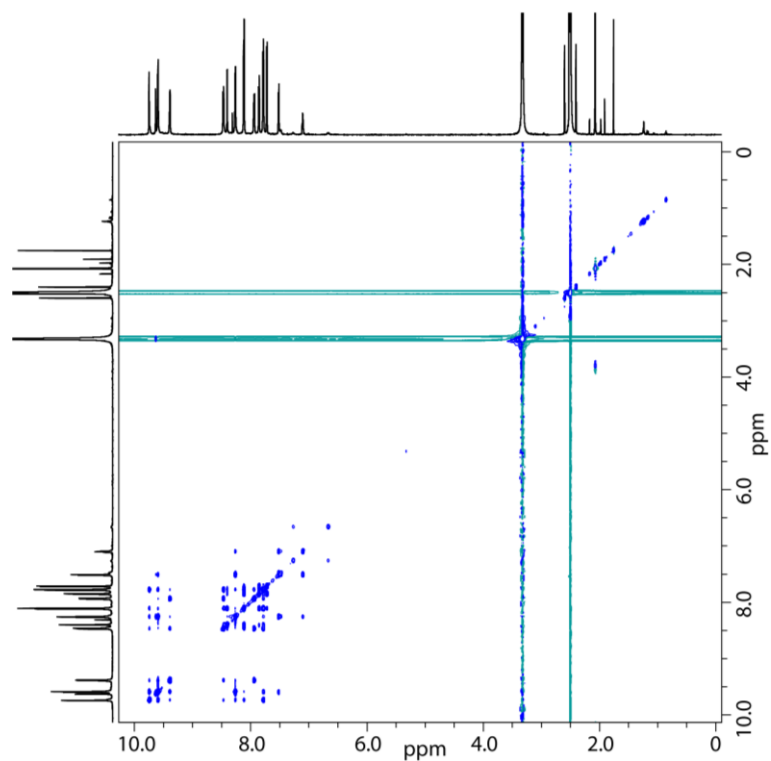
Figure 290: Full ^{1}H-^{1}H NOESY NMR spectrum (700 MHz, 298 K, DMSO-d_6) of Pd$_3$**L^{F2}**$_3$**L^{S5}**$_3$.
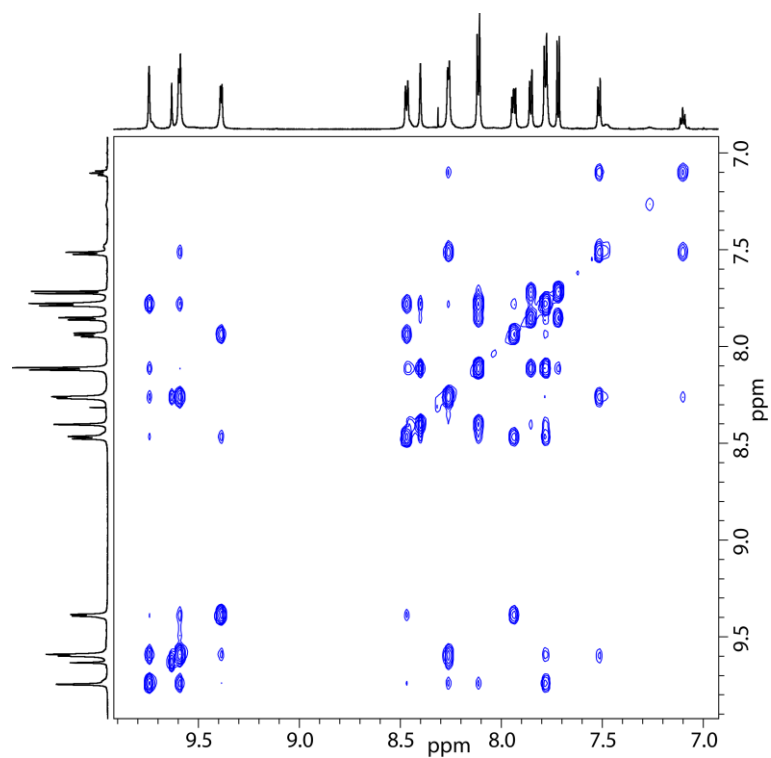
Figure 291: Partial ^{1}H-^{1}H NOESY NMR spectrum (700 MHz, 298 K, DMSO-d_6) of Pd$_3$L$^{F2}_3$L$^{S5}_3$.

$D = 7.764 \pm 0.009 \cdot 10^{-11}$ m$^2 \cdot$ s^{-1}
$r_H = 14.135 \pm 0.016$ Å
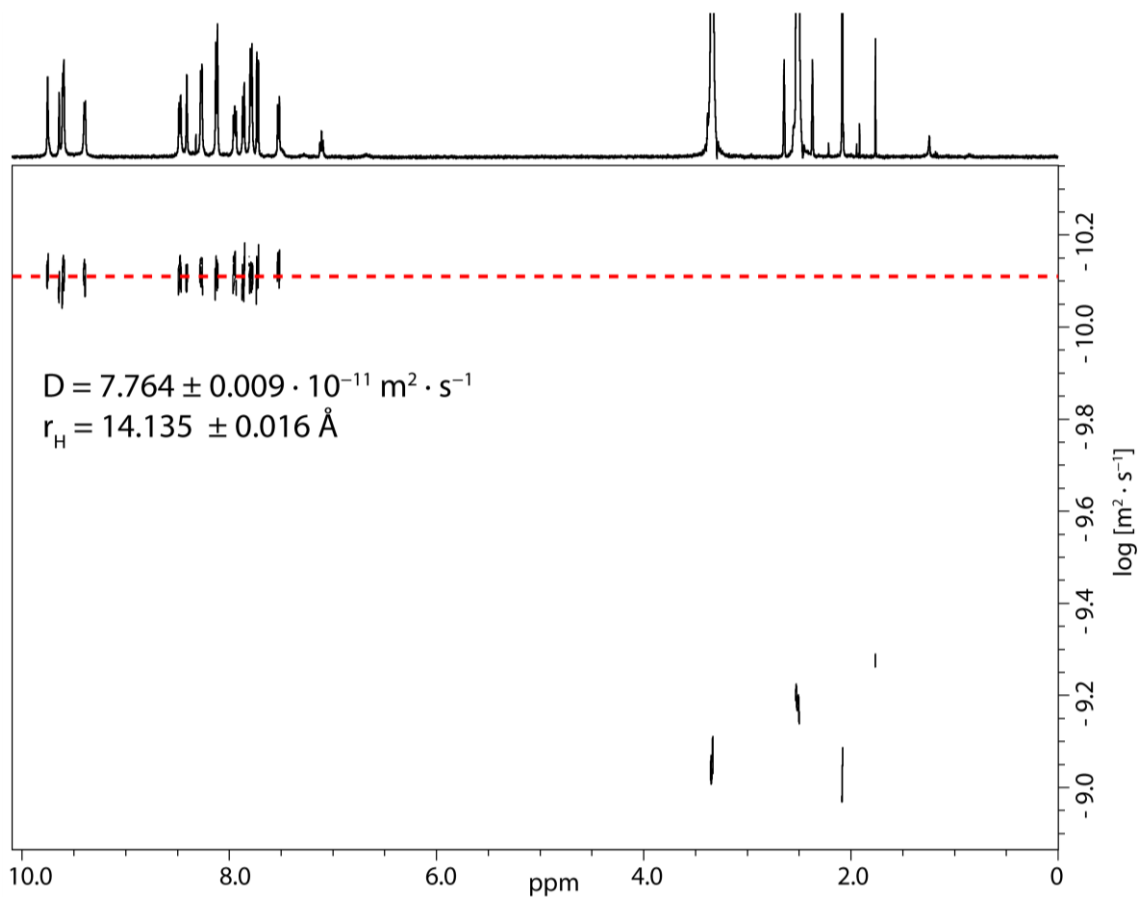
Figure 292: ^{1}H DOSY NMR spectrum (500 MHz, 298 K, DMSO-d_6) of Pd$_3$L$^{F2}_3$L$^{S5}_3$. Values for diffusion coefficient and resulting hydrodynamic radius are given.
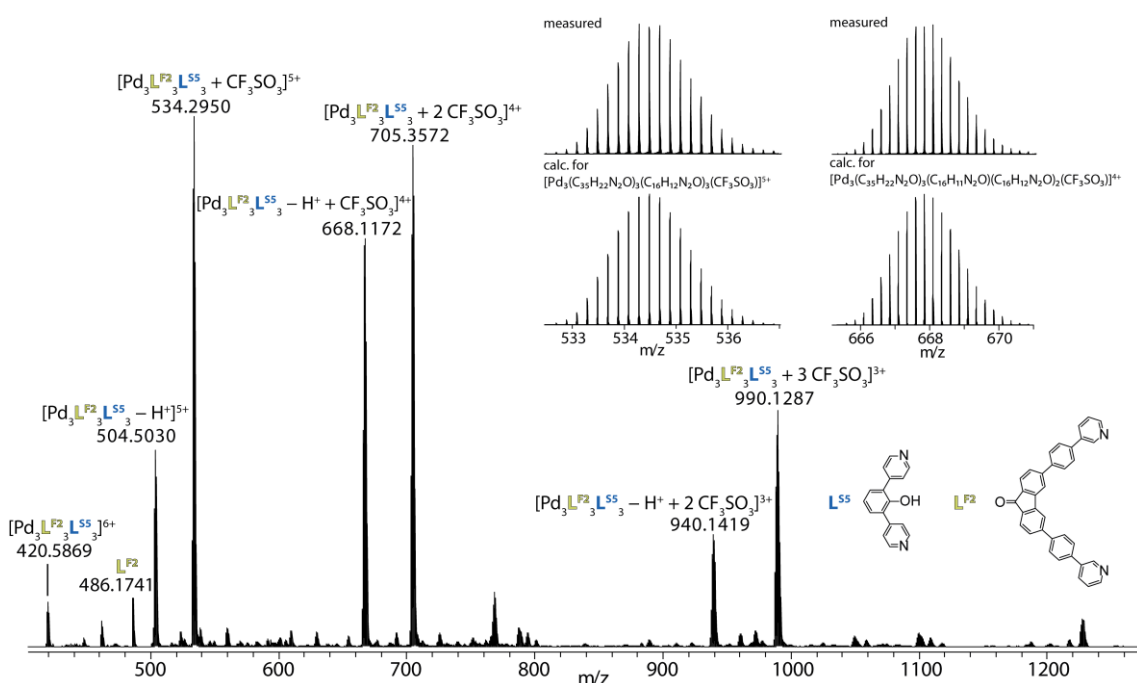
Figure 293: CSI-MS spectrum of $Pd_3L^{F2}_3L^{S5}_3$. Peaks could be assigned to $[Pd_3L^{F2}_3L^{S5}_3 -yH + xCF_3SO_3]^{(6-y-x)}$ (x = 0-3; y = 0, 1). The observed and calculated isotopic patterns are shown in the inset.
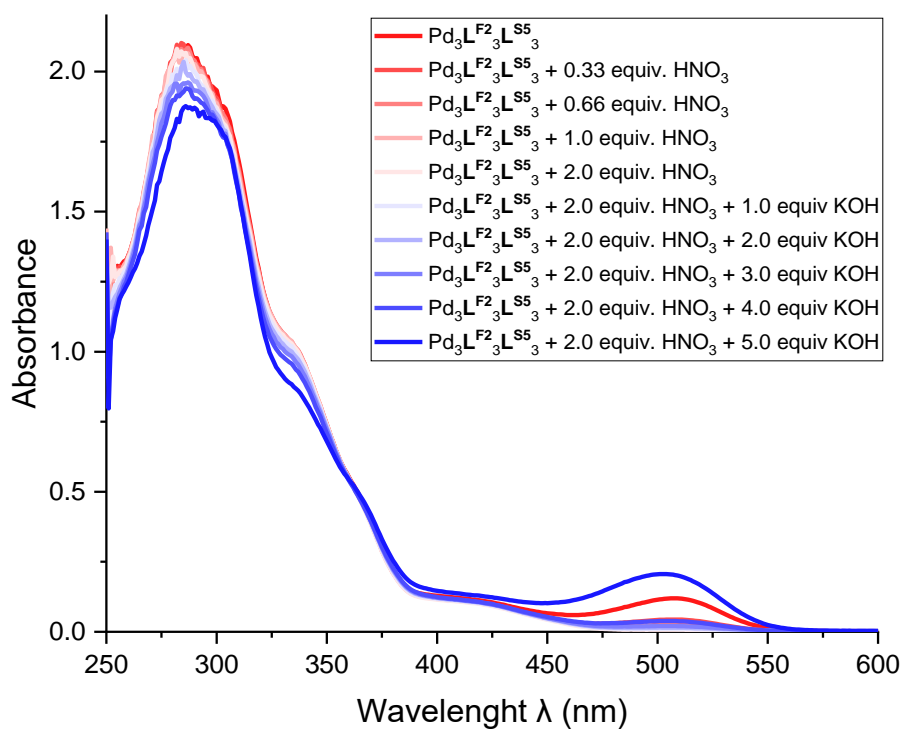
Figure 294: Full measured absorption spectra of $Pd_3L^{F2}_3L^{S5}_3$ (red) and consecutive addition of HNO_3 followed by KOH.

3.4.7.2.6 Pd₄L**F2**₄L**S6**₄

A mixture of ligand **L^{F2}** (270 µL of a 3.11 mM solution in DMSO-d_6), **L^{S6}** (270 µL of a 3.11 mM solution in DMSO-d_6), and [Pd(CH₃CN)₄](OTf)₂ (60 µL of a 15 mM solution in DMSO-d_6) was left to rest at room temperature for 2 h to afford clean Pd₄L**F2**₄L**S6**₄.
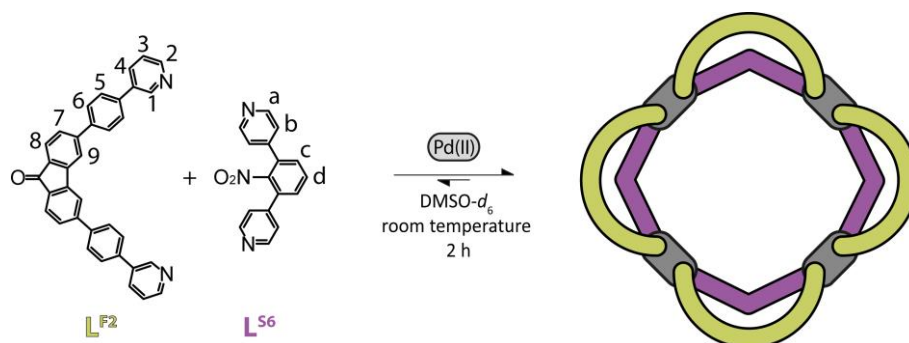
Scheme 44: Formation of Pd₄L**F2**₄L**S6**₄ with consecutive proton labels.
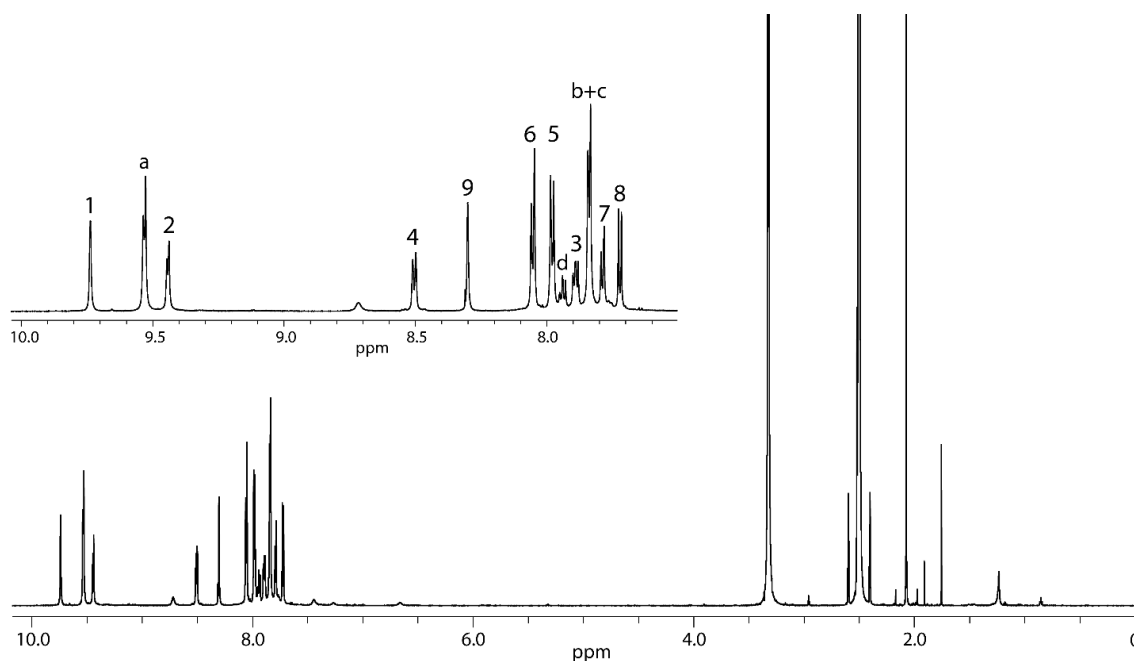
Figure 295: ^{1}H NMR spectrum (700 MHz, 298 K, DMSO-d_6) of Pd₄L**F2**₄L**S6**₄. A zoom into the aromatic region including proton assignment is shown in the inset.

^{1}H (700 MHz, 298 K, DMSO-d_6) δ 9.74 (s, 8H, H^1), 9.53 (d, ^3J = 6.4 Hz, 16H, H^a), 9.44 (d, ^3J = 5.6 Hz, 8H, H^2), 8.50 (d, ^3J = 8.3 Hz, 8H, H^4), 8.30 (s, 8H, H^9), 8.05 (d, ^3J = 8.4 Hz, 16H, H^6), 7.98 (d, ^3J = 8.3 Hz, 16H, H^5), 7.94 (t, ^3J = 7.8 Hz, 4H, H^d), 7.89 (dd, ^3J = 8.4, 5.8 Hz, 8H, H^3), 7.82-7.86 (m, 24H, H^b+H^c), 7.79 (d, ^3J = 7.8 Hz, 8H, H^7), 7.72 (d, ^3J = 7.6 Hz, 8H, H^8) ppm.
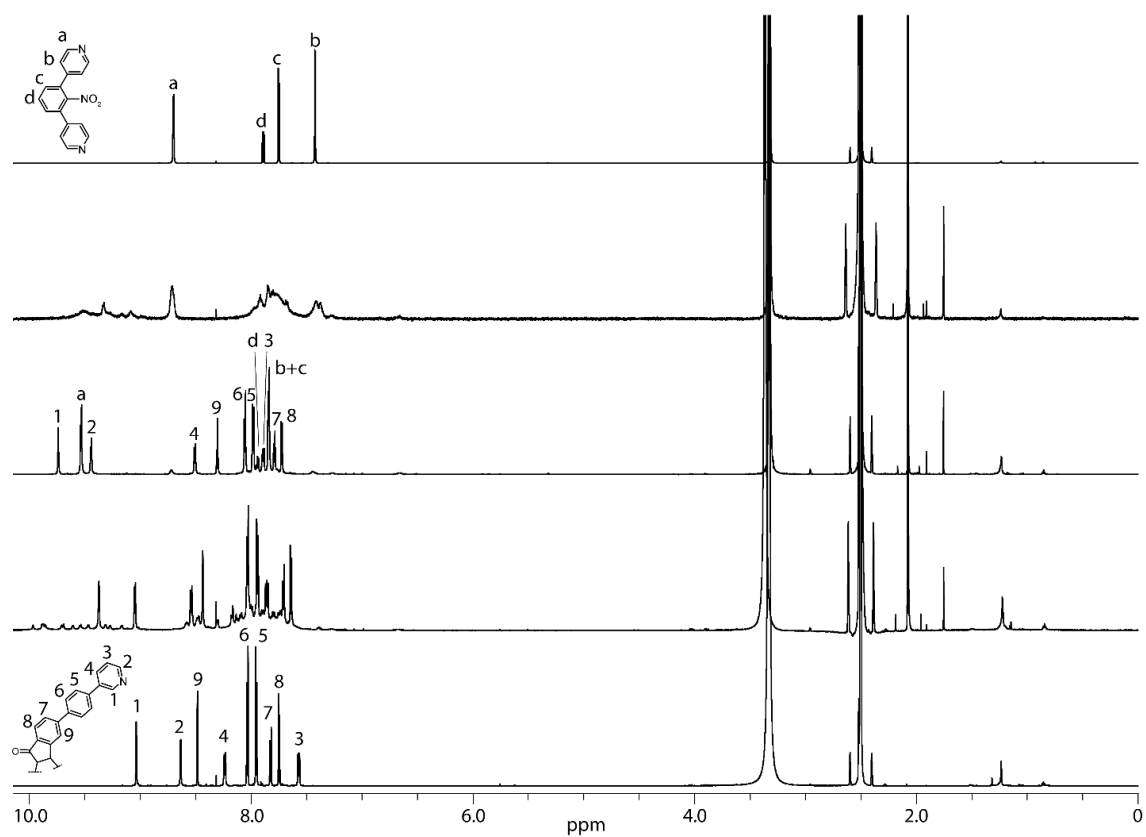
Figure 296: Full ^{1}H NMR spectra (298 K, DMSO-d_6)of ligand $\mathbf{L^{F2}}$ (700 MHz); homoleptic $Pd_2\mathbf{L^{F2}}_4$ cage and the $Pd_n\mathbf{L^{F2}}_{2n}$ (n=3-5) rings formed upon addition of 0.55 equiv. Pd(II) cations to ligand $\mathbf{L^{F2}}$ (600 MHz); heteroleptic $Pd_4\mathbf{L^{F2}}_4\mathbf{L^{S6}}_4$ (700 MHz); ligand $\mathbf{L^{S6}}$ upon addition of 0.55 equiv. Pd(II) cations (500 MHz); ligand $\mathbf{L^{S6}}$ (700 MHz)(listed bottom to top).
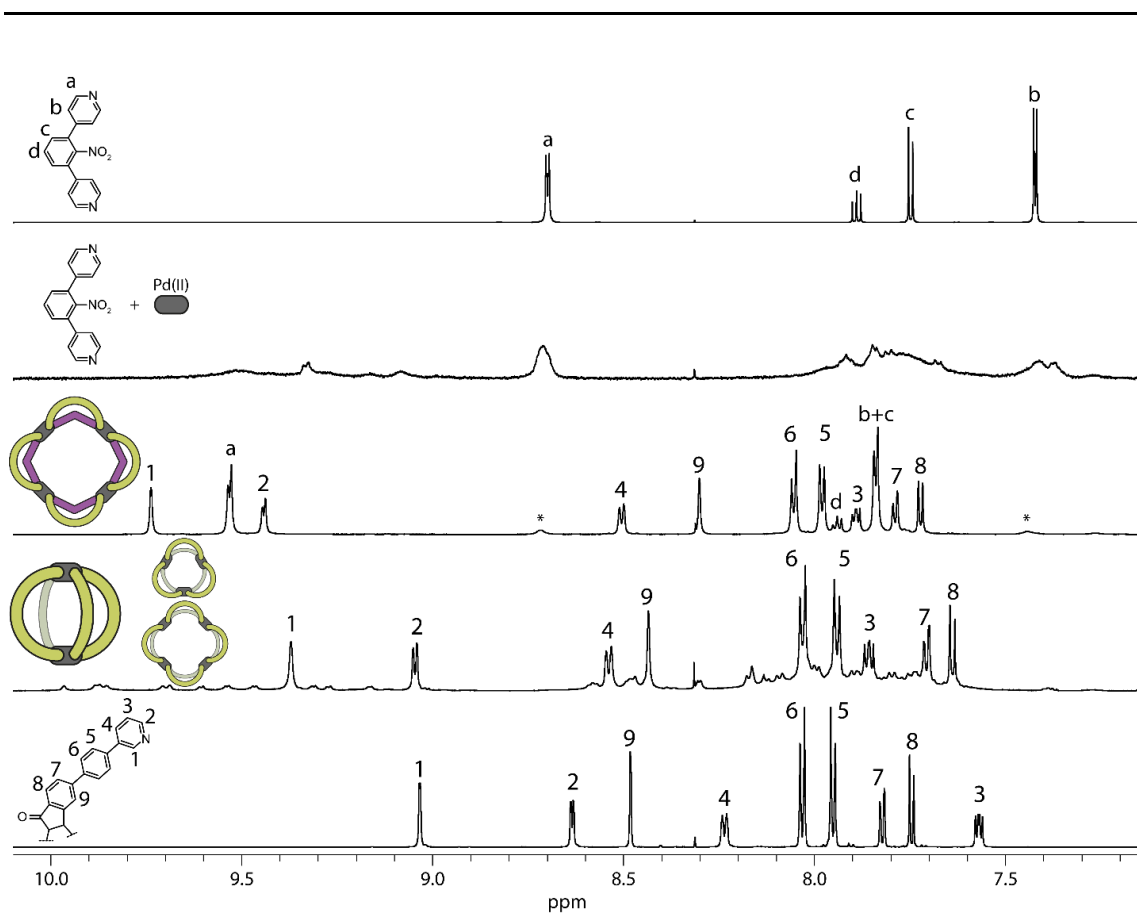
Figure 297: Partial ^{1}H NMR spectra (298 K, DMSO-d_6) of ligand $\mathbf{L^{F2}}$ (700 MHz); homoleptic $Pd_2\mathbf{L^{F2}}_4$ cage and the $Pd_n\mathbf{L^{F2}}_{2n}$ (n=3-5) rings formed upon addition of 0.55 equiv. Pd(II) cations to ligand $\mathbf{L^{F2}}$ (600 MHz); heteroleptic $Pd_4\mathbf{L^{F2}}_4\mathbf{L^{S6}}_4$ (700 MHz); ligand $\mathbf{L^{S6}}$ upon addition of 0.55 equiv. Pd(II) cations (500 MHz); ligand $\mathbf{L^{S6}}$ (700 MHz)(listed bottom to top).
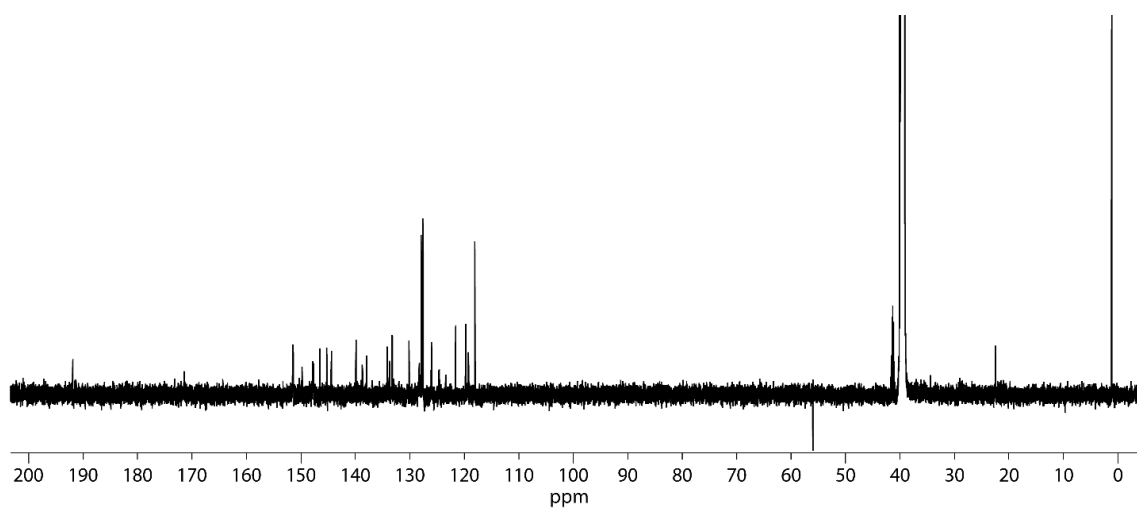
Figure 298: ^{13}C NMR spectrum (176 MHz, 298 K, DMSO-d_6) of $Pd_4\mathbf{L^{F2}}_4\mathbf{L^{S6}}_4$.

^{13}C{^{1}H} (176 MHz, 298 K, DMSO-d_6) δ 191.9, 151.5, 150.3, 149.8, 147.9, 147.7, 146.5, 145.3, 144.4, 139.9, 138.7, 137.9, 134.1, 133.8, 133.2, 133.0, 130.2, 128.3, 127.9, 127.6, 126.0, 124.6, 119.3 ppm.
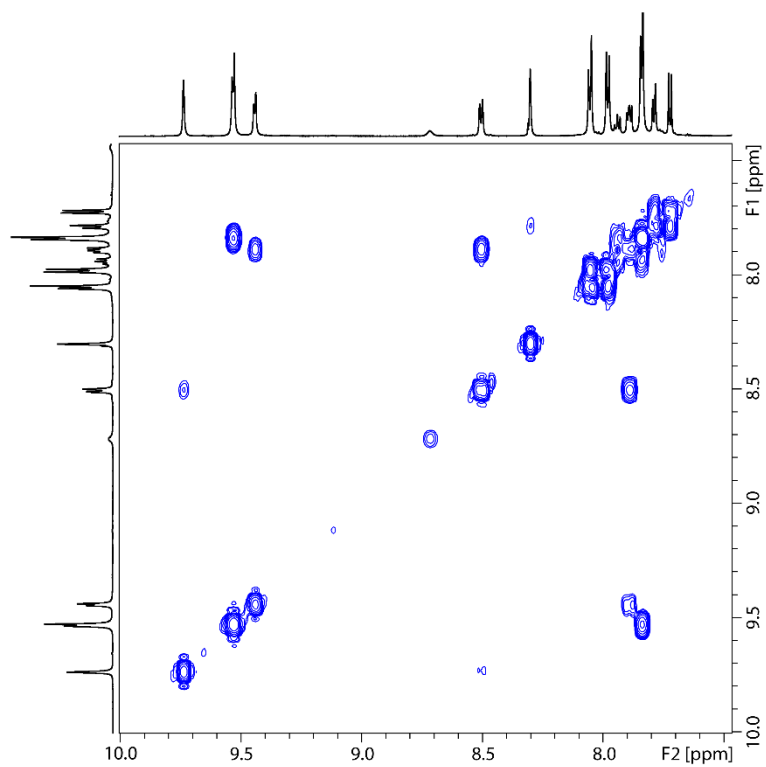
Figure 299: Partial ^{1}H-^{1}H COSY NMR spectrum (700 MHz, 298 K, DMSO-d_6) of Pd$_4$**L**$^{F2}_4$**L**$^{S6}_4$.
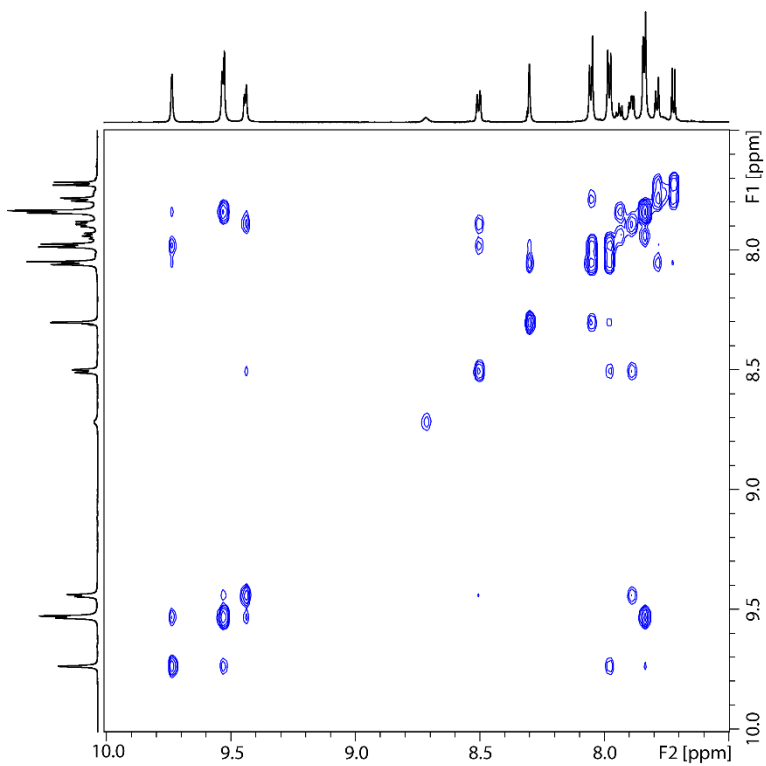
Figure 300: Partial ^{1}H-^{1}H NOESY NMR spectrum (700 MHz, 298 K, DMSO-d_6) of Pd$_4$**L**$^{F2}_4$**L**$^{S6}_4$.
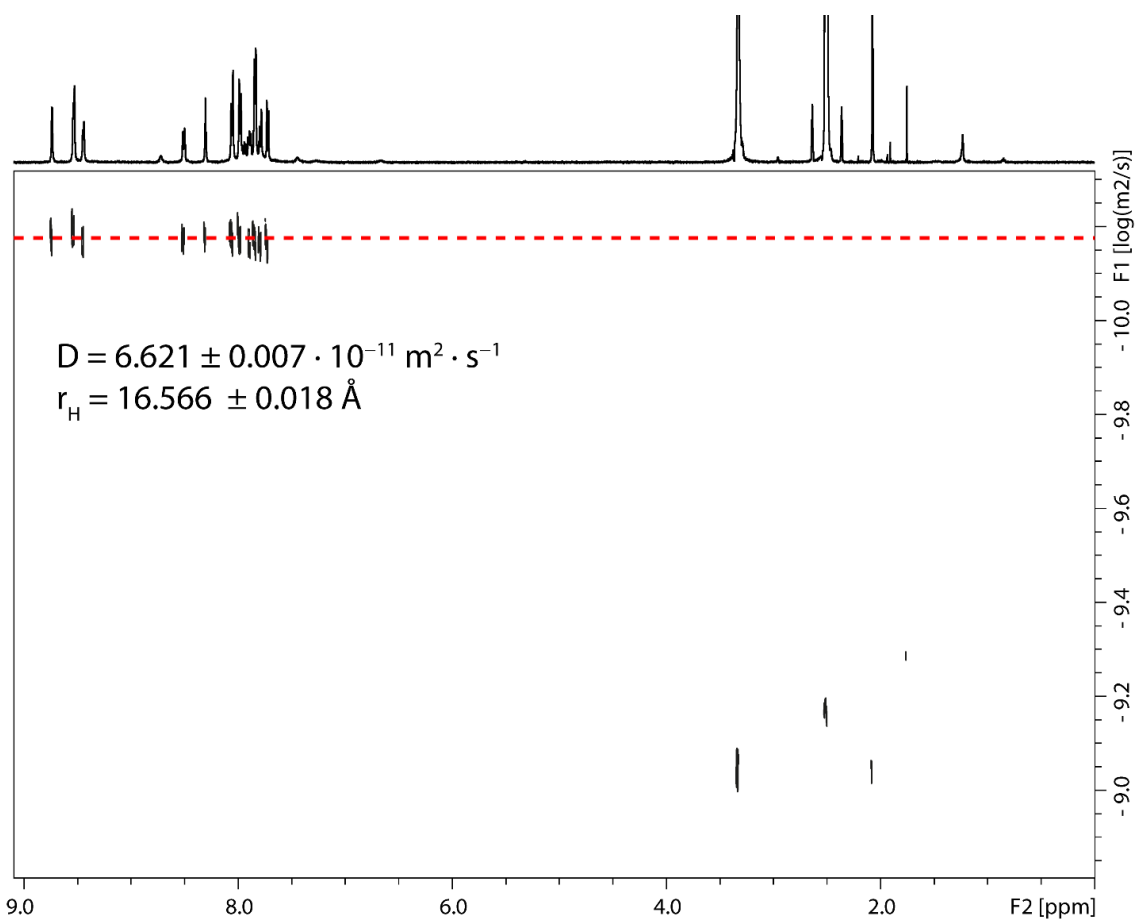
Figure 301: ^{1}H DOSY NMR spectrum (500 MHz, 298 K, DMSO-d_6) of Pd$_4$**L^{F2}**$_4$**L^{S6}**$_4$. Values for diffusion coefficient and resulting hydrodynamic radius are given.

In the figure:

$$D = 6.621 \pm 0.007 \cdot 10^{-11} \, \text{m}^2 \cdot \text{s}^{-1}$$
$$r_H = 16.566 \pm 0.018 \, \text{Å}$$
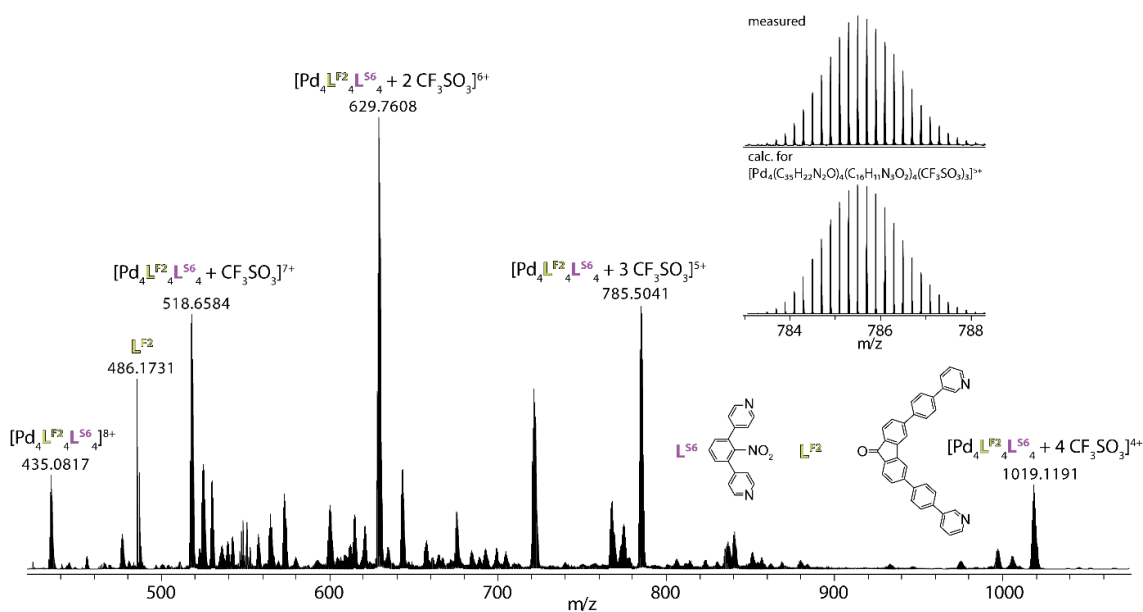
Figure 302: CSI-MS spectrum of Pd$_4$**L^{F2}**$_4$**L^{S6}**$_4$. Peaks could be assigned to [Pd$_4$**L^{F2}**$_4$**L^{S6}**$_4$ + xCF$_3$SO$_3$]$^{(8-x)}$ (x = 0-4). The observed and calculated isotopic patterns are shown in the inset.

3.4.7.2.7 Mixture of Pd$_3$L$^{F2}_3$L$^{S7}_3$ and Pd$_4$L$^{F2}_4$L$^{S7}_4$

A mixture of ligand **L^{F2}** (270 µL of a 3.11 mM solution in DMSO-d_6), **L^{S7}** (270 µL of a 3.11 mM solution in DMSO-d_6), and [Pd(CH$_3$CN)$_4$](OTf)$_2$ (60 µL of a 15 mM solution in DMSO-d_6) was left to rest at room temperature for 2 h to afford a mixture of Pd$_3$L$^{F2}_3$L$^{S7}_3$ and Pd$_4$L$^{F2}_4$L$^{S7}_4$.
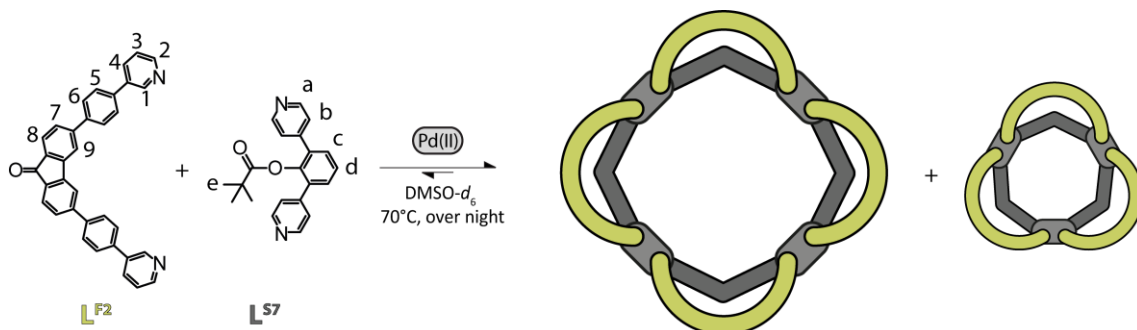
Scheme 45: Formation of the mixture of Pd$_3$L$^{F2}_3$L$^{S7}_3$ and Pd$_4$L$^{F2}_4$L$^{S7}_4$ from a 1:1 mixture of **L^{F2}** and **L^{S7}** with 0.55 equiv. Pd(II) with consecutive proton labels.
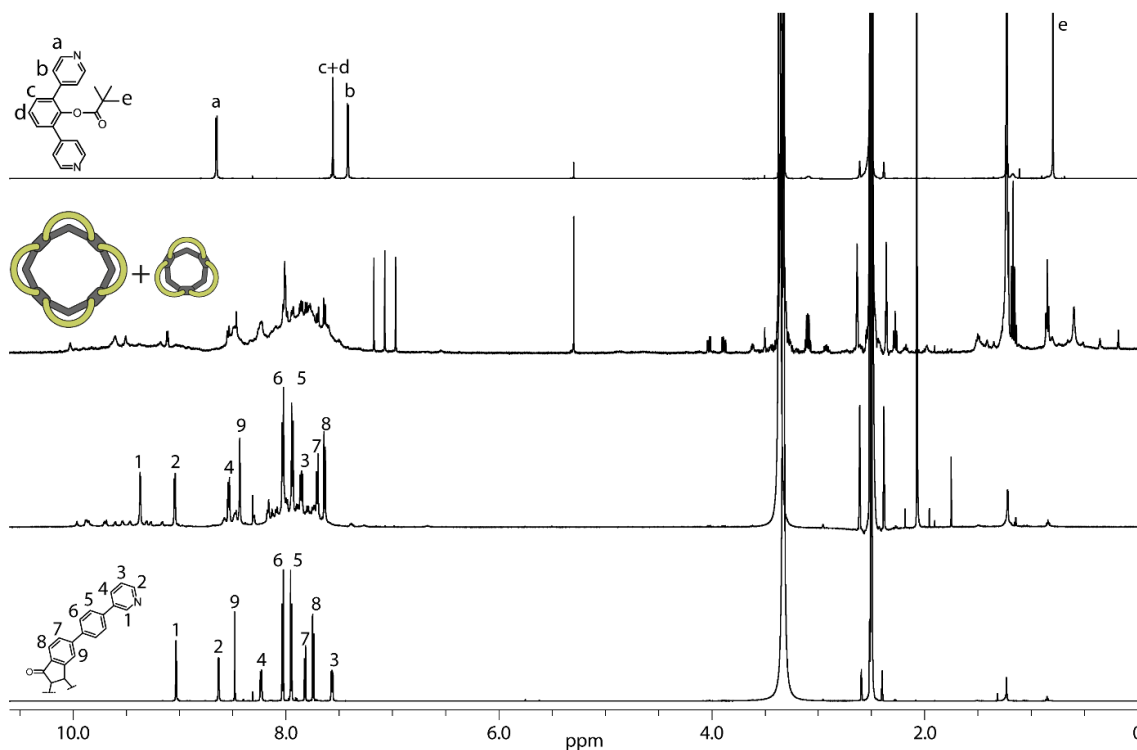
Figure 303: Full ^{1}H NMR spectra (298 K, DMSO-d_6)of ligand **L^{F2}** (700 MHz); homoleptic Pd$_2$L$^{F2}_4$ cage and the Pd$_n$L$^{F2}_{2n}$ (n=3-5) rings formed upon addition of 0.55 equiv. Pd(II) cations to ligand **L^{F2}** (600 MHz); heteroleptic mixture of Pd$_3$L$^{F2}_3$L$^{S7}_3$ and Pd$_4$L$^{F2}_4$L$^{S7}_4$ formed upon Pd(II) addition to a 1:1 mixture of **L^{F2}** and **L^{S7}** (500 MHz); ligand **L^{S7}** (600 MHz)(listed bottom to top).
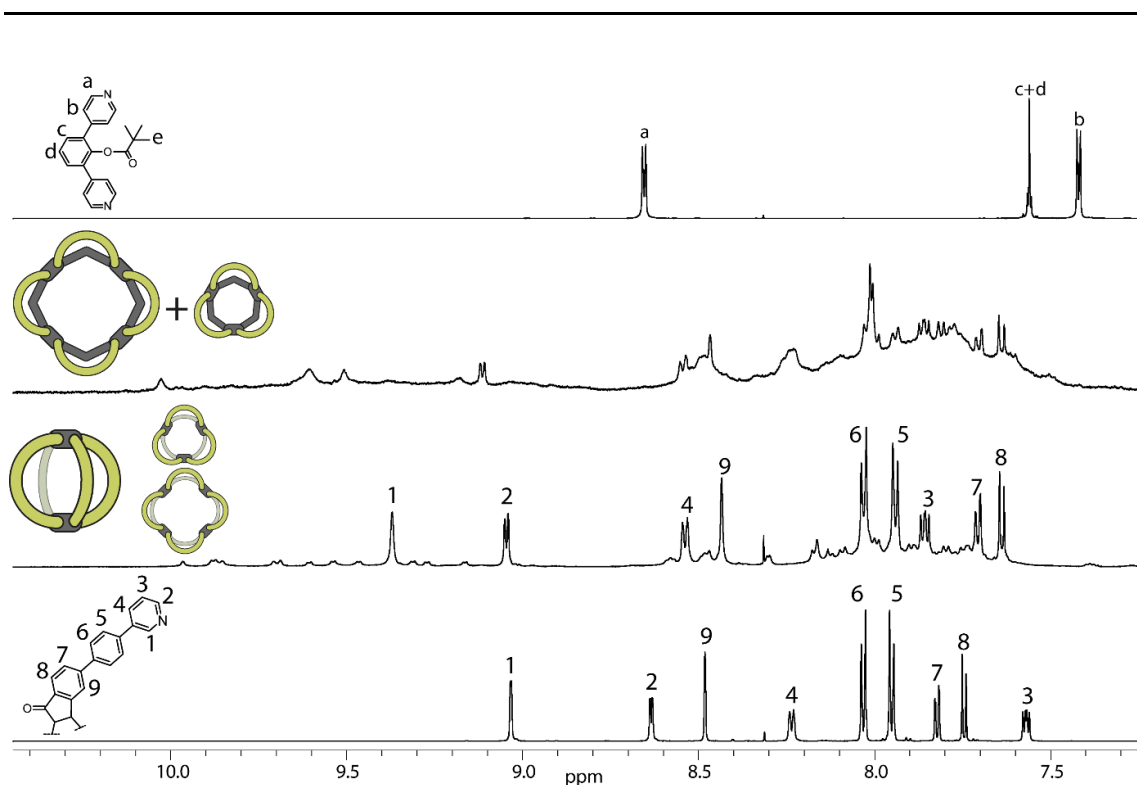
Figure 304: Partial ^{1}H NMR spectra (298 K, DMSO-d_6)of ligand $\mathbf{L^{F2}}$ (700 MHz); homoleptic $Pd_2\mathbf{L^{F2}}_4$ cage and the $Pd_n\mathbf{L^{F2}}_{2n}$ (n=3-5) rings formed upon addition of 0.55 equiv. Pd(II) cations to ligand $\mathbf{L^{F2}}$ (600 MHz); heteroleptic mixture of $Pd_3\mathbf{L^{F2}}_3\mathbf{L^{S7}}_3$ and $Pd_4\mathbf{L^{F2}}_4\mathbf{L^{S7}}_4$ formed upon Pd(II) addition to a 1:1 mixture of $\mathbf{L^{F2}}$ and $\mathbf{L^{S7}}$ (500 MHz); ligand $\mathbf{L^{S7}}$ (600 MHz)(listed bottom to top).
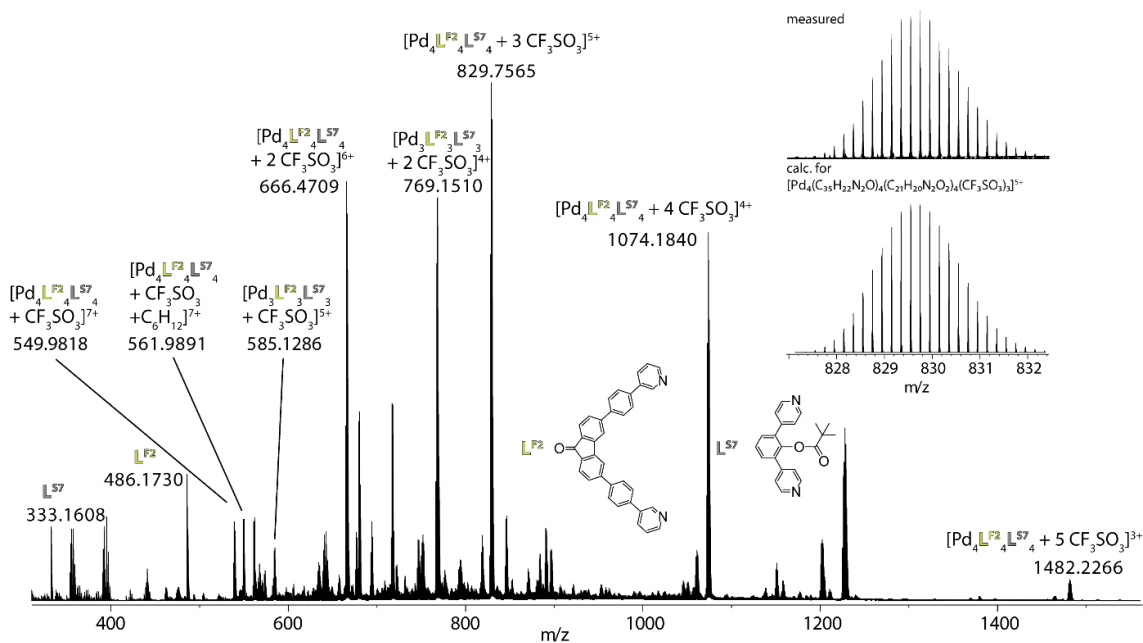
Figure 305: ESI-MS spectrum of the mixture of $Pd_3\mathbf{L^{F2}}_3\mathbf{L^{S7}}_3$ and $Pd_4\mathbf{L^{F2}}_4\mathbf{L^{S7}}_4$ formed upon Pd(II) addition to a 1:1 mixture of $\mathbf{L^{F2}}$ and $\mathbf{L^{S7}}$. The observed and calculated isotopic pattern of the highest peak are shown in the inset.

3.4.7.2.8 Pd$_4$L$^{F2}_4$L$^{S8}_4$

A mixture of ligand **L^{F2}** (270 µL of a 3.11 mM solution in DMSO-d_6), **L^{S8}** (270 µL of a 3.11 mM solution in DMSO-d_6), and [Pd(CH$_3$CN)$_4$](OTf)$_2$ (60 µL of a 15 mM solution in DMSO-d_6) was left to rest at room temperature for 2 h to afford Pd$_4$L$^{F2}_4$L$^{S8}_4$.
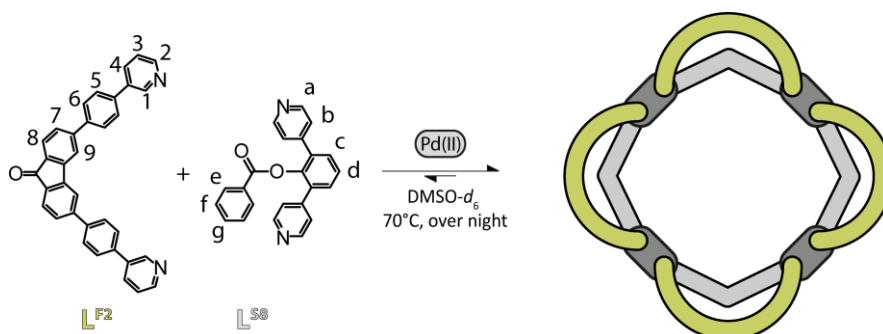
Scheme 46: Formation of Pd$_4$L$^{F2}_4$L$^{S8}_4$ with consecutive proton labels.
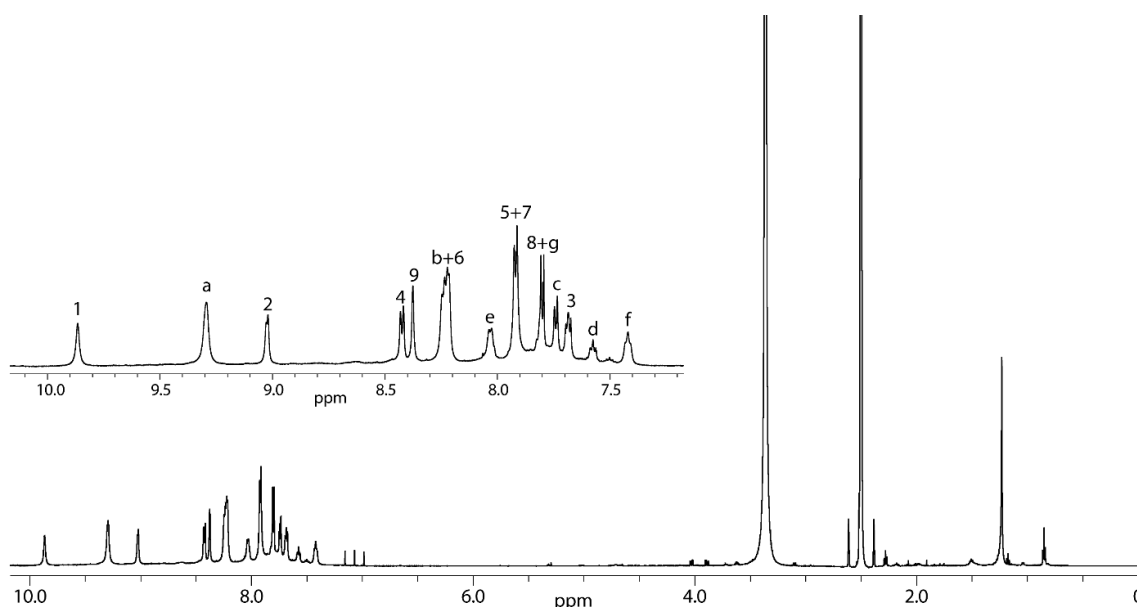
Figure 306: ^{1}H NMR spectrum (600 MHz, 298 K, DMSO-d_6) of Pd$_4$L$^{F2}_4$L$^{S8}_4$. A zoom into the aromatic region including proton assignment is shown in the inset.

^{1}H (600 MHz, 298 K, DMSO-d_6) δ 9.87 (s, 8H, H^1), 9.29 (s (br), 16H, H^a), 9.02 (d, ^3J = 4.5 Hz, 8H, H^2), 8.43 (d, ^3J = 7.8 Hz, 8H, H^4), 8.38 (s, 8H, H^9), 8.18 – 8.29 (m, 32H, H$_b$+H^6), 8.03 (d, ^3J = 7.2 Hz, 8H,H^e), 7.87 – 7.96 (m, 24H, H^5+H^7), 7.78 – 7.84 (m, 12H, H$_g$+H^8), 7.74 (d, ^3J = 7.4 Hz, 8H, H^c), 7.68 (t, ^3J = 6.3 Hz, 8H, H^3), 7.58 (t, ^3J = 7.8 Hz, 8H, H^d), 7.42 (t, ^3J = 6.7 Hz, 8H, H^f) ppm.
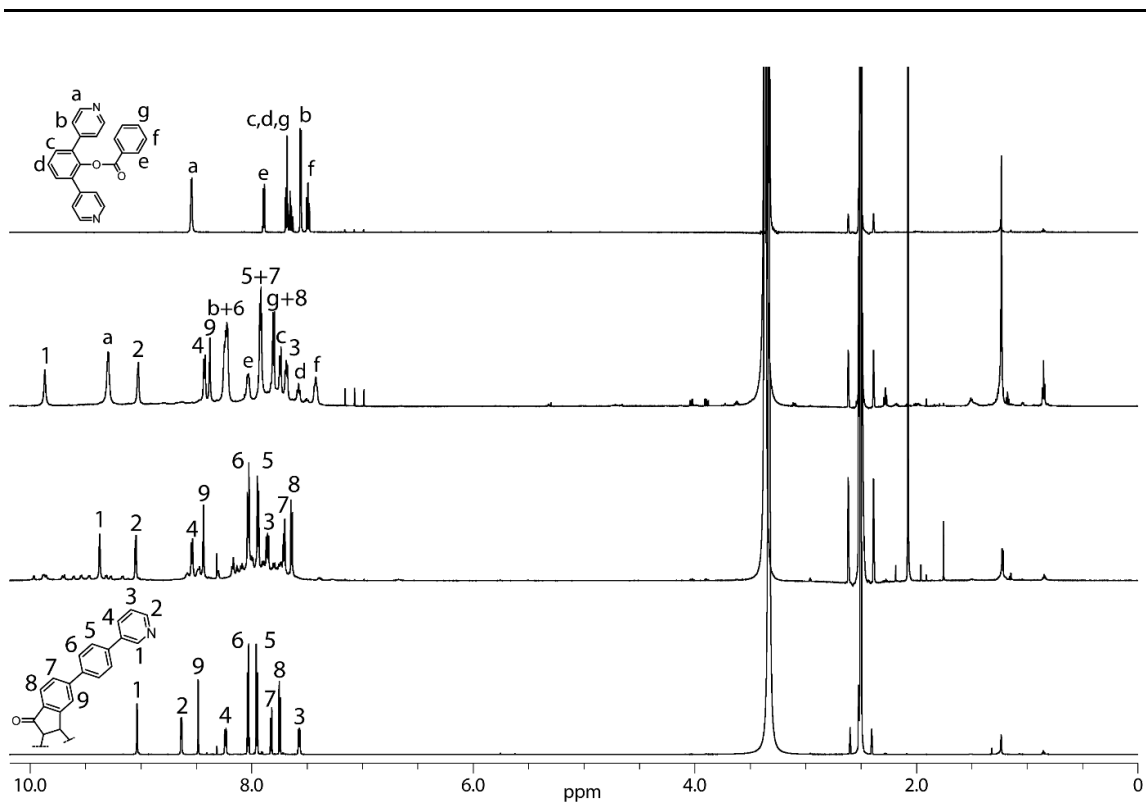
Figure 307: Full ^{1}H NMR spectra (298 K, DMSO-d_6) of ligand $\mathbf{L^{F2}}$ (700 MHz); homoleptic $Pd_2\mathbf{L^{F2}}_4$ cage and the $Pd_n\mathbf{L^{F2}}_{2n}$ (n=3-5) rings formed upon addition of 0.55 equiv. Pd(II) cations to ligand $\mathbf{L^{F2}}$ (600 MHz); heteroleptic $Pd_4\mathbf{L^{F2}}_4\mathbf{L^{S8}}_4$ (600 MHz); ligand $\mathbf{L^{S8}}$ (600 MHz)(listed bottom to top).
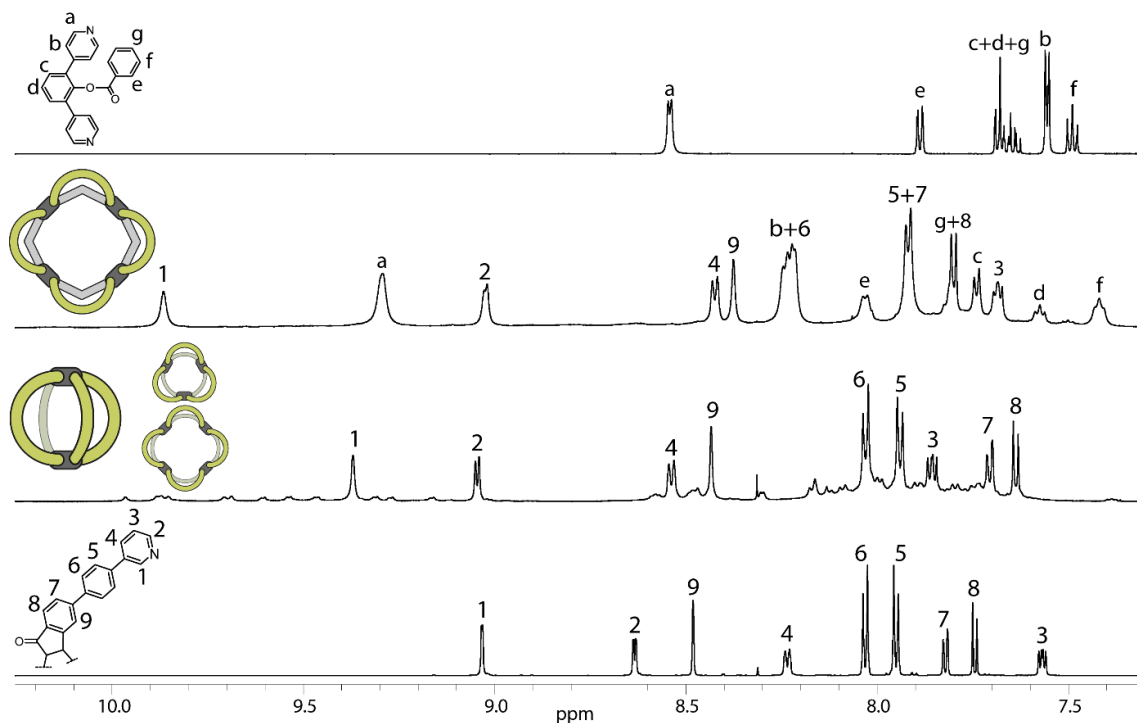
Figure 308: Partial ^{1}H NMR spectra (298 K, DMSO-d_6) of ligand $\mathbf{L^{F2}}$ (700 MHz); homoleptic $Pd_2\mathbf{L^{F2}}_4$ cage and the $Pd_n\mathbf{L^{F2}}_{2n}$ (n=3-5) rings formed upon addition of 0.55 equiv. Pd(II) cations to ligand $\mathbf{L^{F2}}$ (600 MHz); heteroleptic $Pd_4\mathbf{L^{F2}}_4\mathbf{L^{S8}}_4$ (600 MHz); ligand $\mathbf{L^{S8}}$ (600 MHz)(listed bottom to top).

300
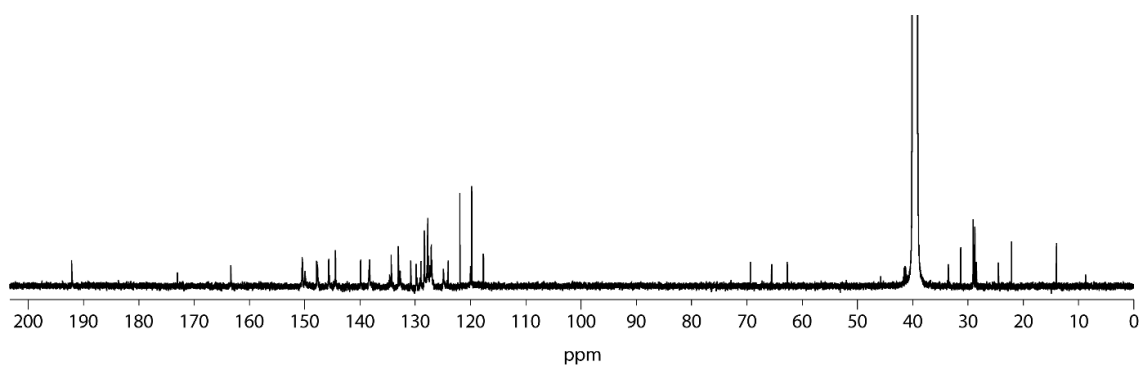
Figure 309: ^{13}C NMR spectrum (176 MHz, 298 K, DMSO-d_6) of Pd$_4$**L^{F2}**$_4$**L^{S8}**$_4$.

^{13}C{^{1}H} (151 MHz, 298 K, DMSO-d_6) δ 192.08, 163.31, 150.38, 149.89, 147.76, 147.62, 145.61, 145.54, 144.38, 139.81, 138.34, 138.20, 134.59, 134.29, 132.99, 132.69, 130.76, 129.79, 129.64, 129.09, 128.91, 128.29, 127.81, 127.66, 127.29, 127.02, 124.84, 119.93 ppm.
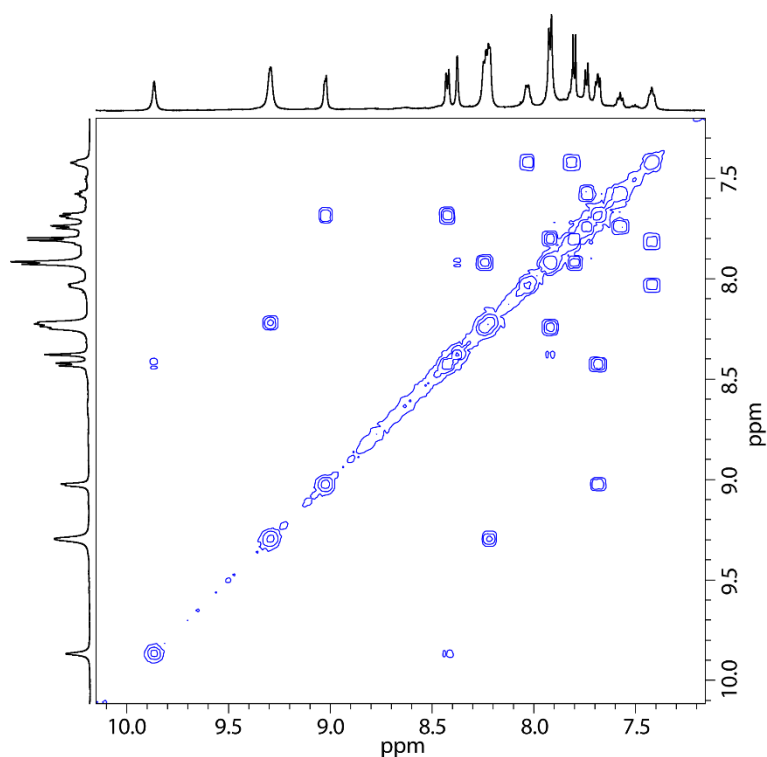
Figure 310: Partial ^{1}H-^{1}H COSY NMR spectrum (600 MHz, 298 K, DMSO-d_6) of Pd$_4$**L^{F2}**$_4$**L^{S8}**$_4$.
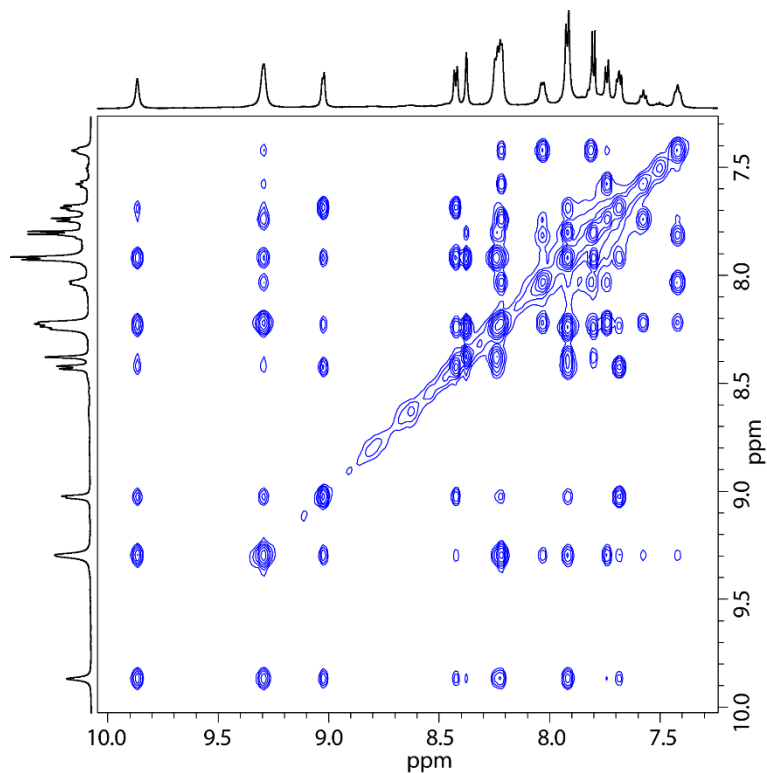
Figure 311: Partial ^{1}H-^{1}H NOESY NMR spectrum (600 MHz, 298 K, DMSO-d_6) of Pd$_4$L$^{F2}_4$L$^{S8}_4$.

$$D = 7.083 \pm 0.006 \cdot 10^{-11}\ \text{m}^2 \cdot \text{s}^{-1}$$
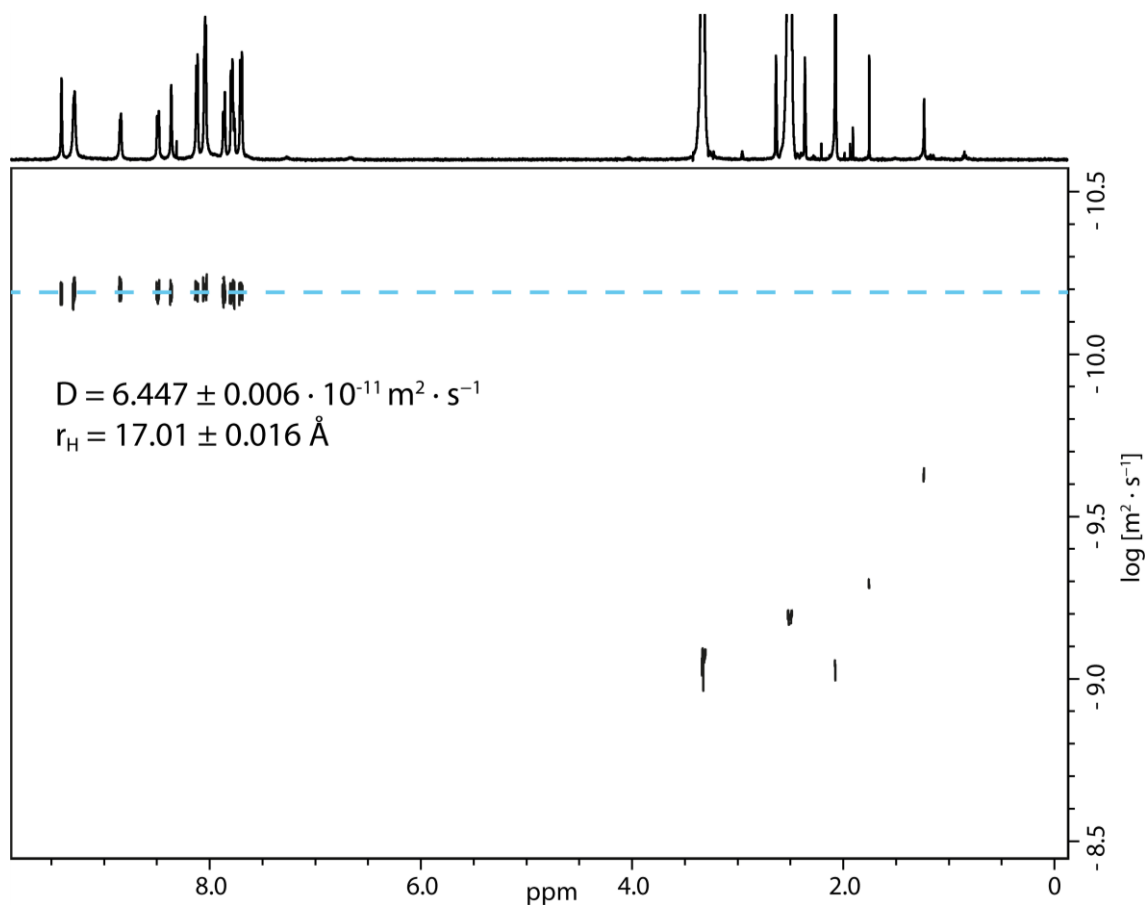$$r_H = 15.486 \pm 0.013\ \text{Å}$$
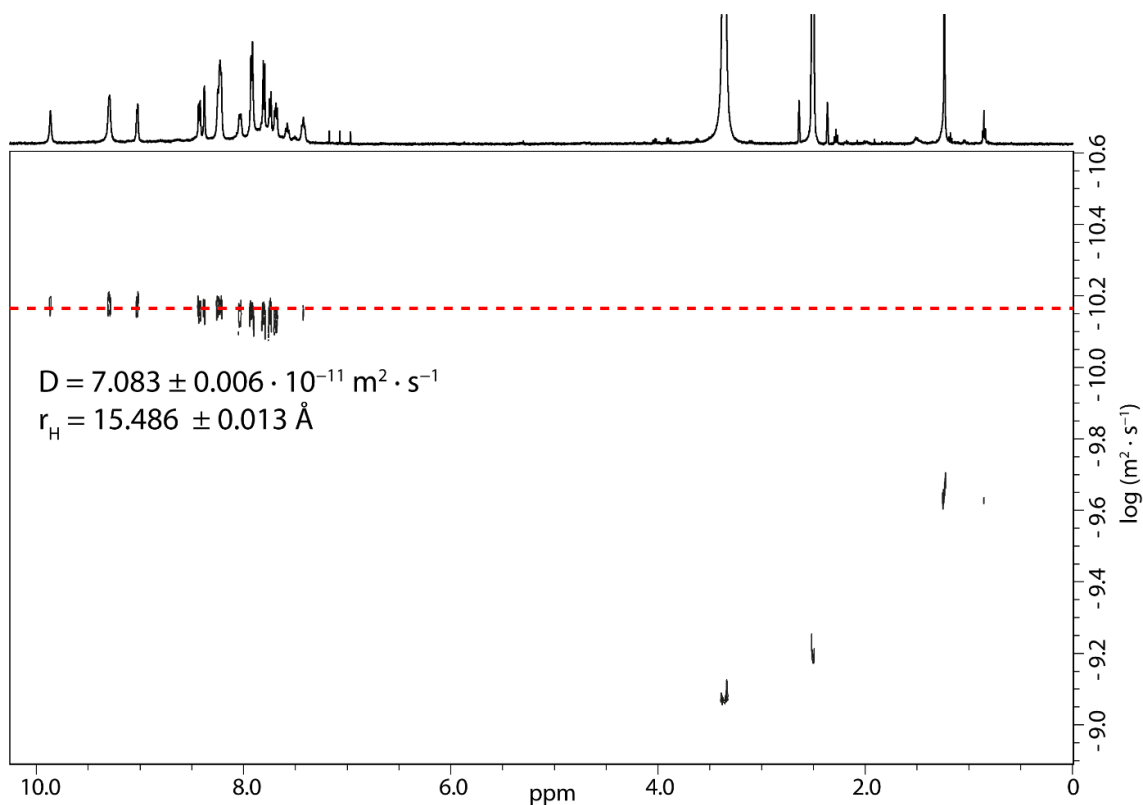
Figure 312: ^{1}H DOSY NMR spectrum (500 MHz, 298 K, DMSO-d_6) of Pd$_4$L$^{F2}_4$L$^{S8}_4$. Values for diffusion coefficient and resulting hydrodynamic radius are given.
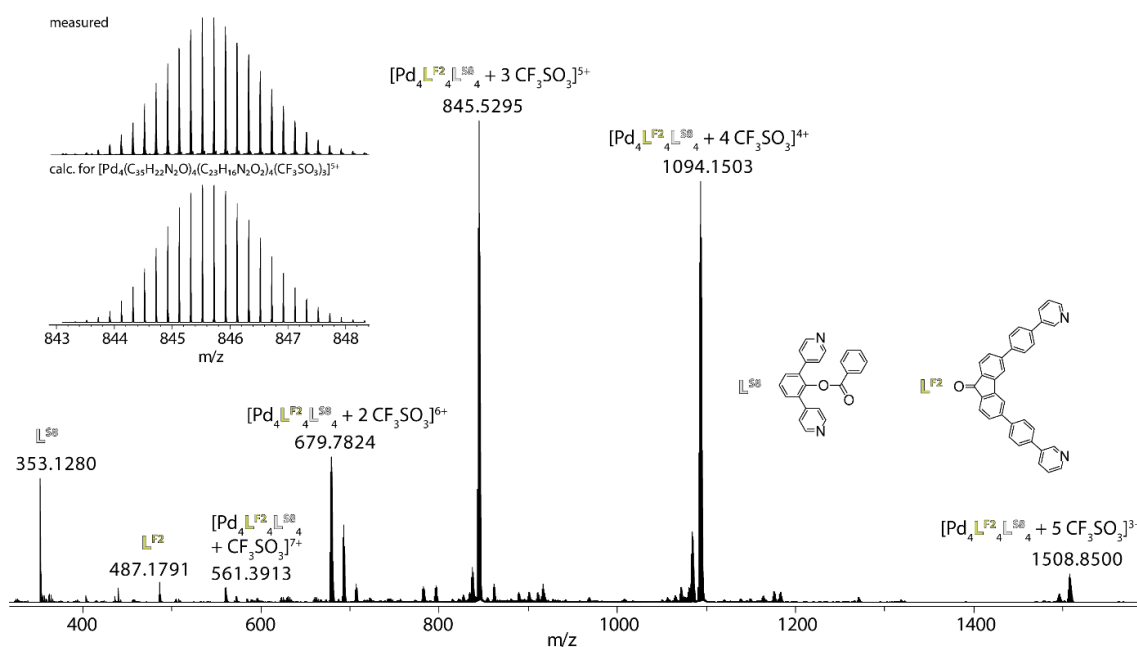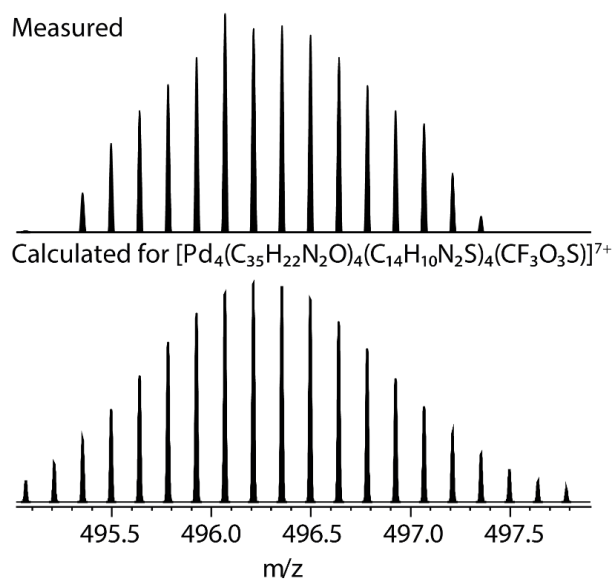
Figure 313: ESI-MS spectrum of Pd$_4$**L**$^{F2}_4$**L**$^{S8}_4$. Peaks could be assigned to [Pd$_4$**L**$^{F2}_4$**L**$^{S8}_4$ + xCF$_3$SO$_3$]$^{(8-x)}$ (x = 0-5). The observed and calculated isotopic patterns are shown in the inset.

3.4.7.2.9 Pd$_4$**L**$^{F2}_4$**L**$^{S9}_4$

A mixture of ligand **L**^{F2} (270 µL of a 3.11 mM solution in DMSO-d_6), **L**^{S9} (270 µL of a 3.11 mM solution in DMSO-d_6), and [Pd(CH$_3$CN)$_4$](OTf)$_2$ (60 µL of a 15 mM solution in DMSO-d_6) was left to rest at room temperature for 2 h to afford clean Pd$_4$**L**$^{F2}_4$**L**$^{S9}_4$.
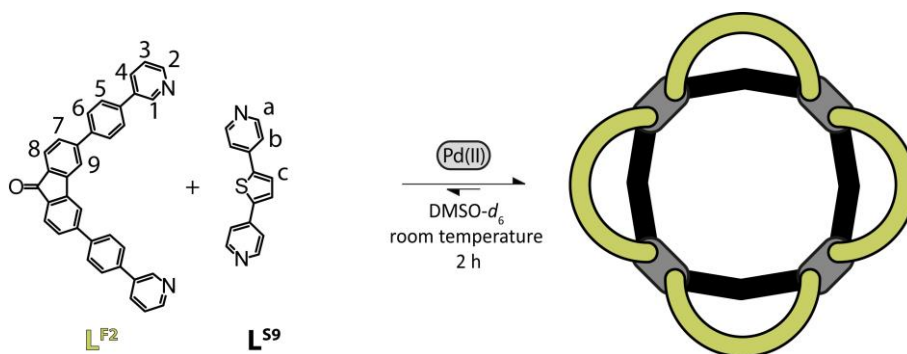
Scheme 47: Formation of Pd$_4$**L**$^{F2}_4$**L**$^{S9}_4$ with consecutive proton labels.
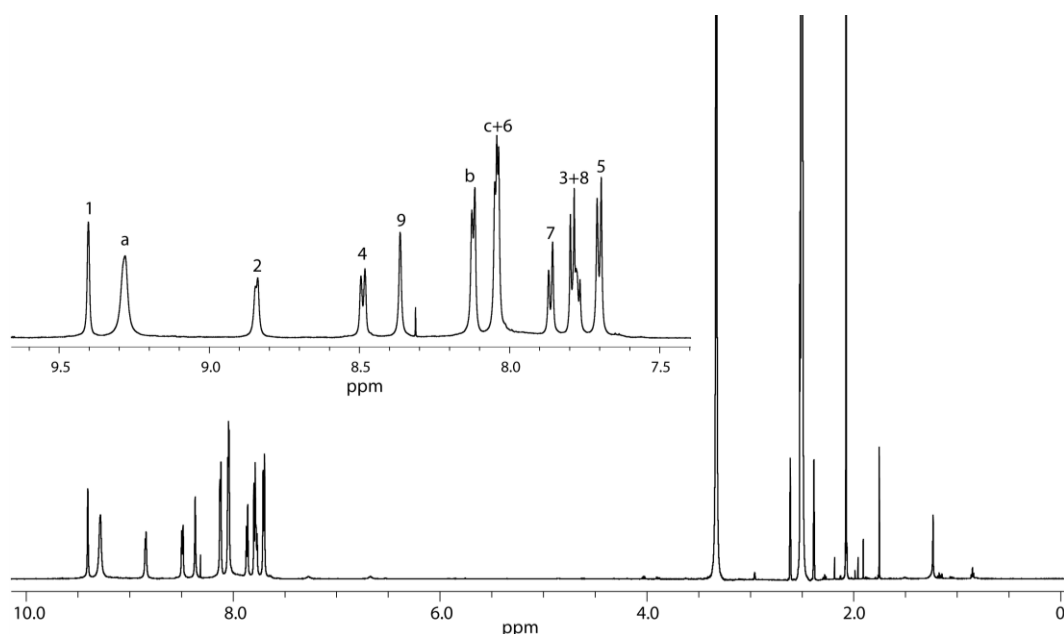
Figure 314: ^{1}H NMR spectrum (600 MHz, 298 K, DMSO-d_6) of Pd$_4$**L**$^{F2}_4$**L**$^{S9}_4$. A zoom into the aromatic region including proton assignment is shown in the inset.

^{1}H (600 MHz, 298 K, DMSO-d_6) δ 9.40 (s, 8H H^1), 9.28 (s (br), 16H, H^a), 8.84 (d, ^3J = 4.9 Hz, 8H, H^2), 8.49 (d, ^3J = 8.15 Hz, 8H, H^4), 8.36 (s, 8H, H^9), 8.12 (d, ^3J = 5.9 Hz, 16H, H^b), 8.01-8.08 (m, 24H, H^c+H^6), 7.86 (d, ^3J = 8.05 Hz, 8H, H^7), 7.74-7.82 (m, 16H, H^3+H^8), 7.70 (d, ^3J = 8.05 Hz, 16H, H^5) ppm.
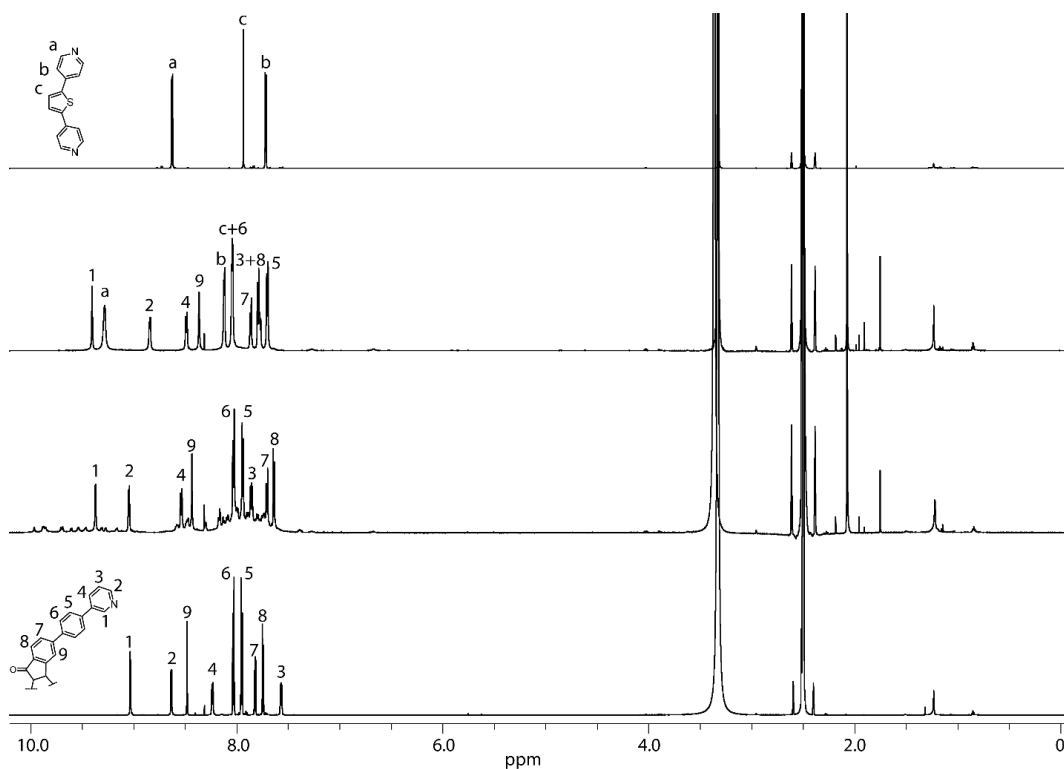
Figure 315: Full ^{1}H NMR spectra (298 K, DMSO-d_6) of ligand **L**^{F2} (700 MHz); homoleptic Pd$_2$**L**$^{F2}_4$ cage and the Pd$_n$**L**$^{F2}_{2n}$ (n=3-5) rings formed upon addition of 0.55 equiv. Pd(II) cations to ligand **L**^{F2} (600 MHz); heteroleptic Pd$_4$**L**$^{F2}_4$**L**$^{S9}_4$ (600 MHz); ligand **L**^{S9} (600 MHz)(listed bottom to top).
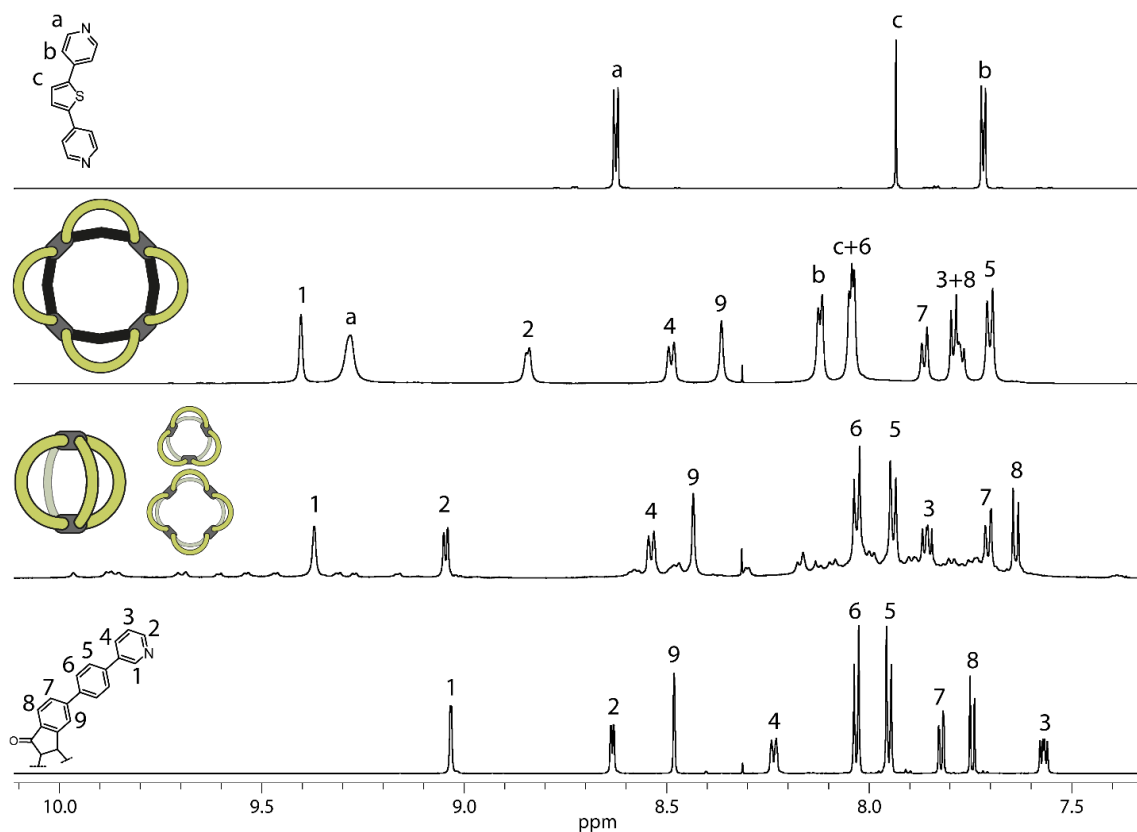
Figure 316: Partial ^{1}H NMR spectra (298 K, DMSO-d_6) of ligand **L^{F2}** (700 MHz); homoleptic Pd$_2$**L^{F2}**$_4$ cage and the Pd$_n$**L^{F2}**$_{2n}$ (n=3-5) rings formed upon addition of 0.55 equiv. Pd(II) cations to ligand **L^{F2}** (600 MHz); heteroleptic Pd$_4$**L^{F2}**$_4$**L^{S9}**$_4$ (600 MHz); ligand **L^{S9}** (600 MHz)(listed bottom to top).
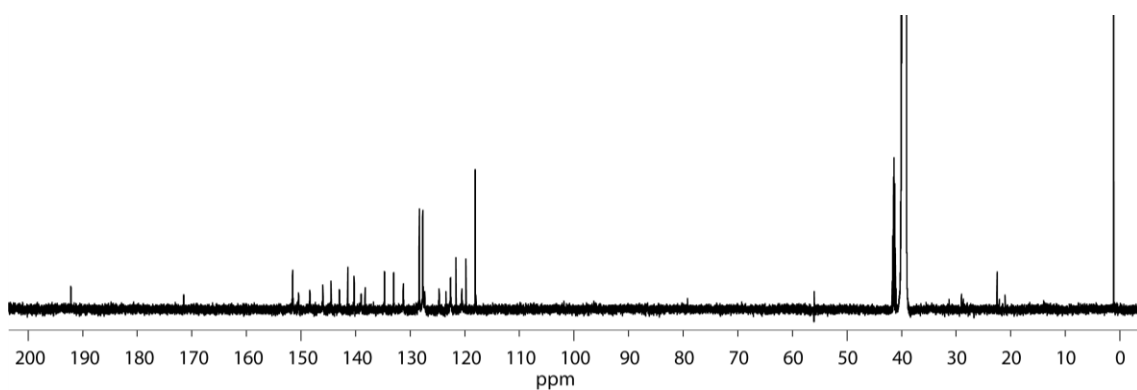
Figure 317: ^{13}C NMR spectrum (176 MHz, 298 K, DMSO-d_6) of Pd$_4$**L^{F2}**$_4$**L^{S9}**$_4$.

^{13}C{^{1}H} (176 MHz, 298 K, DMSO-d_6) δ 192.1, 151.5, 150.4, 148.4, 146.0, 144.5, 143.0, 141.4, 140.3, 139.0, 138.2, 134.7, 133.0, 131.3, 128.3, 127.7, 127.6, 127.4, 124.7, 122.6, 120.5 ppm.
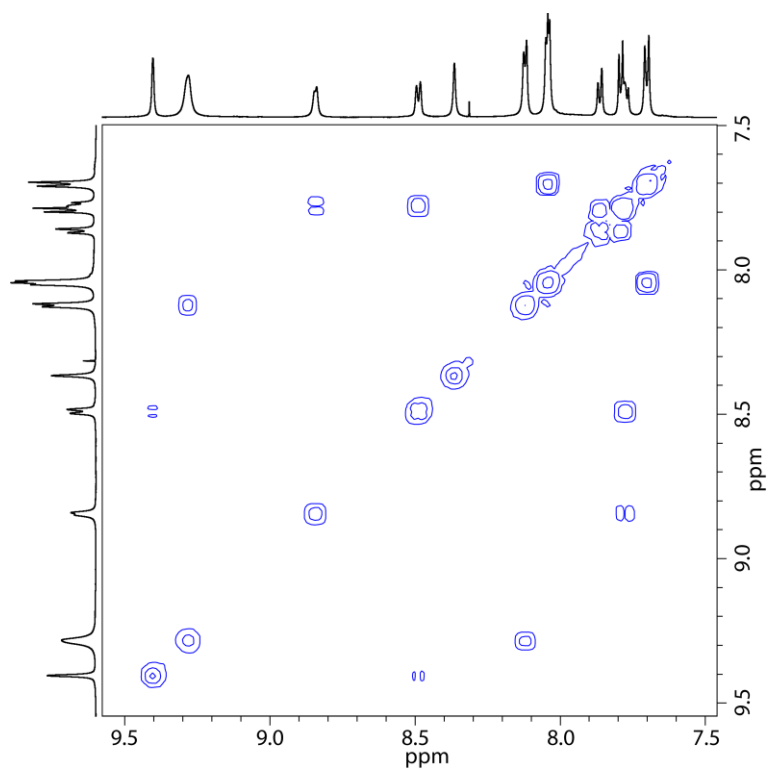
Figure 318: Partial ^{1}H-^{1}H COSY NMR spectrum (600 MHz, 298 K, DMSO-d_6) of Pd$_4$**L**$^{F2}_4$**L**$^{S9}_4$.
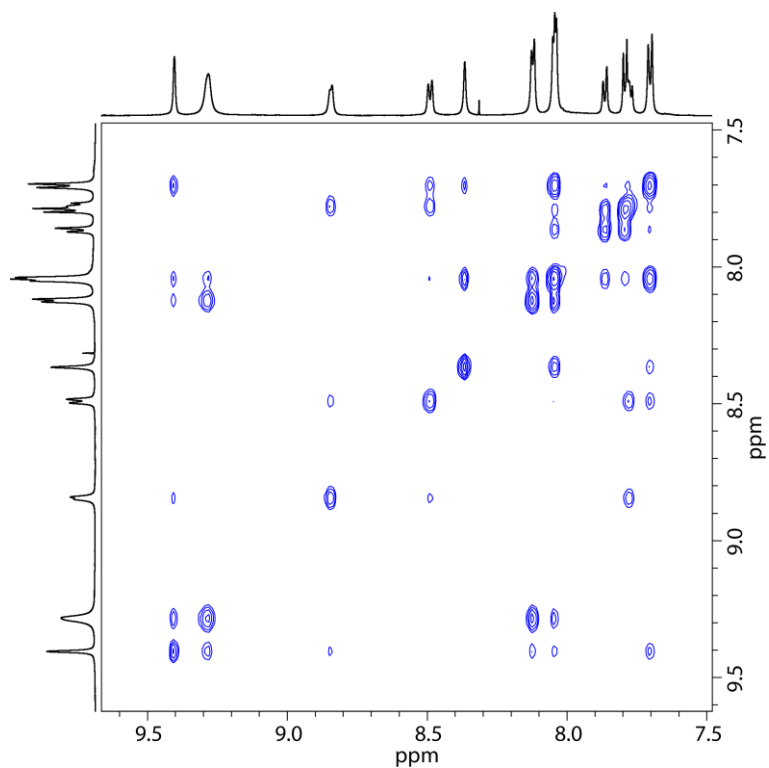
Figure 319: Partial ^{1}H-^{1}H NOESY NMR spectrum (600 MHz, 298 K, DMSO-d_6) of Pd$_4$**L**$^{F2}_4$**L**$^{S9}_4$.
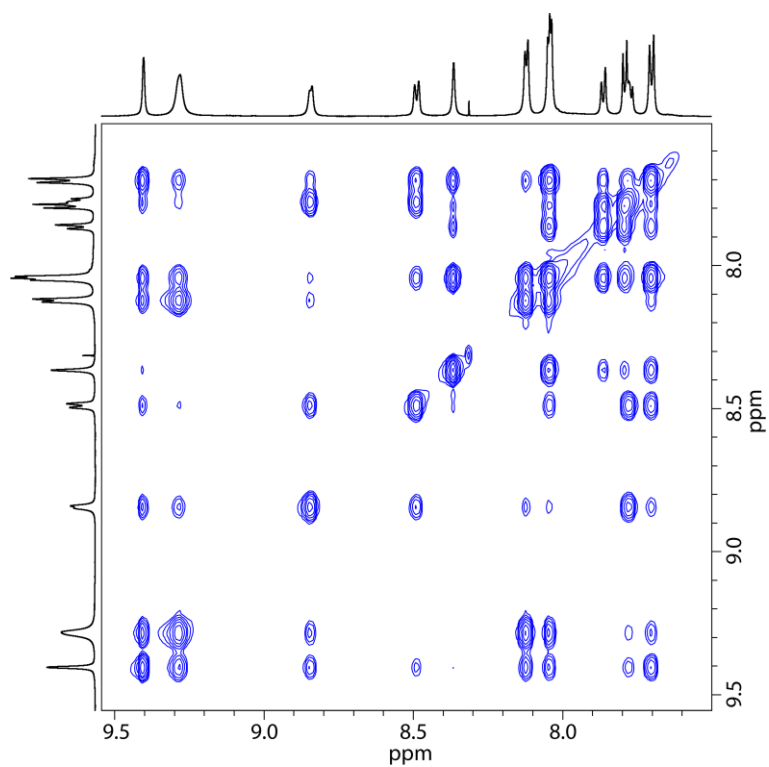
Figure 320: Partial ^{1}H-^{1}H NOESY NMR spectrum (600 MHz, 298 K, DMSO-d_6) of Pd$_4$**L**$^{F2}_4$**L**$^{S9}_4$ with increased signal intensity.

$$D = 6.447 \pm 0.006 \cdot 10^{-11}\,m^2 \cdot s^{-1}$$
$$r_H = 17.01 \pm 0.016\,Å$$

Figure 321: ^{1}H DOSY NMR spectrum (500 MHz, 298 K, DMSO-d_6) of Pd$_4$**L**$^{F2}_4$**L**$^{S9}_4$. Values for diffusion coefficient and resulting hydrodynamic radius are given.

Figure 322: Partial ESI-MS spectrum of Pd$_4$**L^{F2}**$_4$**L^{S9}**$_4$. Neither species with a nuclearity of n = 3 nor of n = 5 could be detected. Cryo-source measurement did not yield better results.
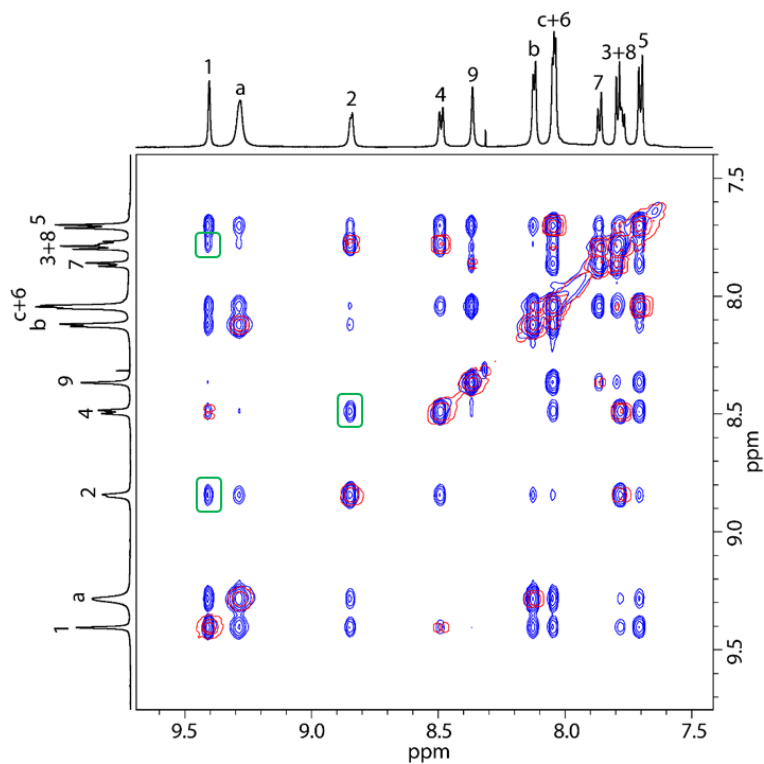
Figure 323: Partial ^{1}H-^{1}H COSY NMR spectrum (600 MHz, 298 K, DMSO-d_6, red) overlayed with a partial ^{1}H-^{1}H NOESY NMR spectrum (600 MHz, 298 K, DMSO-d_6, blue) of Pd$_4$**L^{F2}**$_4$**L^{S9}**$_4$ inclusing proton assignments.

3.4.7.2.10 Pd$_4$L$^{F2}_4$L$^{S10}_4$

A mixture of ligand **L^{F2}** (270 µL of a 3.11 mM solution in DMSO-d_6), **L^{S10}** (270 µL of a 3.11 mM solution in DMSO-d_6), and [Pd(CH$_3$CN)$_4$](OTf)$_2$ (60 µL of a 15 mM solution in DMSO-d_6) was left to rest at room temperature for 2 h to afford clean Pd$_4$L$^{F2}_4$L$^{S10}_4$.
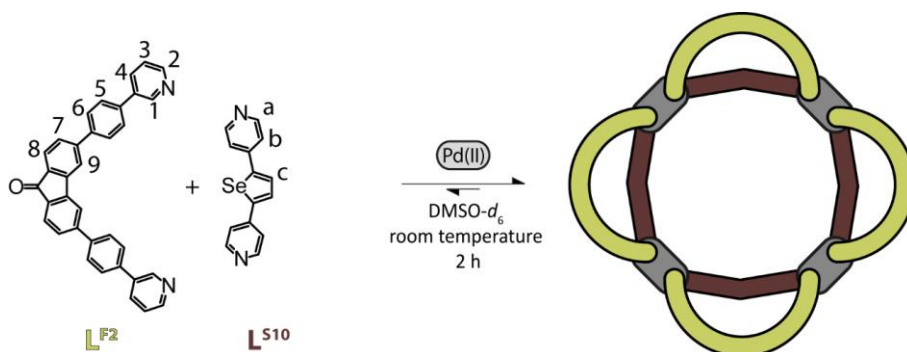
Scheme 48: Formation of Pd$_4$L$^{F2}_4$L$^{S10}_4$ with consecutive proton labels.
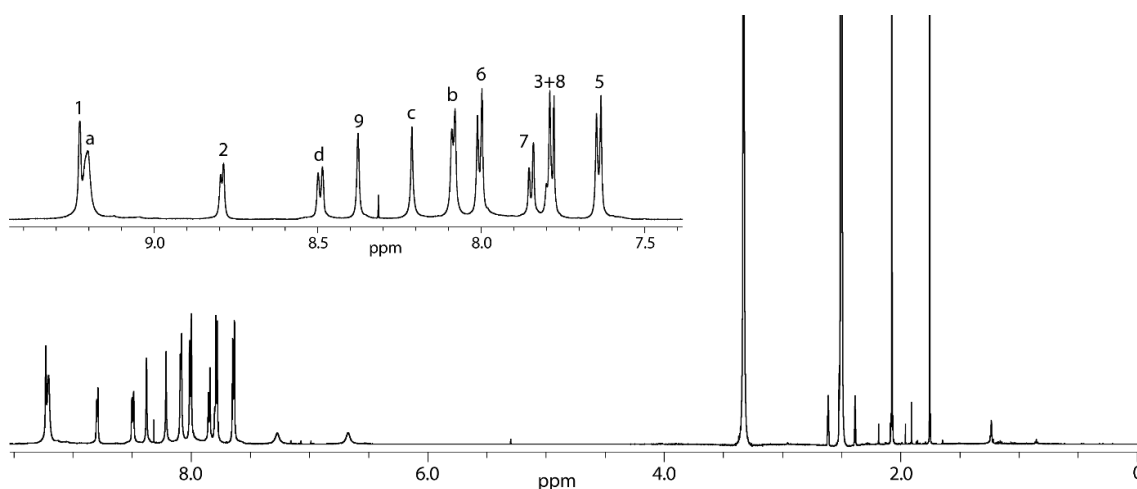
Figure 324: ^{1}H NMR spectrum (600 MHz, 298 K, DMSO-d_6) of Pd$_4$L$^{F2}_4$L$^{S10}_4$. A zoom into the aromatic region including proton assignment is shown in the inset.

^{1}H (600 MHz, 298 K, DMSO-d_6) δ 9.23 (s, 8H, H^1), 9.20 (s (br), 16H, H^a), 8.79 (d, ^3J = 5.2 Hz, 8H, H^2), 8.49 (d, ^3J = 7.9 Hz, 8H, H^4), 8.38 (s, 8H, H^9), 8.21 (s, 8H, H^c), 8.08 (d, ^3J = 5.9 Hz, 16H, H^b), 8.00 (d, ^3J = 8.2 Hz, 16H, H^6), 7.85 (d, ^3J = 8.2 Hz, 8H, H^7), 7.76-7.82 (m, 16H, H^3 + H^8), 7.64 (d, ^3J = 8.2 Hz, 16H, H^5) ppm.
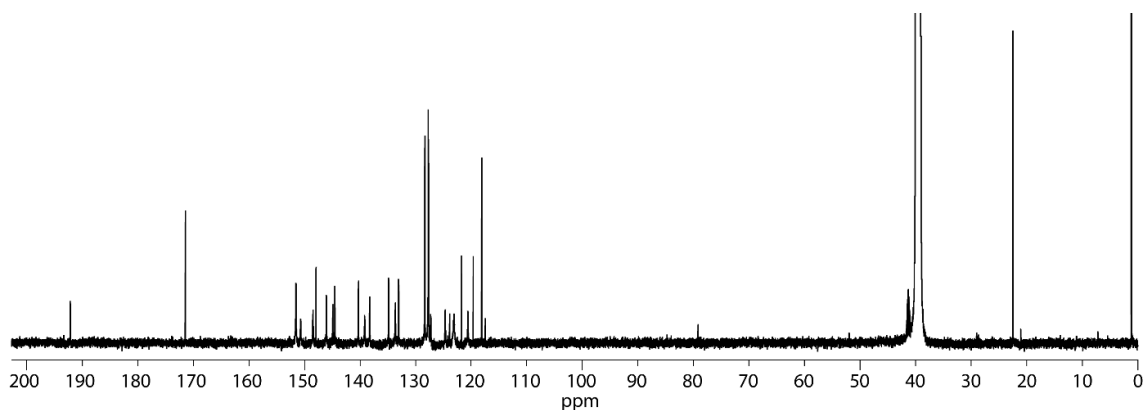
Figure 325: ^{13}C NMR spectrum (176 MHz, 298 K, DMSO-d_6) of Pd$_4$**L^{F2}**$_4$**L^{S10}**$_4$.

^{13}C{^{1}H} (151 MHz, 298 K, DMSO-d_6) δ 192.13, 151.51, 150.67, 148.46, 147.91, 146.05, 144.87, 144.55, 140.27, 139.17, 138.24, 134.82, 133.62, 133.03, 128.33, 127.70, 127.28, 124.64, 123.09, 120.58 ppm.
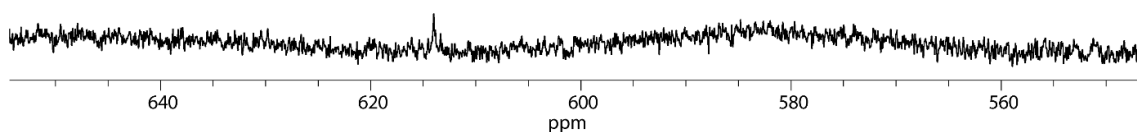
Figure 326: ^{77}Se NMR spectrum (114.5 MHz, 298 K, DMSO-d_6) of Pd$_4$**L^{F2}**$_4$**L^{S10}**$_4$.

^{77}Se{^{1}H} (114.5 MHz, 298 K, DMSO-d_6) δ 613.97 ppm.
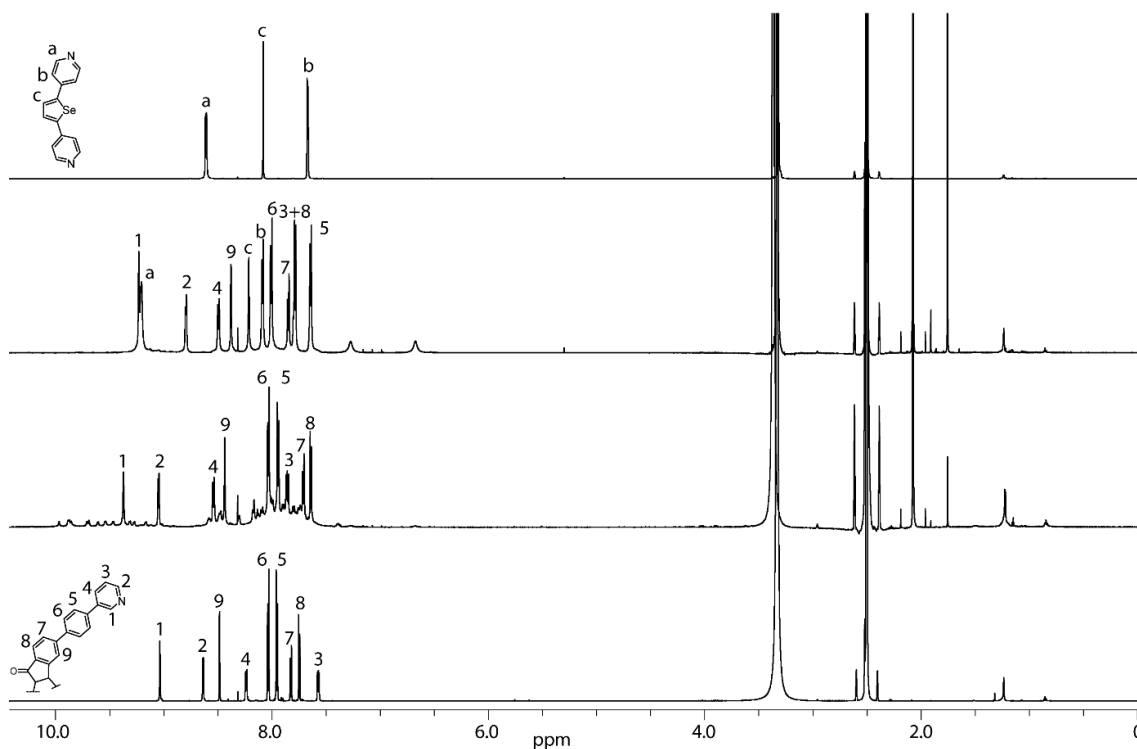
Figure 327: Full ^{1}H NMR spectra (298 K, DMSO-d_6) of ligand **L^{F2}** (700 MHz); homoleptic Pd$_2$**L^{F2}**$_4$ cage and the Pd$_n$**L^{F2}**$_{2n}$ (n=3-5) rings formed upon addition of 0.55 equiv. Pd(II) cations to ligand **L^{F2}** (600 MHz); heteroleptic Pd$_4$**L^{F2}**$_4$**L^{S10}**$_4$ (600 MHz); ligand **L^{S10}** (600 MHz)(listed bottom to top).
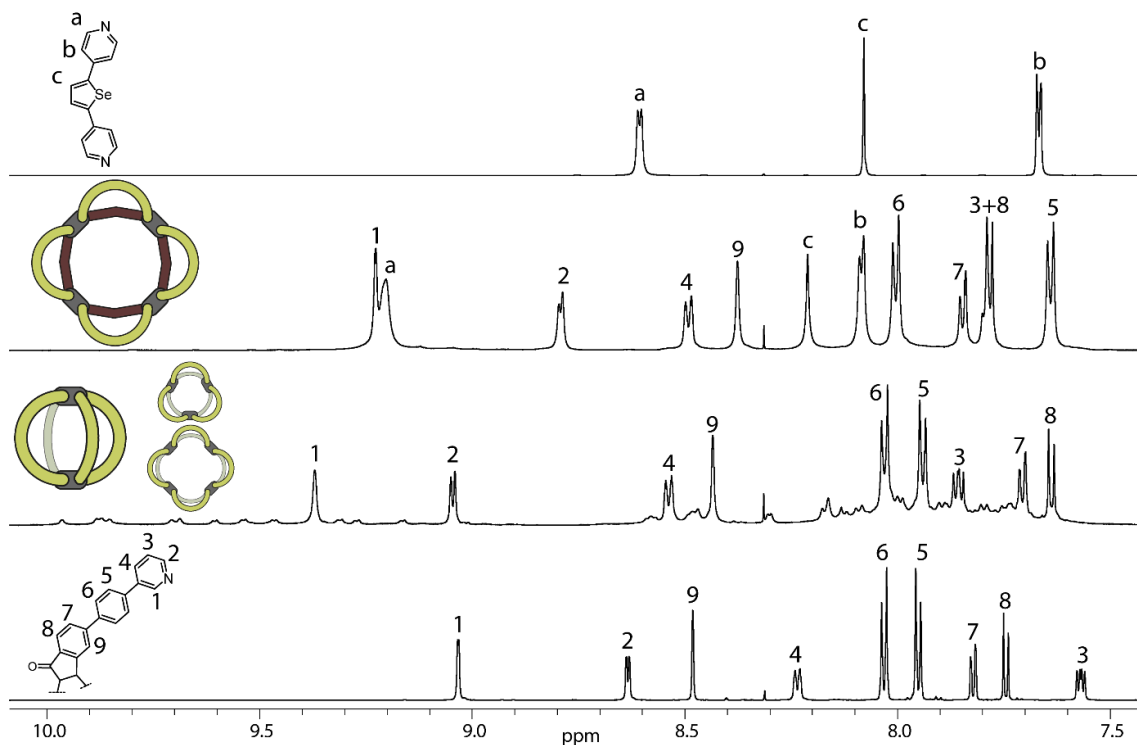
Figure 328: Partial ^{1}H NMR spectra (298 K, DMSO-d_6) of ligand $\mathbf{L^{F2}}$ (700 MHz); homoleptic $Pd_2\mathbf{L^{F2}}_4$ cage and the $Pd_n\mathbf{L^{F2}}_{2n}$ (n=3-5) rings formed upon addition of 0.55 equiv. Pd(II) cations to ligand $\mathbf{L^{F2}}$ (600 MHz); heteroleptic $Pd_4\mathbf{L^{F2}}_4\mathbf{L^{S10}}_4$ (600 MHz); ligand $\mathbf{L^{S10}}$ (600 MHz)(listed bottom to top).
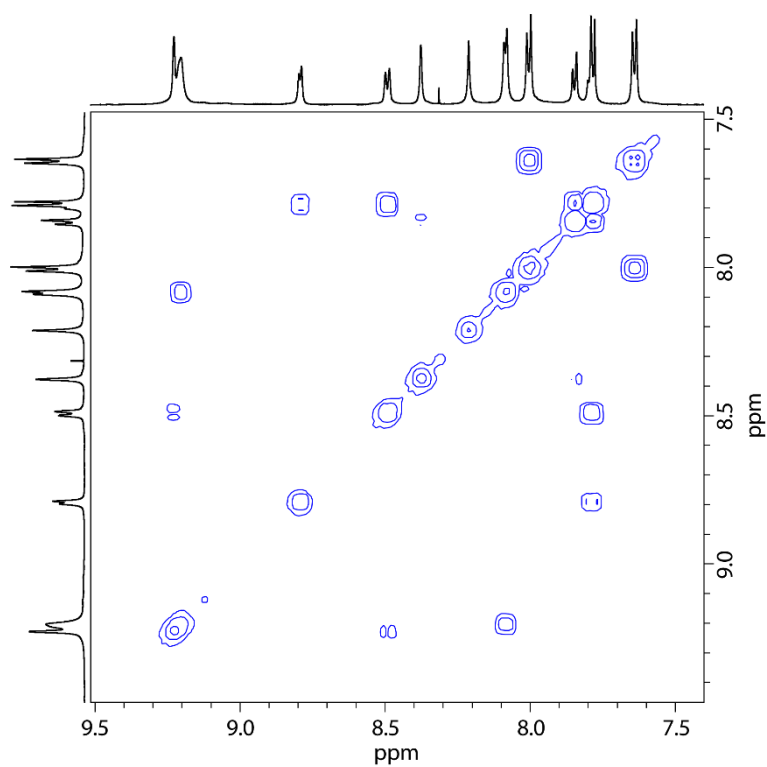
Figure 329: Partial ^{1}H-^{1}H COSY NMR spectrum (600 MHz, 298 K, DMSO-d_6) of $Pd_4\mathbf{L^{F2}}_4\mathbf{L^{S10}}_4$.

311
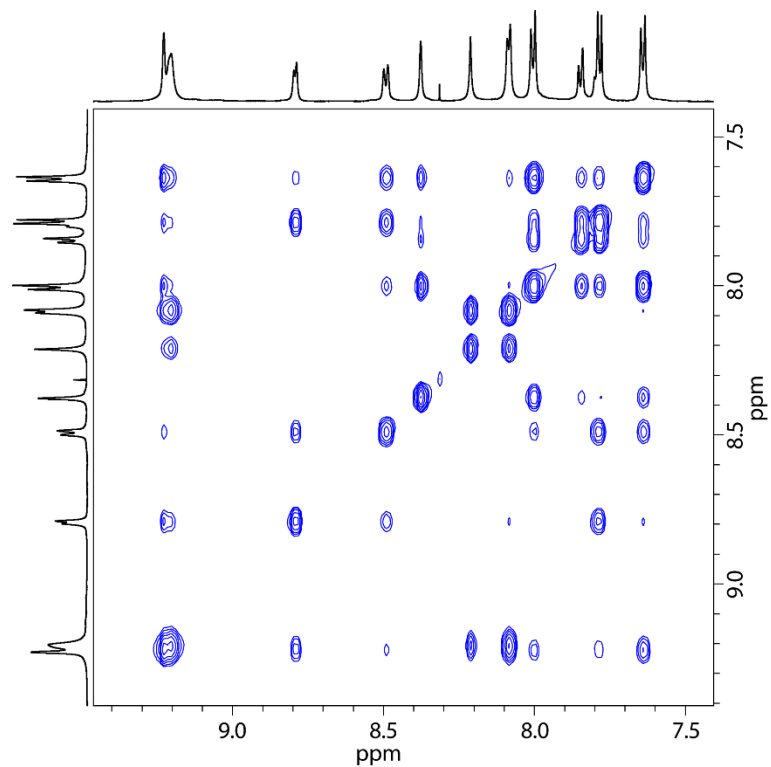
Figure 330: Partial ^{1}H-^{1}H NOESY NMR spectrum (600 MHz, 298 K, DMSO-d_6) of Pd$_4$L$^{F2}_4$L$^{S10}_4$.
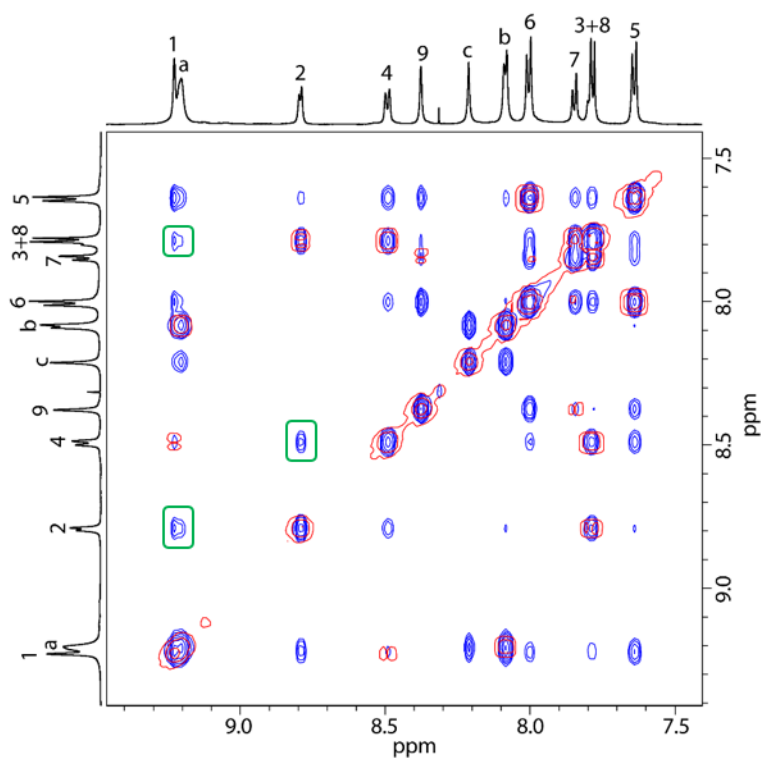
Figure 331: Partial ^{1}H-^{1}H COSY NMR spectrum (600 MHz, 298 K, DMSO-d_6, red) overlayed with a partial ^{1}H-^{1}H NOESY NMR spectrum (600 MHz, 298 K, DMSO-d_6, blue) of Pd$_4$L$^{F2}_4$L$^{S10}_4$ inclusing proton assignments.

$$D = 6.174 \pm 0.004 \cdot 10^{-11}\ m^2 \cdot s^{-1}$$
$$r_H = 17.766 \pm 0.012\ \text{Å}$$
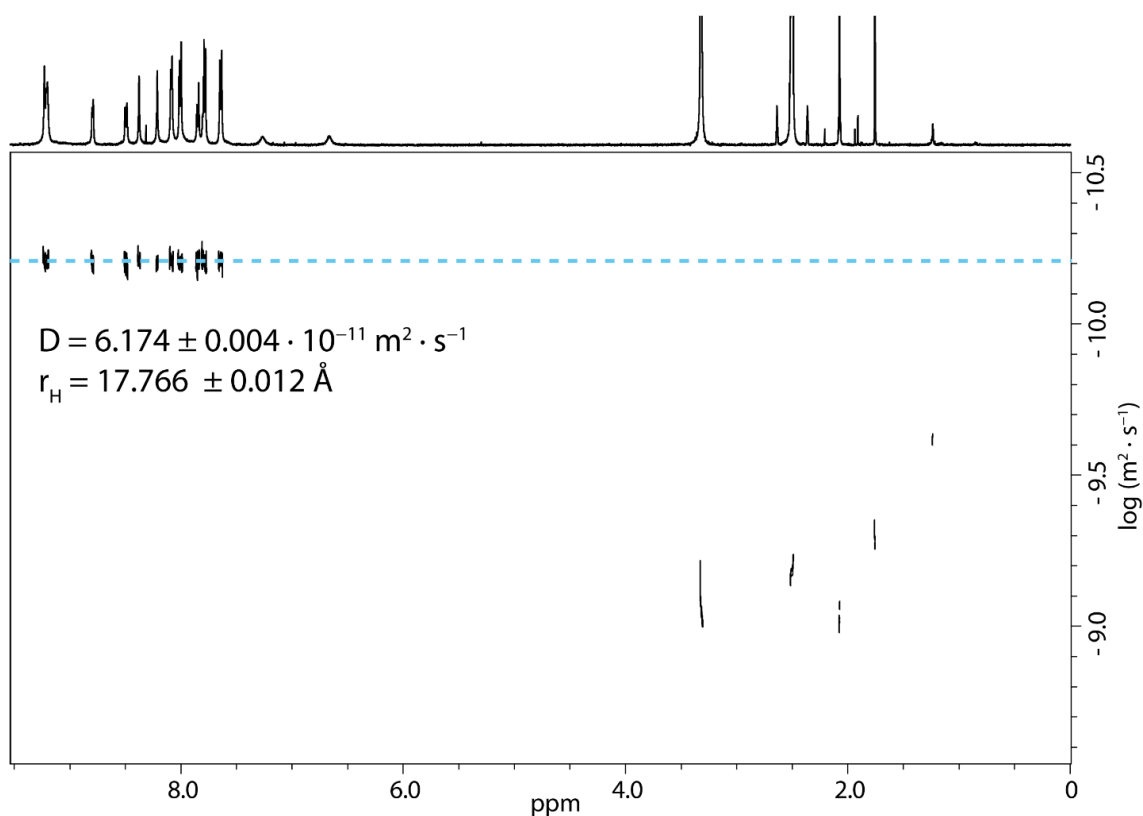
Figure 332: ^{1}H DOSY NMR spectrum (500 MHz, 298 K, DMSO-d_6) of Pd$_4$**L^{F2}**$_4$**L^{S10}**$_4$. Values for diffusion coefficient and resulting hydrodynamic radius are given.
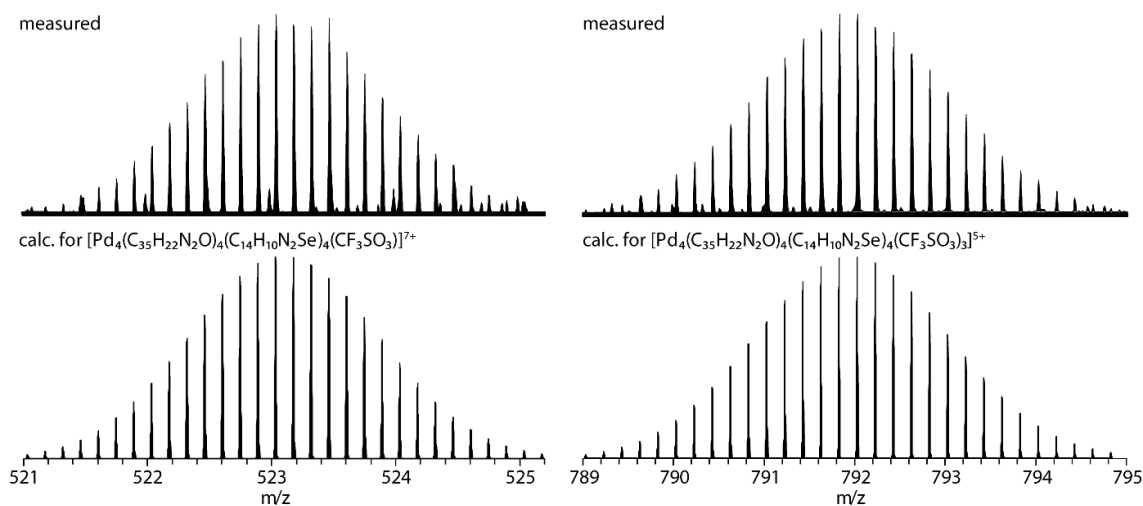
Figure 333: Partial ESI-MS spectrum of Pd$_4$**L^{F2}**$_4$**L^{S10}**$_4$. Neither species with a nuclearity of n = 3 nor of n = 5 could be detected. Cryo-source measurement did not yield better results.

3.4.7.3 Photophysical Characterization

a)

b)
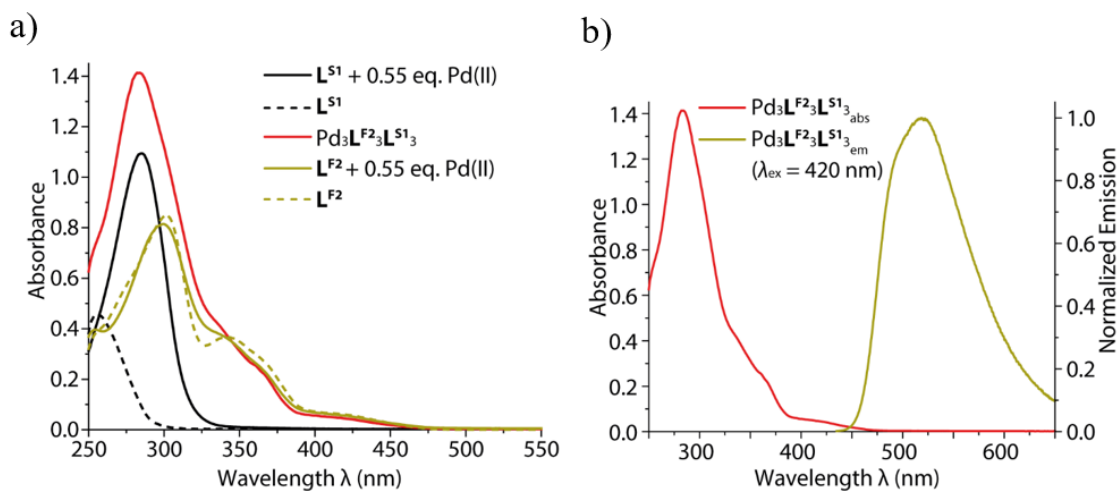
Figure 334: a) UV/VIS spectra of L^{S1}, L^{S1} upon addition of 0.55 equiv. Pd(II), heteroleptic Pd$_3$L$^{F2}_3$L$^{S1}_3$, L^{F2} and L^{F2} upon addition of 0.55 equiv. Pd(II), b) absorbance and normalized emission of heteroleptic Pd$_3$L$^{F2}_3$L$^{S1}_3$.
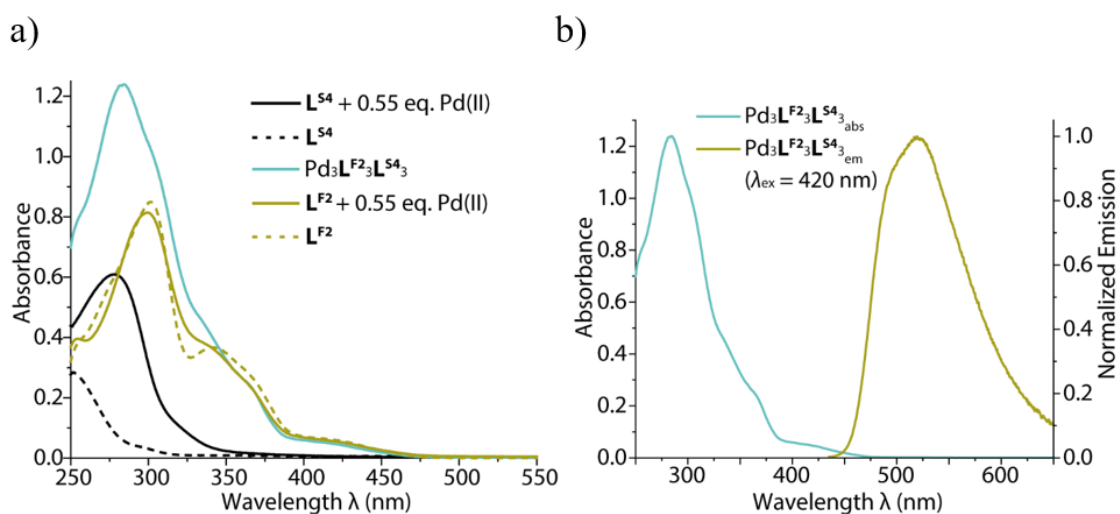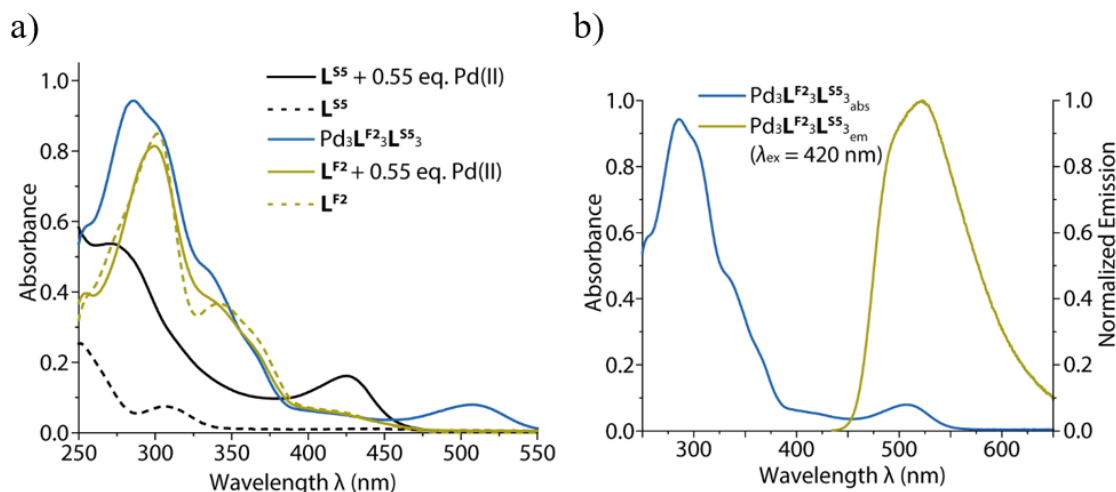
a)

b)
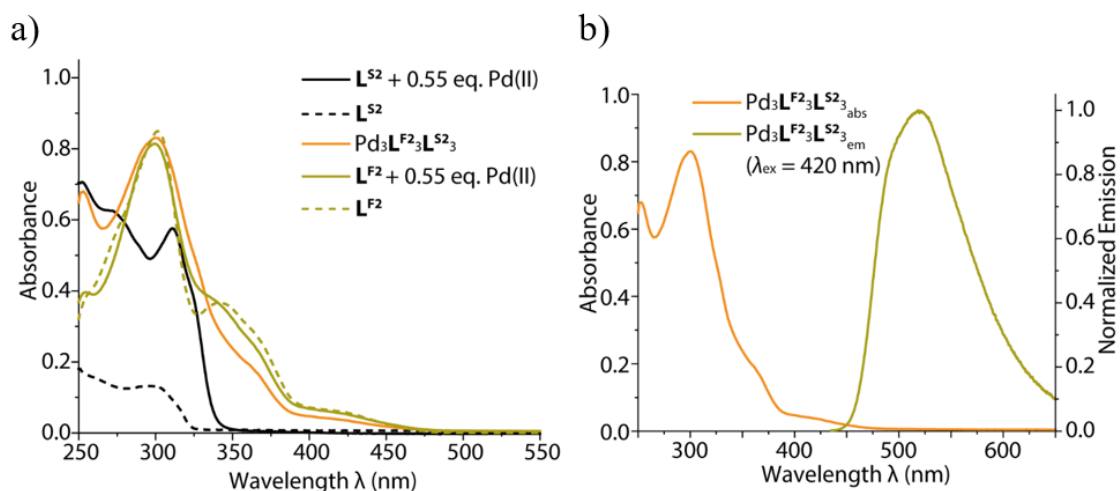
Figure 335: a) UV/VIS spectra of L^{S2}, L^{S2} upon addition of 0.55 equiv. Pd(II), heteroleptic Pd$_3$L$^{F2}_3$L$^{S2}_3$, L^{F2} and L^{F2} upon addition of 0.55 equiv. Pd(II), b) absorbance and normalized emission of heteroleptic Pd$_3$L$^{F2}_3$L$^{S2}_3$.
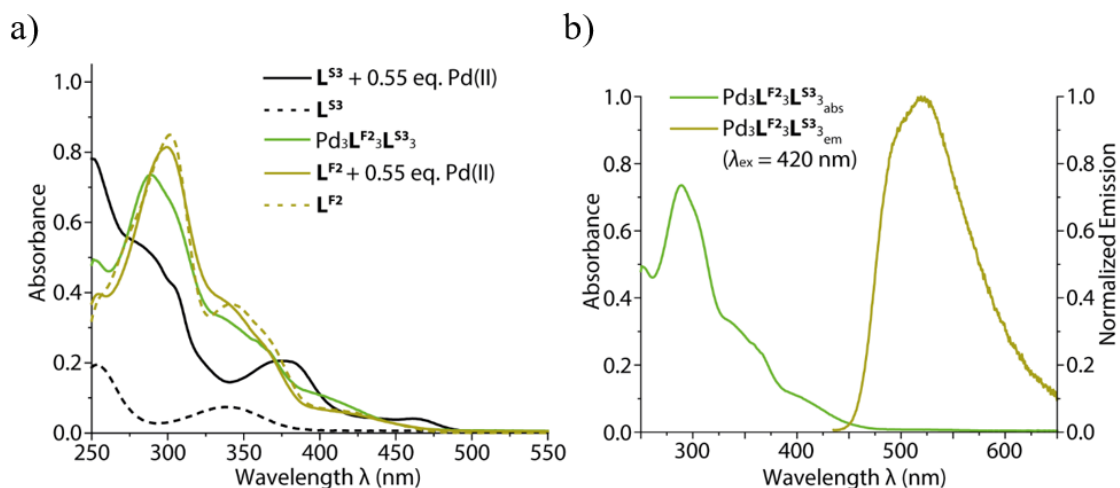
Figure 336: a) UV/VIS spectra of **L**^{S3}, **L**^{S3} upon addition of 0.55 equiv. Pd(II), heteroleptic Pd$_3$**L**$^{F2}_3$**L**$^{S3}_3$, **L**^{F2} and **L**^{F2} upon addition of 0.55 equiv. Pd(II), b) absorbance and normalized emission of heteroleptic Pd$_3$**L**$^{F2}_3$**L**$^{S3}_3$.

Figure 337: a) UV/VIS spectra of **L**^{S4}, **L**^{S4} upon addition of 0.55 equiv. Pd(II), heteroleptic Pd$_3$**L**$^{F2}_3$**L**$^{S4}_3$, **L**^{F2} and **L**^{F2} upon addition of 0.55 equiv. Pd(II), b) absorbance and normalized emission of heteroleptic Pd$_3$**L**$^{F2}_3$**L**$^{S4}_3$.

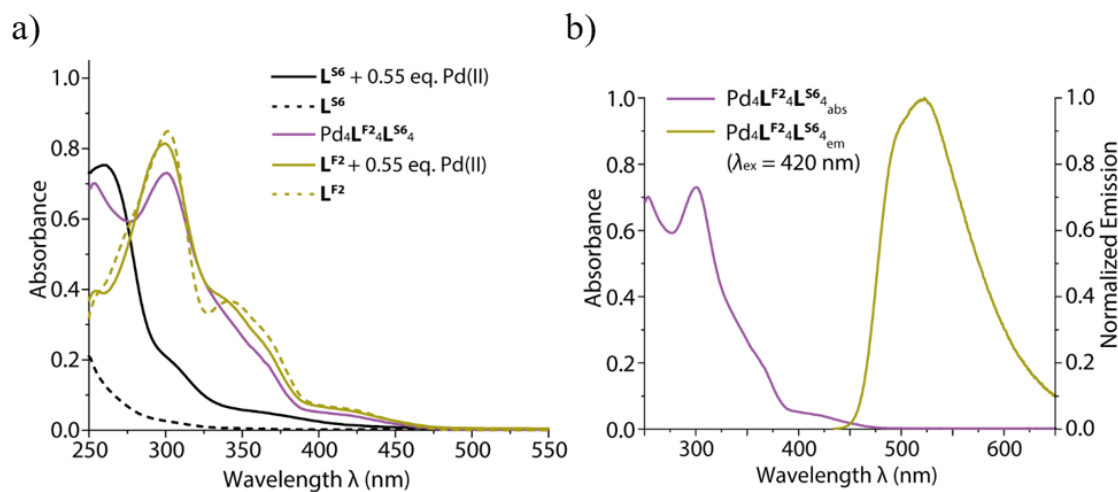Figure 338: a) UV/VIS spectra of L^{S5}, L^{S5} upon addition of 0.55 equiv. Pd(II), heteroleptic $Pd_3L^{F2}_3L^{S5}_3$, L^{F2} and L^{F2} upon addition of 0.55 equiv. Pd(II), b) absorbance and normalized emission of heteroleptic $Pd_3L^{F2}_3L^{S5}_3$.
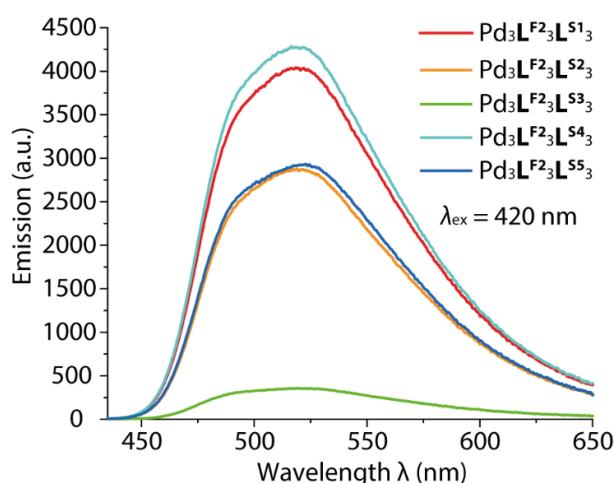
Figure 339: Absolute emission measured of $Pd_3L^{F2}_3L^{S1\text{-}5}_3$. Measurement parameters were kept constant throughout the test series.

Table 13: Quantum yield values measured for all species with nuclearity n = 3 ($Pd_3L^{F2}_3L^{S1\text{-}5}_3$) and the fluorescent ligand L^{F2} (λ_{ex} = 420 nm). Chromophore concentration c = 0.14 mM.

Structure	Quantum Yield (%)
L^{F2}	13.406
$Pd_nL^{F2}_{2n}$ (n = 2-5)	0.824
$Pd_3L^{F2}_3L^{S1}_3$	1.102
$Pd_3L^{F2}_3L^{S2}_3$	0.835
$Pd_3L^{F2}_3L^{S3}_3$	0.256
$Pd_3L^{F2}_3L^{S4}_3$	1.122
$Pd_3L^{F2}_3L^{S5}_3$	0.920

Figure 340: a) UV/VIS spectra of L^{S6}, L^{S6} upon addition of 0.55 equiv. Pd(II), heteroleptic $Pd_4L^{F2}_4L^{S6}_4$, L^{F2} and L^{F2} upon addition of 0.55 equiv. Pd(II), b) absorbance and normalized emission of heteroleptic $Pd_4L^{F2}_4L^{S6}_4$.
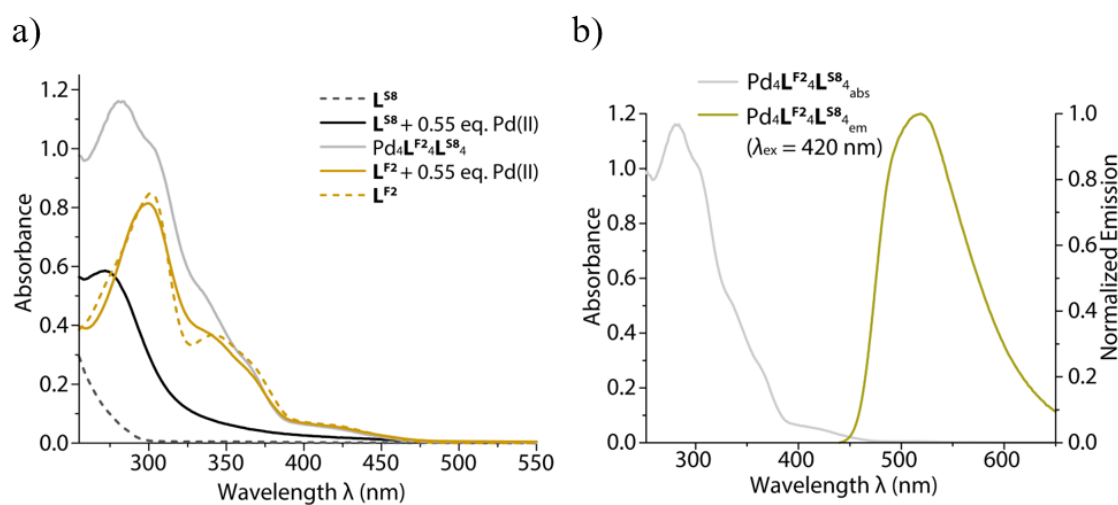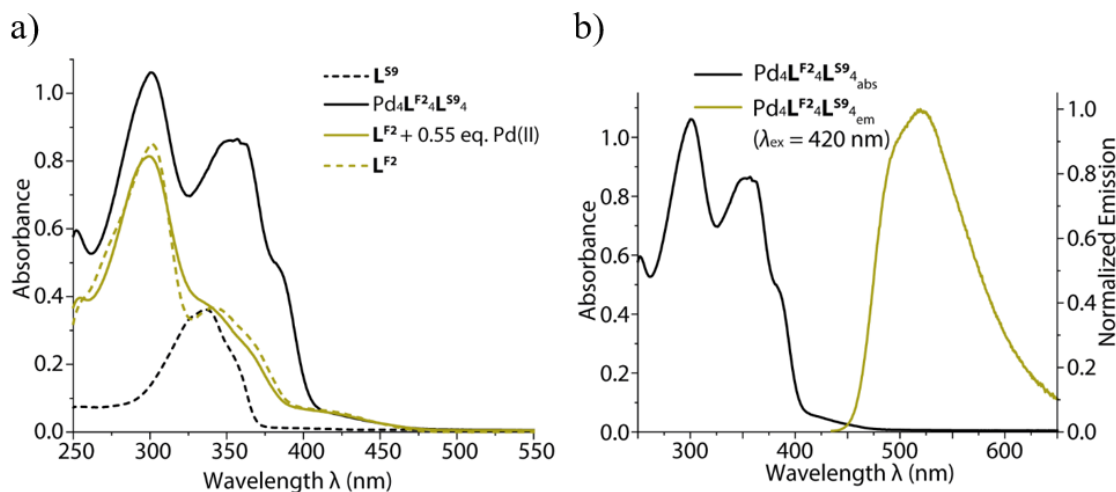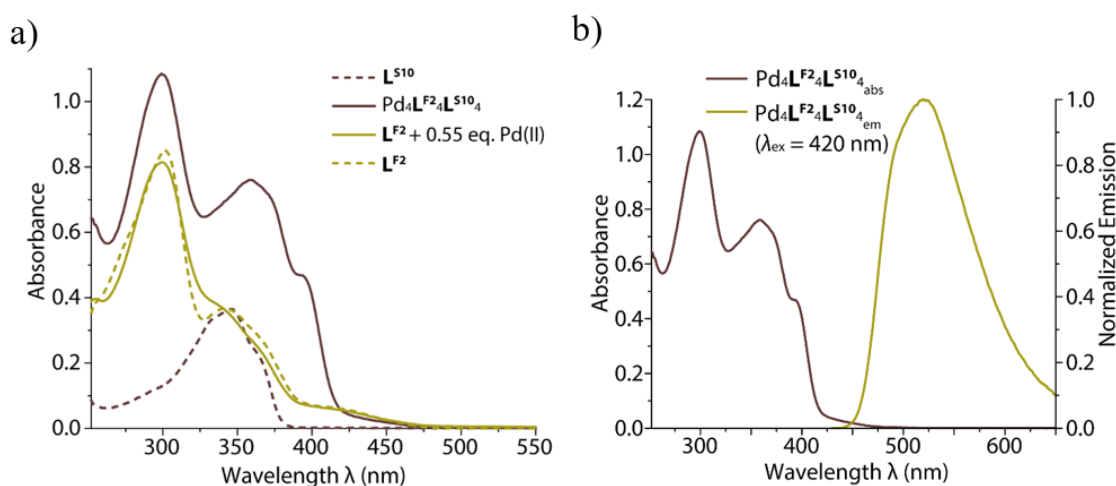

Figure 341: a) UV/VIS spectra of L^{S8}, L^{S8} upon addition of 0.55 equiv. Pd(II), heteroleptic $Pd_4L^{F2}_4L^{S8}_4$, L^{F2} and L^{F2} upon addition of 0.55 equiv. Pd(II), b) absorbance and normalized emission of heteroleptic $Pd_4L^{F2}_4L^{S8}_4$.

Figure 342: a) UV/VIS spectra of L^{S9}, heteroleptic $Pd_4L^{F2}_4L^{S9}_4$, L^{F2} and L^{F2} upon addition of 0.55 equiv. Pd(II), b) absorbance and normalized emission of heteroleptic $Pd_4L^{F2}_4L^{S9}_4$.

Figure 343: a) UV/VIS spectra of L^{S10}, heteroleptic $Pd_4L^{F2}_4L^{S10}_4$, L^{F2} and L^{F2} upon addition of 0.55 equiv. Pd(II), b) absorbance and normalized emission of heteroleptic $Pd_4L^{F2}_4L^{S10}_4$.

3.4.7.4 Host Guest Chemistry

3.4.7.4.1 Chiral Guests **G$^{1-3}$**

G^1 – *(R)*-BINSO
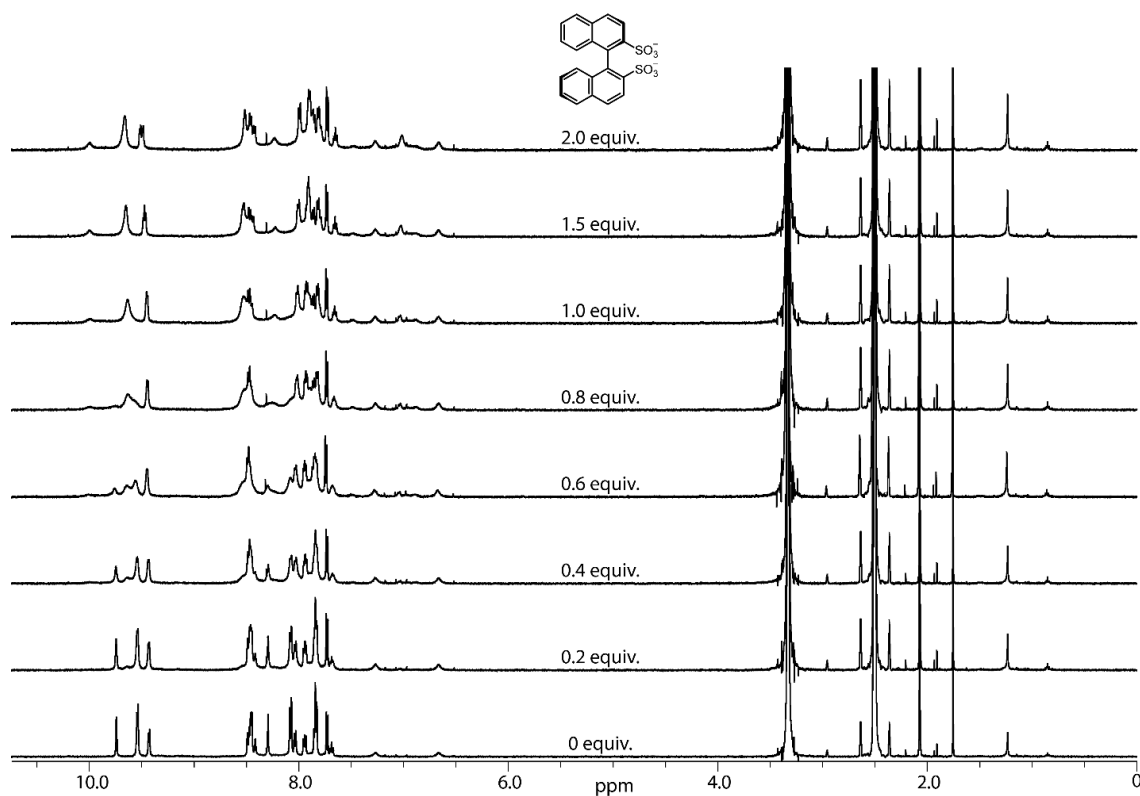
Figure 344: Full ^{1}H NMR spectra (500 MHz, 298 K, DMSO-d_6) of the titration of (*R*)-BINSO (**G^1**) to Pd$_3$**L^{F2}**$_3$**L^{S1}**$_3$.
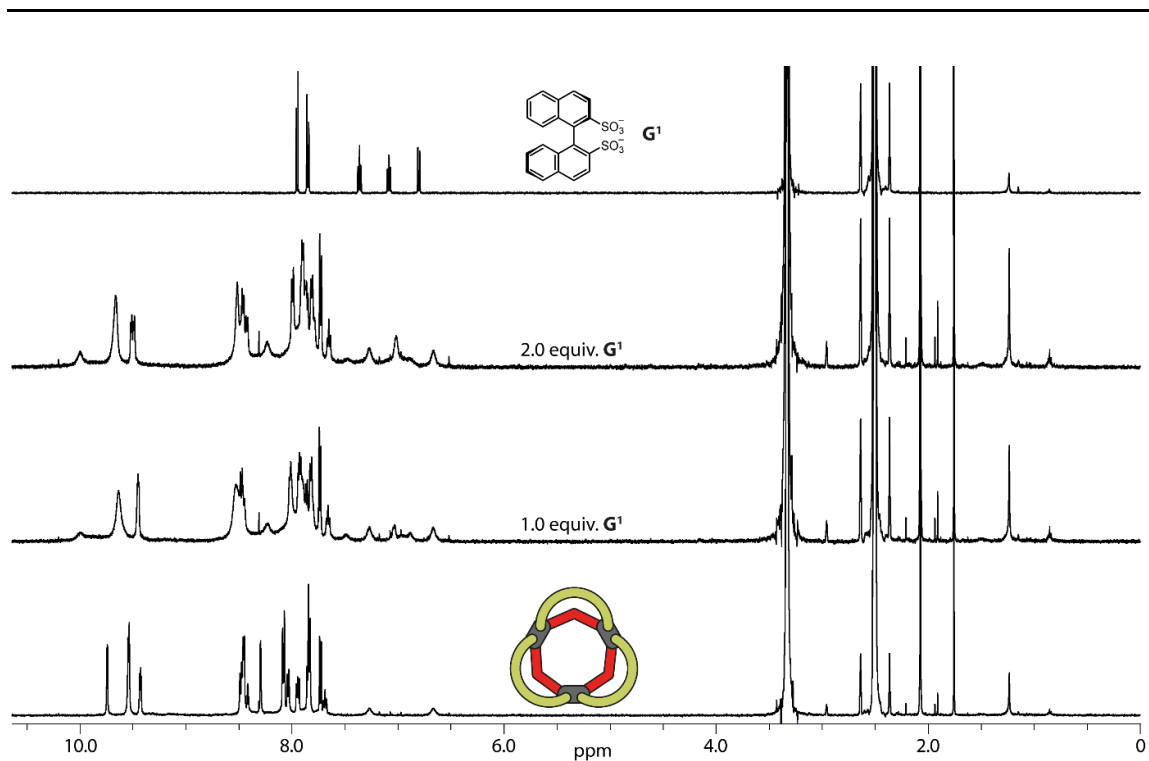
Figure 345: Full ^{1}H NMR spectra (500 MHz, 298 K, DMSO-d_6) of Pd$_3$L$^{F2}_3$L$^{S1}_3$; Pd$_3$L$^{F2}_3$L$^{S1}_3$ with 1 equiv. **G^1**; Pd$_3$L$^{F2}_3$L$^{S1}_3$ with 2 equiv. **G^1** and **G^1** (bottom to top).
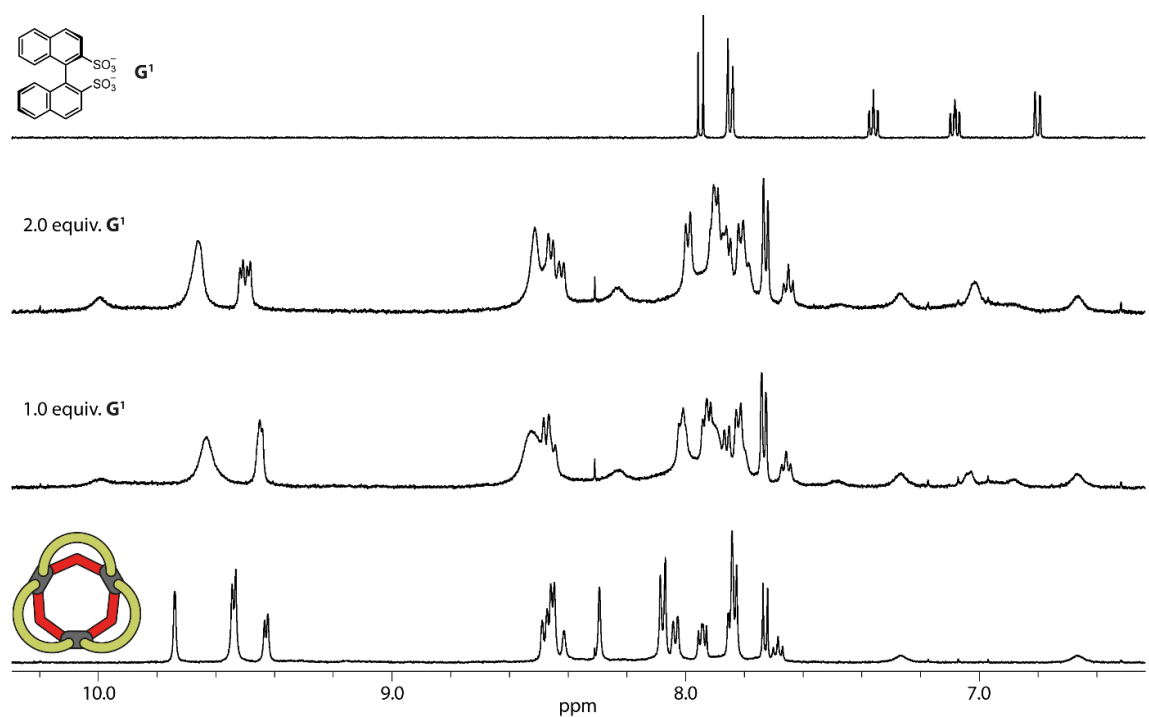
Figure 346: Partial ^{1}H NMR spectra (500 MHz, 298 K, DMSO-d_6) of Pd$_3$L$^{F2}_3$L$^{S1}_3$; Pd$_3$L$^{F2}_3$L$^{S1}_3$ with 1 equiv. **G^1**; Pd$_3$L$^{F2}_3$L$^{S1}_3$ with 2 equiv. **G^1** and **G^1** (bottom to top).

320

Figure 347: CSI-MS spectrum of $[Pd_3L^{F2}_3L^{S1}_3]^{(6-x)+}$ (x = 1;2) after addition of 1 equiv. G^1. Observed and calculated pattern for $[G^1@Pd_3L^{F2}_3L^{S1}_3 + CF_3SO_3]^{3+}$ is shown in the inset.
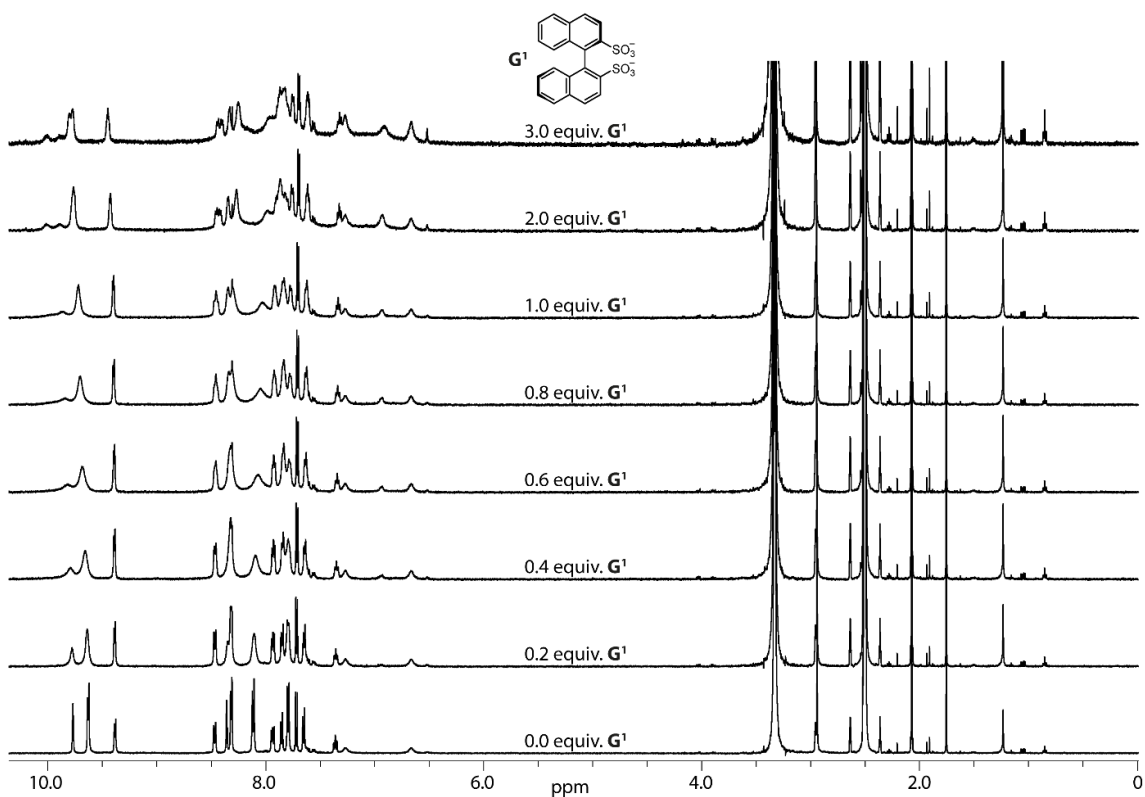

Figure 348: Full ^{1}H NMR spectra (500 MHz, 298 K, DMSO-d_6) of the titration of (R)-BINSO (G^1) to $Pd_3L^{F2}_3L^{S4}_3$.
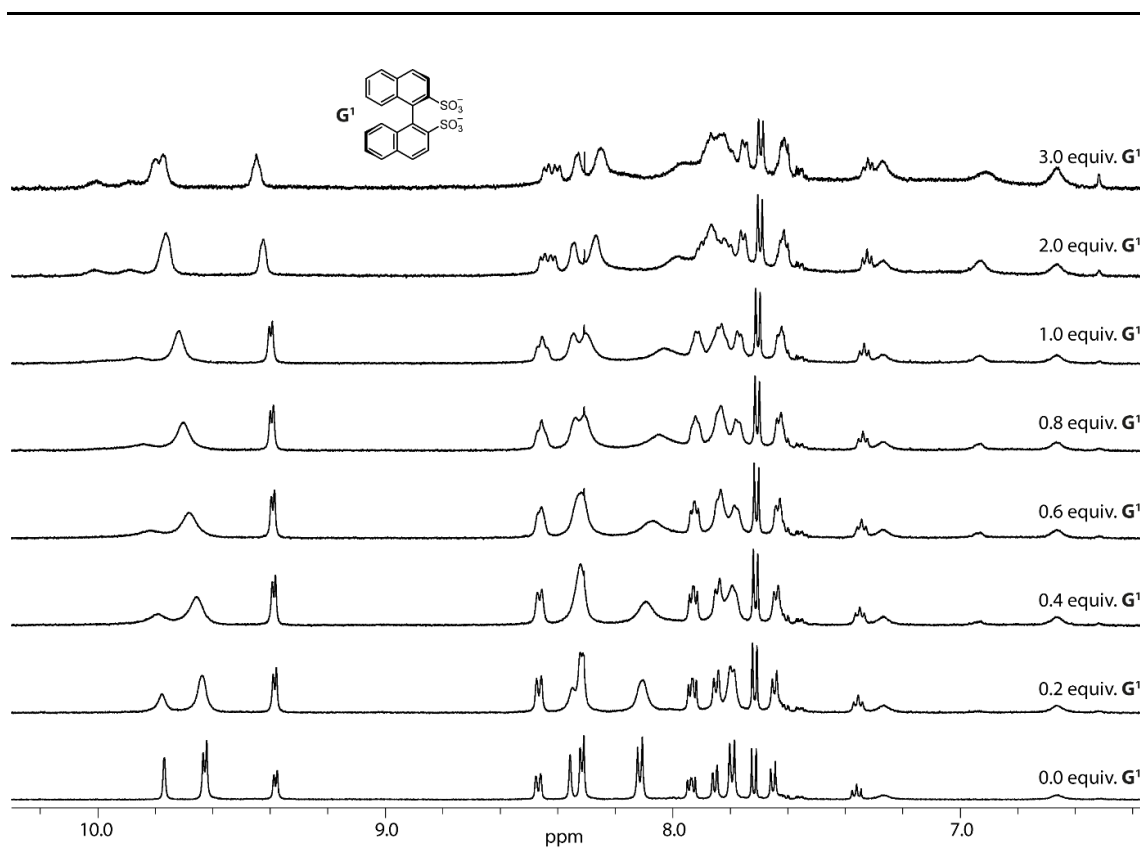
Figure 349: Partial ^{1}H NMR spectra (500 MHz, 298 K, DMSO-d_6) of the titration of (*R*)-BINSO (**G^1**) to Pd$_3$**L^{F2}**$_3$**L^{S4}**$_3$.
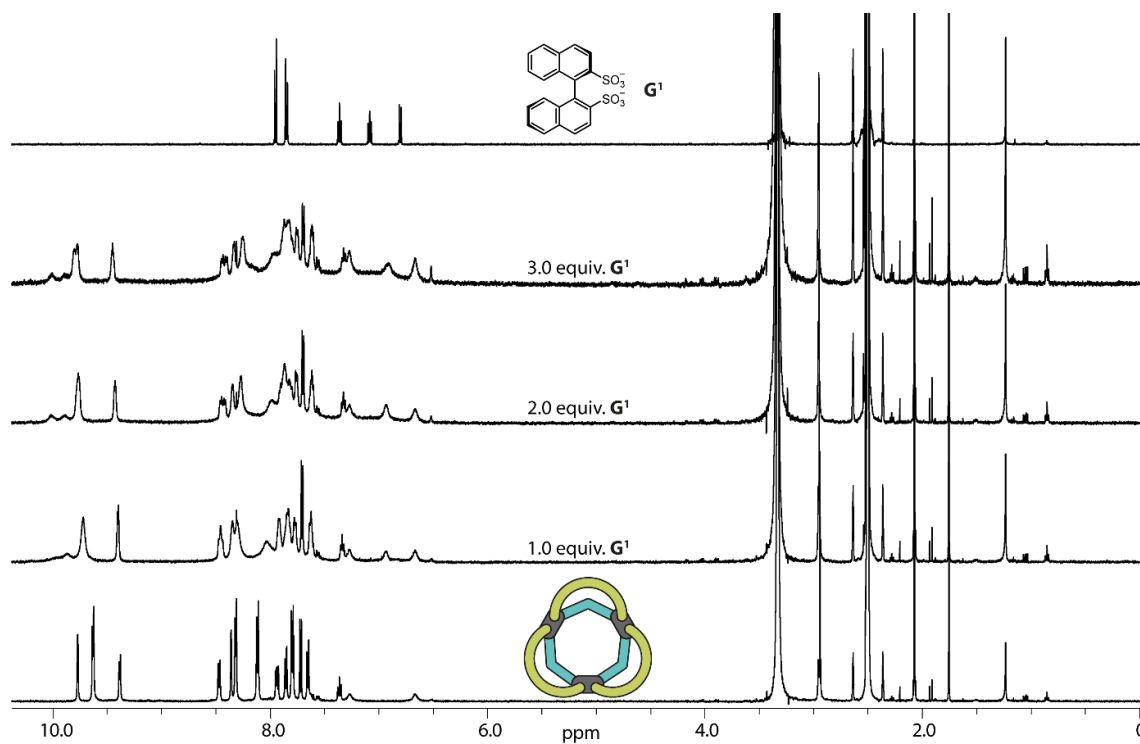
Figure 350: Partial ^{1}H NMR spectra (500 MHz, 298 K, DMSO-d_6) of Pd$_3$**L^{F2}**$_3$**L^{S4}**$_3$; Pd$_3$**L^{F2}**$_3$**L^{S4}**$_3$ with 1 equiv. **G^1**; Pd$_3$**L^{F2}**$_3$**L^{S4}**$_3$ with 2 equiv. **G^1**; Pd$_3$**L^{F2}**$_3$**L^{S4}**$_3$ with 3 equiv. **G^1** and **G^1** (bottom to top).

322
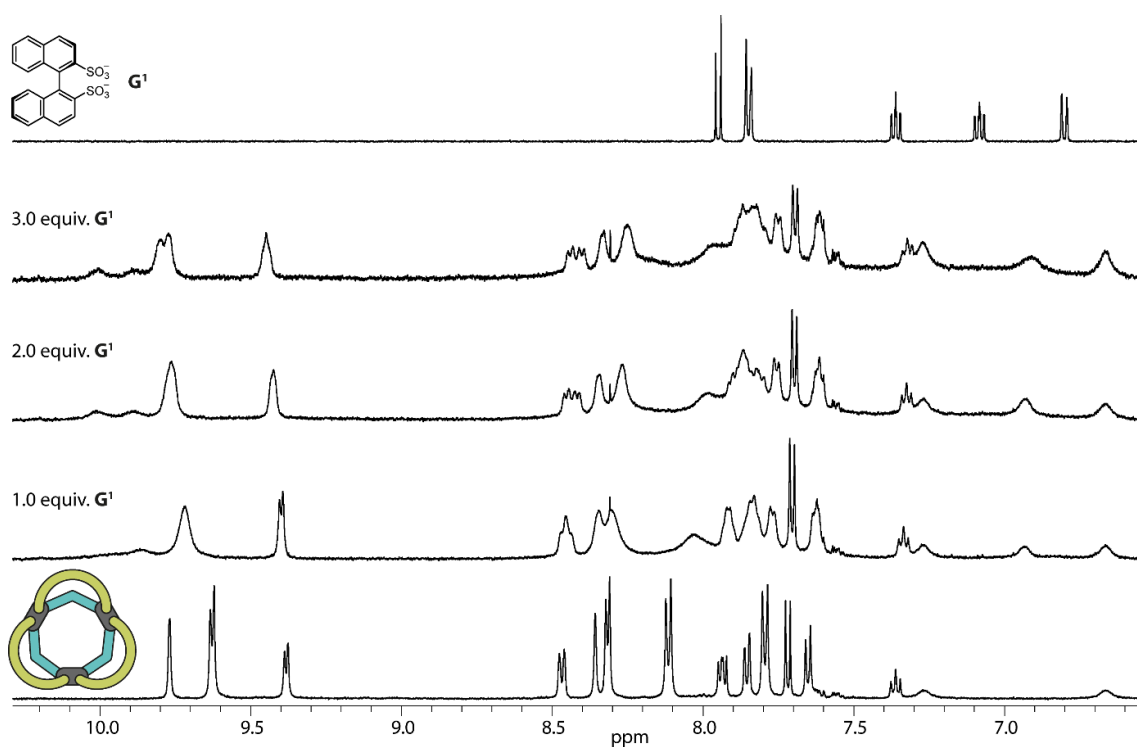
Figure 351: Partial ^{1}H NMR spectra (500 MHz, 298 K, DMSO-d_6) of Pd$_3$L$^{F2}_3$L$^{S4}_3$; Pd$_3$L$^{F2}_3$L$^{S4}_3$ with 1 equiv. **G^1**; Pd$_3$L$^{F2}_3$L$^{S4}_3$ with 2 equiv. **G^1**; Pd$_3$L$^{F2}_3$L$^{S4}_3$ with 3 equiv. **G^1** and **G^1** (bottom to top).

Binding constant K = 139.19 ± 6.53 M^{-1}
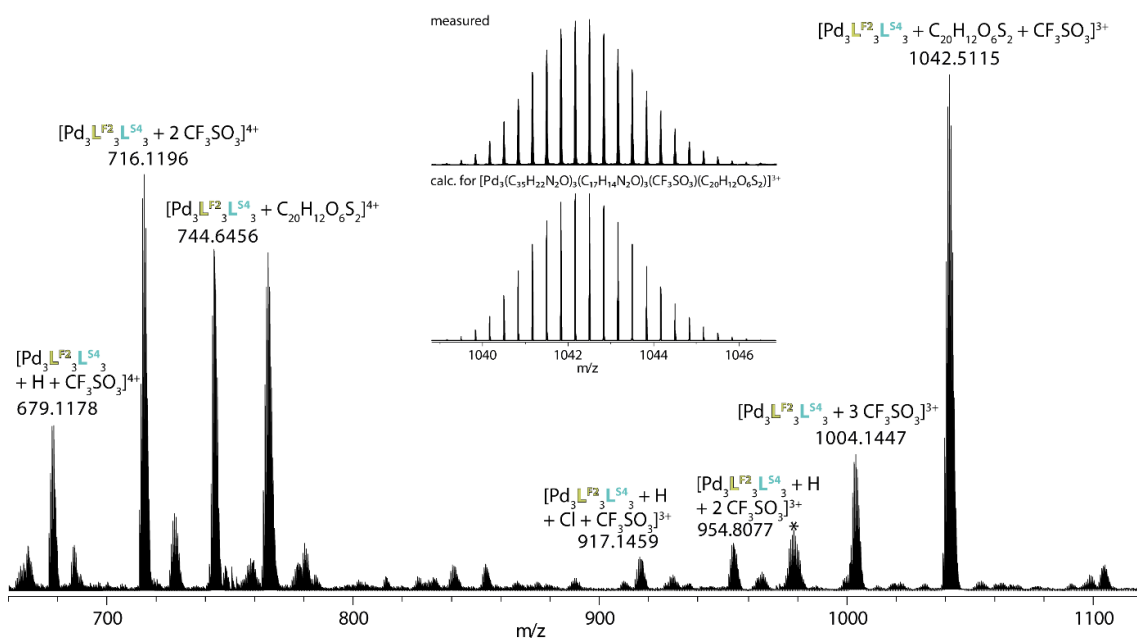
Figure 352: ESI-MS spectrum of [Pd$_3$L$^{F2}_3$L$^{S4}_3$]$^{(6-x)+}$ (x = 1-3) after addition of 1 equiv. **G^1**. Observed and calculated pattern for [**G^1**@Pd$_3$L$^{F2}_3$L$^{S4}_3$ + CF$_3$SO$_3$]$^{3+}$ is shown in the inset.
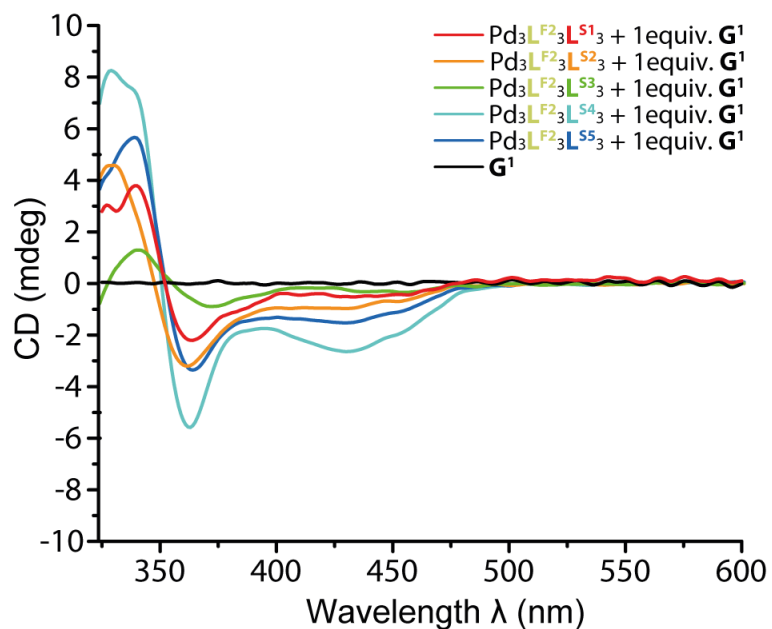
Figure 353: Circular dichroism of $\mathbf{G^1}$ and $Pd_3\mathbf{L^{F2}}_3\mathbf{L^{S1\text{-}5}}_3$ after addition of 1 equiv. $\mathbf{G^1}$ each. Chromophore concentration $c = 0.14$mM. All spectra smoothed using Sawitzki-Golay method with a factor of 10.

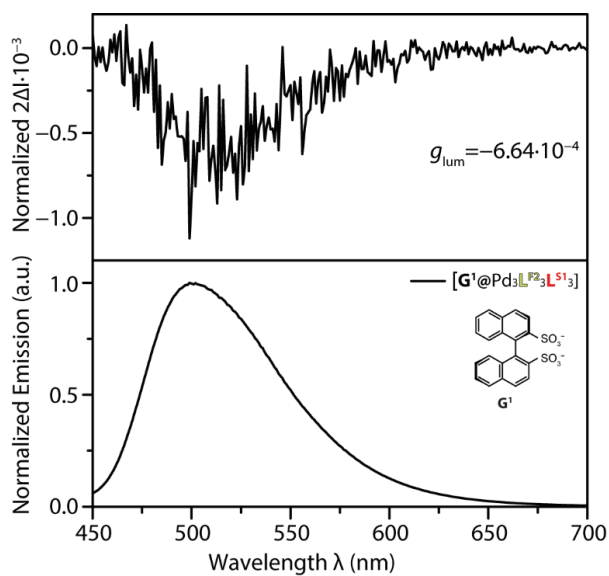Figure 354: Normalized emission and CPL signal of $Pd_3\mathbf{L^{F2}}_3\mathbf{L^{S1}}_3$ after addition of 1 equiv. $\mathbf{G^1}$. Exited at $\lambda = 365$ nm.
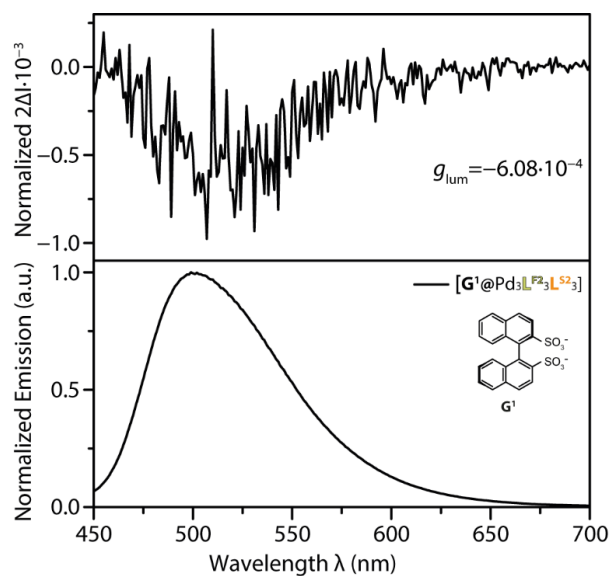
Figure 355: Normalized emission and CPL signal of $Pd_3L^{F2}_3L^{S2}_3$ after addition of 1 equiv. **G¹**. Exited at $\lambda = 365$ nm.

Figure 356: Normalized emission and CPL signal of $Pd_3L^{F2}_3L^{S3}_3$ after addition of 1 equiv. **G¹**. Exited at $\lambda = 365$ nm.

Figure 357: Normalized emission and CPL signal of Pd$_3$L$^{F2}_3$L$^{S4}_3$ after addition of 1 equiv. **G^1**. Exited at λ = 365 nm.
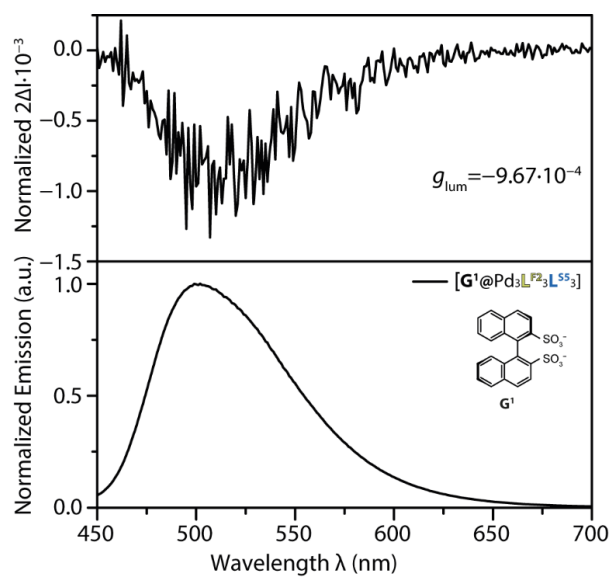
Figure 358: Normalized emission and CPL signal of Pd$_3$L$^{F2}_3$L$^{S5}_3$ after addition of 1 equiv. **G^1**. Exited at λ = 365 nm.
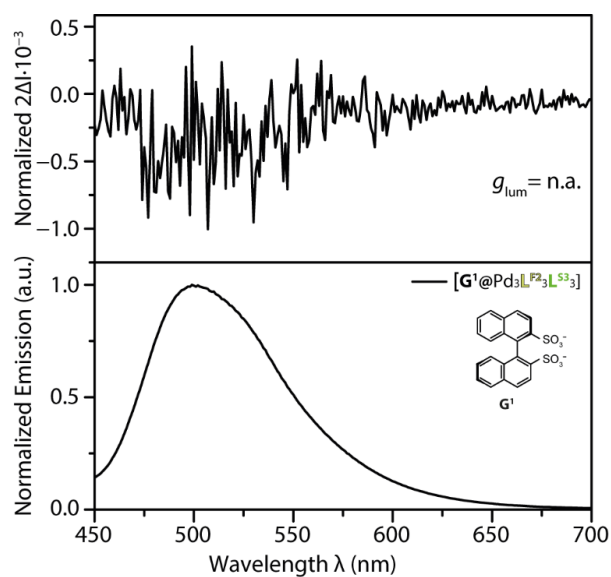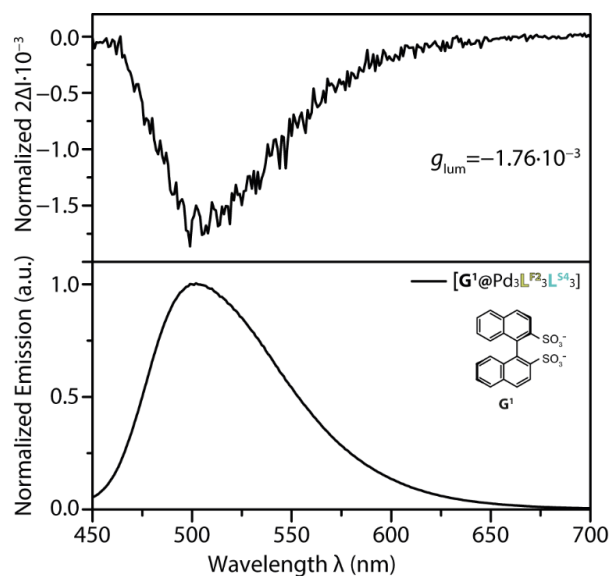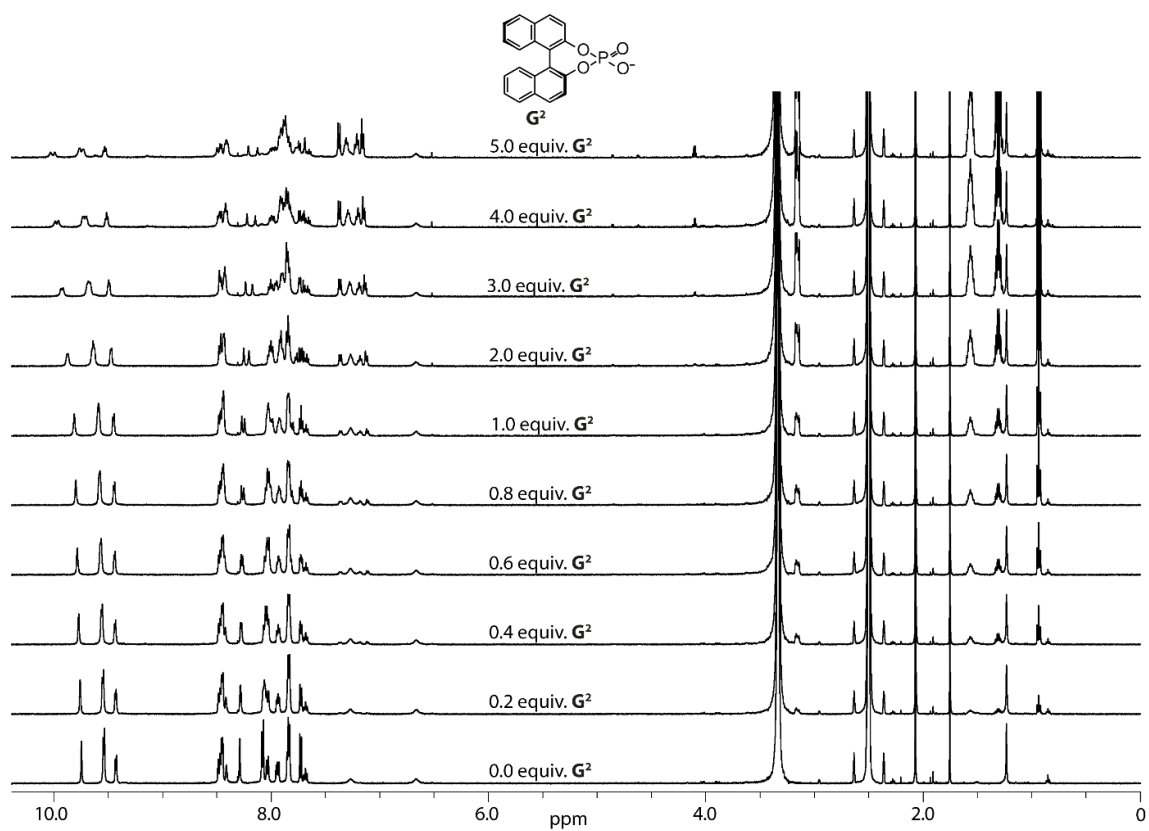
$\mathbf{G^2}$ – *(S)*-BINPHOS

Figure 359: Full ^{1}H NMR spectra (500 MHz, 298 K, DMSO-d_6) of the titration of (*S*)-BINPHOS ($\mathbf{G^2}$) to Pd$_3$L$^{F2}_3$L$^{S1}_3$.
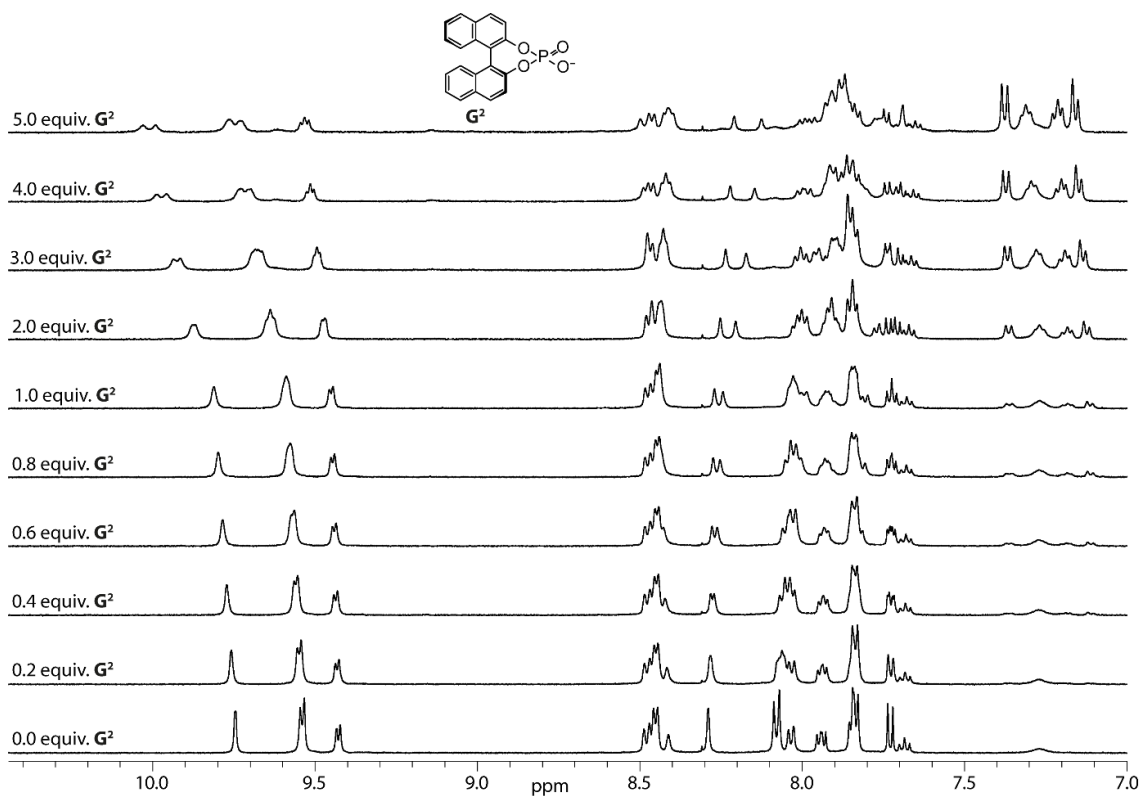
Figure 360: Partial ^{1}H NMR spectra (500 MHz, 298 K, DMSO-d_6) of the titration of (*S*)-BINPHOS (**G²**) to Pd₃**L**^{F2}₃**L**^{S1}₃.
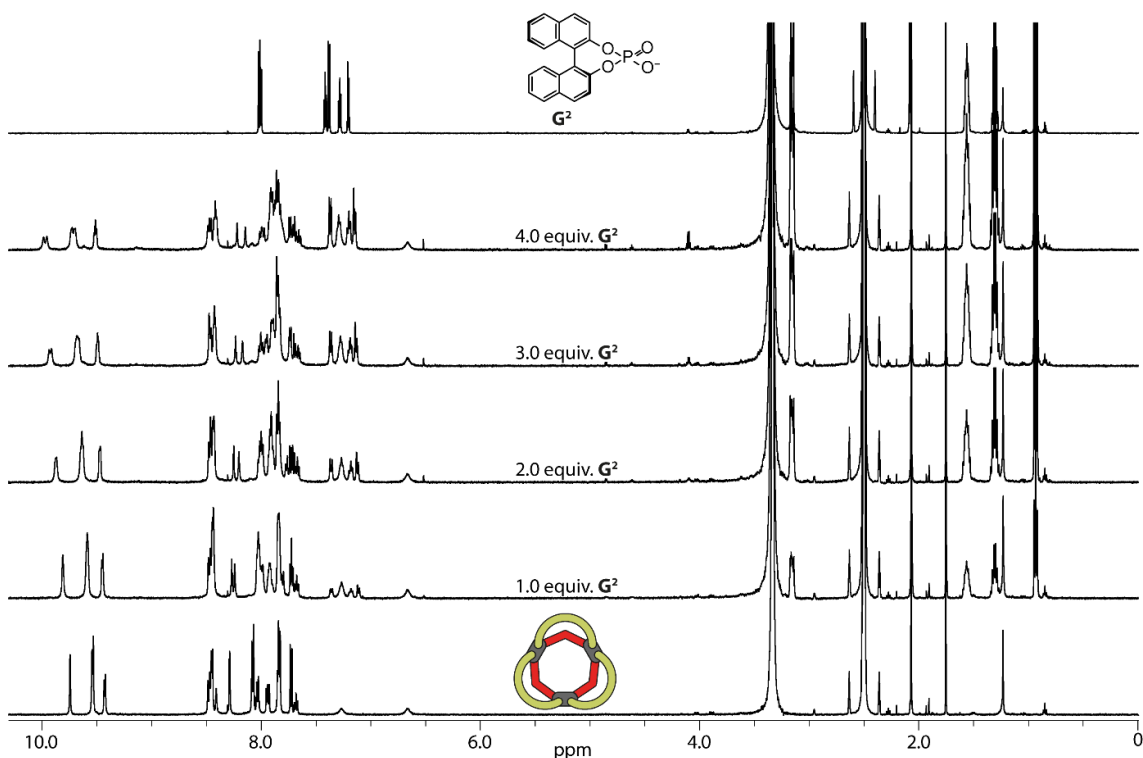
Figure 361: Full ^{1}H NMR spectra (500 MHz, 298 K, DMSO-d_6) of Pd₃**L**^{F2}₃**L**^{S1}₃; Pd₃**L**^{F2}₃**L**^{S1}₃ with 1 equiv. **G²**; Pd₃**L**^{F2}₃**L**^{S1}₃ with 2 equiv. **G²**; Pd₃**L**^{F2}₃**L**^{S1}₃ with 3 equiv. **G²**; Pd₃**L**^{F2}₃**L**^{S1}₃ with 4 equiv. **G²** and **G²** (bottom to top).
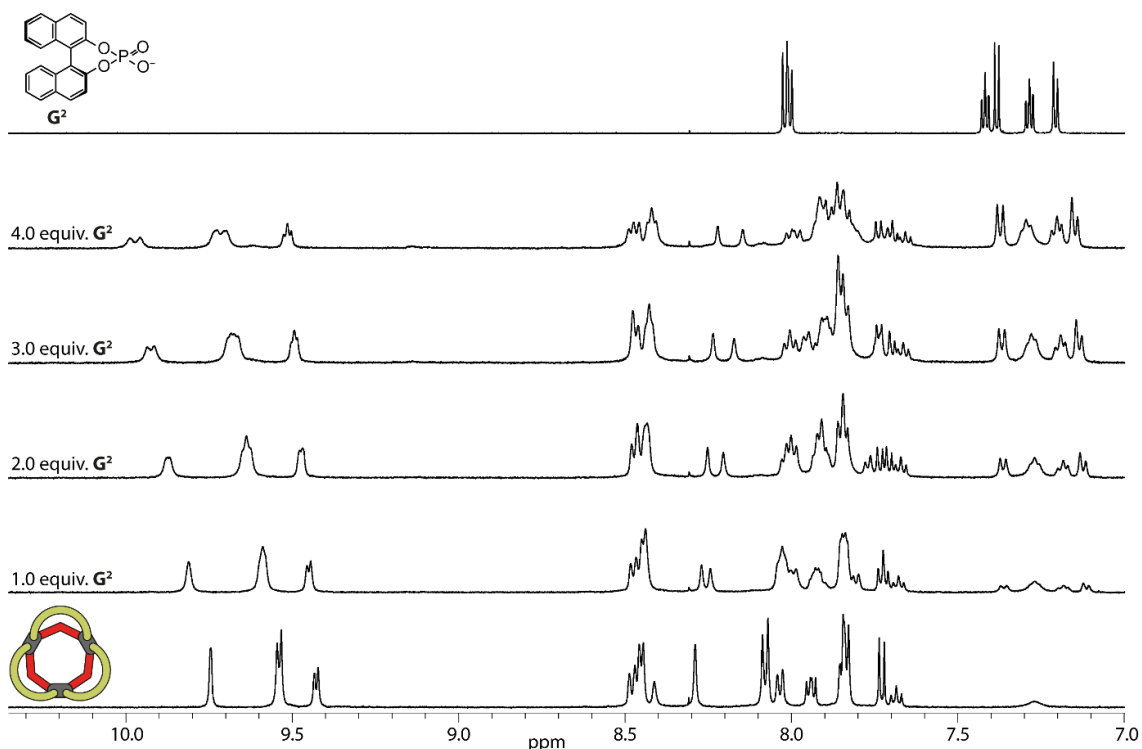
Figure 362: Partial ^{1}H NMR spectra (500 MHz, 298 K, DMSO-d_6) of Pd$_3$**L^{F2}**$_3$**L^{S1}**$_3$; Pd$_3$**L^{F2}**$_3$**L^{S1}**$_3$ with 1 equiv. **G^2**; Pd$_3$**L^{F2}**$_3$**L^{S1}**$_3$ with 2 equiv. **G^2**; Pd$_3$**L^{F2}**$_3$**L^{S1}**$_3$ with 3 equiv. **G^2**; Pd$_3$**L^{F2}**$_3$**L^{S1}**$_3$ with 4 equiv. **G^2** and **G^2** (bottom to top).

Binding constant K = 85.9 ± 0.96 M^{-1}
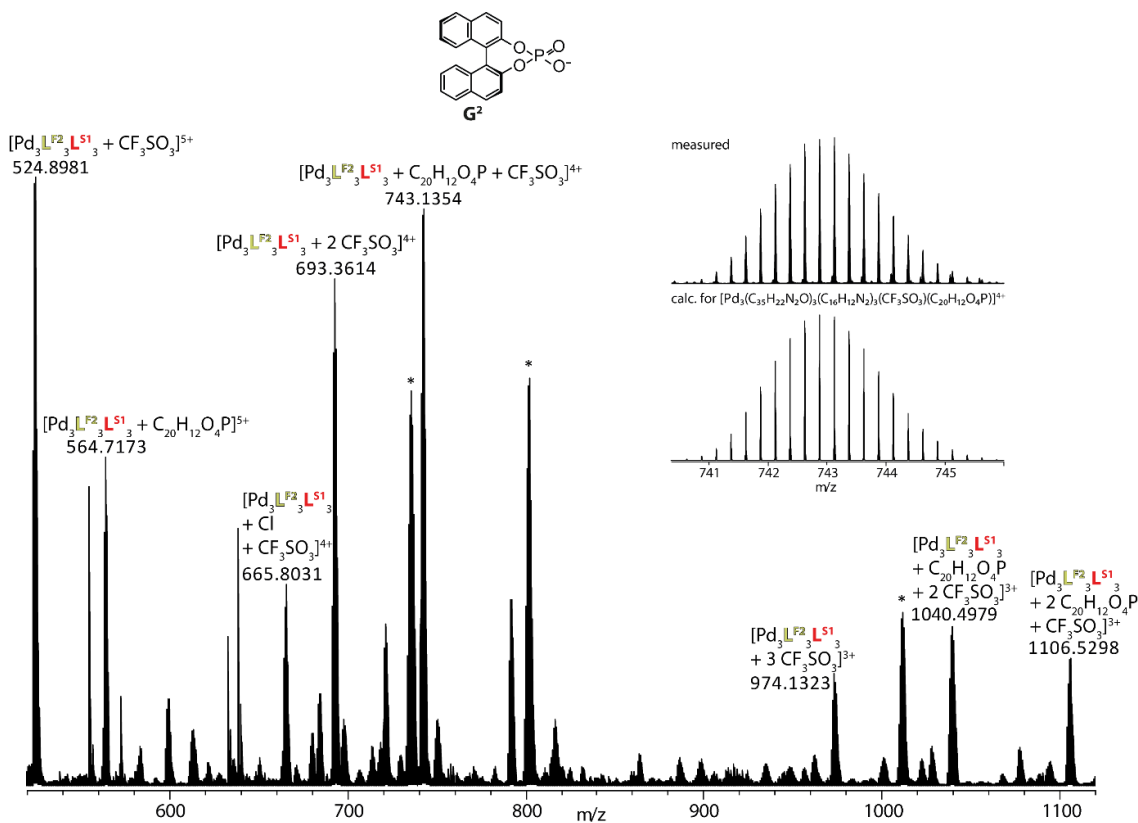
Figure 363: ESI-MS spectrum of [Pd$_3$**L^{F2}**$_3$**L^{S1}**$_3$]$^{(6-x)+}$ (x = 1-3) after addition of 1 equiv. **G^2**. Observed and calculated pattern for [**G^2**@Pd$_3$**L^{F2}**$_3$**L^{S1}**$_3$ + CF$_3$SO$_3$]$^{4+}$ is shown in the inset.

329
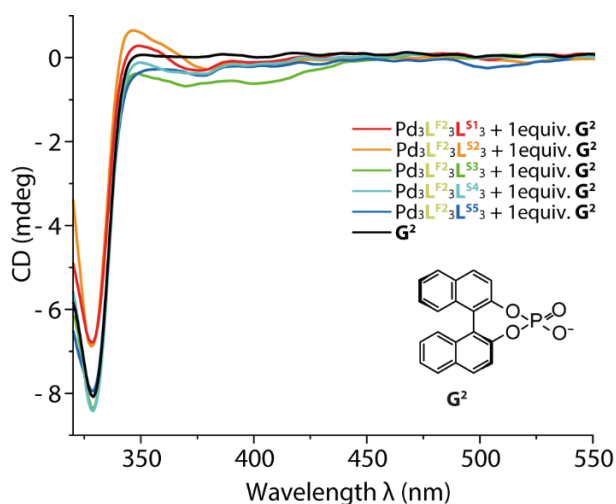
Figure 364: Circular dichroism of **G²** and Pd₃**L**^{F2}₃**L**$^{S1-5}$₃ after addition of 1 equiv. **G²** each. All spectra smoothed using Sawitzki-Golay method with a factor of 10.

G³ – *(R)*-Camphorsulfonate
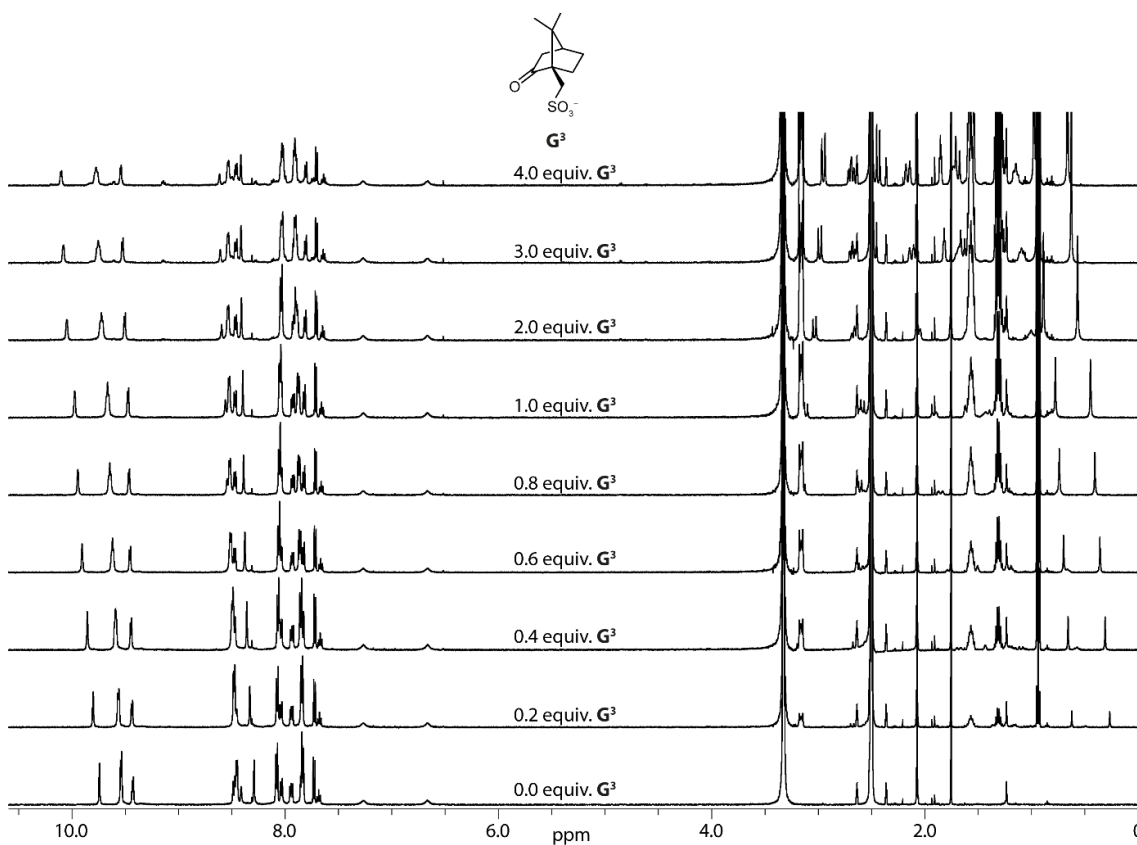
Figure 365: Full ¹H NMR spectra (500 MHz, 298 K, DMSO-*d₆*) of the titration of (*R*)-Camphorsulfonate (**G³**) to Pd₃**L**^{F2}₃**L**^{S1}₃.
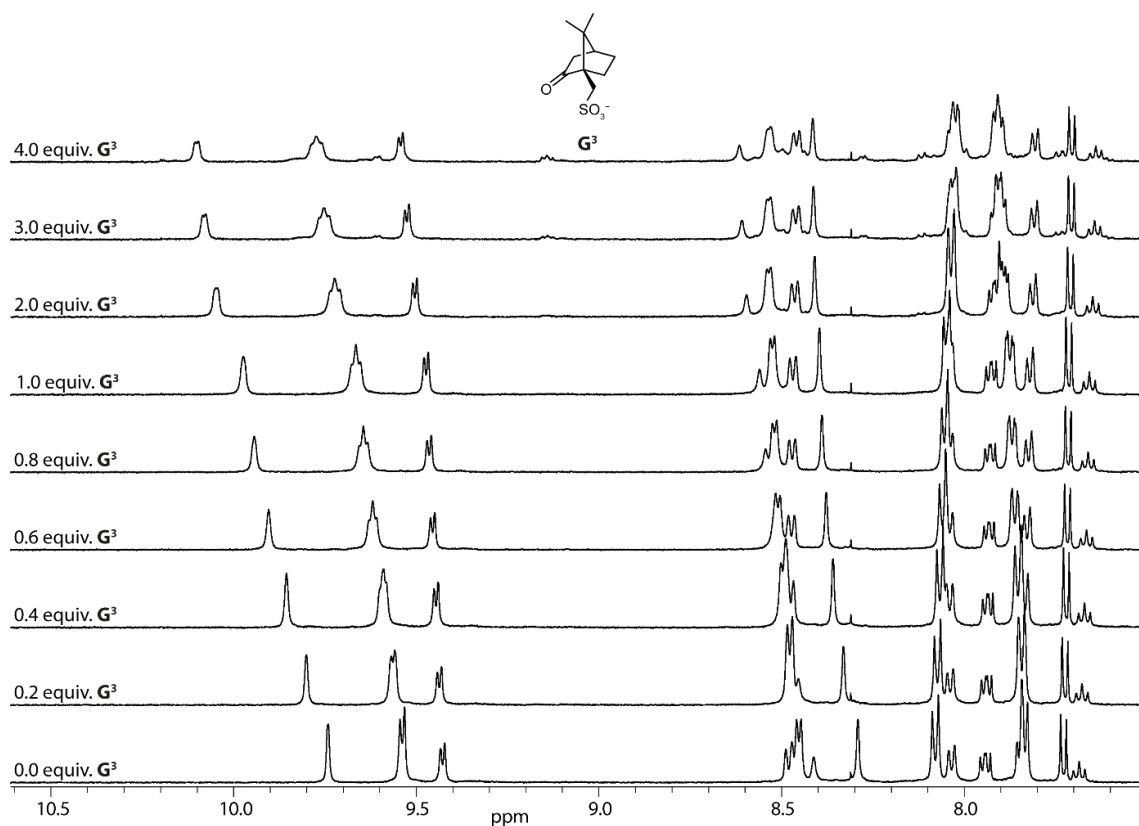
Figure 366: Partial ^{1}H NMR spectra (500 MHz, 298 K, DMSO-d_6) of the titration of (R)-Camphorsulfonate (**G^3**) to Pd$_3$**L$^{F2}_3$L$^{S1}_3$**.

Binding constant $K = 8472.76 \pm 963.79$ M^{-1}
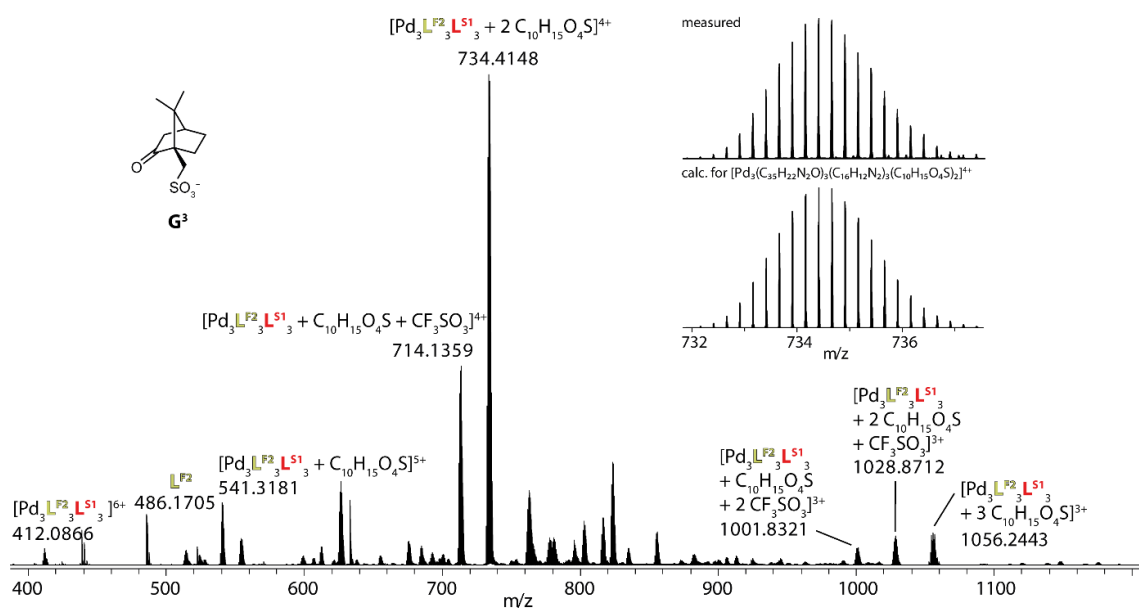
Figure 367: ESI-MS spectrum of [Pd$_3$**L$^{F2}_3$L$^{S1}_3$**]$^{(6-x)+}$ (x = 1;2) after addition of 1 equiv. **G^3**. Observed and calculated pattern for [2**G^3**@Pd$_3$**L$^{F2}_3$L$^{S1}_3$**]$^{4+}$ is shown in the inset.
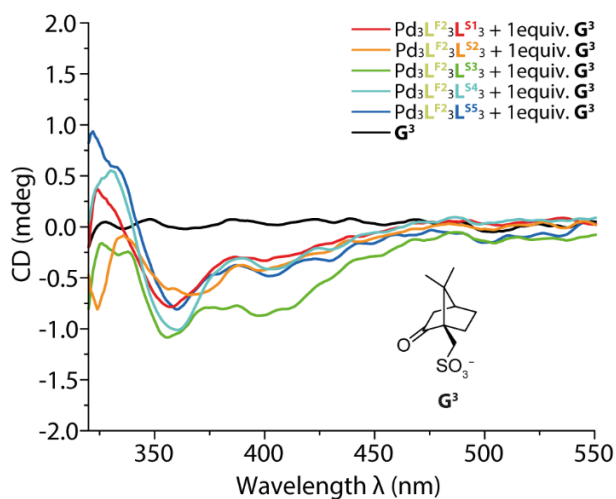
Figure 368: Circular dichroism of **G³** and Pd₃**L**^{F2}₃**L**$^{S1-5}$₃ after addition of 1 equiv. **G³** each. All spectra smoothed using Sawitzki-Golay method with a factor of 10.
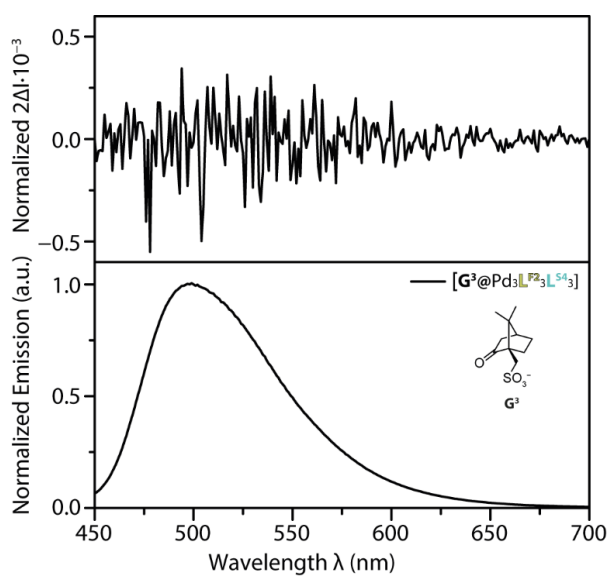
Figure 369: Normalized emission and CPL signal of Pd₃**L**^{F2}₃**L**^{S4}₃ after addition of 1 equiv. **G³**.

3.4.7.4.2 Dye Guests D[1-5]

6-hydroxy-5-[(4-sulfophenyl)azo]-2-naphthalenesulfonate – **D[1]**
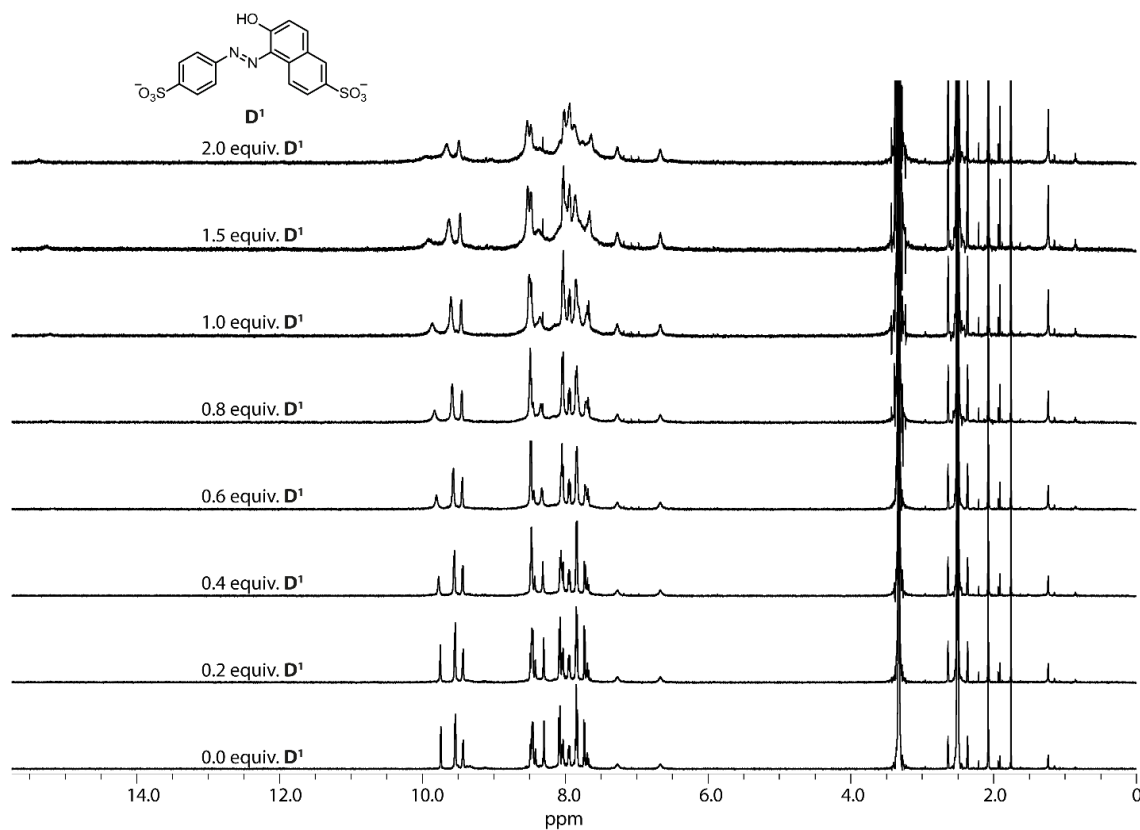
Figure 370: Full ^{1}H NMR spectra (500 MHz, 298 K, DMSO-d_6) of the titration of 6-hydroxy-5-[(4-sulfophenyl)azo]-2-naphthalenesulfonate (**D[1]**) to Pd₃**L**$^{F2}_3$**L**$^{S1}_3$.
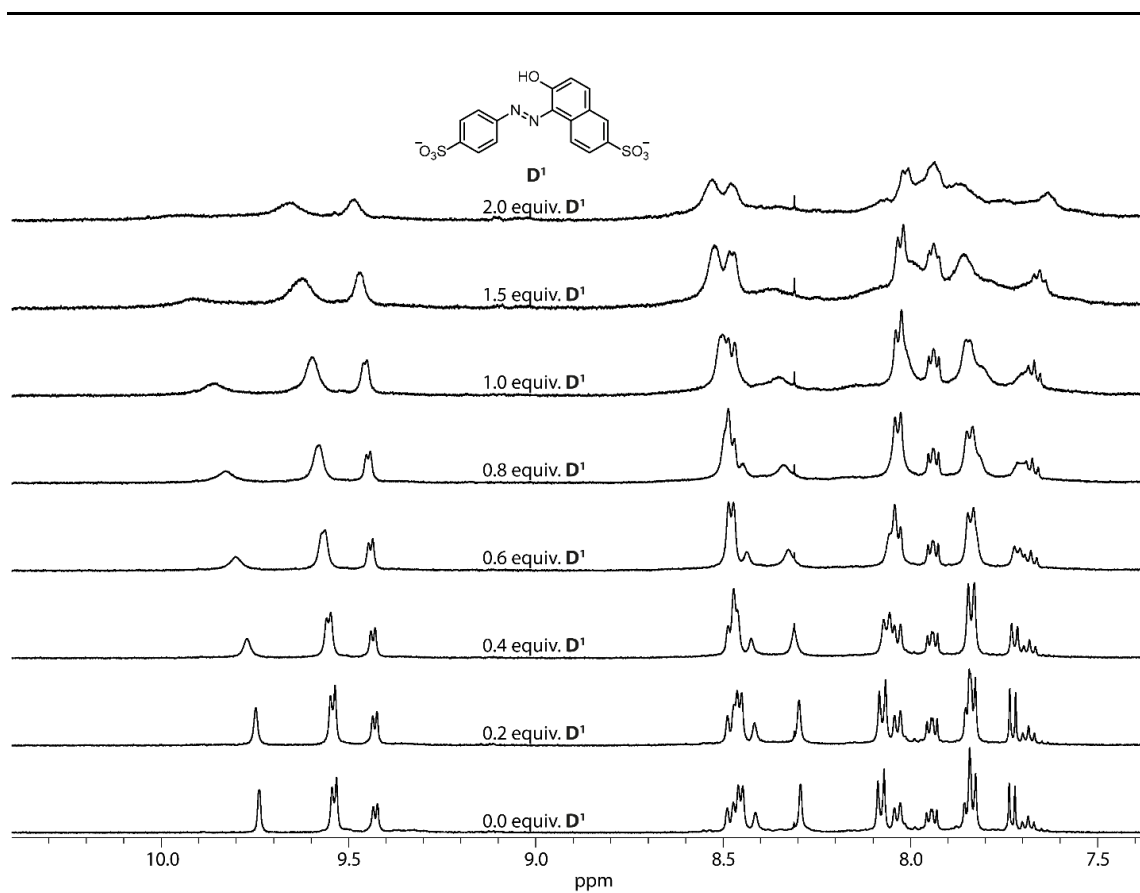
Figure 371: Partial ^{1}H NMR spectra (500 MHz, 298 K, DMSO-d_6) of the titration of 6-hydroxy-5-[(4-sulfophenyl)azo]-2-naphthalenesulfonate (D^1) to Pd$_3$L$^{F2}_3$L$^{S1}_3$.
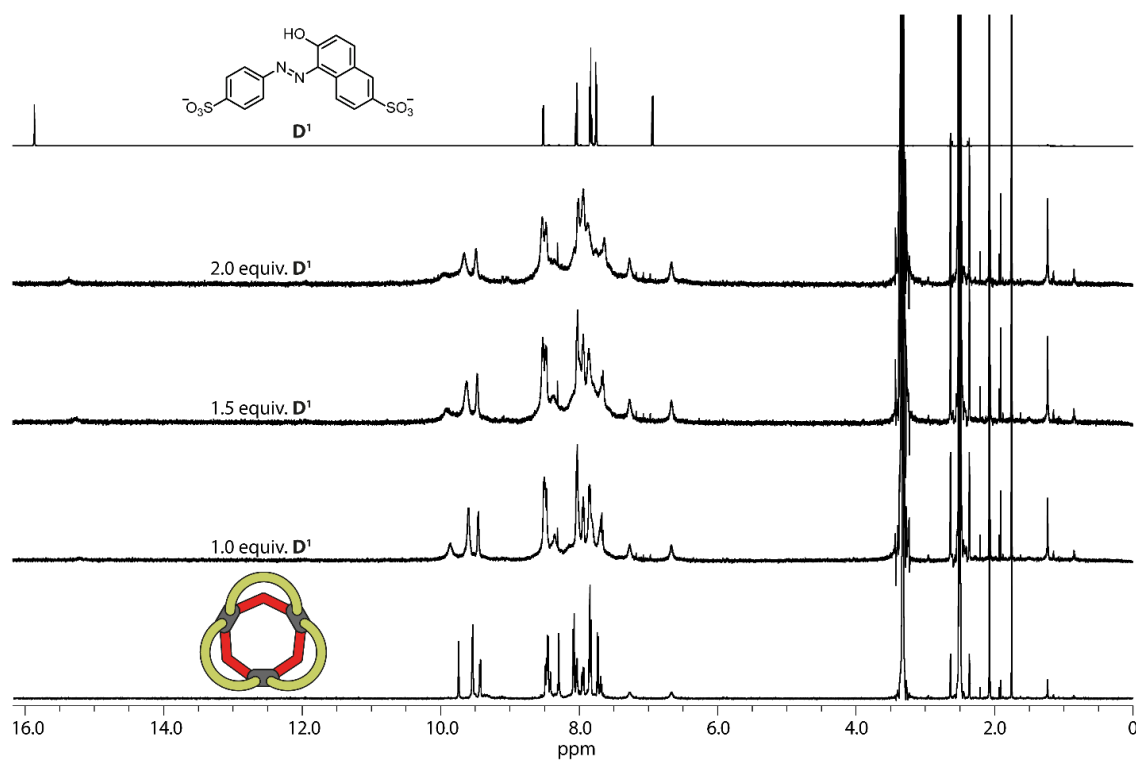
Figure 372: Full ^{1}H NMR spectra (500 MHz, 298 K, DMSO-d_6) of Pd$_3$L$^{F2}_3$L$^{S1}_3$; Pd$_3$L$^{F2}_3$L$^{S1}_3$ with 1 equiv. D^1; Pd$_3$L$^{F2}_3$L$^{S1}_3$ with 2 equiv. D^1; and D^1 (bottom to top).
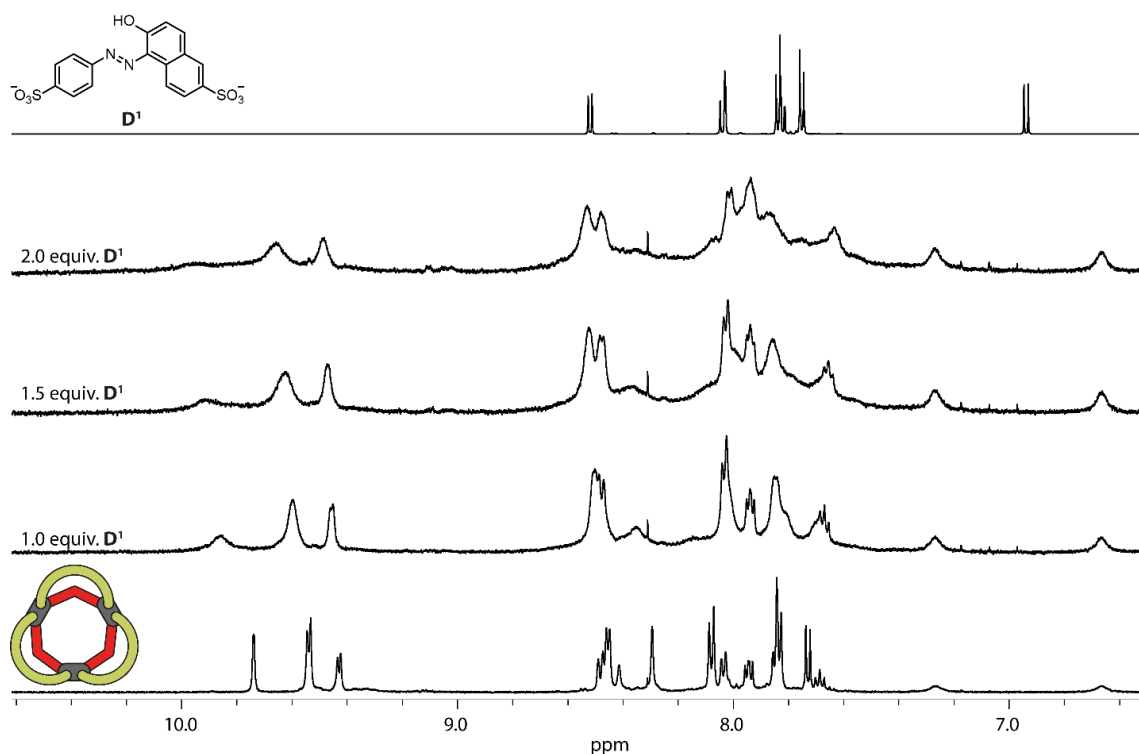
Figure 373: Partial ^{1}H NMR spectra (500 MHz, 298 K, DMSO-d_6) of Pd$_3$**L^{F2}**$_3$**L^{S1}**$_3$; Pd$_3$**L^{F2}**$_3$**L^{S1}**$_3$ with 1 equiv. **D^1**; Pd$_3$**L^{F2}**$_3$**L^{S1}**$_3$ with 2 equiv. **D^1**; and **D^1** (bottom to top).
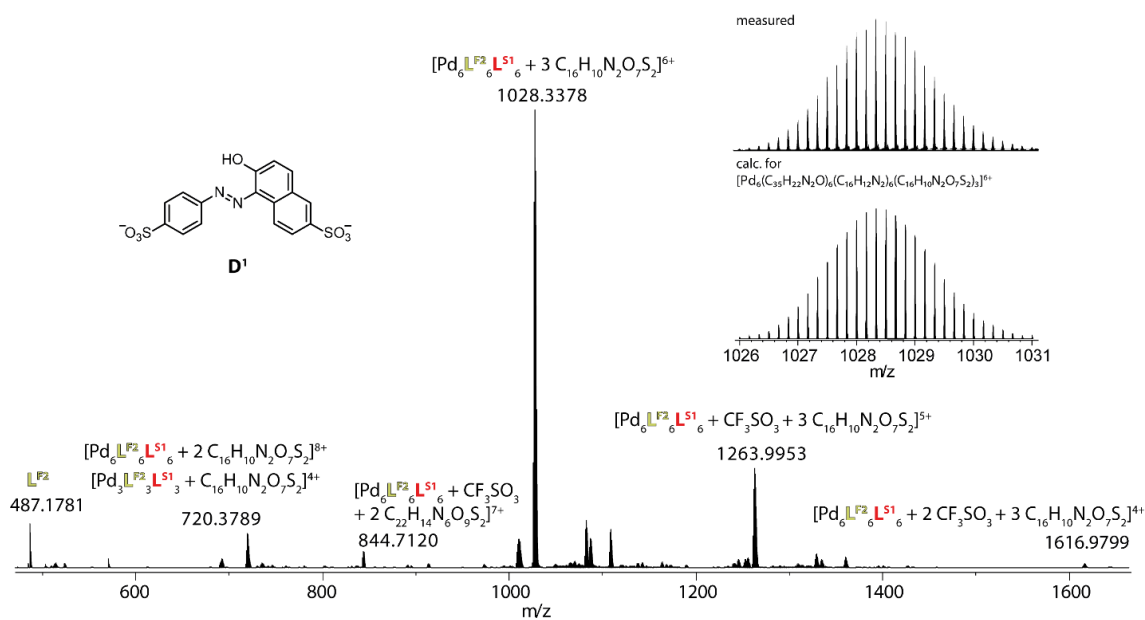
Figure 374: CSI-MS spectrum of [Pd$_3$**L^{F2}**$_3$**L^{S1}**$_3$]$^{(6-x)+}$ (x = 1;2) after addition of 1 equiv. **D^1**. Observed and calculated pattern for [3**D^1**@2Pd$_3$**L^{F2}**$_3$**L^{S1}**$_3$]$^{6+}$ is shown in the inset.
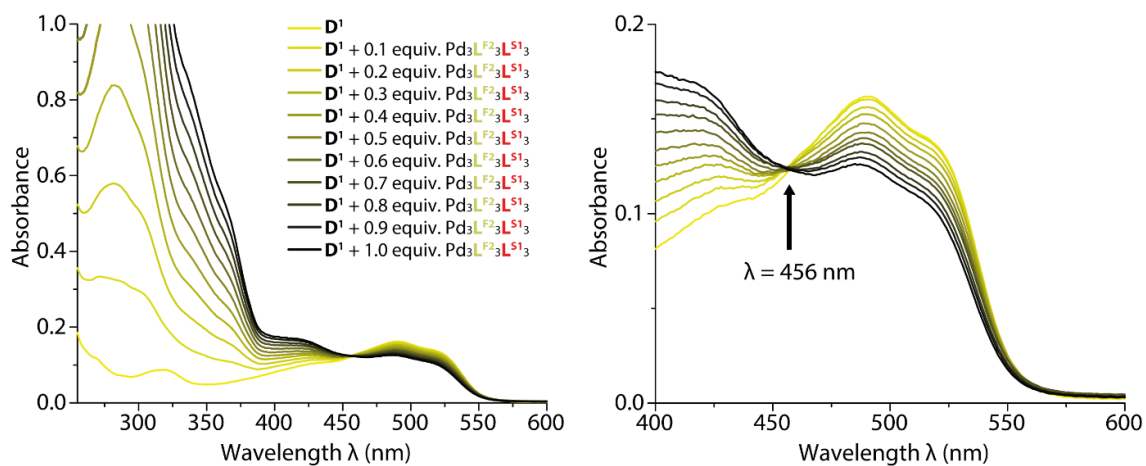
Figure 375: UV/VIS spectra of the reverse titration of Pd₃L**F²**₃L**S¹**₃ to **D¹**. Left: Wavelength coverage from 255-600 nm; right: Wavelength coverage from 400-600 nm with annotated isosbestic point.

6-hydroxy-5-[(2-methoxy-5-methyl-4-sulfonatophenyl)diazenyl]naphthalene-2-sulfonate - **D²**
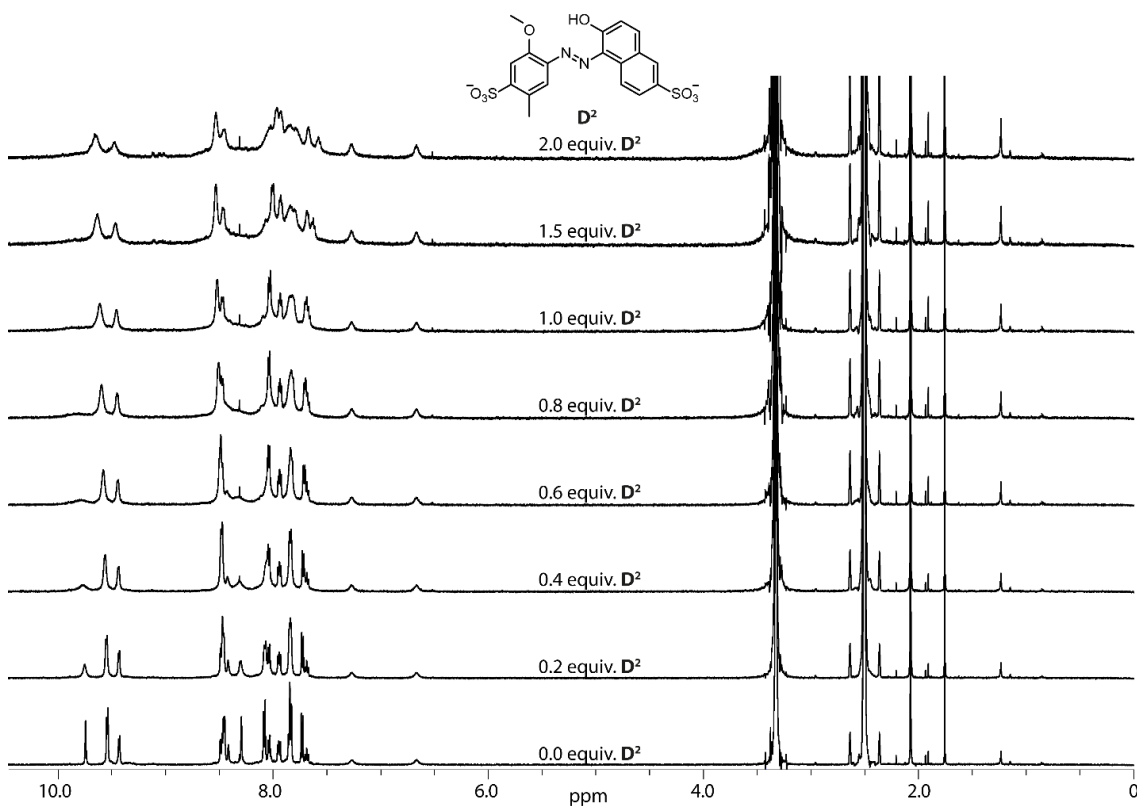
Figure 376: Full ¹H NMR spectra (500 MHz, 298 K, DMSO-*d₆*) of the titration of 6-hydroxy-5-[(2-methoxy-5-methyl-4-sulfonatophenyl)diazenyl]naphthalene-2-sulfonate (**D²**) to Pd₃L**F²**₃L**S¹**₃.
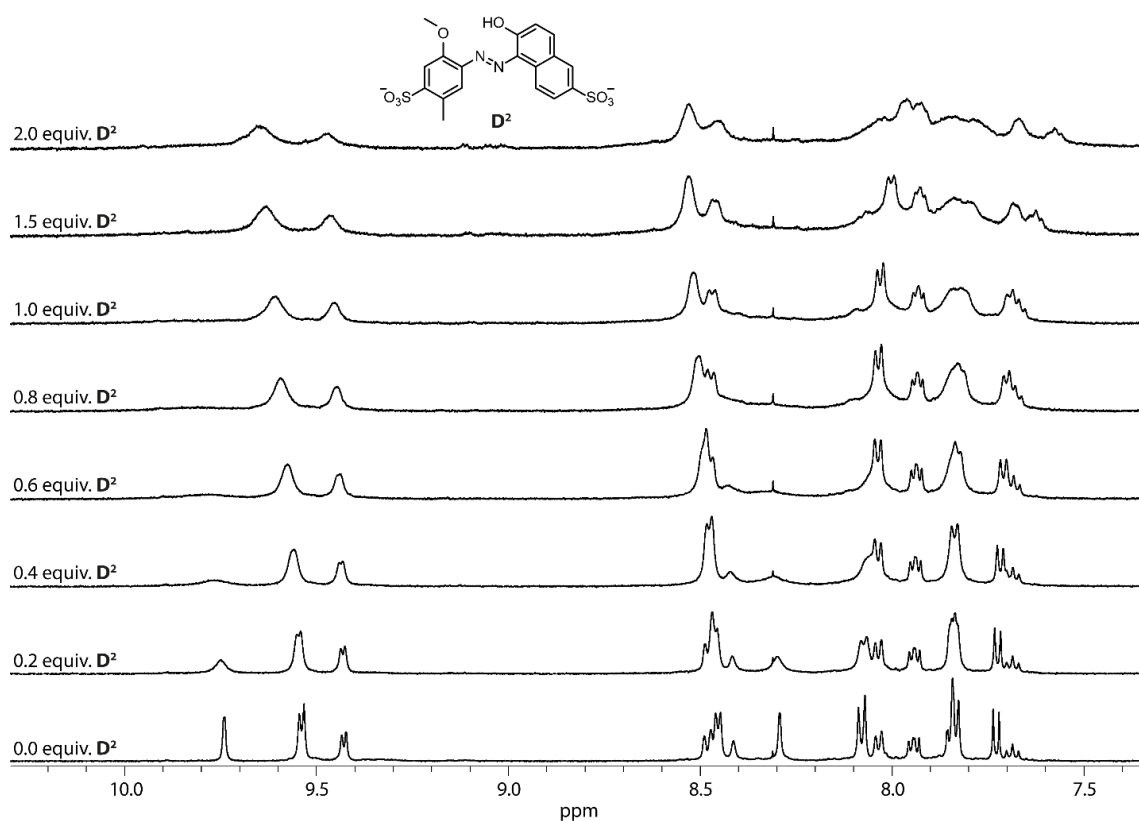
Figure 377: Partial ^{1}H NMR spectra (500 MHz, 298 K, DMSO-d_6) of the titration of 6-hydroxy-5-[(2-methoxy-5-methyl-4-sulfonatophenyl)diazenyl]naphthalene-2-sulfonate ($\mathbf{D^2}$) to $Pd_3\mathbf{L^{F2}}_3\mathbf{L^{S1}}_3$.
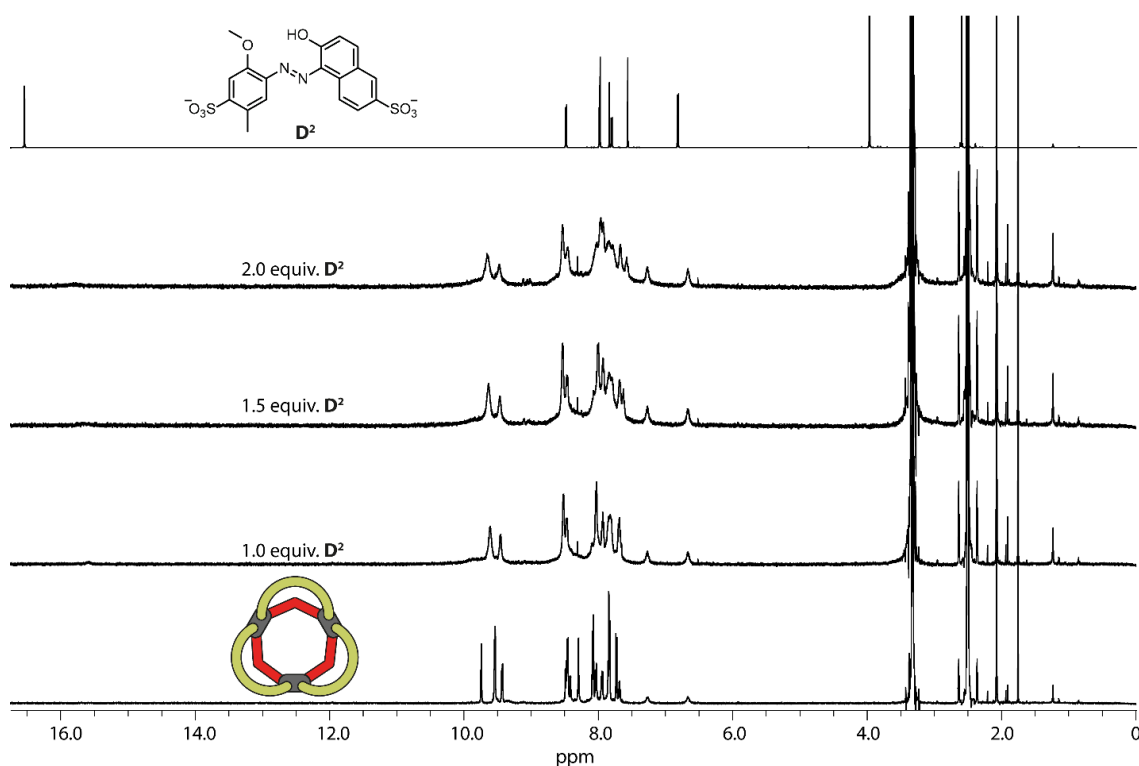
Figure 378: Full ^{1}H NMR spectra (500 MHz, 298 K, DMSO-d_6) of $Pd_3\mathbf{L^{F2}}_3\mathbf{L^{S1}}_3$; $Pd_3\mathbf{L^{F2}}_3\mathbf{L^{S1}}_3$ with 1 equiv. $\mathbf{D^2}$; $Pd_3\mathbf{L^{F2}}_3\mathbf{L^{S1}}_3$ with 1.5 equiv. $\mathbf{D^2}$; $Pd_3\mathbf{L^{F2}}_3\mathbf{L^{S1}}_3$ with 2 equiv. $\mathbf{D^2}$ and $\mathbf{D^2}$ (bottom to top).
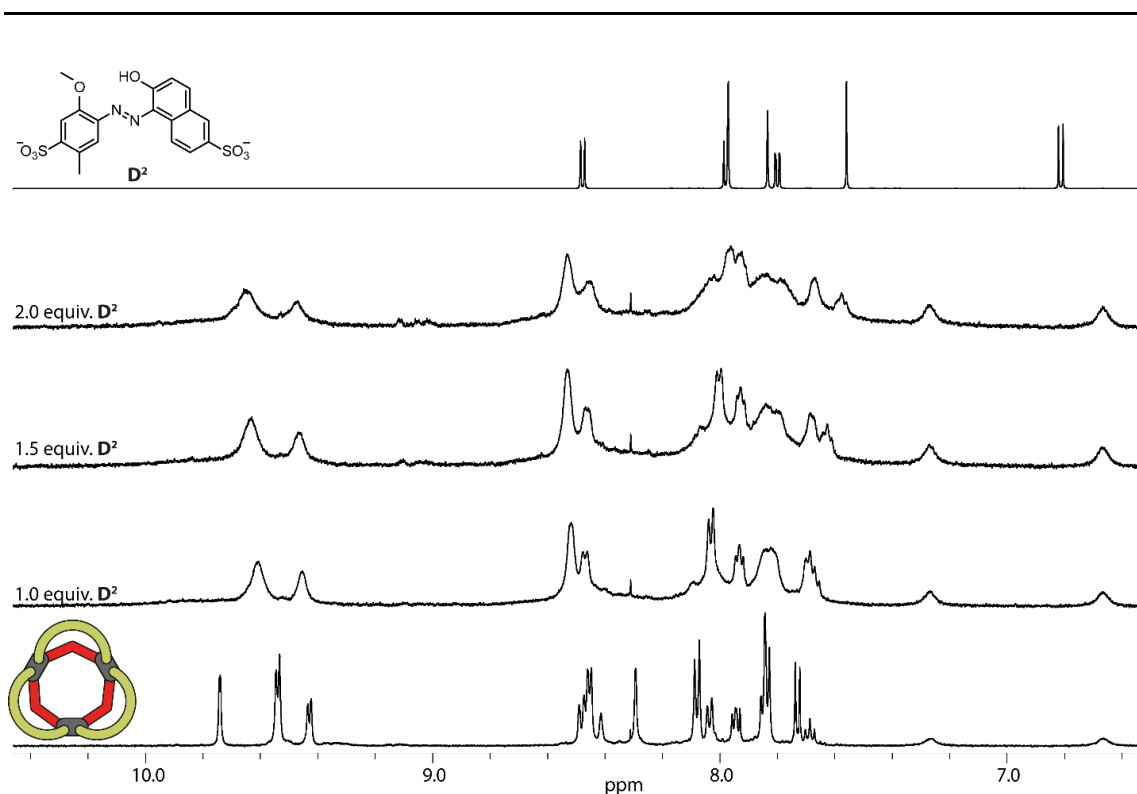
Figure 379: Partial ^{1}H NMR spectra (500 MHz, 298 K, DMSO-d_6) of Pd$_3$**L^{F2}**$_3$**L^{S1}**$_3$; Pd$_3$**L^{F2}**$_3$**L^{S1}**$_3$ with 1 equiv. **D^2**; Pd$_3$**L^{F2}**$_3$**L^{S1}**$_3$ with 1.5 equiv. **D^2**; Pd$_3$**L^{F2}**$_3$**L^{S1}**$_3$ with 2 equiv. **D^2** and **D^2** (bottom to top).
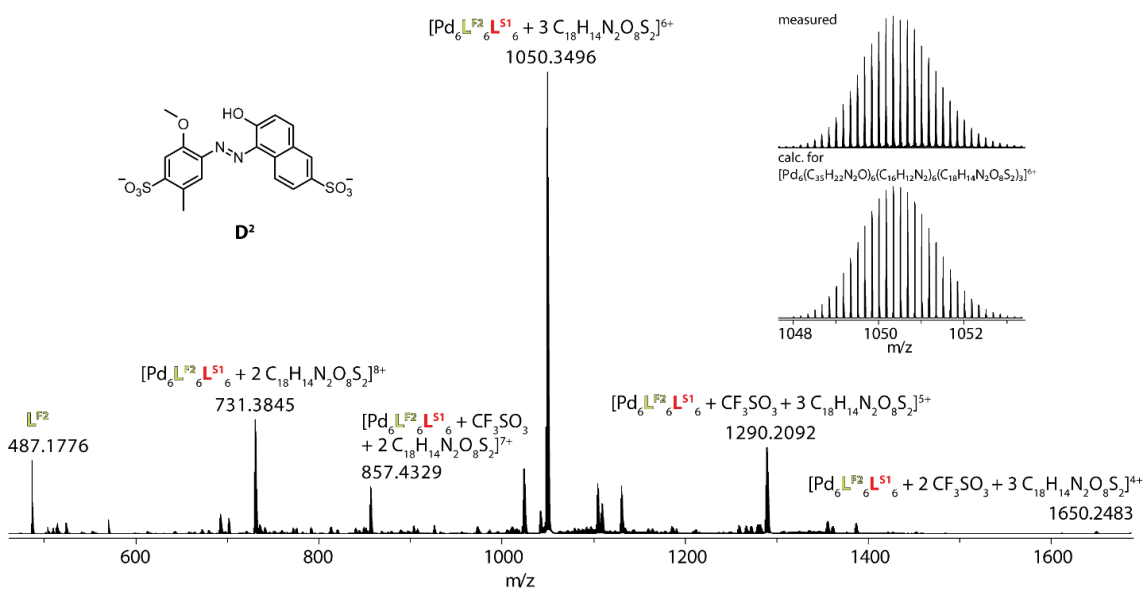
Figure 380: CSI-MS spectrum of [Pd$_3$**L^{F2}**$_3$**L^{S1}**$_3$]$^{(6-x)+}$ (x = 1;2) after addition of 1 equiv. **D^2**. Observed and calculated pattern for [3**D^2**@2Pd$_3$**L^{F2}**$_3$**L^{S1}**$_3$]$^{6+}$ is shown in the inset.
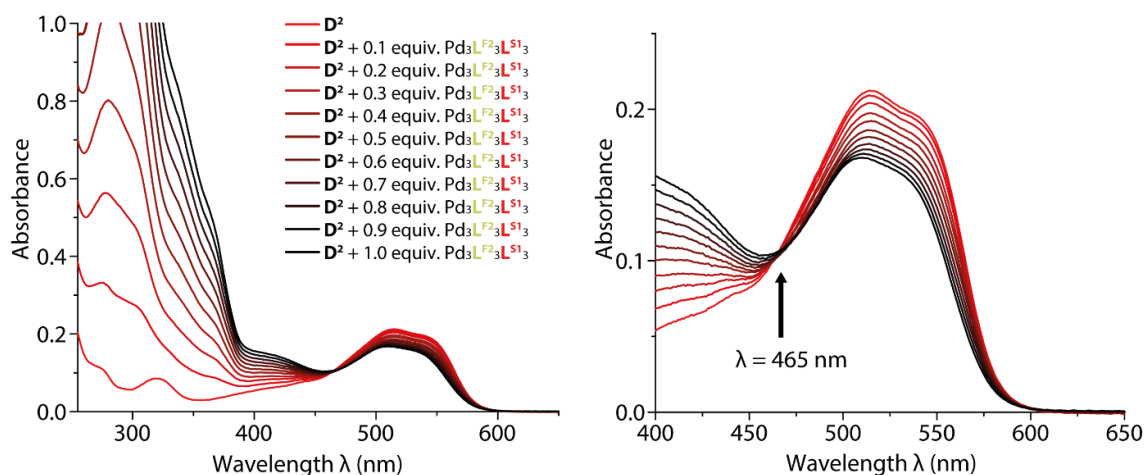
Figure 381: UV/VIS spectra of the reverse titration of Pd$_3$**L**^{F2}$_3$**L**^{S1}$_3$ to **D**^{2}. Left: Wavelength coverage from 255-600 nm; right: Wavelength coverage from 400-600 nm with annotated isosbestic point.

4-hydroxy-2-[(*E*)-(4-sulfonato-1-naphthyl)diazenyl]naphthalene-1-sulfonate – **D**^{3}
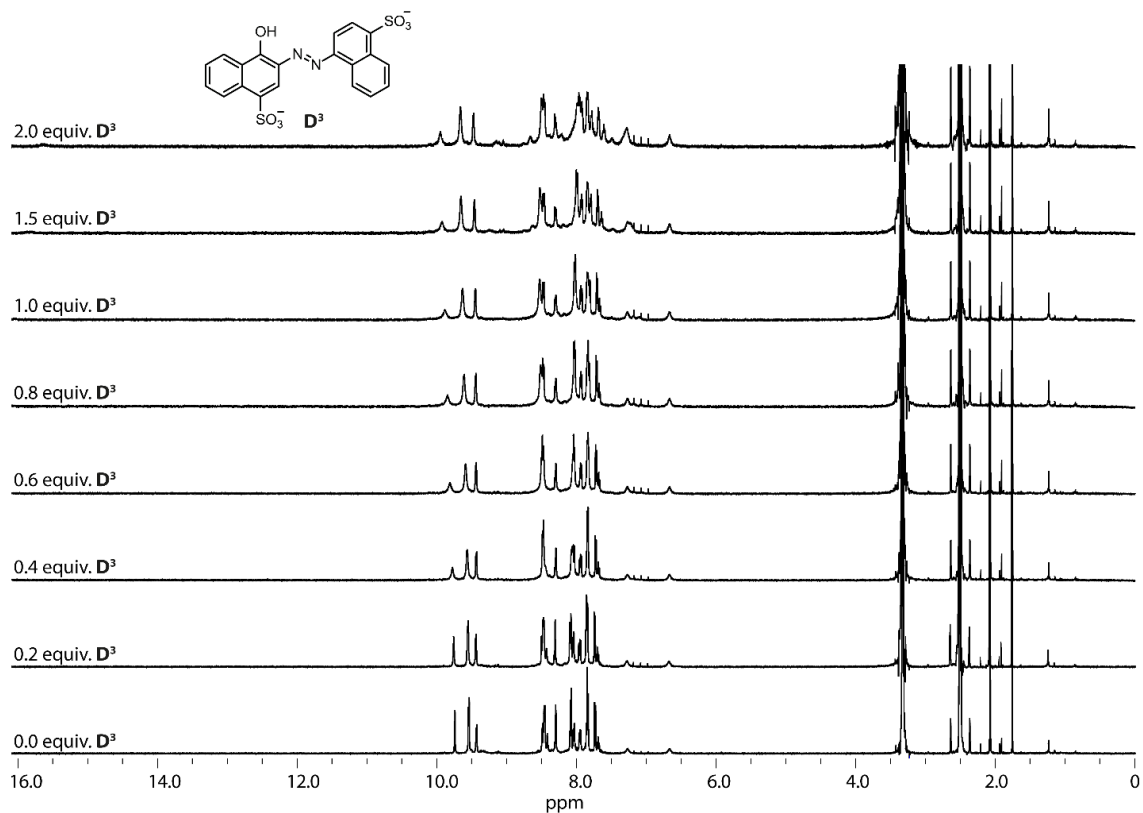
Figure 382: Full ^{1}H NMR spectra (500 MHz, 298 K, DMSO-*d$_6$*) of the titration of 4-hydroxy-2-[(E)-(4-sulfonato-1-naphthyl)diazenyl]naphthalene-1-sulfonate (**D**^{3}) to Pd$_3$**L**^{F2}$_3$**L**^{S1}$_3$.
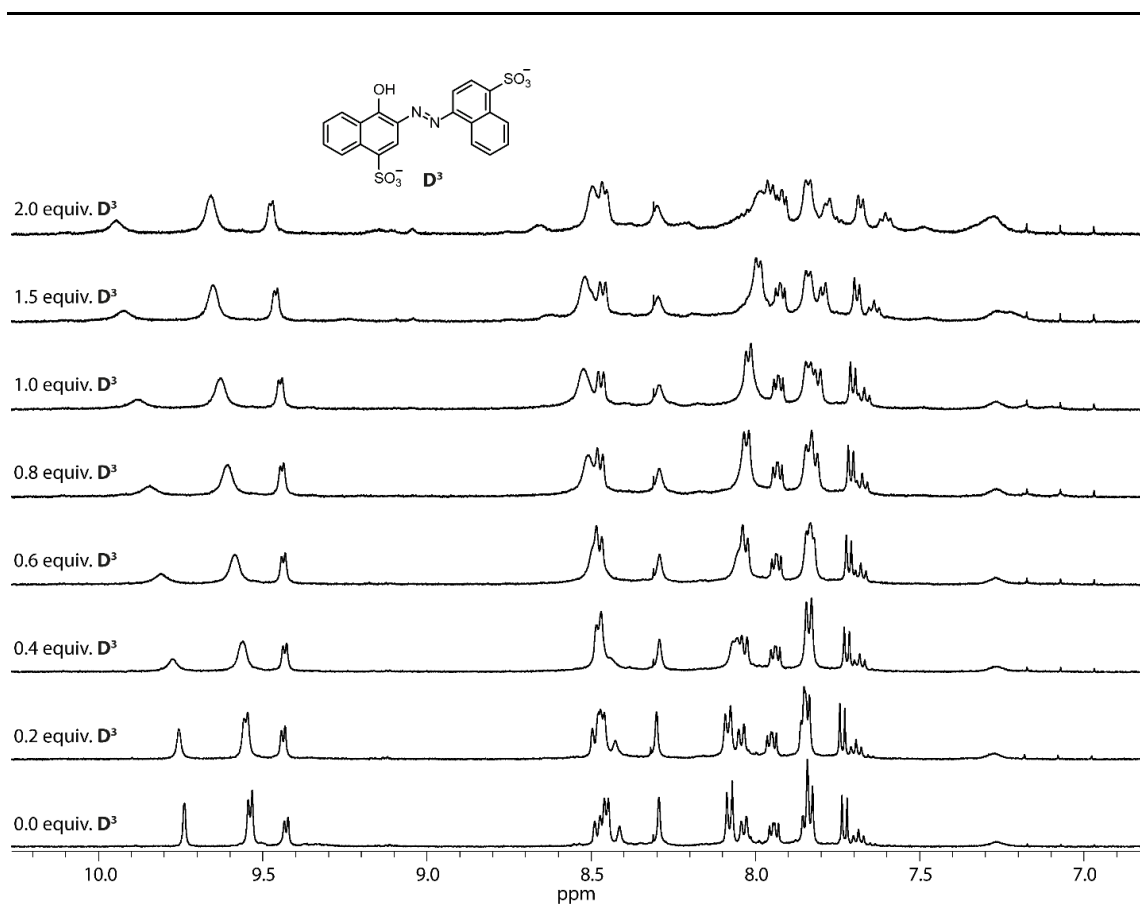
Figure 383: Partial ^{1}H NMR spectra (500 MHz, 298 K, DMSO-d_6) of the titration of 4-hydroxy-2-[(E)-(4-sulfonato-1-naphthyl)diazenyl]naphthalene-1-sulfonate (**D^3**) to Pd$_3$**L$^{F2}_3$L$^{S1}_3$**.
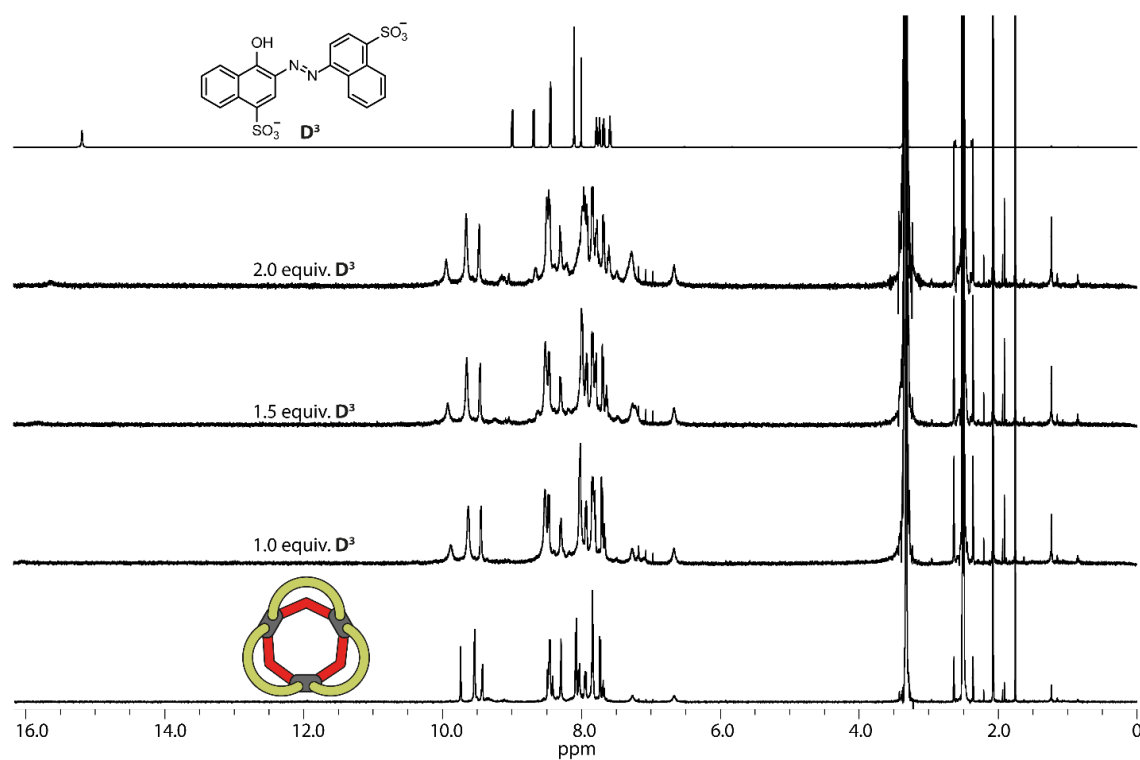
Figure 384: Full ^{1}H NMR spectra (500 MHz, 298 K, DMSO-d_6) of Pd$_3$**L$^{F2}_3$L$^{S1}_3$**; Pd$_3$**L$^{F2}_3$L$^{S1}_3$** with 1 equiv. **D^3**; Pd$_3$**L$^{F2}_3$L$^{S1}_3$** with 1.5 equiv. **D^3**; Pd$_3$**L$^{F2}_3$L$^{S1}_3$** with 2 equiv. **D^3** and **D^3** (bottom to top).
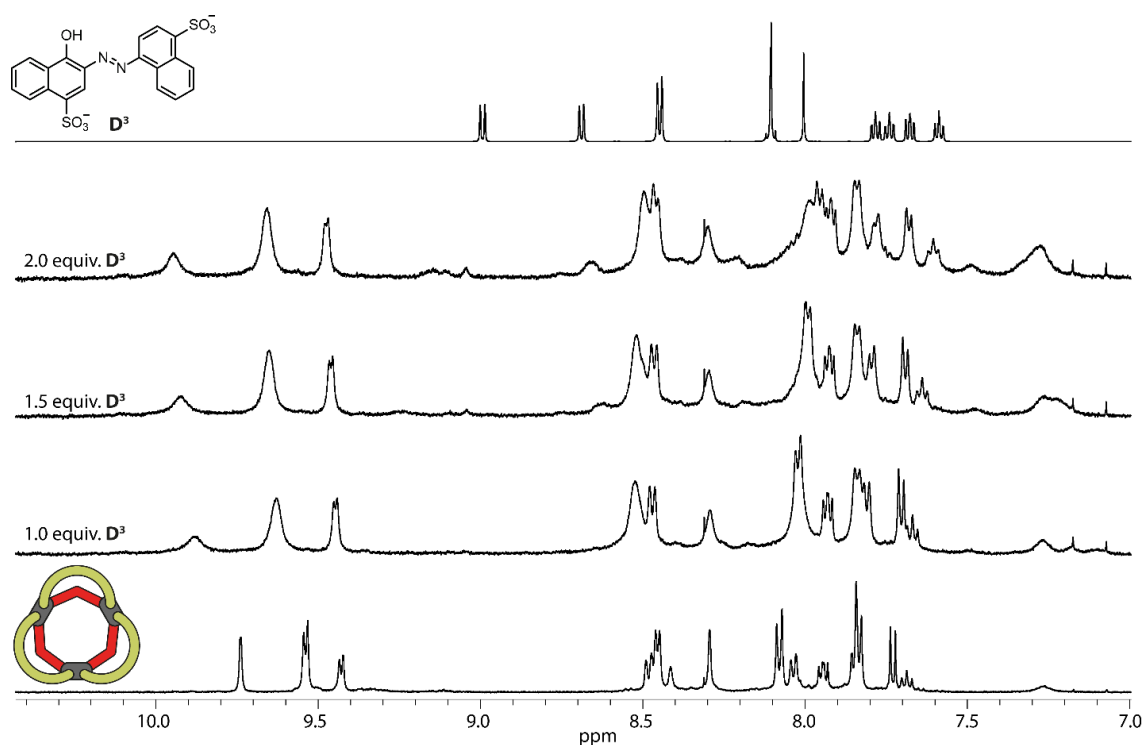
Figure 385: Partial ^{1}H NMR spectra (500 MHz, 298 K, DMSO-d_6) of Pd$_3$L$^{F2}_3$L$^{S1}_3$; Pd$_3$L$^{F2}_3$L$^{S1}_3$ with 1 equiv. D^3; Pd$_3$L$^{F2}_3$L$^{S1}_3$ with 1.5 equiv. D^3; Pd$_3$L$^{F2}_3$L$^{S1}_3$ with 2 equiv. D^3 and D^3 (bottom to top).

Binding constant K = 341.34 ± 25.37 M^{-1}
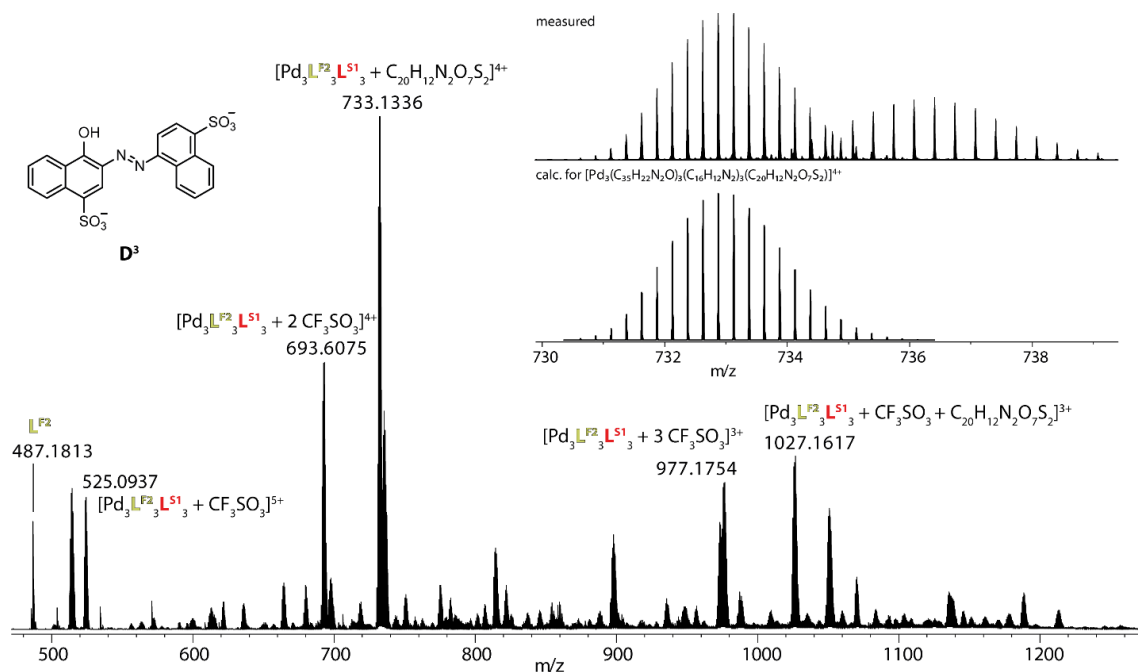
Figure 386: ESI-MS spectrum of [Pd$_3$L$^{F2}_3$L$^{S1}_3$]$^{(6-x)+}$ (x = 1-3) after addition of 1 equiv. D^3. Observed and calculated pattern for [D^3@Pd$_3$L$^{F2}_3$L$^{S1}_3$]$^{4+}$ is shown in the inset.
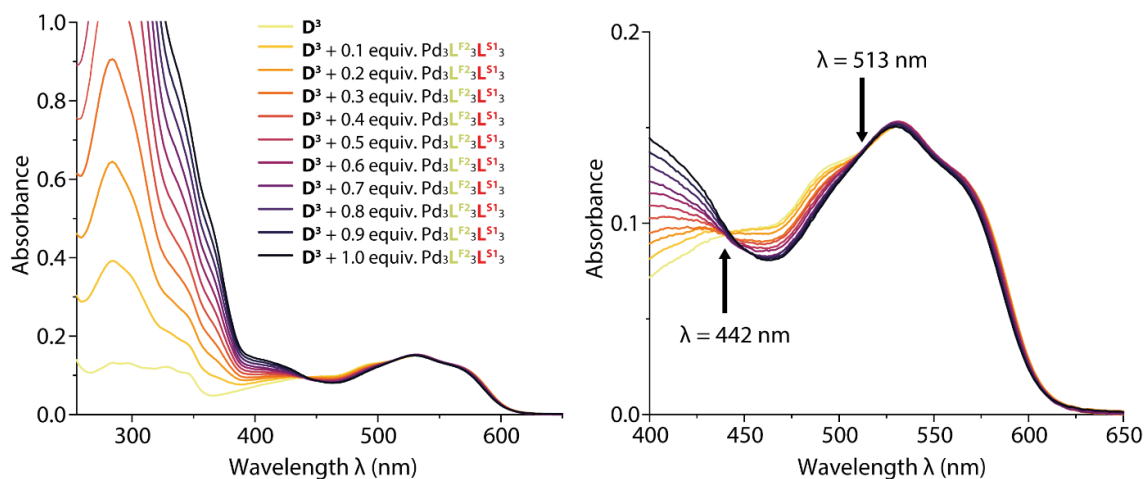
Figure 387: UV/VIS spectra of the reverse titration of $Pd_3L^{F2}{}_3L^{S1}{}_3$ to D^3. Left: Wavelength coverage from 255-600 nm; right: Wavelength coverage from 400-600 nm with annotated isosbestic points.

4-Amino-5-hydroxy-3-[(4-nitrophenyl)azo]-6-(phenylazo)-2,7-naphthalene disulfonate – $\underline{D^4}$
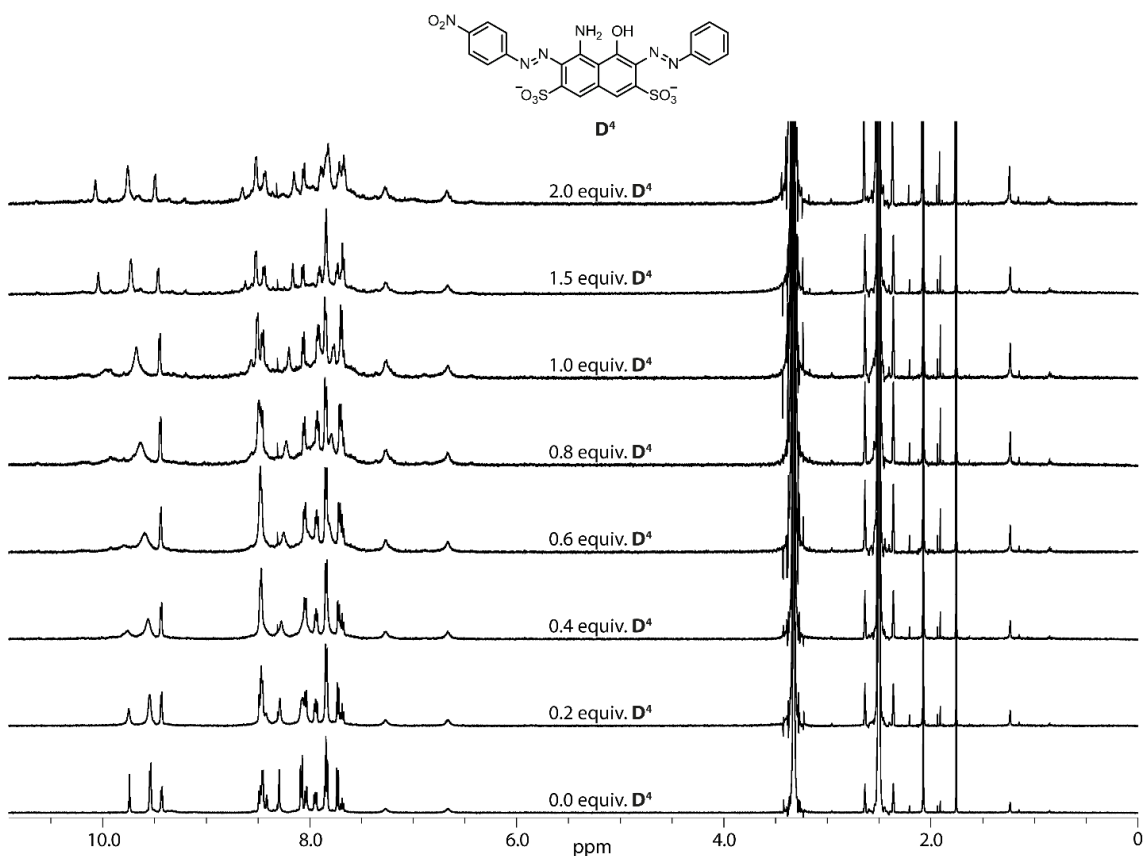
Figure 388: Full ^{1}H NMR spectra (500 MHz, 298 K, DMSO-d_6) of the titration of 4-Amino-5-hydroxy-3-[(4-nitrophenyl)azo]-6-(phenylazo)-2,7-naphthalene disulfonate (D^4) to $Pd_3L^{F2}{}_3L^{S1}{}_3$.
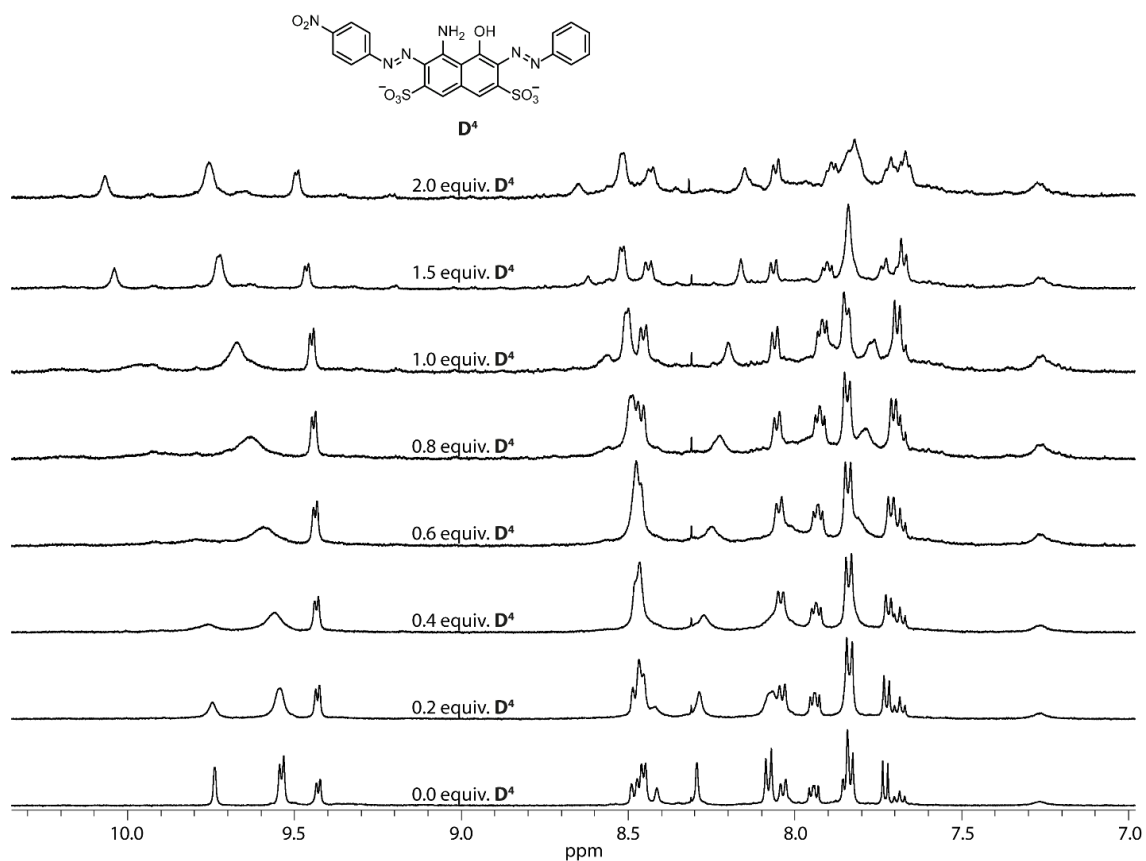
Figure 389: Partial ^{1}H NMR spectra (500 MHz, 298 K, DMSO-d_6) of the titration of 4-Amino-5-hydroxy-3-[(4-nitrophenyl)azo]-6-(phenylazo)-2,7-naphthalene disulfonate (**D^4**) to Pd$_3$**L**$^{F2}_3$**L**$^{S1}_3$.
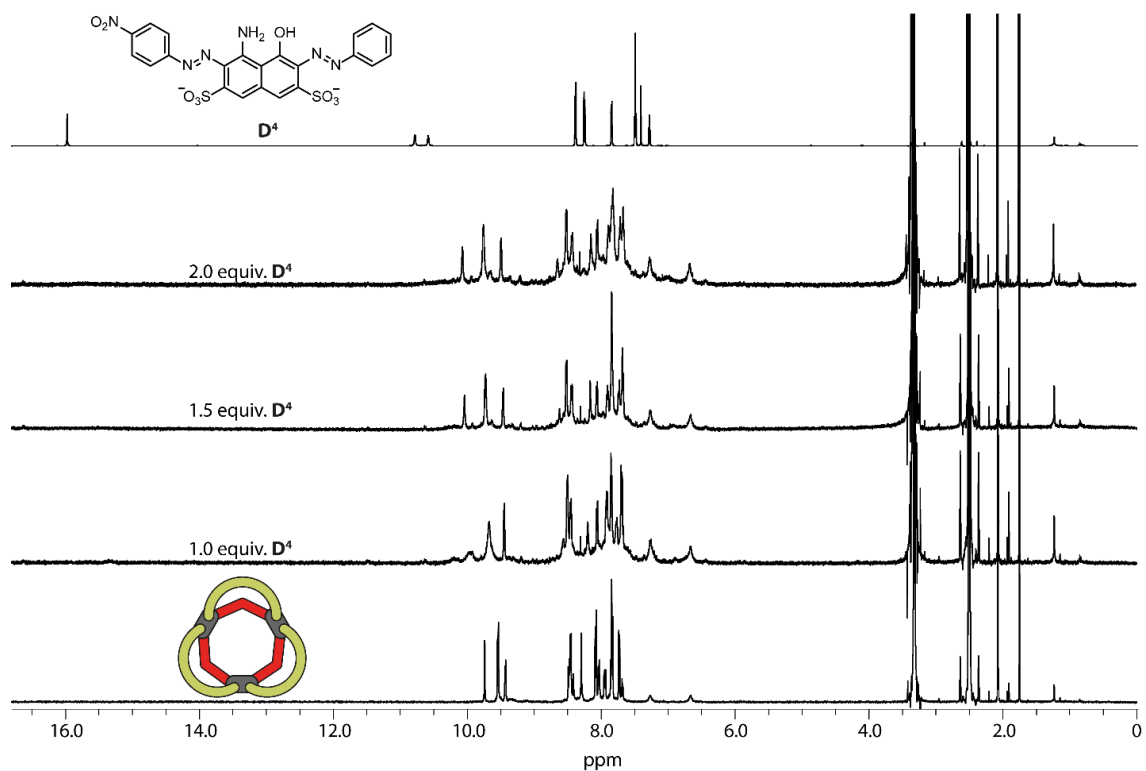
Figure 390: Full ^{1}H NMR spectra (500 MHz, 298 K, DMSO-d_6) of Pd$_3$**L**$^{F2}_3$**L**$^{S1}_3$; Pd$_3$**L**$^{F2}_3$**L**$^{S1}_3$ with 1 equiv. **D^4**; Pd$_3$**L**$^{F2}_3$**L**$^{S1}_3$ with 1.5 equiv. **D^4**; Pd$_3$**L**$^{F2}_3$**L**$^{S1}_3$ with 2 equiv. **D^4** and **D^4** (bottom to top).
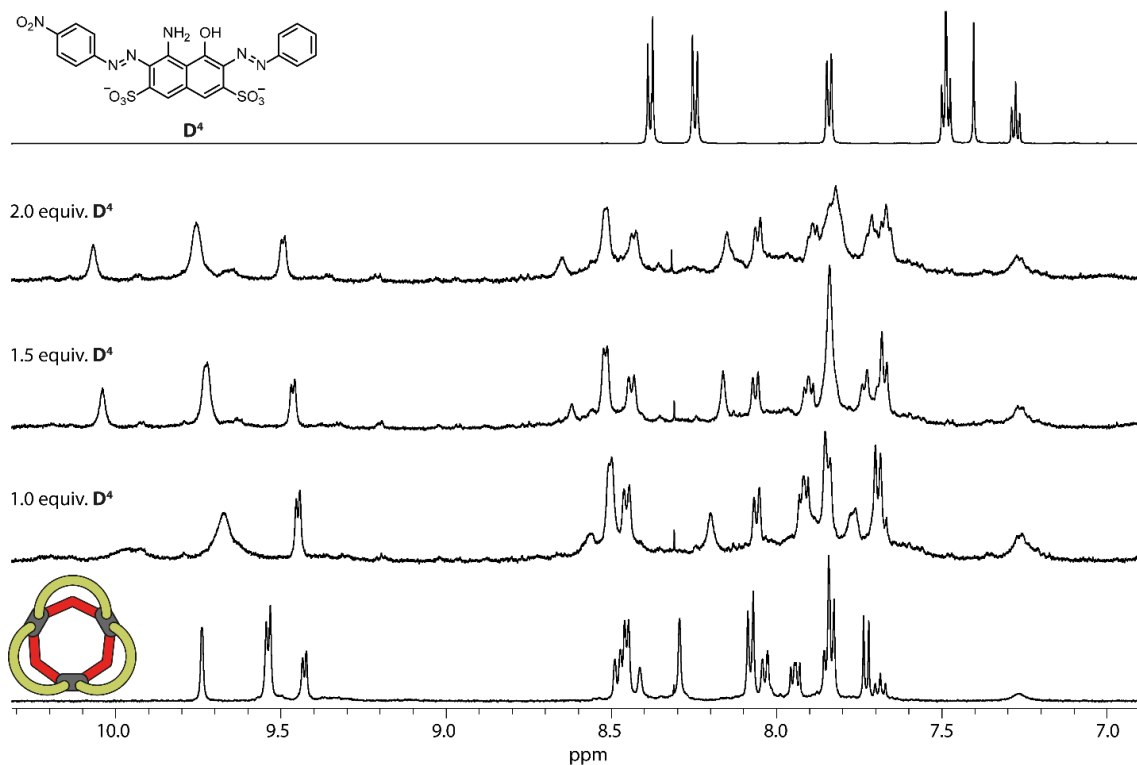
Figure 391: Partial ^{1}H NMR spectra (500 MHz, 298 K, DMSO-d_6) of Pd$_3$L$^{F2}_3$L$^{S1}_3$; Pd$_3$L$^{F2}_3$L$^{S1}_3$ with 1 equiv. **D^4**; Pd$_3$L$^{F2}_3$L$^{S1}_3$ with 1.5 equiv. **D^4**; Pd$_3$L$^{F2}_3$L$^{S1}_3$ with 2 equiv. **D^4** and **D^4** (bottom to top).

Binding constant K = 151.92 ± 11.51 M^{-1}
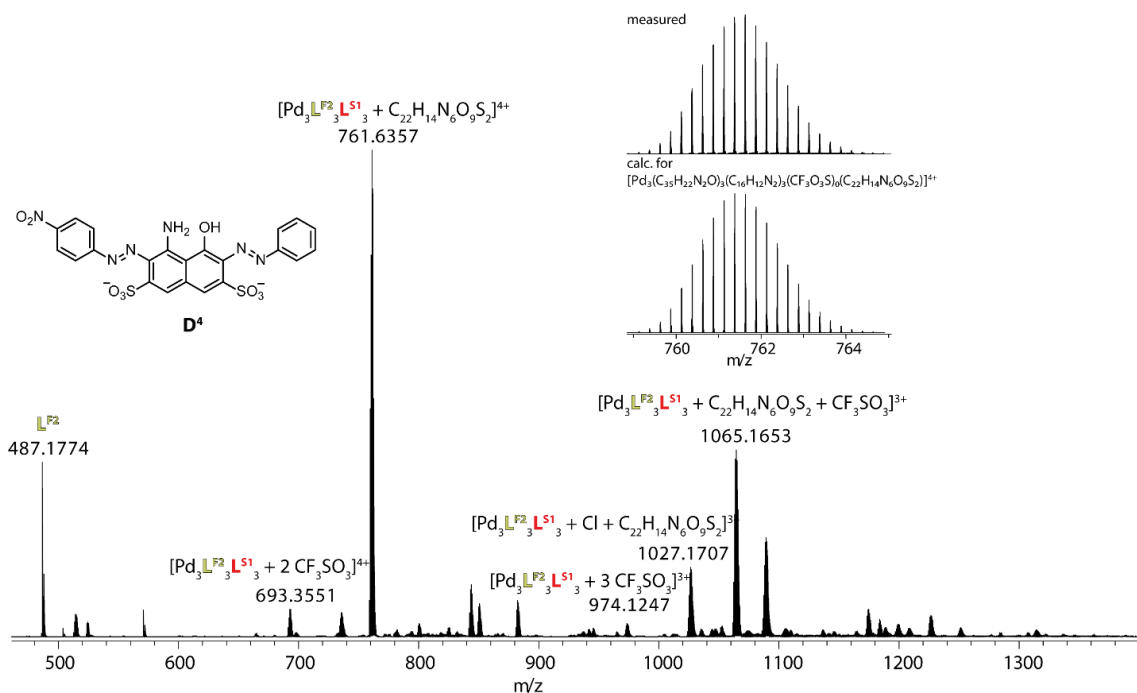
Figure 392: CSI-MS spectrum of [Pd$_3$L$^{F2}_3$L$^{S1}_3$]$^{(6-x)+}$ (x = 1-3) after addition of 1 equiv. **D^4**. Observed and calculated pattern for [**D^4**@Pd$_3$L$^{F2}_3$L$^{S1}_3$]$^{4+}$ is shown in the inset.

344
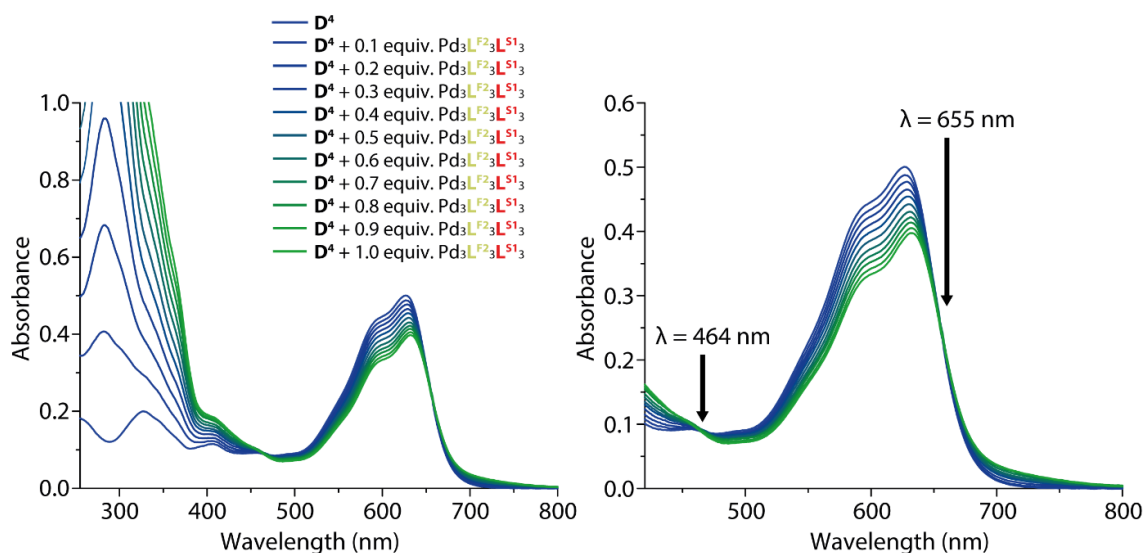
Figure 393: UV/VIS spectra of the reverse titration of $Pd_3L^{F2}{}_3L^{S1}{}_3$ to D^4. Left: Wavelength coverage from 255-600 nm; right: Wavelength coverage from 400-600 nm with annotated isosbestic points.

Sulforhodamin 101 – D^5
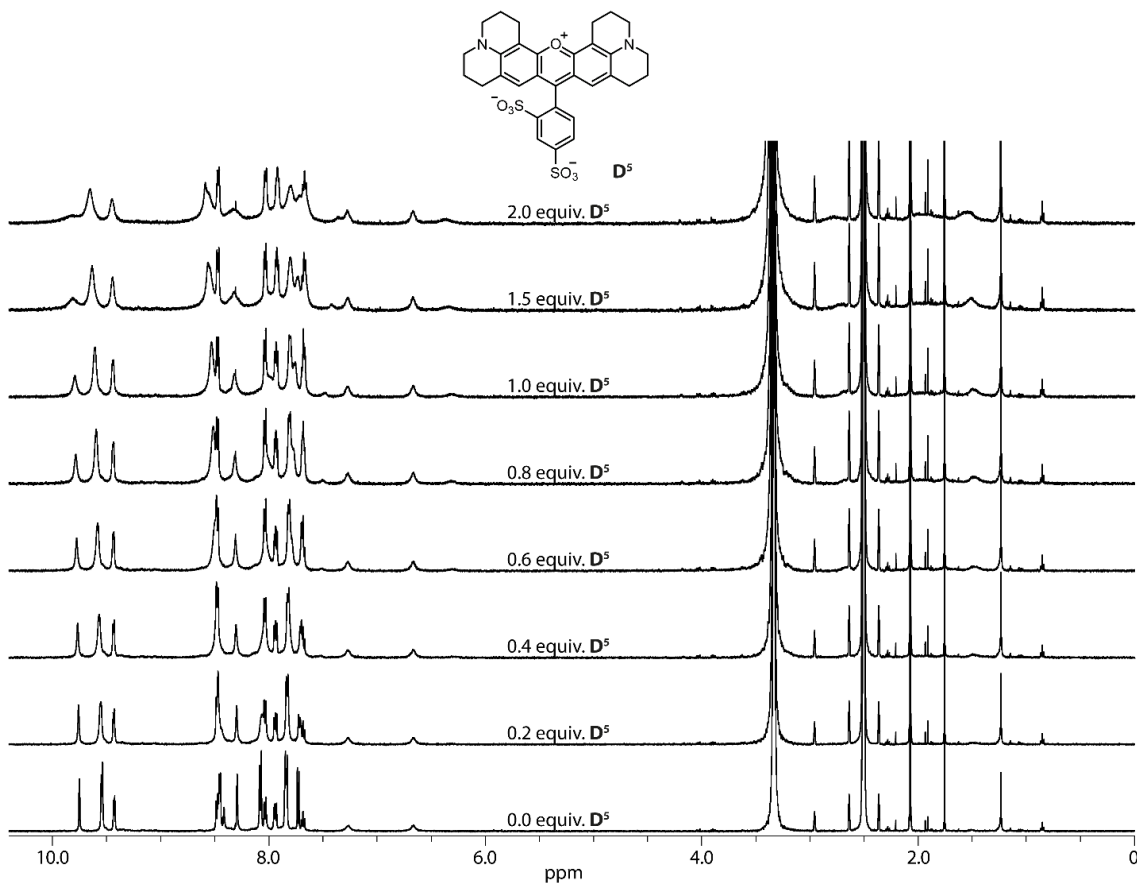
Figure 394: Full ^{1}H NMR spectra (500 MHz, 298 K, DMSO-d_6) of the titration of Sulforhodamine 101 (D^5) to $Pd_3L^{F2}{}_3L^{S1}{}_3$.
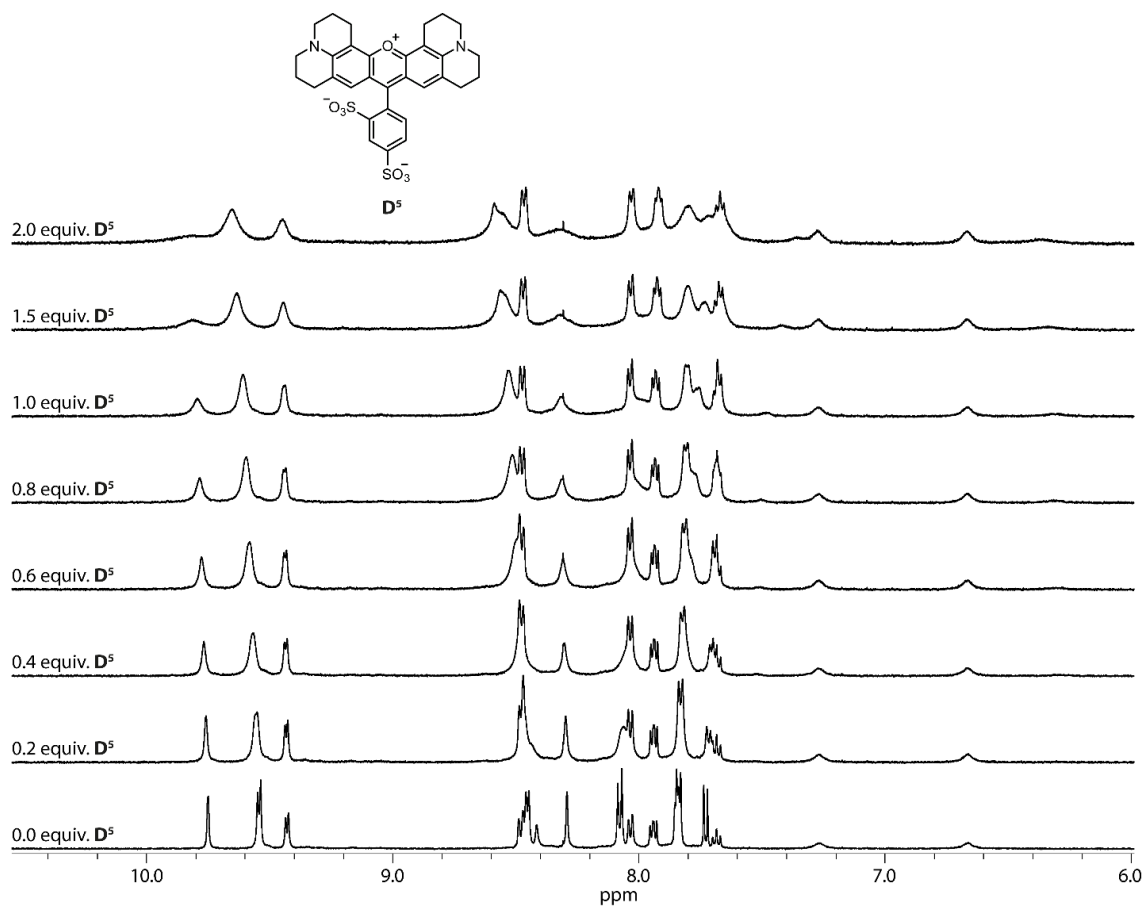
Figure 395: Partial ^{1}H NMR spectra (500 MHz, 298 K, DMSO-d_6) of the titration of Sulforhodamine 101 (**D^5**) to Pd$_3$**L$^{F2}_3$L$^{S1}_3$**.
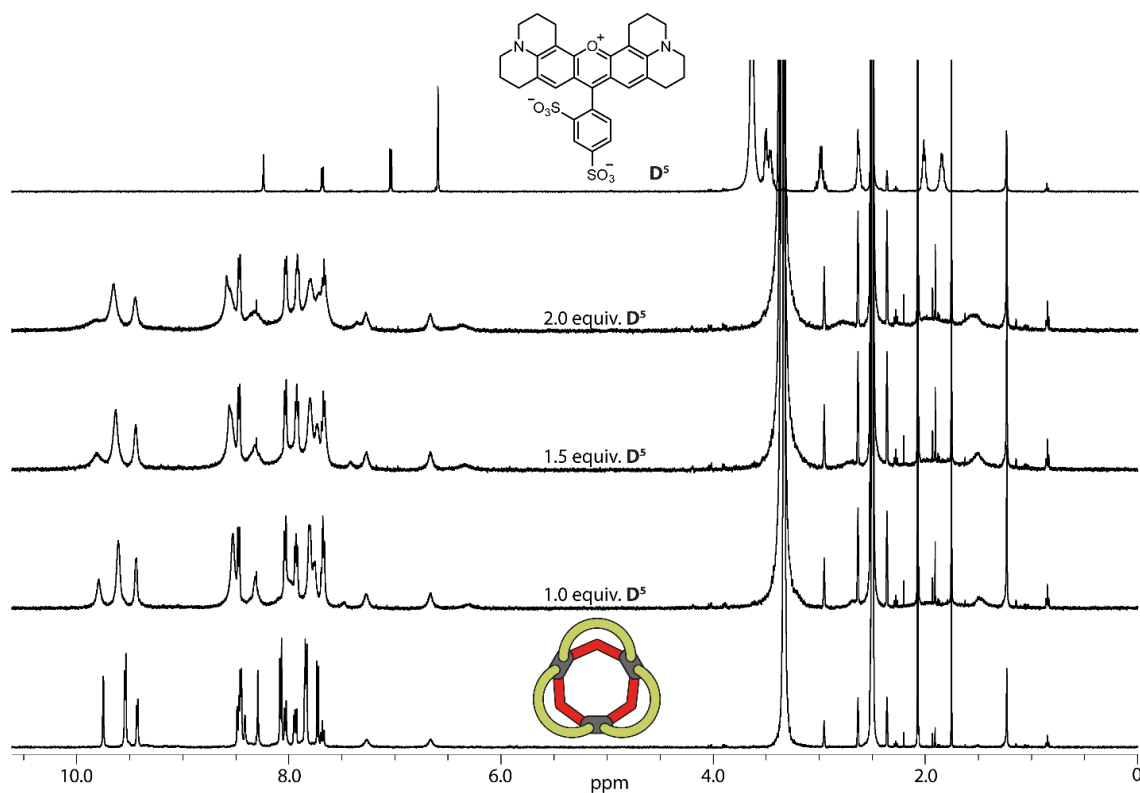
Figure 396: Full ^{1}H NMR spectra (500 MHz, 298 K, DMSO-d_6) of Pd$_3$L$^{F2}_3$L$^{S1}_3$; Pd$_3$L$^{F2}_3$L$^{S1}_3$ with 1 equiv. **D^5**; Pd$_3$L$^{F2}_3$L$^{S1}_3$ with 1.5 equiv. **D^5**; Pd$_3$L$^{F2}_3$L$^{S1}_3$ with 2 equiv. **D^5** and **D^5** (bottom to top).
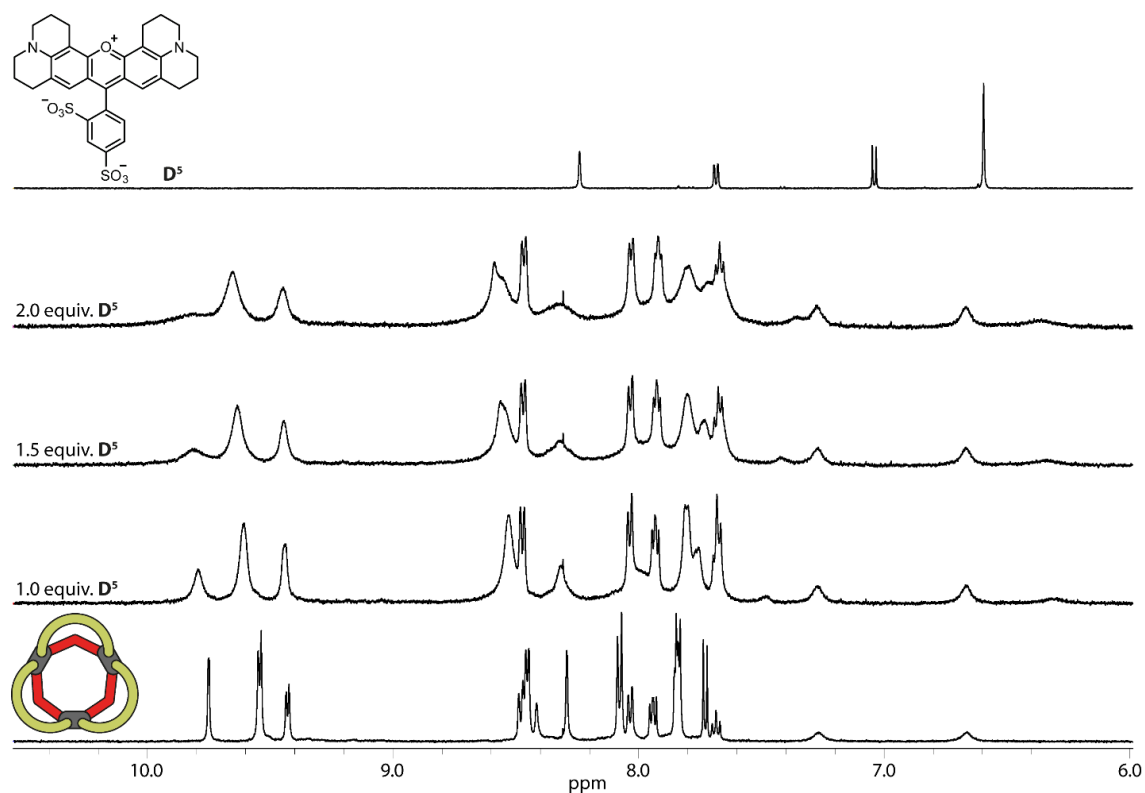
Figure 397: Partial ^{1}H NMR spectra (500 MHz, 298 K, DMSO-d_6) of Pd$_3$L$^{F2}_3$L$^{S1}_3$; Pd$_3$L$^{F2}_3$L$^{S1}_3$ with 1 equiv. **D^5**; Pd$_3$L$^{F2}_3$L$^{S1}_3$ with 1.5 equiv. **D^5**; Pd$_3$L$^{F2}_3$L$^{S1}_3$ with 2 equiv. **D^5** and **D^5** (bottom to top).

Binding constant K = 607.24 ± 15.14 M^{-1}

347
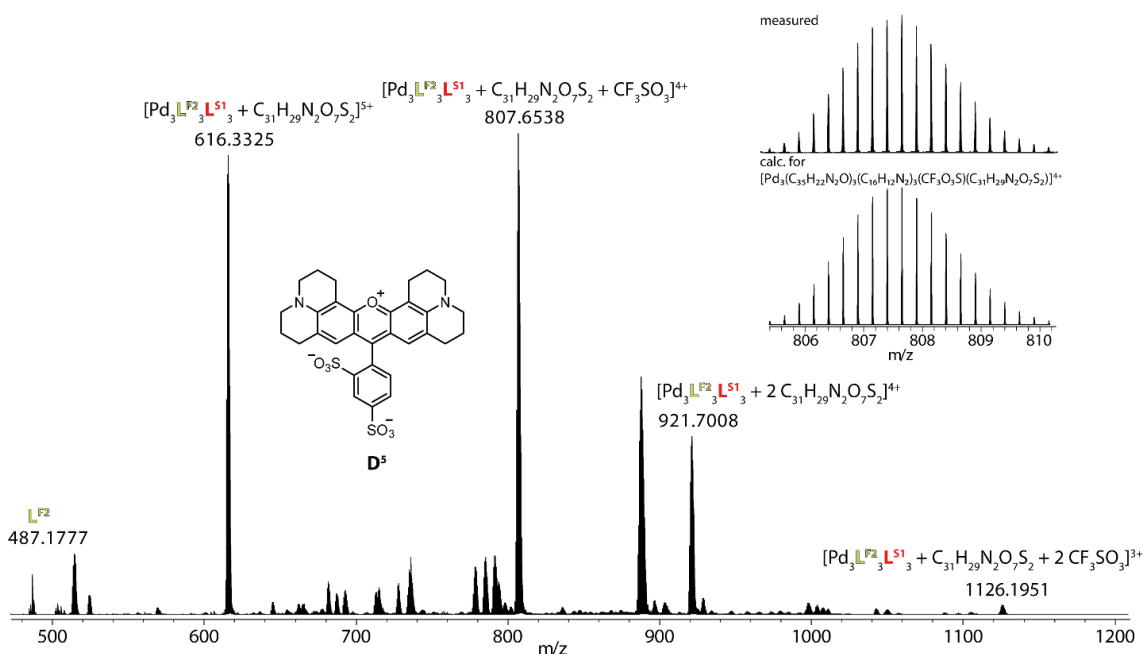
Figure 398: ESI-MS spectrum of $[Pd_3\mathbf{L^{F2}}_3\mathbf{L^{S1}}_3]^{(6-x)+}$ (x = 1;2) after addition of 1 equiv. $\mathbf{D^5}$. Observed and calculated pattern for $[\mathbf{D^5}@Pd_3\mathbf{L^{F2}}_3\mathbf{L^{S1}}_3 + CF_3SO_3]^{4+}$ is shown in the inset.
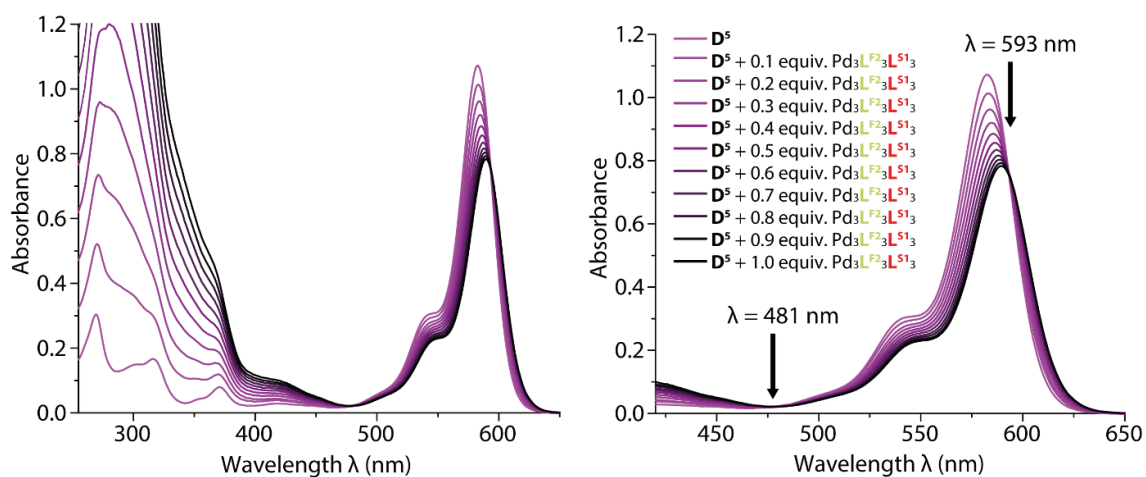
Figure 399: UV/VIS spectra of the reverse titration of $Pd_3\mathbf{L^{F2}}_3\mathbf{L^{S1}}_3$ to $\mathbf{D^5}$. Left: Wavelength coverage from 255-600 nm; right: Wavelength coverage from 380-650 nm with annotated isosbestic points.
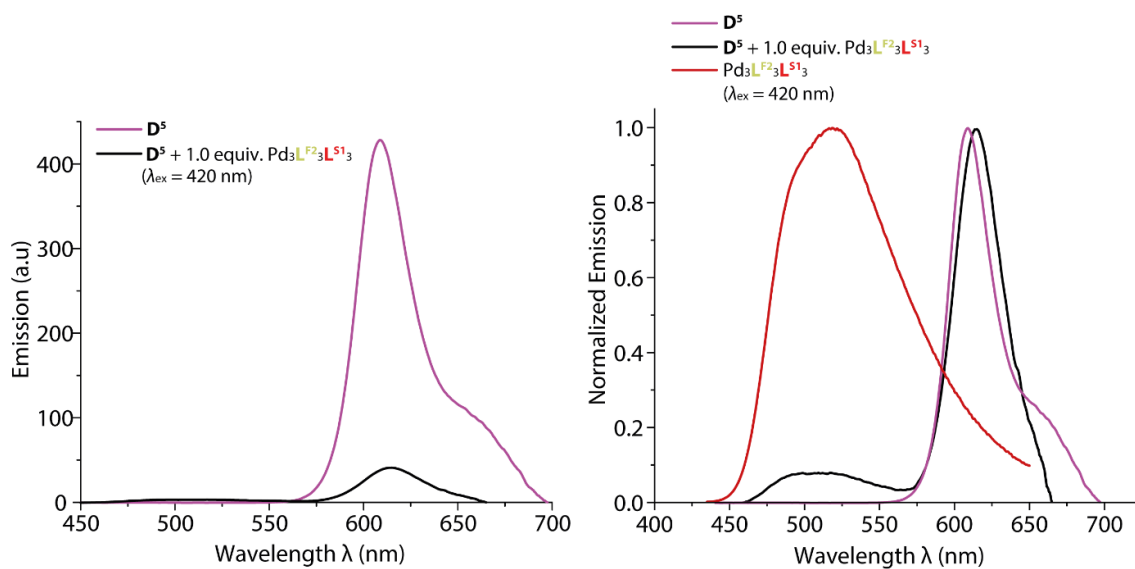
Figure 400: Absolute emission of **D⁵** and **D⁵** after addition of 1 equiv. Pd₃**L^{F2}**₃**L^{S1}**₃ (left) and normalized emission of **D⁵** and **D⁵** after addition of 1 equiv. Pd₃**L^{F2}**₃**L^{S1}**₃ compared to just Pd₃**L^{F2}**₃**L^{S1}**₃ (right).

3.4.7.5 pH Studies on Pd$_3$L$^{F2}_3$L$^{S5}_3$
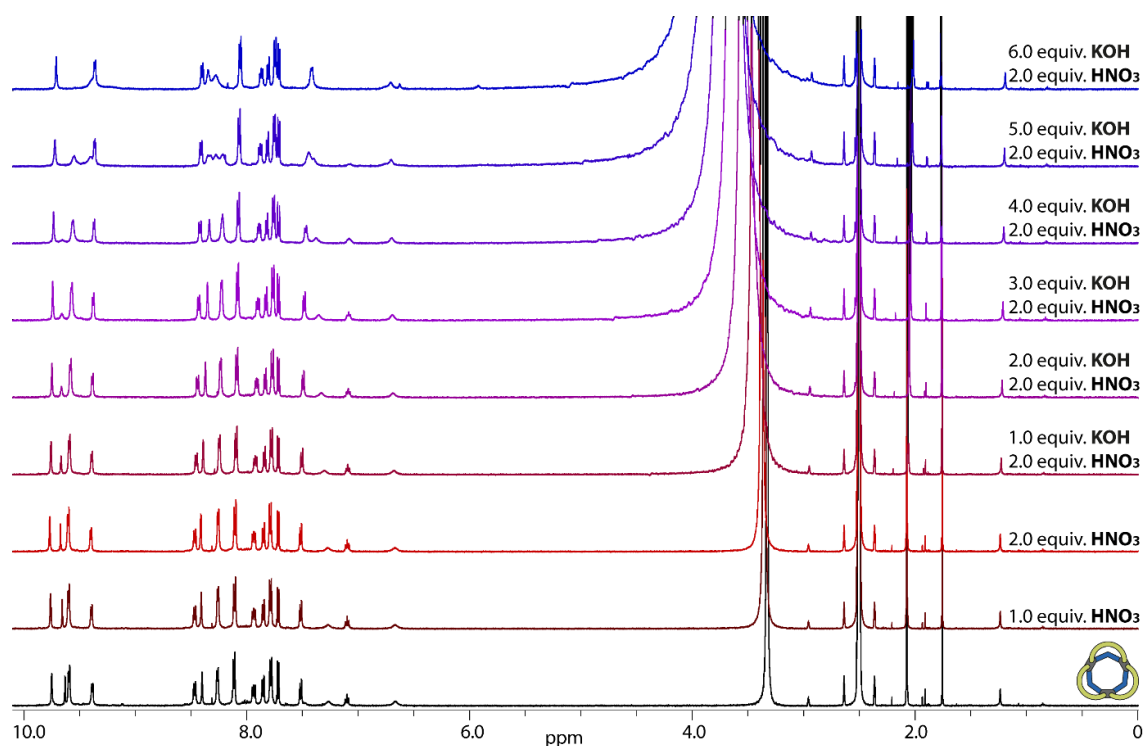
Figure 401: Full ^{1}H NMR spectra (500 MHz, 298 K, DMSO-d_6) of Pd$_3$L$^{F2}_3$L$^{S5}_3$ after successive addition of HNO$_3$ (17.5 mM in DMSO-d_6) and KOH (17.5 mM in D$_2$O).
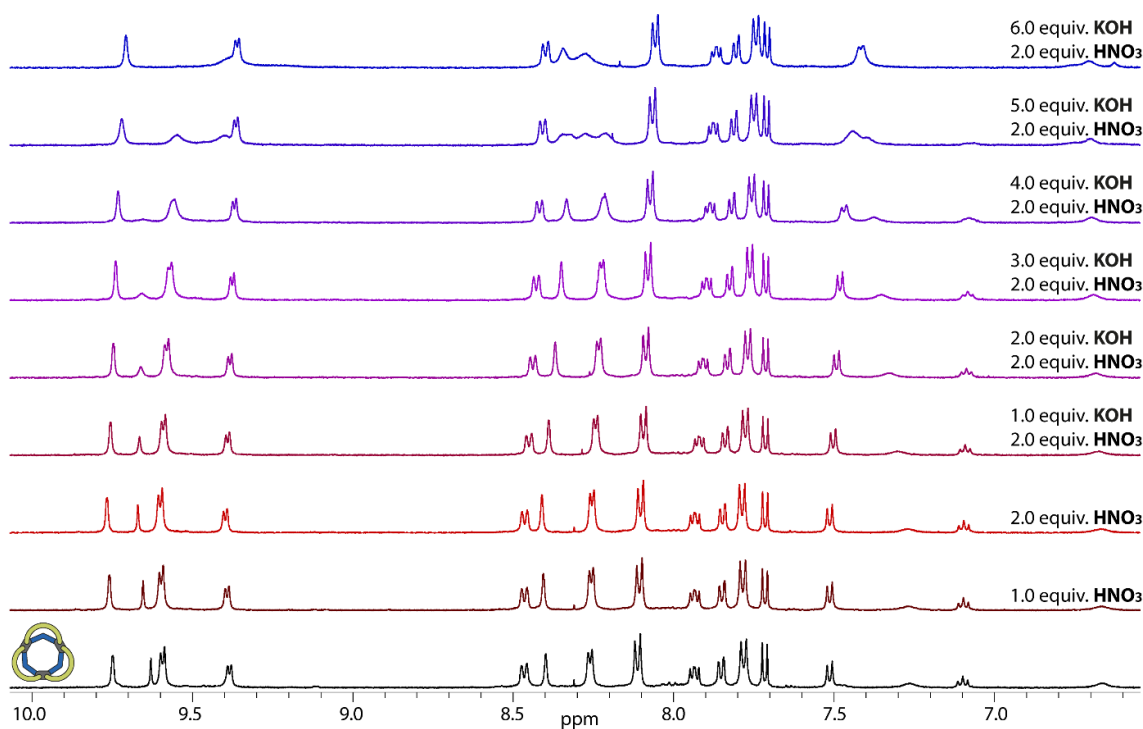
Figure 402: Partial ^{1}H NMR spectra (500 MHz, 298 K, DMSO-d_6) of Pd$_3$L$^{F2}_3$L$^{S5}_3$ after successive addition of HNO$_3$ (17.5 mM in DMSO-d_6) and KOH (17.5 mM in D$_2$O).

350
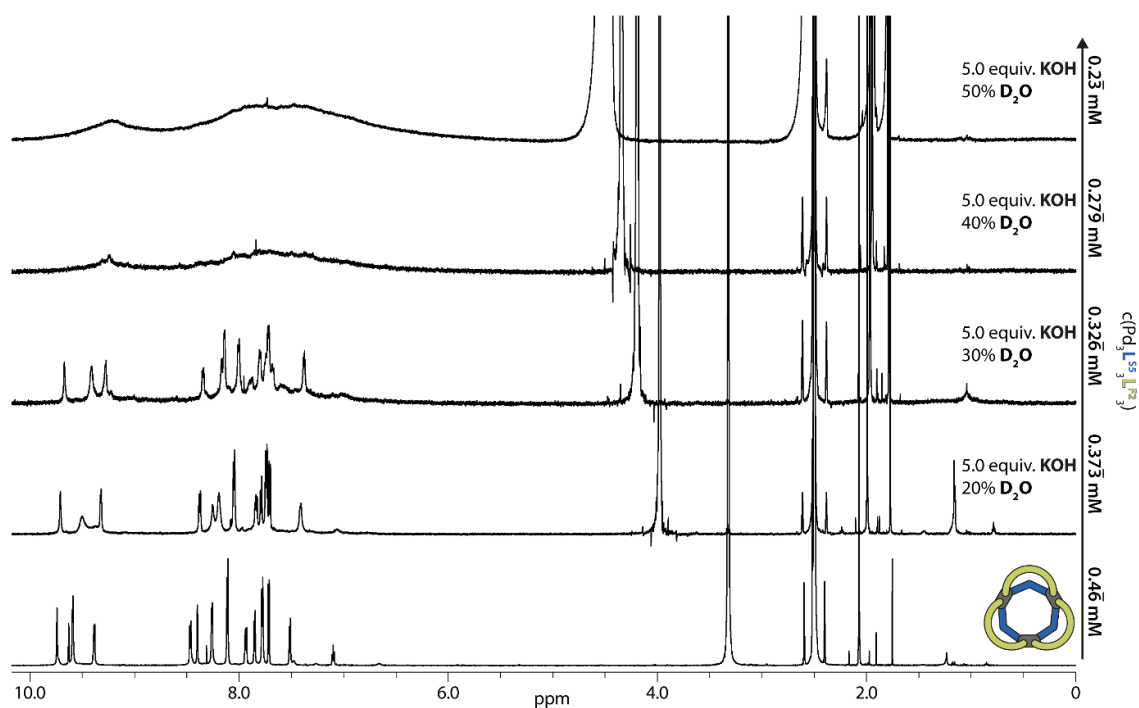
Figure 403: Full ^{1}H NMR spectra (500 MHz, 298 K, DMSO-d_6) of Pd$_3$**L**$^{F2}_3$**L**$^{S5}_3$ after addition of 5 equiv. KOH (17.5 mM in D$_2$O) and increasing dilution with D$_2$O.
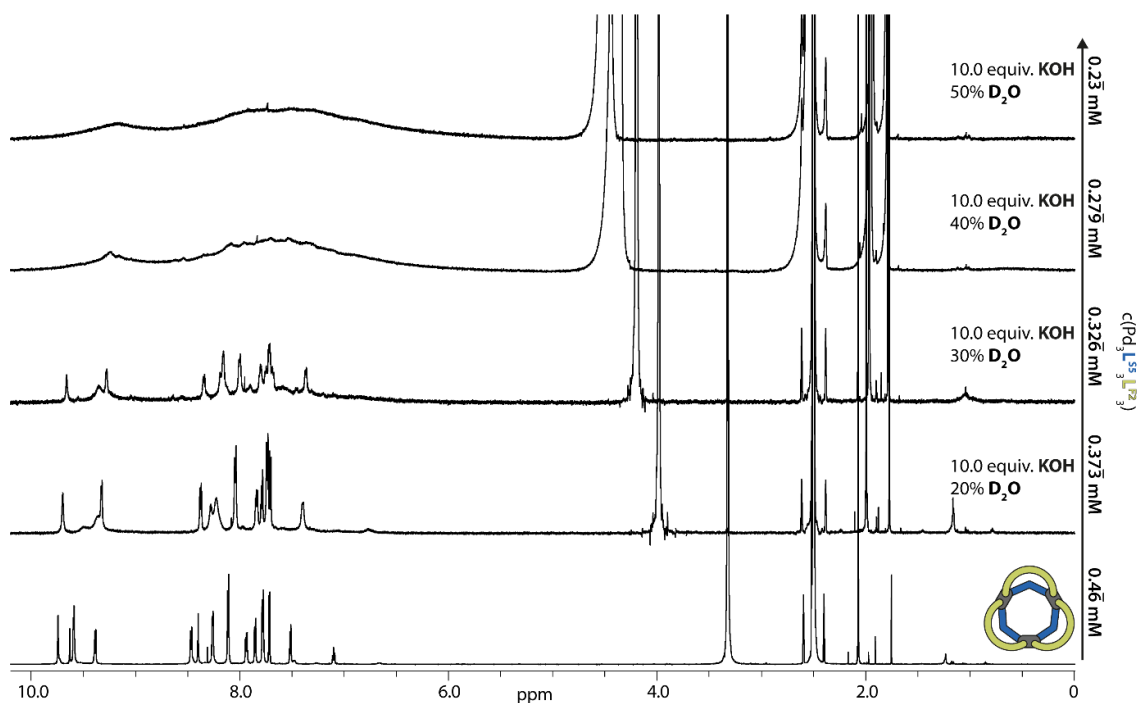
Figure 404: Full ^{1}H NMR spectra (500 MHz, 298 K, DMSO-d_6) of Pd$_3$**L**$^{F2}_3$**L**$^{S5}_3$ after addition of 10 equiv. KOH (17.5 mM in D$_2$O) and increasing dilution with D$_2$O.

3.4.7.6 Interlude Water-soluble Cage Pd₂L^{AQ}₄
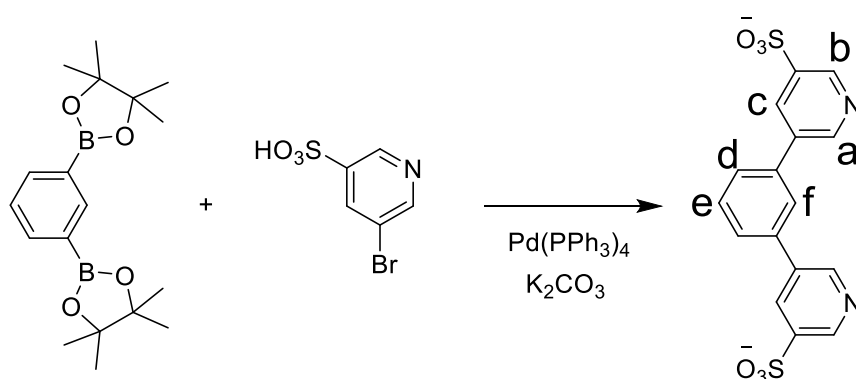
Scheme 49: Synthesis of **L^{AQ}** with proton assignment.

1,3-bis(4,4,5,5-tetramethyl-1,3,2-dioxaborolan-2-yl)benzene (200 mg, 0.606 μM, 1 equiv.), 5-bromopyridine-3-sulfonic acid (108 mg, 0.455 mM, 0.75 equiv.), K_2CO_3 (251 mg, 1.82 mmol, 3 equiv.) and Pd(PPh₃)₄ (28 mg, 0.024 mmol, 0.04 equiv.) were suspended in a mixture of toluene/ethanol/H_2O (2:1:1; 20 ml). The mixture was degassed three times using the *Freeze-Pump-Thaw*-method, heated to reflux and stirred overnight. After cooling down to room temperature, the reaction mixture was extracted thrice with chloroform. The aqueous phase was subjected to TLC control and the solvent was removed under reduced pressure. Crude ¹H NMR showed residual boronic ester species which could be removed by washing with pure EtOH. The residual solid was washed consecutively with MeOH, which led to precipitation of residual carbonate. Decanting the MeOH solution and successive removal of the solvent yielded pure **L^{AQ}**. The yield of the final product has not been determined.

It is noted, that careful choice of CO_3^{2-} source can help adjusting ligand solubility by means of counter cation modification. Furthermore, carbonate removal is of the essence, since it disturbs cage formation later on.
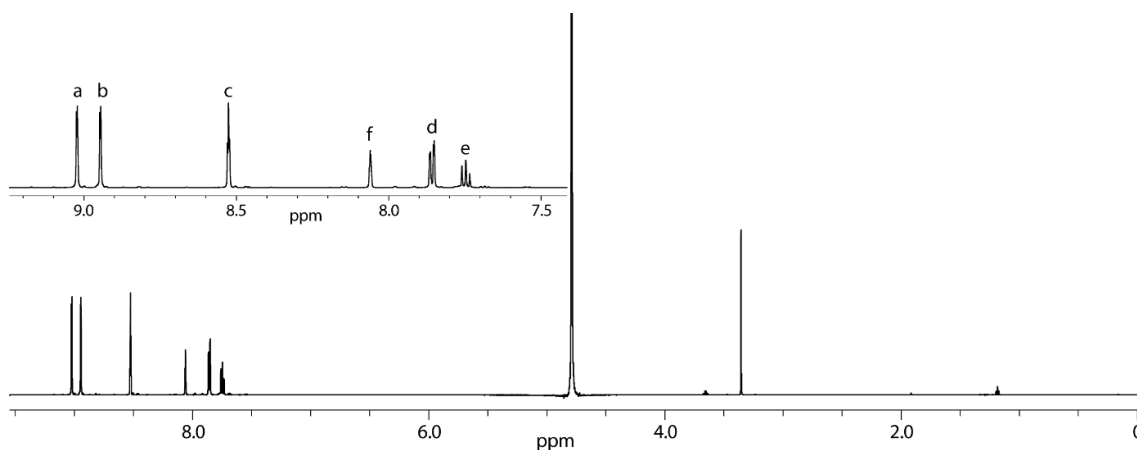
Figure 405: ¹H NMR spectrum (600 MHz, 298 K, D_2O) of **L^{AQ}**. A zoom into the aromatic region including proton assignment is shown in the inset.

^{1}H NMR (600 MHz, 298 K, D$_2$O) δ 9.02 (d, ^4J = 2.05 Hz, 2H, H^a), 8.95 (d, ^4J = 2.05 Hz, 2H, H^b), 8.53 (t, ^4J = 2.05 Hz, 2H, H^c), 8.06 (t, ^4J = 1.55 Hz, 1H, H^f), 7.86 (dd, ^3J = 7.75 Hz, ^4J = 1.55 Hz, 2H, H^d), 7.75 (t, ^3J = 7.75 Hz, 1H, H^e).
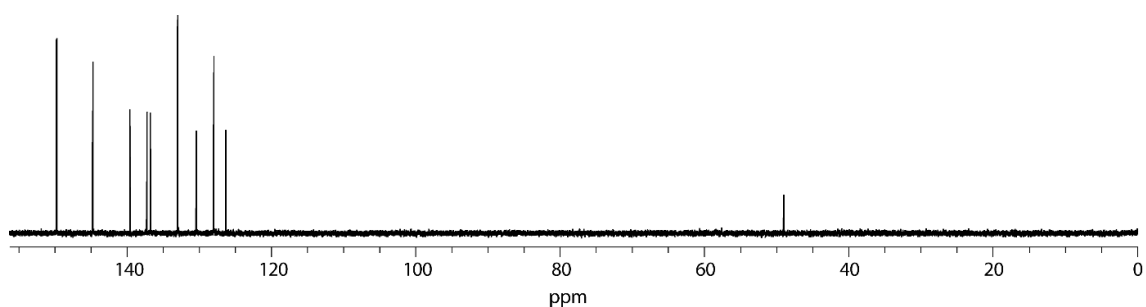
Figure 406: ^{13}C spectrum (151 MHz, 298 K, D$_2$O) of **L^{AQ}**.

^{13}C NMR (151 MHz, 298 K, D$_2$O) δ 149.70, 144.70, 139.56, 137.20, 136.74, 132.95, 130.38, 127.93, 126.29 ppm.

ESI-MS (negative mode)

Calc: 194.9996 (2−) m/z

Found: 195.0060 (2−) m/z
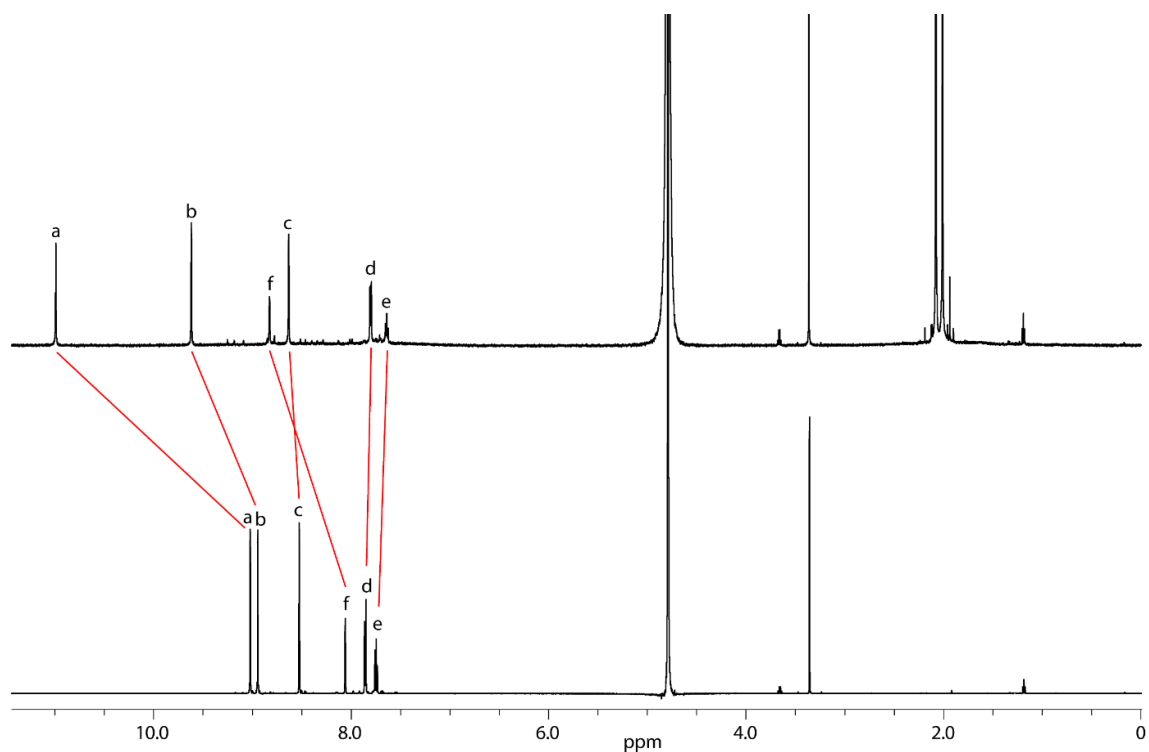
Figure 407: Full ^{1}H NMR spectrum (600 MHz, 298 K, D$_2$O) of **L^{AQ}** (bottom) and Pd$_2$**L^{AQ}**$_4$ (top) with indicated proton shifts.
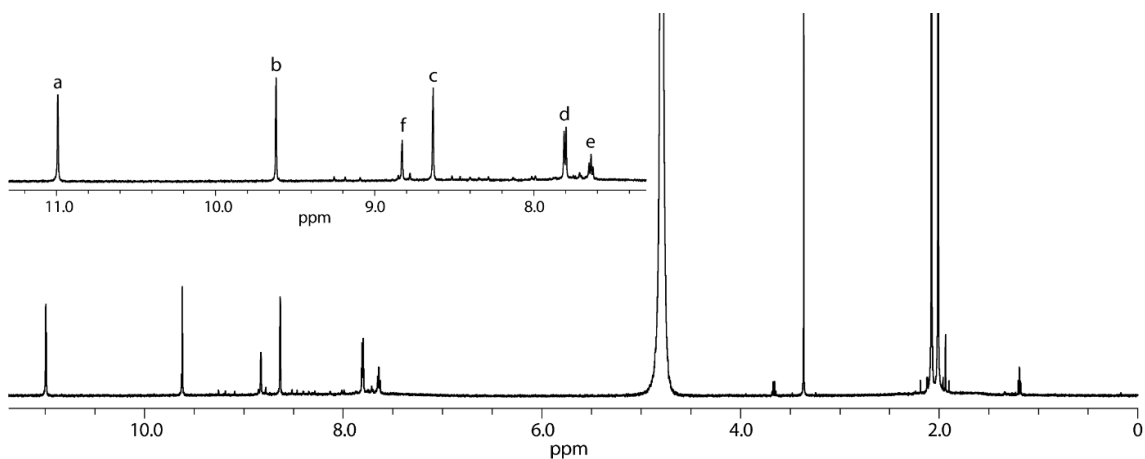
Figure 408: ^{1}H NMR spectrum (600 MHz, 298 K, D_2O) of Pd$_2$**L**$^{AQ}_4$. A zoom into the aromatic region including proton assignment is shown in the inset.

^{1}H NMR (600 MHz, 298 K, D_2O) $δ$ 10.99 (s, 8H, H^a), 9.62 (s, 8H, H^b), 8.83 (s, 4H, H^f), 8.63 (s, 8H, H^c), 7.80 (d, ^3J = 7.75 Hz, 8H, H^d), 7.64 (t, ^3J = 7.75 Hz, 4H, H^e) ppm.
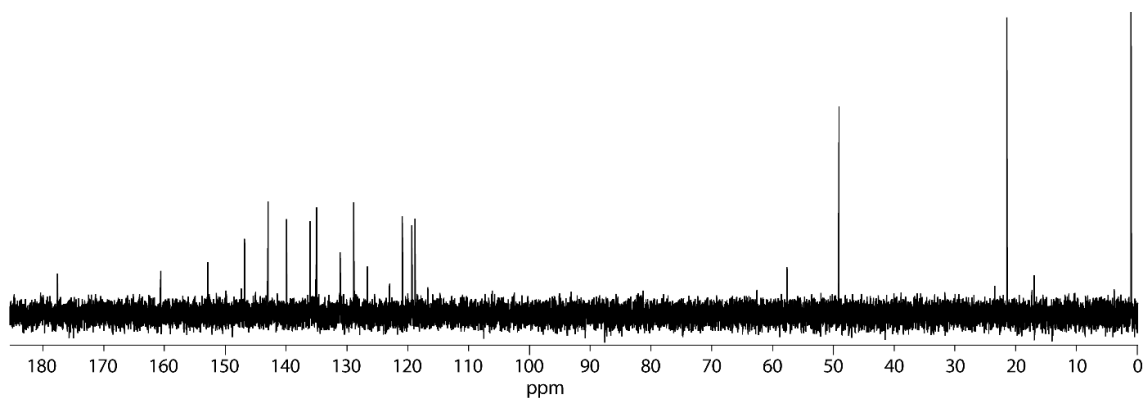
Figure 409: ^{13}C spectrum (151 MHz, 298 K, D_2O) of Pd$_2$**L**$^{AQ}_4$.

^{13}C NMR (151 MHz, 298 K, D_2O) $δ$ 152.82, 146.77, 142.93, 139.86, 136.00, 134.95, 131.05, 128.81, 126.60 ppm.

354
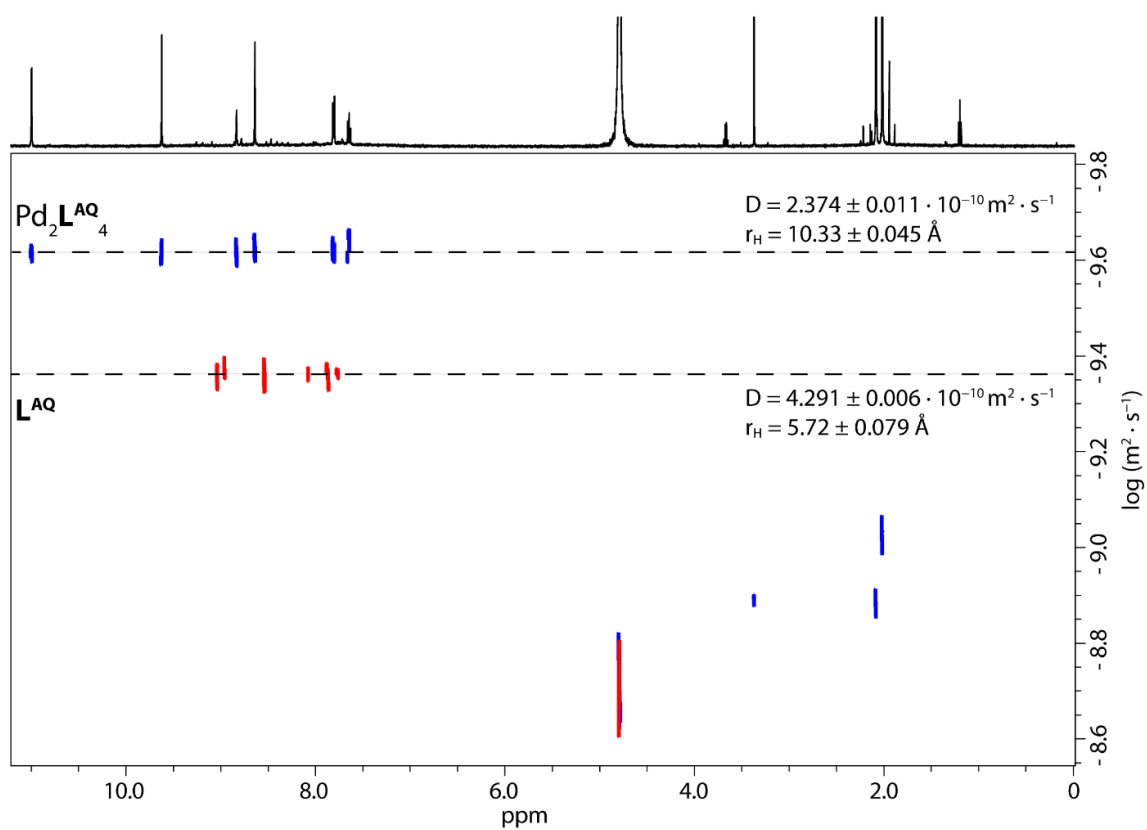
Figure 410: Overlayed ^{1}H DOSY NMR spectra (500 MHz, 298 K, D$_2$O) of **L^{AQ}** (red) and Pd$_2$**L^{AQ}**$_4$ (blue) with given diffusion coefficient D and hydrodynamic radius r_H.
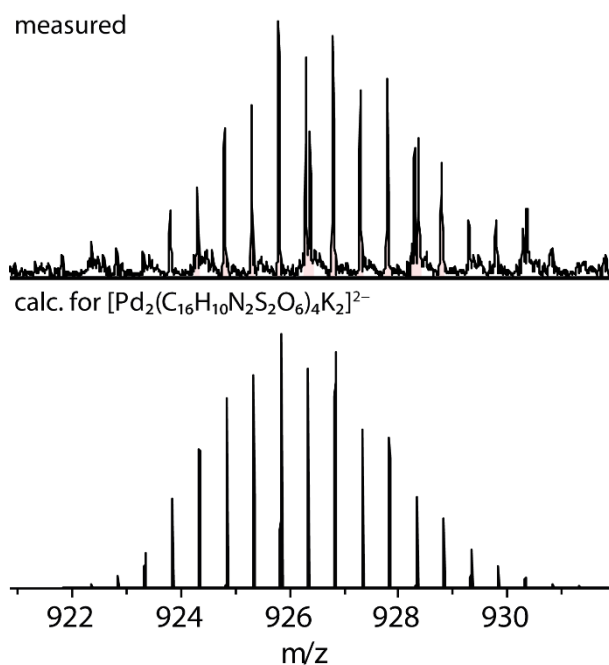
Figure 411: Partial ESI-MS spectrum of Pd$_2$**L^{AQ}**$_4$.

4 Conclusion and Outlook

In summary, the shape complementarity approach has been utilized to form a wide variety of heteroleptic coordination assemblies.

These assemblies have been analyzed in method application studies (chapter 3.1) as a complex model system to successfully challenge the resolving power of ion mobility mass spectrometry in complex coordination systems with special regard to miniscule size differences. Using this method, we could show minimal size differences within a *cis*- and *trans*-Pd$_2$L^{A}L^{B}L^{C}L^D coordination cage, which are structurally extremely closely related, thus helping to establish ion-mobility further as a powerful tool for the analysis of said differences in supramolecular structures.

In chapter 3.2, the SCA was used to prepare heteroleptic Pd$_2$L$^A_2$L$^B_2$ coordination cages incorporating strained alkyne linkers. The system contained four different heteroleptic cages, of which only one showed intriguing solvent switching behavior. This solvent switch could be used for the selective and clean guest-induced post-assembly separation of the two utilized ligands, one alongside the guest, and in host-guest competition experiments. Furthermore, calculations regarding the strain of the alkyne-linkers are on the way help understand the underlying enthalpic effect and complex solvent model calculations to access an explanation as to why the system shows this kind of solvent dependent behavior.

As the SCA is a powerful tool, to purposefully combine complementary functional groups, chapter 3.3 dealt with the combination of two complementary chromophores effectively realizing FRET in between the aforementioned. Furthermore, the cavity of the formed Pd$_2$L$^A_2$L$^B_2$ coordination cage has been used to bind a chiral guest molecule, which led to the alteration of the photophysical properties of the **HG** system. This has been analyzed using CD and CPL spectroscopy. It is further mentioned, that this system is one of the rare examples, in which chromophores directly incorporated in the backbone of a Pd(II) coordination cage were not fully quenched. These results show, how the SCA can be used to access complex materials with the formation of the assembly not only bringing two complementary functional groups together in a clean and controlled fashion, but additionally opening up the cavity inside to enable further applications and features via guest binding.

Chapter 3.4 dealt with the analysis of unique, fluorescent, open structures (UFOS). The combination of rigid ligands led to the formation of yet unprecedented symmetric, heteroleptic Pd$_3$L$^F_3$L$^{SX}_3$ assemblies with an open bowl conformation: The assemblies

maintained the fluorescent properties of its chromophore-based ligand $\mathbf{L^F}$ and showed high functional group tolerance for ligand $\mathbf{L^{SX}}$. The systematics of nuclearity increase were studied using electrostatic repulsion, bulk and bite angle increase. Furthermore, host-guest studies with the $Pd_3\mathbf{L^F}_3\mathbf{L^{SX}}_3$ assemblies showed CPL responses with a chiral (*R*)-BINSO guest molecule. Promising results were also obtained for the binding of common food dyes $\mathbf{D^{1\text{-}5}}$ to $Pd_3\mathbf{L^F}_3\mathbf{L^{S1}}_3$, of which it was feasible to deduce a systematic behavior correlating photophysical properties and binding motif. These insights pave the way for further studies regarding their photophysical properties and their stability allows a vast array of experiments to be done, like e.g. bridging them with guest molecules to form even higher-ordered structures.

5   General Measurement Information

5.1   NMR

NMR spectroscopic data was measured on the spectrometers Bruker AV 500 Avance NEO, AV 600 Avance III HD and AV 700 Avance III HD. For ^{1}H and ^{13}C NMR spectra, chemical shifts were calibrated to the solvent lock signal. Chemical shifts δ are given in ppm, coupling constants J in Hz. The following abbreviations are used to describe signal multiplicity for ^{1}H NMR spectra: s: singlet, d: doublet, t: triplet, dd: doublet of doublets; dt: doublet of triplets; m: multiplet, br: broad. All proton and carbon signals were assigned with the aid of 2D NMR spectra. ^{1}H DOSY NMR spectra were recorded with a *dstebpgp3s* pulse sequence with diffusion delays D20 of 0.08-0.10 s and gradient powers P30 of 1200 to 2800 µs.[186] T1 analyses of the corresponding signals in the 1D spectra were performed to obtain the diffusion coefficients D using the Stejskal-Tanner-Equation.[187] Hydrodynamic radii were calculated using the Stokes-Einstein-Equation.[188] All spectra were recorded in standard 5 mm NMR tubes at room temperature (25 °C) if not stated otherwise.

5.2   Mass Spectrometry

Mass spectrometry data were measured on Bruker ESI-timsTOF (electrospray ionization-trapped ion mobility-time of flight) and Bruker compact high-resolution LC mass spectrometers (positive/negative mode). For calibration of the TIMS and TOF devices, Agilent ESI-Low Concentration Tuning Mix was used.

5.3   X-Ray Single Crystal Structure Determination

Synchrotron beamline P11@DESY: Single crystal X-ray diffraction data was collected at macromolecular beamline P11, Petra III, DESY (a member of the Helmholtz Association, HGF), Hamburg, Germany. Samples were mounted using the Stäubli TX60L robotic arm. A wavelength of l = 0.6889 Å was chosen using a liquid N_2 cooled double crystal monochromator. Single crystal X-ray diffraction data was collected at 100(2) K on a single axis goniometer, equipped with an Oxford Cryostream 800 device and an Eiger 2 12M detector.

5.4 GPC

Recycling gel permeation chromatography was performed on Japan Analytical Industry NEXT and LaboACE instruments using JAIGEL 1-HH and 2-HH columns, 20 mm x 600 mm, flowrate 7 mL/min.

5.5 UV/Vis Spectroscopy

UV vis spectra were recorded on a DAD HP-8453 UV/Vis spectrometer.

5.6 CD Spectroscopy

Circular dichroism spectra were recorded on an Applied Photophysis qCD Chirascan CD spectrometer with a temperature-controlled cuvette holder.

5.7 Experimental Procedures

Where necessary, experiments were performed under argon atmosphere using standard Schlenk techniques. Chemicals and standard solvents were purchased from Sigma Aldrich, Acros Organics, Carl Roth, TCI Europe, VWR, ABCR or other suppliers and used as received, if not mentioned differently. Dry solvents were purchased or purified and dried over absorbent-filled columns on a GS-Systems solvent purification system (SPS). Reactions were monitored with thin layer chromatography (TLC) using silica coated aluminum plates (Merck, silica 60, fluorescence indicator F254, thickness 0.25 mm). For column chromatography, silica (Merck, silica 60, 0.02–0.063 mesh ASTM) was used as the stationary phase, if not mentioned otherwise.

6   Abbreviations

(R)-BINSO	*(R)*-1,1'-Binaphthyl-2,2'-disulfonate
(R)-CSA	(*R*)-camphor sulfonate
(S)-BINPhos	(*S*)-1,1'-Binaphthyl-2,2'-phosphate
BODIPY	Boron-dipyrromethene
CD	Circular dichroism
CSE	Coordination sphere engineering
COSY	Correlation spectroscopy
CPL	Circular polarized luminescence
CSI	Cryo-spray ionization
D	Dye
DCC	Dynamic covalent chemistry
DCM	Dichloromethane
DFT	Density-functional theory
DMF	Dimethylformamide
DMS	Differential mobility mass spectrometry
DMSO	Dimethyl sulfoxide
DOSY	Diffusion ordered spectroscopy
DPP	Diketopyrrolopyrrole
DTIMS	Drift tube ion mobility mass spectrometry
eCCS	Experimental collisional cross section
Equiv.	Equivalents
ESI	Electron spray ionization
EtOAc	Ethyl acetate
EtOH	Ethanol
FAIMS	Field asymmetric ion mobility mass spectrometry
FRET	Förster-resonance energy transfer
G	Guest
GPC	Gel permeation chromatography
H	Host
HR	High resolution
L	Ligand
LC	Liquid chromatography
M	Metal
Me	Methyl

MeOH	Methanol
MS	Mass spectrometry
NMR	Nuclear magnetic resonance
NOESY	Nuclear Overhauser enhancement spectroscopy
OTf	Triflate
PDB	Protein data base
PEG	Polyethylene glycol
Ph	Phenyl
POC	Porous organic cage
PM6	Parametrization method 6
ppm	Parts per million
rt	Room temperature
SCA	Shape complementarity approach
eCCS	Experimental collisional cross section
tCCS	Theoretical collisional cross section
THF	Tetrahydrofuran
TIMS	Trapped ion mobility mass spectrometry
TLC	Thin layer chromatography
TOF	Time-of-flight
TPE	Tetraphenyl ethylene
TWIMS	Travelling wave ion mobility mass spectrometry
UFOS	Unique fluorescent open structures
UV/Vis	Ultraviolet/visible
VT	Variable temperature

Dedication

I want to dedicate this thesis to my parents:

Mama, Papa ohne euch wäre diese Arbeit niemals möglich gewesen! Ihr habt immer an mich geglaubt, mir von klein auf meine nervigen "Warum?"-Fragen beantwortet und mich von Anfang bis Ende unterstützt, auch wenn ich mal vom Weg abgekommen bin.

Danke für alles, ihr könnt euch nicht vorstellen, wie sehr.

Ich hab euch lieb!

7 Acknowledgements

First, I want to thank Prof. Dr. Guido Clever for giving me the chance to prepare this thesis within his group including scientific discussions and the chance to present this work around the globe and Prof. Dr. Christian Merten for taking over the role of my second supervisor.

Furthermore, I want to thank Dr. Ananya Baksi for special MS measurements and Dr. Julian Holstein for X-ray analysis.

Additionally, I want to thank Heidi Auer for going out of her way (like well after working hours) jumping to answer questions regarding thesis submission and helping to file all documents in time and order.

I want to thank the students I supervised over these years for helping me work on my projects and learn more about teaching and myself. Thank you, Nicole, Laura, Seyma and most prominently Erti!

I want to thank the NMR-Team, Basti, Ben and Jan for always enduring my weird requests and suggesting better alternatives. Also, thanks Ben for only scaring the shit out of me once.

Thanks to my subgroup leaders, Irene, Elie and Jacopo for all the helpful suggestions and discussion regarding my research and dealing with my not always happy-go-lucky attitude. Thank you for dealing with my stubborn ass and teaching me a lot.

Irene, thank you for being my older lab sister (not literally, you're not old). All the best for your future career! If you've been to India together, you are poo-friends forever!

Elie, don't be so hard on yourself, you almost look my age dude! I wish you all the best, you will be an amazing professor!

A special thanks goes to Dr. Jacopo Tessarolo: You were a scary guy when you first arrived in the lab, but I'm really happy now being able to call you a good friend. You taught me a lot and your humor is just on point for me. Also, I'm sorry to have caused you so much exasperation and I'm very grateful, that you never gave up on my stubborn ass measuring UV/Vis.

Thank you, Christoph, for all the calculations and helping me with all my weird requests and ideas regarding computational science I had over the course of this PhD. You always indulged me, even if the requests were weird and turned super weird ones down in a very kind way.

I was extremely lucky, to prepare my thesis at the time of overabundance of Postdocs. There was always a more experienced researcher to help me out and answer questions (however stupid they were). Thank you so much Haeri, Sudhakar, Pedro and of course Jacopo and Kai! I learned a lot and wish you all the best for your future!

A big thanks also to Birgit and Gabi! You are literally angels of this group, you listened to every problem and sorrow I had and kept my spirits high. There was no problem, that could not be solved in one way or another and you were supportive through all my time in the CleverLab! I know, this thanks doesn't do justice to what you did but still: Thank you so much!

Special thanks goes to Simon, my partner in crime regarding lab supervision in ACF and BioAC practical courses. Dude! I was so happy to have you around as a well-organized but strict (to the students) "bad cop". Supervising practical courses was still not my favorite thing to do but you made it so much more enjoyable, that I (almost) looked forward to it! You cared for the students to learn something, which was all the more important since at least BioAC was one of the courses, that I personally learned a lot from back when I was just starting out the master.

Speaking of BioAC, I want to thank my little Eumel for adopting the old hag, that just came out of hiding in the basement. You don't know it, but you had a huge impact on me actually finishing my studies and going through with this. Thank you!

I want to thank Robin, for being the big bro everyone needs in their (lab)-life – always helpful, kind and with just the right amount of sarcasm. Looking at the next generation (looking at you Björn!) I hope everyone starting their PhD in this lab will have one.

I also want to thank the crazy blonde giant for showing me how close genius and madness can be at times. Never change, madman!

Thank you Q2 for being literally the cutest little rascal I have ever encountered. Looking forward to visiting you in China <3.

I want to further thank our technicians, at first Alex and Kristian and then Maike, Franzi and Laura for providing everything, from materials to work with and chemicals to a shoulder to cry on when shit hit the fan. The door was always open for me and I appreciated this to no end.

In this regard, I want to convey special thanks to Laura. Sweety you are like a little sister to me ever since we did our first steps in the academic world together sending molecules flying. Hell, we made a paper and an application note without anyone telling us to, it was all ours! But let me tell you something (thanks Subhadeep, for always having this phrase

364

in mind…): It's not all there is, and the wise hag says: Just do, what makes you happy! Having ambitions is nice but don't fret it if something doesn't work. – Wort zum Sonntag Ende –

I want to thank Magi and Julia for all these wine-clad evenings talking about everything and nothing, raging, cursing, laughing, crying, hating, loving wine and all good or bad things. Wine is a solution after all.

Speaking of alcohol, Fridays are for Pfeffi! A well-loved tradition, that I'm a bit bummed not being able to enjoy frequently anymore. I can't express enough how happy I am, that you guys even came up here to Hanover for a sleepover party and we were able to keep this up even over the distance of more than 200 km. Thank you for all the fun and weird things (looking at you, Jenny) that made PhDing so much more bearable (guess the alcohol helped a bit too). Thank you gals and guys, Björn (Robin 2.0, keep up your chill attitude!), Franzi (never stop cleaning – you had André as a supervisor, you will manage just fine), Hannah (seeing your development throughout the years was amazing, you were so shy in the beginning and now you are super confident! Keep it up, you can do it (and if not alone, reach out) - und Tobi is spülen), Ingo (thin line between Opa André and Ingo Urlaub – love it), Jenny (never stop doing Jenny things), Kathi (your stories are amazing, don't let others get you down and just between us: don't put too much effort in teaching, it's way too exhausting), Maike (crazy cat lady <3, you're a real sweetheart but I love it, when you go into "Alex-mode"), Robin (Robin 1.0, das original), Shaian (sleeping ON the box in a club on a metal party is respectfully the most chill thing, I have ever seen), Simon (the only guy I can and ever will send heart emojis to aside from a certain someone)

All of you: You are amazing!

And now on a very personal note, thank you Shota for letting me basically adopt you into our little family. Family is not only by blood but also who we chose to be. We might be the weirdest patchwork family with a ridiculous background, but I think that's pretty darn amazing. You always made me do my best and try new, exciting recipes. Your gratefulness was what motivated me to give it my all and cook up healthy meals throughout the years. And your sassiness was hilarious. I'm looking forward to visiting you in Japan soon! Miss you very much.

And finally, I'd have to convey my thanks to a very special someone. I consider myself extremely lucky to not have been alone in this but to have my partner with me. You always held my spirits high, taught me things I had yet to learn and got me back to the ground, when I way having a little too crazy ideas. You tested (and fractured) my patience

more than once and drove me all kinds of mad (still to this day) but you balance me, complete me. I'm not gonna name you as it's already too fucking cheesy and that wouldn't be us, right? I love you.

I'm not going to sugarcoat it, the PhD was hard and tough and at some points even seemed impossible, but knowing you are NOT alone in this and you have friends to help you and get you through this is so comforting. I had amazing colleagues in the Flab, always helpful, supportive and - one thing not to be neglected in lab work - clean! Thank you, Bin, Jacopo, Kai and Shota, for making lablife amazing!

Knowing all I know now, I would do all of it again, not because it was so enjoyable but because I made friends for life and experiences, that shaped my personality in more than one way. I would not say "I'm smarter than before!" but more like "I'm wiser than before".

It was shit – I'd do it again!

For a solitary animal egoism is a virtue, that tends to preserve and improve the species; in any kind of community it becomes a destructive vice."

Erwin Schrödinger

8 Literature

[1] S. Tsunasawa, T. Masaki, M. Hirose, M. Soejima, F. Sakiyama, *J. Biol. Chem.* **1989**, *264*, 3832–3839.

[2] A. E. Eriksson, T. A. Jones, A. Liljas, *Proteins: Struct., Funct., Bioinf.* **1988**, *4*, 274–282.

[3] S. E. V. Phillips, *J. Mol. Biol.* **1980**, *142*, 531–554.

[4] M. Lim, T. A. Jackson, P. A. Anfinrud, *J. Biol. Inorg. Chem.* **1997**, *2*, 531–536.

[5] A. J. Thomson, H. B. Gray, *Curr. Chem. Biol.* **1998**, *2*, 155–158.

[6] P. Carter, *Biochem. J.* **1986**, *237*, 1–7.

[7] E. Fischer, *Dtsch. Chem. Ges.* **1894**, *27*, 2985–2993.

[8] G. R. Desiraju, *Nature* **2001**, *412*, 397–400.

[9] D. J. Cram, G. M. Lein, *J. Am. Chem. Soc.* **1985**, *107*, 3657–3668.

[10] C. J. Pedersen, *J. Am. Chem. Soc.* **1967**, *89*, 2495–2496.

[11] J. M. Lehn, *Pure Appl. Chem.* **1978**, *50*, 871–892.

[12] B. Dietrich, J. M. Lehn, J. P. Sauvage, *Tetrahedron Lett.* **1969**, *10*, 2889–2892.

[13] B. Dietrich, J. M. Lehn, J. P. Sauvage, *Tetrahedron Lett.* **1969**, *10*, 2885–2888.

[14] J.-M. Lehn, *Acc. Chem. Res.* **1978**, *11*, 49−57.

[15] D. J. Cram, T. Kaneda, G. M. Lein, R. C. Helgeson, *Chem. Commun.* **1979**, 948–9950.

[16] G. Crini, *Chem. Rev.* **2014**, *114*, 10940–10975.

[17] T. Ogoshi, S. Kanai, S. Fujinami, T. Yamagishi, Y. Nakamoto, *J. Am. Chem. Soc.* **2008**, *130*, 5022–5023.

[18] W. A. Freeman, W. L. Mock, and N. Y. Shih, *J. Am. Chem. Soc.* **1981**, 7367–7368.

[19] C. D. G. and J. A. Levine, *J. Am. Chem. Soc.* **1982**, 2652–2653.

[20] M. Mastalerz, *Acc. Chem. Res.* **2018**, *51*, 2411–2422.

[21] Y. Jin, C. Yu, R. J. Denman, W. Zhang, *Chem. Soc. Rev.* **2013**, *42*, 6634–6654.

[22] Royal Swedish Academy of Sciences, *Nobel Lecture*, **1987**.

[23] G. W. Gokel, W. M. Leevy, M. E. Weber, *Chem. Rev.* **2004**, *104*, 2723–2750.

[24] R. Behrend, E. Meyer, F. Rusche, *Liebigs Ann. Chem.* **1905**, *339*, 1–37.

[25] A. Villiers, *Bull. Soc. Chim. Fr.* **1891**, 470.

[26] L. Vial, F. Perret, J. Leclaire, *Eur. J. Org. Chem.* **2022**, *e202101274.*

[27] X. Yang, D. Yuan, J. Hou, A. C. Sedgwick, S. Xu, T. D. James, L. Wang, *Coord. Chem. Rev.* **2021**, *428*, 213609.

[28] M. W. Schneider, I. M. Oppel, A. Griffin, M. Mastalerz, *Angew. Chem. Int. Ed.* **2013**, *52*, 3611–3615.

[29] G. Zhang, O. Presly, F. White, I. M. Oppel, M. Mastalerz, *Angew. Chem. Int. Ed.* **2014**, *53*, 1516–1520.

[30] X. Yang, Z. Ullah, J. F. Stoddart, C. T. Yavuz, *Chem. Rev.* **2023**, *123*, 4602–4634.

[31] D. Chakraborty, P. S. Mukherjee, *Chem. Commun.* **2022**, *58*, 5558–5573.

[32] C. R. P. Fulong, S. Kim, A. E. Friedman, T. R. Cook, *Front. Chem.* **2019**, *7*, 567.

[33] R. Chakrabarty, P. S. Mukherjee, P. J. Stang, *Chem. Rev.* **2011**, *111*, 6810–6918.

[34] S. J. Dalgarno, N. P. Power, J. L. Atwood, *Coord. Chem. Rev.* **2008**, *252*, 825–841.

[35] D. Bardhan, D. K. Chand, *Chem. Eur. J.* **2019**, *25*, 12241−12269.

[36] S. Pasquale, S. Sattin, E. C. Escudero-Adán, M. Martínez-Belmonte, J. de Mendoza, *Nat Commun* **2012**, *3*, 785.

[37] X. Yan, F. Wang, B. Zheng, F. Huang, *Chem. Soc. Rev.* **2012**, *41*, 6042–6065.

[38] D. A. Poole, E. O. Bobylev, B. de Bruin, S. Mathew, J. N. H. Reek, *Inorg. Chem.* **2023**, *62*, 5458–5467.

[39] S. Saha, I. Regeni, G. H. Clever, *Coord. Chem. Rev.* **2018**, *374*, 1–14.

[40] K. Harris, Q.-F. Sun, S. Sato, M. Fujita, *J. Am. Chem. Soc.* **2013**, *135*, 12497–12499.

[41] Q.-F. Sun, J. Iwasa, D. Ogawa, Y. Ishido, S. Sato, T. Ozeki, Y. Sei, K. Yamaguchi, M. Fujita, *Science* **2010**, *328*, 1144–1147.

[42] D. Fujita, Y. Ueda, S. Sato, H. Yokoyama, N. Mizuno, T. Kumasaka, M. Fujita, *Chem.* **2016**, *1*, 91–101.

[43] D. Fujita, Y. Ueda, S. Sato, N. Mizuno, T. Kumasaka, M. Fujita, *Nature* **2016**, *540*, 563.

[44] K. Suzuki, M. Tominaga, M. Kawano, M. Fujita, *Chem. Commun.* **2009**, 1638–1640.

[45] S. Ghorai, S. Maji, B. Paul, K. Samanta, S. K. Sen, R. Natarajan, *Chem. Asian J.* **2023**, e202201312.

[46] E. O. Bobylev, D. A. Poole, B. de Bruin, J. N. H. Reek, *J. Am. Chem. Soc.* **2022**, *144*, 15633–15642.

[47] K. Suzuki, M. Kawano, M. Fujita, *Angew. Chem. Int. Ed.* **2007**, *46*, 2819–2822.

[48] D. R. Martir, L. Delforce, D. B. Cordes, A. M. Z. Slawin, S. L. Warriner, D. Jacquemin, E. Zysman-Colman, *Inorg. Chem. Front.* **2020**, *7*, 232-238

[49] T. Zhang, L.-P. Zhou, X.-Q. Guo, L.-X. Cai, Q.-F. Sun, *Nat. Commun.* **2017**, *8*, 15898.

[50] M. Han, Y. Luo, B. Damaschke, L. Gómez, X. Ribas, A. Jose, P. Peretzki, M. Seibt, G. H. Clever, *Angew. Chem. Int. Ed.* **2016**, *55*, 445–449.

[51] J. Tessarolo, H. Lee, E. Sakuda, K. Umakoshi, G. H. Clever, *J. Am. Chem. Soc.* **2021**, *143*, 6339–6344.

[52] C. Klein, C. Gütz, M. Bogner, F. Topić, K. Rissanen, A. Lützen, *Angew. Chem. Int. Ed.* **2014**, *53*, 3739–3742.

[53] T. Tateishi, T. Kojima, S. Hiraoka, *Inorg. Chem.* **2018**, *57*, 2686–2694.

[54] A. Schmidt, A. Casini, F. E. Kühn, *Coord. Chem. Rev.* **2014**, *275*, 19–36.

[55] C. Desmarets, T. Ducarre, M. N. Rager, G. Gontard, H. Amouri, *Materials* **2014**, *7*, 287–301.

[56] W. M. Bloch, S. Horiuchi, J. J. Holstein, C. Drechsler, A. Wuttke, W. Hiller, R. A. Mata, G. H. Clever, *Chem. Sci.* **2023**, *14*, 1524–1531.

[57] W. M. Bloch, Y. Abe, J. J. Holstein, C. M. Wandtke, B. Dittrich, G. H. Clever, *J. Am. Chem. Soc.* **2016**, *138*, 13750-13755.

[58] I. Regeni, B. Chen, M. Frank, A. Baksi, J. J. Holstein, G. H. Clever, *Angew. Chem. Int. Ed.* **2020**, *60*, 5673–5678.

[59] M. D. Johnstone, M. Frank, G. H. Clever, F. M. Pfeffer, *Eur. J. Org. Chem.* **2013**, *2013*, 5848–5853.

[60] D. Ogata, J. Yuasa, *Angew. Chem. Int. Ed.* **2019**, *58*, 18424-18428.

[61] J. E. M. Lewis, A. Tarzia, A. J. P. White, K. E. Jelfs, *Chem. Sci.* **2019**, *11*, 677-683

[62] J. Lewis, J. Crowley, *ChemPlusChem* **2020**, *85*, 815-827.

[63] K. Wu, B. Zhang, C. Drechsler, J. J. Holstein, G. H. Clever, *Angew. Chem. Int. Ed.* **2020**, *60*, 6403–6407.

[64] W. M. Bloch, J. J. Holstein, W. Hiller, G. H. Clever, *Angew. Chem. Int. Ed.* **2017**, *56*, 8285–8289.

[65] A. Platzek, S. Juber, C. Yurtseven, S. Hasegawa, L. Schneider, C. Drechsler, K. E. Ebbert, R. Rudolf, Q. Yan, J. J. Holstein, L. V. Schäfer, G. H. Clever, *Angew. Chem. Int. Ed.* **2022**, *61*, e202209305.

[66] K. E. Ebbert, L. Schneider, A. Platzek, C. Drechsler, B. Chen, R. Rudolf, G. H. Clever, *Dalton Trans.* **2019**, *48*, 11070-11075.

[67] K. Wu, J. Tessarolo, A. Baksi, G. H. Clever, *Angew. Chem. Int. Ed.* **2022**, *61*, e202205725.

[68] J. Tessarolo, E. Benchimol, A. Jouaiti, M. W. Hosseini, G. H. Clever, *Chem. Commun.* **2023**, *59*, 3467–3470.

[69] I. Regeni, Dye-Based Coordination Cages, Dissertation, TU Dortmund University, **2020**.

[70] H. Lee, J. Tessarolo, D. Langbehn, A. Baksi, R. Herges, G. H. Clever, *J. Am. Chem. Soc.* **2022**, *7*, 3099–3105.

[71] R.-J. Li, J. Tessarolo, H. Lee, G. H. Clever, *J. Am. Chem. Soc.* **2021**, *143*, 3865–3873.

[72] R.-J. Li, J. J. Holstein, W. G. Hiller, J. Andréasson, G. H. Clever, *J. Am. Chem. Soc.* **2019**, *141*, 2097–2103.

[73] M. Frank, J. Ahrens, I. Bejenke, M. Krick, D. Schwarzer, G. H. Clever, *J. Am. Chem. Soc.* **2016**, *138*, 8279–8287.

[74] T. R. Schulte, J. J. Holstein, G. H. Clever, *Angew. Chem. Int. Ed.* **2019**, *58*, 5562–5566.

[75] B. Chen, J. J. Holstein, A. Platzek, L. Schneider, K. Wu, G. H. Clever, *Chem. Sci.* **2022**, *13*, 1829–1834.

[76] B. Chen, J. J. Holstein, S. Horiuchi, W. G. Hiller, G. H. Clever, *J. Am. Chem. Soc.* **2019**, *141*, 8907–8913.

[77] B. Chen, S. Horiuchi, J. J. Holstein, J. Tessarolo, G. H. Clever, *Chem. Eur. J.* **2019**, *25*, 14921-14927.

[78] S. Hasegawa, S. L. Meichsner, J. J. Holstein, A. Baksi, M. Kasanmascheff, G. H. Clever, *J. Am. Chem. Soc.* **2021**, *143*, 9718–9723.

[79] S. Hasegawa, G. H. Clever, *Chem.* **2020**, *6*, 5–7.

[80] S. Pullen, J. Tessarolo, G. H. Clever, *Chem. Sci.* **2021**, *12*, 7269–7293.

[81] W. M. Bloch, G. H. Clever, *Chem. Commun.* **2017**, *53*, 8506–8516.

[82] M. Yamashina, T. Yuki, Y. Sei, M. Akita, M. Yoshizawa, *Chem. Eur. J.* **2015**, *21*, 4200–4204.

[83] A. M. Johnson, R. J. Hooley, *Inorg. Chem.* **2011**, *50*, 4671–4673.

[84] S. Pullen, G. H. Clever, *Acc. Chem. Res.* **2018**, *51*, 3052–3064.

[85] D. Preston, J. E. Barnsley, K. C. Gordon, J. D. Crowley, *J. Am. Chem. Soc.* **2016**, *138*, 10578–10585.

[86] R. Zhu, W. M. Bloch, J. J. Holstein, S. Mandal, L. V. Schäfer, G. H. Clever, *Chem. Eur. J.* **2018**, *24*, 12976–12982.

[87] Q. Sun, S. Sato, M. Fujita, *Angew. Chem. Int. Ed.* **2014**, *53*, 13510–13513.

[88] S. Sudan, R.-J. Li, S. M. Jansze, A. Platzek, R. Rudolf, G. H. Clever, F. Fadaei-Tirani, R. Scopelliti, K. Severin, *J Am Chem Soc* **2021**, *143*, 1773–1778.

[89] R. Li, F. Fadaei-Tirani, R. Scopelliti, K. Severin, *Chem. Eur. J.* **2021**, *27*, 9439–9445.

[90] C. Schalley, *Analytical Methods in Supramolecular Chemistry*, Wiley-VCH, Weinheim, **2007**.

[91] B. Reif, S. E. Ashbrook, L. Emsley, M. Hong, *Nat. Rev. Methods Primers* **2021**, *1*, 2.

[92] A. Pastor, E. Martínez-Viviente, *Coord. Chem. Rev.* **2008**, *252*, 2314–2345.

[93] P. Comba, *Modeling of Molecular Properties*, Wiley-VCH, Weinheim, **2011**.

[94] M. Lehr, T. Paschelke, E. Trumpf, A. Vogt, C. Näther, F. D. Sönnichsen, A. J. McConnell, *Angew. Chem. Int. Ed.* **2020**, *59*, 19344–19351.

[95] R. G. Bryant, *J. Chem. Educ.* **1983**, *60*, 933–935.

[96] Y.-L. Lu, J.-Q. Song, Y.-H. Qin, J. Guo, Y.-H. Huang, X.-D. Zhang, M. Pan, C.-Y. Su, *J. Am. Chem. Soc.* **2022**, *144*, 8778–8788.

[97] Z. Qi, T. Heinrich, S. Moorthy, C. A. Schalley, *Chem. Soc. Rev.* **2014**, *44*, 515–531.

[98] L. Polewski, A. Springer, K. Pagel, C. A. Schalley, *Acc. Chem. Res.* **2021**, *54*, 2445–2456.

[99] A. R. Johnson, E. E. Carlson, *Anal. Chem.* **2015**, *87*, 10668–10678.

[100] G. Carroy, C. Daxhelet, V. Lemaur, J. D. Winter, E. D. Pauw, J. Cornil, P. Gerbaux, *Chem. Eur. J.* **2016**, *22*, 4528–4534.

[101] E. V. Peris, C. Vicent, V. Martinez-Agramunt, V. Gandhi, C. Larriba-Andaluz, D. Gusev, *Angew. Chem. Int. Ed.* **2021**, *60*, 15412-15417

[102] M. M. Zimnicka, *Mass Spectrom. Rev.* **2023**, DOI 10.1002/mas.21851.

[103] E. A. Mason, E. W. McDaniel, *Transport Properties of Ions in Gases*, **1988**, 193–224.

[104] J. N. Dodds, E. S. Baker, *J. Am. Soc. Mass Spectrom.* **2019**, *30*, 2185–2195.

[105] K. Michelmann, J. A. Silveira, M. E. Ridgeway, M. A. Park, *J. Am. Soc. Mass Spectrom.* **2015**, *26*, 14–24.

[106] D. R. Hernandez, J. D. DeBord, M. E. Ridgeway, D. A. Kaplan, M. A. Park, F. Fernandez-Lima, *Analyst* **2014**, *139*, 1913–1921.

[107] M. E. Ridgeway, M. Lubeck, J. Jordens, M. Mann, M. A. Park, *Int. J. Mass Spectrom.* **2018**, *425*, 22–35.

[108] J. A. Silveira, M. E. Ridgeway, M. A. Park, *Anal. Chem.* **2014**, *86*, 5624–5627.

[109] K. Ebbert, Systematic Studies on Heteroleptic $Pd_2L^A_2L^B_2$ Coordination Cages, Master Thesis, TU Dortmund University, **2018**.

[110] G. Joos, I. M. Freeman, *Theoretical Physics*, Dover Publications, New York, **1986**.

[111] P. Atkins, J. de Paula, *Physical Chemistry for the Life Sciences*, **2008**.

[112] N. Mehio, S. Dai, D. Jiang, *J. Phys. Chem. A* **2014**, *118*, 1150–1154.

[113] C. Larriba, C. J. Hogan, *J. Phys. Chem.* **2013**, *117*, 3887–3901.

[114] C. Larriba, C. J. Hogan, *J. Comput. Phys.* **2013**, *251*, 344–363.

[115] M. F. Mesleh, J. M. Hunter, A. A. Shvartsburg, G. C. Schatz, M. F. Jarrold, *J. Phys. Chem.* **1996**, *100*, 16082–16086

[116] I. Campuzano, M. F. Bush, C. V. Robinson, C. Beaumont, K. Richardson, H. Kim, H. I. Kim, *Anal. Chem.* **2012**, *84*, 1026–1033.

[117] R. Zhu, J. Lübben, B. Dittrich, G. H. Clever, *Angew. Chem. Int. Ed.* **2015**, *54*, 2796–2800.

[118] J.-F. Greisch, J. Chmela, M. E. Harding, D. Wunderlich, B. Schäfer, M. Ruben, W. Klopper, D. Schooss, M. M. Kappes, *Phys. Chem. Chem. Phys.* **2017**, *19*, 6105–6112.

[119] F. A. Fernandez-Lima, D. A. Kaplan, M. A. Park, *Rev. Sci. Instrum.* **2011**, *82*, 126106.

[120] T.-Z. Xie, K. J. Endres, Z. Guo, J. M. Ludlow, C. N. Moorefield, M. J. Saunders, C. Wesdemiotis, G. R. Newkome, *J. Am. Chem. Soc.* **2016**, *138*, 12344–12347.

[121] W. Cullen, C. A. Hunter, M. D. Ward, *Inorg. Chem.* **2015**, *54*, 2626–2637.

[122] T. Xie, K. Guo, Z. Guo, W. Gao, L. Wojtas, G. Ning, M. Huang, X. Lu, J. Li, S. Liao, Y. Chen, C. N. Moorefield, M. J. Saunders, S. Z. D. Cheng, C. Wesdemiotis, G. R. Newkome, *Angew. Chem.* **2015**, *127*, 9356–9361.

[123] L. Xu, D. Zhang, T. K. Ronson, J. R. Nitschke, *Angew. Chem. Int. Ed.* **2020**, *59*, 7435–7438.

[124] S. M. Jansze, K. Severin, *J. Am. Chem. Soc.* **2019**, *141*, 815–819.

[125] K. Matsumoto, S. Kusaba, Y. Tanaka, Y. Sei, M. Akita, K. Aritani, M. Haga, M. Yoshizawa, *Angew. Chem. Int. Ed.* **2019**, *58*, 8463–8467.

[126] B. Kilbas, S. Mirtschin, R. Scopelliti, K. Severin, *Chem. Sci.* **2011**, *3*, 701–704.

[127] F. J. Rizzuto, J. P. Carpenter, J. R. Nitschke, *J. Am. Chem. Soc.* **2019**, *141*, 9087–9095.

[128] S. Wang, T. Sawada, K. Ohara, K. Yamaguchi, M. Fujita, *Angew. Chem. Int. Ed.* **2016**, *55*, 2063–2066.

[129] T. K. Ronson, J. P. Carpenter, J. R. Nitschke, *Chem.* **2022**, *8*, 557–568.

[130] T. Tsutsui, L. Catti, K. Yoza, M. Yoshizawa, *Chem. Sci.* **2020**, *11*, 8145-8150.

[131] D.-N. Yan, L.-X. Cai, P.-M. Cheng, S.-J. Hu, L.-P. Zhou, Q.-F. Sun, *J. Am. Chem. Soc.* **2021**, *143*, 16087–16094.

[132] S. Freye, J. Hey, A. Torras-Galán, D. Stalke, R. Herbst-Irmer, M. John, G. H. Clever, *Angew. Chem. Int. Ed.* **2012**, *51*, 2191–2194.

[133] R. Zhu, I. Regeni, J. J. Holstein, B. Dittrich, M. Simon, S. Prévost, M. Gradzielski, G. H. Clever, *Angew. Chem. Int. Ed.* **2018**, *57*, 13652–13656.

[134] L. Yang, X. Jing, B. An, C. He, Y. Yang, C. Duan, *Chem. Sci.* **2017**, *9*, 1050–1057.

[135] W. M. Bloch, J. J. Holstein, B. Dittrich, W. Hiller, G. H. Clever, *Angew. Chem. Int. Ed.* **2018**, *57*, 5534–5538.

[136] M. Frank, M. D. Johnstone, G. H. Clever, *Chem. Eur. J.* **2016**, *22*, 14104–14125.

[137] R. Sekiya, M. Fukuda, R. Kuroda, *J. Am. Chem. Soc.* **2012**, *134*, 10987–10997.

[138] M. Scherer, D. L. Caulder, D. W. Johnson, K. N. Raymond, *Angew. Chem. Int. Ed.* **1999**, *38*, 1587–1592.

[139] D. Zhang, T. K. Ronson, L. Xu, J. R. Nitschke, *J. Am. Chem. Soc.* **2020**, *142*, 9152–9157.

[140] A. M. Castilla, N. Ousaka, R. A. Bilbeisi, E. Valeri, T. K. Ronson, J. R. Nitschke, *J. Am. Chem. Soc.* **2013**, *135*, 17999–18006.

[141] L.-J. Wang, X. Li, S. Bai, Y.-Y. Wang, Y.-F. Han, *J. Am. Chem. Soc.* **2020**, *142*, 2524–2531.

[142] X.-Z. Li, L.-P. Zhou, S.-J. Hu, L.-X. Cai, X.-Q. Guo, Z. Wang, Q.-F. Sun, *Chem. Commun.* **2020**, *56*, 4416–4419.

[143] S. Bandi, D. K. Chand, *Chem. Eur. J.* **2016**, *22*, 10330–10335.

[144] D. Samanta, P. S. Mukherjee, *Chem. Eur. J.* **2014**, *20*, 12483–12492.

[145] I. A. Riddell, T. K. Ronson, J. K. Clegg, C. S. Wood, R. A. Bilbeisi, J. R. Nitschke, *J. Am. Chem. Soc.* **2014**, *136*, 9491–9498.

[146] D. Zhang, Q. Gan, A. J. Plajer, R. Lavendomme, T. K. Ronson, Z. Lu, J. D. Jensen, B. W. Laursen, J. R. Nitschke, *J. Am. Chem. Soc.* **2022**, *144*, 1106–1112.

[147] F. J. Rizzuto, P. Pröhm, A. J. Plajer, J. L. Greenfield, J. R. Nitschke, *J. Am. Chem. Soc.* **2019**, *141*, 1707–1715.

[148] D. A. Roberts, B. S. Pilgrim, G. Sirvinskaite, T. K. Ronson, J. R. Nitschke, *J. Am. Chem. Soc.* **2018**, *140*, 9616–9623.

[149] S. Saha, Y.-T. Chen, S. Ganta, M. Gilles, B. Holzapfel, P. Lill, H. Rehage, C. Gatsogiannis, G. H. Clever, *Chem. Eur. J.* **2022**, e202103406.

[150] I. Regeni, B. Chen, M. Frank, A. Baksi, J. J. Holstein, G. H. Clever, *Angew. Chem.* **2020**, *133*, 5736-5741.

[151] A. Schmidt, M. Hollering, J. Han, A. Casini, F. E. Kühn, *Dalton Trans.* **2016**, *45*, 12297–12300.

[152] M. Käseborn, J. J. Holstein, G. H. Clever, A. Lützen, *Angew. Chem. Int. Ed.* **2018**, *57*, 12171–12175.

[153] V. Helms, *Principles of Computational Cell Biology*, WILEY-VCH, Weinheim, **2008**.

[154] P.-P. Jia, Y.-X. Hu, Z.-Y. Peng, B. Song, Z.-Y. Zeng, Q.-H. Ling, X. Zhao, L. Xu, H.-B. Yang, *Inorg. Chem.* **2022**, *62*, 1950–1957.

[155] Z. Zhang, Z. Zhao, L. Wu, S. Lu, S. Ling, G. Li, L. Xu, L. Ma, Y. Hou, X. Wang, X. Li, G. He, K. Wang, B. Zou, M. Zhang, *J. Am. Chem. Soc.* **2020**, *142*, 2592–2600.

[156] C. He, D. Li, X. Liu, L. Yang, H. Li, G. Guo, X. Li, *Chem. Sci.* **2023**, *14*, 2237-2244.

[157] S. Prusty, K. Yazaki, M. Yoshizawa, D. K. Chand, *Chem. Eur. J.* **2017**, *23*, 12456–12461.

[158] P. Howlader, P. Das, E. Zangrando, P. S. Mukherjee, *J. Am. Chem. Soc.* **2016**, *138*, 1668–1676.

[159] D. Fujita, K. Suzuki, S. Sato, M. Yagi-Utsumi, Y. Yamaguchi, N. Mizuno, T. Kumasaka, M. Takata, M. Noda, S. Uchiyama, K. Kato, M. Fujita, *Nat. Commun.* **2012**, *3*, 1093.

[160] H. Lee, T. H. Noh, O. Jung, *Angew. Chem. Int. Ed.* **2016**, *55*, 1005–1009.

[161] J. A. Findlay, K. M. Patil, M. G. Gardiner, H. I. MacDermott-Opeskin, M. L. O'Mara, P. E. Kruger, D. Preston, *Chem. Asian J.* **2022**, *17*, e202200093.

[162] M. Tominaga, K. Suzuki, M. Kawano, T. Kusukawa, T. Ozeki, S. Sakamoto, K. Yamaguchi, M. Fujita, *Angew. Chem. Int. Ed.* **2004**, *43*, 5621–5625.

[163] D. Fujita, H. Yokoyama, Y. Ueda, S. Sato, M. Fujita, *Angew Chem.* **2015**, *127*, 157–160.

[164] I. Drienovská, C. Mayer, C. Dulson, G. Roelfes, *Nat. Chem.* **2018**, *10*, 946–952.

[165] D. Larsen, M. Pittelkow, S. Karmakar, E. T. Kool, *Org. Lett.* **2015**, *17*, 274–277.

[166] R. Rudolf, Creating a Modifiable Heteroleptic Pd(II) Metallo-Cage System, Dissertation, TU Dortmund University, **2021**.

[167] K. Roy, P. L. A. Popelier, *J. Phys. Org. Chem.* **2009**, *22*, 186–196.

[168] F. G. Bordwell, R. J. McCallum, W. N. Olmstead, *J. Org. Chem.* **1984**, *49*, 1424–1427.

[169] D. Chu, W. Gong, H. Jiang, X. Tang, Y. Cui, Y. Liu, *CCS Chem.* **2022**, *4*, 1180–1189.

[170] L. R. Holloway, P. M. Bogie, Y. Lyon, C. Ngai, T. F. Miller, R. R. Julian, R. J. Hooley, *J. Am. Chem. Soc.* **2018**, *140*, 8078–8081.

[171] F. Jiang, N. Wang, Z. Du, J. Wang, Z. Lan, R. Yang, *Chem. Asian J.* **2012**, *7*, 2230–2234.

[172] K. Suzuki, M. Kawano, S. Sato, M. Fujita, *J. Am. Chem. Soc.* **2007**, *129*, 10652–10653.

[173] J. W. Steed, J. L. Atwood, *Supramolecular Chemistry*, John Wiley & Sons Ltd, Chichester, **2022**.

[174] S. T. Jung, J. Podlech, *J. Org. Chem.* **2020**, *85*, 10951–10957.

[175] G. Schenck, K. Baj, J. A. Iggo, M. Wallace, *Anal. Chem.* **2022**, *94*, 8115–8119.

[176] E. L. Jones, A. J. Mlotkowski, S. P. Hebert, H. B. Schlegel, C. S. Chow, *J. Phys. Chem.* **2022**, *126*, 1518–1529.

[177] R. Stewart, M. G. Harris, *Can. J. Chem.* **1977**, *55*, 3807–3814.

[178] P. Mal, D. Schultz, K. Beyeh, K. Rissanen, J. R. Nitschke, *Angew. Chem.* **2008**, *120*, 8421–8425.

[179] V. Sivalingam, S. Krishnaswamy, D. K. Chand, *Chem. Eur. J.* **2023**, *29*, e202300891.

[180] S. Grimme, C. Bannwarth, P. Shushkov, *J. Chem. Theory Comput.* **2017**, *13*, 1989–2009.

[181] S. Sato, Y. Ishido, M. Fujita, *J. Am. Chem. Soc.* **2009**, *131*, 6064–6065.

[182] M. Tominaga, K. Suzuki, T. Murase, M. Fujita, *J. Am. Chem. Soc.* **2005**, *127*, 11950–11951.

[183] C. R. Jones, C. P. Butts, J. N. Harvey, *J. Org. Chem.* **2011**, *7*, 145–150.

[184] C. P. Butts, C. R. Jones, E. C. Towers, J. L. Flynn, L. Appleby, N. J. Barron, *Org. Biomol. Chem.* **2010**, *9*, 177–184.

[185] R. A. Bell, J. K. Saunders, *Can. J. Chem.* **1970**, *48*, 1114–1122.

[186] A. Jerschow, N. Müller, *J. Magn. Reson.* **1997**, *125*, 372–375.

[187] J. E. Tanner, E. O. Stejskal, *J. Chem. Phys.* **1968**, *49*, 1768–1777.

[188] A. Einstein, *Ann. Phys.* **1905**, *322*, 549–560.